NUCLEOSYNTHESIS AND ABUNDANCES OF ELEMENTS WITH RELEVANT OPTICAL LINES IN MAIN SEQUENCE DWARFS

2023, v.2

Institut für Physik und Astronomie, Universität Potsdam
Astronomical Institute of the Czech Academy of Sciences
Dpto. de Química "Profesor José Carlos Vílchez Martín", Universidad de Huelva

Francisco Molina
Supervisor: Dr Joris Vos

Contents

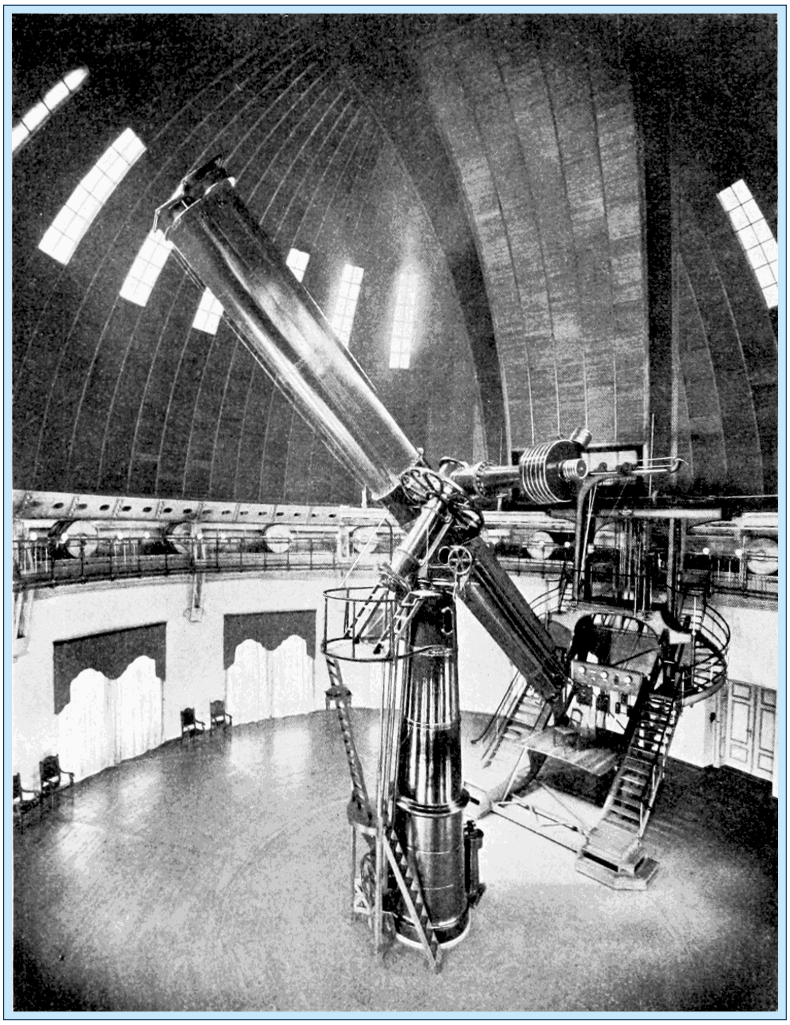

Refracting Telescope at Potsdam, 1901

Compiled using LaTeX

Note

Please, do not take this document as an original piece in any sense. It isn't. It is the work of a beginner for beginners, including all kind of defects and faults that can be expected.

When one is about to initiate a new job, skill or learning from scratch, maybe the initiation is the tough moment: What is all about, where to look for new information, what is important, what is not, what piece of information links with which one, how to structure the information within a general context...

Once a basic and very imperfect framework has been established the learning gets a bit easier and the work is about to start producing a real knowledge or basic understanding on the matter: New readings and ideas are faced against the preliminary framework and one can see how they fit or not, how much of the initial simple and schematic ideas were wrongly understood or not. New readings increase, in an accelerated pace, real knowledge by confronting against first notions, even utterly wrong ones.

An initially wrong, imperfect, incomplete framework is at least a first foundation on which to begin building real knowledge.

The only purpose of this document is to provide a firstly schematic beginner's insight into the matter of the stellar nucleosynthesis. Hence, do not look for any glimpse of originality in this work, it is just the imperfect try to ensemble different basic ideas from original works and sources about the matter, in a particular selection.

Sometimes literal paragraphs have been used when have been intended the basic information was nicely presented and understandable for a beginner. Others, the information has been summarized using different sources, from a beginner understanding point of view.

It is hoped to help the reader building that preliminary and schematic, even partially wrong by author understanding, framework on which to build real knowledge by their followings years of reading, work and expertise.

If it just is used as a first readings incomplete guide, by far the purpose of this document is accomplished.

Prologue

Only during the first minutes of the big bang were the conditions for nuclear reactions to take place correct. These reactions yielded the light primordial nuclei of elements that would later form the first generation of stars.

They are reactions well known by nuclear physics and calculations have been made for ^{1}H, ^{2}H, ^{3}He, ^{4}He, ^{6}Li and ^{7}Li plus others unstable isotopes. And the overall predictions match astonishingly with the observed abundances in our current universe (Krauss 2012).

For instance, the calculation predicts around 24-25% (w/w) of primordial He (Peimbert et al. 2016; Aver et al. 2015; Izotov et al. 2014). The sun shows an abundance of 28% in He I plus a 2% in metals. Similar abundances are found in stars with sun-like old-age and metallicity.

The predicted primordial and the current abundances are very alike, but where originate the differences?.

Taking aside local conditions, the sun is a relatively young star (5 Gyr old) in an older universe (13-14 Gyr), arisen from gaseous clouds and dust that gathered nuclear burning products of precedent generation stars (populations II and III). The universe and stellar evolution have enriched the interstellar medium in helium and heavier elements giving place to new generations of stars with increasingly higher metallicity contain.

This work is intended as a structured summary, more or less fortunate, of basic ideas from studies about the nucleosynthesis sources, certainties and uncertainties, about that 2% in metals, from which our current universe, chemistry, life and ourselves, are made up.

Chapter 1

Introduction: Nucleosynthesis Sources

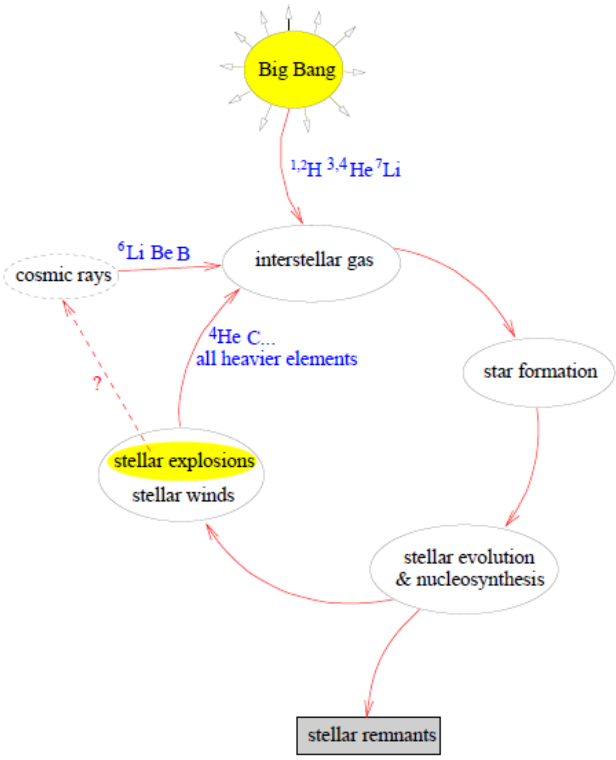

Figure 1.1: *Schematic depiction of cosmic chemical evolution and recycling of the elements. Credit* https://astro.uni-bonn.de/~nlanger/siu_web/nucscript/Nucleo.pdf.

1.1. From hydrogen to helium: main sequence stars

The stars spend most of their lifetime in the main sequence phase. Depending on their mass they will occupy one or another point of the diagonal relation between luminosity/mass/radius and surface temperature in the Hertzsprung-Russell diagram (see Fig. 1.2).

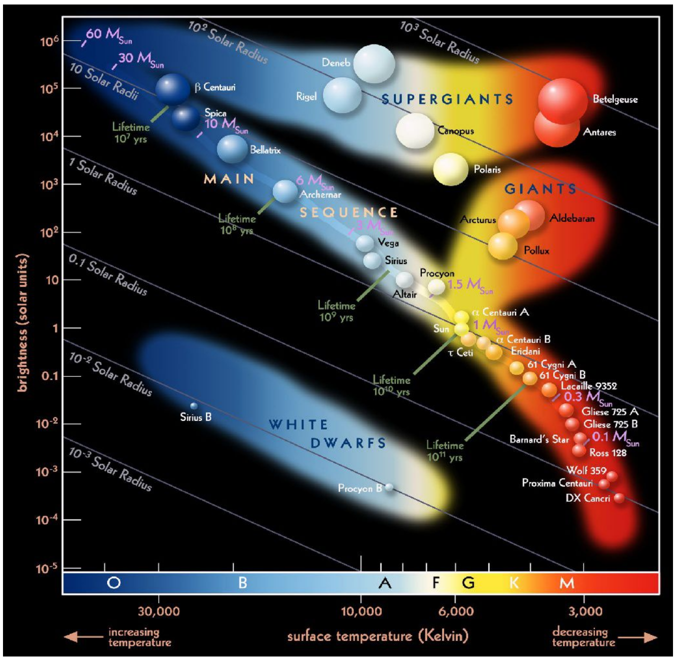

Figure 1.2: *Hertzprung-Russel diagram.*

What all stars from this diagonal have in common is that they are in the longer and more stable phase of their lifetime, the burning hydrogen in the core to produce helium. Once the hydrogen exhausts in the core, the star will evolve off the main-sequence stage leading to new ones that dramatically will change star physical features, producing a nucleosynthesis and a stellar death very different depending on the initial star mass.

1.1.1 Proton-proton chain reactions

This mechanism involves stars with mass < 1.3 $M_\odot$ and temperatures in the core of $4{\cdot}10^6$ K. Basically, successive fusion of protons lead to the ^{4}He formation. The PPI chain is by far the main mechanism of helium production but others side reactions take place, PPII and III, involving nuclei as ^{7}Be, ^{7}Li and unstable ^{8}B that eventually will equally lead to the ^{4}He nucleosynthesis, as next described:

Proton-Proton (PP)

Initial reactions...

$^1_1H +^1_1 H \rightarrow^2_1 H + e^+ + \nu_e$

$^2_1H +^1_1 H \rightarrow^3_2 He + \gamma$

...leading to PPI chain (69%)...

$^3_2He +^3_2 He \rightarrow^4_2 He + 2\,^1_1H$

...or to the precursor reaction of PPII and PPIII chains (31%)...

$^3_2He +^4_2 He \rightarrow^7_4 Be + \gamma$

...mostly producing PPII chain (99.7%)...

$^7_4Be + e^- \rightarrow^7_3 Li + \nu_e$

$^7_3Li +^1_1 H \rightarrow 2\,^4_2He$

...or minoritary PPIII chain (0.3%)

$^7_4Be +^1_1 H \rightarrow^8_5 B + \gamma$

$^8_5B \rightarrow^8_4 Be + e^+ + \nu_e$

$^8_4Be \rightarrow 2\,^4_2He$

1.1.2 CNO cycle

For stars with mass > 1.3 $M_\odot$ and temperatures in the core upper than $17{\cdot}10^6$ K, an additional mechanism is triggered to produce helium. This mechanism involves the previous presence of carbon, nitrogen and oxygen nuclei (^{12}C and ^{13}C; ^{13}N, ^{14}N and ^{15}N and ^{15}O) that play a role as catalysts. Hence, this mechanism was not available for the primordial first generations of massive stars (population III), only made up of hydrogen and helium. It was activated by the universe evolution and the progressive enrichment of the interstellar medium with metals later gathered by new stellar generations.

Though this mechanism was proposed in 1938 and long-held considered as main source of helium production in massive stars, it has not been validated until right now by direct observations (Agostini et al. 2020).

1.2. Evolving off the main sequence

Once the core exhausts its hydrogen, the star continues H-burning in shell surrounding the He core, expanding and cooling the outer layers. Stars are moving off the main sequence phase, starting the last and accelerated stages of their lifetime whose physical characteristics and final fate will be determined by their masses. As they will be, the most interesting reactions of nucleosynthesis that take place at the very end of the star's lifetime, lasting hardly a few milion years.

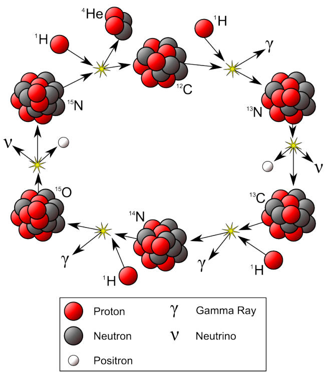

Figure 1.3: *CNO cycle, the CNO isotopes working as catalyst in the helium production from hydrogen.*

Very different will be the element yields obtained and used nucleosynthesis mechanisms from stars with lower masses than 8 $M_\odot$ transiting throughout the AGB phase than the ones derived from the previous burning phases, or than the later nucleosynthesis of a supernova (SNeII) originated by core collapse in massive stars (> 8 $M_\odot$). Or indeed, very different to the nucleosynthesis produced in a thermonuclear nova by binary interactions (SNeIa) between a compact object as a dying white dwarf and an evolving star or a second white dwarf.

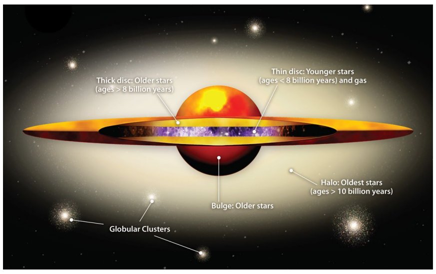

Figure 1.4: *Milky Way structure. Credit* `https://www.universetoday.com/83315/`.

All the mechanisms interact and have evolved as the galaxy evolution did, deriving the current galactic chemical abundances that are also determined by surrounding local medium and star location, either in the thin or thick disk, either in the halo or the bulge of the galaxy (see Fig. 1.4).

It is worth to give a basic look into the main production mechanisms that have enriched the galaxy and universe in metals. They will be described in function of the star mass, starting with the low mass stars.

1.3. Low and intermediate mass stars (< 8$M_\odot$)

In the Fig. 1.6 is shown the life of a sun-like star. For lower or intermediate mass stars is similar.

Once the star is evolving off the main sequence by the exhaustion of hydrogen in core, the hydrogen fusion transits to the burning-shell around the formed helium core. The star

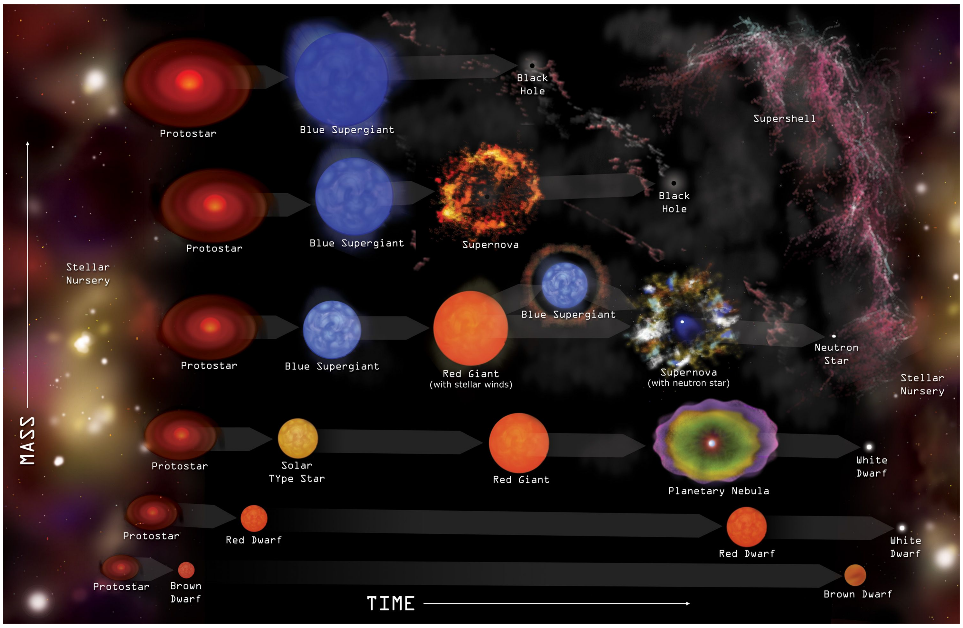

Figure 1.5: *Star life and death in function of mass.*

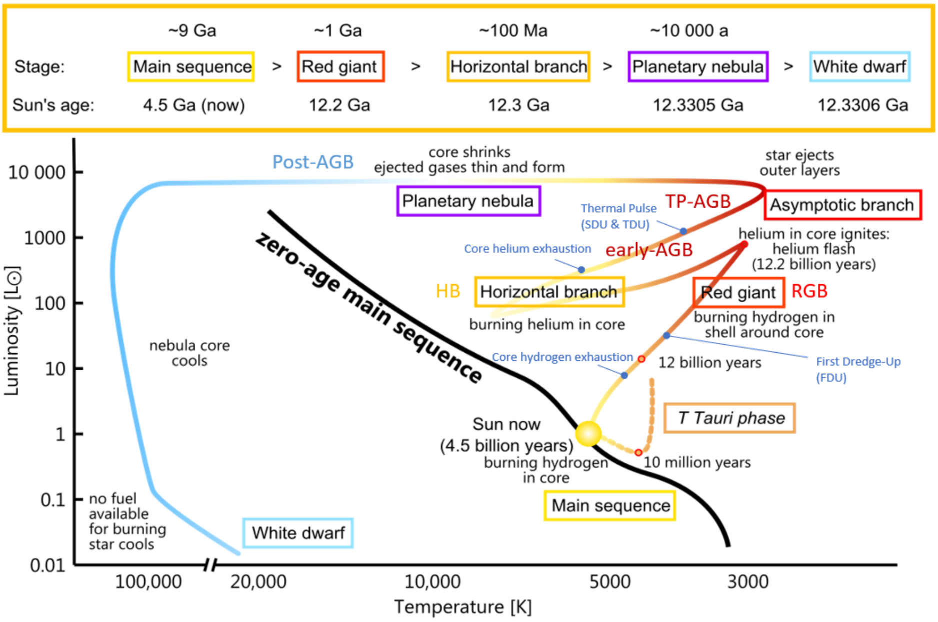

Figure 1.6: *Lifetime path of a sun-like star on the Hertzsprung-Russel diagram.*

expands outer layers, cooling them, but the inner layers contract, increasing the temperature and the hydrogen burning rate in shell around the core. The star increases its luminosity, ascending the Red Giant Branch (RGB) phase.

Physical changes take place, the First Dredge-Up (FDU) process (Karakas & Lattanzio 2014, see Fig. 1.7) mixes layers and jointly with later extra-mixing episodes, they vary the chemical composition on the surface by the mixing of newly fresh formed material in deeper layers closer to the core. The nitrogen abundance increases while the carbon decreases (see Fig. 1.8).

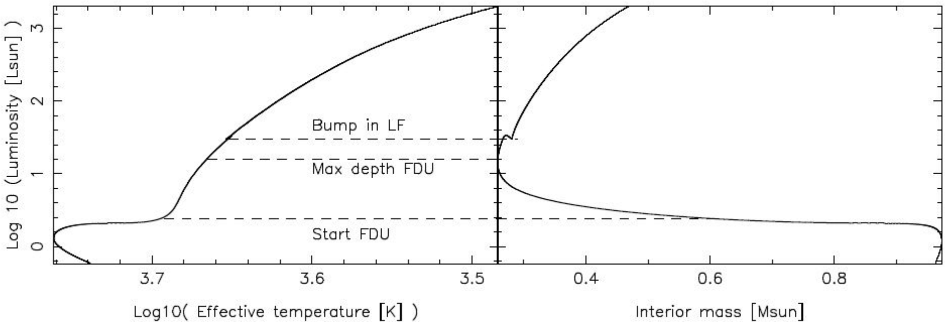

Figure 1.7: *First dredge-up in the 1 $M_{\odot}$, Z = 0.02 model. The left panel shows the HR diagram and the right panel shows the luminosity as a function of the mass position of the inner edge of the convective envelope. It is clearly observed that the envelope begins to deepen just as the star leaves the main sequence, and reaches its deepest extent on the RGB, marking the end of FDU. Further evolution sees the star reverse its evolution and descend the RGB briefly before resuming the climb. This corresponds to the observed bump in the luminosity function of stellar clusters. From Karakas & Lattanzio (2014).*

Once the temperature in core increases enough, the helium ignites, entering star into the Horizontal Branch new phase that leads to the stable helium burning in core. Later, hardly 100 Myr, the helium also exhausts in the core and helium burning transits to the shell around a degenerate C/O core. An outer hydrogen burning shell surrounds it, forming the typical structure of an Asymptotic Giant Branch star (AGB) as shown in Fig. 1.13.

The AGB is the most interesting phase of lower or intermediate mass stars from the nucleosynthesis point of view. The main mechanism of helium burning is called the triple-α reaction (100-300·10^6 K) that produces ^{12}C and ^{16}O as a byproduct (see Fig. 1.9).

^{14}N (in addition to carbon and oxygen) is efficiently produced from the CN cycle by the hot bottom burning mechanism (see Sect. 1.3 and Fig. 1.20). The AGBs are the main nucleosynthesis site for the production of nitrogen and important of oxygen, although this last element is mostly produced in the massive SNeII supernovae. Likewise, the AGBs were thought to be the main site for production of C, although nowadays this is an open issue with increasing number of studies arguing the majority contribution from massive stars (see Sect. 2.2).

The production of these light elements will be key for understanding the nucleosynthesis of the heavier elements produced during the most unstable phases of the AGB. The instability triggers thermal pulses and convective streams produce the mixing through layers and

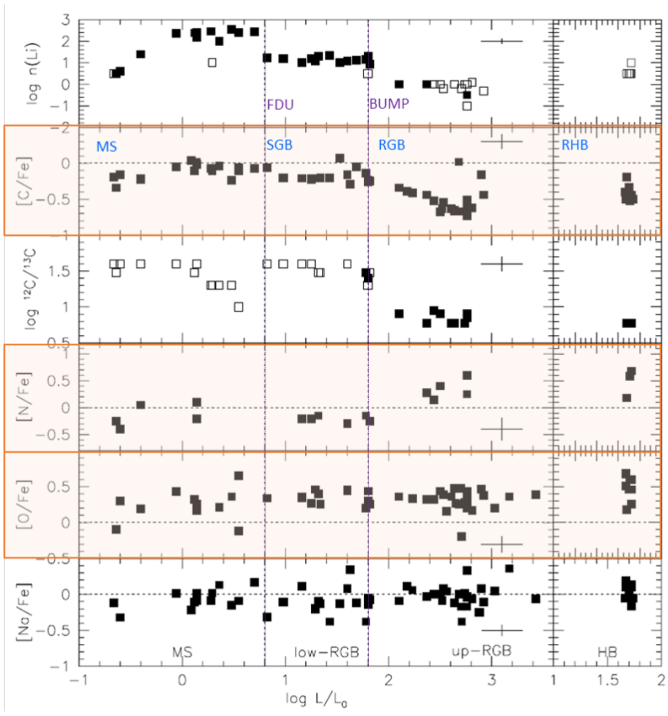

Figure 1.8: *Chemical changes on the photospheric layer from Main Sequence to Horizontal Branch phase. Adapted from Gratton et al. (2000).*

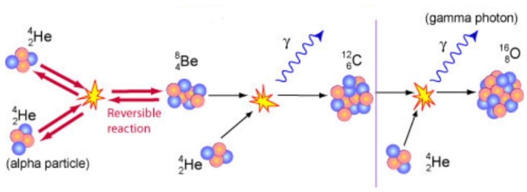

Figure 1.9: *Triple alpha fusion process.*

material (Second and Third Dredge-Up, SDU & TDU), giving place to the most interesting reactions of nucleosynthesis by neutron capture, the main-s process. The thermal pulses enrich the surface on heavy metals but too in ^{12}C and ^{16}O from the deeper layers nearby the core giving place to carbon (C/O>1, C-type) or oxygen-rich stars (C/O<1, M-type).

Finally, the AGB will lost the 50-70% of its mass, forming circumstellar disks and later planetary nebula, enriching the medium in chemicals, processed by UV radiation. The star composition determines the type of condensates forming in the circumstellar envelope (see Fig. 1.10). Oxides and silicates form in O-rich AGB stars (M, S), while C-rich stars are parents to SiC and graphite dust (Hedrosa et al. 2013).

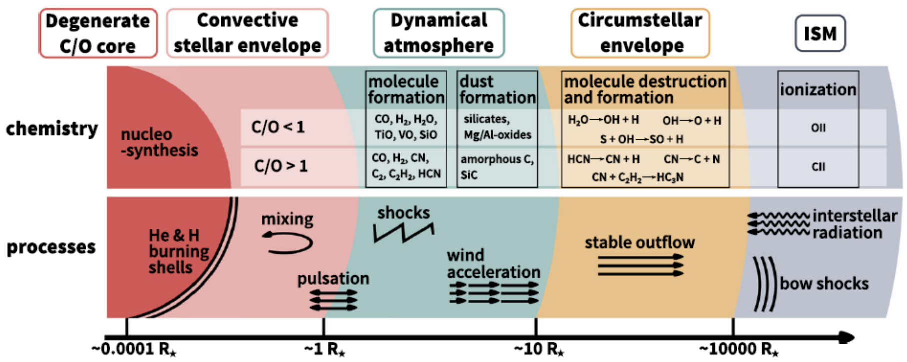

Figure 1.10: *Schematic chemical structure of the circumstellar environment of an AGB star enriching the medium with chemicals by mass loss winds. From Höfner & Olofsson (2018).*

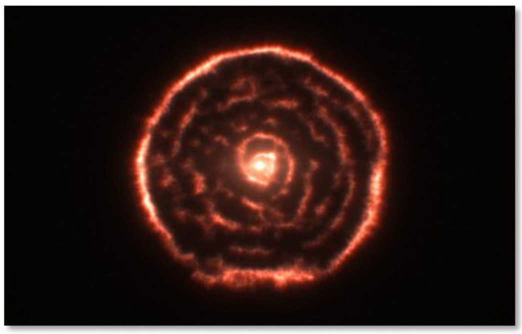

Figure 1.11: *AGB R-Sculptoris losing outer layers. ALMA radio-observation by ESO. Credit* `https://www.eso.org/public/spain/news/eso1239/`.

Figure 1.12: *NGC6543, planetary nebula. Formed during TP- and Post-AGB stages, from the expelled outer layers of the star, that leads to the star death as white dwarf. ACS Camera, Hubble, NASA. Credit* `https://www.esa.int/Science_Exploration/Space_Science/Cat_s_Eye_Nebula_NGC_65432`.

1.3.1 Nucleosynthesis AGB < $4M_{\odot}$: Main s-process

Nuclear fusions to produce heavier elements than iron are not favoured energetically. Hence, the nucleosynthesis of heavy metals only develops in processes involving neutron capture.

The flux of neutrons and its origin, will classify the neutron capture as a slow-process (s-process) or rapid process (r-process). The firsts are produced in the last stages of stars of low (main s-process) or intermediate mass (weak s-process) in AGBs, or massive stars > 8 $M_{\odot}$ (weak s-process). The r-process will occur in massive stars by core collapse (SNeII) or thermonuclear (SNeIa) supernovae where the flux of neutrons available are much higher due to the explosion. Depending on the neutron source the nucleosynthesis and abundances of some heavy elements are favoured over the others.

Main s-process is the responsible of contributions in abundance of isotopes $90 \leq A \leq 204$ that is to say, from Sr to heavier elements like Pb, the termination point of the reaction, and occurs in AGBs of low or intermediate mass progenitors, up to $4M_{\odot}$, during thermal inter-pulse periods. The neutron source comes from the formation of a ^{13}C pocket when the convective envelope rich in protons engulfs into the intershell layer, rich in ^{12}C (by the triple-α reaction from helium) and reacts (see Fig. 1.13).

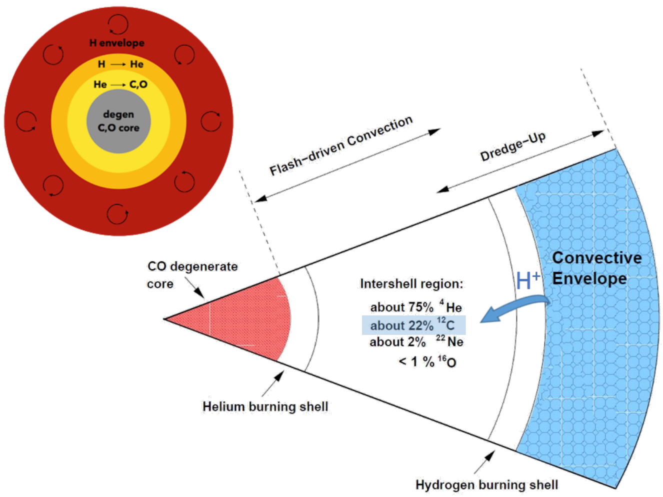

Figure 1.13: *Structure of an AGB star. The thermal pulses produces the engulfment of the convective envelope rich in protons (H^+) into the intershell layer, enriched in ^{12}C to produce ^{13}C. Adapted from Karakas et al. (2002).*

The formed ^{13}C later will fusion with helium to yield ^{16}O liberating neutrons that are the source for the neutron capture by surrounding elements as iron (Fe) producing heavier elements that finally will be lifted and mixed up on the star surface by Dredge Up episode (see Fig. 1.14). The very hot base of the Thermal Pulse just above the He burning shell also allows for the weak s-process mechanism to take place. However, this process contributes little to the final abundances.

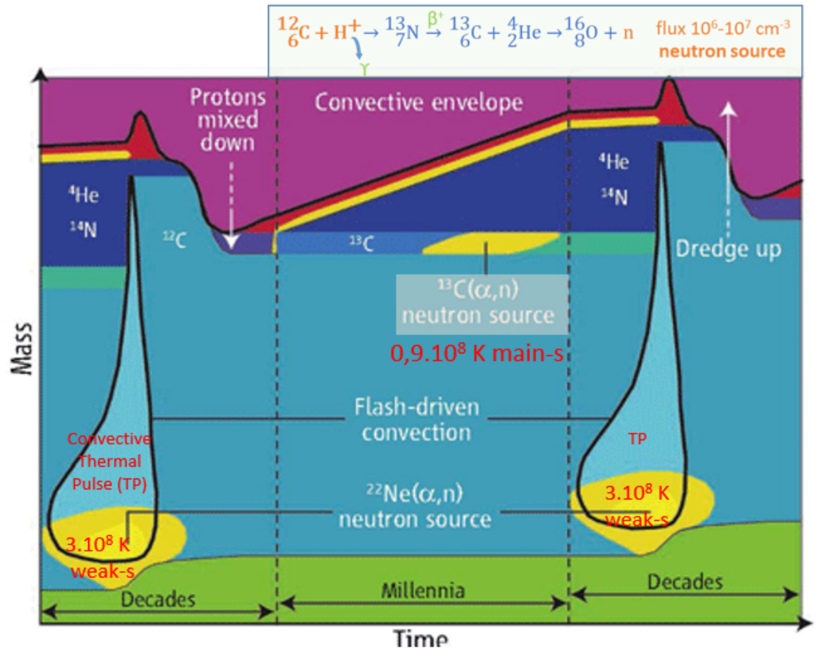

Figure 1.14: *The ${}^{13}C$ pocket formation by engulfment of convective envelope due to thermal pulses. The pocket becomes the neutron source of the main s-process nucleosynthesis by reaction with helium to produce oxygen at ca 100·10^6 K. Adapted from El Eid (2015).*

The production in main s-process elements are favoured for some elements due to the especial stability of their nuclei. In the Fig. 1.15 is shown the relative abundances (against Si) in the Solar System (based on the Sun and meteorites abundances studies) of heavy metals due to the main s-process in function of the mass number. Three peaks of higher abundances are observed which matches with elements showing "magic" number of neutrons (50, 82, 126) in their nuclei that contribute to a especial stability to the isotopes.

The development of the nuclear shell model at the late forties found experimental evidences of shells closure and especial stability at certain number of neutrons or protons (Mayer 1948, 1949), based on the spin-orbit coupling, using the Pauli exclusion principle, in an analogous way as applied to electronic atomic arrangement but for describing the atomic nucleus. And as it happens in the quantum electronic structure, the filling of nuclear quantum energetic shells, determined by certain number of neutrons and protons, the "magic" numbers, confers an especial stability to the nuclei (isotopes) over incomplete shell configurations.

These three peaks of greater stability involve elements as Sr, Y and Zr for the first; Ba,

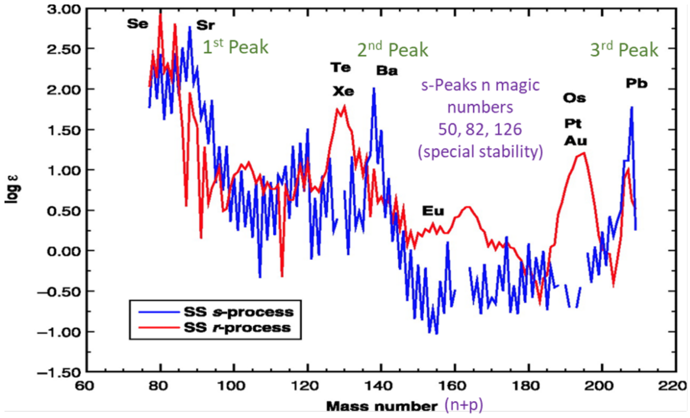

Figure 1.15: *Three main s-process peaks (blue) in the isotopes abundances of the solar systems due to the greater stability of their nuclei. Adapted from Sneden & Cowan (2003).*

La, Ce, Pr, Nd for the second; and Pb for the third.

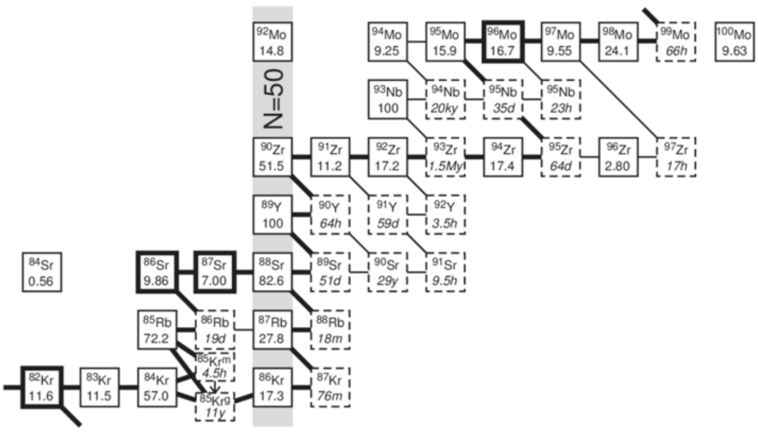

Figure 1.16: *Neutron capture around the first peak of the main s-process. Isotopes with N=50 are more stable, increasing their abundances. From Lugaro et al. (2003).*

However, it must be clear that the s-process distribution in solar system is the average result of previous generations AGB stars contributions in the galaxy (Gallino et al. 2006). Hence the production for a specific AGB will depend on factors as the ^{13}C pocket size and efficiency (neutron flux) and especially on the metallicity.

The main s-process is a linear process that involves neutron capture producing isotopes of one element with increasing mass number. When an unstable isotope is reached, a β^{-} disintegration advances the neutron capture to a next heavier element (see Fig. 1.17).

Hence, n-capture in s-process synthesis occurs near these nuclei close to the "valley of β-stability" (see Fig. 1.32). The sides of the valley correspond to increasing instability reached when neutron is captured by stable nuclei, producing unstable nuclei whose β^- disintegration will advance the reaction to a new heavier element and more stable isotope.

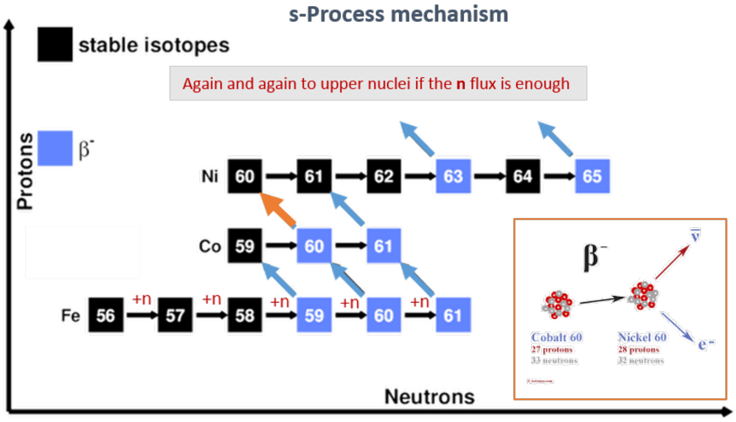

Figure 1.17: *Neutron capture mechanism from ^{56}Fe, neutron capture + β^- disintegration push the main s-process to higher mass number isotopes and new elements. Adapted from Reifarth et al. (2016).*

But the three peaks become bottlenecks for the neutron capture advance to heavier isotopes. To overcome the greater stability, is needed the neutron flux being high enough and hold along the time. And the metallicity (Fe abundance) becomes a very important factor.

The production of main s-process elements has increased with the evolution of the universe due to the increasing number of low or intermediate mass star, and the necessary temporal delay for evolving off the Main-Sequence to the AGB phase.

However, the production of the heavier s-process elements (as Pb) is favoured to poorer metallicities. The reason can be found in the greater neutrons per Fe seed, what pushes ahead the reaction to heavier elements, reaching the third peak, to Pb (Travaglio et al. 2004). Another way of seeing it, if Fe is in excess, it will monopolize the neutron capture for forming continuously lighter elements nearby Fe and will not leave enough neutron flux for heavier elements to overcome the greater stability of the first peak elements (or second). For a given ^{13}C pocket size, decreasing the metallicity, the s-process progressively feeds the first s-peak elements Sr, Y, Zr (light s, ls) then the second s-peak at Ba, La, Ce, Pr, Nd (heavy s, hs) and eventually the third s-peak at the termination point of the s-process, Pb (Gallino et al. 2006). How far is displaced the production to Pb, the second or only to the first peak elements will depend on the metallicity and of course, the initial flux of neutrons (^{13}C pocket size). Hence, the overproduction of Pb relative to Ba in the primordial stars (Population III) is expected, contrary what occurs in more metal-rich AGB stars (Karlsson et al. 2013). The Fig. 1.18 shows the production of s-process three peaks elements in function of the metallicity.

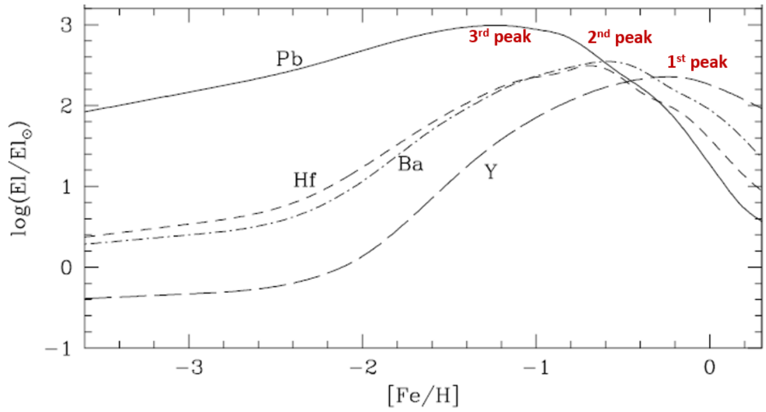

Figure 1.18: *Production of s-process elements in function of metallicity for a 1.5$M_\odot$ AGB (Travaglio et al. 2004). To lower metallicity, the neutron capture is seeded of an excess of neutrons per Fe for displacing the production to the termination point, Pb.*

1.3.2 Nucleosynthesis AGB > 4$M_\odot$: Hot Bottom Burning

This is an alternative nucleosynthesis site and mechanism in AGBs with masses higher than 4$M_\odot$ that provide higher temperatures in the bottom of the hydrogen burning shell (> $100{\cdot}10^6$ K). New reactions take place when the convective envelope reaches it after a thermal pulse, producing ^{7}Li or ^{14}N, later lifted and mixed up on the surface by the Dredge-Up episode, TDU (see Fig. 1.19).

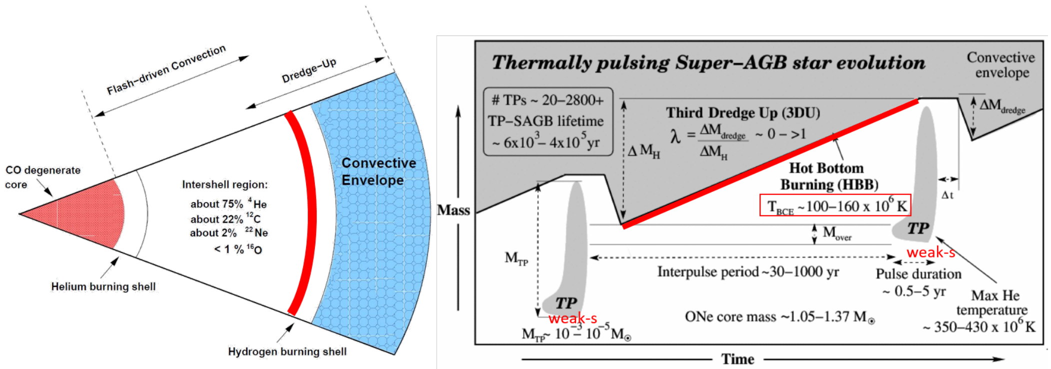

Figure 1.19: *Site of the hot bottom burning (in red). Super-AGB structure adapted from Karakas et al. (2002) and schematic Kippenhahn diagram of two consecutive thermal pulses adapted from Doherty et al. (2017).*

This mechanism inhibits in part the main s-process and prevents the ^{12}C enrichment of the surface, burnt in the hot temperature-induced CN cycling (enriching the star in ^{14}N, see Fig. 1.20 and Sect. 2.3). Unlike AGBs of low mass progenitors, the HBB mechanism produces O-Li rich stars (C/O<1). This composition will determine the type of condensates forming in the next circumstellar envelope, mostly oxides and silicates (see Fig. 1.10).

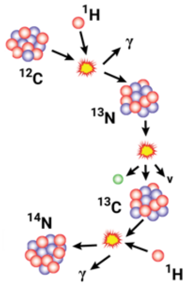

Figure 1.20: *^{14}N production from ^{12}C through CN-cycling induced by the hot temperature at the convective base and the HBB process.*

1.4. Massive stars (> $8M_\odot$)

The helium burning is the last stage in the lifetime of a low or intermediate mass star. The temperatures provided by the gravitational pressure of the outer layers are not high enough to ignite carbon and heavier elements. The star will die leaving a compact C and O core, while its outer layers are ejected forming planetary nebula (see Fig. 1.5, 1.6 and 1.12).

However, the pressure in massive stars is much higher, providing increasingly higher temperatures in the core. Once every fuel is exhausted, the radiation pressure decreases and the core contracts, allowing the successive burning of carbon, neon, oxygen and silicon, produced at the previous burning stage. The successive burning stages trigger a rich nucleosynthesis and reactions by α particle capture, being the main source of the galaxy enrichment in α-elements as O, Mg, Si, S, Ca and Ti.

On the other hand, like in low or intermediate mass AGB, s-process elements are produced although the mechanism is not the main s-process. The stellar structure, temperature and neutron source are different with respect to the AGB ones, and hence, are the nucleosynthesis yield. It is the weak s-process mechanism that yields lighter isotopes than the first s-process peak, from Co to Sr ($60 \leq A \leq 90$).

And finally, the massive nature of the star determines its explosive death. Once the ^{56}Ni element (unstable decaying to ^{56}Fe) is reached, the burning is not energetically sustainable. The balance between radiation and gravitational pressure ceases and the outer layers precipitate against the core in minutes provoking a shock-wave and the violent explosion as a supernova by core collapse (SNeII).

The explosion provides an extremely high flux of neutrons and the conditions for rapid neutron capture that overwhelms the β-disintegration times, producing isotopes far from the β-stability valley: it is the r-process mechanism that will provide a wide source of heavier elements than Fe, depending on the initial chemical and physical parameters of the star (mass, metallicity, etc.).

Besides, the shock-wave of the supernova with the interstellar medium will provide an additional nucleosynthesis and reactions enriching the interstellar medium (ISM) of chemicals.

1.4.1 Weak s-process

The weak s process is responsible of contributions in abundance of isotopes with mass number 60 to 90, that is to say, from Co to Sr. Their nucleosynthesis sites are located in the core He burning of massive stars, and in shell C burning where the temperature is high enough to develop reactions with ^{22}Ne, the main neutron source, producing elements as Mg and Na.

The nucleosynthesis paths are different in one or another burning (see Fig. 1.22 and 1.23). Later the elements, unprocessed, will be ejected into the ISM by SNeII explosion.

	core He-burning	shell C-burning
Temperature	$3\text{-}3.5\cdot10^{8}$ K	$\sim1\cdot10^{9}$ K
	kT=25 keV	kT=90 keV
Neutron density	10^{6} cm^{-3}	$10^{11}\text{-}10^{12}$ cm^{-3}
Neutron source	^{22}Ne(α,n)	^{22}Ne(α,n) unburned in core He-burning
	↓	^{13}C(α,n)^{16}O^{13}C via ^{12}C(p,γ)^{13}N(β^{+})^{13}C
		^{17}O(α,n)^{20}Ne via ^{16}O(n,γ)^{17}O
	^{25}Mg	^{12}C(^{12}C,α)^{20}Ne, ^{12}C(^{12}C,p)^{23}Na

Figure 1.21: *Neutron source in weak s-process depending on the massive star burning.*

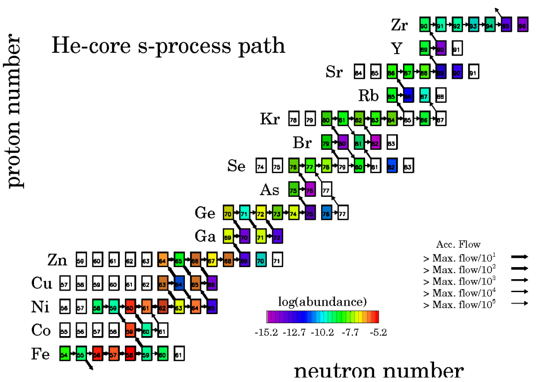

Figure 1.22: *Neutron capture path for weak s-process elements, in He core burning of massive stars (The et al. 2007).*

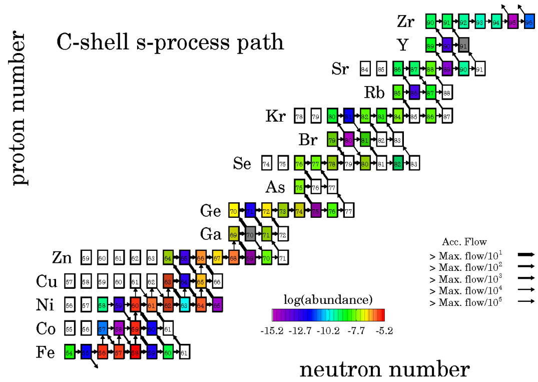

Figure 1.23: *Neutron capture path for weak s-process elements, in C shell burning of massive stars (The et al. 2007).*

The percentage in the Solar System of the different elements or isotopes from Co to Mo are shown in Fig. 1.24. The Sr, light main s-process first-peak element, is the breaking point of the main s-process domination over weak s.

s-PROCESS CONTRIBUTION AT $t = t_{\odot}$

Element	Massive Stars[a] Weak *s* (%)	AGB Stars[b] LMSs (%)	IMSs (%)	Total AGB (%)	Total *s* Weak *s* + Main *s* (%)
Co	6	1	2	3	9
Ni	1	0	0	0	1
Cu	22	2	3	5	27
Zn	8	2	1	3	11
Ga	44	7	4	11	55
Ge	43	8	4	12	55
As	17	5	3	8	25
Se	25	9	5	14	39
Br	11	9	6	15	26
Kr	19	17	12	29	48
Rb	14	18	21	39	53
Sr	9	62	9	71	80
Y	5	62	7	69	74
Zr	2	55	10	65	67
Nb	2	55	12	67	69
Mo	1	34	4	38	39

Low mass   Int. mass

[a] Raiteri et al. 1992.
[b] This paper.

Figure 1.24: *Contribution of s-process mechanisms to abundances of elements from Co to Mo in Solar System (Travaglio et al. 2004).*

1.4.2 Burning Stages proceeding Supernovae II: α-elements

Burning phases before a core-collapse SNeII is the main production site of the α-elements as O, Mg, Si, S, Ca and Ti. Schematically, the net reaction is the α particle capture,

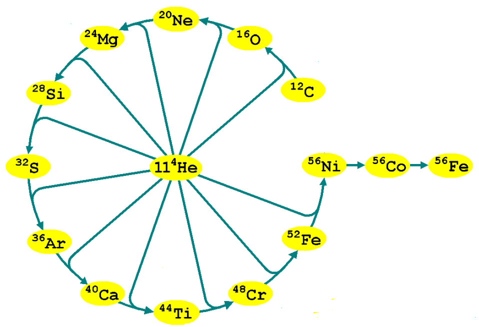

Figure 1.25: *Schematic α-reactions.*

yielding successively heavier elements with even atomic and mass number (see Fig. 1.25).

They are (and other additional elements) progressively formed in the consecutive and accelerated burning stages after the helium exhaustion:

Carbon Burning

500-800·10^6 K, ca 1000 years. Main formed elements: O, Ne, Na, Mg

$$^{12}_{6}C +^{12}_{6} C \rightarrow^{20}_{10} Ne +^{4}_{2} He$$
$$^{12}_{6}C +^{12}_{6} C \rightarrow^{23}_{11} Na +^{1}_{1} H$$
$$^{12}_{6}C +^{12}_{6} C \rightarrow^{23}_{12} Mg + n$$
$$^{12}_{6}C +^{12}_{6} C \rightarrow^{24}_{12} Mg + \gamma$$
$$^{12}_{6}C +^{12}_{6} C \rightarrow^{16}_{8} O + 2\,^{4}_{2}He$$

Neon Burning

1200-1500·10^6 K, ca 10 years. Main formed elements: O, Mg

$$^{20}_{10}Ne + \gamma \rightarrow^{16}_{8} O +^{4}_{2} He$$
$$^{20}_{10}Ne +^{4}_{2} He \rightarrow^{24}_{12} Mg + \gamma$$
$$^{20}_{10}Ne + n \rightarrow^{21}_{10} Ne + \gamma$$
$$^{21}_{10}Ne +^{4}_{2} He \rightarrow^{24}_{12} Mg + n$$

Oxygen Burning

1500-2600·10^6 K, ca 1 years. Main formed elements: Mg, Si, P, S

$$^{16}_{8}O +^{16}_{8} O \rightarrow^{28}_{14} Si +^{4}_{2} He$$
$$^{16}_{8}O +^{16}_{8} O \rightarrow^{31}_{15} P +^{1}_{1} H$$
$$^{16}_{8}O +^{16}_{8} O \rightarrow^{31}_{16} S + n$$
$$^{16}_{8}O +^{16}_{8} O \rightarrow^{30}_{14} Si + 2\,^{1}_{1}H$$
$$^{16}_{8}O +^{16}_{8} O \rightarrow^{30}_{15} P +^{2}_{1} D$$

$$^{16}_{8}O +^{16}_{8} O \rightarrow^{32}_{16} S + \gamma$$
$$^{16}_{8}O +^{16}_{8} O \rightarrow^{24}_{12} Mg + 2^{4}_{2}He$$

Silicon Burning

2700-3500·10^6 K, ca 1 day. See Fig. 1.26. Even Z-elements from S to Zn

$$^{28}_{14}Si +^{4}_{2} He \rightarrow^{32}_{16} S$$
$$^{32}_{16}S +^{4}_{2} He \rightarrow^{36}_{18} Ar$$
$$^{36}_{18}Ar +^{4}_{2} He \rightarrow^{40}_{20} Ca$$
$$^{40}_{20}Ca +^{4}_{2} He \rightarrow^{44}_{22} Ti$$
$$^{44}_{22}Ti +^{4}_{2} He \rightarrow^{48}_{24} Cr$$
$$^{48}_{24}Cr +^{4}_{2} He \rightarrow^{52}_{26} Fe$$
$$^{52}_{26}Fe +^{4}_{2} He \rightarrow^{56}_{28} Ni$$
$$^{56}_{28}Ni +^{4}_{2} He \rightarrow^{60}_{30} Zn^{*}$$

* Energetically demanding, see Fig. 2.1 in Chapt. 2

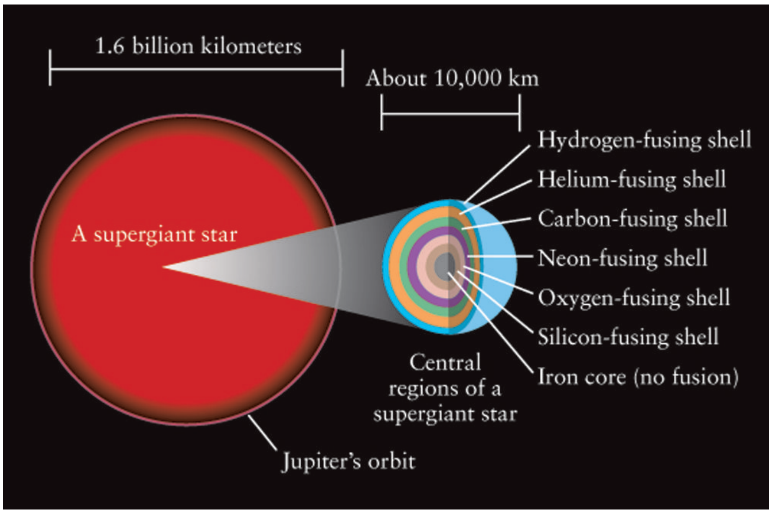

Figure 1.26: *Onion layer structure of pre-supernova star (SNeII) during the last silicon burning stage (ca 1 day). Credit* https://sites.ualberta.ca/~pogosyan/teaching/ASTRO_122/lect18/lecture18.html.

The profile of the α-elements with respect to the metallicity is typical (see Fig. 1.27). The nucleosynthesis sites of α-elements and the ones for Fe or others light elements are different.

As above commented, the α-elements are formed in previous burning phases of a SNeII, meanwhile Fe peak elements are mainly produced in thermonuclear supernovae (SNeIa, see Sect. 1.5), where the α-elements are not so efficient in their production.

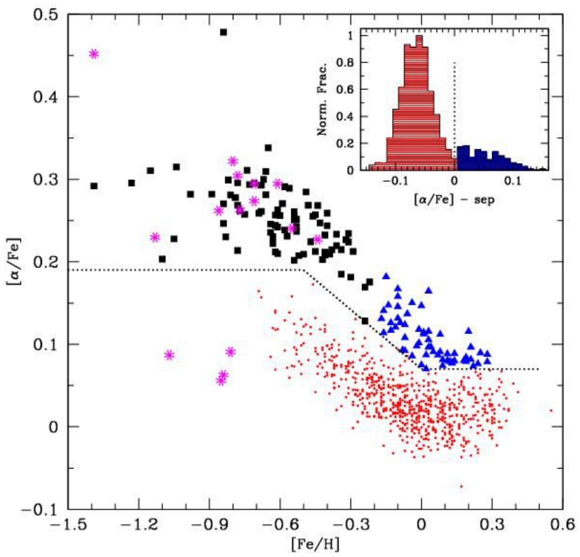

Figure 1.27: *Sample of FGK main sequence stars. α-index (from average weighed abundances of Si, Ca, Ti) with respect to the metallicity. Metallicity can be understood as a galactic evolution time parameter. The black filled squares refer to the thick disk stars, blue triangles to the hαmr (high alpha metal rich stars), and the red dots to the thin disk stars. Magenta asterisks represent the stars belonging to the halo by their kinematics. The blackdotted line is the fiducial for division into thin and thick disk populations. From* Adibekyan et al. (2013)*.*

The early Universe was enriched in α-elements because SNeII occurred on a much faster time-scale than SNeIa (Edvardsson et al. 1993). This time factor determines the abundance slope in function of metallicity. To higher metallicities we are closer to the current universe (and metallicity) where the α-elements have been diluted by the higher number of SNeIa events and AGB production.

Like this, the trend shows an enhancement in α-elements to metal poor stars of the thick disk, older stars which gathered material from previous generations in an early universe. The breaking point in galactic evolution terms is reached at a metallicity of [Fe/H] = -1.0 dex, when mainly SNeII or very massive and energetic novae (Hypernovae, HNe) were contributing to element abundances. In that point the α-elements reach a steady plateau at +0.3 over scaled solar abundances.

The diagram is too a tool for the assignment of the stars to the thin or thick disk from the chemical point of view, in addition to the traditional orbital or kinematic features assignment. Chemically the α-elements show a gap between thin or thick stars, hinting a different chemical nature and galactic forming evolution of the thin or thick disks.

1.4.3 Core Collapse Supernovae SNeII: r-process elements

The stars lifetime is a delicate balance between two opposing forces determining their evolution and stages. On one side, radiation pressure as a result of the fusion reactions along the different burning phases (H, C, Ne, O, Si in case of massive stars > 8 $M_{\odot}$). On the other, gravity, pushing the enormous mass of the outer star layers against the core and inner layers (see Fig. 1.28).

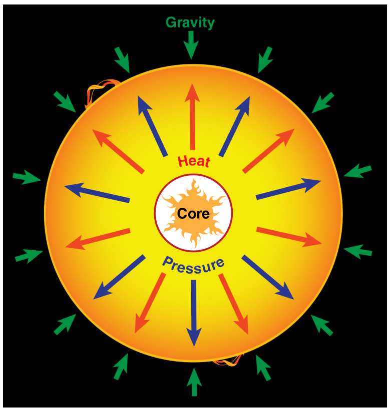

Figure 1.28: *Star balance. Credit* https://spaceplace.nasa.gov/supernova/en/.

Once the burning fuels are exhausted, gravity wins the war and the successive layers fall violently at a fraction of the speed of light (around 23%) against the core, that reaches 10^{11} K and contracts to the limit of the electronic degeneracy.

When the compacted core mass exceeds the Chandrasekhar limit (1.4 $M_{\odot}$), even this matter resistance is overwhelmed and the core implosions, collapsing, only stopped by the neutron degeneracy, the last resistance of the star's core to becoming a black hole. Outer layers rebound over this collapsed core, provoking an expanding shock-wave, completely disrupting the rest of the star and the ejection of the outer layers as a supernova explosion (see Fig. 1.29).

Behind, the collapsed core has become a neutron star or black hole depending on the initial mass of the star and experienced gravity pressure (see Fig. 1.30).

The supernovae by core collapse will enrich the ISM with the α-elements produced during the previous burning stages. But in addition, the very high flux of neutrons that the core collapse and explosion provide, will seed the rapid neutron capture process (r-process) and the nucleosynthesis of heavy elements.

The classic scenario for r-process production is the neutrino-driven winds from the core-collapse supernovae, SNeII > 10 $M_{\odot}$ (Woosley et al. 1994). Extremely energetic neutrinos are produced during the collapse of the SNeII, and they are potentially able to interact with the dense material (see Fig. 1.31) that is falling onto the core of the star. This

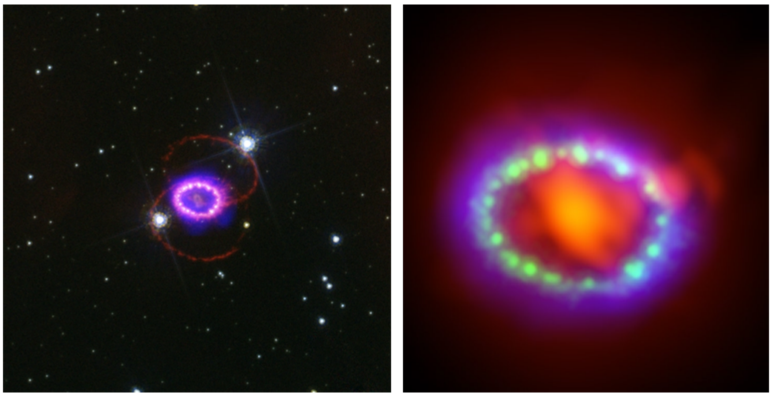

Figure 1.29: *Core-collapse Supernova SN1987A .*
Left: *Hubble optical image. Bright spots along the inner ring of gas surrounding the exploded star as a consequence of the material unleashed by the stellar blast slamming into regions along the inner ring, heating them up, and causing them to glow. Credit NASA/ESA* https://hubblesite.org/contents/news-releases/2007/news-2007-10.html
Right: *Composite of ALMA radio observation (red) showing dust in the remnant center, Hubble optical observation (green) and eventually the more energetic R-Ray emissions by Chandra X ray observation (blue/purple), showing where the expanding shock wave is colliding with a ring of material around the supernova. Credit ALMA (ESO/NAOJ/NRAO)/A* https://www.eso.org/public/images/eso1401a/.

interaction can heat the material, giving it the additional energy needed to reach the observed energy output of $\simeq 10^{51}$erg (Battistini & Bensby 2016) [1].

Neutrino-driven winds from proto-NS (neutron stars) following the delayed explosions of very massive stars ($> 20\ M_{\odot}$, Hypernovae) have been suggested as a promising site to form the solar r-process abundances (Matteucci et al. 2014). However, recent hydrodynamicals simulations have shown that the neutrino winds are proton rich (Arcones et al. 2007; Fischer et al. 2010; Hüdepohl et al. 2010) but never very neutron rich, only slightly rich as best (Martínez Pinedo et al. 2012; Roberts et al. 2012), unlike the pioneer simulations by Woosley et al. (1994) and Takahashi et al. (1994).

These studies casts serious doubts on the validity of the neutrino wind scenario and it seems now established that neutrino-driven winds from proto-NS cannot be the main origin of the r-process elements beyond A $\simeq$ 110. Prompt explosions of massive stars in the 8–10 $M_{\odot}$ range may lead to an ejected amount of r-process matter consistent with the observed Galactic abundances but it is not clear whether these prompt explosions do occur and the right yields (Matteucci et al. 2014).

[1]Green brackets indicate that the information of the paragraph or partially the paragraph itself has been extracted from this article, including other references in the paragraph as primary sources regarding some statements, issues or studies.

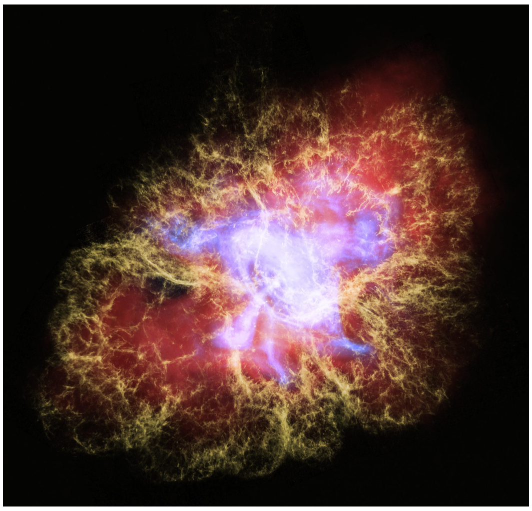

Figure 1.30: *Crab Nebula and remnant neutron star/pulsar. Composite of the more energetic X-Ray emissions by Chandra X ray observation (blue) showing the neutron star/pulsar, core-collapsed remnant of the supernova's progenitor star, rotating 30 times per second. A disk of X-ray-emitting material, spewing jets of high-energy particles perpendicular to the disk, surrounds the pulsar; visible light as a result of emission from oxygen that has been heated by higher-energy (ultraviolet and X-ray) synchrotron radiation, from the Hubble Space Telescope (in yellow), showing the characteristic nebula image; and eventually infrared light seen by the Spitzer Space Telescope (in red), showing synchrotron radiation, formed from streams of charged particles/electrons spiraling around the pulsar's strong magnetic field. Credit NASA/ESA* `https://hubblesite.org/contents/media/images/2020/03/4601-Image?news=true`.

In addition, the high temperatures, energies and radiation produce the nucleosynthesis of other lighter elements in the shock-wave with the different ejected shells (α-freeze outs, see next section) or ISM medium.

The element yields and star fate will depend on the initial parameters of the SNeII progenitor (or Hypernovae, HNe, when more massive and energetic) as are shown (Population III) in the Tables 1.1 and 1.2, about the primordial stars in a very early, extremely metal-poor universe (Karlsson et al. 2013).

1.4.4 α-Freeze-outs in SNeII

During the core collapse of a dying massive star, a shock wave develops as matter falls supersonically onto the collapsed stellar core. The shock, aided by a push from neutrinos from the cooling nascent neutron star, expands out into, heats, and expels the overlying stellar matter (see Fig. 1.31).

Mass range ($\mathcal{M}_\odot$)	Final fate	Metal ejection	Remnant
$m \lesssim 9$	Planetary nebula[a]	Yes	White dwarf
$9 \lesssim m < 10$	O/Ne/Mg core collapse SN[a]	Yes	Neutron star
$10 \leq m < 25$	Fe core collapse SN[a]	Yes	Neutron star
$25 \leq m < 40$	Weak Fe core collapse SN[a] (fallback)	Yes	Black hole
$25 \leq m < 40$	Hypernova[b] (fallback)	Yes	Black hole
$40 \leq m < 100$	Direct collapse[a] (no SN)	No	Black hole
$100 \leq m < 140$	Pulsational pair-instability SN[a] (fallback)	No?	Black hole
$140 \leq m < 260$	Pair-instability SN[a]	Yes	No remnant
$260 \leq m \lesssim 10^5$	Direct collapse[c]/core collapse[c,d] (no SN?)	No?	Black hole
$10^5 \lesssim m$	Direct collapse before reaching main sequence[d]	No	Black hole

a: Heger et al. (2003)
b: Nomoto et al. (2006)
c: Fryer et al. (2001)
d: Ohkubo et al. (2006)

Table 1.1: *Final fates and remnants of massive primordial stars for different initial masses. First line referred to AGB stars. From Karlsson et al. (2013).*

Mass range ($\mathcal{M}_\odot$)	Expl. energy ($\times 10^{51}$ erg)	Ejected Fe ($\mathcal{M}_\odot$)	Metal enrichment	Nucleosynthetic characteristics
$m \lesssim 9$	Wind	0	^{7}Li(?), C, N, O, Na, Mg, s-process	$(C+N)/O > 1$ e.g., $[Pb/Ba] \simeq 1.2$
$9 \lesssim m < 10$	~ 0.1	$\sim 0.002 - 0.004$	Carbon to Fe-peak[a] r-process?	$[C,\alpha/Fe] \ll 0$ $[Mg/Ca] \ll 0$ $[Ni, Zn/Fe] \gg 0$ e.g., $[Ba/Eu] \simeq -0.6$[b]
$10 \leq m < 25$	~ 1	~ 0.07	Carbon to Fe-peak	$[\alpha/Fe] > 0$
$25 \leq m < 40$	< 1	$\lesssim 0.01$	Carbon to Fe-peak r-process?	$[C, O/Fe] \gg 0$ e.g., $[Ba/Eu] \simeq -0.6$[b]
$25 \leq m < 40$	$\gtrsim 10$	$\sim 0.08 - 0.3$	Carbon to Fe-peak	larger [Si,S/C,O] larger [V,Co,Cu,Zn/Fe] smaller [Mn,Cr/Fe]
$40 \leq m < 100$	No expl.	0	–	–
$100 \leq m < 140$	~ 1	0	Only H, He(?)	–
$140 \leq m < 260$	$\sim 10 - 10^2$	$\sim 0.01 - 40$	Carbon to Fe-peak	$[Mg, Si/Na, Al] \gg 0$ $[Si, S/C] \sim 1 - 1.5$ $[Zn/Fe] \ll 0$, no r-proc.
$260 \leq m \lesssim 10^5$	$\sim 10^3 - 10^4$	$\sim 5 - 20$	Carbon to Fe-peak[c]	$[Mg, Si/Na, Al] \gg 0$ $[C,\alpha/Fe] \ll 0$ $[Zn/Fe] \gg 0$
$10^5 \lesssim m$	No expl.	0	–	–

a: Based on a solar metallicity 8.8 $M_\odot$ 1D-model Wanajo et al. (2009)
b: Deduced from observations of metal-poor stars Barklem et al. (2005)
c: Ejection of metals may only occur if bipolar jets are generated Ohkubo et al. (2006)

Table 1.2: *Nucleosynthetic signatures of massive primordial stars. First line referred to AGB stars. From Karlsson et al. (2013).*

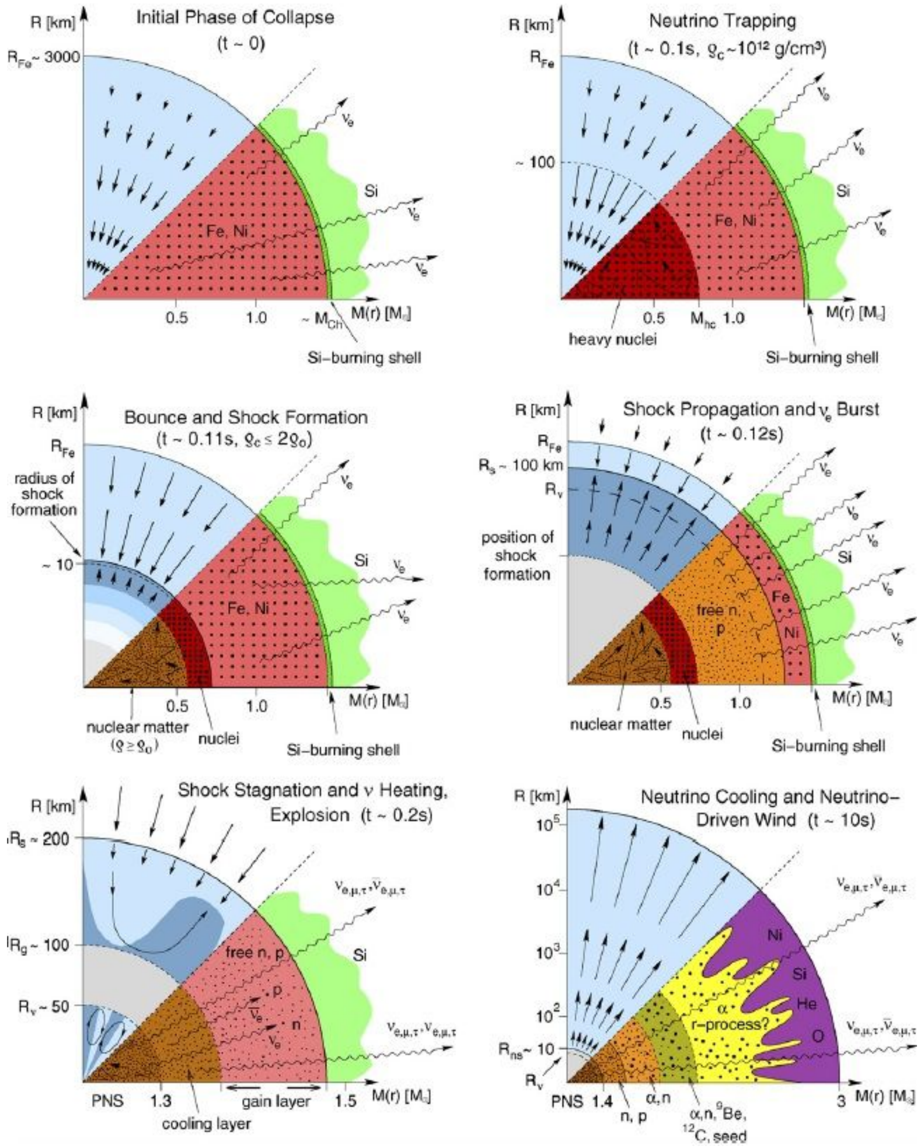

Figure 1.31: *Schematic representation of the evolutionary stages from stellar core collapse through the onset of the supernova explosion to the neutrino-driven wind during the neutrino-cooling phase of the proto-neutron star (PNS). The panels display the dynamical conditions in their upper half, with arrows representing velocity vectors. The nuclear composition as well as the nuclear and weak processes are indicated in the lower half of each panel. The horizontal axis gives mass information. MCh means the Chandrasekhar mass and Mhc the mass of the subsonically collapsing, homologous inner core. The vertical axis shows corresponding radii, with RFe, Rs, Rg, Rns, and R being the iron core radius, shock radius, gain radius, neutron star radius, and neutrino sphere, respectively. The PNS has maximum densities ρ above the saturation density of nuclear matter (ρ_0). From* Janka et al. *(*2007*).*

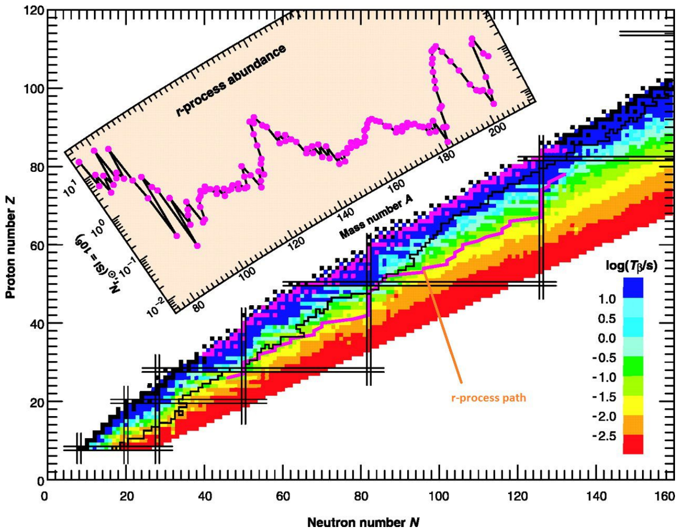

Figure 1.32: *r-process path (magenta). At a given proton (atomic) number, isotopes toward the left are proton-rich, and those to the right are the neutron-rich ones. The stable nuclides are marked by black boxes; n-capture in s-process synthesis occurs near these nuclei close to the "valley of β-stability." The jagged diagonal black line represents the limit of experimentally determined properties of nuclei. Vertical and horizontal black lines represent closed neutron or proton shells, sometimes referred to as "magic numbers." Color shading denotes the different (log) time scales for β-decay. From Sneden & Cowan (2003).*

In the initial heating of the inner most regions of the ejecta, when the supernova shock wave passes through the Si-rich shell of the star, post-shock temperatures are sufficiently high that nuclei are broken down into nucleons and α-particles. As the material subsequently expands and cools, the nucleons and α-particles reassemble to form heavy nuclei. Because of the fast expansion of the matter, however, not all α-particles reassemble, and, as a result, the final abundances freeze out with a significant number α-particles remaining, hence the name α-rich freezeout.

A number of significant astronomical observables are produced in this process, contributing to the abundances of some Fe-peak and α-elements (Jordan et al. 2003).

Later study by Magkotsios et al. (2011) suggests that a larger number of isotopes (12 ≤ A ≤ 122) are produced and that they can be classified in two families, depending on the mechanism of nucleosynthesis. But although the alternative mechanism is able to produce all the range of isotopes, A from 12 to 122, however it is the aforementioned mechanism that dominates the final production with isotopes related to nuclei near the magic numbers 28, 50 and 82.

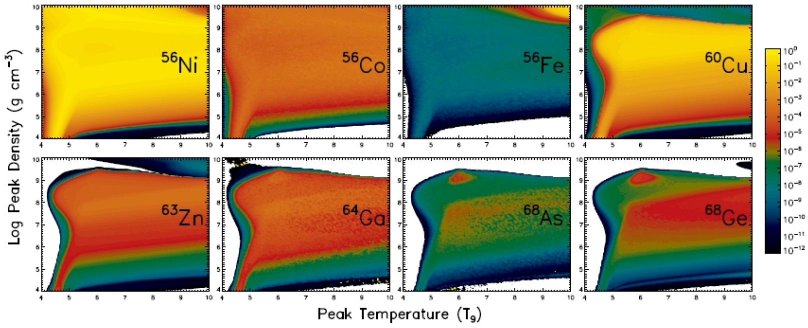

Figure 1.33: *Final mass fractions of isotopes with protons and neutrons near the magic number 28 (main mechanism) in the peak temperature–density plane for the power-law profile at initial electron fraction, Ye = 0.52. The white colored space corresponds to values below the color scale shown. From left to right, the first row corresponds to ^{56}Ni, ^{56}Co, ^{56}Fe and ^{60}Cu, and the second row corresponds to ^{63}Zn, ^{64}Ga, ^{68}As and ^{68}Ge. From Magkotsios et al. (2011).*

1.4.5 Magnetohydrodynamics Supernovae (MHD-SNeII)

Polar jets from rotating Magnetohydrodynamics (MHD) core-collapse Supernovae (Nishimura et al. 2006; Winteler et al. 2012) have been recently proposed as strong r-process sites that greatly would impact the metal poor abundance trends and nucleosynthesis at early stages of the galaxy.

An important step in the study of neutron-capture elements (r- and s-process) was the discovery that metal-poor stars show high relative abundances of certain neutron-capture elements compared to Fe, meaning that the r- and s-processes were already active at early times. Specifically the significant number of stars with high levels of r-process element as Eu, at extremely low metallicities (galactic halo stars) show the impact of the early r-process. The s-process (AGB/LIMS) needs at least 500 Myr time delay, after the formation of the first population of stars (Sneden et al. 2008). However r-process linked with core-collapse of massive stars might develop very soon after the appearance of the first stars.

MHD-SNeII, characterized by high rotation rates and large magnetic fields, is observed as an interesting and promising site for the strong r-process observed in the early Galaxy that deserve further investigation. The rarity of the MHD-SNeII progenitors, might provide a natural explanation for the observed scatter in the abundances of r-process elements (and indirectly for the s-process ones) in extremely metal poor stars at very early stage of the universe.

1.5. Binary interactions and mergers

Binary interactions rule the late stages in the stellar evolution of a high percentage of systems. It is not a surprising data: Approximately half of the sun-like star population

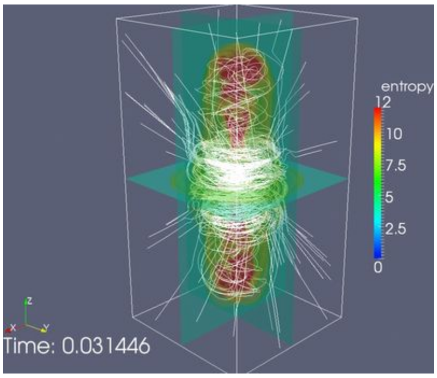

Figure 1.34: *3D entropy contours spanning the coordinates planes with magnetic field lines (white lines) of the Magneto-Hydrodynamic Core-Collapse Supernovae (MHD-SNeII) simulation ≃ 31 ms after bounce. From Winteler et al. (2012).*

resides in binary or higher order systems (see Fig. 1.35) and this fraction increases with higher mass stars (Raghavan et al. 2010; Hilditch 2001).

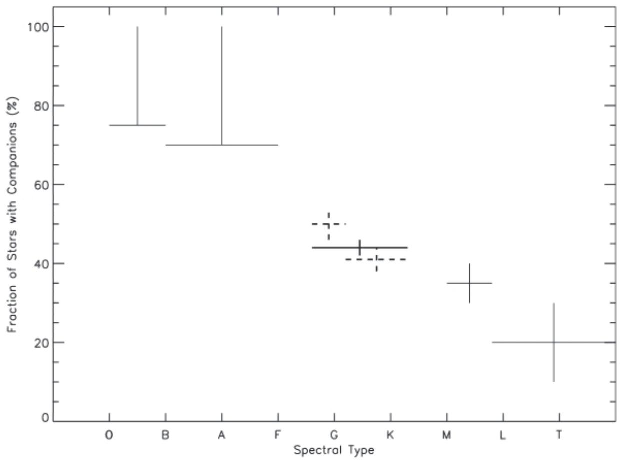

Figure 1.35: *Multiplicity statistics by spectral type. The thin solid lines represent stars and brown dwarfs beyond the spectral range of the Raghavan et al. (2010) study. For the FGK stars studied by Raghavan et al. (2010), the thick dashed lines show the observed multiplicity fractions, i.e., the percentage of stars with confirmed stellar or brown dwarf companions, for spectral types F6–G2 and G2–K3. The thick solid lines show the incompleteness-adjusted fraction for the entire F6–K3 sample. From Raghavan et al. (2010).*

The evolution possibilities of binary systems are wide depending on the initial masses and orbital periods of the companion stars. See Fig. 1.36 for a complete understanding of possible evolution paths.

In the Fig. 1.37 is described a particular and partial channel for the production of a pair of black holes (that finally might merge) from very massive blue super-giants, once one of them evolves off the main sequence. But for no so massive stars, the evolution might dramatically change producing neutron star pair or follow other different evolutionary paths. For low or intermediate mass stars (LIMS/AGB) in close binaries, once more the evolution leads to different possibilities. For this case, the Fig. 1.38 describes one possible standard path.

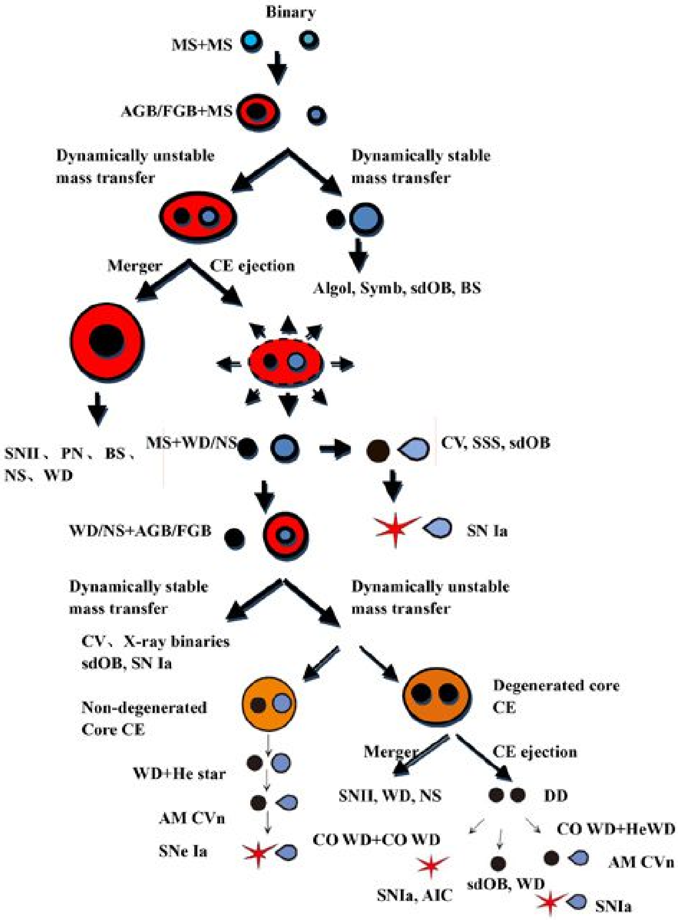

Figure 1.36: *Evolution paths of binary systems. Credit* `http://www1.ynao.ac.cn/~zhanwenhan/jpeg/flchart.jpg`*, Dr. Zhanwen Han, Yunnan Observatories.*

Due to the complexity of the binary interactions, the nucleosynthesis possibilities in these systems are rich, linked to the initial system features and stages the binary system goes through.

Higher orders of the systems, increase the complexity of the possible evolutionary paths depending on a more complex set of initial orbital and involved stellar objects features. As an example, the Fig. 1.39 shows the outcomes of a theoretical study about the rich evolutionary possibilities of the sizable population of binaries around a third object, the

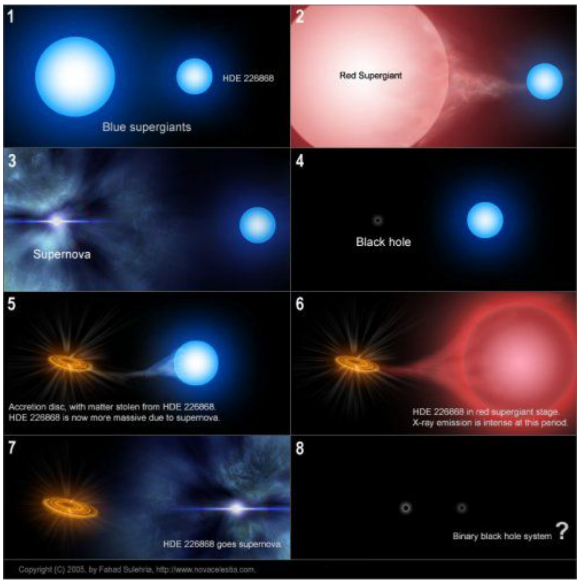

Figure 1.37: *Example of a binary system evolution from massive blue super-giants to a pair of black holes. Credit: NovaCelestia* `http://www.stronggravity.eu/public-outreach-tmp/black-hole-evolution/`.

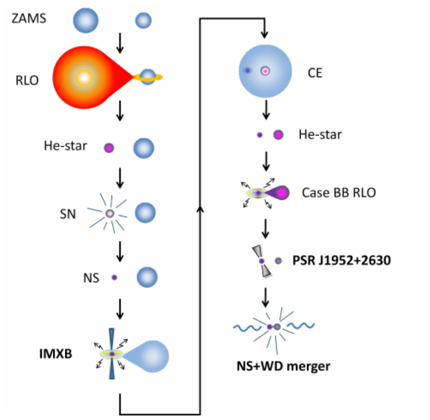

Figure 1.38: *An illustration of a full binary stellar evolution from the zero-age main sequence (ZAMS) to the final merger stage. The initially more massive star evolves to initiate Roche-Lobe Overflow (RLOF), leaving behind a naked helium core which collapses into a neutron star (NS) remnant, following a supernova explosion (SN). Thereafter, the system becomes a wide-orbit intermediate- mass X-ray binary (IMXB), leading to dynamically unstable mass transfer and the formation of a common envelope (CE), when the 6–7 $M_{\odot}$donor star initiates RLOF. The post-CE evolution, calculated is responsible for recycling the NS via Case BB RLOF when the helium star companion expands to initiate a final mass-transfer episode, leading to a radio pulsar orbiting a massive white dwarf (WD). Credit Lazarus et al. (2014).*

Super-massive Black Hole (SMBH, Sagittarius A*) in the Galaxy Center (Stephan et al. 2019).

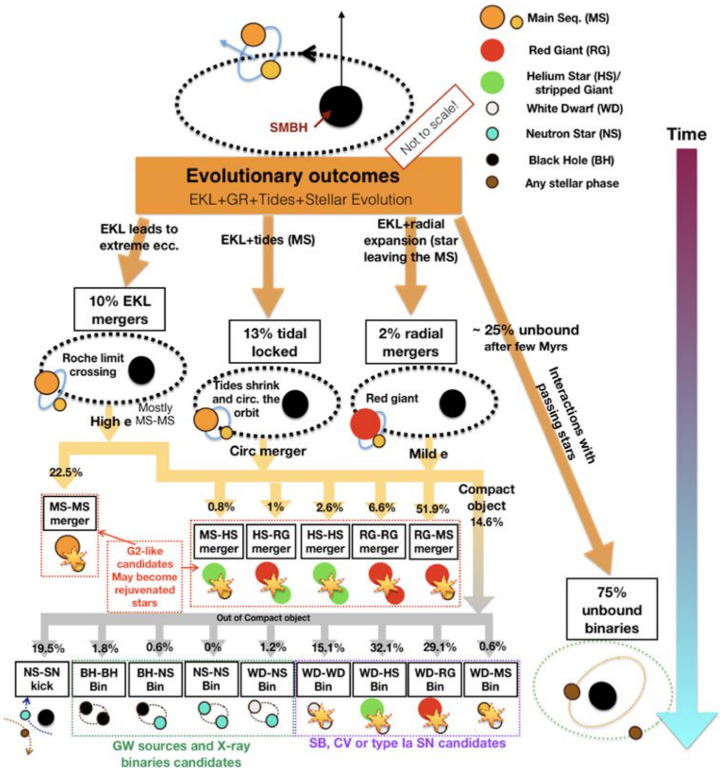

Figure 1.39: *The diagram shows the outcomes of binary evolution in the inner 0.1 pc of the Galactic Center, around Sagittarius A*. Dynamical effects such as scattering with other stars separate 75% of all binaries into independent singles before they can interact with each other. 10% of binaries will collide or have grazing encounters due to Eccentric Kozai–Lidov evolution (EKL)-induced high eccentricities. 2% will merge simply due to radial expansion of one of the binary members due to stellar evolution.13% of binaries will tidally shrink their orbits and become decoupled from gravitational perturbations by the super-massive black hole (SMBH, Sagittarius A*). Stephan et al. (2019) determined the further evolution of these binary pairs and their evolutionary phases during merging, using binary stellar evolution code BSE (Hurley et al. 2002). The different possible outcomes are shown in the figure. Generally, the most likely combinations for merging binaries are pairs of main-sequence stars, main-sequence and red giant stars, pairs of red giant stars, and white dwarfs with evolved stellar companions. There is also a sizable population of binaries that were separated due to neutron star kicks, producing single neutron stars orbiting the SMBH, as well as a small population of binaries containing black holes or neutron stars that can become gravitational wave sources and might have been X-ray sources at some point, marked by the green box (see Bortolas et al. (2017); Hoang et al. (2018)). Mergers involving white dwarfs are candidates for SBs, CVs, and SNe Ia (purple box), while mergers involving red giants, stripped giants, or main-sequence stars are candidates for G2-like objects or progenitors of rejuvenated stars (red boxes; e.g., Witzel et al. (2014, 2017); Stephan et al. (2016)). From Stephan et al. (2019).*

1.5.1 Thermonuclear Supernovae SNeIa and Classical Novae

The thermonuclear supernovae (SNeIa) are formed by binary interactions between a white dwarf (WD) and an evolved companion (Red Giant) or another white dwarf. The matter accretion (see Fig. 1.40) by the white dwarf that finally surpasses a critical mass point, the Chandrasekhar limit (ca 1.4 $M_{\odot}$), produces the collapse of the core by an uncontrolled fusion reaction, leading to the explosion that might eject the companion, leaving behind a neutron star or black hole.

However, there is to remark that different channels are available to produce SNeIa depending on the system features as shown by Fig. 1.42. Although no consensus has been reached, it can be summarized in some SNIa scenarios currently considered. They are listed next (Bear & Soker 2018; Tsebrenko & Soker 2015):

SNIa scenarios

- The Core-Degenerate (CD) scenario

  A CO WD merges with the core of a massive asymptotic giant branch (AGB) star at the final stages of the common envelope evolution. Explosion might occur shortly or a long time after merger. According to some studies, this channel accounts for most SNe Ia, though the population synthesis study by Wang et al. (2017) concluded only up to 20%.

- The Double Degenerate (DD) scenario

  Two WDs merge most likely in a violent process a long time after the common envelope evolution has ended. There is no specification of the later evolution, e.g. how long after merger explosion occurs.

- The Detonation (DDet) scenario

  A sub-Chandrasekhar mass WD accumulates a layer of helium-rich material on its surface, accreted from a companion. The helium layer detonates and leads to a second detonation near the centre of the CO WD.

- The Single Degenerate (SD) scenario

  The WD accretes mass from a non-degenerate stellar companion and explodes when it reaches close the Chandrasekhar mass limit.

- The WD-WD Collision (WWC) scenario

  Two WDs collide at about their free fall velocity and immediately ignite.

In spite of this summary, other scenarios are possible and can be considered as those emerging from the interaction between WD and circumstellar matter.

A variant of the SNeIa, is the Classical Novae (see Fig. 1.41), usually a close WD + MS system with orbital periods lower than 12 hours. In the Classical Novae, the thermonuclear runaway occurs only on the surface of the star, allowing the white dwarf and the binary system to remain intact, unlike the SNeIa whose explosion occurs within the white dwarf itself, destroying the binary system.

The SNeIa are key in the nucleosynthesis for the Fe-peak group elements as manganese (Mn) and iron (Fe) but too in different yields for vanadium (V), chromium (Cr), cobalt (Co), nickel (Ni), copper (Cu) and zinc (Zn). Besides, an estimable contribution in other lighter elements as it is the case of some α-elements as S, Ca and Ti.

In situ electron captures significantly lowers the electron fraction and drives the yields toward more neutron-rich isotopes. The net yield nucleosynthesis predicted by the models, will depend on the initial parameters as the central density of the WD (Seitenzahl & Townsley 2017).

1.5.2 Compact Binary Mergers (CBM)

Laser Interferometer observatories for the detection of gravitational waves as LIGO and Virgo, will mean a dramatic advance in the comprehension of gravitating compact mergers of neutron stars or black holes (see Fig. 1.43 and 1.44).

Already it has provided an opportunity to observe the counter part electromagnetic emission of a neutron merger in real time (not electromagnetic counterpart for black hole merger) as it was the case of GW170817 (see Fig. 1.45), a neutron stars merger whose gravitational waves were detected by LIGO/Virgo observatories in August 2017, the source located and the emissions studied in the full wide extent of electromagnetic ranges producing abundant scientific information in a multidisciplinary effort (see e.g. series of Soares-Santos et al. 2017 from I to VIII papers or Lyman et al. 2018; Troja et al. 2017; Mooley et al. 2018; Pratten et al. 2020, etc.).

From this unique event surged the opportunity to study the glow thermal emission of the radiactive decay of the heavy elements isotopes freshly synthesized by r-process (Kasen et al. 2017). Two distinct components of ejecta were inferred: one composed of primarily of light elements (mass number $\leq$ 140) and one of heavy r-process elements ($\geq$ 140).

The substantial ejecta masses inferred from GW170817 suggest that neutron-star mergers may be the dominant contributors to r-process production in the Galaxy, and could account for all the gold (Au) (although the last study by Kobayashi et al. (2020a) does point this only source to be insufficient for explaining the total abundance), platinum (Pt) and many other heavy elements. For light components are observed numerous Fe-peak group signatures and from heavy r-process elements contain a substantial fraction (1-10% mass)

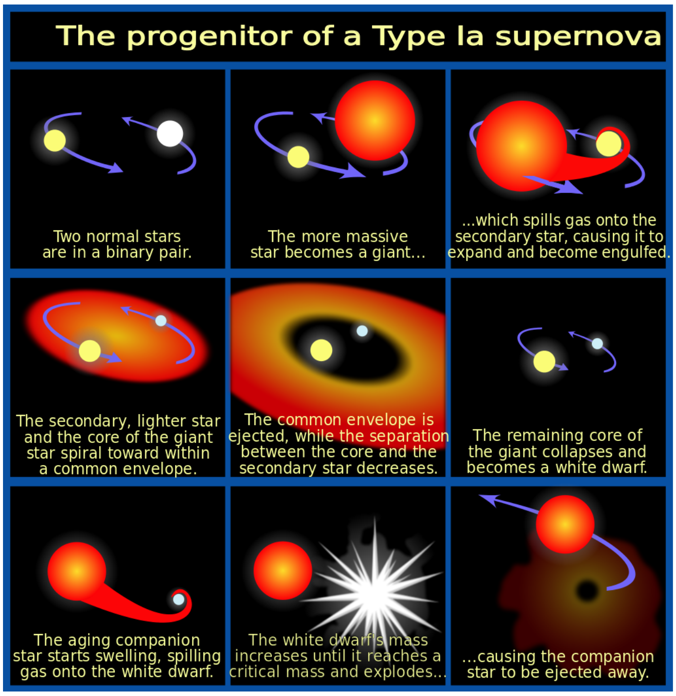

Figure 1.40: *Supernova Ia formation. Credit NASA/ESA/A.*

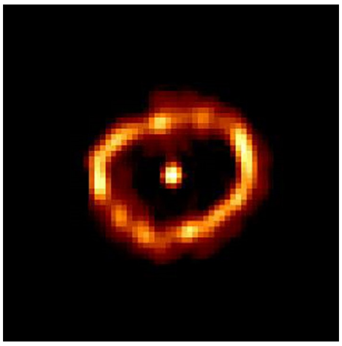

Figure 1.41: *Classical Nova, Cygni 1992. From Hubble/NASA. Credit* https://hubblesite.org/contents/media/images/1994/06/136-Image.html.

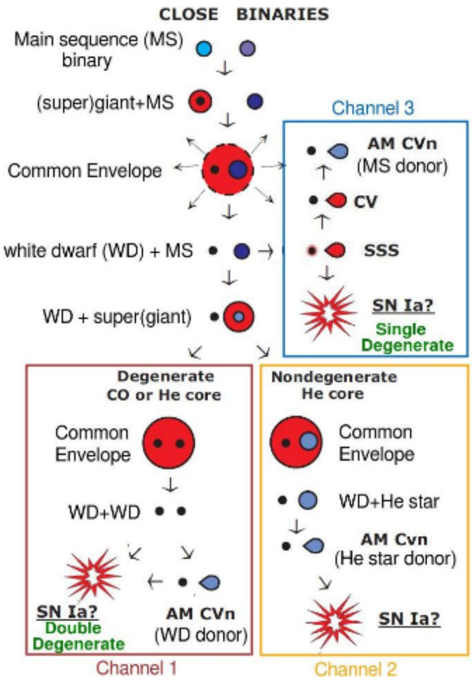

Figure 1.42: *Evolution of close binary, resulting in mergers or systems with high-(SSSs) and low accretion rates (CVs and AM CVns) and finally leading to thermonuclear SN Ia supernovae. From Toloza et al. (2019).*

of lanthanides ($58 \leq Z \leq 71$). In the heavy r-process spectra are observed some features corresponding to neodymium (Nd, Z=60) and cerium (Ce, Z=58).

Light r-process production dominates the first few hours after the merger, after which the heavy r-process takes over as the main nucleosynthesis process (see spectra in Fig. 1.47).

The theoretical neutron stars (Freiburghaus et al. 1999) and/or neutron-star/black hole merger (Surman et al. 2008) abundance patterns are practically indistinguishable and are uniquely referred as compact binary mergers (CBM).

At least up than 10^{-2} $M_{\odot}$ of r-process matter may be ejected in a single coalescence event, orders of magnitude higher than the average r-process ejecta obtained from SNeII, though the rate of CBM events should be significantly lower than the core-collapse ones in the galaxy. CBM might be one of the natural explanation for the scatter of r-process element abundances at low metallicity, given their rarity and high r-process element production (Matteucci et al. 2014), jointly with the MHD-SNeII (see Sect. 1.4) and Spinstars production

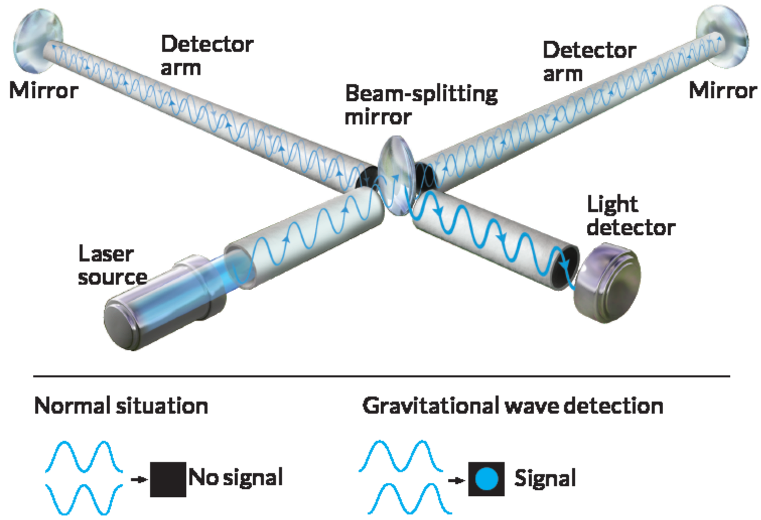

Figure 1.43: *LIGO detects gravitational waves by splitting a laser beam in two, sending light down two arms. The light reflects back and forth between mirrors in the arms. The beams then recombine and are sent to a detector. If the arms are the same length, the light beams cancel each other out. Any length difference — such as that caused by gravitational waves stretching one arm while shortening the other — will allow some light through to the detector. From* https://www.sciencenewsforstudents.org/article/trio-wins-physics-nobel-detecting-gravity-waves.

(see next Sect.).

1.6. Fast-rotators: spinstars

Widely used yields models as Woosley & Weaver (1995) and Nomoto et al. (2006) did not include mass loss but observational abundance data seem to corroborate that this factor is important and affect the yields of light elements as He, C, N, O or Ne as well as other weak s-process elements (see Sect. 1.21), especially in massive stars > 25 $M_{\odot}$ (Prantzos et al. 2018).

The first hint of fast-rotators at the early stages of the universe (lower metallicity range) was found by Maeder et al. (1999) and later corroborated by Martayan et al. (2007), studying Be stars frequency in solar neighborhood compared to the Large and Small Magellanic Clouds (Maeder et al. 2015).

Theoretical models of the formation of the first stars indicated that stars of very low Z (metallicity) should have very high rotational velocities, and thus experience mixing (Stacy et al. 2011). The prototype model of a spinstar is a massive star with low metallicity, fast rotation, strong mixing processes and a high mass loss rate (Meynet et al. 2010; Maeder & Meynet 2012).

Since then, increasingly number of works have confirmed and remarked the importance

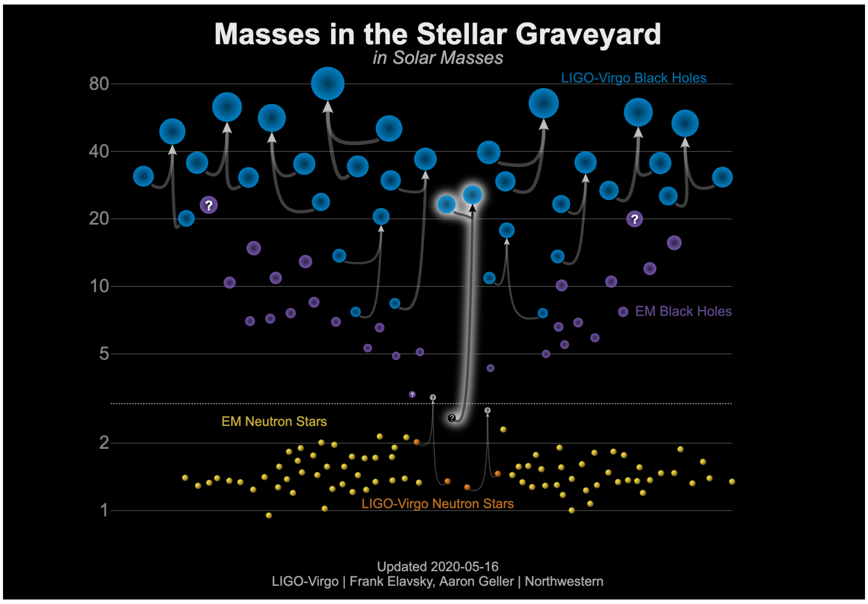

Figure 1.44: *Masses of Neutron Stars and Black Holes detected by LIGO-Virgo observatories through time (x axe). The masses of stellar remnants are measured in many different ways. This graphic shows the masses for black holes detected through electromagnetic observations (purple); the black holes measured by gravitational-wave observations (blue); neutron stars measured with electromagnetic observations (yellow); and the masses of the neutron stars that merged in an event which were detected in gravitational waves (orange). The remnant of GW170817, the first neutron star merger, is unclassified, and labeled as a question mark. Credit LIGO-Virgo* `https://www.ligo.caltech.edu/image/ligo20200623a`.

of the taking into account this factor, especially at the early stages of the universe, for the understanding and correct evaluation of element nucleosynthesis yields and analysis of chemical abundance trends. The general impact of fast rotation on massive stars in yields might be summarised in three key effects (Prantzos et al. 2018):

Fast Rotation Stellar Effects

- The mixing of layers putting in contact nuclear species which would otherwise remain separated.
- Changes of convective regions (core and shell) and hence the physical evolution of a star.
- Altered surface properties making the star eager to lose enormous amount of mass in comparison with no rotating stars.

Maeder et al. (2015) describe some of the important effects on GCE:

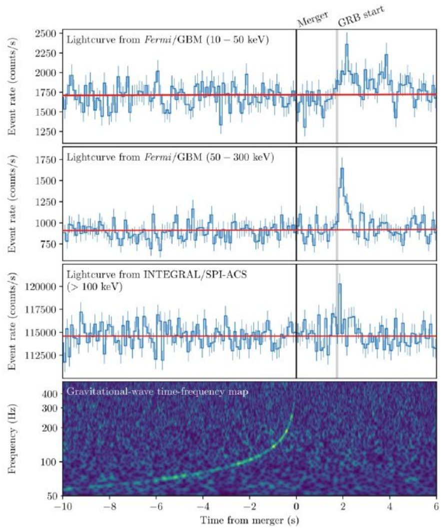

Figure 1.45: *Gamma-ray burst detected by Fermi (Gamma-ray space telescope), and INTEGRAL (Gamma-ray and X-ray space telescope); and gravitational waves by LIGO. From Abbott et al. (2017a).*

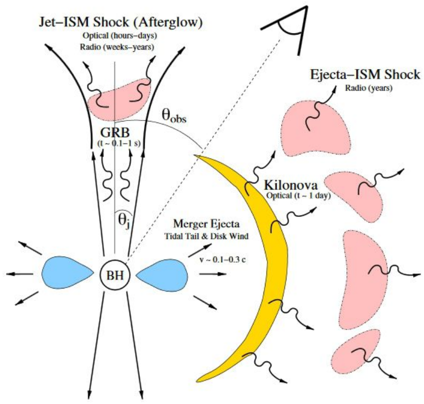

Figure 1.46: *Summary of potential electromagnetic counterparts of NS–NS/NS–BH mergers, as a function of the observer angle, θobs. Following the merger a centrifugally supported disk (blue) remains around the central compact object (usually a BH). Rapid accretion lasting ≤ 1s powers a collimated relativistic jet, which produces a short-duration gamma-ray burst. Due to relativistic beaming, the gamma-ray emission is restricted to observers with θobs ≤ θj, the half-opening angle of the jet. Non-thermal afterglow emission results from the interaction of the jet with the surrounding circumburst medium (pink). Optical afterglow emission is observable on timescales up todays–weeks by observers with viewing angles of θobs ≤ 2. θj. Radio afterglow emission is observable from all viewing angles (isotropic) once the jet decelerates to mildly relativistic speeds on a timescale of weeks–months, and can also be produced on timescales of years from sub-relativistic ejecta. Short-lived isotropic optical emission lastingfew days (kilonova; yellow) can also accompany the merger, powered by the radioactive decay of heavy elements synthesized in the ejecta (Metzger & Berger 2012).*

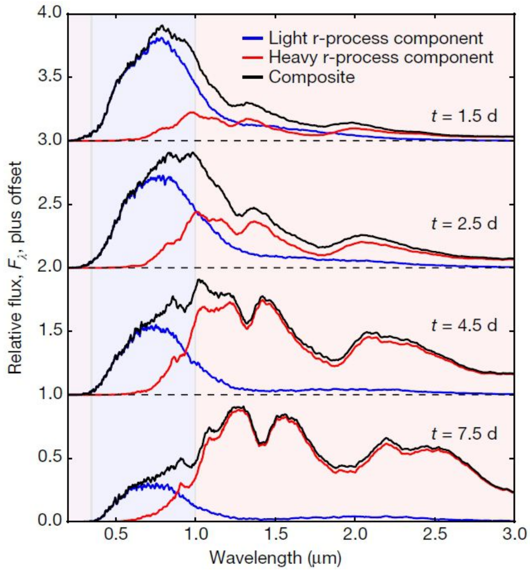

Figure 1.47: *A unified kilonova model explaining the optical/infrared counterpart of GW170817. The model is the superposition of the emission from two spatially distinct ejecta components: a 'blue' kilonova (light r-process ejecta with $M = 0.025M_\odot$, $V_k = 0.3c$ and $X_{lan} = 10^{-4}$) plus a 'red' kilonova (heavy r-process ejecta with $M = 0.04M_\odot$, $V_k = 0.15c$ and $X_{lan} = 10^{-1.5}$). Optical–infrared spectral time series, where the black line is the sum of the light r-process (blue line) and heavy r-process (red line) contributions (Kasen et al. 2017). Heavy r-process dominates the spectra after the first hours.*

Fast Rotation Nucleosynthesis Effects

- Production of quasi-primary ^{13}C at very low metallicities by massive stars, helping to understand the low ^{12}C/^{13}C ratio observed in halo stars (Chiappini et al. 2008).

- Production of large amounts of ^{14}N at low metallicity, from both rotating AGB and massive stars, via production channels that lose their effectiveness at higher metallicities (Meynet & Maeder 2002b), explaining the observed primary behaviour of N in the Galactic halo (Chiappini et al. 2006).

- Production of Galactic Cosmic Rays (GCR) mainly from the accelerated winds of massive stars, explaining the observed GCR excess of ^{22}Ne (Prantzos 2012a) and helping to understand the observed primary production of Be by GCR spallation (Prantzos 2012b).

- Production of substantial amounts of "light s-process nuclei" resulting from the weak s-process in massive stars which may help to understand the large dispersion of the "light/heavy" s-element ratio in halo stars (Cescutti et al. 2013). See Fig. 1.48.

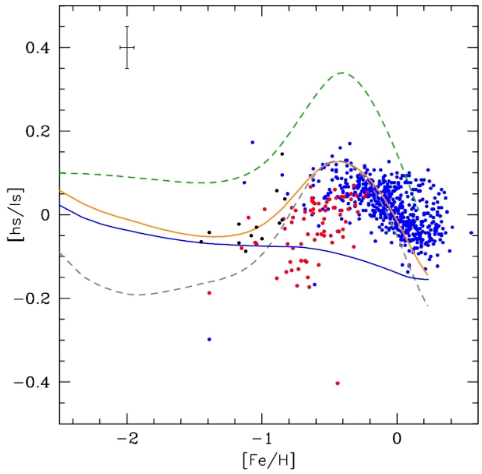

Figure 1.48: *Observed heavy-s (Ba, Ce, Nd) to light-s (Sr, Y, Zr) ratio [hs/ls] vs [Fe/H] compared with Prantzos et al. (2018) GCE model predictions. Observational data are from Delgado Mena et al. (2017) for thin (blue dots) and thick (red dots) disk stars. Black dots are the thick disk stars in Fishlock et al. (2017). Solid orange curve shows the prediction from Prantzos et al. (2018) baseline model, green dashed curve the one for the non-rotating massive stars, and gray dashed curve the non-rotating case where the r-component is not considered. The blue solid curve shows the prediction when the contribution from Low and Intermediate Mass Stars is omitted. From Prantzos et al. (2018).*

In the last years, the taking into account of this effect in nucleosynthesis yields term is changing the understanding the analysis of galactic chemical trends, in especial at early stages of the universe (see e.g. for K in Fig. 2.77 of Chapt. 2).

In addition, changing the understanding of nucleosynthesis sites of elements so important as e.g. carbon, traditionally thought to be mainly synthesized in LIMS/AGBs (up to 80% according to Mattsson 2010), but that however in the recent study by Romano et al. (2020), including fast rotators nucleosynthesis impact (Romano et al. 2019), is argued to be mainly produced, more than 60% of solar system carbon, by massive fast-rotators stars (see Sect. 2.2 about C element).

1.7. Galactic evolution models: thin-, thick-disks and halo stars

The three main stellar populations of the Milky Way in the solar neighborhood are the thin disk, the thick disk, and the halo (see Fig. 1.4). Thin and thick disks were firstly identified by Gilmore & Reid (1983). These two populations have different kinematics and chemical properties. Thick disk is thought to be composed of relatively older, metal-poorer and α-elements enhanced stars than with respect to the thin one (Adibekyan et al. 2013).

As observed in Fig. 1.27 from the Sect. 1.4, the α-element abundances are a good chemical proxy to identify stars belonging to one or another disk, showing a striking gap between the two populations, in addition to kinematic features.

Kinetically, differences are equally remarkable as shown in Toomre diagrams from HARPS sample (see Fig. 1.49). Thick disk population is kinetically hotter than the thin disk one. And even more for the stars from the halo with respect to both disk populations. This kinetically hotter behaviour has too its implication in the orbital eccentricity of the stars belonging to one or another disk, as shown in Fig. 1.50.

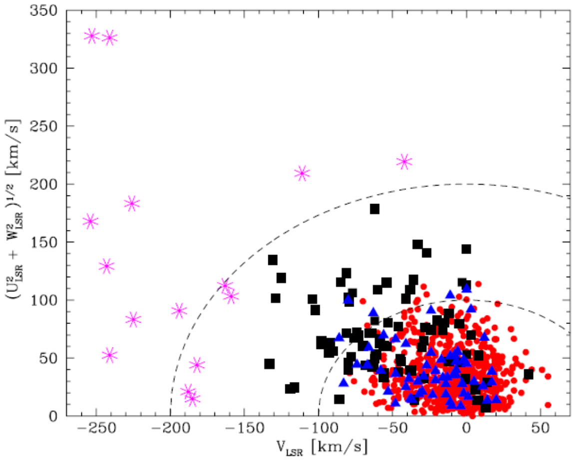

Figure 1.49: *Toomre diagram, kinematic information from HARPS FGK dwarfs sample. The black filled squares refer to the thick disk stars, blue triangles to the hαmr stars (high α metal rich), and the red dots to the thin disk stars. Magenta asterisks represent the stars belonging to the halo by their kinematics. From Adibekyan et al. (2013).*

These differential features, chemical and kinematics, seem to hint to a nature or evolutionary path different, for the halo, thick and thin disks. Several theoretical models try to explain the observed properties of the thick disk as consequence from the scattering or radial migration of stars by spiral arms (Sellwood & Binney 2002; Schönrich & Binney 2009; Schönrich & McMillan 2017; Roškar et al. 2012), where stars are transported outwards and gain vertical height above the galactic plane to form a thick disk. As well as from external heating processes such as accretion of stars from disrupted satellite dwarf galaxies (Abadi et al. 2003) or the thickening of a pre-existing thin disk through a minor merger events (Quinn et al. 1993; Villalobos & Helmi 2008) or other possibility, from in situ triggered star formation during/after gas-rich mergers (Brook et al. 2004, 2005).

Data from high resolution massive spectroscopic surveys (GAIA, APOGEE, GALAH, 4MOST, WEAVE) will help to understand the formation of thick disk whose rapid formation

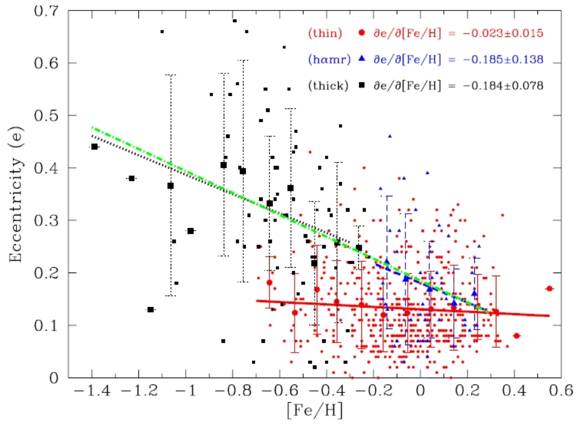

Figure 1.50: *Trends of eccentricities as a function of metallicity for stars assigned to different stellar populations. The black filled squares refer to the thick disk stars, blue triangles to the hαmr, and the red dots to the thin disk stars. The smaller symbols correspond to the real stars and the larger symbols present the eccentricities and standard deviations for each metallicity bin. The slopes are obtained for the unbinned data (green slope refers to hαmr trend). From Adibekyan et al. (2013).*

and old population means that it provides a detailed snap-shot of the conditions in the early Galaxy, becoming a seemingly ubiquitous feature of disk galaxy evolution (Duong et al. 2018).

Results, such as the lack of thick disk vertical metallicity gradient observed by Gilmore et al. (1995) and the observed orbital eccentricity distributions by Sales et al. (2009) and Dierickx et al. (2010), favoured merger scenarios (Duong et al. 2018), as argued by Helmi et al. (2018), supported from the GAIA kinematic and APOGEE α-chemical abundance observational data. Kinematics show (see Fig. 1.51) that a considerable fraction of the halo stars in the nearby neighborhood of the Sun are associated with a single large kinematic structure showing a slightly retrograde mean motion and dominating the blue sequence of the Hertzsprung–Russell diagram revealed in the Gaia data (Gaia Collaboration et al. 2018). On the other hand APOGEE survey has revealed that majority of the halo-retrograde structure is linked with a distinctive lower [α/Fe] index than thick disk and the large metallicity spread of the stars of the retrograde structure implies that they did not form in a single burst in a low-mass system (see Fig. 1.51).

These features have been argued as a proof of the inner halo to be dominated by debris from a merger with an object that at infall held a 1:4 mass ratio with respect to the Milky Way, and which the authors refer to as Gaia–Enceladus, contributing to the dynamical heating of the precursor of the Galactic thick disk and thus to its formation 10 Gyr years ago (Helmi et al. 2018).

Whatever the causes, the Galaxy Chemical Evolution (GCE) models (see Appendix A) assume an infall of primordial gas from outside the disk region. It is rather well established

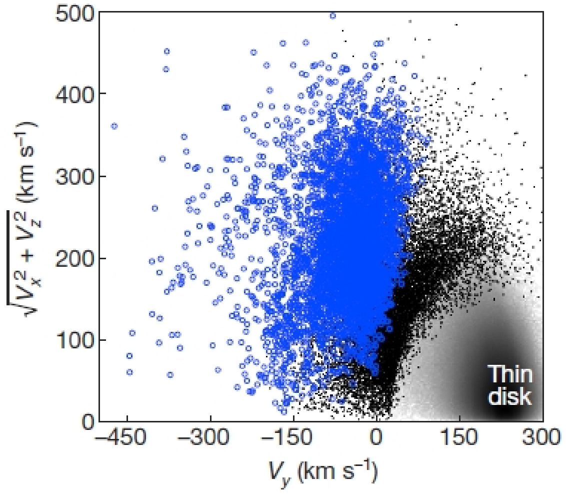

Figure 1.51: *Measured velocity distribution of stars in the solar vicinity. Velocities of stars in the disk are plotted with grey density contours (because of the large number of stars), and halo stars are shown as black points. The blue points are part of a prominent structure with slightly retrograde mean rotational. From Helmi et al. (2018).*

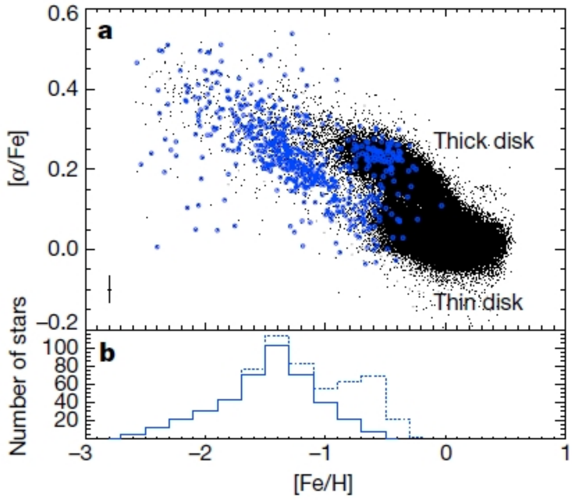

Figure 1.52: *Astrophysical properties of stars in Gaia–Enceladus. Chemical abundances for a sample of stars located within 5 kpc from the Sun, obtained from cross-matching Gaia and APOGEE data. Blue circles correspond to 590 stars, showing a clear separation between the thick disk and the sequence defined by the majority of the stars in the halo retrograde structure, except for a small amount of contamination (17%) by thick-disk stars (that is, in the α-rich sequence). In* ***b****, metallicity distribution of the retrograde structure without (with) the subset of α-rich stars. The distribution peaks at [Fe/H] $\simeq -1.6$ dex, as a reminiscence of the distribution of the stellar halo of the Galaxy. From Helmi et al. (2018).*

that the halo/thick disc and the thin disc components of the Galaxy were assembled on different time-scales (Mattsson 2010) and majority of models, usually employed on the analysis of chemical abundance trends (see next Chapt. 2 and 3 or Appendix A), assume it and are based on the "two-infall" chemical evolution model for the Milky Way halo and disks, originally developed by Chiappini et al. (1997, 2001) and their later evolution versions with improved or modified prescriptions. This model divides the Galactic disk into several concentric annuli 2 kpc wide that evolve independently, without exchanges of matter between them. The inner halo and thick disc are assumed to form fast, in less than 1 Gyr, out of a first episode of accretion of virgin gas. During these earlier evolutionary stages, the star formation proceeds very efficiently and turns a large fraction of the available gas into stars. Eventually, the critical gas density threshold is reached below which the star formation halts. Later, on a second infall episode, which is delayed 1 Gyr with respect to the previous one, starts replenishing the disc with fresh gas and star formation is reignited (Romano et al. 2020). The thin disc thence forms on longer timescales that are functions of the Galactocentric distance (Matteucci & Francois 1989).

Though an overall continuity in the vertical metallicity profile, two distinct α-enhancement tracks as a function of z (distance to galactic plane) observed by Duong et al. (2018, see Fig. 1.53), have some implications, in this direction, for the stars formation history in the galaxy.

Comparing models with respect to APOGEE data, Haywood et al. (2016) proposed that the star formation rate dropped significantly at ages of 10 Gyr before increasing again at about 7 Gyr to a lower maximum value. This could indicate the transition between thick to thin disk formation (Duong et al. 2018).

Thus, stellar ages seem to be an additional good separator between thin and thick disks, e.g. studies by Bensby et al. (2014) and Battistini & Bensby (2015) consider thick disk to consist of stars older than 9 Gyr and thin disk of stars younger than 7 Gyr. Relations between abundances of different elements, especially involving α-elements (e.g. see Sect. 2.14 about Ti element), and stellar ages are very used and useful for tracking the evolution of the galaxy formation.

Summarizing, observational data and theoretical models describe a complex and still not fully understood galaxy formation in which the galaxy components show a rich and differential chemical and kinematics features due to their likely different origins, time formation and evolution paths as the Fig. 1.54 shows.

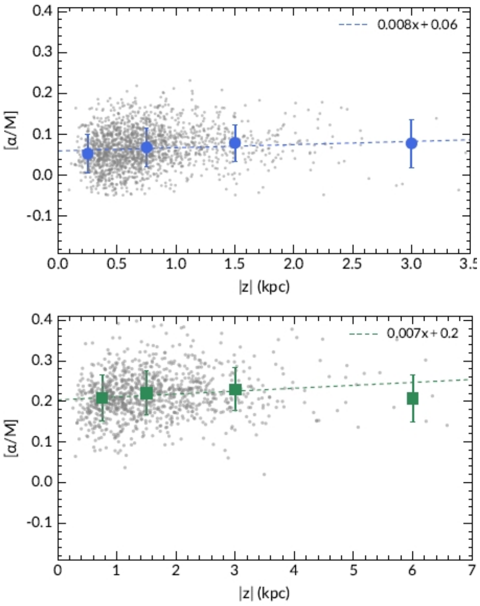

Figure 1.53: *Variation of [α/M] with distance from the galactic plane for each of the high and low-α population. Top panel: vertical abundance gradient for the low-α stars. Bottom panel: vertical abundance gradient of the high-α stars. Both populations show a flat-positive trend. The high-α population shows a higher dispersion in [α/M] values. The trends are fitted over grey data points, over-plotted are averaged values of four height bins and their one sigma error bars. The binned values were not used in the gradient fitting. From Duong et al. (2018).*

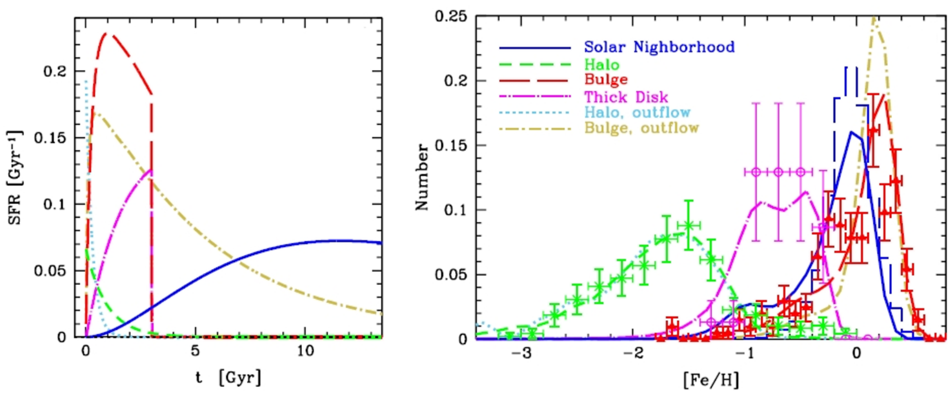

Figure 1.54: *Star formation histories (left), and metallicity distribution functions (right) for the solar neighborhood (blue solid lines), halo (green short-dashed lines), halo with stronger outflow (light-blue dotted lines), bulge (red long-dashed lines), bulge with outflow (olive dot-short-dashed lines) and thick disk (magenta dot-long-dashed lines). The observational data sources are: histogram, Casagrande et al. (2011); crosses, Chiba & Yoshii (1998); filled triangles, Zoccali et al. (2008); open circles, Wyse & Gilmore (1995). From Kobayashi et al. (2020a).*

Chapter 2

To the Iron...

Fusion of heavier elements needs of extreme conditions of pressure and temperature to exceed the electrostatic repulsion and bring closer nuclei so that the strong nuclear force begins to act. However, the fusion of increasingly heavier elements are less energetically favoured by two factors:

Firstly, the likewise increasing electrostatic repulsion by electronic shells leads to the need of more extreme temperatures and pressures for producing the fusion. Secondly, the binding energy released by fusion decreases for heavier isotopes (see Fig. 2.1). For heavier isotopes than ^{56}Fe the fusion is not energetically sustainable. Massive stars able to provide extreme conditions necessary to sustain silicon burning reach the terminal phase of the fusion possibilities, triggering the next chain reactions by α-particle capture:

Silicon Burning

2700-3500·10^6 K, ca 1 day

$$
\begin{aligned}
{}^{28}_{14}Si + {}^{4}_{2}He &\rightarrow {}^{32}_{16}S \\
{}^{32}_{16}S + {}^{4}_{2}He &\rightarrow {}^{36}_{18}Ar \\
{}^{36}_{18}Ar + {}^{4}_{2}He &\rightarrow {}^{40}_{20}Ca \\
{}^{40}_{20}Ca + {}^{4}_{2}He &\rightarrow {}^{44}_{22}Ti \\
{}^{44}_{22}Ti + {}^{4}_{2}He &\rightarrow {}^{48}_{24}Cr \\
{}^{48}_{24}Cr + {}^{4}_{2}He &\rightarrow {}^{52}_{26}Fe \\
{}^{52}_{26}Fe + {}^{4}_{2}He &\rightarrow {}^{56}_{28}Ni \\
{}^{56}_{28}Ni + {}^{4}_{2}He &\rightarrow {}^{60}_{30}Zn
\end{aligned}
$$

However, when the chain reaches the fusion of ^{56}Ni (unstable decaying to ^{56}Fe) the star runs out of nuclear combustible as the next fusion reaction to produce ^{60}Zn is energetically-demanding (see Fig. 2.1). Without the radiative pressure provided by fusion reactions, the core and the entire star begins to contract, it is entering the last few seconds of its lifetime before the core-collapse and the ejecta as supernova (SNeII).

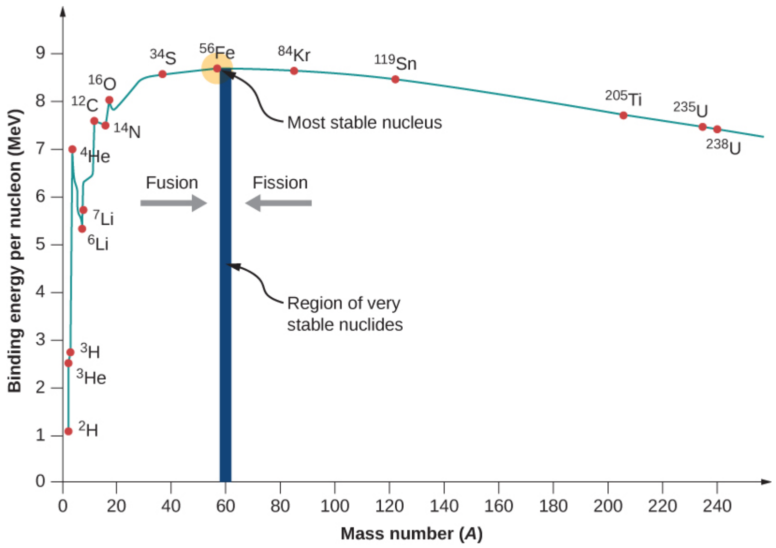

Figure 2.1: *Energy binding per nucleon. From ^{56}Fe production by fusion is energetically-demanding and not sustainable.*

Hence, some lighter elements than Fe are mainly produced by burning phases in massive stars (< 8 M$_{\odot}$) before SNeII explosion. Very favoured by this nucleosynthesis site are the α-elements as O, Mg, Si, S, Ca and Ti. Their theoretical models are generally confirmed by galactic chemical evolution distributions in spite of some remaining uncertainties (as example see abundances against metallicity diagrams and models of Fig. 2.42, 2.63, 2.72 and 2.83 respectively for O, Si, S and Ca).

They show a typical profile indicating their enrichment in an early universe (see Fig. 1.27) where this mechanism was predominant over the thermonuclear SNeIa production by a time evolution delay (Edvardsson et al. 1993) between SNeII (core-collapse of massive stars, quicker evolution) and the SNeIa that need more time to evolve the companions of the binary system.

The SNeIa will be the second contribution to elements lighter than Fe (and some heavier ones), especially favouring the iron-group elements production as V, Cr, Mn, Fe, Co, Ni, Zn. Nevertheless, each element presents their own peculiarities and some uncertainties remains about the main nucleosynthesis sites for some of them (see every element section).

Two key elements for life and very light ones as C and N (and Li) are mainly thought to be produced in the last burning phase of the low- and intermediate-mass stars (LIMS), in AGB stars, by triple-α reaction (He burning) and the CN cycle. However, the importance of fast rotating massive stars to nucleosynthesis is becoming increasingly clear. Especially during the early stages of the universe when they were more frequent. Even so, more work will remain necessary to constrain their net contribution (see C element in Sect. 2.2).

The ^{12}C abundance as progenitor of the ^{13}C pocket, will be key for the production of heavier elements than Fe in AGBs by main s-process neutron capture (three stable s-peaks of elements) as Y, Sr, Zr, Nb, Mo, Ba, La, Ce, Pr, Nd and Pb but also being an important contribution to other heavy isotopes.

Oxygen is equally produced in AGB stars as a side-product (by α-capture particle) of the ^{12}C production (by triple-α reaction from He) but it will be mostly produced in burning phases of massive stars preceding to the SNeII explosion similar to the other α-elements, with higher yields in very massive stars > 15 $M_{\odot}$, enriching the ISM at very early stages of the universe.

The nucleosynthesis of Be, B and partially Li is a special case. These elements are not produces by stellar nucleosynthesis as they are easily destroyed inside stars. The main mechanism is spallation by cosmic rays, with a small contribution of spallation by supernovae neutrinos (Vangioni-Flam & Cassé 1999; Vangioni-Flam et al. 2000). Nevertheless, these elements will not be included in this work because the absence of relevant optical lines.

2.1. Lithium ($_3$Li)

Determination of the origins and contribution of nucleosynthesis sites to the lithium abundances is likely the most challenging from all the elements of the periodic table (Miller 2015).

At least three different processes are likely to contribute to their abundances:

Lithium Nucleosynthesis Sites

- Primordial big bang nucleosynthesis (SBBN, see Fig. 2.2).
- Spallation of galactic cosmic-ray particles on interstellar matter nuclei (GCR).
- Stellar nucleosynthesis (HBB in AGBs).

Theoretical study supports that the GCR nucleosynthesis is accelerated as consequence of forward shocks of supernova explosions, propagating through the winds of massive stars and the ISM (Prantzos 2012b) although other scenarios are proposed (see Fig. 2.3).

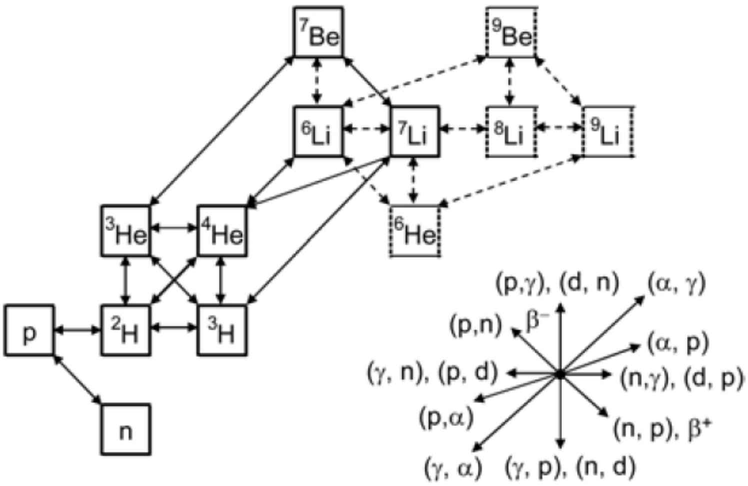

Figure 2.2: *Reaction network for Big Bang Nucleosynthesis (BBN). From Li et al. (2011).*

On the other hand, stellar nucleosynthesis is a controversial matter. Charbonnel & Balachandran (2000) linked the enrichment episodes of Li with extra-mixing episodes in the early AGB of intermediate mass giants and the bump phase in the RGB ascend (see Fig. 1.7 in Chapt. 1) of the low mass Red giants.

The enrichment in intermediate AGB stars develops by Hot Bottom Burning (see

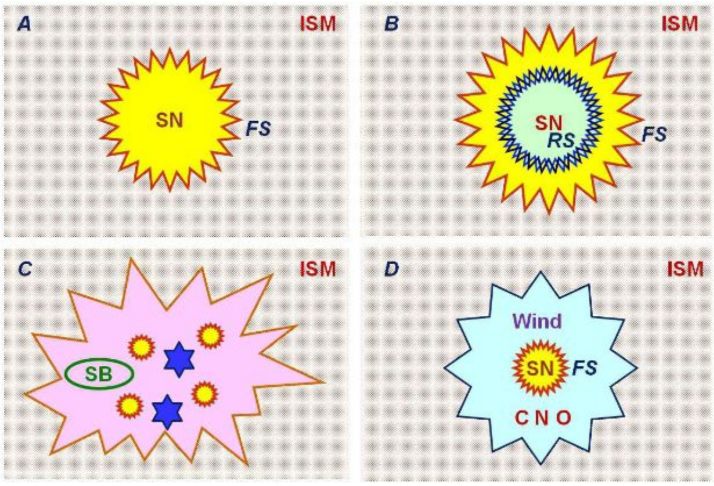

Figure 2.3: *Scenarios for the origin of GCR.* ***A:*** *GCR originate from the interstellar medium (ISM) and are accelerated from the forward shock (FS) of SN.* ***B:*** *GCR originate from the interior of supernovae and are accelerated by the reverse shock (RS), propagating inwards.* ***C:*** *GCR originate from superbubble (SB) material, enriched by the metals ejected by supernovae and massive star winds; they are accelerated by the forward shocks of supernovae and stellar winds.* ***D:*** *GCR originate from the wind material of massive rotating stars,always rich in CNO (but not in heavier nuclei) and they are accelerated by the forward shock of the SN explosion. From Prantzos (2012b).*

Sect. 1.3) via Cameron-Fawler mechanism (Cameron & Fowler 1971; Ventura & D'Antona 2010). The convective layer enters the H-burning shell providing the means to bring the fresh Li to the surface.

Cameron-Fawler Mechanism

$^{3}He +^{4} He \rightarrow^{7} Be \rightarrow^{7} Li$

Nevertheless both, ^{7}Be and ^{7}Li are easily destroyed inside the stars at relatively low temperatures (2.5-2.6·10^6 K) by proton captures (Travaglio et al. 2001b; Silva Aguirre et al. 2014):

Beryllium and Lithium destruction

$^{7}Be + p \rightarrow^{8} B \rightarrow ...$
$^{7}Li + p \rightarrow 2\,^{4}He$

The basic idea of the Cameron-Fawler mechanism is the use of convection to remove ^{7}Be from hot region before it can complete the PP chains destroying beryllium, so that later lithium can be formed by disintegration.

The mechanisms of Li enrichment observed in some low mass Red Giants seem more complex and remain unclear. Once the star abandon the main sequence stage, Li abundance is expected to decrease due to the inward penetration of the convective envelope during the FDU (Salaris et al. 2002; Lagarde et al. 2012). Nevertheless, about 1–2% of the known giants have been found to be rich in Li (Brown et al. 1989; Kirby et al. 2016; Casey et al. 2016). As above mentioned, Li nuclei are easily destroyed via proton capture. This happens to temperatures exceeding $\sim 2.6 \cdot 10^6$ K. An extra mixing mechanism is required to produce Li and lift it to the surface before it is destroyed in a reaction with protons of the medium at this temperature (Smiljanic et al. 2018).

It is unclear how this mixing develops although some mechanisms have been proposed as the "cool-bottom processing" by Sackmann & Boothroyd (1999) and linked to the bump in the RGB ascend as above mentioned by Charbonnel & Balachandran (2000). Nevertheless, the lithium enhancement in the bump phase (extremely short lived) should quickly deplete before the stars reach the RGB tip (Silva Aguirre et al. 2014). However, Li-rich giants have been observed at different luminosities along the RGB. And on the other hand, some Li-rich giants were found to be instead core He-burning giants (da Silva et al. 2012; Kumar et al. 2011; Monaco et al. 2014). This suggests a different scenario triggered by non-canonical mixing at the RGB tip, maybe related with the core helium ignite (Silva Aguirre et al. 2014).

Li enhancement alternative mechanisms during RGB ascend have been proposed. By Denissenkov (2012), due to fast internal rotation that produces an enhanced mixing across the radiative zone. Or connected to a phase of enhanced mass loss in K-type Giant stars by de la Reza et al. (2015).

Or as a result of an external pollution. Some authors, e.g. Aguilera-Gómez et al. (2016); Delgado Mena et al. (2016); Reddy & Lambert (2016), have proposed the engulfment of close planets or planetesimals before evolving up the RGB to explain the Li-rich giants. The location in HR diagram of Li-rich giants observed within the Gaia-ESO Survey seemed to be consistent with this scenario. However, expected engulfment signatures as the enrichment in other light elements as ^{6}Li and Be have never observed. The complexity of the evolutionary mixing events affecting Li and other elements might prevent the discovery of clear abundance signatures related to planet engulfment (Smiljanic et al. 2018).

In addition, other nucleosynthesis sites are proposed to the mentioned:

Additional Lithium Sources

- Thermonuclear novae SNeIa with explosive nucleosynthesis in the He layer accreted onto the white dwarf (Hernanz et al. 1996).
- Core collapse supernovae SNeII, helped by the neutrinos of the explosion producing ^{3}He through excitation and subsequent de-excitation of the ^{4}He (α particles) in the He shell, named ν-process (Woosley et al. 1990).

Recently, signatures of lithium production (radiactive ^{7}Be$^+$ line resonances in near-UV) have been found in one studied SNeIa (Miller 2015), hinting a production of 3 to 10 times larger than models predict for SNeIa. This shows that more work will remain necessary to constrain yields of the proposed nucleosynthesis sites.

2.1.1 Chemical galactic evolution abundances

The stellar abundance studies increases the uncertainties about the nucleosynthesis origins of lithium (see Fig. 2.4).

From the striking homogeneity of the stars abundance, from the early universe to metallicity ca [Fe/H]= -1.0 dex, it is assumed that it corresponds to the primordial ^{7}Li production by the Big Bang nucleosynthesis (Travaglio et al. 2001b).

The Fig. 2.4 shows this plateau of abundance mainly found in the halo star population (population II). It is known as the Spite plateau, named after the astronomers who published the discovery (Spite & Spite 1982).

However, in the same figure, is shown the theoretical prediction by the Standard Big Bang nucleosynthesis model (SBBN, solid green curve). It corresponds to the cosmic baryon density provided by WMAP results (Steigman 2010; Iocco et al. 2009). And do not match with the observational abundance found in old stars. There is evidently a gap between the primordial estimation of ^{7}Li by SBBN which is 3 times higher than the stellar abundances at the Spite plateau.

Stellar photospheric abundances in the Spite plateau most probably do not reflect the true value of ^{7}Li in the gas clouds from which the halo stars were formed. This is because the depletion processes of Li, so far poorly understood.

And the same probably holds for disk (thin or thick) stars (Prantzos 2012b). In the Fig. 2.4 are likewise included the theoretical model predictions that correspond with some of the above mentioned additional nucleosynthesis sources:

- ν-process from SNeII (in dashed blue).
- HBB in AGBs + Low mass RG + SNeIa (in dashed pink).
- GPR spallation of ^{7}Li and ^{6}Li (dot dashed and dotted brown).

They do not have a striking contribution but at high metallicity (ca [Fe/H]>-1.0), belonging to stars of the disks (thick and thin) populations. Like in the halo stars abundances, remains a gap between the total Li abundance predicted by models and the observational abundance data derived from disks stars (Lambert & Reddy 2004), shown as green dots.

Models by Prantzos (2012b) estimate around a 30% accounted for by Big Bang nucleosynthesis (SBBN) and cosmic-ray spallation (GCR), 20% core-collapse supernova (SNeII) and 50% for the rest of sites: ν-nucleosynthesis, novae SNeIa and AGBs (hot bottom burning, HBB).

However, it is difficult to get a full understanding of Li nucleosynthesis and the observed galactic chemical evolution trend. This is due to the uncertainties in yields of the different nucleosyntheis mechanisms, combined with poorly understood depletion mechanisms.

As initially commented, lithium nucleosynthesis remains like the most challenging and mysterious from all the elements of the periodic table.

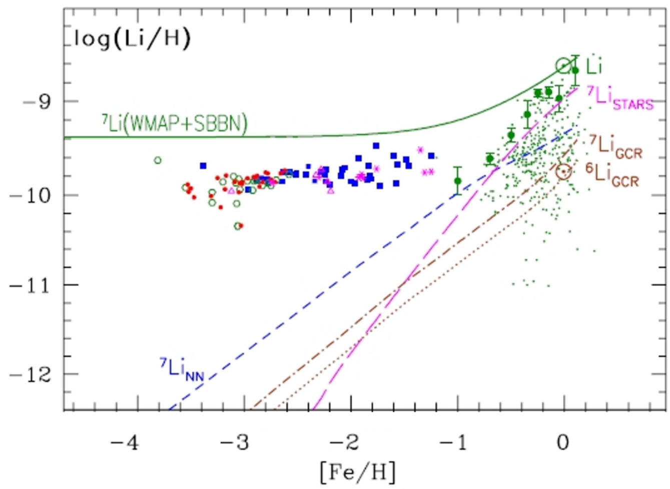

Figure 2.4: *Abundance data for halo stars are taken from Charbonnel & Primas (2005) (filled squares), Sbordone et al. (2010) (filled circles), Bonifacio et al. (2007) (open circles), García Pérez et al. (2009) (open triangles), Asplund et al. (2006) (asterisks) and for disc stars from Lambert & Reddy (2004) (green dots). In the latter case, points with error bars indicate the average values of the six most Li-rich stars in the corresponding metallicity bins.*
Evolution of Li according to one of the models by Prantzos (2012b): ^{7}Li from GCR (dot-dashed), ^{6}Li from GCR (dotted), ^{7}Li from ν-nucleosynthesis (NN,dashed) and ^{7}Li from a delayed stellar source (novae and/or AGB stars,long dashed). Solid curve indicate total and primordial Li (SSBN, Standard Big Bang nucleosynthesis tested by WMAP, cosmic microwave background anisotropy measurements). Credit: Adapted from Prantzos (2012b).

2.2. Carbon ($_6$C)

Carbon is one of the most common elements that can be found in just about any astrophysical environment (Mattsson 2010).

The triple-α reaction (Salpeter 1952) is the main source of carbon in low and intermediate-mass AGB-Carbon (C) stars (see Fig. 1.9 and section 1.3). The envelope mass loss during the TP-AGB and Post-AGB enriches the interestellar medium in C-based chemicals (see Fig. 1.10 and 1.11).

Nevertheless other nucleosynthesis site has been suggested: Maeder (1992) proposed that radiatively driven winds from high mass stars should provide huge amounts of carbon, becoming the main C source.

Chemical evolution models from recent works deepen the uncertainty about the balance of the nucleosynthesis sites yields, leading to opposite conclusions. Meanwhile the Mattsson (2010) models assume that the low and intermediate-mass stars provide at least 80% of the carbon to the interstellar medium (ISM). Contrary, the study by Romano et al. (2020) concludes than more of 60% of the solar C abundance comes from massive stars (fast rotators/spinstars) with especial relevance in an early universe and galactic formation when they were more frequent (see Fig. 2.12 by Prantzos et al. 2018 as an example of prescription about rotational velocities in function of metallicity).

Hence, a full understanding of the galaxy C evolution (see Sect. 2.2) has not been reached and will need additional observations to constrain models.

2.2.1 Carbon evolution in low and intermediate masss stars: from MS to AGB

In Fig. 1.8 of Sect. 1.3, by Gratton et al. (2000) was shown the carbon abundance changes and evolution on the photospheric layer once the star evolves off the main sequence, going through the First Dredge-Up in the low-RGB to the Horizontal Branch stage (RHB).

The net yield of the whole evolution is a depletion of the carbon abundance on surface, when FDU and specifically the Bump take place. This differentiates the lower- from the upper-RGB phase. The trend holds until the Horizontal Branch stage.

However, the helium burning (AGB phase) and thermal pulses will change that trend. This can be observed in the C/O evolution in the models of Abia et al. (2017, see Fig. 2.5).

Another remarkable change has to do with the ^{12}C/^{13}C isotopic ratio on the photospheric surface layer. After FDU and bump on the low-RGB, the mixing produces the depletion of total carbon (mostly ^{12}C) on surface but conversely an increment of ^{13}C is noted due to the freshly processed material by the CNO cycle (see Sect. 1.1 and Fig. 1.3) from inner layers around the core, later mixed up on the surface (see Fig. 2.6).

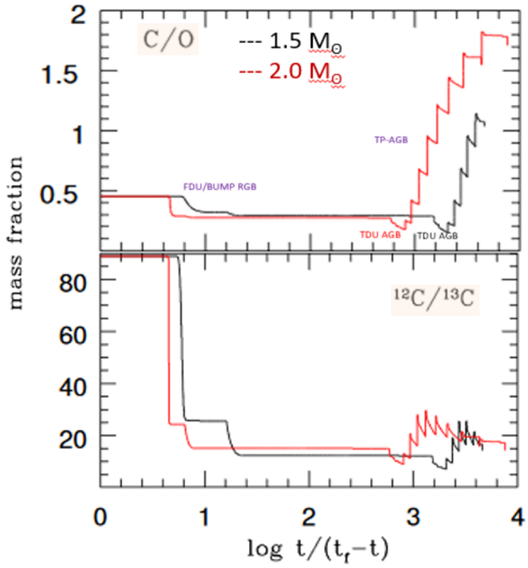

Figure 2.5: *Evolution up to the AGB tip from RGB, of C/O and $^{12}C/^{13}C$ isotopic ratios in models with 1.5 $M_{\odot}$(black line) and 2 $M_{\odot}$(red line). Evolutionary timescale has been re-scaled to the final time (tf) in the computation time (2.91 and 1.196 Gyr respectively). The first dredge-up occurs at log t/(tf-t) ~ 0,9 (1.5 $M_{\odot}$) and 0,6 (2 $M_{\odot}$), while the RGB bump takes place at log t/(tf-t) ~ 1,2 and 0,8 respectively. The combined actions of the third dredge-up and the AGB extra mixing arise at log t/(tf-t) > 3,2 and 2,8. Adapted from Abia et al. (2017).*

As consequence, the $^{12}C/^{13}C$ ratio dramatically decreases from 90 to usual values < 20. Even lower than 10, approximately, in metal-poor RGB stars (see Fig. 2.5). This ratio will increase in the AGB stage due to the triple-α reaction of helium which produces C. This gets transferred to the surface by the TDU episodes during the TP-AGB. So that this isotopic ratio may be observed as a proxy of the evolution along the AGB lifetime (Abia et al. 2017).

2.2.2 Carbon evolution in low and intermediate mass stars: AGB

As above commented in Sect. 1.3 of Chapt. 1, AGB stage (low and intermediate mass stars) triggers He shell burning by triple-α reaction (see Fig. 1.9) as an additional nucleosynthesis mechanism mainly producing ^{12}C and ^{16}O as a byproduct.

Once the helium exhausts in the core and helium burning transits to the shell around a

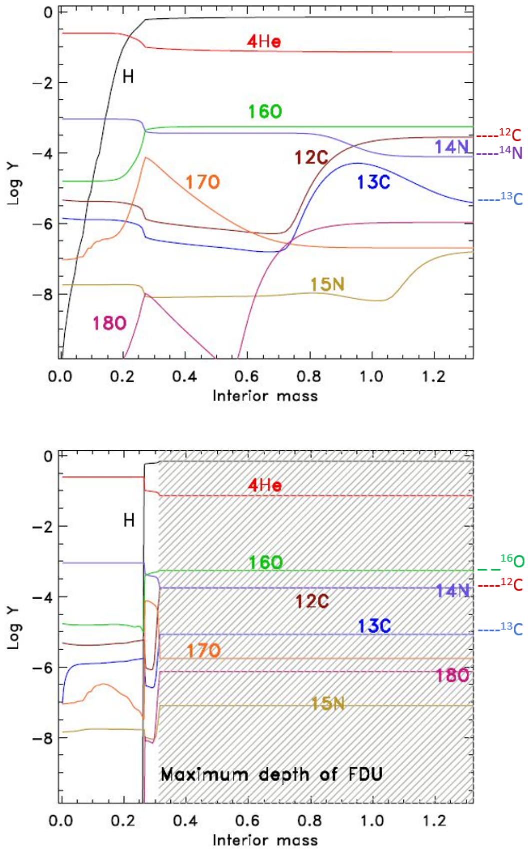

Figure 2.6: *Isotopic abundances along a 2 $M_\odot$ and Z = 0.02 star. Upper pannel, after MS but previous to FDU; lower, after FDU in low-RGB phase. Decreasing of -0.1/-0.2 dex in ^{12}C, increasing of +0.4/+0.5 dex in ^{13}C and +0.2/+0.3 in ^{14}N. ^{16}O, not appreciable change. Adapted from Karakas & Lattanzio (2014).*

degenerate C/O core the instability triggers thermal pulses. The H shell burning remains jointly taking place or in turns with the He shell burning. Convective streams produce the mixing through layers and material that will trigger the nucleosynthesis of new elements. They will emerge to the surface due to the Second and Third Dredge-Up (SDU & TDU). The carbon formed in the intershell region (about 22%, see Fig. 1.13) will be key for giving place to the main s-process nucleosynthesis by neutron capture (see Sect. 1.3 in Chapt. 1). The successive thermal pulses, will enrich the surface in carbon (and the main s-process elements), becoming a carbon star (see Fig. 2.9).

The large-scale convective flows bring newly formed chemical elements to the stellar surface and, together with pulsations, trigger shock waves in the extended stellar atmosphere. There, massive outflows of gas and dust have their origin, which enrich the interstellar medium and, eventually, lead to a transformation of the cool luminous giants into white dwarfs. Dust grains forming in the upper atmospheric layers (see Fig. 2.7) play a critical role in the wind acceleration process, by scattering and absorbing stellar photons and transferring their outward-directed momentum to the surrounding gas through collisions (Höfner & Olofsson 2018).

C-rich stars are the origin to SiC and graphite dust condensates forming in the dynamical atmosphere. While O-rich AGB stars, M (C/O<1) and S (C/O~1) spectral classes, are parents to oxides and silicates dust condensates (Abia et al. 2017; Lodders & Fegley 1995).

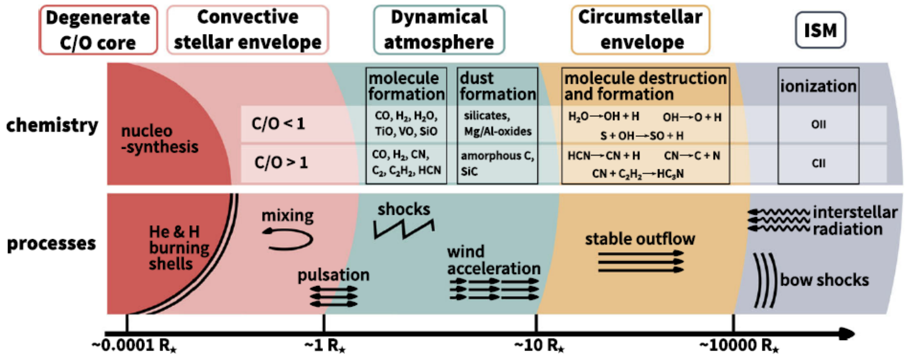

Figure 2.7: *Schematic chemical structure of the circumstellar environment of an AGB star enriching the medium with chemicals by mass loss winds. From Höfner & Olofsson (2018).*

The envelope mass loss during the Post-AGB enriches the interestellar medium in these C- and O-based chemicals (see Fig. 2.7, 2.8, 1.11 and 1.12).

However, the chemical composition and physical conditions of dust and gas seen in the AGB circumstellar envelope are found to be different from what is observed in the ISM. Several processes related to dust formation, shock-induced chemistry, or photodissociation by cosmic rays, are known to play a role in this transition (Hillen 2013).

Meanwhile the naked degenerate C/O core becomes the progenitor of the dying white dwarf.

2.2.3 Chemical galactic evolution abundances

As mentioned in the introduction, the nucleosynthesis sites balance is still a controversial issue. Historically, low- and intermediate-mass AGB stars have been considered the main nucleosynthesis site of the carbon abundances, up to 80% according to Mattsson (2010, see Fig. 2.10).

However, some recent studies by Prantzos et al. (2018) and Romano et al. (2020) point to a higher contribution of massive stars (fast rotators/spinstars) for explaining galactic chemical evolution and the different populations of thin-, thick-disks and halo stars in function of metallicity. The higher contribution from massive stars at very low metallicity

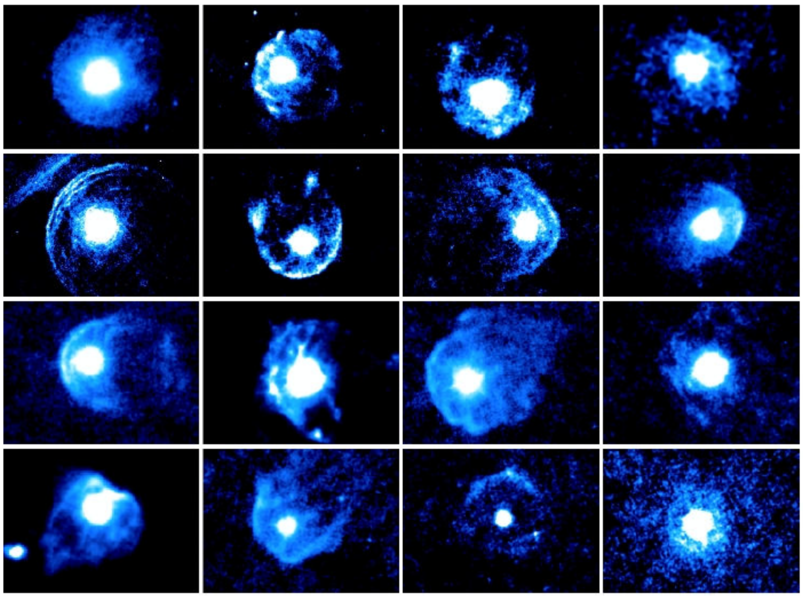

Figure 2.8: *HERSCHEL/PACS images of the ISM/CSE (Circumstellar envelope) interaction seen around many mass-losing AGB and red supergiant stars. Included in PhD thesis by Michel Hillen* `https://lirias.kuleuven.be/retrieve/236997`*, figure courtesy N.Cox.*

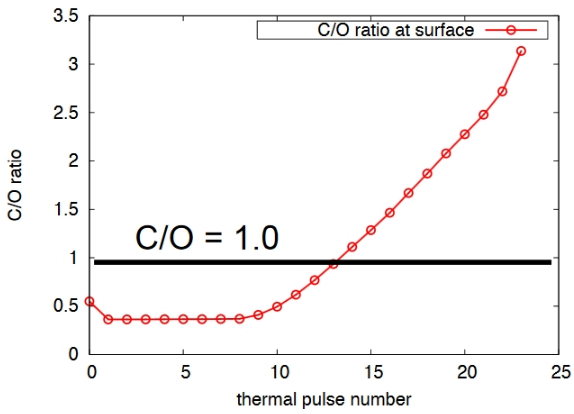

Figure 2.9: *C/O ratio increasing with every Thermal Pulse in TP-AGB phase. If the ratio C/O>1 is becoming a carbon star (C), if =1 M star, if < 1 a oxygen-rich star (M) usually by Hot Bottom Burning process in intermediate mass stars (see Sect. 1.3).*

already was a possibility argued by Maeder (1992) and Chiappini et al. (2006).

The models of the recent study by Romano et al. (2020) fit satisfactory to the abundance distribution in the Galaxy when is assumed an abrupt transition occurring between a regime that favours the formation of massive fast rotators at low metallicities (early universe in halo and thick disk stars), and a regime that mostly leads to slowly- or non-rotating stars

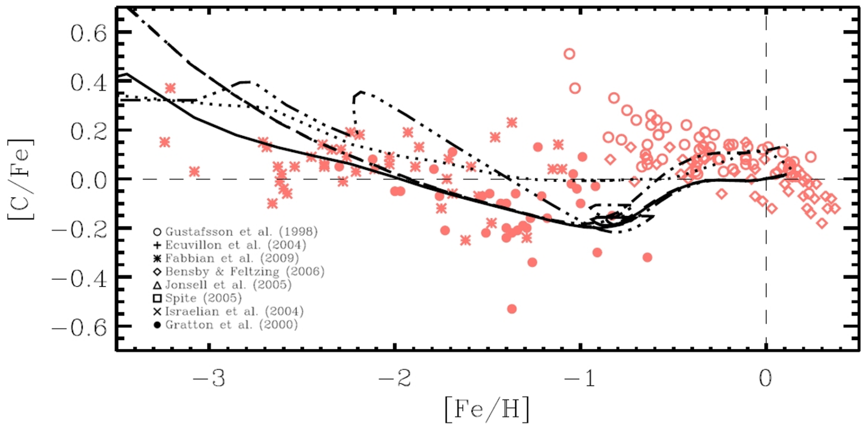

Figure 2.10: *Chemical galactic evolution abundances from some studies. Including thin, thick disk and halo stars. Adapted from Mattsson (2010). Lines referred to C chemical evolution models in the paper.*

above [Fe/H] = -1.0 (Romano et al. 2019). This way, higher abundances would be expected at early galactic stages due to the higher presence of very massive fast rotators. A source that decreases over time (see Fig. 2.12, based on the Prantzos et al. 2018 models and their rotational velocities assumptions as example).

The decreasing C trend due to the lower presence of massive fast rotators is balanced by the C supply from AGBs. As it happens in the different α-elements trends, the abundance profiles are impacted by the increasingly enrichment of the ISM by the SNeIa production, from [Fe/H]~ -1 to nowadays. However, the SNIa nucleosynthesis is rich in some Fe-peak group elements but not efficient in C, unlike AGBs.

The Fe increase through SNeIa at higher metallicities is balanced by C production from long lived AGB/LIM stars (Prantzos et al. 2018). However, the net result of their relation [C/Fe] shows a decay in this metallicity range due to the increasing impact of the SNeIa and their C-poor, Fe-rich production.

Another factor that determines the abundance trend of C within this metallicity range (as for the rest of elements) is the galaxy formation of the disks stars populations: thin and thick disks (see Sect. 1.7 in Chapt. 1). It is rather well established that the halo/thick disk and the thin disk components of the Galaxy were assembled on different time-scales (Mattsson 2010). Thick disk is thought to be composed of relatively older, metal-poorer and α-elements enhanced stars than with respect to the thin one (Adibekyan et al. 2013).

The differential features, chemical and kinematics (see Fig. 1.27 and 1.49 in Chapt. 1), seem to hint to a nature or evolutionary path different, for the halo, thick and thin disks. Several theoretical models try to explain the observed properties of the thick disk as consequence from the scattering or radial migration of stars by spiral arms (Sellwood &

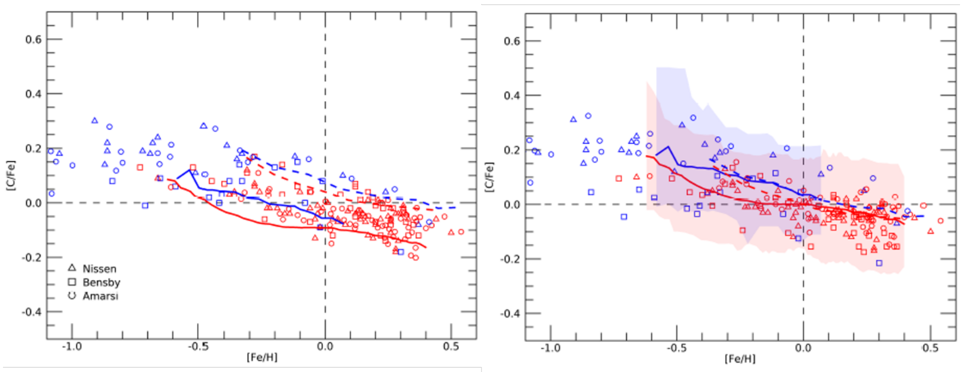

Figure 2.11: *Carbon-to-iron abundance ratios as functions of [Fe/H] in the solar neighbourhood, thin and thick disk stars.*
Left panel*: The red and blue symbols represent abundance estimates from targeted observations of thin- and thick-disc stars, respectively (triangles correspond to Nissen et al. 2014; the squares correspond to Bensby & Feltzing 2006; the circles correspond to Amarsi et al. 2019b).*
The red and blue lines represent trends of abundance ratios of thin- and thick-disc stars, respectively, which were derived from: (i) nearly 1300 thin-disc and 100 thick-disc dwarf stars from GES iDR5 (Gaia), which were selected on the basis of chemical criteria (continuous lines; Franchini et al. 2020); (ii) more than 12 000 stars from GALAH DR2, divided into high-Ia and low-Ia sequences (dashed lines; Griffith et al. 2019). No zero-point offsets were applied to the data.
Right panel*: Same, but zero-point offsets (see text) were applied to the data so that thin-disc stars with [Fe/H]=0 also have a solar chemical composition ([C/Fe]=0). Pale red and blue areas show the spread in thin- and thick-disc GES data (Gaia) within boundaries corresponding to the 10th and 90th percentiles. Adapted from Romano et al. (2020).*

Binney 2002; Schönrich & Binney 2009; Schönrich & McMillan 2017; Roškar et al. 2012), where stars are transported outwards and gain vertical height above the galactic plane to form a thick disk. As well as from external heating processes such as accretion of stars from disrupted satellite dwarf galaxies (Abadi et al. 2003) or the thickening of a pre-existing thin disk through a minor merger events (Quinn et al. 1993; Villalobos & Helmi 2008) or other possibility, from in situ triggered star formation during/after gas-rich mergers (Brook et al. 2004, 2005) (Duong et al. 2018).

The "two-infall" model was firstly developed by Chiappini et al. (1997, 2001). Their formalism is an approach of the galaxy evolution based on the premise that components of the Galaxy were assembled on different time-scales and suggesting some separation in time between the disks formation. This model divides the Galactic disk into several concentric annuli 2 kpc wide that evolve independently, without exchanges of matter between them. The inner halo and thick disk are assumed to form fast, in less than 1 Gyr, out of a first episode of accretion of virgin gas. During these earlier evolutionary stages, the star formation proceeds very efficiently and turns a large fraction of the available gas into stars. Eventually, the critical gas density threshold is reached below which the star formation halts. Later, on a second infall episode, which is delayed 1 Gyr with respect to the previous one, starts replenishing the disc with fresh gas and star formation is reignited (Romano et al. 2020). The thin disc thence forms on longer timescales that are functions of the Galactocentric distance (Matteucci & Francois 1989).

Some later models have updated and evolved their assumptions. Either the original or evolved models, are used extensively in GCE studies of elements as e.g. the C by the mentioned Mattsson (2010) and Romano et al. (2020).

Nevertheless, a numerous alternative prescriptions and galaxy formation approaches are used in the GCE models. Some times according to the study purpose. As an example, the mentioned galaxy chemical evolution study by Prantzos et al. (2018) from C to Pb, uses a simple one-zone model by Goswami & Prantzos (2000). They argue to be fully aware that the adopted model reflects poorly the physical processes in the halo, thick and thin disks. However it is enough for their purpose, to test the implications of a new grid of stellar yields from rotating massive stars (Prantzos et al. 2018).

The recent proposed GCE models for elements from C to U by Kobayashi et al. (2020a) follow a different approach. Nevertheless, whatever the model used, it is assumed a distinct formation and chemical evolution of the halo, and the thick and thin disks. This is observed in the Fig. 2.13 that shows the star formation history and metallicity distribution functions of the galaxy components based on observational data.

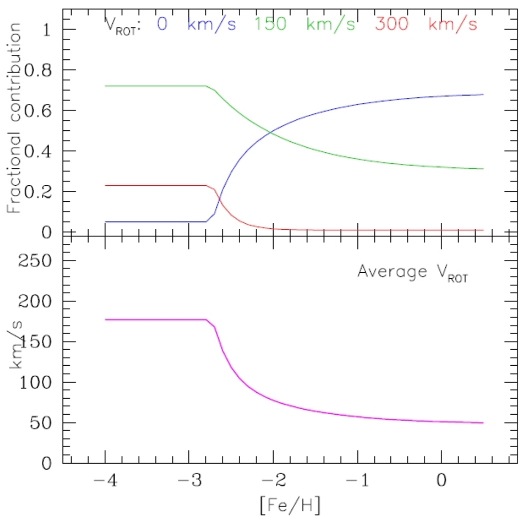

Figure 2.12: ***Top***: *Adopted fractional contribution with metallicity of the yields of rotating massive stars.* ***Bottom***: *Resulting average initial rotational velocity of massive stars as a function of metallicity. From Prantzos et al. (2018).*

In the Fig. 2.14 by Prantzos et al. (2018) models are quite coincident considering or not the rotating component assumptions along the galaxy evolution. Nevertheless, the rotating

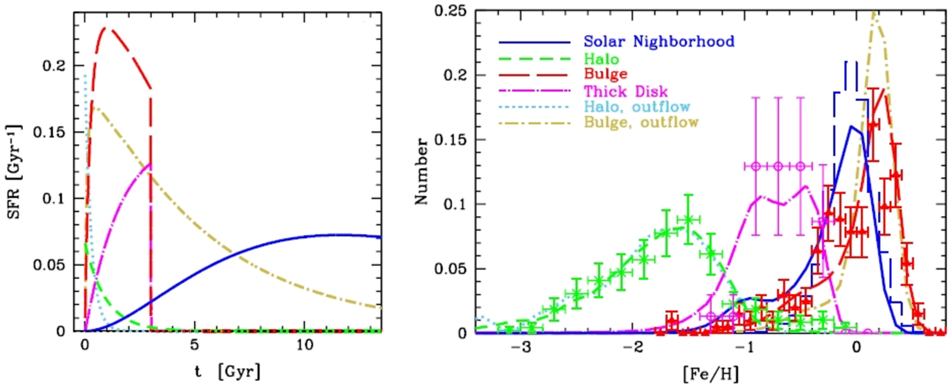

Figure 2.13: *Star formation histories (left), and metallicity distribution functions (right) for the solar neighborhood (blue solid lines), halo (green short-dashed lines), halo with stronger outflow (light-blue dotted lines), bulge (red long-dashed lines), bulge with outflow (olive dot-short-dashed lines) and thick disk (magenta dot-long-dashed lines). The observational data sources are: histogram, Casagrande et al. (2011); crosses, Chiba & Yoshii (1998); filled triangles, Zoccali et al. (2008); open circles, Wyse & Gilmore (1995). From Kobayashi et al. (2020a).*

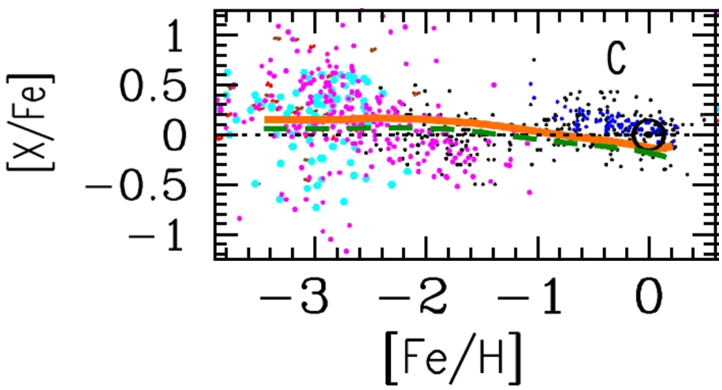

Figure 2.14: *Evolution of abundance ratio [C/Fe] as a function of [Fe/H] and comparison to observational data. Prantzos et al. (2018) model from massive (2/3) and AGB/LIMS (1/3) stars productions is in solid green curve; the same model but with enhanced C yields from rotating massive stars is in orange curve. Observational data from Yong et al. (2013), Roederer et al. (2014a) and Lai et al. (2008) based on LTE assumptions. From Prantzos et al. (2018).*

yields assumption improves the fit. There is to remember that this study is not specifically develop for C but for the most of the periodic table elements and on the other hand it is adopting a simpler galaxy formation model (one-zone by Goswami & Prantzos 2000) in order to test the impact of rotating yields on the elements models fits.

What it might be more significant, both models by Prantzos et al. (2018) (assuming rotating yields or not) are based on a 2/3 contribution from massive stars and 1/3 from

LIMS/AGB. This is a change on the perspective over the traditional expected contributions from these nucleosynthesis sources. Even the LIM/AGB stars contributions should be considered as an upper limit since the authors have not included net yields from stars in the mass range 7-10 $M_\odot$. These stars may undergone hot hydrogen burning at the base of the convective envelope (HBB) at the end of their evolutionary phase (the super-AGB phase) and, in consequence, they may deplete ^{12}C and produce some ^{14}N.

The Fig. 2.15 shows the models fit to the observational data by Romano et al. (2020). It is used a galaxy formation approach based on the "two-infall" model (Chiappini et al. 1997, 2001) and a later review of the model by Spitoni et al. (2019).

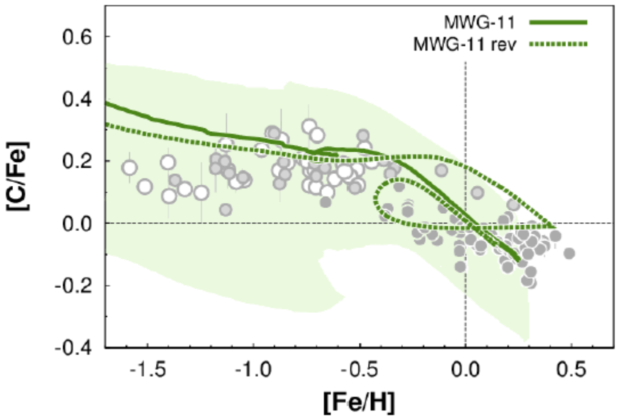

Figure 2.15: *Carbon-to-iron and carbon-to-oxygen abundance ratios as functions of [Fe/H] in the solar vicinity. The solid lines show the predictions of model MWG-11 by Romano et al. (2019) based on the "two-infall" model of galaxy formation; the theoretical uncertainties arising from stellar nucleosynthesis are highlighted by the pale green areas. The dashed lines show the predictions of model MWG-11 revised following Spitoni et al. (2019) improvements in their reviewed "two-infall" model. The symbols represent 3D non-LTE abundance estimates from high-resolution spectra of thin-disc, thick-disc, and high-α halo stars (dark grey filled circles, light grey filled circles and empty circles, respectively; Amarsi et al. 2019b); in most cases, the observational error lies within the symbol size. From Romano et al. (2020).*

Nevertheless, the C nucleosynthesis sources contributions is an open question and the increasing abundance data from GAIA and other surveys will help to constraint models of future studies.

Another observed feature in the data is the C abundance scatter at low metallicities. The rotating massive stars yields at the early galaxy change in function of the physical parameters (wide range of rotating velocities or massive stars) and this is used as a natural explanation of the scatter. Other rare nucleosynthesis sources acting at low metallicities: MHD-SNeII (see Sect. 1.4) and CBM (see Sect. 1.5), are equally argued to be natural explanations for abundance scatter observed in some s- and r-process elements by their low event rates but expected large yields in some elements. Due to the uncertainties in the yield, this can indirectly impact the abundances of other elements.

In addition, halo formation features should be taken into account as additional factors. Merging of sub-halos (each one with its own history and timescale for chemical enrichment) as forming mechanism of the early Galaxy or the imperfect gas mixing have been suggested as promising factors of the abundance scatter need to be studied in-depth (Prantzos et al. 2018).

An important note is that optical lines of carbon at low metalicities are very weak. This complicates observations and increases the uncertainties of C abundances in low metalicities stars.

$^{12}C/^{13}C$ galaxy evolution

An additional effect of high rotational velocity in fast rotators, due to the layer mixing, is the production of quasi-primary ^{13}C. GCE models with non-rotating stars predict a secondary production channel for ^{13}C, similar to the one of ^{14}N. This results in a very high $^{12}C/^{13}C$ ratio at low metallicity, of the order of several 10^3 (Prantzos et al. 1996; Kobayashi et al. 2011a; Chiappini et al. 2008) much higher than the solar value of 90 (Prantzos et al. 2018). However, GCE models by Prantzos et al. (2018) predict a significant reduction of the $^{12}C/^{13}C$ ratio at lower metallicities, also pointed by the Chiappini et al. (2008) model for rotating stars, although not so striking at extremely poor metallicity range.

Unfortunately, observational data can not help to understand the role played by rotation. $^{12}C/^{13}C$ ratios can only be determined in red giant stars, where various processes are active that alter the initial ratios (e.g.the FDU) (Prantzos et al. 2018). Nevertheless, the depletion effect of FDU at several metallicities and mass star models, have been quantified and taken into account. The Fig. 2.16 shows that rotating massive stars, GCE model by Prantzos et al. (2018) looks to fit better the observational Red Giants ratios.

However, it is argued by the same authors that $^{12}C/^{13}C$ ratio observed in Red Giants is affected mainly by internal stellar processes and can hardly be used to infer their initial $^{12}C/^{13}C$.

Likewise, there exist some unevolved very metal poor stars which show extremely low $^{12}C/^{13}C$ (<15) ratios (e.g. Lucatello et al. (2003); Cohen et al. (2006); Masseron et al. (2012). However, the overwhelming majority of these stars are known to be carbon enhanced metal-poor stars with s-element enhancements (CEMP-s), see next Sect. 2.2. These objects belong to binary systems, in which they accreted mass from the primary star (now a WD) when it was on the AGB phase (Prantzos et al. 2018).

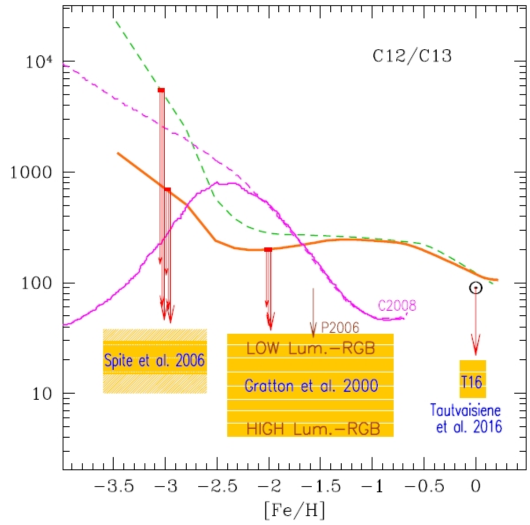

Figure 2.16: *Evolution of the $^{12}C/^{13}C$ isotopic ratio in the baseline Prantzos et al. (2018) rotating massive stars model (orange solid) and with non-rotating massive stars (green dashed). The magenta curves represent the results of Chiappini et al. (2008) for non-rotating stars (dashed) and for rotating ones (solid). Shaded regions indicate the range of observations for red giants at various metallicities, from Spite et al. (2006); Gratton et al. (2000); Tautvaišienė et al. (2016); the latter correspond to open clusters of age ∼ 1 Gyr, i.e. turn-off mass of ∼ 2 $M_\odot$.*
Arrows (in triplets) indicate internal depletion in red-bump stars of 0.8, 0.85 and 0.9 $M_\odot$ (from left to right), starting from initial $^{12}C/^{13}C$ ratios obtained in the Prantzos et al. (2018) GCE model: ∼ 6500 for non-rotating and 750 for the baseline rotating model at [Fe/H]= -3 dex, and 200 for the baseline model at [Fe/H]= -2. P2006 indicates the result by Palacios et al. (2006) for a 0.85 $M_\odot$ model with solar initial $^{12}C/^{13}C$. At solar metallicity it is showed a 2 $M_\odot$ model, as appropriate for clusters of age ∼ 1 Gyr. From Prantzos et al. (2018).

NLTE effect corrections

Another remaining question is the impact of NLTE effects of the optical C lines on the derived abundances. As above commented, C optical (or near IR) lines are strikingly weak in dwarfs. Takeda & Honda (2005) used the permitted C I 5052 and 5380 Å lines and the forbidden [C I] 8727 Å line. The authors developed NLTE estimations based on the equivalent widths as a funtion of the T_{eff} of the two permitted lines, because the [C I] line was proved to be in agreement with LTE derived abundances. The NLTE corrections calculated by this method, were found to be negligible in the FGK dwarfs sample.

Later 1D NLTE derived corrections based on these and additional lines (as C I 7111 and 7119 Å lines), e.g. by Takeda et al. (2013), Nissen et al. (2014) and Zhao et al. (2016) found quite similar non significant NLTE corrections.

However, when observing the 3D NLTE (T_{eff}, logg and metallicity) corrections by Amarsi et al. (2019b), 3D hydrodynamic model atmospheres were adopted from the

STAGGER-grid (Magic et al. 2013), applied to literature abundances (see Fig. 2.17), one can be aware about the importance that these effects might have for determining abundances on e.g. the metal poorer and older stars. This study is based on the more relevant C I lines from 505 to 966 nm and the authors find that the absolute 3D non-LTE versus 1D LTE abundance corrections can be as severe as e.g. -0.3 dex for C I lines in low-metallicity F dwarfs.

The taking into account or not of these effects by 3D NLTE corrections over LTE assumptions, might impact the analysis of the galaxy chemical evolution as the Fig. 2.17 shows. As one example, the above mentioned theoretical Romano et al. (2020) study on rotating massive stars contribution to C abundances, is based on this NLTE 3D corrected abundance distribution by Amarsi et al. (2019b).

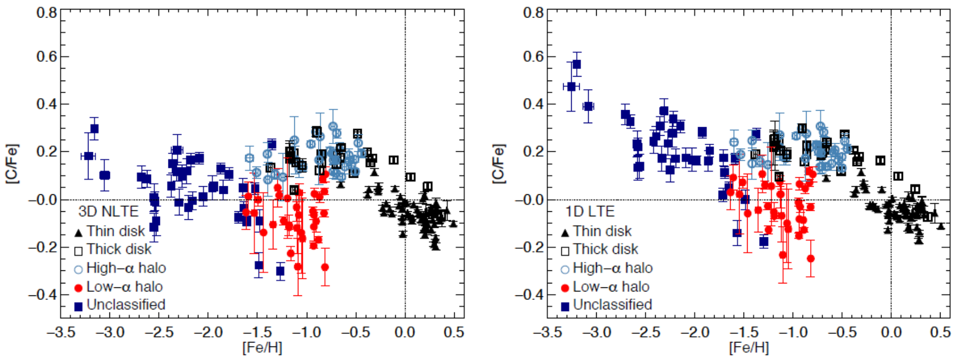

Figure 2.17: *Carbon to iron abundance ratios. Panels show results based on different line formation models, the 3D non-LTE model being preferred. The sample consists of three different data sets of F and G dwarfs used by Amarsi et al. (2019b): the 67 disk stars (mainly of the thin disk, and including the Sun) in the HARPS-FEROS sample of Nissen et al. (2014); the 85 thick-disk and halo stars in the UVES-FIES sample of Nissen et al. (2014); and the 40 halo stars in the VLT/UVES sample of Nissen et al. (2007) which were recently re-analysed by Amarsi et al. (2019a). From Amarsi et al. (2019b).*

2.2.4 [C/O] ratio versus [O/H] abundance

This is a ratio particularly useful when discussing the origin and Galactic evolution of carbon (Nissen et al. 2014). Given that oxygen is exclusively produced in very massive stars on a relatively short timescale after the appearence of the first stars, ~ 10 Myr, the change in [C/O] as a function of [O/H] depends on the yields and timescales of carbon production in various types of stars (Chiappini et al. 2003; Akerman et al. 2004; Carigi et al. 2005; Cescutti et al. 2009; Carigi & Peimbert 2011).

The Fig. 2.18 by Amarsi et al. (2019b) shows the traditional [C/O] profile in 1D LTE assumptions as well as the profile with the 3D NLTE corrections applied (see latter section).

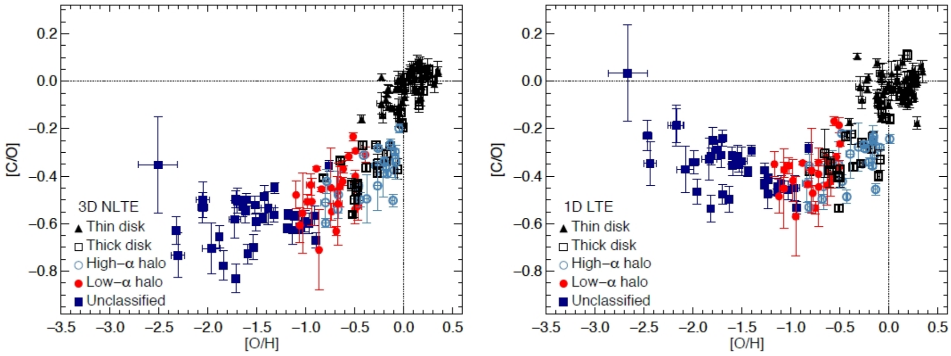

Figure 2.18: *Carbon to oxygen abundance ratios for the entire stellar sample. The unclassified stars are from the VLT/UVES sample. The panels show results based on different line formation models, the 3D non-LTE model being preferred. From Amarsi et al. (2019b).*

The 3D NLTE corrections greatly change the correlations between [C/O] and [O/H] at the low [O/H] range.

The observed separation between the thin and thick disk appears consistent with the Milky Way having had two main infall episodes (Amarsi et al. 2019b). The latter of those episodes is responsible for the formation of the thin disk (Chiappini et al. 1997, 2001).

The increasing [C/O] with increasing [O/H], could reflect an increasing rate of carbon enrichment from AGB stars at later epochs, or an increasing rate of carbon enrichment from metallicity-dependent winds from massive stars (Amarsi et al. 2019b).

From studies as Nissen et al. (2014), it would be expected that also low-α halo population would show similar increase. However this is not not observed. The explanation offered by the authors is that intermediate mass AGB stars (4–8 $M_\odot$) contribute very little carbon (Kobayashi et al. 2011b). Furthermore, the evolution timescales of low-mass AGB stars (1-3 $M_\odot$) which have a high carbon yield, is longer than the timescale for enriching the low-α stars with Fe from Type Ia SNe.

However, in the Fig. 2.18 by Amarsi et al. (2019b), is not observed clear evidence (3D NLTE correction) for an offset between the low-α halo population and the thick disk/high-α halo population. Rather, the low-α halo population continues the trend of decreasing [C/O] with decreasing [O/H]. The unclassified stars, which are possibly dominated by the low-α halo population, form a plateau of [C/O] $\sim$ -0.6 below [O/H] $\sim$ -1.0 dex. This plateau could be interpreted as reflecting primary carbon and oxygen nucleosynthesis from the cores of massive stars at earlier epochs, with a negligible contribution from AGB stars or metallicity-dependent winds from massive stars.

As final remark, this [C/O] ratio is being used as a marker for stars hosting planets in some studies along the last years with the increasing number of confirmed exoplanets (see

Fig. 2.19).

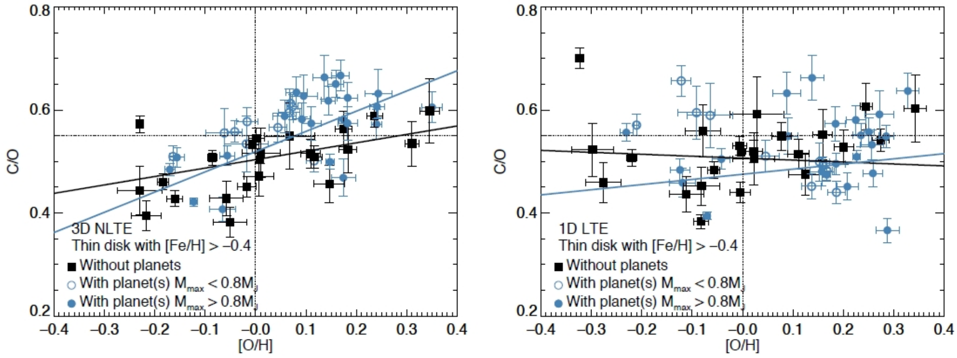

Figure 2.19: *Carbon to oxygen abundance ratios, for thin-disk stars without and with confirmed planet detection. The latter are further separated according to the maximum planet mass in the system. The panels show results based on different line formation models, the 3D non-LTE model being preferred. The nominal solar value C/O = 0.55 is shown as a horizontal dashed line. Also plotted are error-weighted lines of best fit for stars without and with confirmed planet detection (irrespective of maximum planet mass). Planet data from the NASA exoplanet archive (Akeson et al. 2013). From Amarsi et al. (2019b).*

2.2.5 Carbon-enhanced metal-poor stars (CEMP)

In the previous section, some [C/O] diagrams were shown whose interpretation might change whether NLTE effect corrections are included or not. The outlier shown in Fig. 2.18 is the most oxygen-poor star known CD24 17504. The authors suggest likely status as a carbon-enhanced metal-poor (CEMP) star (Amarsi et al. 2019b).

Indeed, when the sample is extended to the early universe, it is clear that the [C/O] upturn, accompanied by higher scattering, is a real and solid trend as is observed in Fig. 2.20. It has been suggested that this upturn is a signature of enrichment by Pop. III stars (Akerman et al. 2004; Pettini et al. 2008).

The stars in the EAGLE simulation by Sharma et al. (2018) that have such low [O/H] and high [C/O] formed before z = 6 (corresponding ~ 1 Gyr after the Big Bang, and only ~ 700 Myrs after the formation of the first stars), which is late enough for the AGB channel to become active. This upturn is due to carbon produced by AGB stars. Somehow, the birth cloud of these stars avoided being enriched by massive stars (SNeII and more massive, that enhances O) for long enough (ca 300 Myr), to allow AGB progenitors to evolve and release carbon (Sharma et al. 2018).

This CEMP population involves the most metal poor stars in the galaxy (at least the 20% with [Fe/H]< -2 according to Lucatello et al. (2006)). In some way, maybe the most

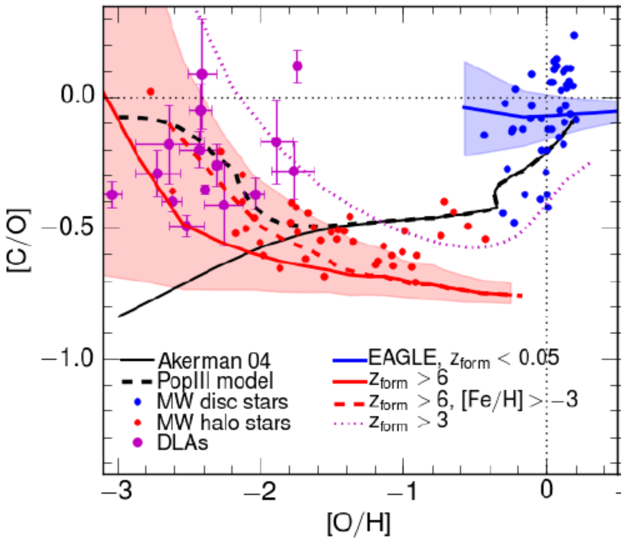

Figure 2.20: *[C/O] abundance as a function of [O/H]. Blue and solid red curves are the median relation for EAGLE simulations (suite of cosmological hydrodynamical simulations star particles by Schaye et al. (2015)) that formed after z = 0.05, or before z = 6, respectively. The dashed red curve is the median predicted eagle relation for stars formed before z = 6 with [Fe/H]> -3. The dotted curve is the median predicted eagle relation for stars formed before z = 3. The black curves are population synthesis models from Akerman et al. (2004), without (solid) and with (dashed) a contribution from Pop. III stars. Blue and red points are observed Milky Way disc and halo stars, respectively, taken from Fabbian et al. (2009). Magenta points with error bars are the Damped Lyman Alpha (DLA) systems from Cooke et al. (2017). From Sharma et al. (2018).*

pristine (Spite et al. 2013). Its proportion increases with the distance to the galactic plane (Frebel et al. 2006). At the lowest metallicities, this proportions increases dramatically (Beers et al. 1992; Norris et al. 1997).

Hence mostly participating in the galactic halo population as observed from the kinematic data of a CEMP sample in the Fig. 2.21 by Hansen et al. (2019).

The observed scattering in the Fig. 2.20 and specifically in the Fig. 2.22 by Sharma et al. (2018) shows [C/Fe] abundance in function of metallicity. This is hinting at a heterogeneous chemical composition and origin of these stars.

The criterion of the carbon abundance ratio in the definition of “carbon-enhanced” objects depends on the authors and studies: varying from [C/Fe] = +0.5 to +1.0. Some study takes the evolutionary stage of the object into consideration. However, distributions of carbon abundance ratios clearly split into two groups, and the estimate of the fraction of carbon-enhanced stars is not significantly changed by the criterion as observed in Fig. 2.23 by Aoki (2010).

What a more complete sample, from Sharma et al. (2018), tell us is that even in

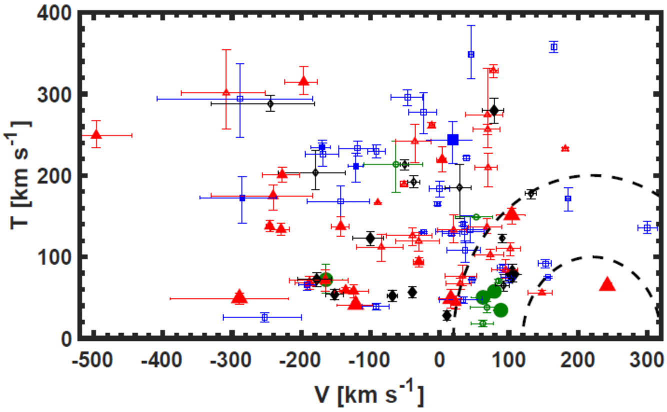

Figure 2.21: *Toomre diagram showing the observational kinematic data of a sample of CEMP stars separated by chemical sub-groups. CEMP-no stars are shown as blue squares, CEMP-s as red triangles, CEMP-r and -r/s as green circles, and C-normal stars as black diamonds. Large, filled symbols are data from Hansen et al. (2019), while small filled symbols refer to the sample of Hansen et al. (2016a). The dashed circles indicate a 3D space velocity relative to the local standard of rest of 100 and 200 km $\cdot$ s^{-1}, respectively, centred on VLSR = 232 km $\cdot$ s^{-1}, indicating the kinematic separation among thin, thick disks and halo. From Hansen et al. (2019).*

the CEMP population, the chemical and formations features are different. Indeed a first separation comes from the s-process element abundances of the CEMP stars (see Fig. 2.22): CEMP-s stars that shows s-process element enrichment with respect to the CEMP-no stars, in which, the s-process abundances are comparable to standard C stars in the disk.

Beers & Christlieb (2005) defined a first clasiffication based on the two main classes according to the following criteria: CEMP-s with [C/Fe] > +0.7 and [Ba/Fe] > +1.0, and the CEMP-no stars that do not show any s-process enhancement and which usually occur at lower metallicities with [C/Fe] > +0.7 and [Ba/Fe] < 0.0 (Arentsen et al. 2019).

And what it is interesting, their abundances and frequency show a dependency with respect to the metallicity and the very early universe. Like this, only CEMP-no (no s-process enhancements) are found in extremely iron-poor range (see EAGLE histogram and CEMP-no population in Fig. 2.22) and are thought to provide a glimpse into interesting info linked with the conditions of the first stars formation (Spite et al. 2013).

Whereas CEMP-s stars may have accreted additional elements during their stellar lifetimes (Lucatello et al. 2005), CEMP-no stars are expected to reflect the chemical composition of their birth environment (Hartwig & Yoshida 2019).

It was found that the CEMP-s stars are almost always in a binary system (e.g. McClure & Woodsworth (1990);Preston & Sneden (2001); Lucatello et al. (2005); Hansen et al. (2016a)), while the CEMP-no stars more often appear to be single stars (Norris et al. (2013); Starkenburg et al. (2014); Hansen et al. (2016b)). CEMP-s stars are thought to have received

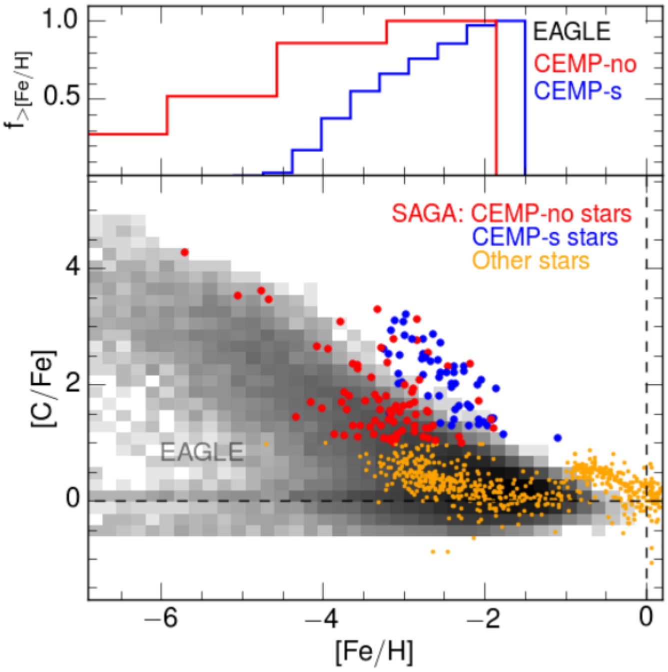

Figure 2.22: *[C/Fe] as a function of [Fe/H]. The predicted distribution of EAGLE stars simulations (suite of cosmological hydrodynamical simulations star particles by Schaye et al. (2015)) formed before Z=6 is shown using a gray-scale 2D histogram. Observed stars, taken from the SAGA database, are shown as red and blue circles for CEMP-no ([C/Fe]> 1, [Ba/H]<-2) and CEMP-s stars ([C/Fe]> 1,[Ba/H]>-2), respectively, with the remainder plotted as orange dots for standard stars. Cumulative probability distribution of [Fe/H] for EAGLE CEMP-no and CEMP-s stars predictions is shown as red and blue histograms, respectively. From Sharma et al. (2018).*

their carbon and s-process elements via mass-transfer from an evolved companion (Abate et al. 2015) that has gone through the Asymptotic Giant Branch (AGB) phase (Arentsen et al. 2019).

This fact is observed in the sample of Fig. 2.24, pointing to the binary interaction from an evolved AGB as the most usual source of CEMP-s stars. In the Fig. 2.25 by Arentsen et al. (2019) and 2.26 by Jorissen et al. (2016) are observed orbital parameters as Period and Eccentricity of binary systems including CEMP stars. They reveal two different groups of systems: one with short orbital periods (P < 1000 d) and mostly circular or almost circular orbits, and another with longer period and eccentric (e > 0.1) orbits (Jorissen et al. 2016).

However, the origin of the CEMP-no is not yet clear and can not be explained by mass transfer from an evolved companion. In the Fig. 2.27 can be observed how the proportion of CEMP-no originated in binary systems, is minority. CEMP-no stars from binary interactions are indicated in yellow and green stars (previously known and 4 new systems found by

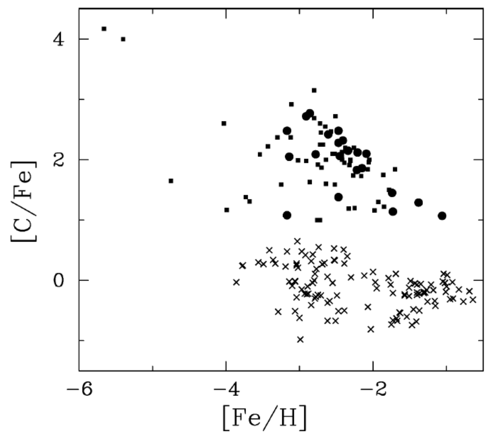

Figure 2.23: *[C/Fe] as a function of [Fe/H]. [C/Fe]= +1.0 is adopted as a the criterion to define CEMP stars (filled symbols) in the Aoki (2010) paper. This figure is based on a figure of Aoki et al. (2007) with additional data from literature. From Aoki (2010).*

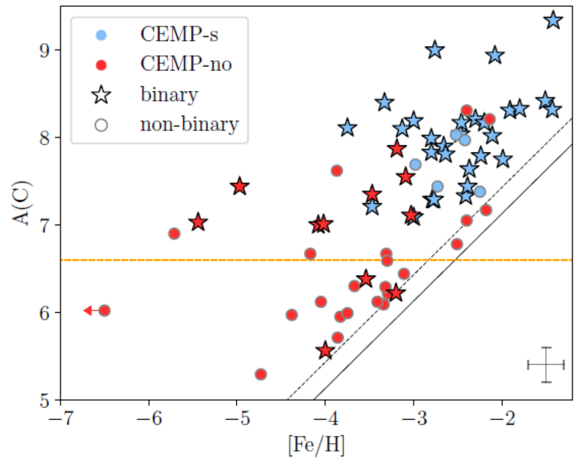

Figure 2.24: *Absolute carbon abundance A(C)[(a)] as a function of [Fe/H] for CEMP stars, where again CEMP-no stars are shown in red and CEMP-s stars in blue. Binary stars are indicated by a star symbol. Most binary systems are CEMP-s. From Arentsen et al. (2019).*
(a) $A(C) = \log \epsilon_C = \log(N_C/N_H)+12$.

Arentsen et al. 2019), with respect to the single CEMP-no population in red circles.

Conventional Pop III core-collapse SNe and high-mass pair instability SNe produce [C/Fe] < 0.7 (Nomoto et al. 2013), thus they can not be the direct origin of these stars at the very early universe.

A special kind of SN has been proposed as their possible origin; faint SNe. These SNe eject less iron, which results in an increased [C/Fe]. If about half of the Pop. III core-collapse SNe are faint, theoretical models might reproduce the fraction of CEMP stars at low metallicities (Ji et al. 2015; de Bennassuti et al. 2017; Hartwig et al. 2018) (Hartwig

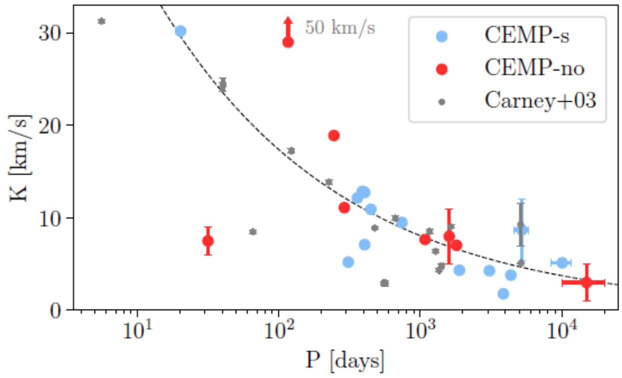

Figure 2.25: *Periods and semi-amplitudes of carbon-normal metal-poor binaries from Carney et al. (2003), CEMP-s binaries from Hansen et al. (2016a) (excluding their CEMP-r/s stars) and CEMP-no binaries from Arentsen et al. (2019). The line indicates what would be expected of Keplerian orbits of a 0.8 $M_\odot$ star with a 0.5 $M_\odot$ companion, for an eccentricity of 0.3 (typical for the stars in the Carney et al. (2003) sample) under an inclination of 60^o. From Arentsen et al. (2019)*

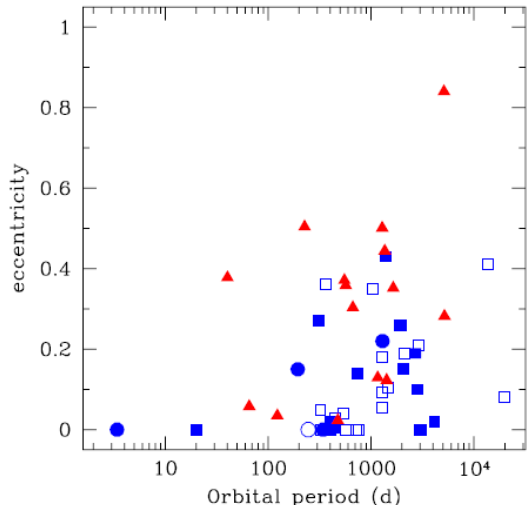

Figure 2.26: *Comparison of CEMP stars (filled symbols) and CH stars (open symbols) in the period – eccentricity diagram. Dwarf carbon stars are represented by circles, giant carbon stars by squares. For comparison, the sample of low-metallicity giants studied by Carney et al. (2003) is represented with red triangles. From Jorissen et al. (2016).*

& Yoshida 2019).

However, inhomogeneous metal mixing from previous standard SNe can lead toward the preferred formation of single CEMP-no stars at low metallicities as argued by the theoretical study of Hartwig & Yoshida (2019). In the Fig. 2.28 is shown the proposed mechanism: After a Pop III SN, gas recollapses and triggers the formation of second-generation stars (Chiaki et al. 2018). During the recollapse, multiple overdensities can form with potentially

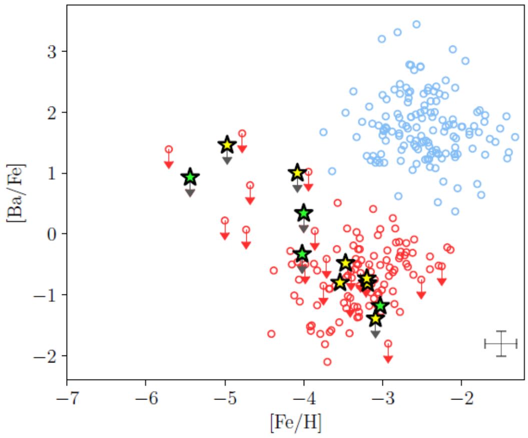

Figure 2.27: *[Ba/Fe] as a function of [Fe/H] for the compilation of CEMP stars from Yoon et al. (2016) to [Fe/H] = -6, where CEMP-s stars are shown in blue and the CEMP-no stars in red. Indicated are the known and new CEMP-no binaries as yellow and green stars respectively. From Arentsen et al. (2019)*

different elemental abundances (top and bottom row in Fig. 2.28). If the collapse time (tcoll) of the carbon-rich clump is short enough, this clump can form stars and prevent star formation in the nearby clump by its energetic photons pressure (Hartwig & Yoshida 2019).

Nevertheless, there are other lines of research in relation with the explanation of the CEMP-no origin. Theoretical stellar models predict that Pop. III and extremely metal-poor stars ([Fe/H] < 4) undergo violent evolutionary episodes not seen at higher metallicities. The more violent of those is expected in the core He flash of low mass stars in which is injected H-rich material down to regions of high temperature. That produces a secondary flash of H, this time. The combination of both flash events, He and H, is called "Dual Core Flash". It is followed by a dredge-up that lifts CNO-rich nuclear ashes to the atmosphere. This is a promising scenario for explaining the enrichment in C of the CEMP-no single stars (Campbell & Lattanzio 2008; Mocák et al. 2010).

Besides the two main CEMP categories, CEMP-s and CEMP-no, are observed some less numerous CEMP populations with their own special features. We review all the CEMP categories (Jorissen et al. 2016) attending to the heavy element abundance patterns (Beers & Christlieb 2005; Masseron et al. 2010):

CEMP Categories

- CEMP-s: [C/Fe] > +1.0, [Ba/Fe] > +1.0, and [Ba/Eu] > +0.5. This most numerous class is characterised by enrichments of neutron-capture elements, with an abundance pattern compatible with the operation of the s process in asymptotic giant branch (AGB) stars. After initial studies of their binary

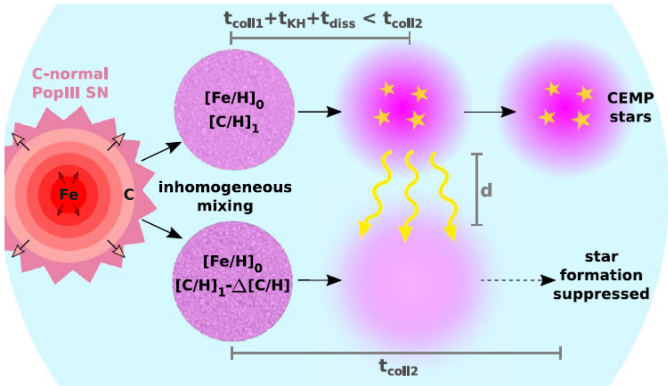

Figure 2.28: *How a standard C and Fe ejecta from Pop III SN ([C/Fe]< 0.7) can trigger the formation of CEMP stars ([C/Fe]> 0.7). The crucial quantities are the separation of the two clumps, d, and their carbonicity difference, Δ[C/H]. From Hartwig & Yoshida (2019).*

frequency by Preston & Sneden (2001), Sneden et al. (2003b), and Lucatello et al. (2005), Starkenburg et al. (2014) finally used a large sample of stars to demonstrate that these stars are all members of binary systems. Thus, it is now established that these CEMP-s stars, along with the closely-related classical CH stars (Keenan 1942), are members of wide binary systems, where the former primary star transferred material during its AGB phase onto the presently observable companion (McClure 1984; McClure & Woodsworth 1990).

- CEMP-rs: [C/Fe] > +1.0, [Ba/Fe] >+0.5 and [Ba/Eu] > 0.0. This other class of CEMP stars, exhibiting large overabundances of elements produced by the s process and elements traditionally related to the r-process, was discovered by Barbuy et al. (1997) and Hill et al. (2000). A number of these stars exhibit radial-velocity variations (Sivarani et al. 2004;Barbuy et al. 2005). Here again the companion could be responsible for the peculiar abundance pattern (e.g. Masseron et al. 2010; Bisterzo et al. 2011).
- CEMP-r: [C/Fe] > +1.0 and [Eu/Fe] > +1.0. This is the signature of a highly r-process-enhanced CEMP star, so far observed in only one object (CS22892-052; Sneden et al. 2003a).
- CEMP-no: [C/Fe] > +1.0 and [Ba/Fe] ∼ 0. Starkenburg et al. (2014) found these CEMP stars with no enhancements in their neutron-capture-element abundances Aoki et al. (2002) to have normal binary frequency. Consequently, a mass-transfer scenario comparable to that occurring in CEMP-s (and possibly in CEMP-rs) stars has not operated here.

However, an alternative attempt to categorize CEMP stars has been presented by Hansen et al. (2019) based on the Sr and Ba abundances (see Fig. 2.29) and kinematics analysis.

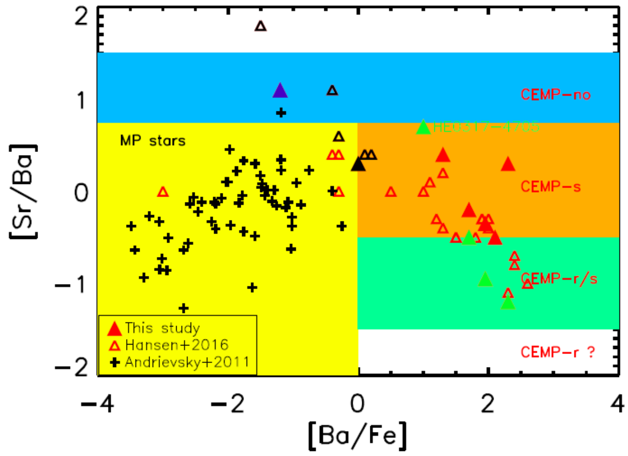

Figure 2.29: *[Sr/Ba] vs. [Ba/Fe] from Hansen et al. (2019) study compared to Hansen et al. (2016a) and NLTE values (+) from Andrievsky et al. (2011). The blue symbol colour indicates CEMP-no stars, red CEMP-s, and green CEMP-r/s, while black (yellow region) shows C-normal metal poor stars. Suggested sub-classifications are highlighted in similar colours to the symbols. From Hansen et al. (2019).*

2.3. Nitrogen ($_7$N)

Carbon is the main product of He burning. The initially AGB O-rich stars are increasingly enriched in carbon and s-process elements over the time with each new thermal pulse in the TP-AGB stage (see Fig. 2.9). They become carbon stars once C/O > 1. This typically occurs between 1.5 and 3-4 $M_\odot$ for solar-like metallicity stars (Abia et al. 2002; Cristallo et al. 2011).

However for masses higher than 4 $M_\odot$, the stars cannot become carbon-rich because of the Hot Bottom Burning (HBB) process: the hot temperatures at the envelope base induces CN cycling, burning the dredged-up carbon (Hedrosa et al. 2013) and preventing carbon enrichment of the surface. They become O-rich stars.

But the activation of the CN cycling by HBB in metal-rich intermediate mass stars during the AGB phase (van den Hoek & Groenewegen 1997) and the small cross section (Henry et al. 2000; Meyer 2005) of the reaction ^{14}N(p,γ)^{15}O (which destroys nitrogen) will allow nitrogen to accumulate over the time (Meynet & Maeder 2002b).

Freshly produced nitrogen may be brought to the surface by the third dredge-up and released in the interstellar medium by the stellar winds (Israelian et al. 2004). This is the source of "secondary" nitrogen whose effective yield depends on the previous enrichment of C and O of the cloud in which the star was formed.

When the nitrogen is obtained from the primordial H and He of the star, it is considered "primary" and for which there are two possible sources: first, intermediate mass stars which experience HBB (Marigo 2001) or rotate (Meynet & Maeder 2002b). Or second, metal poor massive fast-rotators stars (more frequent in an early universe), by rotational diffusion of ^{12}C into the He-burning layer (Meynet & Maeder 2002b).

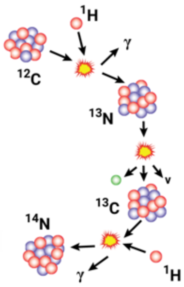

Figure 2.30: *^{14}N production from ^{12}C through CN-cycling induced by the hot temperature at the convective base and the HBB process.*

Like in the C nucleosynthesis, fast rotators (Maeder 1992; Maeder et al. 1999; Romano et al. 2020) have been argued to stimulate the production of nitrogen in an early universe, in metal poor stars (see Fig. 2.31 and 2.32).

The nitrogen production of these rotators is mostly primary (from original H and He) in intermediate AGB stars, enriching the medium through ejecta driven by stellar winds (fast rotators > 100 $km \cdot s^{-1}$, most in the early universe) or during formation of planetary nebula (low rotators currently more abundant at higher metallicity, Romano et al. 2019).

However, the same models at Z= 0.02, do not produce any primary nitrogen (Meynet & Maeder 2000). The mechanism which produces primary nitrogen in rotating AGB stars, only works efficiently for Z less than ~ 1/5 of solar (Meynet & Maeder 2002b).

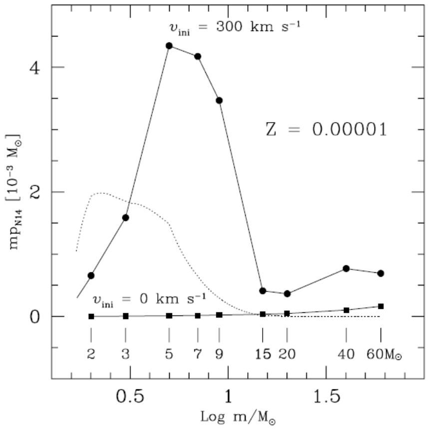

Figure 2.31: *Nitrogen yield theoretical study by Meynet & Maeder (2002b), calculated at metallicity Z = 0,00001 from the zero age sequence (ZAMS) to the phase of thermal pulses for models below or equal to 7$M_\odot$(AGB), and up to the end of central C-burning for the more massive stars. Amount of nitrogen (mainly primary in rotating models) produced as a function of the initial stellar mass. The initial rotation velocity on the ZAMS is indicated. For the initial mass stars between 3 and 15 $M_\odot$, the average rotational velocity during the Main Sequence is around 230 $km \cdot s^{-1}$.*

2.3.1 Primary or secondary? The [N/O] question

Oxygen is mainly produced in last burning phases of the massive stars, especially those with mass > 15 $M_\odot$ at very early stages of the universe, hardly a few million years after first star population appeared.

Hence, the [N/O] ratio might be a good tracer about the nitrogen origin. Several largely known metal-poor halo star studies favours the idea of primary origin of the nitrogen from massive stars at low metallicity (early universe) but the main support comes from the abundance studies in H ii regions of nearby metal-poor galaxies. The plateau log(N/O)= -1.5 at lower metallicity (log(O/H) ≤ -4.0) observed in the Fig. 2.33 by Henry et al. (2000) suggests a coupling between both, N and O productions, supporting the idea of a common

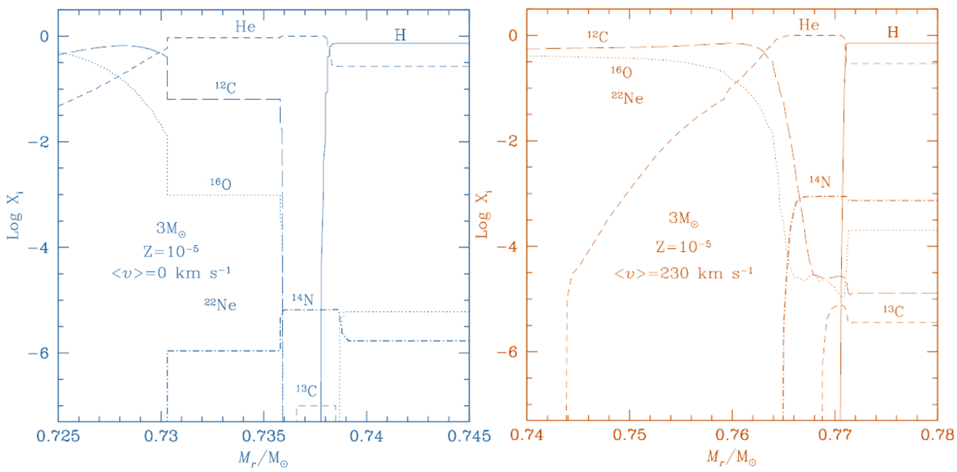

Figure 2.32: *Distribution of the main elements in the region of the helium- and hydrogen-burning shells during the TP-AGB phase of an initial non-rotating (left, blue) and rotating during the Main Sequence at 230 km $\cdot$ s^{-1} (right, orange), 3 $M_\odot$ star at Z = 0.00001. The models between 2 and 7 $M_\odot$ show a similar behaviour. Adapted from Meynet & Maeder (2002b).*

origin from massive stars at early universe.

Nevertheless, other models based on massive stars yielding O and intermediate mass stars producing primary N with a delay of ~ 250 Myr at very low stellar formation rate (Henry et al. 2000; Israelian et al. 2004), may reproduce likewise this plateau.

Hence, the question is open, some studies support the mostly primary production of N in intermediate mass stars (Liang et al. 2001; Henry et al. 2000), others do not, arguing the low scatter of the log(N/O) in galaxies observed at different evolutionary stages, deducing no time delay in the injection of N and O abundance, so hinting at a common origin in very massive stars (Thuan et al. 1995; Izotov et al. 2001).

However it is reasonable that the above mechanisms likely are able to produce primary as well as secondary nitrogen in any stellar population. Hence this element should show a behaviour neither purely primary nor secondary (Israelian et al. 2004).

2.3.2 Nitrogen evolution: from MS to AGB

The dominant nitrogen production mode lies in the re-arrangement of nuclei which occur in the CNO cycle, increasing ^{14}N at expense of ^{12}C and ^{16}O.

The CNO hydrogen burning in Main Sequence (MS) stars (more massive than sun) occurs the core and models do not expect that the freshly processed material reaches the surface. Except if extra mixing processes would be active as e.g. fast rotation. These are

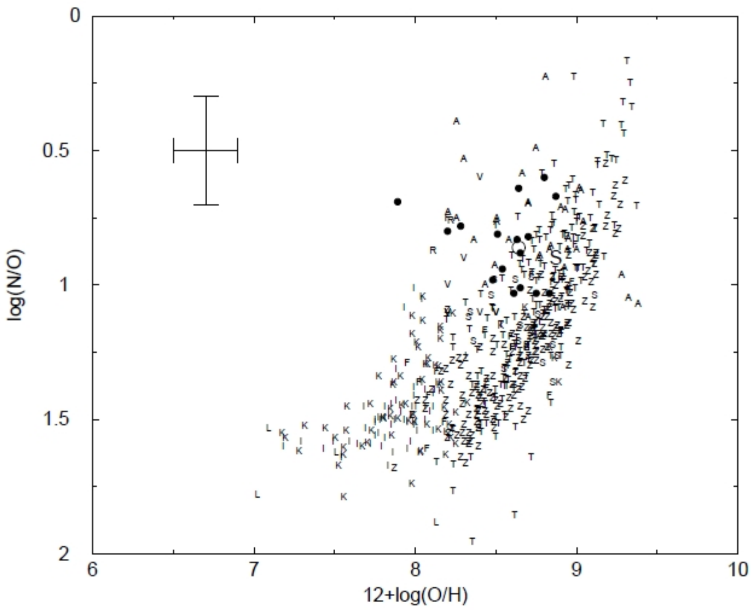

Figure 2.33: *log (N/O) vs. 12+log (O/H) for H* II *regions and stars in the Milky Way disk, extra-galactic spirals, and irregulars. Data for the Milky Way are from Afflerbach et al. (1997) (A) ; Fich & Silkey (1991) (F) ; Shaver et al. (1983) (S) ; Rudolph et al. (1997) (R) ; and Vilchez & Esteban (1996) (V). Extragalactic data are from Izotov & Thuan (1999) (i) ; Kobulnicky & Skillman (1996) (K) ; Thurston et al. (1996) (T) ; and van Zee et al. (1998) (Z). Filled circles are stellar data from Gummersbach et al. (1998). The circle indicates the position of the Orion Nebula (Esteban et al. 1998), the large S shows the position of the Sun (Grevesse et al. 1996), and the L symbols at extremely low oxygen show upper limits for two high-redshift damped Lyα objects in Lu et al. (1996). From Henry et al. (2000).*

more likely to occur in the early universe.

Fig.1.8 in Chapt. 1 from Gratton et al. (2000) shows the unaltered evolution of nitrogen abundance during the MS phase for a regular metal poor stars sample.

However during the hydrogen shell burning along the RGB ascend, there are several mechanisms which might mix up the freshly processed nitrogen on the surface, producing primary or secondary nitrogen in massive or intermediate mass stars. Hence, during the RGB the nitrogen enriches the surface as it is observed likewise, in the sample of Fig. 1.8.

The isotopic $^{14}N/^{15}N$ dramatically increases in AGBs as shown in the Fig. 2.34 though this study is limited to 1.5 (black line) and 2.0 $M_{\odot}$ (red line).

2.3.3 Nitrogen evolution in AGB

During interpulse in AGBs are working different nucleosynthesis mechanisms transforming hydrogen in helium as pp chain and CNO cycle in the H burning shell.

The CNO cycle leads to the production of ^{13}C that finally feeds the overproduction of ^{14}N via (see Fig.2.30):

^{14}N enrichment

$^{12}C +^{1} H \rightarrow^{13} N + \gamma$
$^{13}N \rightarrow^{13} C + e^{+} + \nu_e$
$^{13}C +^{1} H \rightarrow^{14} N + \gamma$

...but also following an alternative branch of the CNO cycle via ^{16}O...
$^{16}O +^{1} H \rightarrow^{17} F + \gamma$
$^{17}F +^{1} H \rightarrow^{17} O + e^{+} + \nu$
...and the ^{17}O is destroyed in deeper and richer hydrogen layers of LIMS
$^{17}O +^{1} H \rightarrow^{14} N +^{4} He$

The high temperatures reached in the bottom of the convective envelope of intermediate mass stars trigger the HBB mechanism which destroy more efficiently ^{12}C to produce ^{14}N via the chain reactions above shown.

This results in AGBs especially enriched in nitrogen, preventing the star to become a carbon star in intermediate mass star due to the regulation of ^{12}C abundance. The C/O ratio is kept under the unity. This mechanism also poisons the neutron flux formation from the ^{13}C pocket to produce ^{16}O via α-particle capture and therefore the nucleosynthesis of main s-process elements are inhibited in intermediate mass stars.

In any case less (low mass stars) or more efficiently (intermediate mass stars), the total abundance of ^{14}N is increased in AGB and the ratio over other rare nitrogen isotope as ^{15}N is strikingly increased during AGB stage (see Fig.2.34).

2.3.4 Chemical galactic evolution abundances

The nitrogen does not present readily available lines in optical or near IR range (4000-9000 Å) but some extremely weak and blended lines in the near IR. The N I 8683 Å line was used in the study of Takeda & Honda (2005). It is constraint to metallicities higher than -0.4 dex, due to its extreme weakness. Even so there are high uncertainties on the derived abundances and the results might not be very reliable.

In spite of this fact, nitrogen has been included in this work due to a great importance from the nucleosynthetic and evolutionary point of view but too with respect to others as chemical or biological aspects.

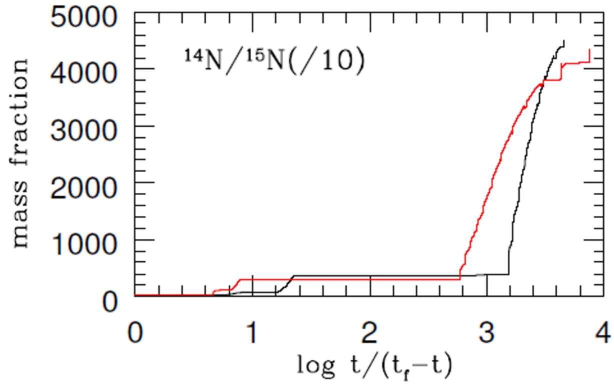

Figure 2.34: *Evolution up to the AGB tip from RGB, of $^{14}N/^{15}N$ isotopic ratios in models with 1.5 $M_\odot$(black line) and 2 $M_\odot$(red line). Evolutionary timescale has been re-scaled to the final time (tf) in the computation time (2.91 and 1.196 Gyr respectively). The first dredge-up occurs at log t/(tf-t) ~ 0,9 (1.5 $M_\odot$) and 0,6 (2 $M_\odot$), while the RGB bump takes place at log t/(tf-t) ~ 1,2 and 0,8 respectively. The combined actions of the third dredge-up and the AGB extra mixing arise at log t/(tf-t) > 3,2 and 2,8. Adapted from Abia et al. (2017).*

The usual way to derive abundances comes from near-UV molecular bands: NH around 3360 Å (see Fig. 2.35), or CN around 3880 Å.

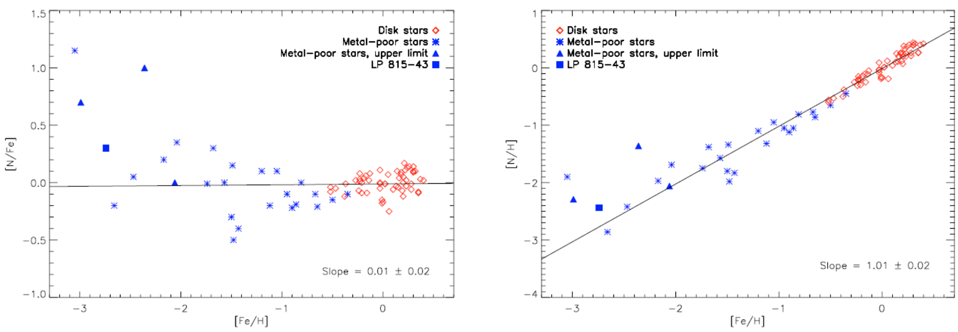

Figure 2.35: *[N/Fe] and [N/H] ratios against [Fe/H] from 3360 Å molecular NH bands by Israelian et al. (2004).*

Theoretical chemical evolution models as the ones by Mattsson (2010, Fig. 2.36) fail to reproduce the increasing nitrogen abundance of extremely metal-poor stars (EMP) derived by Israelian et al. (2004). Though is argued that these N-rich stars might be exceptional and the sample is no representative of general trend. The difficulties (opacity uncertainties in the near-UV) to derive data (and scarceness) especially from EMP stars does not allow to obtain right conclusions about nucleosynthesis sites and evolution from galactic chemical abundance pattern.

Similar conclusions can be reached based on the theoretical GCE study by Romano et al. (2010). That, in spite of the different prescriptions applied in their models, over a

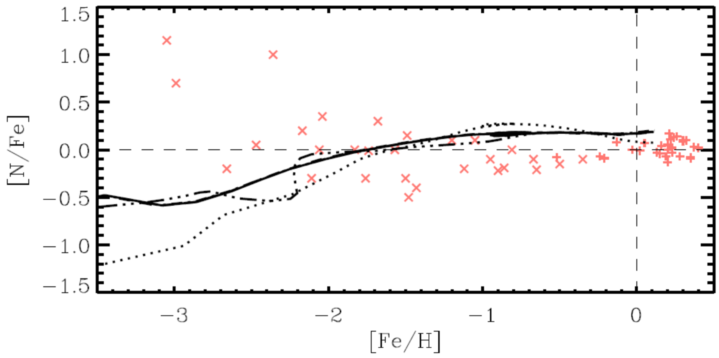

Figure 2.36: *Stellar abundances of nitrogen by Israelian et al. (2004) (cross) and Ecuvillon et al. (2004) (plus). Different chemical evolution models (solid and dashed lines) by Mattsson (2010).*

similar observational data sample from historical nitrogen determinations (see Fig. 2.37).

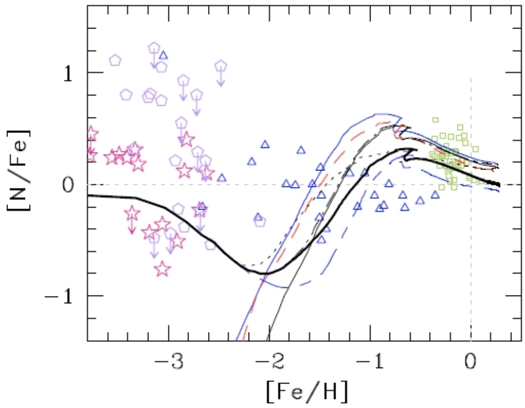

Figure 2.37: *N galactic chemical distribution in function of metallicity. Observational abundance data from Spite et al. (2005)(empty stars), Lai et al. (2008)(open pentagons), Israelian et al. (2004)(open triangles) and Reddy et al. (2003)(open squares). Some chemical evolution models have been added (solid and dashed lines). From Romano et al. (2010).*

However, when Prantzos et al. (2018) include in their models nitrogen yields from rotating massive stars (spinstars or fast rotators), greatly improves its fit to the observational data (see Fig. 2.38). Especially at the early universe, though is not perfect.

The Prantzos et al. (2018) model uses a mixture of stars with different rotational velocities, the fastest rotating at 300 $\mathrm{km \cdot s^{-1}}$. Meanwhile, however, the Chiappini et al. (2006) model uses and suggests 800 $\mathrm{km \cdot s^{-1}}$for explaining the overall appearance of primary N in the early Galaxy.

The inclusion of fast rotating massive stars, hence might explain the primary nitrogen abundance at the early universe although the used rotational velocities and adopted prescriptions greatly impact the GCE models and the issue remains unsettled (Prantzos et al. 2018).

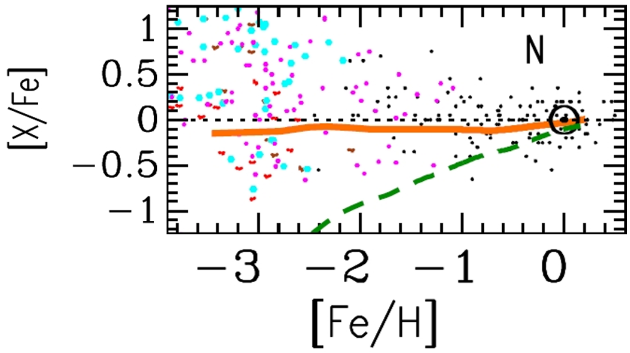

Figure 2.38: *Evolution of abundance ratio [N/Fe] as a function of [Fe/H] and comparison to observational data. Prantzos et al. (2018) model from massive and AGB/LIMS stars productions is in dashed green curve; the same model but with enhanced yields from rotating massive stars is in orange curve. Observational data from Yong et al. (2013), Roederer et al. (2014a) and Lai et al. (2008) based on LTE assumptions. From Prantzos et al. (2018).*

2.4. Oxygen ($_8$O)

Oxygen is by far the most abundant element produced by stars, being a dominant player in chemistry taking place in stellar outflows and in the interstellar medium (Meyer 2005).

Although it is efficiently produced in AGB stars ($< 8\ M_\odot$), the main source is the hydrostatic helium burning in the core of massive stars ($> 8\ M_\odot$). Which is later released into the interstellar medium by core collapsed supernovae (SNeII).

Oxygen fossil records are very important when modeling galactic evolution as they constrain the rates of core collapse supernovae (SNeII) and thermonuclear supernovae SNeIa with time (Woosley et al. 1990). The overabundance of oxygen ([O/Fe] > 0) indicates a fast chemical enrichment and a high star formation rate (Bensby et al. 2004).

Hence, this points to the burning phases before SNeII as the main source of oxygen in early stages of the galactic formation. Especially in very massive stars $> 15\ M_\odot$. They began to enrich the ISM, hardly few million years after the appearance of the first generation of stars. The later SNeIa appearance, as nucleosynthesis source of Fe-peak elements, balanced the oxygen abundances.

The abundance studies show the typical profile of an α-element (see Fig. 1.27 and 2.40). Metal poor stars from the halo are enhanced in oxygen ([O/Fe]) with respect to the thick but especially the thin disk richer-metal stars. Oxygen ratio ([O/Fe]) decreases, diluted by the richer Fe-peak elements contribution from thermonuclear supernovae (SNeIa).

Hence, its galactic chemical distribution reflects two main key ideas about galactic evolution, determining its profile:

α-elements galactic evolution keys

- Firstly, the early Universe was enriched in α-elements (Si in this case) because SNeII occurred on a much faster time-scale than SNeI (Edvardsson et al. 1993) in which α-elements production is not efficient but do for elements as Fe. This assumption determines the observed plateau in the abundances for older and metal-poorer stars ([Fe/H]<-1.0 dex) and the later dilution by SNeIa production (mainly Fe).
- Secondly, the galaxy formation of the disks stars populations: thin and thick disks (see Sect. 1.7 in Chapt. 1). It is rather well established that the halo/thick disk and the thin disk components of the Galaxy were assembled on different time-scales (Mattsson 2010). Thick disk is thought to be composed of relatively older, metal-poorer and α-elements enhanced stars than the thin one

(Adibekyan et al. 2013). The differential features, chemical and kinematical (see Fig. 1.27 and 1.49 in Chapt. 1), seem to hint to a different nature or evolutionary path, for the halo, thick and thin disks. Several theoretical models try to explain the observed properties of the thick disk as consequence from the scattering or radial migration of stars by spiral arms (Sellwood & Binney 2002; Schönrich & Binney 2009; Schönrich & McMillan 2017; Roškar et al. 2012), where stars are transported outwards and gain vertical height above the galactic plane to form a thick disk. As well as from external heating processes such as accretion of stars from disrupted satellite dwarf galaxies (Abadi et al. 2003) or the thickening of a pre-existing thin disk through a minor merger events (Quinn et al. 1993; Villalobos & Helmi 2008) or other possibility, from in situ triggered star formation during/after gas-rich mergers (Brook et al. 2004, 2005) (Duong et al. 2018).

However, the determination of oxygen abundances is unfortunately often troublesome due to the limited number of available oxygen lines (Bensby et al. 2004). As in the Sect. 2.4 will be indicated, the intense O I 770 nm triplet, are strongly impacted by NLTE effects.

2.4.1 Isotopic oxygen evolution

^{16}O is the main oxygen isotope, and the third most abundant isotope in the galaxy. ^{18}O (0.2% that of ^{16}O) and ^{17}O (0.03%) are also sufficiently abundant to be measured in stellar atmospheres.

The relations among the three isotopes are key to understand the evolutionary life of a star, as they are predominantly produced in different burning epochs: ^{17}O during H burning, ^{18}O during early stages of the helium burning and the ^{16}O during last part of the helium burning (Meyer 2005). However due to the ^{16}O domination, oxygen abundances on stellar atmospheres are not significantly altered (see Fig. 1.8) from the MS to the Horizontal Branch (Gratton et al. 2000).

^{16}O is a primary isotope. It can be synthesized by stars only made-up of hydrogen by the triple-α reaction from the previously formed helium (see Fig. 1.9 in Chapt. 1). It does not need the participation of metallic nuclei from previous stellar generations in their production. However it is not the case of ^{17}O (CNO cycle, dependant of the chemical composition of the cloud from which the star was formed) or ^{18}O.

CNO cycle that produces helium from hydrogen burning is activated when the core reaches temperatures exceeding 17.10^6 K. This happens in intermediate, and especially, massive stars in which becomes the main hydrogen burning mechanism (over PP chains).

Observing the CNO cycle (see Fig. 1.3 in Chapt. 1), proton capture by ^{15}N to form ^{12}C and ^{4}He (the main and neat production of the cycle due to the catalytic role of the CNO nuclei) close the cycle. However, roughly 0.1% of the time, the proton capture by ^{15}N produces ^{16}O triggering the NO cycle: -

NO cycle

$^{15}N +^{1} H \rightarrow^{16} O + \gamma$
$^{16}O +^{1} H \rightarrow^{17} F + \gamma$
$^{17}F +^{1} H \rightarrow^{17} O + e^{+} + \nu$
$^{17}O +^{1} H \rightarrow^{14} N +^{4} He$
An alternative and minor pathway involves ^{18}O formation throughout:
$^{17}O +^{1} H \rightarrow^{18} F + \gamma$
$^{18}F \rightarrow^{18} O + e^{+} + \nu$
$^{18}O +^{1} H \rightarrow^{15} N +^{4} He$

The ^{18}O destruction via proton capture quickly depletes its abundance meanwhile ^{17}O enhances around 10 times its initial abundances, though later reaches a steady state, balanced by the proton capture forming ^{14}N.

However, in the early stages of the helium burning by triple-α production (100-300$\cdot 10^{6}$ K), the temperatures and the abundance of ^{14}N will enrich the ^{18}O with respect to the ^{16}O and ^{17}O via α capture and later ^{18}F decay:

^{18}O Enrichment

$^{14}N +^{4} He \rightarrow^{18} F + \gamma$
$^{18}F \rightarrow^{18} O + e^{+} + \nu$

The ^{18}O captures an α particle to form ^{22}Ne, strongly depleting its abundance in only a year time. After this first year, the stable triple-α will sufficiently enrich the star in ^{12}C becoming the dominant α capturing isotope, leading to the ^{16}O formation and preventing the formation of ^{18}O via α capture by ^{14}N.

2.4.2 Chemical galactic evolution abundances

As above commented, oxygen shows a typical α-element profile from current metallicities to the plateau at ca -1.0 dex. It is hinting that the early Universe was enriched in α-elements because SNeII occurred on a much faster time-scale than SNeIa due to the evolutionary time delay.

In the Fig. 2.40 is observed the typical chemical gap (around +0.1 at -0.5 dex of metal-

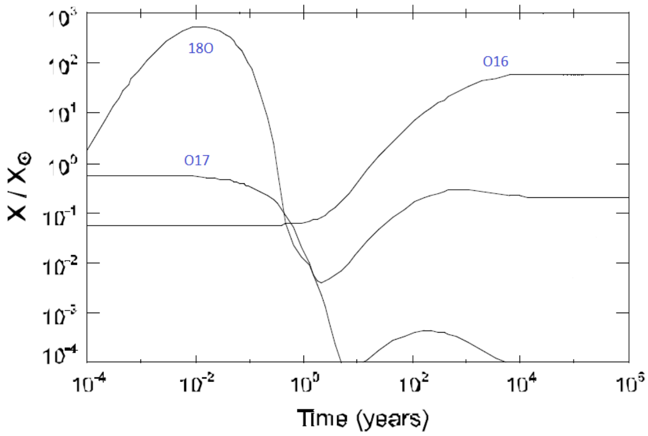

Figure 2.39: *Evolution of the mass fractions of the oxygen isotopes with respect to their solar abundances during helium burning at 250·10^6 K and a density of 1·10^3 g/cm3. Adapted from Meyer (2005).*

licity) between thin and thick disks hinting their different chemical nature and evolutionary formation.

NLTE corrections

The typically used lines of the O ɪ 777 nm triplet, are strongly impacted by NLTE effects. Different authors use different procedures (1D or 3D) and reach different effect corrections, e.g. Takeda & Honda (2005); Bensby et al. (2004); Amarsi et al. (2015, 2019b). As a consequence, high uncertainties about the oxygen NLTE corrections have prevented their use in α-element index about the thin and thick chemical properties in studies like the ones by Duong et al. (2018) or Adibekyan et al. (2013).

The 3D NLTE corrections for the O ɪ 777 nm triplet by Amarsi et al. (2015, 2019b) are the most exhaustive so far, being used in recent chemical evolution model studies as the ones by Romano et al. (2020) or Kobayashi et al. (2020a).

Other optical lines have been used as the forbidden [O ɪ] 6300 and 6363 Å lines but they are very gravity-dependent and very weak or not present in dwarfs and sub-giants (Fulbright & Johnson 2003). Besides, the [O ɪ] 6300 Å line is severely blended by Ni ɪ line at high metallicities (Allende Prieto et al. 2001) and the surrounding interval, is impacted by telluric bands.

Similar chemical distribution in Fig. 2.42 includes the impact of fast rotating massive star prescriptions in CGE model that improves the fit with respect to the observational data at early universe stages.

As above mentioned, the oxygen fossil record is very important for constraining models of galactic evolution. It is very used for comparing with respect to the chemical evolution

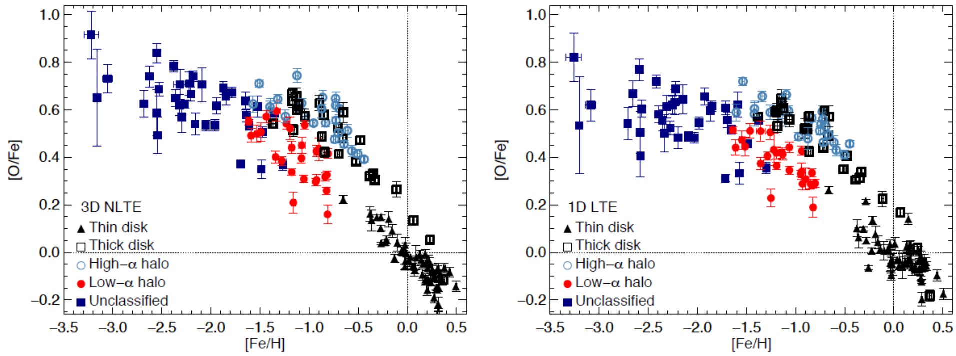

Figure 2.40: *Oxygen to iron abundance ratios for the entire stellar sample. The unclassified stars are from the VLT/UVES sample. 3D NLTE corrected (left) and LTE results (right). The sample consists of three different data sets of F and G dwarfs: the 67 disk stars (mainly of the thin disk, and including Sun) in the HARPS-FEROS sample of Nissen et al. (2014); the 85 thick-disk and halo stars in the UVES-FIES sample of Nissen et al. (2014); and the 40 halo stars in the VLT/UVES sample of Nissen et al. (2007). From Amarsi et al. (2019b).*

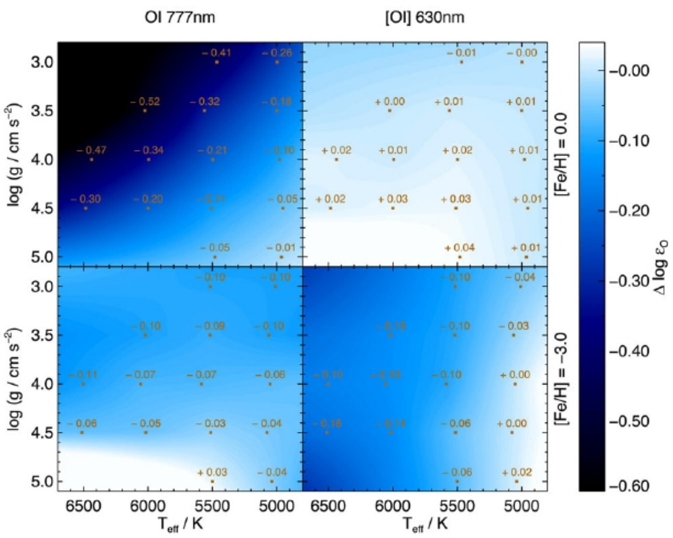

Figure 2.41: *Abundance corrections across the STAGGER grid (T_{eff}, log g, [Fe/H]) of 3D stellar atmospheres by Amarsi et al. (2015). NLTE abundance corrections for the permitted O I 777 nm line and the forbidden [O I] 630 nm are shown across T_{eff}–log g planes.*

and nucleosynthesis sites of the other elements: light elements as e.g. the carbon (see Fig. 2.18) and nitrogen (see Fig. 2.33) or heavy elements as the s-process element, barium (see Fig. 3.47) or as the r-process, europium.

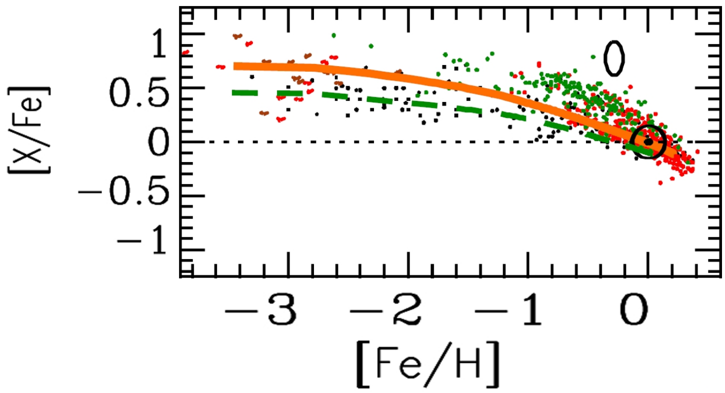

Figure 2.42: *Evolution of abundance ratio [O/Fe] as a function of [Fe/H] and comparison to observational data. Prantzos et al. (2018) model from massive and AGB/LIMS stars productions is in dashed green curve; the same model but with enhanced yields from rotating massive stars is in orange curve. Observational data from Bensby et al. (2014), Roederer et al. (2014a), Chen et al. (2000) and Lai et al. (2008) based on LTE assumptions. From Prantzos et al. (2018).*

2.5. Fluorine ($_9$F)

The odd-Z element, Fluorine, does not show any relevant lines in the optical or near IR range and abundance studies are based on the molecular vibration-rotation transitions of the hydrogen fluoride (HF) lines in the K band at 2.3 μm.

Hence, it should not be included in this nucleosynthesis summary. Nevertheless, the low and intermediate mass AGBs, the only nucleosynthesis production so far validated by observational data and chemical evolution models from AGB, Post-AGB and planetary nebulae studies by Jorissen et al. (1992), Forestini et al. (1992), Werner et al. (2005), Otsuka et al. (2008), Uttenthaler et al. (2008), Abia et al. (2010, 2015, 2019), Lucatello et al. (2011), invite to give a close look on the matter and the relation with other involved elements.

These observational and theoretical studies show that the abundance origin of the only stable isotope ^{19}F remains uncertain. The AGB is not sufficient as only source (Abia et al. 2015) to explain galactic chemical evolution models (Renda et al. 2004; Kobayashi et al. 2011a). Especially when comparing with the evolution inferred from observations (Recio-Blanco et al. 2012; Jönsson et al. 2014a).

There are several proposed nucleosynthesis sources (Abia et al. 2015; Guerço et al. 2019):

Fluorine Nucleosynthesis Sources

- As mentioned before, AGB stars via neutron and proton captures during He-burning thermal pulses (TP-AGB) and later TDU episodes (above commented literature).
- Neutrino spallation ν-process in core collapse SNeII (Woosley & Haxton 1988; Woosley et al. 1990; Kobayashi et al. 2011a).
- Core He-burning in Wolf-Rayet stars undergoing high mass loss rates by stellar winds (Meynet & Arnould 2000).
- Low-metallicity and high-mass fast rotators (Prantzos et al. 2018).
- Dwarf mergers (Woosley et al. 1990; Forestini et al. 1992; Meynet & Arnould 2000; Longland et al. 2011).

2.5.1 Fluorine production in AGB stars

Although there are several sources needed to explain and fit chemical evolution models with galactic chemical abundance evolution, no doubt AGB production is one of the main contributors. It is also the only one validated by observations.

In AGB, fluorine is mainly produced in core and shell-helium burning in the mass 2-4 $M_{\odot}$ range, being destroyed by proton capture in the convective base (Hot Bottom Burning) of intermediate AGB stars (4-7 $M_{\odot}$) and α-capture at temperatures above $2.5{\cdot}10^8$ K. However, when the HBB ceases, the intermediate AGB could overproduce fluorine. Although they produce less that the low mass AGBs, they will expel more material into the interstellar medium (Pilachowski & Pace 2015).

So, there are two main chain reactions proposed for obtaining ^{19}F, triggered by the neutron or α-capture of ^{14}N (Guerço et al. 2019):

Low mass AGB channel

Cristallo et al. (2014)

$$^{14}N + n \rightarrow ^{14}C + ^{1}H$$
$$^{14}C + ^{4}He \rightarrow ^{18}O + \gamma$$
$$^{18}O + ^{1}H \rightarrow ^{15}N + ^{4}He$$
$$^{15}N + ^{4}He \rightarrow ^{19}F + \gamma$$

Intermediate AGB channel

Meynet & Arnould (2000)

$$^{14}N + ^{4}He \rightarrow ^{18}F + \gamma$$
$$^{18}F \rightarrow ^{18}O + e^{+} + \nu$$
$$^{18}O + ^{1}H \rightarrow ^{15}N + ^{4}He$$
$$^{15}N + ^{4}He \rightarrow ^{19}F + \gamma$$

The neutron source might be the ^{13}C pocket (see Fig. 1.13 and 1.14 and Sect. 1.3) formed during the inter-thermal pulses, in the TP-AGB stage, by engulfment of the convective envelope (rich in H^{+}) into the intershell region (enriched in ^{12}C by triple-α-reaction), evolving to the ^{16}O formation:

$$^{13}C + ^{4}He \rightarrow ^{16}O + nflux$$

The proton source is triggered by ^{14}C from neutron capture by ^{14}N (first reaction above indicated).

The formation of ^{14}N (and later fluorine) might be seen as a poisoning reaction of the neutron production by the ^{13}C pocket, common neutron source of main s-process elements production. Although there is not a straightforward connection between F and s-process, a clear correlation between F and the s-element enhancements can be found in carbon-rich stars (C-type) (Abia et al. 2010).

2.5.2 Chemical galactic evolution abundances

Abundances derived from molecular HF lines are limited by temperature because the HF feature disappears in stars hotter than about 4700 K due to molecular dissociation, so effective samples are limited to M and late K type dwarfs.

With such a variety of possible sources and somewhat varied nuclear reaction chains, the chemical evolution of fluorine in the Galaxy may be complex. No single chemical evolution model satisfactorily describes the observed behavior of the derived fluorine abundances as a function of metallicity (Guerço et al. 2019; Kobayashi et al. 2011a).

No evident trends are observed in Fig. 2.43, indicating a complex relation and different nucleosynthesis sites contributions.

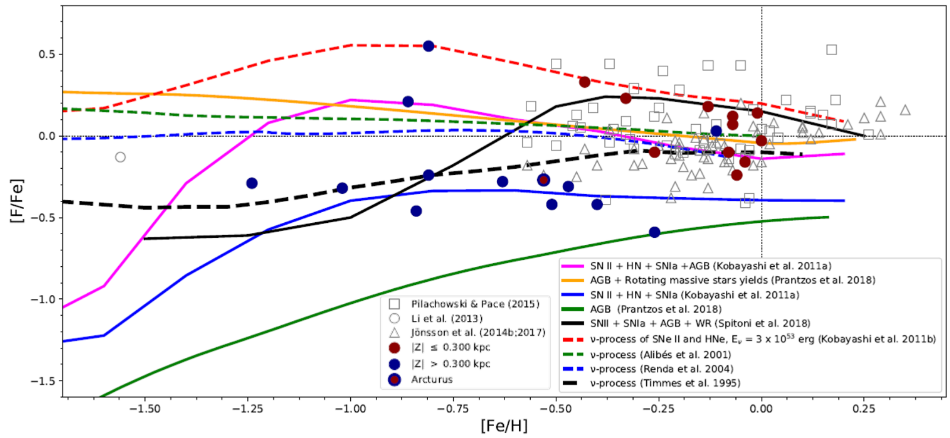

Figure 2.43: *The chemical evolution of fluorine viewed as [F/Fe] versus [Fe/H]. The blue circles represent stars with distances from the mid-plane |Z| > 300 pc, corresponding to the geometric thick disk/halo, while the red circles correspond to probable thin disk stars (|Z| < 300 pc). Other fluorine abundance results by Pilachowski & Pace (2015), Li et al. (2013) and Jönsson et al. (2014b, 2017) are also shown as open symbols. Several chemical evolution GCE models from the literature with different combination of likely fluorine sources by Kobayashi et al. (2011b), Prantzos et al. (2018) and Spitoni et al. (2018) are included. Sample limited to dwarfs and giants with T_{eff} < 4700 K. From Guerço et al. (2019).*

Nevertheless, some hints are observed. For instance, the evidence of the contribution of neutrino spallation ν-processes in core-collapse supernovae SNeII in the abundances of thin disk stars (Pilachowski & Pace 2015). At lower metallicities the models are in conflict though the fluorine seems to behave as a primary-like element, with increasing contributions from ν-processes and fast rotating massive stars.

However GCE models including AGBs (Prantzos et al. 2018, see Fig. 2.43 and 2.44) as fluorine sources show large discrepancies due to the uncertainties in the reaction rates and yields (Guerço et al. 2019).

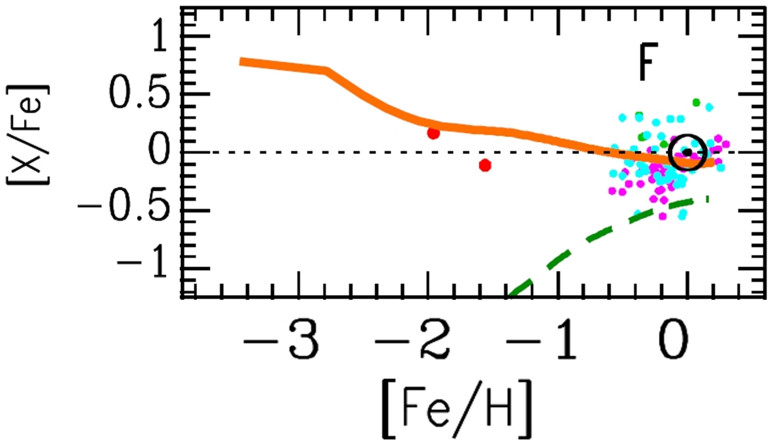

Figure 2.44: *Evolution of abundance ratio [F/Fe] as a function of [Fe/H] and comparison to observational data. Prantzos et al. (2018) model from massive and AGB/LIMS stars productions is in dashed green curve; the same model but with enhanced yields from rotating massive stars is in orange curve. Observational data from Recio-Blanco et al. (2012), Jönsson et al. (2014a), Pilachowski & Pace (2015), Jönsson et al. (2017), Li et al. (2013), Maiorca et al. (2014), Nault & Pilachowski (2013) and Cunha et al. (2008) based on LTE assumptions. From Prantzos et al. (2018).*

2.6. Sodium ($_{11}$Na)

The Odd-Z element, Sodium, has an only stable isotope ^{23}Na. As an odd-Z (neutron-rich) element, its production is sensitive to neutron excess and is therefore metal-dependent (Takeda et al. 2003).

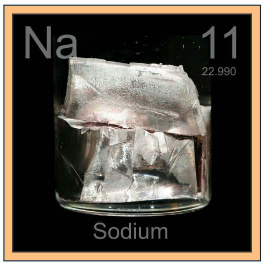

Basically, two main sources contribute to the sodium abundances (Smiljanic et al. 2016):

Na Nucleosynthesis Sources

- Hydrostatic carbon burning in massive stars, where final abundances are sensitive to neutron excess.
- In high-temperature H-burning regions through the NeNa cycle in low or intermediate mass stars.

But others are suspected contributing in less proportion as thermonuclear supernovae SNeIa or Classical Novae.

Production by hydrostatic C burning is developed throughout the reaction:

C Burning

$$^{12}C +^{12} C \rightarrow^{23} Na +^{1} H$$

Later, the SNeII supernovae will enrich the interstellar medium with the Na production.

The Na production by the NeNa cycle (see Fig. 2.45) in low or intermediate mass stars, might be mixing to the stellar photosphere during First Dredge-Up (FDU) though it is not clear to what extent. Models predict that mixing is deep enough to change Na abundance only in giants (RGB) above 1.5-2 $M_{\odot}$but particularly in intermediate-mass above 4 $M_{\odot}$. Observationally, it is well known that evolved intermediate-mass stars show some Na enhancement after the FDU (Smiljanic et al. 2016). However, low-mass metal-poor field giants (< 2 $M_{\odot}$) do not show an indication of changes in their surface Na abundances (Gratton et al. 2000), see Fig. 1.8 in Chapt. 1.

Likewise, mixing might occur later during AGB phase, enriching the medium by the stellar winds and outer layers loss during AGB and Post-AGB.

The ^{23}Na production by NeNa cycle results from:

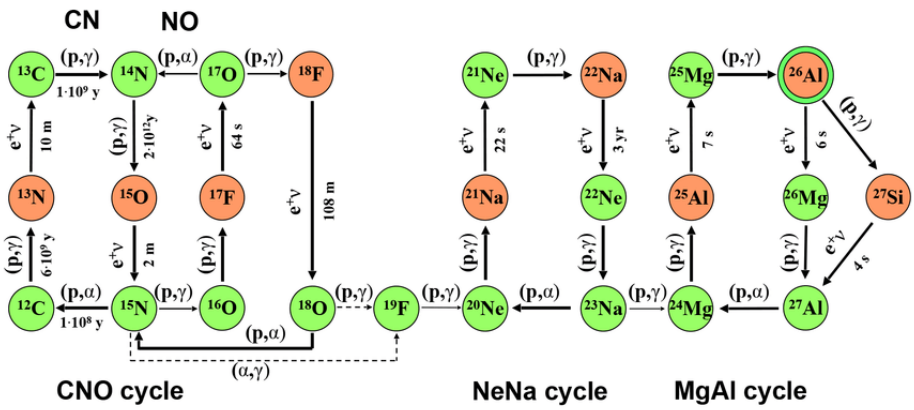

Figure 2.45: *Linked CNO, NeNa and MgAl cycles. Stable and long lived radioactive nuclei are shown in green, while short lived are shown in orange.* ^{26}*Al is long lived nuclide in its ground state, while its metastable state decays directly to* ^{26}*Mg with a short half-life. Characteristic time scales and lifetimes are indicated for some of the processes. From Boeltzig et al. (2016).*

H Burning NeNa cycle

$$^{22}Ne +^{1} H \rightarrow^{23} Na + \gamma$$

while the reactions...

Na destruction

$$^{23}Na +^{1} H \rightarrow^{24} Mg + \gamma$$
$$^{23}Na +^{1} H \rightarrow^{20} Ne +^{4} He$$

...are responsible for its destruction, which can be substantial at T > $60{\cdot}10^6$ K (Arnould et al. 1999).

2.6.1 Chemical galactic evolution abundances

Chemical evolution models still have problems reproducing the observed behavior of the Na. The enhancement in super-solar metallicities is a particular challenge. For instance, none of the models computed by Romano et al. (2010, see Fig. 2.46), with different stellar yields, was able to reproduce such behavior (Smiljanic et al. 2016).

Chemical galactic abundances from Gaia-ESO observational data (see Fig. 2.47) for dwarfs and giants at higher metallicities show the Na enhancement in giants due to the FDU, especially for intermediate mass stars, though it is likely caused by systematic problems in

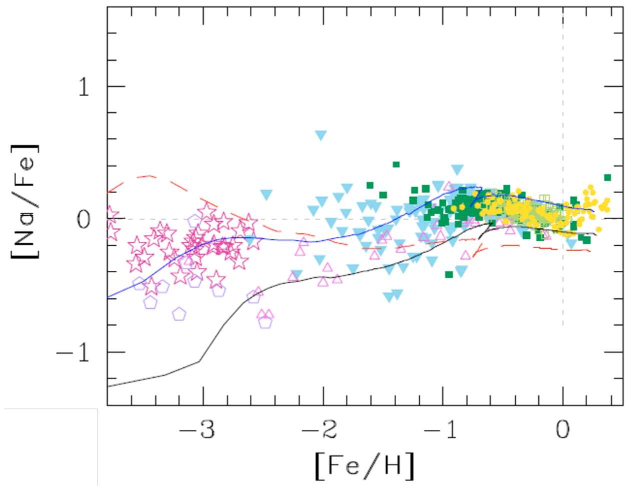

Figure 2.46: *Na galactic chemical distribution in function of metallicity. Observational abundance data from Andrievsky et al. (2007)(stars), Lai et al. (2008)(open pentagons), Gratton et al. (2003)(blue upside-down triangles), Gehren et al. (2006)(open triangles), Reddy et al. (2006)(filled squares), Reddy et al. (2003)(open squares) and Bensby et al. (2005)(filled circles). Some chemical evolution models have been added (dashed and solid lines). From Romano et al. (2010).*

the analysis and it is still under investigation (Smiljanic et al. 2016).

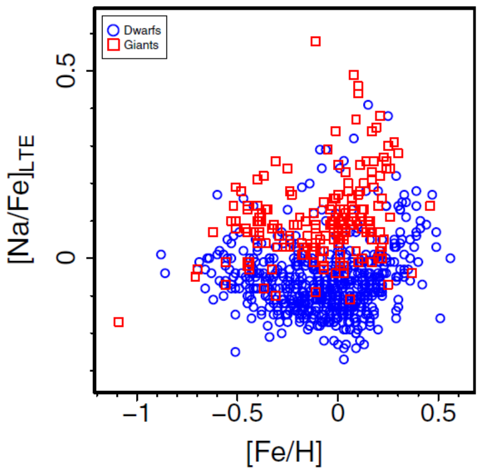

Figure 2.47: *Sodium abundances in dwarfs and giants, as a function of metallicity. From Smiljanic et al. (2016).*

In spite of the new and high quality observational data and the use of up-to-date stellar yields, the disagreement between models and observations remains and the explanation does not seem to lie in low and intermediate-mass stars (NeNa cycle) whose contribution to the galactic abundance seem to be negligible (Smiljanic et al. 2016), but by the massive stars (carbon burning stage) production modelling (novae type, rotational effects on nucleosynthesis,...).

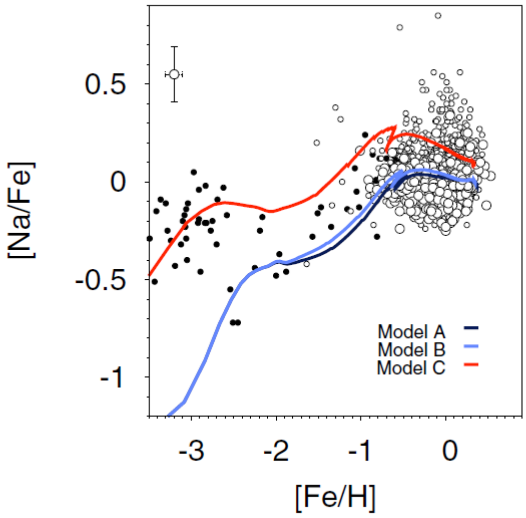

Figure 2.48: *Na galactic chemical distribution in function of metallicity. Observational abundance data from Gaia-ESO (open circles) and low-metallicity stars (filled circles) from Gehren et al. (2006) and Andrievsky et al. (2007). Models A (Romano et al. 2010), B and C, explained in text. From Smiljanic et al. (2016).*

When observing the Fig. 2.48, model C seems to be doing a better job. Model A is one of the models from Romano et al. (2010), discussed above. Model B is the same as A but including updated yields for low and intermediate-mass stars (not much change in abundance terms with respect to the model A) by Ventura et al. (2013, 2014b,a). Finally, model C is the same as B but limiting massive star explosions. In model C the massive stars are modeled to undergo core-collapse supernovae (SNeII) with energies on the order of 10^{51} erg (Kobayashi et al. 2006). In models A and B, the same massive stars are modeled as hypernovae explosions with energies on the order of 10^{52} erg.

Clearly, the inclusion of massive stars into the model greatly impacts the theoretical abundances. Even in the case of the best fitting model C, it greatly fails in overestimating aluminum (Al) production (very related to the Na one) when applied at lower metallicites. This fact is hinting some failure in the basic premises of the nucleosynthesis sites (sodium or aluminum).

Moreover, all of them are failing in explaining uprising Na abundances at supersolar metallicities [Fe/H] > 0, which is suggesting the model is missing a nucleosynthesis source. It might be SNeIa, though the contribution seems negligible (Iwamoto et al. 1999).

Classical Novae (see Fig. 1.41 and Sect. 1.40 in Chapt. 1) might be an alternative good candidate because they equally (as SNIa) supply the products of explosive H burning on relative long-time scales, and have been already detected to be contributing with important amounts of ^{7}Li, ^{13}C, ^{15}N, ^{17}O, ^{22}Na and ^{26}Al. Maybe, it might too with ^{23}Na. However, the explanation of the increasing trend with time might lie elsewhere (Smiljanic et al. 2016) and new data are needed for obtaining a better understanding on the Na nucleosynthesis.

NLTE effect corrections

Finally, several are the authors that have studied the non-LTE effects and their impact in Na abundance determination as e.g. Mashonkina et al. (2000), Gehren et al. (2004, 2006) or Andrievsky et al. (2007).

Depending on the chosen lines, they show to be strong corrections, especially at low metallicity (see Fig. 2.49). Photoionization rates tend to increase with decreasing metal abundance and the neutral atoms become a minority that is sensitively reacting with particle interactions (Gehren et al. 2004, 2006).

The abundance distribution figures of Na show the theoretical expected Odd-Z element behaviour: a lower production at lower metallicities. However the high NLTE effects at low metallicity preclude any strong conclusions from comparing GCE model to observational data based on LTE assumptions (Prantzos et al. 2018). And it points to the need of exact determination studies of NLTE effects at low metallicity.

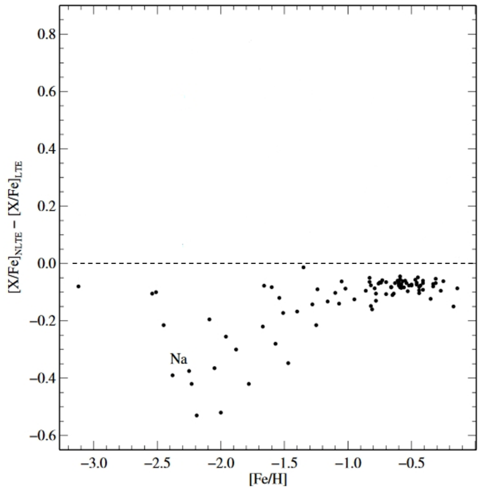

Figure 2.49: *NLTE corrections for Na in function of the metallicity by Gehren et al. (2006) (adapted). Averaged corrections from Na* I *5889.96, 5895.93, 6154.23, 6160.75, 5682.64 and 5688.21 Å lines.*

2.7. Magnesium ($_{12}$Mg)

Magnesium is an α-element. It is mostly formed in the final burning stages of massive stars preceding core-collapse supernova (SNeII). It is a product of hydrostatic carbon ensuing neon-burning in massive stars.

Carbon Burning

$$^{12}C +^{12} C \rightarrow^{23} Mg + n$$

Neon Burning

$$^{20}Ne +^{4} He \rightarrow^{24} Mg + \gamma$$

The amount of freshly synthesized magnesium depends on the available fuel, e.g. the size of the C-O core after hydrostatic He burning (Argast et al. 2002).

Like of the other α-elements its chemical distribution reflects two main key ideas about galactic evolution (see introduction to oxygen element in Sect. 2.4 for additional details) that determines its profile (see Fig. 1.27):

α-elements galactic evolution keys

- The early Universe was α-enriched because SNeII occurred on a much faster time-scale than SNeIa.
- The halo, thick and thin disks show their own chemical and kinematical features as a result of a different formation and evolutionary path.

2.7.1 Chemical galactic evolution abundances

Several magnesium abundance surveys show similar profiles in line with the latter two key galaxy evolution ideas, as e.g. Gehren et al. (2006); Adibekyan et al. (2012); Bensby et al. (2014); Prantzos et al. (2018).

In the Fig. 2.50 is observed the chemical abundance gap (around +0.1 dex at [Fe/H] = -0.5 dex) between thin and thick disk stars. Older thick disk stars were arisen from metal-poorer clouds which gathered material from the first stellar generations, hence highly enhanced by material from SNeII ejecta in which the yields of α-elements (as Mg) were higher.

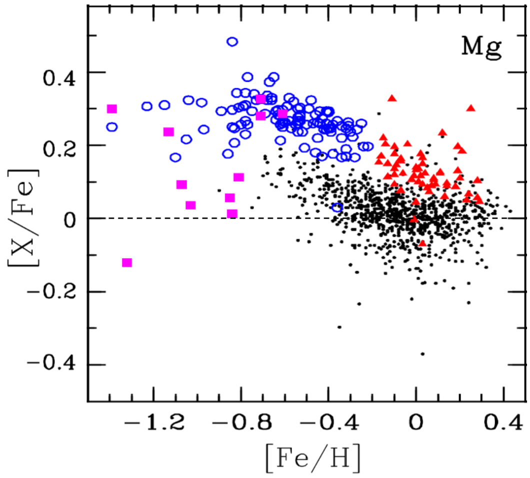

Figure 2.50: *[Mg/Fe] ratio abundance with respect to the metallicity [Fe/H]. The blue circles and black dots refer to the chemically selected thick- and thin disk stars, and the red filled triangles are the hαmr stars (high alpha metal rich thin disk stars). Magenta squares represent the stars belonging to the halo according to their kinematics. Sample of 1111 FGK stars from HARPS GTO planet search program, Adibekyan et al. (2012).*

Thus, the relative abundance in Mg increases at lower metallicity, reaching a plateau at ca [Fe/H] ~ -1.0 dex, the breaking point in the galaxy evolution from which the SNeIa began to dilute the older and more abundant SNeII production.

However, when metal-poorer stars are studied, nearby- and extremely metal poor stars (mostly thought to be halo stars), the distribution scatters (see Fig. 2.51, 2.52 and especially 2.53).

This fact implies that the interstellar medium (ISM) was not well mixed at early stages of the galaxy formation. Two main reason might explain the abundance scattering at very low metallicity (Argast et al. 2000, 2002):

Scattering at low metallicity

- Firstly, strong dependence of the nucleosynthesis and ejected mass with the wider range of SNeII's progenitors masses at early stages of the universe. The ejected Mg but too other elements as O or Ne vary by a factor of 10-20 between a 13 $M_{\odot}$and a 25 $M_{\odot}$progenitor star (Argast et al. 2002). This in-homogeneously enriched the medium in some α and other elements, see e.g. Karlsson et al. (2013) paper and Table 1.2 in Chapt. 1. Accurate nucleosynthesis yields as a function of progenitor mass are crucial for the understanding of the earliest stages of galaxy formation.
- Secondly, as a consequence, a wide range of stellar features which are very dependent of the local chemical conditions due to the in-homogeneous pro-

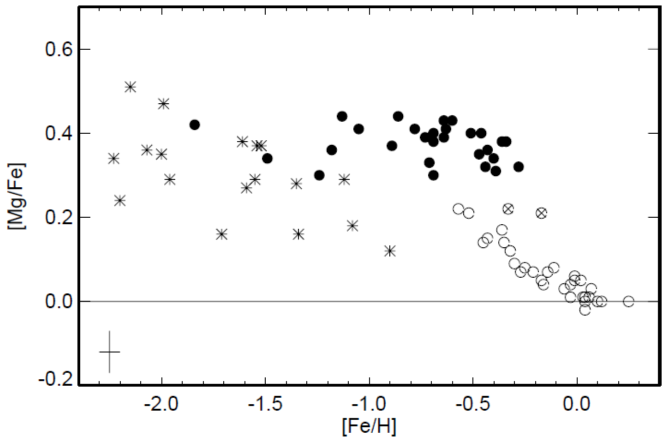

Figure 2.51: *[Mg/Fe] ratio abundance with respect to the metallicity [Fe/H] of a sample of cool dwarf stars. Symbols correspond to thin disk (open circles), thick disk (filled circles), and halo stars (asterisks). The two stars indicated by a cross in an open circle are transition stars between thin and thick disk according to Fuhrmann (1998). From Mashonkina et al. (2003).*

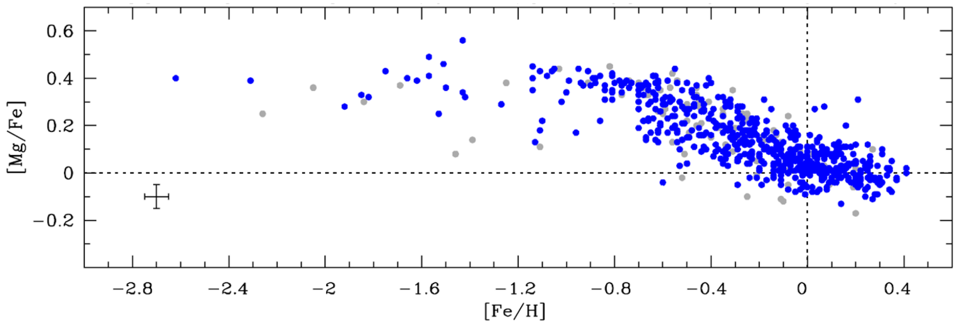

Figure 2.52: *[Mg/Fe] ratio abundance (LTE) with respect to the metallicity [Fe/H] of a sample of 714 dwarf and sub-giant stars. Grey dots indicate stars with T_{eff} < 5400 K. From Bensby et al. (2014).*

duction from SNeII of previous generations.

Base on these assumptions, however some models fail in reproducing Mg abundance, even though they are successful in predicting other α-elements (Argast et al. 2000). This is a strong indication that the progenitor mass dependence of existing nucleosynthesis models is not fully understood. It is not only in the case of elements as Mg but especially in the correct determination of iron amounts in ejecta.

Even the inclusion of fast rotators massive star yields, unlike other elements, fail to improve the fit of GCE models with respect to the observational data, as shown in Fig.2.53.

NLTE effect corrections

As an additional factor, one has to take into account stronger NLTE effects at lower metallicities. Though negligible for thick and thin disk stars (< +0.1 dex), for metal poorer stars belonging to the halo, the average NLTE effects on main Mg lines can be significant (+0.2 dex, see Fig. 2.54).

Other studies claim negative corrections for the high excitation Mg II lines and Mg I triplet at 517 nm, which is only concerning at very low metallicities (-0.05 and -0.2 dex corrections at most, respectively, at metal poor range) (Romano et al. 2010).

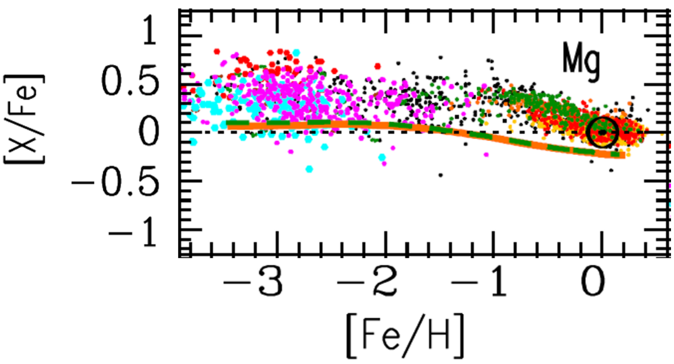

Figure 2.53: *Evolution of abundance ratio [Mg/Fe] as a function of [Fe/H] and comparison to observational data. Prantzos et al. (2018) model from massive and AGB/LIMS stars productions is in dashed green curve; the same model but with enhanced yields from rotating massive stars is in orange curve. Observational data from Yong et al. (2013), Bensby et al. (2014), Roederer et al. (2014a), Adibekyan et al. (2012) and Chen et al. (2000) based on LTE assumptions. From Prantzos et al. (2018).*

As final remark, there is to indicate the helpful use of magnesium as an α-element prototype, in ratios against elements of different character. E.g., as a proxy to stellar ages when compared with respect to a main s-process element as Y (Feltzing et al. 2017) like it is observed in Fig. 3.33, hinting the different nucleosynthesis sites and the time delay between SNeII (Mg) and the main s-process first peak AGB production (Y). Or against a r-process element as Eu, for documenting the coupling of chemical abundances (see Fig. 3.55) and suggesting a common origin (SNeII of 8-10 $M_{\odot}$), although throughout different nucleosynthesis mechanisms. Or with respect to Mg-like (α-like) elements as K for confirming coupled nucleosynthesis (see Fig. 2.76).

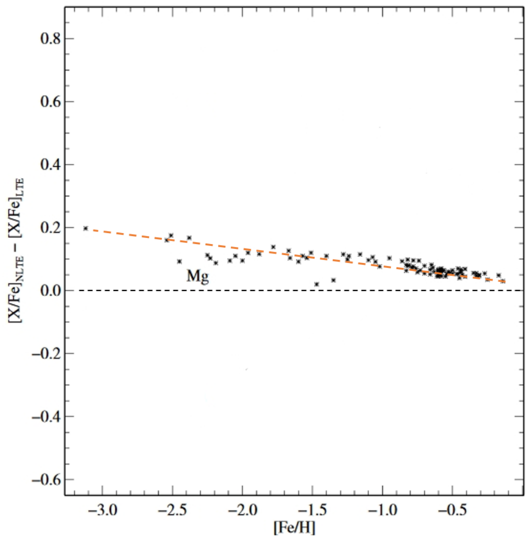

Figure 2.54: *NLTE corrections for Mg (averaged main optical lines) in function of the metallicity by Gehren et al. (2006) (adapted). Averaged corrections from Mg* I *4571.09, 5172.70, 5183.62, 5711.07, 5528.41, 4730.03 and 4702.99 Å lines.*

2.8. Aluminum ($_{13}$Al)

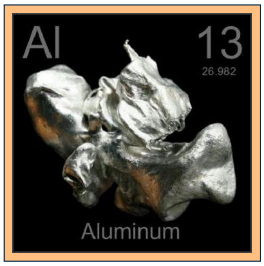

The only stable isotope ^{27}Al is mainly synthesized in carbon and neon burning phases of massive stars (Arnett & Thielemann 1985; Thielemann & Arnett 1985; Woosley & Weaver 1995).

But also in intermediate AGB (Ventura et al. 2014b; Doherty et al. 2014a) above 5 $M_{\odot}$ experiencing HBB through the MgAl cycle (see Fig. 2.45). This cycle is triggered above $50{\cdot}10^6$ K but it would be at temperatures exceeding $70 \cdot 10^6$ K when the cycle pushes forward the production for ^{27}Al accumulation (Arnould et al. 1999).

An odd-Z element as Al might have been expected to behave like Na but it doesn't in terms of galactic chemical abundances. Al is Mg-like, an α-like element in other words (Reddy et al. 2006). At higher metallicities (>-1.0 dex) corresponding to thick and thin disk stars, the behaviour is alike to the α-elements one (see Fig. 1.27). This is understandable because of the common origin in late burning stages of massive stars before they become core-collapse supernovae (SNeII).

2.8.1 Chemical galactic evolution abundances

In spite of being linked to the same burning phases than Na (C and Ne burning phases in massive stars, and the NeNaMgAl cycle in AGBs though different activation temperatures by different stellar masses), Al shows an strikingly α-like profile (see Fig. 2.55), unlike Na (see Fig. 2.46 and 2.47) at higher metallicities > -1.0 dex.

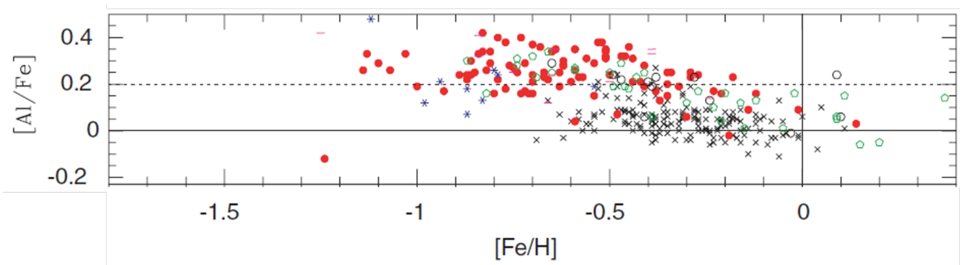

Figure 2.55: *Al galactic chemical distribution in function of metallicity for a dwarf sample from Hipparcos catalogue by Reddy et al. (2006). Using accurate radial velocities combined with the Hipparcos astrometry, kinematics (U, V and W) and Galactic orbital parameters it is estimated the probability for a star to belong to the thin disc, the thick disc or the halo: thick disc (filled red circles), the thin disc (open red circles), the halo (blue circles), and the stars which might belong to either the thin or the thick disc (green pentagons), and stars which might belong to either the halo and the thick disc (magenta dashes).*

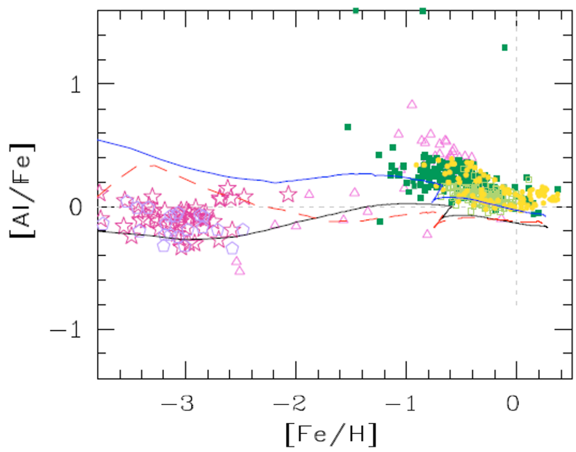

Figure 2.56: *Al galactic chemical distribution in function of metallicity. Observational abundance data from Andrievsky et al. (2007)(stars), Lai et al. (2008)(open pentagons), Gehren et al. (2006)(open triangles), Reddy et al. (2006)(filled squares), Reddy et al. (2003)(open squares) and Bensby et al. (2005)(filled circles). Some chemical evolution models have been added (lines). From Romano et al. (2010).*

Even more striking, at lower metallicities (halo EMP stars) the models that nicely reproduce Na observations (see Sect. 2.6 model explanations) constantly overproduce Al (see Fig. 2.57, model C in red). Besides the EMP stars seem to show a lower scatter than Na ones.

For galaxy thick and thin disks stars, they fail by under-producing abundances with respect to the observations. It is a strong indication that a better understanding about the Al nucleosynthesis is needed. E.g. next studies about the impact of stellar rotations (fast rotators are more frequent in an early universe) on nucleosynthesis might help to reach a better understanding (Smiljanic et al. 2016). The activation of the MgAl chain in the central regions of rotating massive stars on the main sequence, followed by transportation of Al-rich matter to the outer envelope and ejection of the outermost layers by slow stellar winds, might lead to a substantial modification of the used Al yields (Romano et al. 2010; Decressin et al. 2007).

However, so far, the study including fast rotators yields into the GCE model by Prantzos et al. (2018) has not improved the fit to observational data (see Fig. 2.58).

NLTE effect corrections

A final consideration to be taken into account are the likely strong NLTE effects that might affect abundances of metal poorer stars. Although non-LTE abundances of Al have been computed in the literature, e.g. corrections by Gehren et al. (2004, see Fig. 2.59), however no comprehensive grid of NLTE effect corrections is currently available for the full metallicity

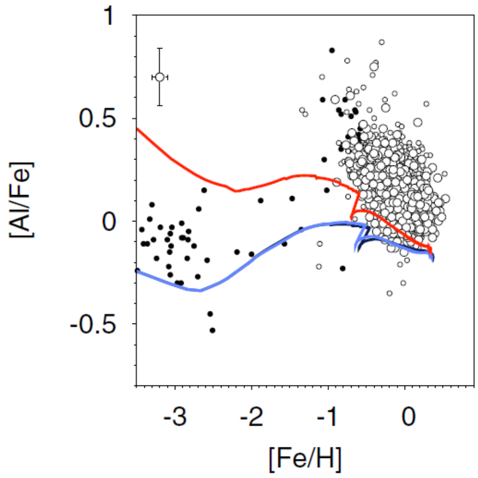

Figure 2.57: *Al galactic chemical distribution in function of metallicity. Observational abundance data from Gaia-ESO (open circles) and low-metallicity stars (filled circles) from Gehren et al. (2006) and Andrievsky et al. (2007). Models A (Romano et al. 2010) (black), B (blue) and C (red), explained in section 2.6. From Smiljanic et al. (2016).*

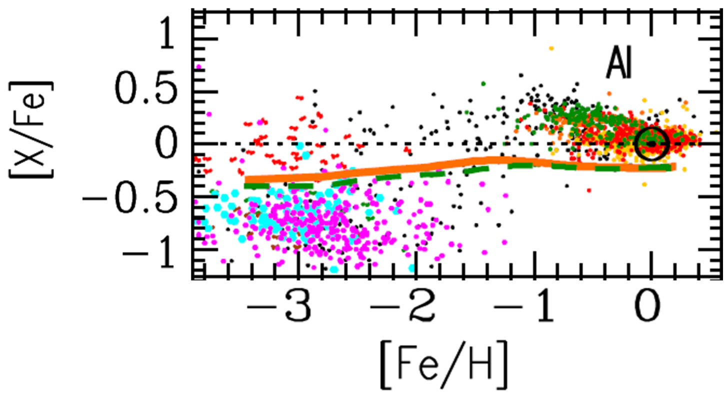

Figure 2.58: *Evolution of abundance ratio [Mg/Fe] as a function of [Fe/H] and comparison to observational data. Prantzos et al. (2018) model from massive and AGB/LIMS stars productions is in dashed green curve; the same model but with enhanced yields from rotating massive stars is in orange curve. Observational data from Yong et al. (2013), Bensby et al. (2014), Roederer et al. (2014a), Adibekyan et al. (2012) and Chen et al. (2000) based on LTE assumptions. From Prantzos et al. (2018).*

range (Smiljanic et al. 2016). Nevertheless, it is a factor that can not be ignored.

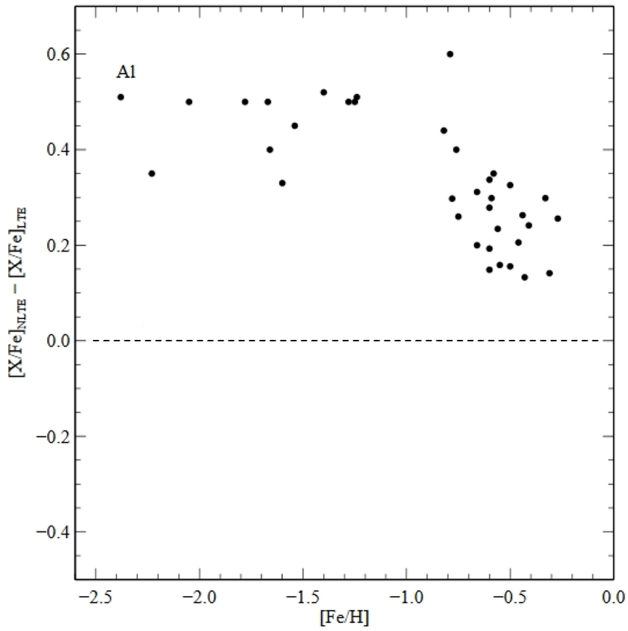

Figure 2.59: *Difference of aluminum abundance ratios calculated under NLTE and LTE assumptions by Gehren et al. (2004). Average NLTE corrections from several Al* I *optical lines: 3961.53, doublet 6696.03 & 6698.67, doublet 8772.88 & 8773.91 and doublet 7835.31 & 7836.13 Å.*

2.9. Silicon ($_{14}$Si)

Silicon is an α-element. It is mostly formed in the final burning stages of massive stars preceding core-collapse supernovae (SNeII). It is a product of neon and specially from the oxygen burning stage (Woosley & Weaver 1995). This burning is maintained for one year and the needed temperature exceeds the 1500-2600 $\cdot 10^6$ K...

Oxygen Burning

$$^{16}O + ^{16}O \rightarrow ^{28}Si + ^{4}He$$

...and the final abundance of Si in the stellar ejecta is sensitive to a variety of factors regarding the evolution and explosion of the progenitor stars (Romano et al. 2010).

SNeIa may also produce some Si, as suggested by Tsujimoto et al. (1995) and Nomoto et al. (1997) but like of the other α-elements its chemical distribution reflects two main key ideas about galactic evolution (see introduction to oxygen element in Sect. 2.4 for additional details) that determines its profile (see Fig. 1.27):

α-elements galactic evolution keys

- The early Universe was α-enriched because SNeII occurred on a much faster time-scale than SNeIa.
- The halo, thick and thin disks show their own chemical and kinematical features as a result of a different formation and evolutionary path.

2.9.1 Chemical galactic evolution abundances

Several silicon abundances surveys show similar profiles in line with these two key evolutionary ideas (e.g. see Fig. 2.60 and 2.61).

Some chemical models (see Fig. 2.62) are in good agreement with the available data, though at supersolar metallicity might require a revision of stellar yields from high-metallicity massive stars and/or SNeIa. It is too suggested that in the very early halo stages the most massive stars exploded as hypernovae (HNe) rather than normal SNeII (Romano et al. 2010).

Nevertheless, the evolution of α-elements as Si, is well reproduced, in general, by most GCE models. This is one of the well established results in the field of stellar nucleosynthesis

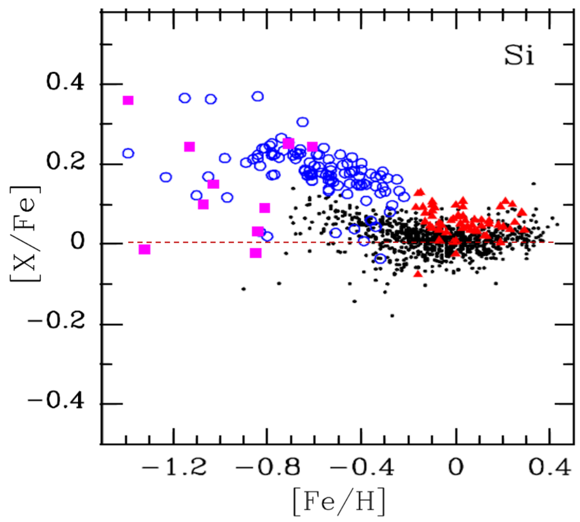

Figure 2.60: *The blue circles and black dots refer to the chemically selected thick- and thin disk stars, and the red filled triangles are the hαmr stars (high alpha metal rich thin disk stars). Magenta squares represent the stars belonging to the halo according to their kinematics. Sample of 1111 FGK stars from HARPS GTO planet search program, Adibekyan et al. (2012).*

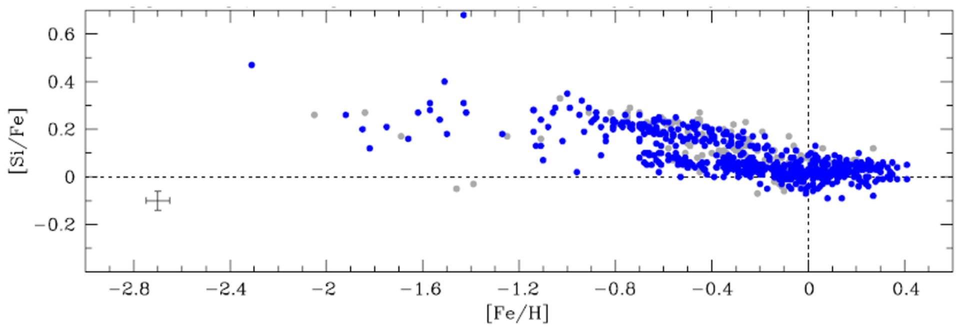

Figure 2.61: *[Si/Fe] ratio abundance (LTE) with respect to the metallicity [Fe/H] of a sample of 714 dwarf and sub-giant stars. Grey dots indicate stars with T_{eff} < 5400 K. From Bensby et al. (2014).*

and GCE studies. A recent study by Prantzos et al. (2018), it is reassuring that rotation does not affect that result (see Fig. 2.63).

NLTE corrections

The scatter in Si abundances are present through all metallicities but are particularly high for extremely metal-poor stars when LTE conditions are assumed (Shi et al. 2009, see Fig. 2.63 or 2.64).

There are two are main causes that might be contributing to an extra-scattered behaviour

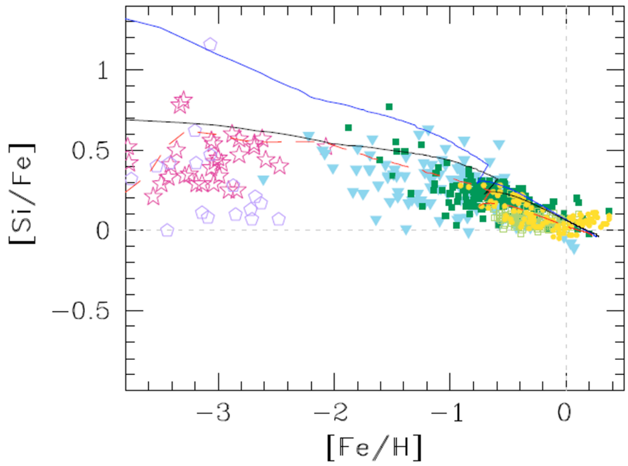

Figure 2.62: *Al galactic chemical distribution in function of metallicity. Observational abundance data from Andrievsky et al. (2007)(stars), Lai et al. (2008)(open pentagons), Gratton et al. (2003)(blue upside-down triangles), Gehren et al. (2006)(open triangles), Reddy et al. (2006)(filled squares), Reddy et al. (2003)(open squares) and Bensby et al. (2005)(filled circles). Some chemical evolution models have been added (dashed and solid lines). From Romano et al. (2010).*

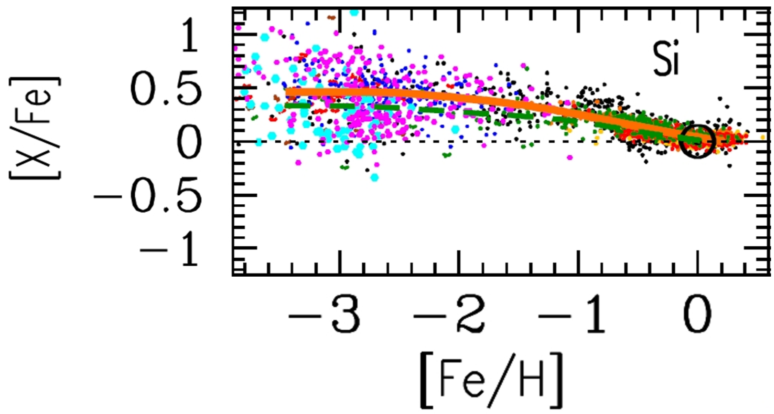

Figure 2.63: *Evolution of abundance ratio [Si/Fe] as a function of [Fe/H] and comparison to observational data. Prantzos et al. (2018) model from massive and AGB/LIMS stars productions is in dashed green curve; the same model but with enhanced yields from rotating massive stars is in orange curve. Observational data from Yong et al. (2013), Bensby et al. (2014), Roederer et al. (2014a), Adibekyan et al. (2012) and Chen et al. (2000) based on LTE assumptions. From Prantzos et al. (2018).*

at lower metallicities. Firstly, the optical Si I lines are very weak in metal-poor stars (Tan et al. 2016) and the two strong Si I 3905 and 4102 Å lines in near-ultraviolet are not perfectly unblended, e.g. the 3905 Å line is affected by CH bands, quite appreciable in cool giant stars. In addition, in case of binary systems including a hot star with high UV flux, deriving abundance from these lines is problematic.

By these motives some studies use IR Si I lines, unblended and stronger, for deriving abundances at lower metallicities or surface temperatures (Jönsson et al. 2011; Shi et al. 2012).

Secondly, the NLTE effects, which differs from line to line showing large departures from LTE in warm metal-poor stars (+0.25 dex). The strong dependence with surface temperature is shown in Fig. 2.65. Stronger lines as Si I 3905 and 4102 Å show stronger NLTE corrections. The weak lines at higher metallicities are better lines for deriving abundances.

Si I NLTE corrections are positive meanwhile two characteristics Si II as 6347.10 and 6371.36 Å lines are negative, helping to remove historical discrepancies between abundances obtained from Si I and Si II under LTE assumptions (Shi et al. 2009).

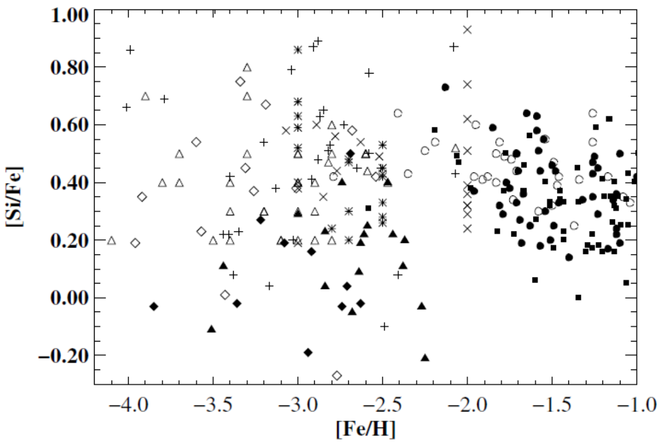

Figure 2.64: *Silicon abundances of metal-poor stars determined from LTE analyses of Fulbright (2000) (filled circles for dwarfs and open circles for giants), McWilliam et al. (1995) (pluses), Honda et al. (2004) (crosses), Aoki et al. (2005) (asterisks), Ryan et al. (1996) (filled diamonds for dwarfs and open diamonds for giants), Gratton et al. (2003) (filled squares), Cayrel et al. (2004) (open triangles), and Cohen et al. (2004) (filled triangles). From Shi et al. (2009).*

However, there might be other direct or indirect factors that contribute to the scatter (Prantzos et al. 2018) as:

Scattering at low metallicity

- Rare events with high mass ejecta (CBM or MHD-SNeII).
- Evolution factors of the early Galaxy as merging of sub-halos, each one with its own history and timescale for chemical enrichment.
- Imperfect gas mixing.

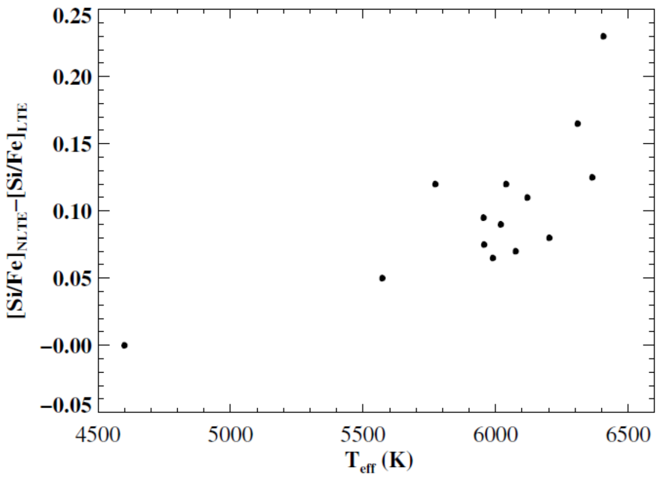

Figure 2.65: *NLTE corrections over LTE assumptions for the two strong Si* I *3905 and 4102 Å lines as a function of surface temperature. From* Shi et al. (2009).

2.10. Sulphur ($_{16}$S)

Sulphur is another α-element, produced in hydrostatic and explosive burning of oxygen and silicon in massive stars (> 8 $M_{\odot}$) (Woosley & Weaver 1995) preceding core-collapse explosion as supernovae SNeII.

Oxygen Burning

$$^{16}O + ^{16}O \rightarrow ^{32}S + \gamma$$
$$^{16}O + ^{16}O \rightarrow ^{31}S + n$$

Silicon Burning

$$^{28}Si + ^{4}He \rightarrow ^{32}S + \gamma$$

Like of the other α-elements its chemical distribution reflects two main key ideas about galactic evolution (see introduction to oxygen element in Sect. 2.4 for additional details) that determines its profile (see Fig. 1.27):

α-elements galactic evolution keys

- The early Universe was α-enriched because SNeII occurred on a much faster time-scale than SNeIa.
- The halo, thick and thin disks show their own chemical and kinematical features as a result of a different formation and evolutionary path.

However, whether sulphur behaves as a typical α-element is a controversial subject fed by IR metal poor stars studies. But analysing the sulfur abundance of metal-poor stars is problematic due to the lack of suitable atomic lines (Korn & Ryde 2005). This makes difficult obtaining conclusions about the nucleosynthesis sources of the S element from GCE model studies. Especially in the early universe as it will be discussed in Sect. 2.10.

Besides sulphur presents an additional interesting property, its striking low condensation temperature with respect to the rest of α-elements:

S, 674 K; Mg, 1340 K; Si, 1340 K; Ca, 1634 K; Ti, 1600 K (Maas et al. 2005).

Hence, S is a volatile element, not eager to form part of grains in the ISM (Savage & Sembach 1996), neither in circumstellar disks around AGB and Post-AGB stars (Maas et al. 2005), nor in circumbinary disks. This characteristic makes sulphur an ideal depletion-independent tracer of the evolution of galaxies (Costa Silva et al. 2020) and suitable for cosmological studies , e.g. as a cosmological clock for tracing the evolution of damped Lyα systems (Nissen et al. 2004, 2007). Which are huge clouds of predominantly neutral hydrogen gas at high redshifts that are thought to play an instrumental role in galaxy formation (Matrozis et al. 2013).

2.10.1 Chemical galactic abundances

As above commented, recent studies based on IR lines for metal poor stars feed the controvercy of the α-nature and the nucleosynthesis origin in early stages of the universe and galactic formation.

Historical studies have been based on S I high-excitation lines in the near-IR: 8693.2 & 8694.0 & 8694.6 (Nissen et al. 2004; Ryde & Lambert 2004) and 9212.9 & 9228.1 & 9237.5 Å (Israelian & Rebolo 2001; Takada-Hidai et al. 2002). Their weakness in halo stars, make the analysis very difficult (Korn & Ryde 2005).

The 2 early studies on S mentioned above Israelian & Rebolo (2001, see Fig. 2.66) and Takada-Hidai et al. (2002) found that the relative sulphur abundance continuously increases in the metallicity range from solar to at least [Fe/H] ≃ -2.5 dex, reaching [S/Fe]= +0.8 dex.

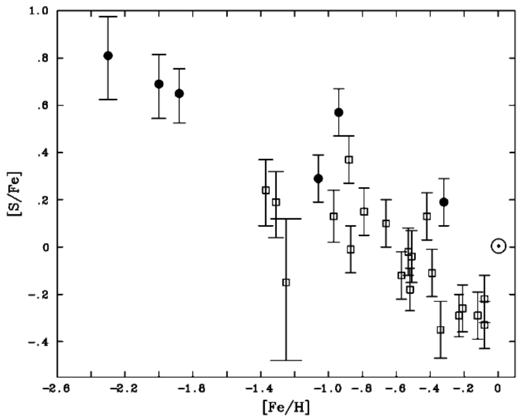

Figure 2.66: *Sulphur abundances with respect to iron. The open squares are the data from Francois (1987, 1988), and the filled circles, new measurements. The Sun is marked with the standard symbol. From Israelian & Rebolo (2001).*

This profile implies a very different nucleosynthesis origin in early stages of the universe. A high rate of sulphur-rich hypernovae HNe (e.g., Nakamura et al. 2001) was proposed as possible explanation.

But most of studies (Chen et al. 2002; Ryde & Lambert 2004; Nissen et al. 2007; Korn & Ryde 2005; Spite et al. 2011; Matrozis et al. 2013; Caffau et al. 2019; Costa Silva et al.

2020), do not find evidences for this uprising at lower metallicities than -1.0 dex. Instead, they show a typical steady plateau abundance enhancement ([S/Fe] $\simeq$ +0.3 dex). This a fairly α-element behaviour, pointing to the SNeII origin of the S (Costa Silva et al. 2020) and fitting quite well to the Kobayashi et al. (2006) model when compared to the Romano et al. (2010) and Prantzos et al. (2018) models (see Fig. 2.69 and 2.70).

A study by Prantzos et al. (2018) shows that rotation hardly improves the fit of the GCE models to observational data, showing the little effect of this nucleosynthesis contribution to α-element abundances (see Fig. 2.72).

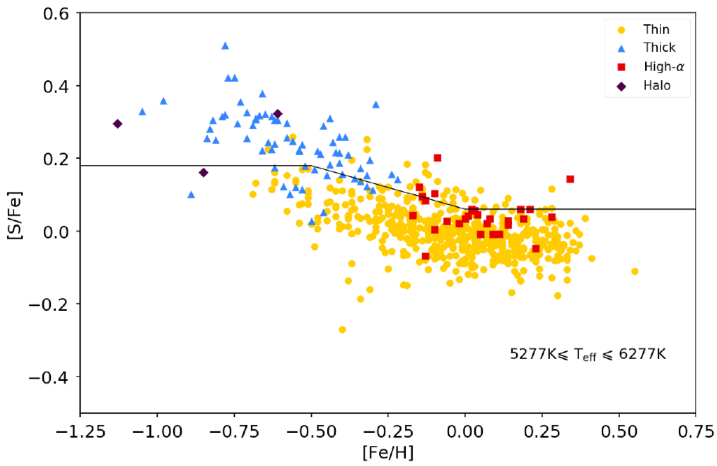

Figure 2.67: *[S/Fe] vs. [Fe/H], with the theoretical α-line chemical separation of thin and thick disks. Symbols: yellow circles are for the thin disc, blue triangles for the thick disc, red squares for the high-α metal-rich stars, and purple diamonds for halo stars. Sample of 1111 FGK stars from the HARPS-GTO planet search, Costa Silva et al. (2020).*

Other additional matter is linked with the lines selection for deriving abundances. As above commented, the traditional near-IR lines are quite weak at lower metallicities. The S I 8693/8694 Å lines have been argued to show negligible NLTE effects (see Fig. 2.68) but are not the case of the S I 9213 and 9237 Å lines (Takeda et al. 2005).

However, applying NLTE corrections, abundances from S I 8693/8694 Å lines are systematically higher than the ones from the S I 9212 and 9237 Å lines (Nissen et al. 2007). On the other hand, other used line as S I 8680 Å is blended with a Si I line with uncertain oscillator strength.

In the case of the S I 9212 and 9237 Å lines other considerations have to be taken into account as the opacity contribution from the wings of the Paschen-ζ hydrogen line at 9229 Å . And the high uncertainties introduced by the strong NLTE effects they look like to suffer (see Fig. 2.68).

These difficulties have encouraged the use of alternative lines as the IR S I at 1045 nm by Caffau et al. (2010), 1082 nm by Matrozis et al. (2013) or the optical S I 6743 and 6757

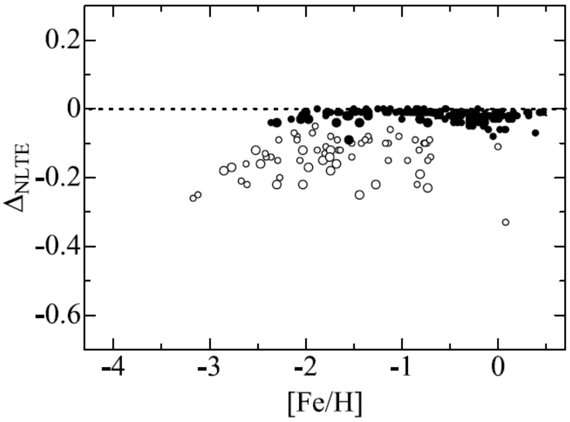

Figure 2.68: *NLTE corrections for S in Takeda et al. (2005). Open circles, corrections for S I 9212 and 9237 Å lines; filled circles, corrections for S I 8693/8694 Å doublet.*

Å lines (weak at lower metallicities) in the recently published work by Costa Silva et al. (2020).

Altogether, when observing the derived abundances from historical studies (see Fig. 2.71) mostly are pointing to the S behaviour as a typical α-element with the usual plateau at lower metallicities. This is a consequence of the early SNeII contribution to the ISM and the time delay of the SNeIa one as validated by models (Kobayashi et al. 2006, 2011b, see Fig. 2.69). Nevertheless, the remaining uncertainties advise the need for further observations and studies.

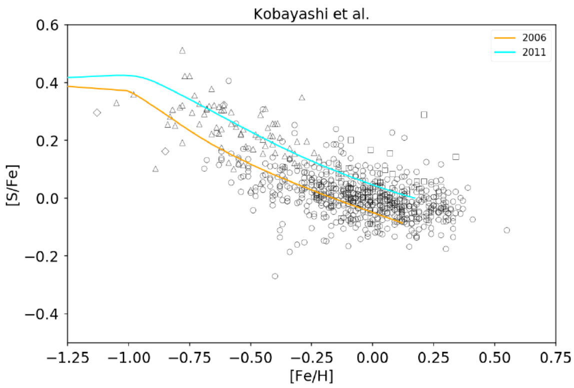

Figure 2.69: *Kobayashi et al. (2006, 2011b) galactic evolution models in the Costa Silva et al. (2020) sample.*

As a final example of this need, the recently derived abundances by Costa Silva et al. (2020, see Fig. 2.67) point to a continued decrease at high metallicities, showing a discrepancy with respect to the best fitted theoretical GCE model by Prantzos et al. (2018) of this region which predicts a flattened trend.

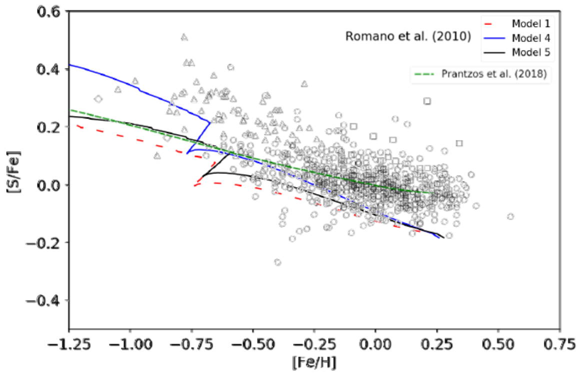

Figure 2.70: *Romano et al. (2010) and Prantzos et al. (2018) galactic evolution models in the Costa Silva et al. (2020) sample. Adapted figure.*

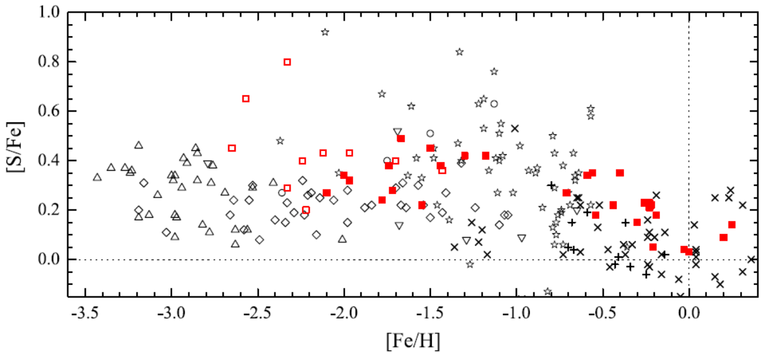

Figure 2.71: *Sulphur abundances derived in Matrozis et al. (2013) (red squeares) and previous works. The symbols denote measurements from Chen et al. (2002) (plus symbols), Takada-Hidai et al. (2002) (crosses), Ryde & Lambert (2004) (downward-pointing triangles), Caffau et al. (2005) (stars), Nissen et al. (2007) (rhombi), Caffau et al. (2010) (circles), and Spite et al. (2011) (upward-pointing triangles).*

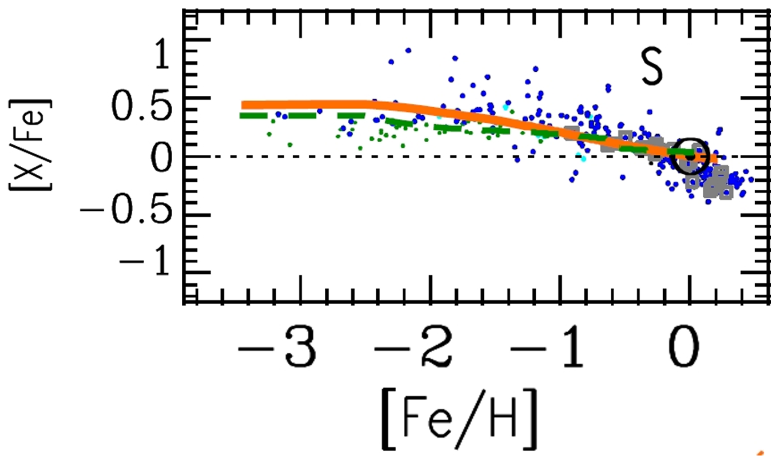

Figure 2.72: *Evolution of abundance ratio [S/Fe] as a function of [Fe/H] and comparison to observational data. Prantzos et al. (2018) model from massive and AGB/LIMS stars productions is in dashed green curve; the same model but with enhanced yields from rotating massive stars is in orange curve. Observational data from Caffau et al. (2005), Caffau et al. (2011) and Maas et al. (2017) based on LTE assumptions. From Prantzos et al. (2018).*

2.11. Potassium ($_{19}$K)

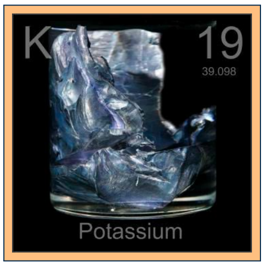

Potassium is an Odd-Z nucleus. Three stable isotopes ^{39}K, ^{40}K, ^{41}K, being the ^{39}K isotope the more abundant (93% in solar-system meteorites, Lodders & Palme 2009), are mainly synthesized in hydrostatic oxygen shell (ca 1 year before SNeII, 1500-2600 $\cdot 10^6$ K) and explosive oxygen burning of core-collapse supernovae SNeII of massive stars (Truran & Arnett 1971; Woosley et al. 1973; Thielemann & Arnett 1985; Woosley & Weaver 1995).

Some authors proposed galactic chemical evolution (GCE) models arguing in favor of hydrostatic equilibrium conditions (Timmes et al. 1995; Goswami & Prantzos 2000), however they show a different trend at higher metallicities with respect to the observational data.

To resolve these contradictions, it was suggested (Chen et al. 2000; Timmes et al. 1995) that there were departures from LTE in the level populations of K I, that can substantially change the potassium abundances derived assuming LTE (Shimansky et al. 2003). Only a couple of strong K I lines are available in optical/near-IR range: 7698.96 and 7664.90 Å but in fact only the 7699 Å line is usually invoked as the 7664 Å tends to be severely blended with telluric lines (Takeda 2020).

Nevertheless, both lines suffer strong departures from LTE caused by an over-recombination on the first level of the K I atom in the atmospheres of the late-type stars, leading to an increase of the equivalent widths of the K I 7664 and 7699 Å lines, see Ivanova & Shimanskiĭ (2000), and the LTE abundance overestimation (Andrievsky et al. 2010).

As a consequence, pioneering studies of stellar K abundances done under the assumption of LTE (e.g., Gratton & Sneden 1987b,a; Chen et al. 2000) are not regarded as reliable as viewed from present-day standard (Takeda 2020).

Strong NLTE corrections, as a consequence, greatly impact arguments about the galactic chemical evolution of potassium, introducing uncertainties in derived abundances despite great effort to investigate the NLTE effects (Takeda et al. 1996; Ivanova & Shimanskiĭ 2000; Takada-Hidai et al. 2002; Shimansky et al. 2003; Zhang et al. 2006; Andrievsky et al. 2010; Reggiani et al. 2019). Accurate determinations of NLTE effects are needed in order to provide better abundance observations.

2.11.1 Chemical galactic abundances

K galactic abundances have been derived from F, G and K dwarfs and recently also from red giants, since potassium is not expected to suffer any change by evolution-induced dredge-up (unlike lighter elements such as CNO or Na), primordial K abundances should be retained at the surface of giants (Takeda 2020).

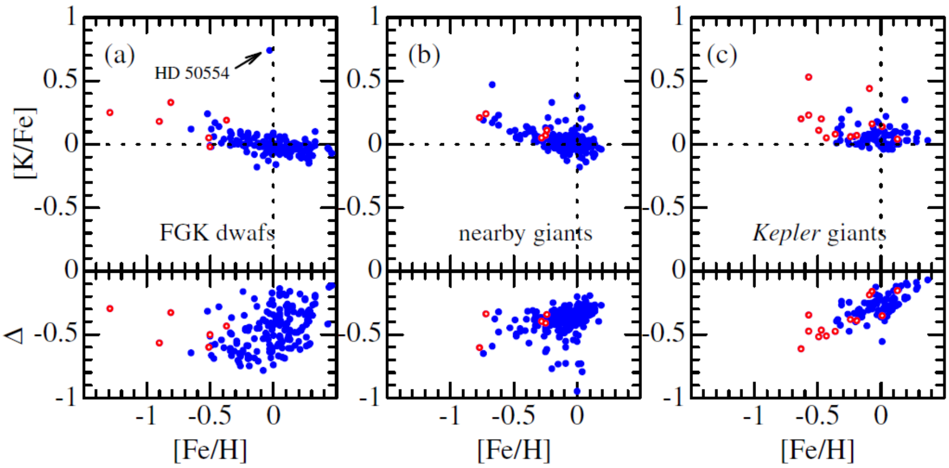

Figure 2.73: *The values of [K/Fe] (non-LTE abundance ratio) and NLTE applied corrections. From left to right: FGK dwarfs, nearby giants, and Kepler giants, respectively. Thin (blue filled) and thick disk stars (red filled). From Takeda (2020).*

NLTE effect corrections

In Fig. 2.73, can be observed the strong NLTE corrections applied by Takeda (2020), around -0.5 dex for undersolar FGK dwarfs. As above commented, great effort of researcher has been put in deriving NLTE corrections. using increasingly more complex atomic models. Though great dispersion of used models and corrections, the use of increasingly more complex atomic models is helping to obtain more accurate estimation of these effects. Fig. 2.74 shows a correction panel by Reggiani et al. (2019) in function of two atmosphere models, not very far from the ones generally observed in Fig. 2.73 by Takeda (2020). Confluence of accurate NLTE corrections, will provide more reliable abundances and hence a better understanding of the chemical galactic evolution models.

Although having this factor in mind, the potassium abundances of halo, thin, and thick disk stars show a distinct trend, such as for the α-elements (see Fig. 2.75) and display a nearly constant [K/Mg] ratio with small scatter (Fig. 2.76), which suggests that the nucleosynthesis of potassium is closely coupled to that of the α-elements (Zhang et al. 2006).

In some way, it is not surprising as similar to the α-elements, K is mainly formed in burning phases prior SNeII. Galactic evolution models fit well to the observational data of the disks and halo stars populations. This is observed in the fit of the GCE Goswami & Prantzos (2000) model to the stars sample of Zhang et al. (2006, see Fig. 2.75).

However at lower metallicities, the SNeII yield show a clear shortage even in more

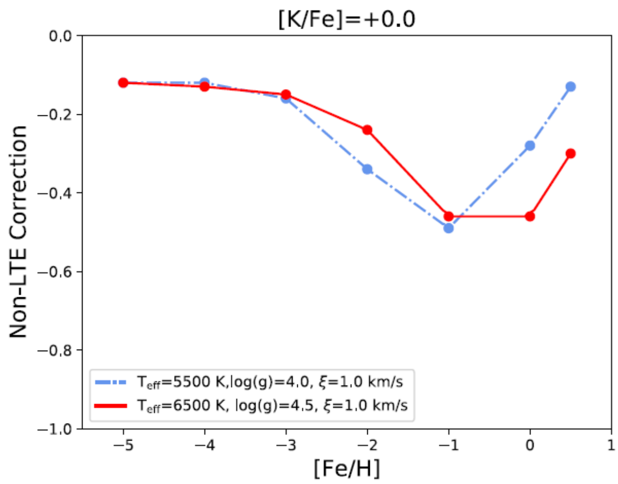

Figure 2.74: *non-LTE correction variation with [Fe/H]. Two different model atmospheres showing the corrections for the K I 7698 Å line. From Reggiani et al. (2019).*

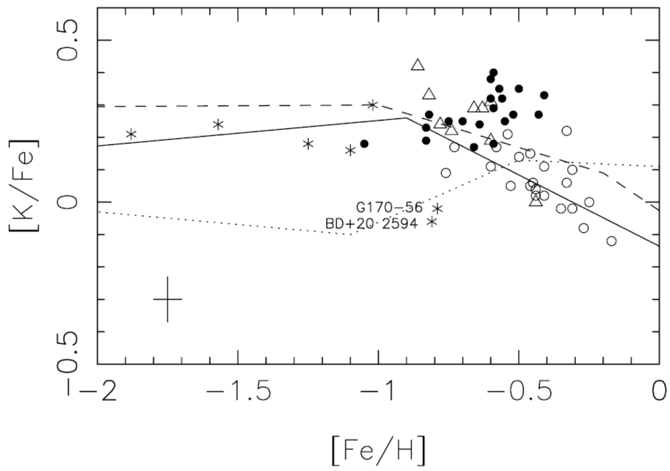

Figure 2.75: *Abundance ratios [K/Fe] for NLTE analysis. Open circles refer to the thin-disk stars, filled circles to the thick-disk stars, asterisks to the halo stars, open triangle to the stars with uncertain population membership. The solid line shows the theoretical predictions of Goswami & Prantzos (2000), the dashed line is the one of Samland (1998), and the dotted line refers to Timmes et al. (1995). From Zhang et al. (2006).*

updated models as the ones from Romano et al. (2010) and Kobayashi et al. (2011a),which include updated star yields or different SNeII and HNe energetic assumptions.

Later introduction in models (Prantzos et al. 2018) of yields of rotating massive stars (very abundant at early stages of the universe) improved the agreement between models and observations (see Fig. 2.78) at least for a metal poor ([Fe/H] ≤ -2 dex) regime (Reggiani et al. 2019), however, without solving the problem of their overall underproduction (Prantzos

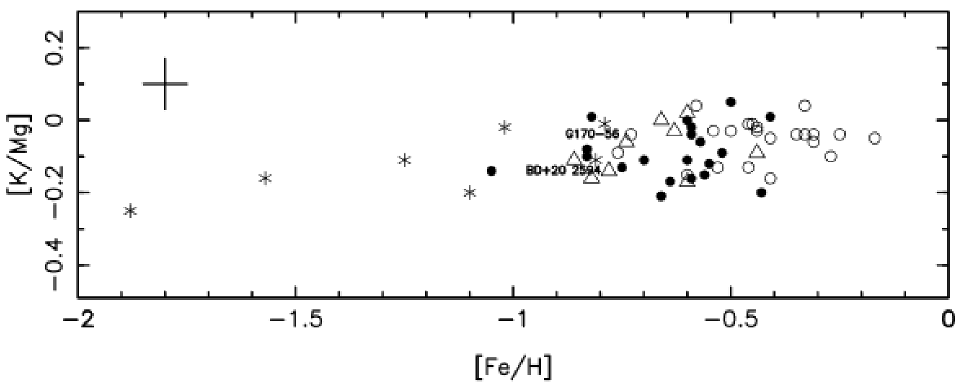

Figure 2.76: *[K/Mg] abundances ratios from NLTE analyses as functions of [Fe/H]. Same symbols as Fig.2.75. From Zhang et al. (2006).*

et al. 2018).

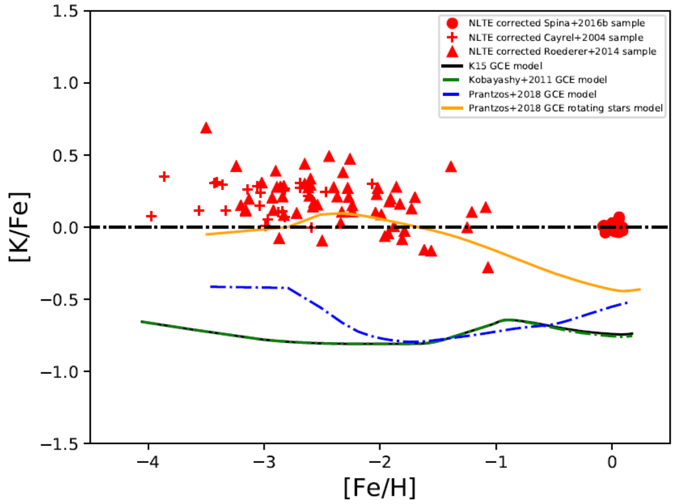

Figure 2.77: *K non-LTE corrected abundances for the metal poor stars sample by Cayrel et al. (2004) and Spina et al. (2016). Included some galactic chemical evolution models (GCE): K15 (Zhao et al. (2016); Sneden et al. (2016)), Kobayashi et al. (2011a) and Prantzos et al. (2018). The model by Prantzos et al. (2018) including fast rotators better matches the observations of extremely metal poor stars than the others only including SNeII or HNe assumptions which greatly underestimates K abundances. From Reggiani et al. (2019).*

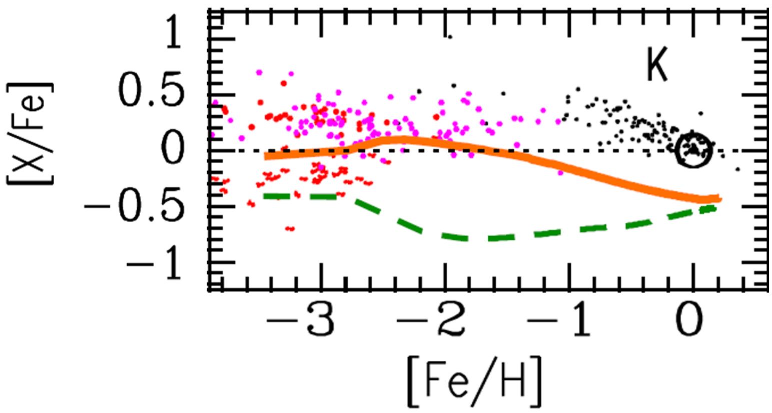

Figure 2.78: *Evolution of abundance ratio [K/Fe] as a function of [Fe/H] and comparison to observational data. Prantzos et al. (2018) model from massive and AGB/LIMS stars productions is in dashed green curve; the same model but with enhanced yields from rotating massive stars is in orange curve. Observational data from Roederer et al. (2014a) based on LTE assumptions. From Prantzos et al. (2018).*

2.12. Calcium ($_{20}$Ca)

The double magic isotope ^{40}Ca is produced mainly by silicon and oxygen burning in massive stars according to Woosley & Weaver (1995) (Hinkel et al. 2014; Romano et al. 2010).

Silicon and Oxygen Burning

$$^{36}Ar +^{4} He \rightarrow^{40} Ca + \gamma$$

^{40}Ca is also obtained from ^{40}K (formed by explosive oxygen burning and neon burning in massive stars or s-process nucleosynthesis) by β^{-}decay.

Explosive Oxygen and Neon Burning

$$^{40}K \rightarrow^{40} Ca + e^{-} + antineutrino$$

Like of the other α-elements its chemical distribution reflects two main key ideas about galactic evolution (see introduction to oxygen element in Sect. 2.4 for additional details) that determines its profile (see Fig. 1.27):

α-elements galactic evolution keys

- The early Universe was α-enriched because SNeII occurred on a much faster time-scale than SNeIa.
- The halo, thick and thin disks show their own chemical and kinematical features as a result of a different formation and evolutionary path.

2.12.1 Chemical galactic abundances

The chemical galactic distribution of the calcium observed in Fig. 2.79 shows the typical profile of an α-element with the usual chemical gap between thick and thin disks and the [Ca/Fe] plateau for metallicities [Fe/H] lower than < -1.0 dex.

The same distribution can be observed in Fig. 2.80 and 2.81, and in addition the plateau is quite homogeneous for metal poor stars. A trend that is continued in EMP stars as observed in Fig. 2.82.

Some difference in the abundance plateau can be observed between the first abundance

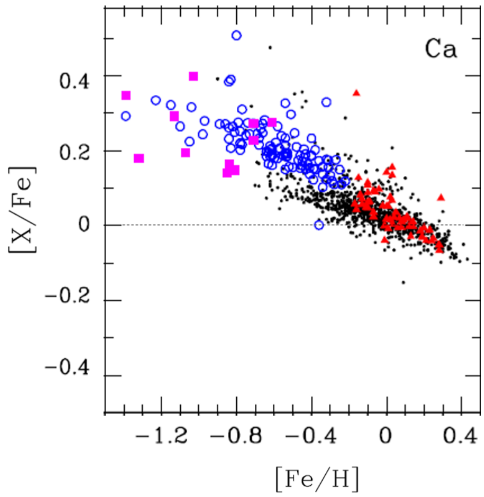

Figure 2.79: *The blue circles and black dots refer to the chemically selected thick- and thin disk stars, and the red filled triangles are the hαmr stars (high alpha metal rich thin disk stars). Magenta squares represent the stars belonging to the halo according to their kinematics. Sample of 1111 FGK stars from HARPS GTO planet search program, Adibekyan et al. (2012).*

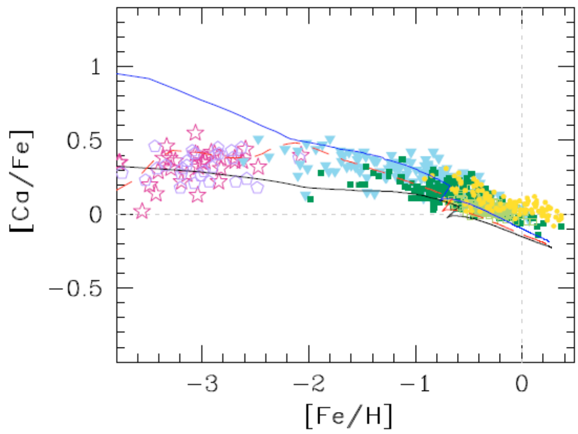

Figure 2.80: *Ca galactic chemical distribution in function of metallicity. Observational abundance data from Cayrel et al. (2004)(stars), Lai et al. (2008)(open pentagons), Gratton et al. (2003)(blue upside-down triangles), Reddy et al. (2006)(filled squares), Reddy et al. (2003)(open squares) and Bensby et al. (2005)(filled circles). Some chemical evolution models have been added (lines). From Romano et al. (2010).*

distributions derived under LTE assumptions with respect to the Spite et al. (2012) NLTE corrected EMP distribution (ca +0.15 dex). However, these corrections vary in function of chosen lines. NLTE effects have been investigated in different studies and ionizing state (Ca I or Ca II) like from Mashonkina et al. (2007) or in extremely metal poor star conditions like the ones from Spite et al. (2012) or the recent work by Sitnova et al. (2019).

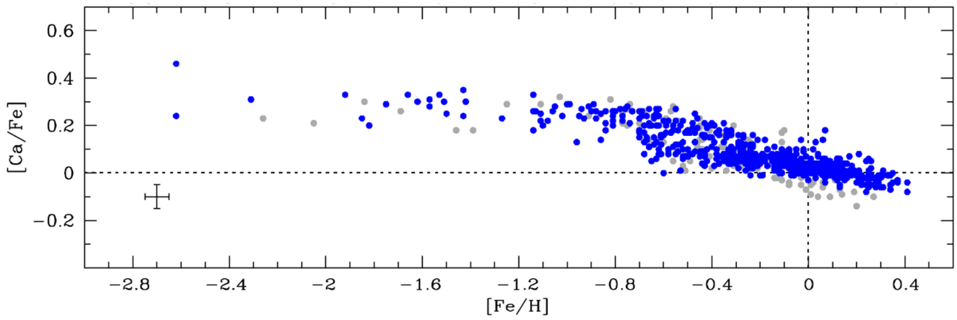

Figure 2.81: *[Ca/Fe] ratio abundance (LTE) with respect to the metallicity [Fe/H] of a sample of 714 dwarf and sub-giant stars. Grey dots indicate stars with T_{eff} < 5400 K. From Bensby et al. (2014).*

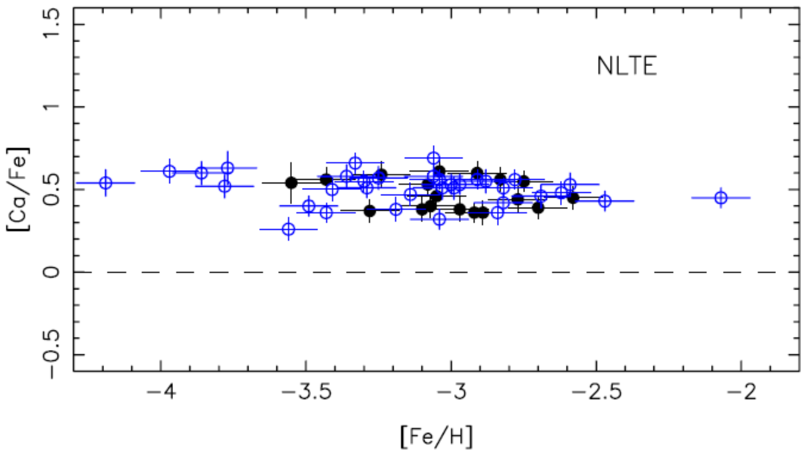

Figure 2.82: *[Ca/Fe] vs. [Fe/H] in a sample of EMP stars, NLTE corrected for the 422.67 Ca* I *and 866.22 nm Ca* II *lines. The filled circles represent the turnoff stars and the open symbols the giants. Turnoff and giant stars agrees quite well, [Ca/Fe] is constant in the range 4.3 < [Fe/H] < 2.5 and the mean value is equal to [Ca/Fe] = 0.5, a value slightly higher than the LTE value [Ca/Fe] = 0.35 (see Bonifacio et al. (2009)). From Spite et al. (2012).*

For Ca I, NLTE corrections depend on T_{eff}, log$g$, [Ca/H] and microturbulence value, and differ in value and sign for different Ca I lines. For Ca II, NLTE effects lead to negative abundance corrections over the whole range of stellar parameters (Romano et al. 2010).

Observed in Fig. 2.80 chemical galactic evolution models based in supernovae SNeII assumptions from Woosley & Weaver (1995) and adopting a two-infall galactic formation, looks like to fit well (red dashed line) for thick disk and halo stars: The inner halo and thick disc of the Milky Way are assumed to form on a relatively short time scale (about 1 Gyr) out of a first infall episode, whereas the thin disc forms inside-out on longer time scales (7 Gyr in the solar vicinity and more than a Hubble time at the outermost radii) during a second independent episode of extra-galactic gas infall (Romano et al. 2010).

Besides, the model by Kobayashi et al. (2006) including yields from Hypernovae (HNe) behaves acceptably well (solid black line). However, all the models fail in a proper description of the thin disk star abundances.

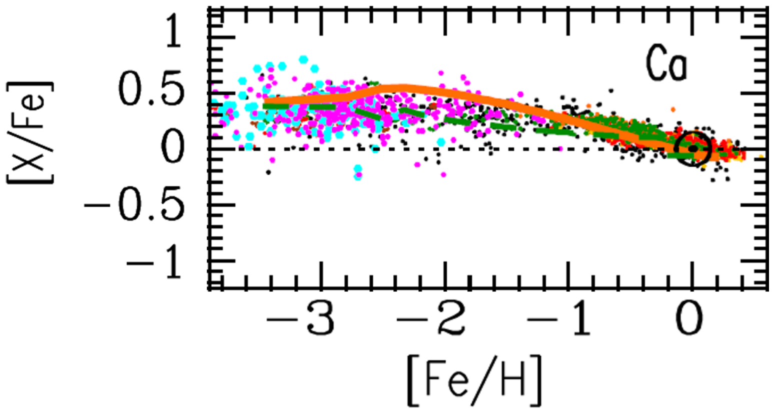

Figure 2.83: *Evolution of abundance ratio [Ca/Fe] as a function of [Fe/H] and comparison to observational data. Prantzos et al. (2018) model from massive and AGB/LIMS stars productions is in dashed green curve; the same model but with enhanced yields from rotating massive stars is in orange curve. Observational data from Yong et al. (2013), Bensby et al. (2014), Roederer et al. (2014a), Adibekyan et al. (2012) and Chen et al. (2000) based on LTE assumptions. From Prantzos et al. (2018).*

Nevertheless, the evolution of α-elements as Ca, is well reproduced in general, by most GCE models. The study by Prantzos et al. (2018) reassures that rotation does not significantly affect that result though the slight improve of the fit at metal poor range (see Fig. 2.83).

2.13. Scandium ($_{21}$Sc)

Scandium is an Odd-Z Iron-peak group element. The iron peak elements (Sc to Ge), though grouped in one broad category, are produced in complex nucleosynthesis processes not always coupled to the Fe production, hinting for some elements a very different nucleosynthesis site than iron, mostly produced in thermonuclear supernovae SNeIa (Battistini & Bensby 2015).

It is the case of the only stable isotope of scandium, ^{45}Sc, whose abundances show an α-like behaviour (Zhang et al. 2014). It is produced during neon burning phases (direct ^{45}Sc formation) and in explosive oxygen and silicon burning (from β^{+} decay of progenitor ^{45}Ti) of massive stars. Its nucleosynthesis occurs in the innermost ejected layers of core-collapse SNeII supernovae. This is a common nucleosynthesis source with the α-elements (Woosley & Weaver 1995).

Additional Sc nucleosynthesis yields might be obtained from a jet-like explosion model (Umeda & Nomoto 2005) and from the SN ejecta by neutrino spallation (ν-process, see Yoshida et al. 2008) occurring in Si-burning regions (Romano et al. 2010).

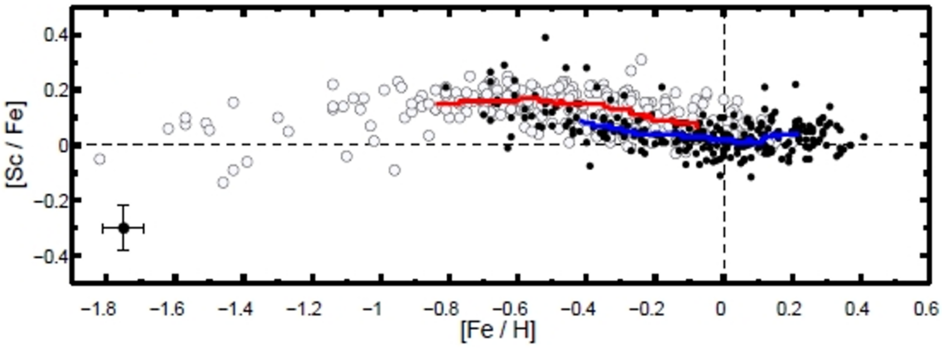

Figure 2.84: *Sc abundance trend of 594 F- and G-type dwarfs in the solar neighborhood. Large white dots are stars older than 9 Gyr (likely thick disk stars), while small black dots are stars younger than 7 Gyr (likely thin disk stars). The blue and red lines represent the running median of thin and thick disk stars. From Battistini & Bensby (2015).*

2.13.1 Chemical galactic abundances

Observing the Fig. 2.84, the trend is quite similar to the α-element profiles: A flat trend at supersolar metallicity and a rise from thin to thick disk stars, reaching [Sc/Fe]= +0.2 dex at [Fe/H]= -0.8 dex. This trend is consistent with the more recent Sc studies as the ones by

Allende Prieto et al. (2004), Brewer & Carney (2006), Reddy et al. (2006), Adibekyan et al. (2012) or Ishigaki et al. (2013). As well as from other pioneering studies by Nissen et al. (2000) and Prochaska et al. (2000).

LTE assumptions are used to derive Sc abundances. There is no in-depth study on NLTE effects though it is expected to be negligible from the only study by Zhang et al. (2008) applied to Sun Sc ii lines.

Abundance trend to metal poorer stars from the halo show a possible slight decrease in [Sc/Fe] and increase scatter in Fig. 2.84 and similarly when extended to EMP stars (Ishigaki et al. 2013) as observed in Fig. 2.85.

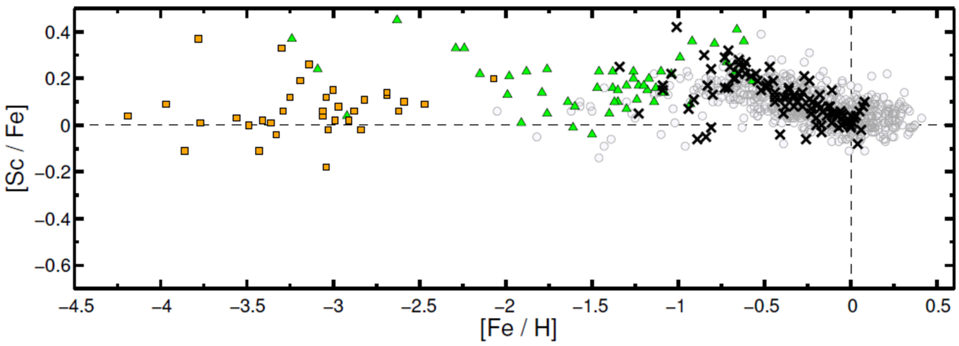

Figure 2.85: *In grey, same population from Fig.2.84. Added sample from Ishigaki et al. (2013) (EMP stars, green triangles), Nissen et al. (2000) (black crosses) and Cayrel et al. (2004) (orange squares). Adapted from Battistini & Bensby (2015).*

In spite of the approximately homogeneous abundances from different studies, models do not predict properly the observational data. All of them severely underestimating the Sc production.

As observed in Fig. 2.86, evolution model adopting core collapse SNeII nucleosynthesis site under prescriptions by Woosley & Weaver (1995) and a two-infall galactic formation (see more detailed explanation in Sect. 1.7) looks like it provides the best fit (red dashed line) though in a very deficient approximation. Meanwhile other models including Kobayashi et al. (2006), independently of the assumed Hypernovae HNe fraction (>20 $M_\odot$, 10^{52} erg), severely disagree with observations (Romano et al. 2010).

Later model by Nomoto et al. (2013) owing to metallicity dependencies of Sc yields for core-collapse supernovae (SNeII) and hypernovae (HNe), is also unable to reproduce observed abundances. Strong dependence of the Sc yields from the initial parameters of the supernovae explosion might be the cause for this disagreement between observational data and galactic chemical models (Battistini & Bensby 2015).

Including fast rotators improves the fit slightly, however, without solving the problem of their overall underproduction (Prantzos et al. 2018, see Fig. 2.87).

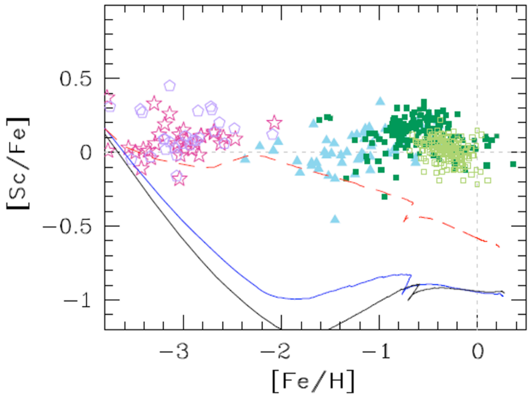

Figure 2.86: *Sc galactic chemical distribution in function of metallicity. Observational abundance data from Cayrel et al. (2004)(stars), Lai et al. (2008)(open pentagons), Gratton et al. (2003)(blue triangles), Reddy et al. (2006)(filled squares), Reddy et al. (2003)(open squares). Some chemical evolution models have been added (lines). From Romano et al. (2010).*

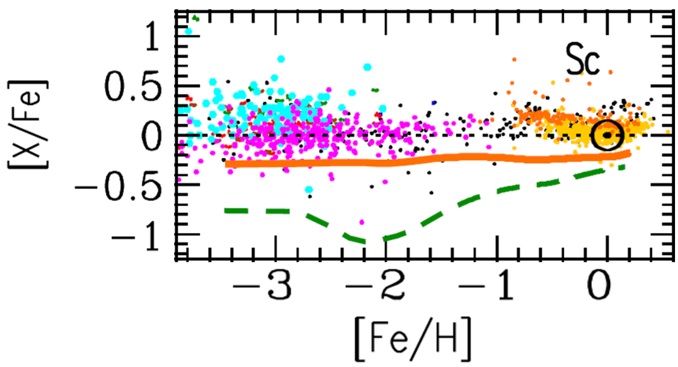

Figure 2.87: *Evolution of abundance ratio [Ca/Fe] as a function of [Fe/H] and comparison to observational data. Prantzos et al. (2018) model from massive and AGB/LIMS stars productions is in dashed green curve; the same model but with enhanced yields from rotating massive stars is in orange curve. Observational data from Yong et al. (2013), Roederer et al. (2014a), Adibekyan et al. (2012) and Lai et al. (2008) based on LTE assumptions. From Prantzos et al. (2018).*

2.14. Titanium ($_{22}$Ti)

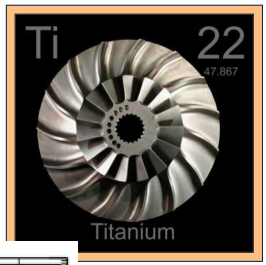

The last of the α-elements, whose main isotopes ^{48}Ti (73.7% Ti abundance in Solar System) and ^{49}Ti (5.4% SS) are predominantly produced in silicon burning stellar layers of massive stars before core-collapse SNeII (Woosley & Weaver 1995, see Fig. 2.88). Additionally, ^{46}Ti (8.2% SS) is predominantly produced by explosive O burning (Sneden et al. 2016).

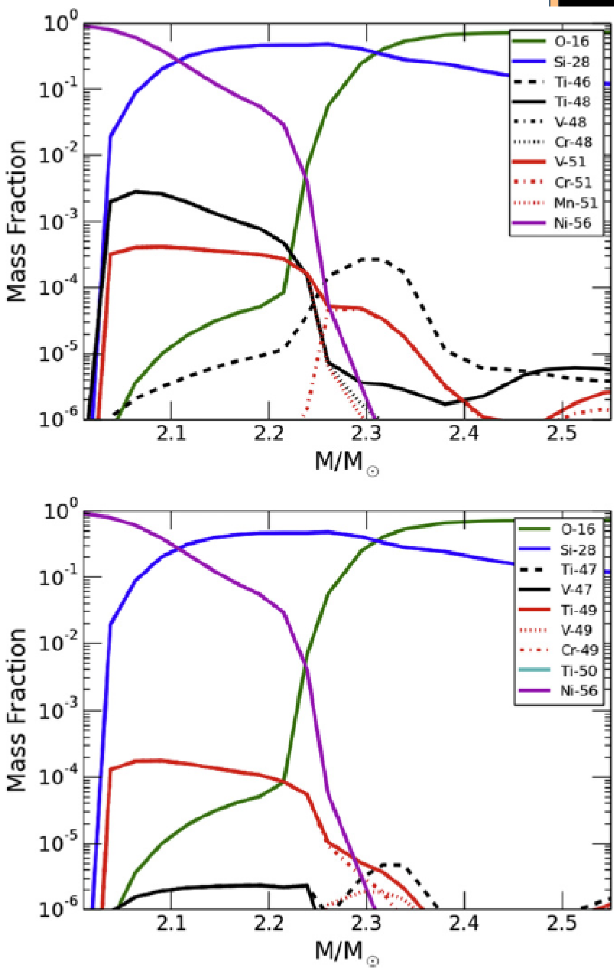

Figure 2.88: *Upper panel: isotopic abundances in the explosive Si-burning and O-burning ejecta of the 15M$_\odot$ SN model (Pignatari et al. 2016). Shown are profiles for ^{16}O, ^{28}Si, ^{46}Ti, ^{48}Ti, and its radiogenic parent isotopes ^{48}V and ^{48}Cr, ^{51}V and its radiogenic parent isotopes ^{51}Cr and ^{51}Mn, and ^{56}Ni. The unstable isotope ^{56}Ni will decay to ^{56}Co and finally to ^{56}Fe, which is most of the Fe SN ejecta. Lower panel: the same of the upper panel, but for ^{47}Ti and its radiogenic parent isotope ^{47}V, ^{49}Ti and its radiogenic parent isotopes ^{49}V and ^{49}Cr, and for ^{50}Ti. From Sneden et al. (2016).*

Like of the other α-elements its chemical distribution reflects two main key ideas about galactic evolution (see introduction to oxygen element in Sect. 2.4 for additional details) that determines its profile (see Fig. 1.27):

α-elements galactic evolution keys

- The early Universe was α-enriched because SNeII occurred on a much faster time-scale than SNeIa.
- The halo, thick and thin disks show their own chemical and kinematical features as a result of a different formation and evolutionary path.

2.14.1 Chemical galactic abundances

Prototypical is the α-profile shown in the Fig. 2.89 by Adibekyan et al. (2012). The abundance gap between thin and thick disk populations is clearly visible (around 0.1 dex) and the enhanced plateau achieved by metal poorer stars at ca -1.0 dex, hinting the SNeII nucleosynthesis site origin and later dilution by SNeIa.

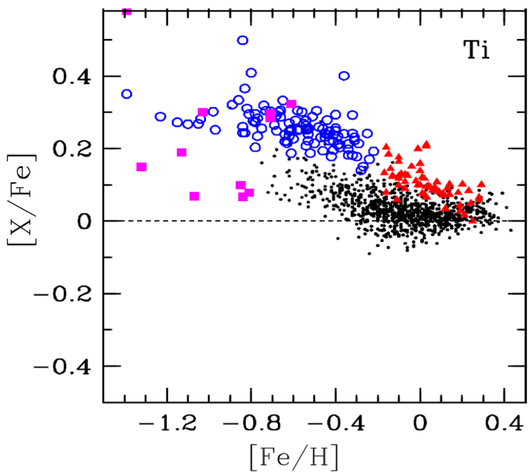

Figure 2.89: *The blue circles and black dots refer to the chemically selected thick- and thin disk stars, and the red filled triangles are the hαmr stars (high alpha metal rich thin disk stars). Magenta squares represent the stars belonging to the halo according to their kinematics. Sample of 1111 FGK stars from HARPS GTO planet search program, Adibekyan et al. (2012).*

When extended to poor and EMP from halo, the plateau looks like to be hold but scatter increases as shown in Fig. 2.90, 2.91 and 2.92. The surveys are quite homogeneous but once again, the striking underproduction predicted by the different models with respect to the observational data can be observed.

For instance in the Fig. 2.91, are used the GCE Kobayashi et al. (2006) and Kobayashi et al. (2011a) models. The contributions from various supernovae with different masses, metallicities, and energies are integrated according to the star-formation history of the system considered. The delay-time distributions of SNeIa are slightly different between the 2006 and 2011 models (Sneden et al. 2016). But both fail along the whole evolution, severely underestimating Ti production. Even when included Hypernovae (>20 $M_{\odot}$, 10^{52} erg) as jet-like explosions, expected to enhance iron-peaks element productions by the strong α-rich freeze-out (see Sect. 1.4 in Chapt. 1) due to high temperatures and high entropies in complete Si burning, the model (blue dashed line) still is very deficient for explaining observational data. Similar analysis can be told about the common models included in Fig. 2.92.

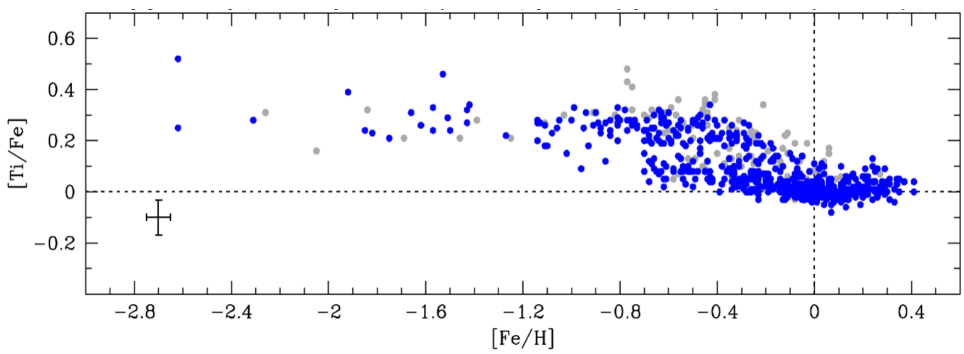

Figure 2.90: *[Ti/Fe] ratio abundance (LTE) with respect to the metallicity [Fe/H] of a sample of 714 dwarf and sub-giant stars. Grey dots indicate stars with T_{eff} < 5400 K. From Bensby et al. (2014).*

As above commented for Sc and others, strong dependence of the yields from the initial parameters of the supernovae explosion might be the cause for disagreements between observational data and galactic chemical models (Battistini & Bensby 2015). Additional neutrino effects (e.g., the spallation ν-processes), may increase the predicted production of Ti abundances (Sneden et al. 2016). And finally, massive fast rotators yields might be important to enhance the production at early stages of the universe when they were more frequent.

The GCE study by Prantzos et al. (2018) including fast rotators contribution at early stages of the universe improved the fit slightly, but does not solve the problem of the overall underproduction (see Fig. 2.93).

Some NLTE effect corrections studies of titanium can be found in bibliography as the ones by Bergemann (2011) and Sitnova et al. (2016). However, the number of NLTE effect studies for cool dwarfs is low in comparison with other elements.

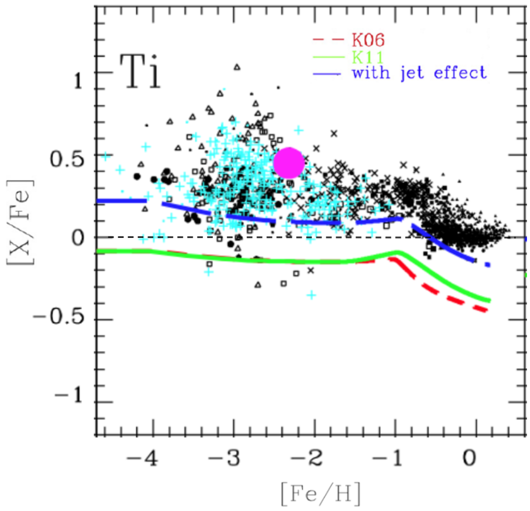

Figure 2.91: *Abundance ratios of Ti plotted as function of [Fe/H] metallicity. The solid magenta circles represent the HD 84937 abundance ratio derived in the Sneden et al. (2016) paper. Black dots represent observational data before 2014: Fulbright (2000), Gratton et al. (2003), Reddy et al. (2003), Cayrel et al. (2004), Honda et al. (2004), Cohen et al. (2013) and Yong et al. (2013). Cyan plus signs are from Roederer et al. (2014a). Overlaid on the figure are GCE models from Kobayashi et al. (2006, 2011b) and the Sneden et al. (2016) paper. From Sneden et al. (2016).*

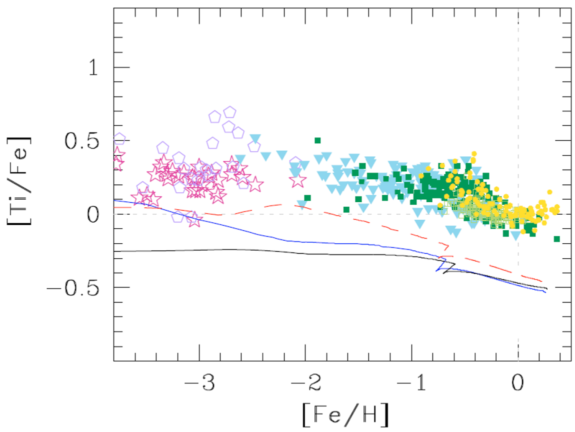

Figure 2.92: *Ti galactic chemical distribution in function of metallicity. Observational abundance data from Cayrel et al. (2004)(stars), Lai et al. (2008)(open pentagons), Gratton et al. (2003)(blue triangles), Reddy et al. (2006)(filled squares), Reddy et al. (2003)(open squares), and Bensby et al. (2005)(filled circles). Some galactic chemical evolution (GCE) models have been added (lines). From Romano et al. (2010).*

2.14.2 Ti as a proxy for stellar age

Identification of different populations by chemical abundances rather than other proper-

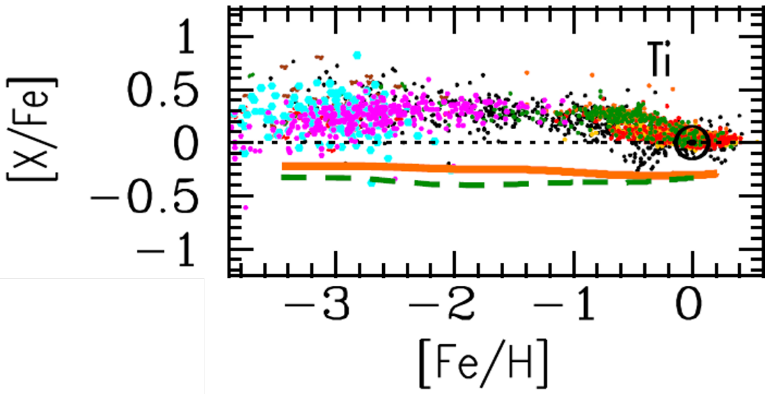

Figure 2.93: *Evolution of abundance ratio [Ti/Fe] as a function of [Fe/H] and comparison to observational data. Prantzos et al. (2018) model from massive and AGB/LIMS stars productions is in dashed green curve; the same model but with enhanced yields from rotating massive stars is in orange curve. Observational data from Yong et al. (2013), Bensby et al. (2014), Roederer et al. (2014a), Adibekyan et al. (2012), Chen et al. (2000) and Lai et al. (2008) based on LTE assumptions. From Prantzos et al. (2018).*

ties such as kinematics was argued by Navarro et al. (2011), and has been an useful followed path by authors as e.g. Adibekyan et al. (2013) and Duong et al. (2018), for the assignment of halo, thick and thin disk star populations based on the α-element abundances (in their studies as weighted averaged of Mg, Si and Ti).

The α-element abundance yields are linked with the universe and galaxy evolution (see Sect. 1.4 and 1.7), and the time delay between the core-collapse SNeII and thermonuclear SNeIa supernovae production.

The two-infall galactic formation model, generally used in GCE models for halo and thick disk and on the other hand, for thin disk formation, leaves an additional fingerprint in the α-element abundance profiles, showing the different chemical nature of the galactic populations, besides of kinematic.

Thus, no wonder that some authors (Liu & van de Ven 2012; Haywood et al. 2013) have suggested the use of α-enhancements as a proxy for stellar ages (Bensby et al. 2014). Hence, titanium, as an α-element prototype, freed from some problems that affect to other α-elements like Ca or O, has been used for this purpose.

Although age is a very difficult property to derive for most stars, the link between Ti abundances and stellar ages, and thus membership of the galactic population, is evident. This can be observed in Fig. 2.94, 2.95, 2.96, 2.97.

In the Fig. 2.98 in which the stars have been separated in two groups (< 7 Gyr and older > 9 Gyr), the younger stars look like concentrated around solar values, hinting their likely belonging to thin disk, meanwhile older distribution is clearly deficient in Fe with respect to the Ti, especially to metal poor stars, expected for thick disk and halo stars. Kinematical

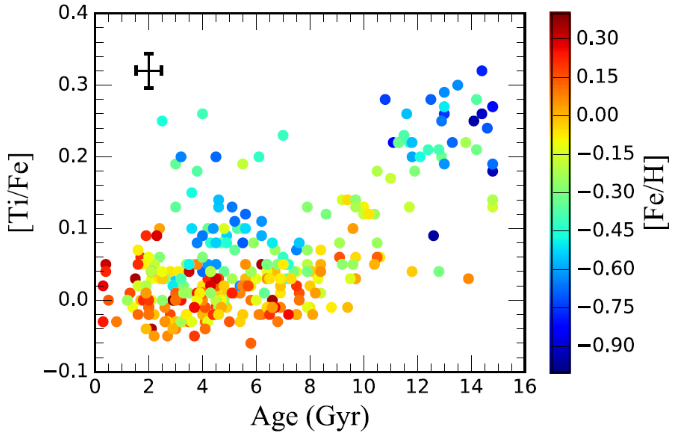

Figure 2.94: *[Ti/Fe] as a function of age (in Gyr) for all stars with σ_{age} < 1 Gyr from Bensby et al. (2014). The stars are colour-coded according to their [Fe/H] (as indicated in the colour bar). A typical error bar is shown. From Feltzing et al. (2017).*

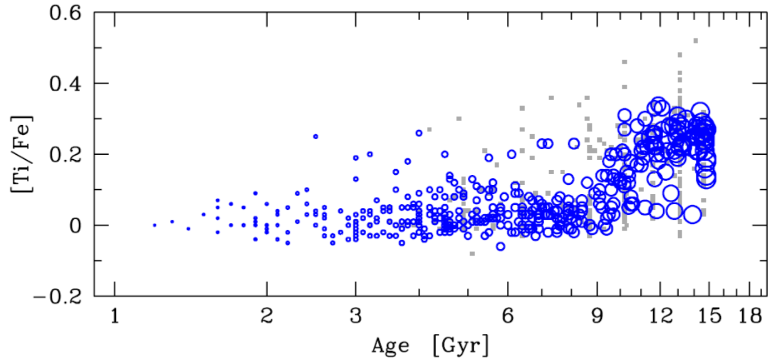

Figure 2.95: *Age-metallicity relation for those stars that have an age difference between upper and lower estimate of less than 4 Gyr. The sizes of the circles have been scaled with the ages of the stars. Stars with larger age uncertainties are shown as small grey dots. From Bensby et al. (2014).*

Toomre diagram indicates how in general the older stars are showing a hotter distribution than the younger, a characteristic of thick disk and halo stars. However, there is a large kinematical overlap, i.e. there are many young stars with hot kinematics and many old stars with cold kinematics. Aside from technical deriving difficulties, stellar ages might be a somewhat better discriminator when selecting thin and thick disk stars from nearby stellar samples than by kinematical reasons (Bensby et al. 2014).

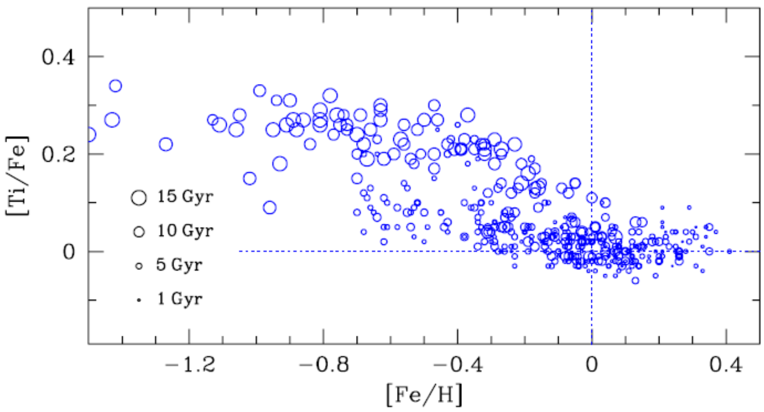

Figure 2.96: *[Ti/Fe] versus [Fe/H] for stars that have low age uncertainties (the differences between upper and lower age estimates are less than 4 Gyr). The sizes of the circles are scaled with the ages of the stars as indicated in the figure. From Bensby et al. (2014).*

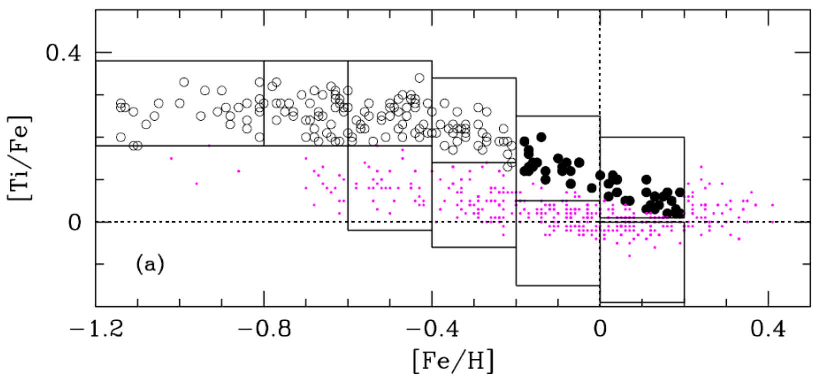

Figure 2.97: *Solid black circles mark stars that are α-enhanced and metal-rich (HAMR stars); the empty black circles mark stars that are α-enhanced at lower [Fe/H] (a.k.a. potential thick disk); and the small pink circles mark stars with low or moderate α-enhancement (a.k.a. potential thin disk stars). From Bensby et al. (2014).*

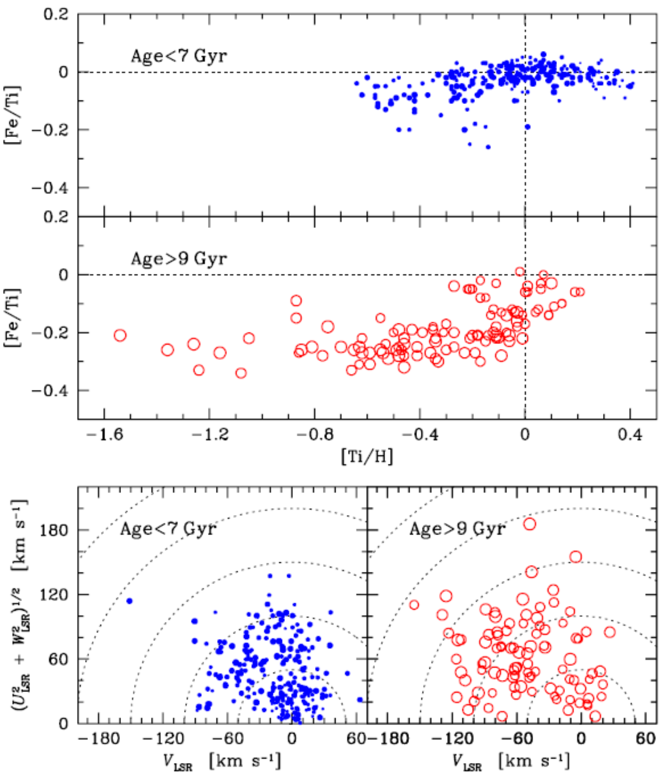

Figure 2.98: *The abundance trends when splitting the sample according to their ages. Upper panel indicates [Fe/Ti] ratio in function of [Ti/H]. Lower panel shows kinematic properties of stars. From Bensby et al. (2014)*

2.15. Vanadium ($_{23}$V)

Vanadium is an Odd-Z Iron-peak element. It is thought to be produced during incomplete explosive silicon burning in core-collapse supernovae SNeII (Woosley & Weaver 1995; Limongi & Chieffi 2003) and to a smaller extent in thermonuclear SNeIa (Bravo & Martínez-Pinedo 2012). V seems to share same nucleosynthesis sites (see abundance profiles) with Sc and Ti (Battistini & Bensby 2015), and as in their cases, slight changes on the initial parameters of the progenitor's and explosion SNeII, dramatically vary the obtained yields. Hence, the tuning of them could explain differences between observational data and GCE models.

The only naturally occurring isotope ^{51}V is produced in explosive silicon burning together with ^{48}Ti and ^{49}Ti, and in explosive O burning with ^{46}Ti. Within this scenario, the elemental ratio V/Ti observed in metal-poor stars can be used to explore the properties of explosive Si-burning and O-burning regions. The observed correlation of V and Ti may be a signature of this common production (Sneden et al. 2016).

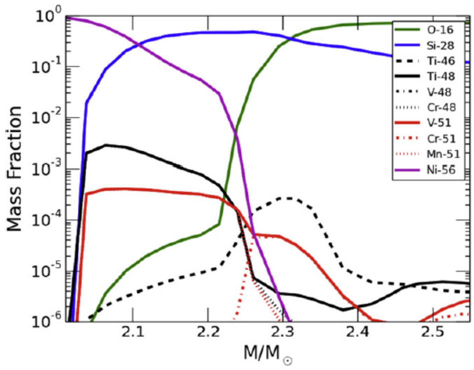

Figure 2.99: *Isotopic abundances in the explosive Si-burning ejecta of the 15M$_\odot$ SN model (Pignatari et al. 2016). Shown are profiles for ^{16}O, ^{28}Si, ^{46}Ti, ^{48}Ti, and its radiogenic parent isotopes ^{48}V and ^{48}Cr, ^{51}V and its radiogenic parent isotopes ^{51}Cr and ^{51}Mn, and ^{56}Ni. The unstable isotope ^{56}Ni will decay to ^{56}Co and finally to ^{56}Fe, which is most of the Fe SN ejecta. From Sneden et al. (2016).*

2.15.1 Chemical galactic abundances

Different abundance studies as Prochaska et al. (2000), Reddy et al. (2006), Brewer & Carney (2006), Adibekyan et al. (2012) are in good agreement at higher metallicities, showing a modest enhancement increase to lower metallicities (ca to [Fe/H] ≃ -0.8 dex), so an only slight metallicitiy dependence is observed (Battistini & Bensby 2015). However, at [Fe/H]< -1.0 dex, the scatter is higher and the trend averages scaled solar abundances (Ishigaki et al. 2013; Sneden et al. 2016, e.g. see Fig. 2.101, 2.102 or 2.103).

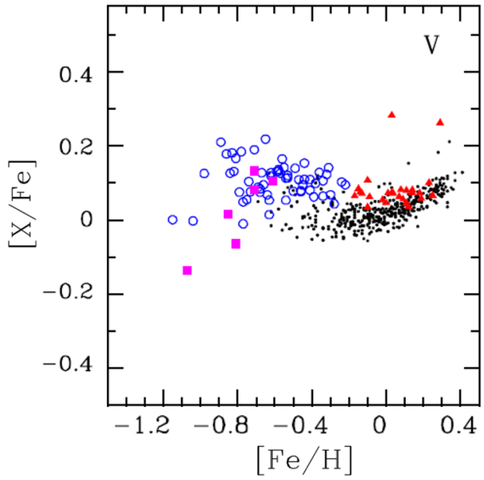

Figure 2.100: *The blue circles and black dots refer to the chemically selected thick- and thin disk stars, and the red filled triangles are the hαmr stars (high alpha metal rich thin disk stars). Magenta squares represent the stars belonging to the halo according to their kinematics. Sample of 1111 FGK stars from HARPS GTO planet search program, Adibekyan et al. (2012).*

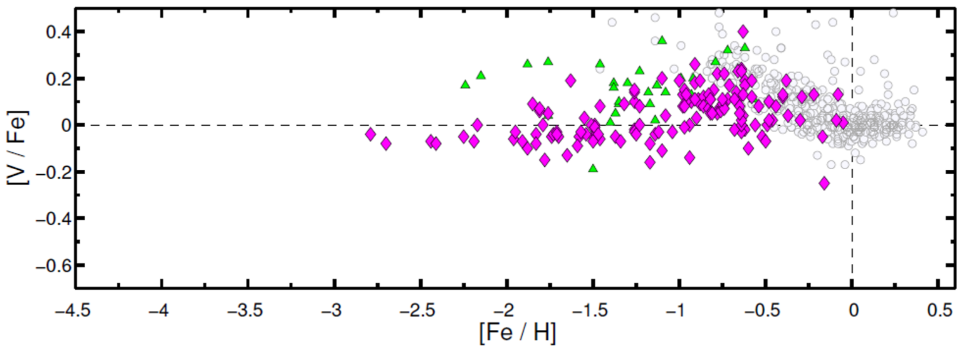

Figure 2.101: *In grey, V abundance trend of 594 F- and G-type dwarfs in the solar neighborhood by Battistini & Bensby (2015). Added sample from Ishigaki et al. (2013) (EMP stars, green triangles) and Fulbright (2000) (magenta diamonds). Adapted from Battistini & Bensby (2015).*

Like in the cases of Sc and Ti, GCE models (e.g. Kobayashi et al. (2006, 2011b)) severely underestimated the V production (see Fig. 2.102 and 2.103). As above commented the tuning of initial parameters on the progenitor's core-collapse star, might dramatically change V yields. The inclusion of effects as enhancement of yields by fast rotators in massive stars, Hypernovae (>20 $M_\odot$, 10^{52} erg) jet-like explosions (see Fig. 2.103) and alternative nucleosynthesis site contributions might help for matching observational data

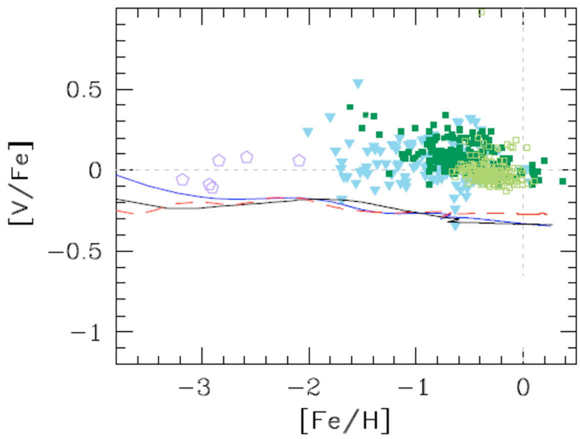

Figure 2.102: *V galactic chemical distribution in function of metallicity. Observational abundance data from Lai et al. (2008)(open pentagons), Gratton et al. (2003)(blue triangles), Reddy et al. (2006)(filled squares) and Reddy et al. (2003)(open squares), Some galactic chemical evolution (GCE) models have been added (lines). From Romano et al. (2010).*

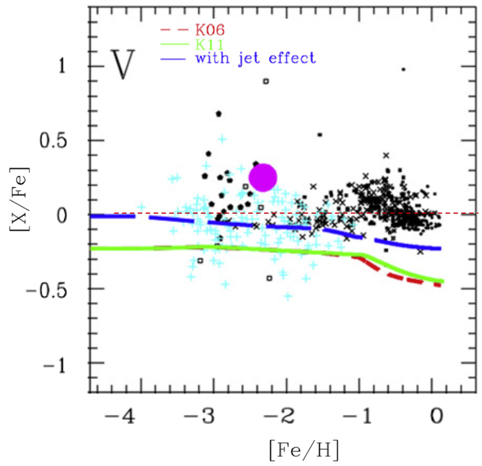

Figure 2.103: *Abundance ratios of V plotted as function of [Fe/H] metallicity. The solid magenta circles represent the HD 84937 abundance ratio derived in the Sneden et al. (2016) paper. Black dots represent observational data from studies before 2014. Cyan plus signs are from Roederer et al. (2014a). Overlaid on the figure are GCE models from Kobayashi et al. (2006, 2011b) and the Sneden et al. (2016) paper. From Sneden et al. (2016).*

and GCE models in the future.

However, so far, the GCE study by Prantzos et al. (2018) including fast rotators contribution at early stages of the universe improves the fit slightly, but does not solve the problem of the overall underproduction (see Fig. 2.104).

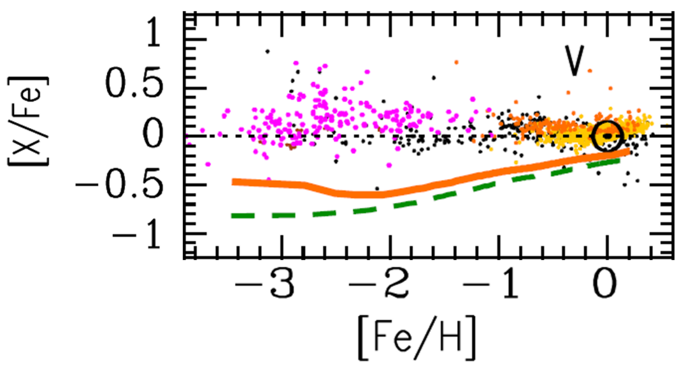

Figure 2.104: *Evolution of abundance ratio [Ti/Fe] as a function of [Fe/H] and comparison to observational data. Prantzos et al. (2018) model from massive and AGB/LIMS stars productions is in dashed green curve; the same model but with enhanced yields from rotating massive stars is in orange curve. Observational data from Roederer et al. (2014a), Adibekyan et al. (2012), and Lai et al. (2008) based on LTE assumptions. From Prantzos et al. (2018).*

2.16. Chromium ($_{24}$Cr)

Chromium is an Even-Z Iron group element thought to be produced in explosive silicon burning (Woosley & Weaver 1995; Hix & Thielemann 1999; Thielemann et al. 2007). 2/3 originates in thermonuclear supernovae SNeIa, the remaining 1/3 results from core collapse supernovae SNeII. (Matteucci & Greggio 1986; Samland 1998). Though the nucleosynthesis sites have been identified, their yields are affected by large uncertainties in function of the explosion parameters (Bergemann & Cescutti 2010), e.g. the energy or the mass ejecta.

Silicon burning produces the neutron-magic isotope ^{52}Cr (83.8% Cr natural abundance) relatively quickly, and thereafter produces ^{56}Fe via a sequence of capture and photo-disintegration processes. As it can be seen in the model of the Fig. 2.105, the results of a one-zone nuclear reaction network calculation starting from pure ^{28}Si and evolved at density temperature conditions during shell Si burning in the 20 $M_\odot$ stellar model about an hour before the SNeII collapse (Côté et al. 2020).

But as above commented, uncertainties are high in function of the supernovae model parameters. Depending on thermonuclear SNeIa model parameters, different isotopic abundance ratios for Cr and Fe can be obtained (Bergemann 2011).

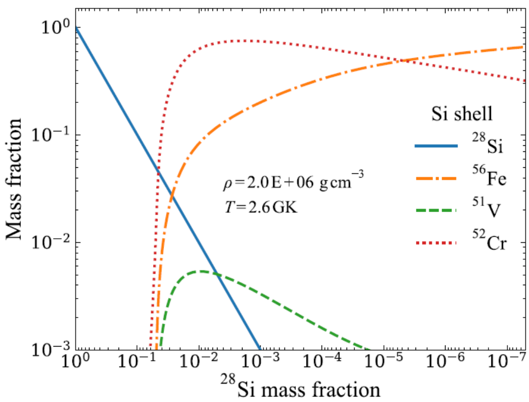

Figure 2.105: *Evolution of key isotopes during a one-zone burn network integration at conditions characteristic of Si-shell burning in a 20 $M_\odot$ star. From Côté et al. (2020).*

2.16.1 Chemical galactic abundances

The coupling between nucleosynthesis sites for chromium and iron is indicated by their correlation of [Cr/Fe] and [Fe/H] as shown in Fig. 2.106. Chromium is the only element for which the thin and the thick disks have the same abundance ratio against iron in the chemical galactic survey by Adibekyan et al. (2012).

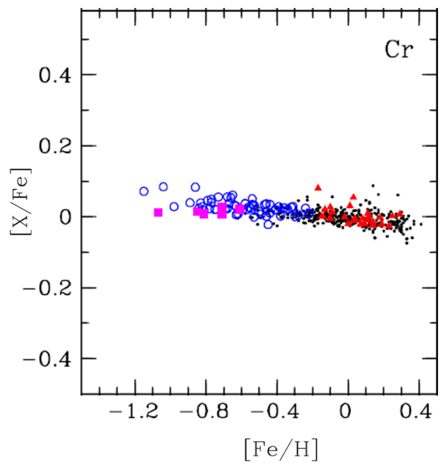

Figure 2.106: *The blue circles and black dots refer to the chemically selected thick- and thin disk stars, and the red filled triangles are the hαmr stars (high alpha metal rich thin disk stars). Magenta squares represent the stars belonging to the halo according to their kinematics. Sample of 1111 FGK stars from HARPS GTO planet search program, Adibekyan et al. (2012).*

When extended to metal poorer stars, this flat trend astonishingly holds as observed in Fig.2.107, although at metal poor range (EMP stars) one can notice the usual scatter (see Fig. 2.108, 2.109 and 2.112), likely due to the usual factors that theoretical models indicate: wide range of yields depending on the parameters of progenitor's supernovae and explosion, HNe (>20 $M_\odot$, 10^{52} erg) fraction, influence of fast rotators nucleosynthesis or additional as theoretical O-C shell mergers in massive stars that potentially might impact Cr abundances (Côté et al. 2020). And always in mind rare but energetic events at early stages of the universe as CBM or MHD-SNeII (see Chapt. 1) that might impact direct or indirectly the element abundances. Or other galaxy evolution factors as merging of sub-halos (each one with its own history and timescale for chemical enrichment) as forming mechanism of the early Galaxy or the imperfect gas mixing (Prantzos et al. 2018).

However, part of the reason for this scatter might be found in an observed offset between Cr i and Cr ii lines (only in giants), appreciable too between giants and turnoff stars (Honda et al. 2004; Lai et al. 2008; Bonifacio et al. 2009). The likely reason is NLTE effects.

NLTE effect corrections

Gratton & Sneden (1991) suggested that the chromium neutral species is affected by overionization and thus using Cr i lines would underestimate the overall Cr abundance (Ishigaki et al. 2013).

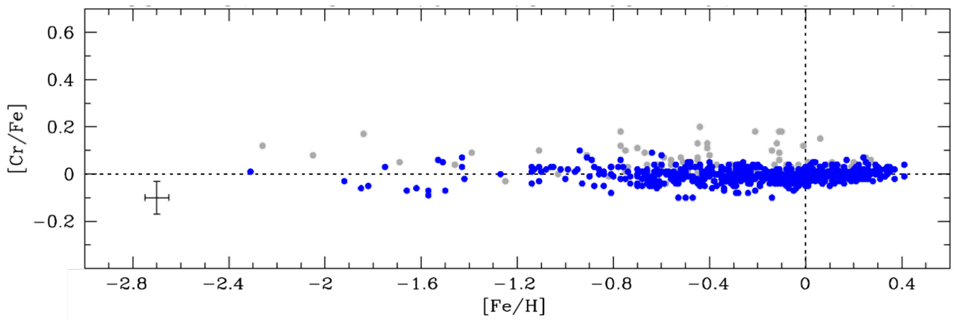

Figure 2.107: *[Cr/Fe] ratio abundance (LTE) with respect to the metallicity [Fe/H] of a sample of 714 dwarf and sub-giant stars. Grey dots indicate stars with T_{eff} < 5400 K. From Bensby et al. (2014).*

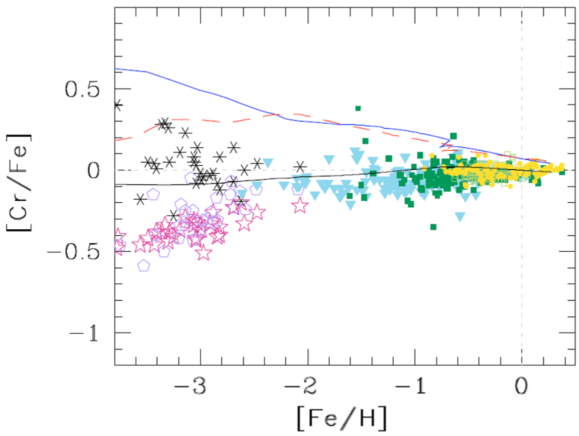

Figure 2.108: *Cr galactic chemical distribution in function of metallicity. Observational abundance data from Cayrel et al. (2004) (stars), Bonifacio et al. (2009) (asterisks, from Cr* II *lines) Lai et al. (2008)(open pentagons), Gratton et al. (2003)(blue triangles), Reddy et al. (2006)(filled squares), Reddy et al. (2003)(open squares) and Bensby et al. (2005) (filled circles). Some galactic chemical evolution (GCE) models have been added (dashed and solid lines). From Romano et al. (2010).*

The differences vary from study to study. In the metal poor stars sample from the Bergemann & Cescutti (2010) study, a 0.2-0.3 offset is observed. The main controlling parameter looks to be metallicity (see Fig.2.110) over surface gravity or temperature, although for giants with $T_{eff} \leq 5000$ K, the studies are coincident in a $\simeq 0.4$ dex offset.

Improved NLTE correction models might increase the homogeneity of the derived abundances at poorer metallicities as observed in the Fig. 2.111 from the Bergemann & Cescutti (2010) NLTE study.

NLTE effects and other reasons causing scattering might play its role in the best fitted GCE models (see e.g. Fig. 2.111 where one or another model fit better in function of LTE

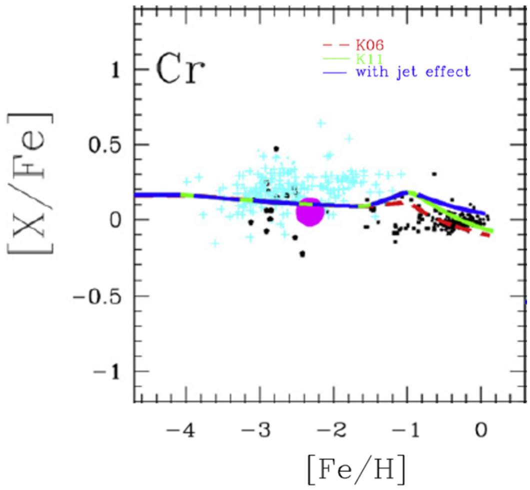

Figure 2.109: *Abundance ratios of Cr plotted as function of [Fe/H] metallicity. The solid magenta circles represent the HD 84937 abundance ratio derived in the Sneden et al. (2016) paper. Black dots represent observational data from studies before 2014. Cyan plus signs are from Roederer et al. (2014a). Overlaid on the figure are GCE models from Kobayashi et al. (2006, 2011b) and the Sneden et al. (2016) paper. From Sneden et al. (2016).*

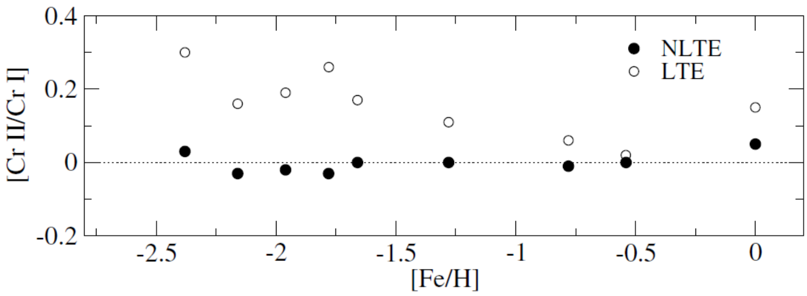

Figure 2.110: *[Cr/Fe] ratios as determined from Cr* I *and Cr* II *lines under NLTE (filled symbols) and LTE (open symbols) as a function of effective metallicity by Bergemann & Cescutti (2010).*

or NLTE derived abundances) but in general models as Kobayashi et al. (2006, 2011a); Woosley & Weaver (1995) work better than in the previous element sections for describing observational data. The two-infall galaxy formation as presented by Chiappini et al. (1997) or revised versions is included in galaxy evolution models, e.g. as the one by François et al. (2004, see Fig. 2.111).

The GCE study by Prantzos et al. (2018) including fast rotators contribution at early stages of the universe, improves the fit slightly but hardly impacts the expected Cr production (see Fig. 2.112).

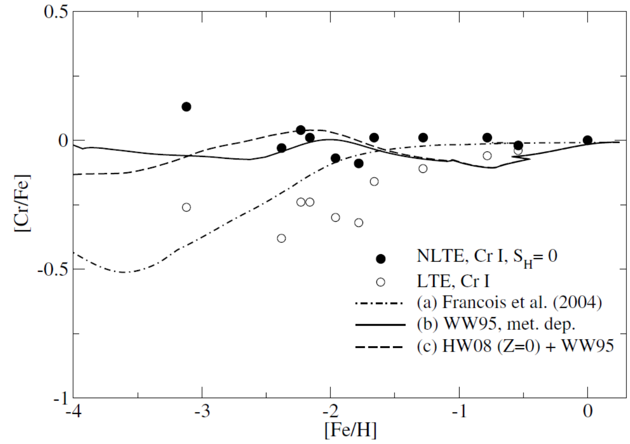

Figure 2.111: *Abundance ratios [Cr/Fe] as a function of metallicity. NLTE and LTE-based Cr abundances in metal-poor stars are marked with filled and open symbols. The evolutionary curves for [Cr/Fe] are computed with the CE model for the solar neighborhood adopting different sets of SN II yields. From Bergemann & Cescutti (2010).*

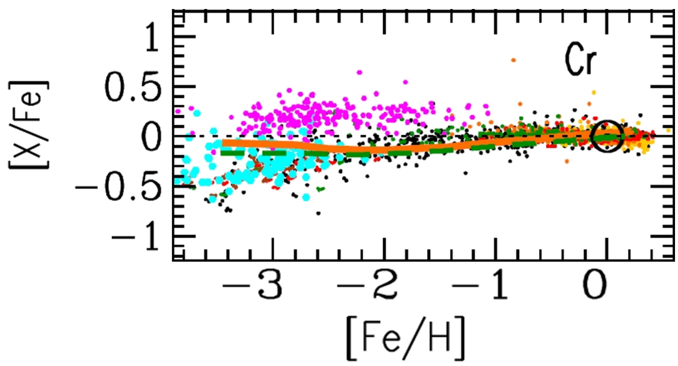

Figure 2.112: *Evolution of abundance ratio [Cr/Fe] as a function of [Fe/H] and comparison to observational data. Prantzos et al. (2018) model from massive and AGB/LIMS stars productions is in dashed green curve; the same model but with enhanced yields from rotating massive stars is in orange curve. Observational data from Yong et al. (2013), Bensby et al. (2014), Roederer et al. (2014a), Adibekyan et al. (2012) and Lai et al. (2008) based on LTE assumptions. From Prantzos et al. (2018).*

2.17. Manganese ($_{25}$Mn)

Manganese is an Odd-Z Iron peak element. The only stable ^{55}Mn isotope is thought mostly produced by explosive silicon burning in massive stars in the outer incomplete Si-burning layers of core-collapse supernovae SNeII (Woosley & Weaver 1995; Umeda & Nomoto 2005) and in thermonuclear supernovae SNeIa (Bravo & Martínez-Pinedo 2012; Iwamoto et al. 1999). Although models of yields do not always coincide with observational data because of the scarce knowledge of certain processes in stellar evolution but also because the production of elements in supernovae explosions are highly sensitive to explosion parameters as argued by Kobayashi et al. (2006, 2011a) (Battistini & Bensby 2015).

2.17.1 Chemical galactic abundances

NLTE effect corrections

One additional factor to be taken into account that leads to very different conclusions on the base of the observational data, is the NLTE effect corrections of the Mn lines. They become more pronounced with the decreasing metallicity by photoionization. It depopulates all Mn I levels and increases effective temperature by ionization from the ground state of Mn I. Nevertheless, collision rates also increase due to a larger kinetic energy of the particles, counteracting the NLTE influence of the radiation field (Bergemann & Gehren 2008).

The NLTE effects depend on the Mn line and inelastic collisional model with hydrogen as observed in Fig. 2.113, although it is observed that at lower metallicity ([Mn/Fe] ~ -3.0 dex), the NLTE corrections may run up to 0.5–0.7 dex. At a secondary level, the surface temperature and gravity might also affect the NLTE corrections although there is no evident trend as it is shown in Battistini & Bensby (2015, see Fig. 2.114).

Hence, NLTE effects introduce severe corrections at lower metallicities (see Fig. 2.115) can thus dramatically change the arguments about galactic chemical evolution trends or Mn nucleosynthesis sites.

When observing LTE abundance trends by different works as Gratton (1989), Prochaska et al. (2000), Reddy et al. (2006), Brewer & Carney (2006), Feltzing et al. (2007), Romano et al. (2010), Adibekyan et al. (2012), Ishigaki et al. (2013) and Sneden et al. (2016), all of them are quite coincident showing under-abundances with respect to the Fe and a behaviour opposite to an α-element.

Although with some differences, this trend can be observed in the LTE abundances of

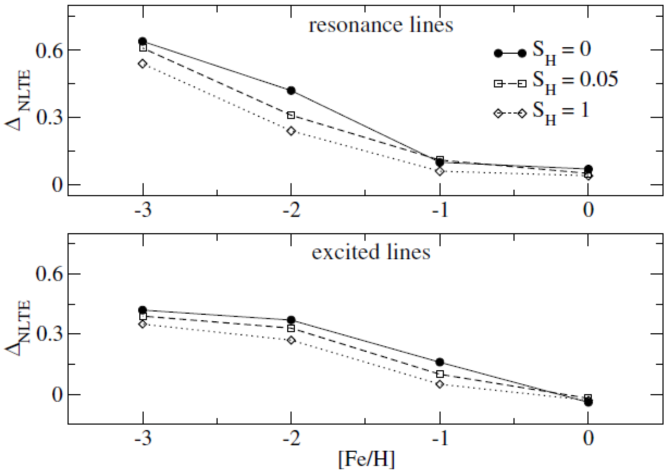

Figure 2.113: *NLTE abundance corrections ΔNLTE calculated with three different values of a scaling factor to inelastic collisions with hydrogen SH = 0, 0.05, 1: the average for the resonance triplet at 403 nm (top), the average for excited lines at 4783 and 4823 Å (down). Calculations were performed for four models with T_{eff} = 6000, log g = 4, [Fe/H] = 0, 1, 2, 3. From Bergemann & Gehren (2008).*

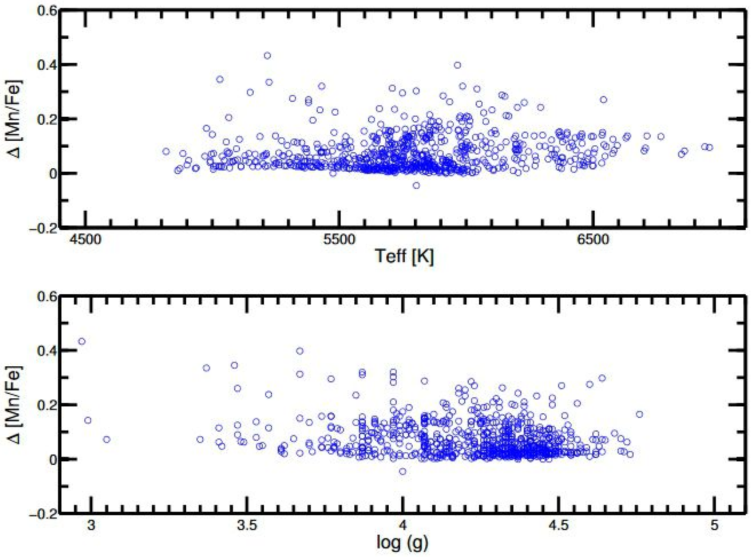

Figure 2.114: *Relation between NLTE corrections for Mn with the T_{eff} and log g of the stellar sample from Battistini & Bensby (2015).*

the Fig. 2.116 and 2.117.

This behaviour contradictory to α-elements is supported by models (Kobayashi et al. 2011a; Nomoto et al. 2013), see e.g. Fig. 2.119 and 2.120, in which Mn is produced in SNeII at low metallicity (Tsujimoto & Shigeyama 1998) while at [Fe/H] ~ -1.0 dex to upper

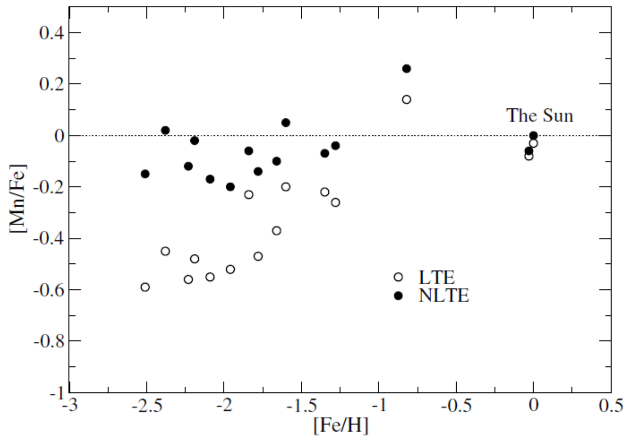

Figure 2.115: *LTE and NLTE corrected [Mn/Fe] vs. [Fe/H] in metal-poor stars by Bergemann & Gehren (2008).*

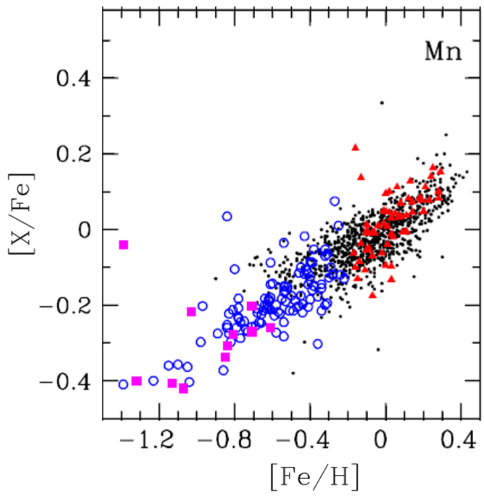

Figure 2.116: *LTE Mn abundances. The blue circles and black dots refer to the chemically selected thick- and thin disk stars, and the red filled triangles are the hαmr stars (high alpha metal rich thin disk stars). Magenta squares represent the stars belonging to the halo according to their kinematics. Sample of 1111 FGK stars from HARPS GTO planet search program, Adibekyan et al. (2012).*

metallicity, it is mainly produced by increasing contribution from thermonuclear supernovae SNIa (Kobayashi et al. 2006) (Battistini & Bensby 2015).

Applying NLTE corrections to Mn corrections (see Fig. 2.118), [Mn/Fe] becomes basically flat over the whole metallicity range, Mn shares the same production sites as Fe and is produced in the same quantity. However, when NLTE corrections are taken into account, no model has been able to explain this trend/behavior (Battistini & Bensby 2015).

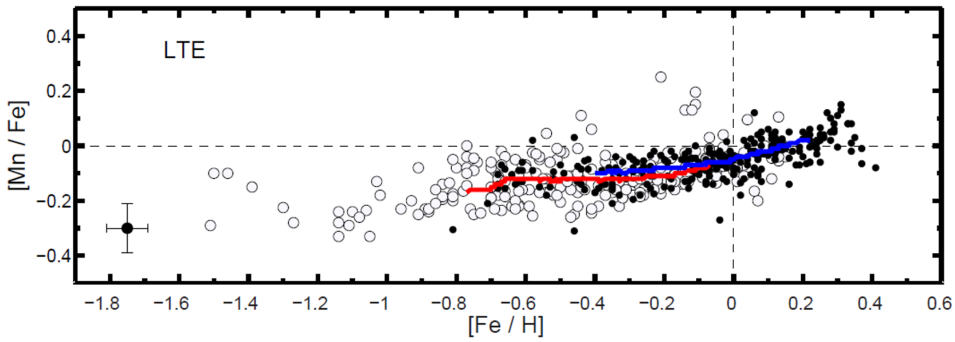

Figure 2.117: *Mn abundance trend under LTE assumptions of 594 F- and G-type dwarfs in the solar neighborhood. Large white dots are stars older than 9 Gyr (likely thick disk stars), while small black dots are stars younger than 7 Gyr (likely thin disk stars). The blue and red lines represent the running median of thin and thick disk stars. From Battistini & Bensby (2015).*

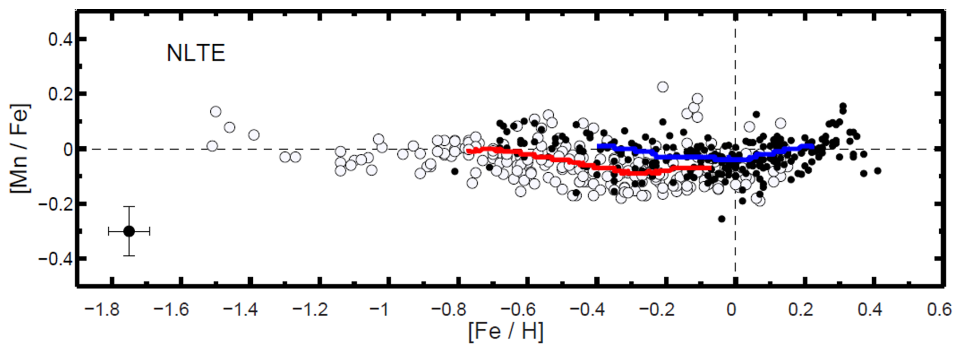

Figure 2.118: *Mn abundance trend under NLTE assumptions of 594 F- and G-type dwarfs in the solar neighborhood. Large white dots are stars older than 9 Gyr (likely thick disk stars), while small black dots are stars younger than 7 Gyr (likely thin disk stars). The blue and red lines represent the running median of thin and thick disk stars. From Battistini & Bensby (2015).*

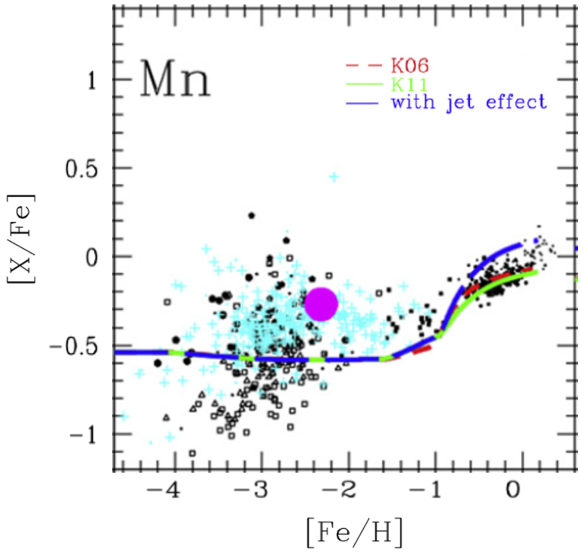

Figure 2.119: *Abundance ratios of Mn plotted as function of [Fe/H] metallicity under LTE assumptions. The solid magenta circles represent the HD 84937 abundance ratio derived in the Sneden et al. (2016) paper. Black dots represent observational data from studies before 2014. Cyan plus signs are from Roederer et al. (2014a). Overlaid on the figure are GCE models from Kobayashi et al. (2006, 2011b) and the Sneden et al. (2016) paper. From Sneden et al. (2016).*

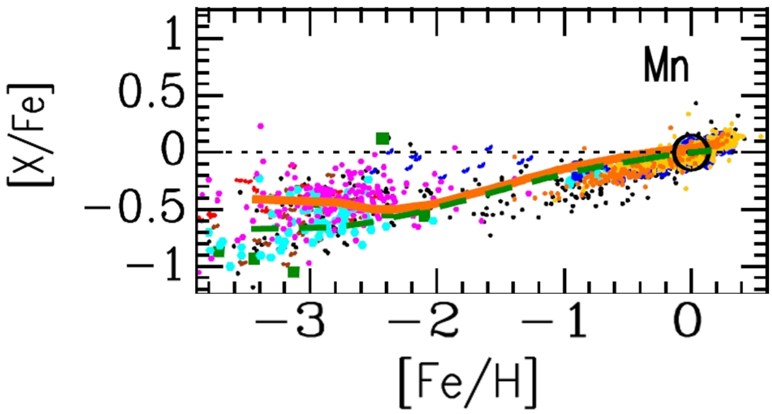

Figure 2.120: *Evolution of abundance ratio [Mn/Fe] as a function of [Fe/H] and comparison to observational data. Prantzos et al. (2018) model from massive and AGB/LIMS stars productions is in dashed green curve; the same model but with enhanced yields from rotating massive stars is in orange curve. Observational data from Yong et al. (2013), Roederer et al. (2014a), Adibekyan et al. (2012) and Lai et al. (2008) based on LTE assumptions. From Prantzos et al. (2018).*

2.18. Iron ($_{26}$Fe)

Iron is a nucleosynthesis product of supernovae, either core-collapse SNeII or thermonuclear SNIa. Most of Fe has been thought to be produced by SNeIa according to classical works. However, this perspective has changed and the contribution from both supernovae is more balanced in recent GCE studies. The freshly published study by Kobayashi et al. (2020a) finds only a 60% originated from SNeIa.

SNeIa converts much of the progenitor white dwarf to iron group elements (Hoyle & Fowler 1960; Seitenzahl et al. 2013b). Although it depends on the kind of SNeIa and the conditions of temperature and density in supernova. An order of 0.4-0.8 $M_\odot$ of ^{56}Ni (Arnett 1982) is expected to be produced in the branch-normal type of SNeIa (Flörs et al. 2018). This radioactive isotope decay to ^{56}Fe, via ^{56}Co (Nomoto et al. 2013, see Fig. 2.121).

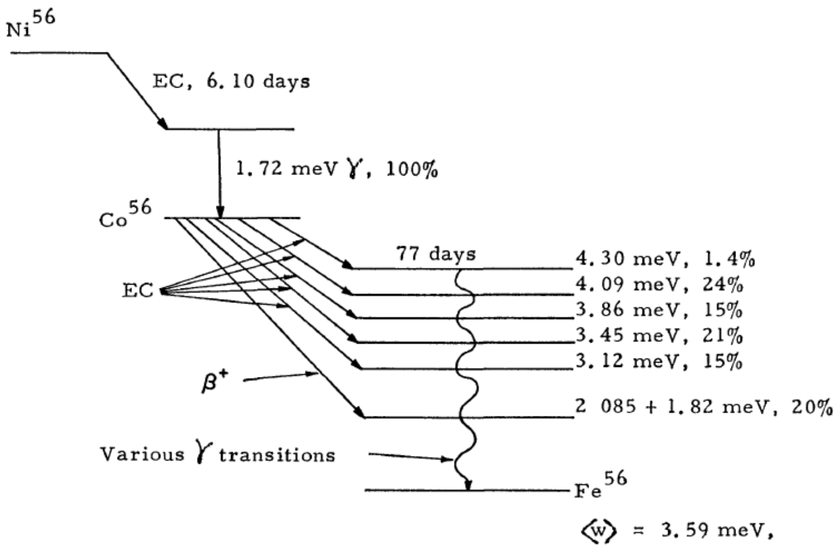

Figure 2.121: *The decay from ^{56}Ni to ^{56}Fe via ^{56}Co develops through electron capture (EC) and β^+ decay. From Lederer et al. (1967).*

On the other hand, the elements produced during the explosion in SNeII likewise depends on the the peak temperature attained through the passage of the shock, the density when the peak temperature is reached, and the number of electrons per nucleon (Y_e). The ^{56}Fe (and ^{57}Fe) are produced in electron rich regions ($Y_e \sim 0.50$) of the explosive Si burning in SNeII. This is as a result of the radioactive decay of ^{56}Ni (and ^{57}Ni) via ^{56}Co (and ^{57}Co), albeit both Fe isotopes might be directly synthesized (Nomoto et al. 2013).

The ^{56}Ni mass ejecta is linked with the progenitor's mass and energy of the explosion. It attains the maximum production of 0.3-0.5 $M_\odot$ in HNe of 30-50 $M_\odot$ (see Fig. 2.122).

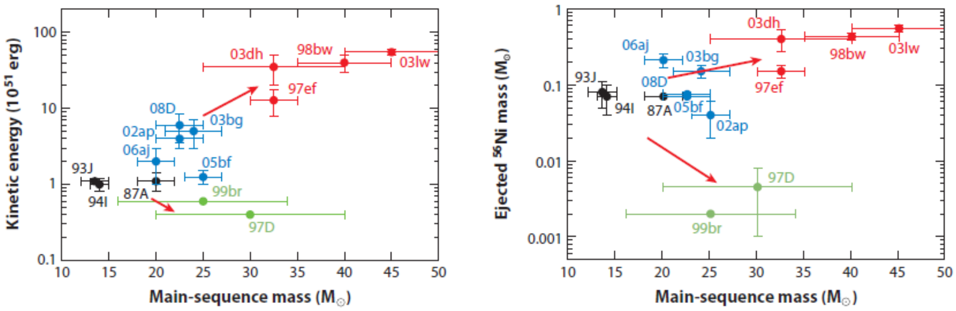

Figure 2.122: *Explosion energy and ejected ^{56}Ni mass as a function of the main-sequence mass of the progenitors for several supernovae/hypernovae. Explosions of 13–25 $M_\odot$ stars cluster at normal supernovae, whereas explosions of 25–40 $M_\odot$ stars have a large variety ranging from hypernovae to faint supernovae. From Nomoto et al. (2013).*

The energy release from this chain (^{56}Ni-^{56}Co-^{56}Fe) is the main driver of SNIa light curve luminosity. And it plays a significant energetic role in many SNeII light curves as well. The final ^{56}Fe yield can therefore be estimated for both types of SN light curves. There is thus a good semi-empirical handle on the total iron yield of different SN types (Maoz & Graur 2017, see Fig. 2.123).

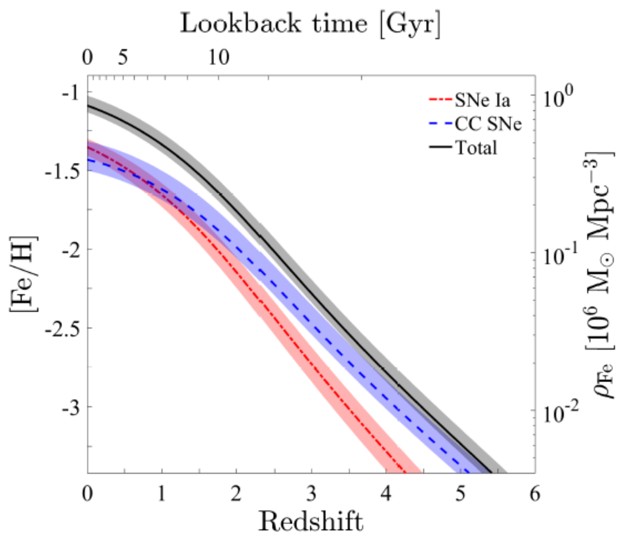

Figure 2.123: *Cosmic mean iron volume density (right-hand axis), and iron abundance, relative to Solar, [Fe/H] (lefthand axis), versus redshift, contributed by core-collapse SNe, by SNe Ia, and by their sum. The shaded regions are indicating uncertainties. From Maoz & Graur (2017).*

Iron lines dominate the optical spectra of dwarfs. It is usually chosen to play the role as

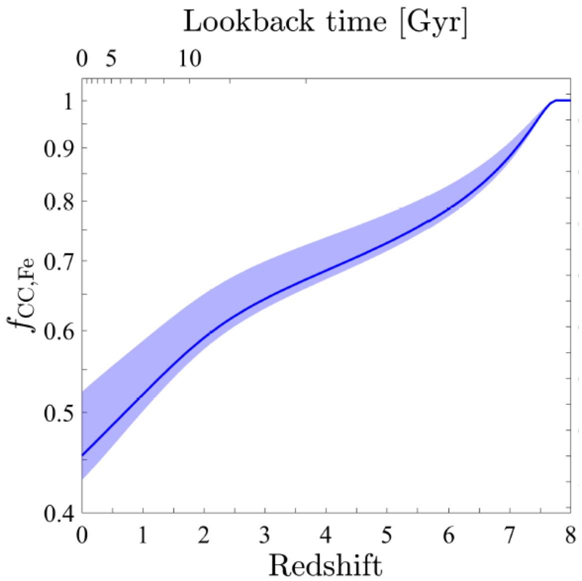

Figure 2.124: *Relative core-collapse SN contribution (left-hand axis) to the total iron budget (from both CC-SNe and SNeIa) as a function of redshift. Adapted from Maoz & Graur (2017).*

the fundamental measure of metallicity because it is relatively easy to determine the stellar abundance of Fe (Wheeler et al. 1989). And the chemical evolution studies present the evolution of the elements abundances referenced with respect to the Fe ([Fe/H]), acting as a parameter related to time.

It is also used to derive other basic stellar parameters as T_{eff} from the excitation equilibrium of Fe I, and the surface gravity, log g, from the ionization equilibrium between Fe I and Fe II (Mashonkina et al. 2011).

Chapter 3

...And Beyond

As pointed out in the beginning of the Chapt. 2, once the fusion in the silicon burning phases reaches the unstable ^{56}Ni, decaying to ^{56}Fe, the fusion process for heavier elements becomes energy-demanding.

Neutron capture (see Chapt. 1) will be the main source for the production of new heavier isotopes in low and intermediate mass stars LIMS/AGB or massive stars by slow mechanisms (s-process) or in energetic events as supernovae SNeII or SNIa (or even more dramatic as neutron stars merger) by rapid mechanisms (r-process), depending on the neutron source and available flux.

The estimated s- and r-process rates for each element in Solar System are shown in Fig. 3.1 by Simmerer et al. (2004).

Element	Z	r-Fraction	s-Fraction
Ga	31	0.431	0.569
Ge	32	0.516	0.484
As	33	0.785	0.215
Se	34	0.655	0.345
Br	35	0.833	0.167
Kr	36	0.437	0.563
Rb	37	0.499	0.501
Sr	38	0.11	0.89
Y	39	0.281	0.719
Zr	40	0.191	0.809
Nb	41	0.324	0.676
Mo	42	0.323	0.677
Tc	43	0.965	0.035
Ru	44	0.61	0.39
Rh	45	0.839	0.161
Pd	46	0.555	0.445
Ag	47	0.788	0.212
Cd	48	0.499	0.501
In	49	0.678	0.322
Sn	50	0.225	0.775
Sb	51	0.839	0.161
Te	52	0.803	0.197
I	53	0.944	0.056
Xe	54	0.796	0.204
Cs	55	0.85	0.15
Ba	56	0.147	0.853
La	57	0.246	0.754
Ce	58	0.186	0.814
Pr	59	0.508	0.492
Nd	60	0.421	0.579
Sm	62	0.669	0.331
Eu	63	0.973	0.027
Gd	64	0.819	0.181
Tb	65	0.933	0.067
Dy	66	0.879	0.121
Ho	67	0.936	0.064
Er	68	0.832	0.168
Tm	69	0.829	0.171
Yb	70	0.682	0.318
Lu	71	0.796	0.204
Hf	72	0.51	0.49
Ta	73	0.588	0.412
W	74	0.462	0.538
Re	75	0.911	0.089
Os	76	0.916	0.084
Ir	77	0.988	0.012
Pt	78	0.949	0.051
Au	79	0.944	0.056
Hg	80	0.42	0.58
Tl	81	0.341	0.659
Pb	82	0.214	0.786
Bi	83	0.647	0.353
Th	90	1.000	0.000
U	92	1.000	0.000

Figure 3.1: *s- and r-process ratio of elements in Solar System. Adapted from Simmerer et al. (2004).*

3.1. Cobalt ($_{27}$Co)

Cobalt is an Odd Iron-peak element. There is neither an agreement on the overall abundance trend of Co in the halo and thin/thick disk nor a generally accepted scenario for the nucleosynthetic production of cobalt (Bergemann et al. 2010).

However, the only stable isotope ^{59}Co is thought to be produced in both, core-collapse SNeII explosive Si burning (central complete-Si-burning regions of the supernova ejecta) and thermonuclear SNIa supernovae (Timmes et al. 1995; Kobayashi et al. 2006). As an element beyond the Fe, Co is too enriched by weak s-process nucleosynthesis in massive stars and main s-process in low and intermediate mass stars (LIMS/AGBs) although in a modest contribution (around 9% in Solar System), see Fig. 1.24 and 1.17 in Chapt. 1.

Umeda & Nomoto (2005); Nomoto et al. (2006, 2013) argued that strong explosion energies in supernovae may lead to enhanced yields of Co: Hypernovae (>20 $M_\odot$, 10^{52} erg) might have played an important role in the early chemical enrichment of the ISM. It may be due to the higher frequency of these events at early stages of the universe and their higher mass ejecta. Additionally, Fe-peak group elements yields might be enhanced by the strong α-rich freeze-out nucleosynthesis (see Sect. 1.4) in bipolar jet-like HNe explosions (Maeda & Nomoto 2003).

3.1.1 Chemical galactic abundances

NLTE effect corrections

The chemical abundance trend shows an α-like element behaviour, an almost flat trend for thin disk stars and an increasingly enhanced abundance trend for thick disk stars towards the metal poor range (ca [Fe/H]= -1.0 dex)(see Fig. 3.2).

Nevertheless, NLTE effects have to be taken into account, they might be severe. Bergemann et al. (2010) found NLTE corrections as large as +0.3 dex for Co II lines and from +0.1 to +0.6 for Co I lines, depending on the metallicity and surface gravity and temperature (see Fig. 3.3).

As usual, the NLTE effects increase the difficulty of the analysis of chemical abundance trends, especially at low metallicity range, where they are calculated to be more severe. Even so, the trend seems to show an over-abundant abundance of Co at very low metallicities (see Fig. 3.4). As above commented, more frequent energetic Hypernovae explosions at the early Universe might be playing an important role in the observed enrichment at low

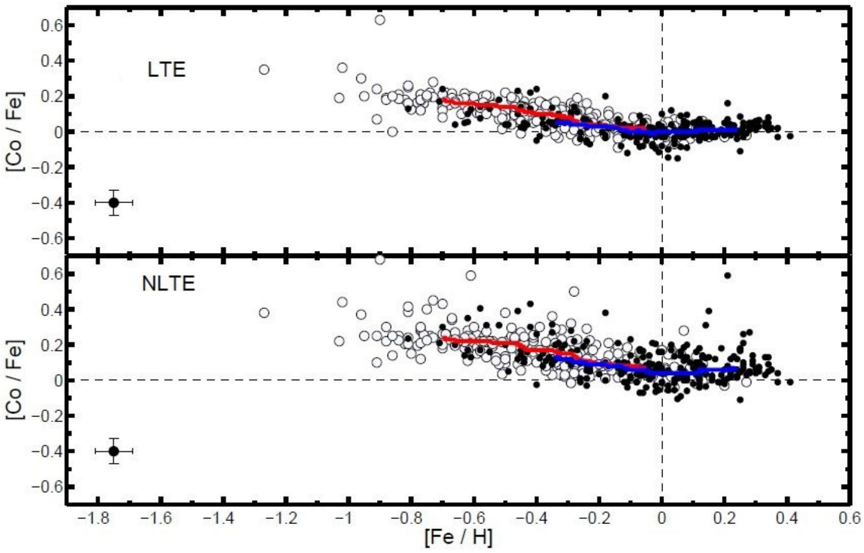

Figure 3.2: *Co abundance trend of 594 F- and G-type dwarfs in the solar neighborhood. Large white dots are stars older than 9 Gyr (likely thick disk stars), while small black dots are stars younger than 7 Gyr (likely thin disk stars). The blue and red lines represent the running median of thin and thick disk stars. LTE and NLTE-corrected assumptions. From Battistini & Bensby (2015).*

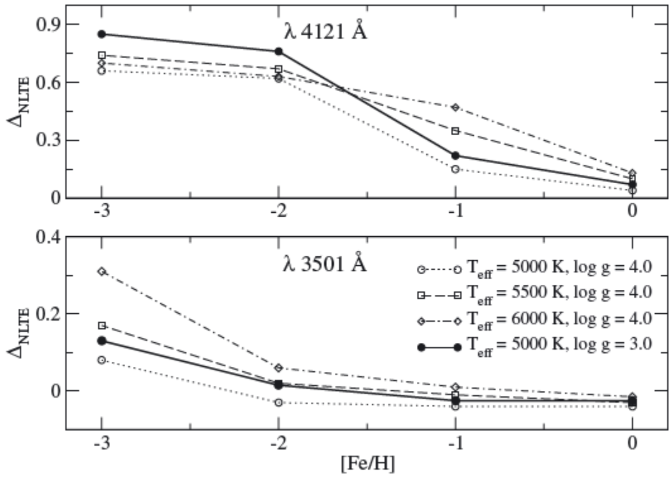

Figure 3.3: *Examples of NLTE corrections on Co* I *4121 Å line and Co* II *3501 Å line. Calculations are performed for 16 models with different surface temperature and gravity, and metallicity. From Bergemann et al. (2010).*

metallities (Battistini & Bensby 2015).

An additional contribution might come from considering that Hypernovae should be jet-like explosions. Maeda & Nomoto (2003) showed that some Fe-peak elements

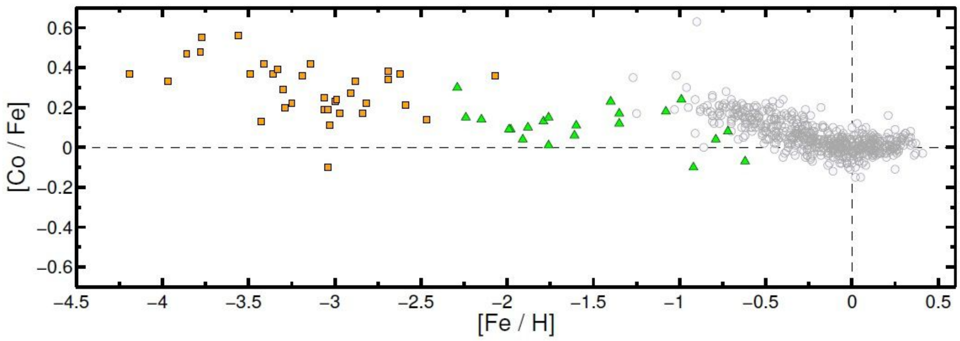

Figure 3.4: *In grey, V abundance trend of 594 F- and G-type dwarfs in the solar neighborhood by Battistini & Bensby (2015). Added nearby and extremely metal poor stars samples from Ishigaki et al. (2013) (EMP stars, green triangles) and Cayrel et al. (2004) (EMP stars, orange squares). From Battistini & Bensby (2015).*

are significantly enhanced by the strong α-rich freeze-out nucleosynthesis due to high temperatures and high entropies in complete Si burning with bipolar models (Sneden et al. 2016).

When included in CGE models, they can reproduce the trends at low metallicity better. However, large deviations are still observed. For example in the models of Kobayashi et al. (2006, 2011b) that include a 50% fraction of HNe and are enhances by the inclusion of the jet effect by Sneden et al. (2016), can still not really reproduce the observed abundance patterns (see Fig. 3.5).

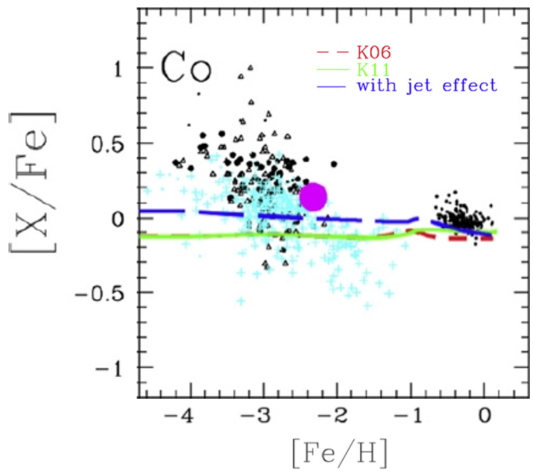

Figure 3.5: *Abundance ratios of Co plotted as function of [Fe/H] metallicity. The solid magenta circles represent the HD 84937 abundance ratio derived in the Sneden et al. (2016) paper. Black dots represent observational data from studies before 2014. Cyan plus signs are from Roederer et al. (2014a). Overlaid on the figure are GCE models from Kobayashi et al. (2006, 2011b) and the Sneden et al. (2016) paper. From Sneden et al. (2016).*

Taking into account the nucleosynthesis contribution from fast rotators (see Fig. 3.6) does not improve GCE models fit to the observational data (Prantzos et al. 2018). As a conclusion, the Co chemical abundance trend explanation, in especial at low metallicity (early universe) remains puzzling.

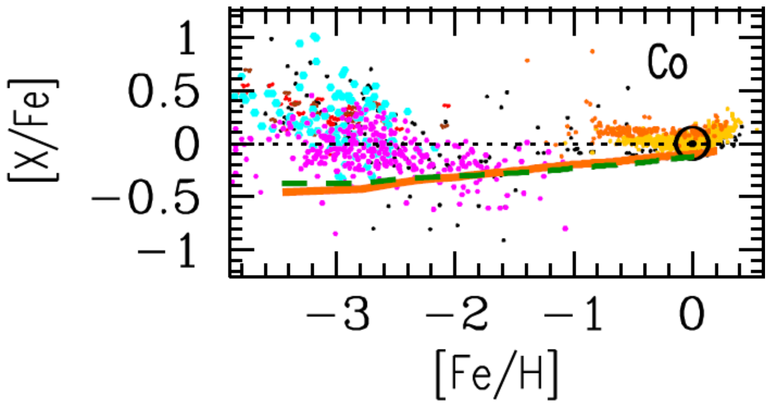

Figure 3.6: *Evolution of abundance ratio [Co/Fe] as a function of [Fe/H] and comparison to observational data. Prantzos et al. (2018) model from massive and AGB/LIMS stars productions is in dashed green curve; the same model but with enhanced yields from rotating massive stars is in orange curve. Observational data from Yong et al. (2013), Roederer et al. (2014a), Adibekyan et al. (2012) and Lai et al. (2008) based on LTE assumptions. From Prantzos et al. (2018).*

3.2. Nickel ($_{28}$Ni)

Nickel is produced by silicon burning, showing similar yields of core-collapse SNeII and thermonuclear SNeIa supernovaes contributions (Nomoto et al. 2013). In the case of the SNeII ejecta, it is synthesized in the more central, complete-Si-burning regions (Sneden et al. 2016). Although it is an element beyond Fe, still the s-process contribution is negligible (hardly 1% from weak s-process in massive stars for the SS, see Fig. 1.24).

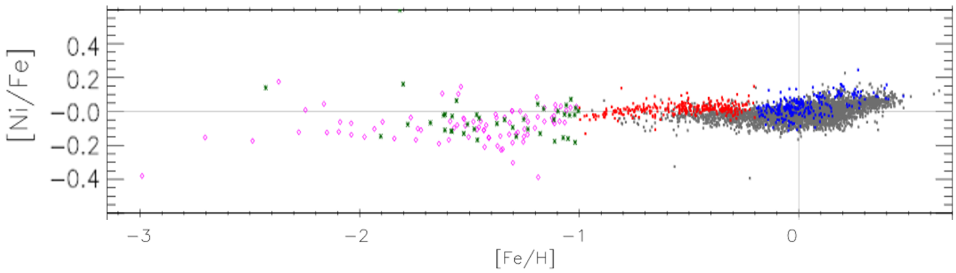

Figure 3.7: *Abundance Ni trend (LTE) againts metallicity in a sample of 4666 stars from AMBRE catalogue. Thin disc (grey dots), thick disc (red dots), metal-rich high-α sequence (blue dots), metal-poor low-α sequence (green asterisk), and metal-poor high-α sequence (magenta rhombus); the light grey lines represent the solar values. From Mikolaitis et al. (2017).*

3.2.1 Chemical galactic abundances

The nickel shows a characteristic almost flat [Ni/Fe] trend against metallicity (Mikolaitis et al. 2017). Other studies in the last years showed similar distributions (Bensby et al. 2014; Adibekyan et al. 2012) in which apparently no chemical separation is observed between thin and thick populations.

Neither between metal-poor low-α stars and metal-poor high-α stars in terms of Ni abundance as observed in Fig. 3.7. Nevertheless, Nissen & Schuster (2010) discovered a separation in [Ni/Fe]-[Na/Fe] distribution between both populations, later studied by Bensby et al. (2014), suggesting different origins of these halo-star populations.

As in other elements, GCE models fail to reproduce observational data. Kobayashi et al. (2006, 2011b) models including Hypernovae explosion (>20 $M_{\odot}$, 10^{52} erg) enhanced fractions and Sneden et al. (2016) including jet-alike HNe explosions, severely undermine the expected production with respect the observational data at low metallicities but however show overproductions at high metallicity which do not match the observational data.

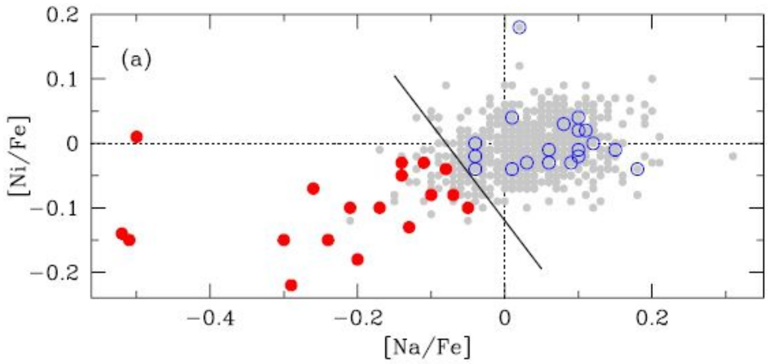

Figure 3.8: *Diagram [Ni/Fe]-[Na/Fe] for metal-poor low-α halo (red) and metal-poor high-α halo stars (blue) showing discovered separation by Nissen & Schuster (2010). From 714 F-and G-dwarf stars sample of Bensby et al. (2014).*

The Prantzos et al. (2018) model fits the low metallicity population better (EMP), independent on including the fast rotator nucleosynthesis prescriptions, but falls into the same overproduction estimation at the high metallicity range as observed in Fig. 3.9.

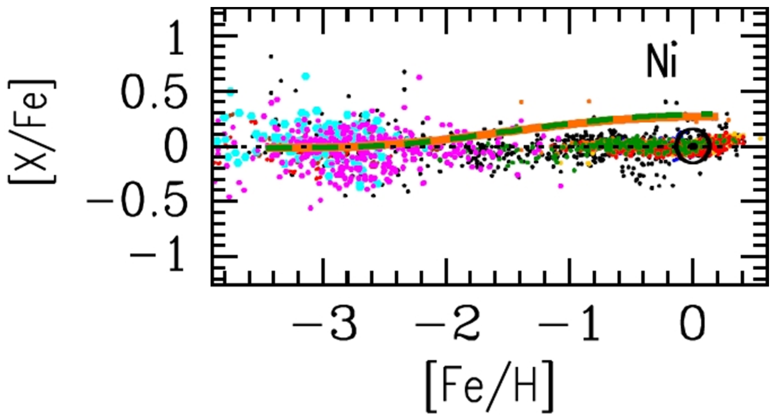

Figure 3.9: *Evolution of abundance ratio [Ni/Fe] as a function of [Fe/H] and comparison to observational data. Prantzos et al. (2018) model with rotating massive star yields is in solid orange curve; the same model but with non-rotating massive star yields is in dashed green curve. Observational data from Yong et al. (2013); Bensby et al. (2014); Roederer et al. (2014a); Adibekyan et al. (2012); Chen et al. (2000). From Prantzos et al. (2018).*

To our knowledge there is no in-depth study on NLTE effects in Ni lines.

3.3. Copper ($_{29}$Cu)

As we go beyond the iron, the neutron capture mechanisms contribution is increasingly dominant on the nucleosynthesis.

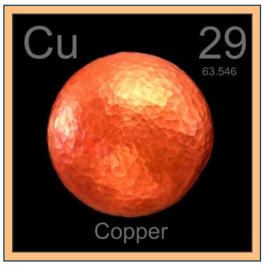

As is the case for Copper, an intermediate element between the iron-peak and a neutron capture element, thus its nucleosynthesis is very complex (Mikolaitis et al. 2017).

According to Travaglio et al. (2004), 27% of the Cu present in the solar system originates from s-process mechanisms. 22% is contributed by the weak s-process mechanism in massive stars and only 5% by main s-process in AGB/LIMS (see Fig. 1.24 in Chapt. 1).

Other sources are the explosive core-collapse SNeII and thermonuclear SNeIa supernovae. Nevertheless, the copper underabundance trend at low metallicity has raised yields corrections in order to reconcile observational data with models (Timmes et al. 1995) and the assumption that SNeIa should start polluting the interstellar media already at [Fe/H] ~ –2.0 dex (Korotin et al. 2018).

Mishenina et al. (2002) argued that at low metallicity the great majority of the copper nuclei were produced by secondary phenomena in massive stars (ca 25%), while a less important contribution comes from primary phenomena in the same environment. These can be either explosive silicon burning in SNeII or from the relatively fast neutron captures called "n-process". Finally, 62-65% originates from SNeIa supernovae on a long time scale. Hence SNeII are only considered as an important contributor at the very early stages of the universe (Korotin et al. 2018).

However, against the preponderance of the SNeIa contribution, Romano & Matteucci (2007) presented a comprehensive study in which they argued, on a galactic scale, that Cu is mainly produced by massive stars rather than by SNeIa (Romano et al. 2010).

After a short phase in which the primary contribution from explosive silicon burning nucleosynthesis in core-collapse SNeII dominates, the evolution of Cu in galaxies of different type is regulated mostly by the weak s-process occurring in massive stars (Romano & Matteucci 2007).

3.3.1 Chemical galactic abundances

Observational data distributions are quite homogeneous throughout most of the abundance studies (see Fig. 3.10, 3.11, 3.12). However, GCE models do not provide a clear

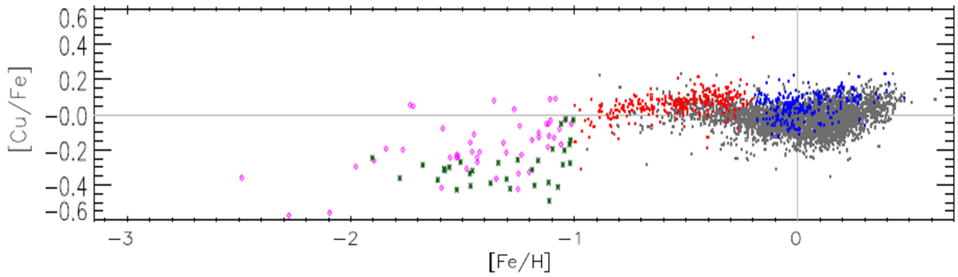

Figure 3.10: *Abundance Cu trend (LTE) againts metallicity in a sample of 4666 stars from AMBRE catalogue. Thin disc (grey dots), thick disc (red dots), metal-rich high-α sequence (blue dots), metal-poor low-α sequence (green asterisk), and metal-poor high-α sequence (magenta rhombus); the light grey lines represent the solar values. From Mikolaitis et al. (2017).*

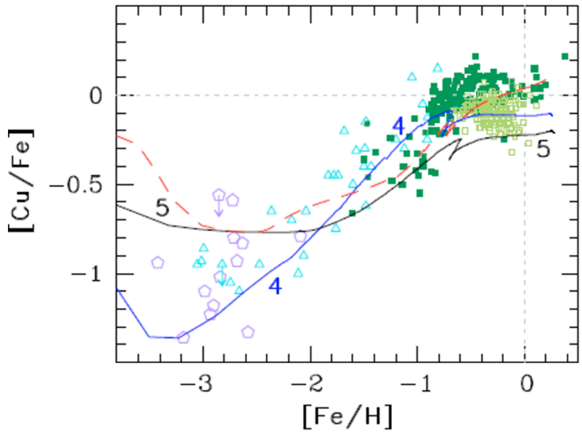

Figure 3.11: *Cu galactic chemical distribution in function of metallicity. Observational abundance data from Lai et al. (2008)(open pentagons), Gratton et al. (2003)(blue triangles), Reddy et al. (2006)(filled squares), Reddy et al. (2003)(open squares). Some galactic chemical evolution (GCE) models have been added (dashed and solid lines). From Romano et al. (2010).*

vision on the contribution evolution from the nucleosynthesis sources.

Models by Romano et al. (2010) in Fig. 3.11 show that the based model of Woosley & Weaver (1995) (dashed red), looks like a better fit but fails at the metal poor range. Model 4 refers to the Kobayashi et al. (2006) model in which SNeII yields were updated and model 5 to the Kobayashi et al. (2011b) model in which an important fraction of energetic Hypernovae (>20 $M_\odot$, 10^{52} erg) was included. An intermediate model between both seems to be working well, taking into account the later preponderance of s-process mechanism by massive stars. However these models lack contributions from s-mechanisms in LIMS/AGB.

Likewise based on Kobayashi et al. (2006, 2011b) prescriptions, the models by Sneden et al. (2016) severely fail when HNe jet-alike explosions are included in the model, overproducing Cu abundances at high metallicity range that do not match the observational abundances.

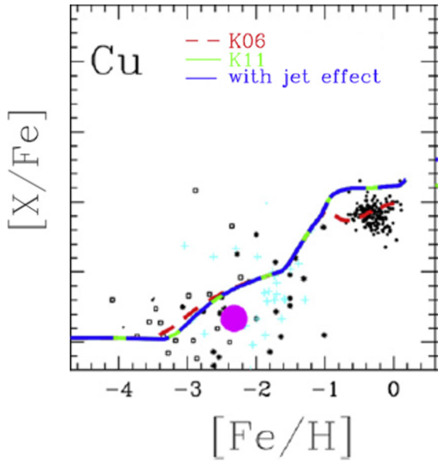

Figure 3.12: *Abundance ratios of Cu plotted as function of [Fe/H] metallicity. The solid magenta circles represent the HD 84937 abundance ratio derived in the Sneden et al. (2016) paper. Black dots represent observational data from studies before 2014. Cyan plus signs are from Roederer et al. (2014a). Overlaid on the figure are GCE models from Kobayashi et al. (2006, 2011b) and the Sneden et al. (2016) paper. From Sneden et al. (2016).*

Finally, the Prantzos et al. (2018) model fits well with the observed distribution (see Fig. 3.13). This model includes the general enhancement of yields due to a higher fraction of fast-rotators during the early stages of the universe.

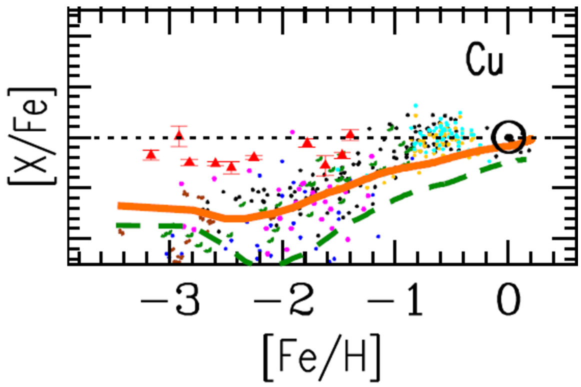

Figure 3.13: *Evolution of abundance ratio [Cu/Fe] against [Fe/H] and comparison to observational data. Prantzos et al. (2018) model with rotating massive star yields is in solid orange curve; the same model but with non-rotating massive star yields is in dashed green curve. Observational data from Roederer et al. (2014a); Yan et al. (2015); Lai et al. (2008); Andrievsky et al. (2018), the first and third, based on LTE assumptions, the second and the later, on NLTE. From Prantzos et al. (2018).*

Summarizing, the undersolar trend in the metal-poor range although studied from different evolutionary perspectives, still lacks an interpretation on the right nucleosynthesis sources contributions (Korotin et al. 2018).

NLTE effect corrections

The NLTE effects on the Cu lines and hence the derived abundances might change the overall view on the nucleosynthesis sites. Especially so in the low metallicity range where the NLTE effect are more exacerbated.

The Fig. 3.13 shows abundances based on LTE assumptions by Roederer et al. (2014a) and Lai et al. (2008) and include the NLTE-corrected ones by Yan et al. (2015) and Andrievsky et al. (2018), in red triangles, which are suggesting a quasi-solar trend at low metallicity range.

The derived corrected abundances by Andrievsky et al. (2018) are separately shown in Fig. 3.14, observing how the NLTE effects might reach +1.0 dex corrections at very low metallicities, much larger than previous NLTE corrections in studies as the one by Yan et al. (2015).

The used Cu I lines by Andrievsky et al. (2018) cover the UV to IR range (Cu I 3247, 3273, 5105, 5153, 5218, 5220, 5700, 5782, 7933, 8092 Å lines plus additional ones into the UV-C range), although at low metallicities the only available lines are an UV resonant doublet (Cu I 3247 and 3273 Å).

Although the results are suggesting a revision of Cu abundance distributions derived under LTE assumptions at low metallity ranges points to the need for a larger sample and performing of 3D-NLTE computations, which are currently not available (Andrievsky et al. 2018).

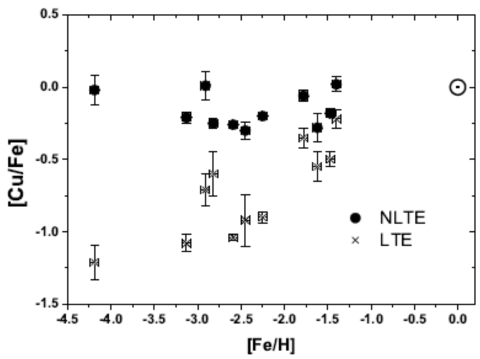

Figure 3.14: *Cu abundances derived from a metal poor sample corrected of NLTE effects (filled circles), calculated by Andrievsky et al. (2018).*

3.4. Zinc ($_{30}$Zn)

This Iron-peak element shares similar nucleosynthesis sites with copper, but in different yields. The ^{64}Zn isotope is mostly produced from α-rich freeze-out in neutrino driven winds environment of Supernovae (Woosley & Hoffman 1992; Bisterzo et al. 2004) or from Hypernovae, >20 M$_{\odot}$, 10^{52} erg (Umeda & Nomoto 2002), meanwhile ^{66,67,68,70}Zn are mainly produced by neutron capture in secondary weak s-process during core He-burning and the subsequent convective shell C-burning phase in massive stars (Bisterzo et al. 2004).

Observing Fig. 1.17 in Chapt. 1 by Travaglio et al. (2004), AGB/LIMS stars (main s-component) contribution to solar Zn is marginal, ca 3%. Meanwhile the total weak s contribution to Zn by massive stars attains ca 8%.

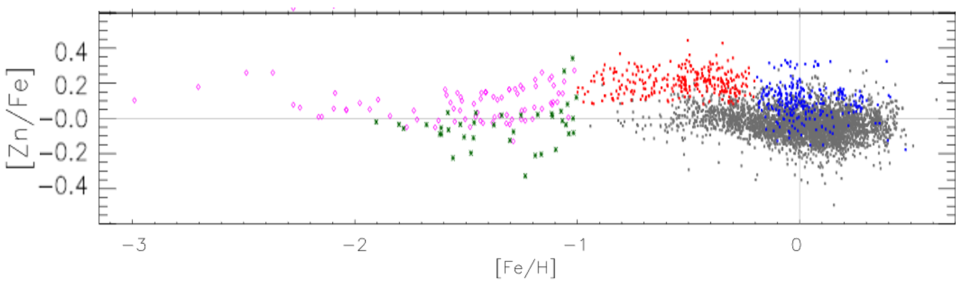

Figure 3.15: *Abundance Zn trend (LTE) againts metallicity in a sample of 4666 stars from AMBRE catalogue. Thin disc (grey dots), thick disc (red dots), metal-rich high-α sequence (blue dots), metal-poor low-α sequence (green asterisk), and metal-poor high-α sequence (magenta rhombus); the light grey lines represent the solar values. From Mikolaitis et al. (2017).*

3.4.1 Chemical galactic abundances

The abundance trend at metallicity [Fe/H]= 0.0-1.0 dex, resembles an α-like behaviour (see Fig. 3.15), with a slight increment of abundance in metal poor stars of the thick disk (around +0.3 dex at [Zn/Fe]=-1.0 dex).

However, at extremely metal poor range, there is a linear increase of [Zn/Fe] (see Fig. 3.16 and 3.17) with decreasing metallicity ([Fe/H] < -2.5 dex), hinting an increasing efficiency in the production from one or several of the named nucleosynthesis channels.

Extreme α-rich freezout in metal poor SNeII supernovae, could explain this raise (Fröhlich et al. 2006) but an alternative contribution enhancement might come, as proposed by Ohkubo et al. (2006), from Pop III core-collapse very massive (500-1000 $M_{\odot}$) stars, in which, at the pre-supernova stage, silicon-burning regions occupy a large fraction, more than 20% of the total mass (Romano et al. 2010).

Not taking into account of a large fraction of energetic Hypernovae (>20 $M_{\odot}$, 10^{52} erg) at the early universe seems to be behind the severe discrepancy and failing of the Prantzos et al. (2018) GCE models (regardless of including fast rotator massive stars yields) to reproduce observational data (see Fig. 3.16).

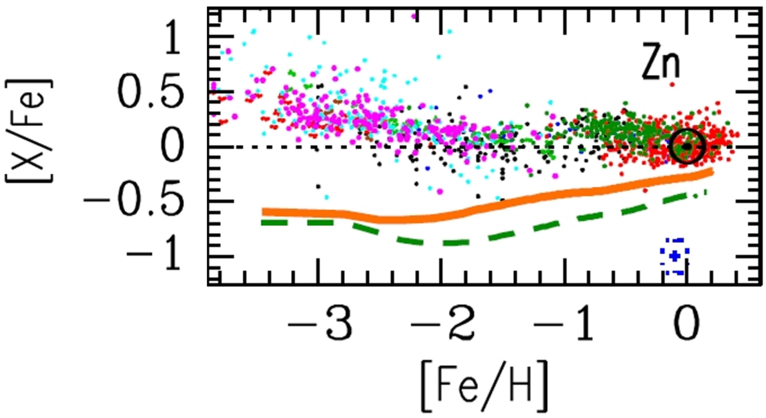

Figure 3.16: *Evolution of abundance ratio [Zn/Fe] as a function of [Fe/H] and comparison to observational data. Prantzos et al. (2018) model with rotating massive star yields is in solid orange curve; the same model but with non-rotating massive star yields is in dashed green curve. Observational data from Bensby et al. (2014), Roederer et al. (2014a) and Lai et al. (2008) based on LTE assumptions. From Prantzos et al. (2018).*

As the Fig. 3.17 by Romano et al. (2010) shows, the based GCE model on Woosley & Weaver (1995) prescriptions (dashed red) underestimates Zn abundances although it predicts the linear increase of abundance at low range metallicity. Model 4 based on the Kobayashi et al. (2006) model in which SNeII yields were updated, dramatically fails to reproduce observational data but model 5 based on the Kobayashi et al. (2011b) model that evolves Kobayashi et al. (2006) with the inclusion of a large fraction of SNeII exploding as energetic HNe (>20 $M_{\odot}$) fits much better. However, it fails to reproduce the increasing abundance trend at [Fe/H]<-2.0 dex to low metallicity.

NLTE effect corrections

To our knowledge there is no updated in-depth study on NLTE effects over Zn lines. The study by Takeda et al. (2005) predicts positive NLTE corrections of little significance ($\leq$ +0.1 dex) in the metal poor range (see Fig. 3.18).

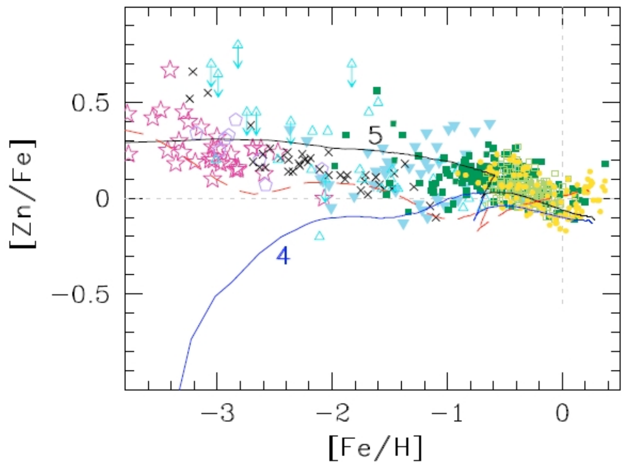

Figure 3.17: *Zn galactic chemical distribution in function of metallicity. Observational abundance data from Cayrel et al. (2004) (stars), Lai et al. (2008) (open pentagons), Nissen et al. (2007) (crosses), Bihain et al. (2004) (open triangles), Gratton et al. (2003)(upside-down triangles), Reddy et al. (2006)(filled squares), Reddy et al. (2003)(open squares) and Bensby et al. (2005) (filled circles). Some galactic chemical evolution (GCE) models have been added (lines). From Romano et al. (2010).*

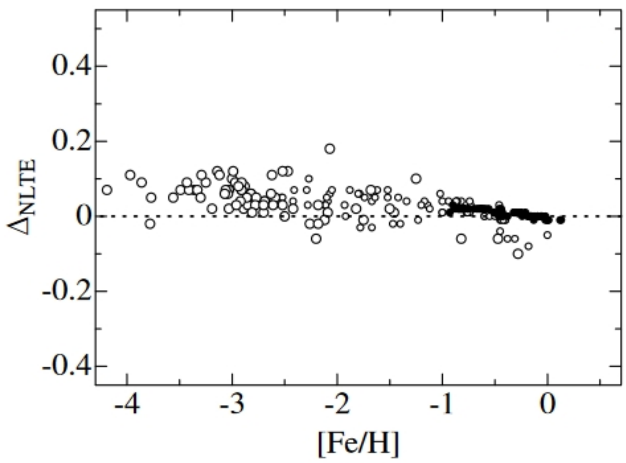

Figure 3.18: *NLTE corrections computed for Zn by Takeda et al. (2005). Open circles, corrections for Zn I 4722/4780 Å lines, used for deriving abundances of metal poor stars; filled circles, corrections for Zn I 6362 Å line.*

3.5. Strontium ($_{38}$Sr)

Strontium is an element that belongs to the first peak of stability in main s-process, a light s-process element (see Sect. 1.3 in Chapt. 1). ^{88}Sr isotope shows increased stability due to its magic number of neutrons, 50 (see Fig. 1.16 in Chapt. 1) and accounts for 82% of the solar system Sr nuclei (Travaglio et al. 2004, see Fig. 3.19). This stability makes these isotopes (^{88}Sr, ^{89}Y, ^{90}Zr) bottle necks in the main slow (s-process) neutron capture mechanism.

s-Process Fractional Contributions at $t = t_{\odot}$ with Respect to Solar System Abundances

Element	Solar[a] Atom (%)	Solar[a] σ (%)	GCE[b] IMSs (%)	GCE[b] LMSs+IMSs (%)	Weak s[c] (%)	TOT s[d] (%)
^{86}Sr	9.86	...	8	52	24	76
^{87}Sr	7.00	...	5	54	16	70
^{88}Sr	82.58	...	10	75	7	82
Sr....................	...	8.1	9	71	9	80
^{89}Y	100	...	7	69	5	74
Y.....................	...	6.0	7	69	5	74
^{90}Zr................	51.45	...	6	53	2	55
^{91}Zr................	11.22	...	18	80	3	83
^{92}Zr................	17.15	...	15	76	3	79
^{94}Zr................	17.38	...	9	79	2	81
^{96}Zr................	2.80	...	40	82	0	82
Zr....................	...	6.4	10	65	2	67
^{93}Nb...............	100	...	12	67	2	69
Nb...................	...	1.4	12	67	2	69
^{95}Mo	15.92	...	4	39	1	40
^{96}Mo	16.68	...	8	78	2	80
^{97}Mo	9.55	...	6	46	1	47
^{98}Mo	24.13	...	6	59	1	60
Mo	...	5.5	4	38	1	39

Interm. mass | Low+Interm. mass | Massive

[a] Anders & Grevesse 1989.
[b] This paper.
[c] Raiteri et al. 1993.
[d] Total from s-process: main s plus weak s.

Figure 3.19: *Isotopic contribution of s-process mechanisms to abundances of elements from Sr to Mo in Solar System (Travaglio et al. 2004).*

This process is developed in AGB/LIMS stars (Karakas & Lattanzio 2014) in which the required free neutrons are supplied mainly by the reaction ^{13}C(α; n)^{16}O and to a lesser extent by the reaction ^{22}Ne(α; n)^{25}Mg (Delgado Mena et al. 2017), see Sect. 1.3. Once it is synthesized during thermal inter-pulse periods, it gets lifted and mixed up in the surface after the third dredge-up (TDU).

The main s-process might account for ca 71% of the System Solar Sr abundance (see Fig. 1.24 in Chapt. 1) plus ca 9% from weak s-process contribution in massive stars.

Nevertheless, some studies argue an increased galactic weak s contribution, e.g. as high as 30% by Pignatari et al. (2010).

Lower mass AGB stars (1–4 $M_{\odot}$), in particular, produce large amounts of main s-process elements, meaning that the enrichment of the ISM (which begun roughly 500 Myr after the formation of the first population of stars) with Sr gradually increases with time (Travaglio et al. 2004). Therefore younger stars will have larger Sr abundances.

This is additionally linked with the metallicity. An excess of Fe over the neutron flux limits the final point of the main s-process production to the lighter elements, the first peak of stability (see Fig. 1.15 and 1.18 in Chapt. 1). The linear reaction is unable to push beyond, to the second or third peaks, due to the scarceness of neutrons. They are eagerly captured by the excess of Fe to form heavier isotopes of Fe or light Fe-peak elements (e.g. see Fig. 1.17 in Sect. 1.3).

In addition, primitive massive stars provide a promising site for the early production of the neutron-capture elements by the r-process throughout classical neutrino-driven wind of core-collapse SNeII or by the weak s-process. This is because the short evolution time needed in contrast with the longer time needed to develop the main s-process in AGB/LIMS. Although it is short with respect to other sources, the enrichment of the interstellar medium (ISM) with main s-process material only begins roughly 500 Myr after the formation of the first population of stars (Sneden et al. 2008).

These ideas are not well reproduced by nucleosynthesis models and might require new or independent channels. However in the Solar System, the global abundances of the heavy elements are the result of late production by the main s-process in addition to an early production by the r-process, and it has been possible to distinguish the fraction produced by each process (Andrievsky et al. 2011).

3.5.1 Chemical galactic abundances

The Sr abundance trend in disk stars shows an almost flat (thin disk) or very slight increase (thick disk stars) with decreasing metallicity as observed in Fig. 3.20. Similar trend is obtained in the larger sample from the HARPS-GTO program by Delgado Mena et al. (2017, see Fig. 3.21 and 3.22 in which some halo stars are likewise present).

The included Bisterzo et al. (2017) GCE models fits the thin disk population abundances quite well, but does not reproduce the thick disk stars. These models are built considering the contributions of r-process (only significant in metal poorer stars), s-process, and the Lighter Element Primary Process (LEPP). The latter a new and unknown s-process proposed by Travaglio et al. (2004) as a contribution to explain an extra over-abundance observed of

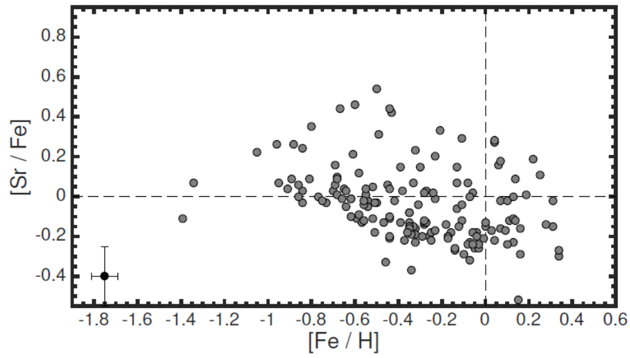

Figure 3.20: *[Sr/Fe] LTE abundance with respect to metallicity in a sample of F and G disk dwarf stars in the solar neighborhood. From Battistini & Bensby (2016).*

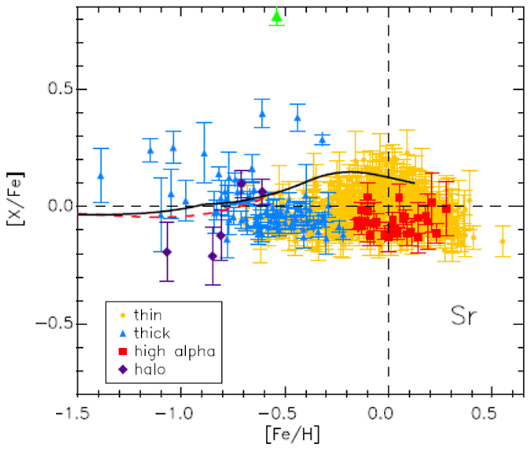

Figure 3.21: *[Sr/Fe] ratio as a function of metallicity for stars with T_{eff} > 5300 K and S/N > 100. The green bigger triangle is the s-enriched star HD 11397. GCE models are included from Bisterzo et al. (2017) for the thin disc (black lines) and the thick disc (red dashed lines). From Delgado Mena et al. (2017).*

light-s elements (Sr, Y and Zr) with respect to heavy ones (e.g. Ba) at lower metallicities.

In the Fig. 3.23 is observed the expected increase in a light s-element as Sr, over a second/heavy element as Ba, towards the metal richer range, especially in stars from the thin disk. This is due to the AGB/LIMS richer contribution in first peak main s-process elements. As above explained, the excess of Fe nuclei captures neutrons and prevents the lineal reaction to go further from the first peak of the main s-process. Like this, their elements are privileged over second or third peak ones towards the metal rich range (see Fig. 1.18 in Sect. 1.3).

Towards the metal poor range, the ratio should hold the decreasing trend due to the higher production of second main s-process elements as Ba. The Fe nuclei are less abundant

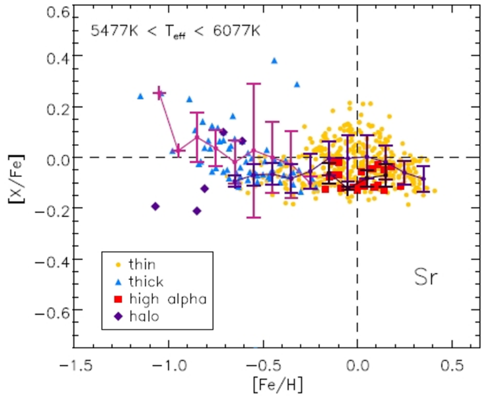

Figure 3.22: *[Sr/Fe] ratio as a function of metalliticy for stars with $T_{eff\odot} \pm 300$ K. The mean abundances in each metallicity bin of 0.1 dex are shown together with the standard deviation. From Delgado Mena et al. (2017).*

in AGB/LIMS. Therefore, a higher excess of neutrons is allowed, eager to push the lineal reaction beyond the first peak of stability. However, that is not the case when observing at lower metallicity [Fe/H] than -0.5 dex. This supports the idea of a lost extra source and mechanism of nucleosynthesis of s-light elements (LEPP suggestion by Travaglio et al. 2004) at lower metallicities, especially affecting the stellar thick disk population.

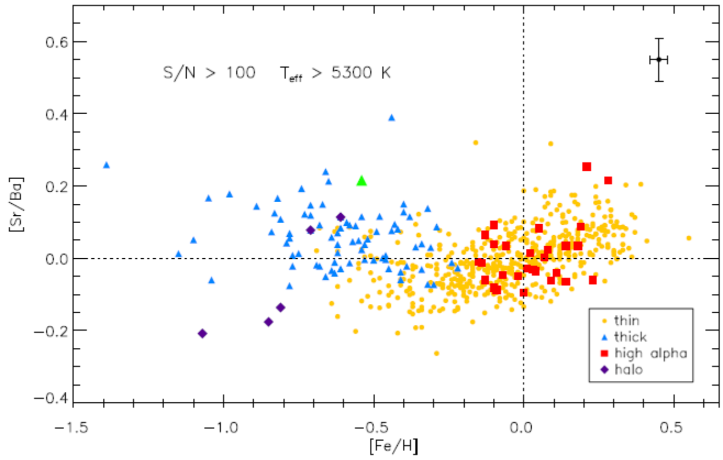

Figure 3.23: *Abundance ratios of a light-s element as Sr with respect to the heavy, main s-process second peak element Ba as a function of [Fe/H] for stars with T_{eff} > 5300 K and S/N > 100. From Delgado Mena et al. (2017).*

Likewise, the change of slope from thin to thick disk populations and excess of s light elements (average of Sr, Y, Zr) with respect to the heavy elements (Ba, Ce and Nd) in the thick disk to metal poor range is shown in Fig. 3.24. As it might be observed in a beautiful way in the Fig. 3.25 by Battistini & Bensby (2016) where the stellar ages are computed from physical and spectral observational data. The change of slope with respect to the stellar age remarks the transition breaking point from thin to thick disk population, linked with the different chemical nature and galaxy evolutionary path of both disks.

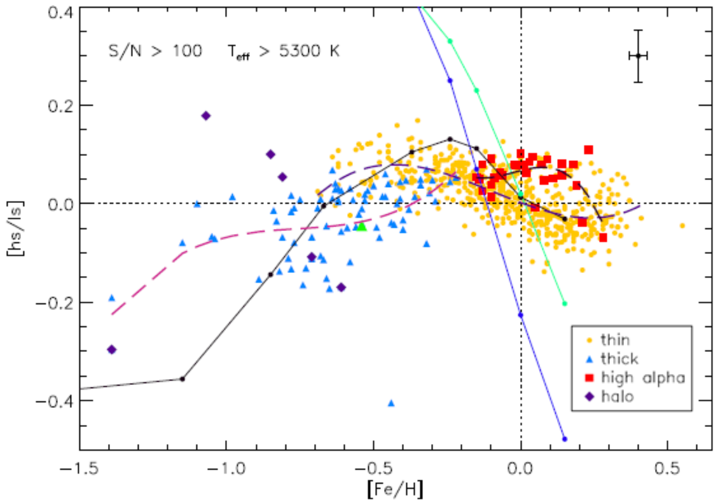

Figure 3.24: *Ratios of heavy-s to light-s as a function of [Fe/H] for stars with T_{eff} > 5300K and S/N > 100. The blue, green, and black lines are AGB models of 2 $M_\odot$, 3 $M_\odot$, and 6 $M_\odot$, respectively, from Cristallo et al. (2015a). The long-dashed lines are polynomial fits to the different populations. From Delgado Mena et al. (2017).*

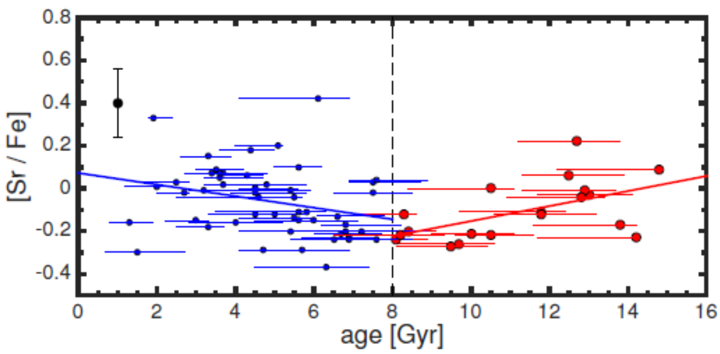

Figure 3.25: *[Sr/Fe] compared to age. Only stars with age uncertainties less than 3 Gyr are plotted. The vertical dotted line at 8 Gyr indicates an approximate age separation between thin and thick disk. Blue dots represent young thin disk stars, while red dots are for old thick disk stars. The blue and red lines indicate the best fit for thin and thick disk stars. The errors on the ages are from Bensby et al. (2014). The average error on the abundance ratio is indicated in black. From Battistini & Bensby (2016).*

Nevertheless, the extra s-process elements contribution by the LEPP mechanism is not fully accepted and is ruled out or discussed by authors as Trippella et al. (2016), Cristallo et al. (2015a) and Prantzos et al. (2018) who argue that the trend might be explained by existent nucleosynthesis sites and the great uncertainties still affecting both stellar and galactic chemical evolution models.

Prantzos et al. (2018) addressed the LEPP issue, including and adjusting weak s-process contributions from rotating massive stars in a model whose nucleosynthesis yields depend on the metallicity. They argued that their model does not require the LEPP mechanism to fit the observed nearby solar abundances quite well (see Fig. 3.26 and especially 3.27).

When abundances are derived from metal poor stars the scatter largely increases. This is consistently observed in abundance studies of metal poor stars, e.g. by Travaglio et al. (2004), Lai et al. (2007, 2008), Andrievsky et al. (2011), Ishigaki et al. (2013) or Hansen et al. (2014). This scatter can be observed in Fig. 3.26 by Prantzos et al. (2018).

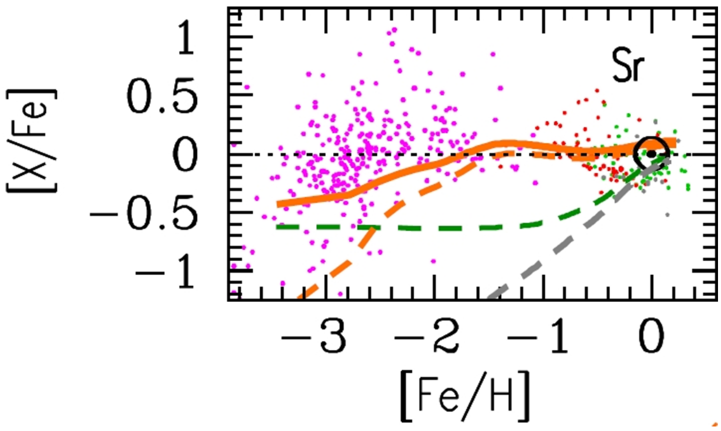

Figure 3.26: *Evolution of abundance ratio [Sr/Fe] as a function of [Fe/H] and comparison to observational data. Prantzos et al. (2018) model including AGB/LIMS, rotating massive and r-process stellar yields is in solid orange curve; the same model but with non-rotating massive star yields is in dashed green curve; model including AGB/LIMS, rotating massive but without r-process stellar yields in orange dashed curve and finally model including AGB/LIMS but without rotating massive nor r-process yields in gray dashed curve. Observational data from Roederer et al. (2014a), Battistini & Bensby (2016) and Lai et al. (2008) based on LTE assumptions. From Prantzos et al. (2018).*

This figure includes their models accounting for different prescriptions relative to yield sources as AGB/LIMS (main s-process), massive stars (early r process) and enhancement of yields in massive fast rotators. These last two yield sources having a stronger incidence at the metal poor range.

It is observed how the inclusion of r-process contribution at early stages of the universe due to their short time evolution with respect to the AGB production, and the Sr yield enhancement in fast rotators, greatly improve the fit of the abundance data.

It is observed that the including of r-process contributions at early stages of the universe greatly improves the fit of abundance data. This is due to their short time evolution compared to the AGB production process. And a second factor is the including of the Sr enhanced yields in fast rotators.

In this direction, the role of the spinstars/fast rotators were studied by Cescutti et al.

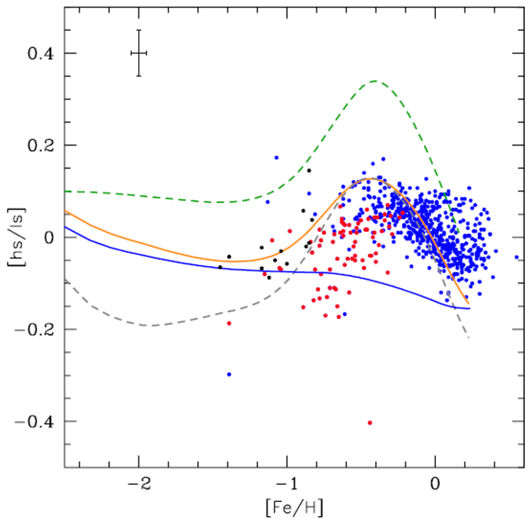

Figure 3.27: *Observed heavy-s (Ba, Ce, Nd) to light-s (Sr, Y, Zr) ratio [hs/ls] vs [Fe/H] compared with Prantzos et al. (2018) GCE model predictions. Observational data are from Delgado Mena et al. (2017) for thin (blue dots) and thick (red dots) disk stars. Black dots are the thick disk stars in Fishlock et al. (2017). Solid orange curve shows the prediction from Prantzos et al. (2018) baseline model, green dashed curve the one for the non-rotating massive stars, and gray dashed curve the non-rotating case where the r-component is not considered. The blue solid curve shows the prediction when the contribution from Low and Intermediate Mass Stars is omitted. From Prantzos et al. (2018).*

(2013); Cescutti & Chiappini (2014), constraining the early s and r-process contribution. The observed scatter in the halo metal-poor stars is explained by Cescutti & Chiappini (2014) assuming different scenarios. The authors developed an inhomogeneous GCE model for the galactic halo as a result of combining contributions:

Contributions Galactic Halo Cescutti & Chiappini (2014) Model

- s-process production in fast rotators (spinstars) more abundant in early stages of the universe
- r-process coming from massive stars by electron-capture Supernovae
- r-process coming from Magnetorotationally driven Supernovae (Winteler et al. 2012). This is a rare progenitor configuration characterized by a high rotation rate and a strong magnetic field necessary for the formation of bipolar jets (see Fig. 1.34 and Sect. 1.4).

However, both r-process contributions are not clearly distinguishable in observational data. Both are able to reproduce the fraction of r-process-rich stars fairly well in the early galaxy abundance. Independently of the r-process scenarios adopted, the weak s-process contribution from massive spin-stars is needed to reproduce the spread in the Sr over the heavy neutron capture element, Ba (Cescutti & Chiappini 2014).

Nevertheless, Prantzos et al. (2018) argues that the inhomogeneous GCE model by Cescutti & Chiappini (2014) is not sufficient to fully explain the halo abundances scatter. They points to the need of an in-depth study taking into account additional factors as merging of sub-halos (each one with its own history and timescale for chemical enrichment) as a forming mechanism of the early Galaxy or the imperfect gas mixing.

The Prantzos et al. (2018) GCE model including rotating massive stars yields are found to have a dramatic impact in the predicted evolution of the s-elements as light as Sr at low metallicity (see Fig. 3.26, solid orange model). However it does not fully explain the abundance scatter in the halo, as commented by the same authors as above.

3.6. Yttrium ($_{39}$Y)

Yttrium is another light s-process element that belongs to the first stability peak in main s-process (see Sect. 1.3 in Chapt. 1). ^{89}Y isotope has increased stability due to its magic number of neutrons, 50 (see Fig. 1.16 in Chapt. 1) and accounts for entirety of the Y nuclei of the solar system (Travaglio et al. 2004, see Fig. 3.19). This special stability makes these isotopes (^{88}Sr, ^{89}Y, ^{90}Zr) bottle necks in the main slow (s-process) neutron capture mechanism.

This process is developed in AGB/LIMS stars (Karakas & Lattanzio 2014) where the required free neutrons are supplied mainly by the reaction ^{13}C(α; n)^{16}O and to a lesser extent by the reaction ^{22}Ne(α; n)^{25}Mg (Delgado Mena et al. 2017), see Sect. 1.3. Once it is synthesized during thermal inter-pulse periods, it gets lifted up and mixed in the surface after the third dredge-up. The main s-process might account for ca 69% of the System Solar Y abundance (see Fig. 1.24 in Chapt. 1) plus ca 5% from weak s-process contribution.

One interesting characteristic of Y is its high condensation temperature at 1622 K, making this element eager to form dust in the early stages of a possible circumstellar disk formation, present in some Post-AGB stars. The radiation pressure prevents the re-accretion on the star, leading to a depletion of the Y abundance on the photospheric layer as it is observed by Maas et al. (2005) in some Post-AGB stars.

The discussion about chemical galaxy distribution, nucleosynthesis sites and time delay with respect other sources, show similar topics with respect to the main s-process first peak partners as Sr and Zr. See latter Sect. 3.5, Sr element, for a general view equally applicable for Y.

3.6.1 Chemical galactic abundances

The galactic chemical abundance of Y is shown in Fig. 3.28 by Delgado Mena et al. (2017) from the HARPS GTO survey. The included Bisterzo et al. (2017) GCE models fits the thin disk population abundances quite well, but does not reproduce the thick disk stars. These models are built considering the contributions of r-process (only significant in metal poorer stars), s-process, and the LEPP.

In the Fig. 3.29 the [Y/Ba] ratio is observed. The same argument than in Subsect. 3.5 (Sr element) can be developed in relation with the increase of the ratio towards metal poor stars from [Fe/H] < -0.5 dex. This indicates an unexpected contribution of s-process light elements in this range. A full discussion about this subject and the relation of the first peak s-process elements with metallicity might be found in the commented subsection of Sr.

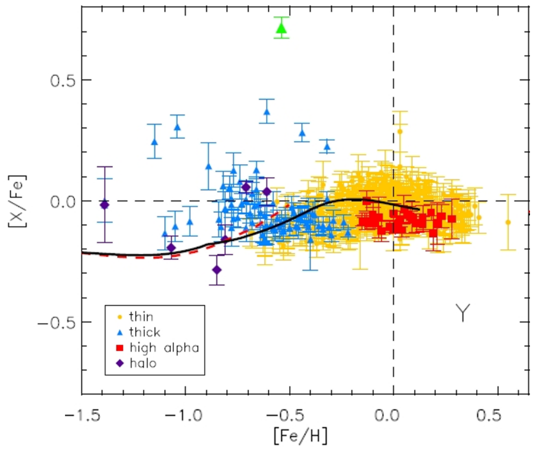

Figure 3.28: *[Y/Fe] ratio as a function of metalliticy for stars with T_{eff} > 5300 K and S/N > 100. The green bigger triangle is the s-enriched star HD 11397. GCE models are included from Bisterzo et al. (2017) for the thin disc (black lines) and the thick disc (red dashed lines). From Delgado Mena et al. (2017).*

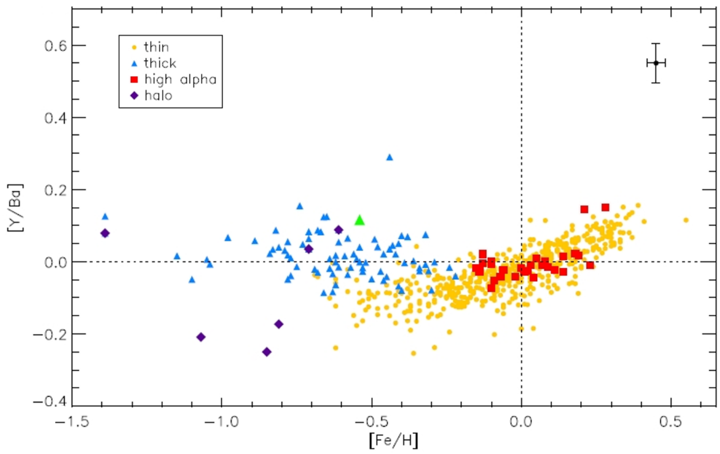

Figure 3.29: *Abundance ratios of a light-s element as Y with respect to the heavy, main s-process second peak element Ba as a function of [Fe/H] for stars with T_{eff} > 5300 K and S/N > 100. From Delgado Mena et al. (2017).*

This gave origin to the LEPP hypothesis, a new and unknown source of light s-process elements proposed by Travaglio et al. (2004). However, this point is under discussion and some studies have been published arguing that known nucleosynthesis sources might explain this apparent anomaly.

Once more, see Subsect. 3.5 for a full development on this subject and abundance trend figures explanation. Or others as the increasing scatter of the stellar abundances towards metal poor stars (halo/EMP) and their proposed causes.

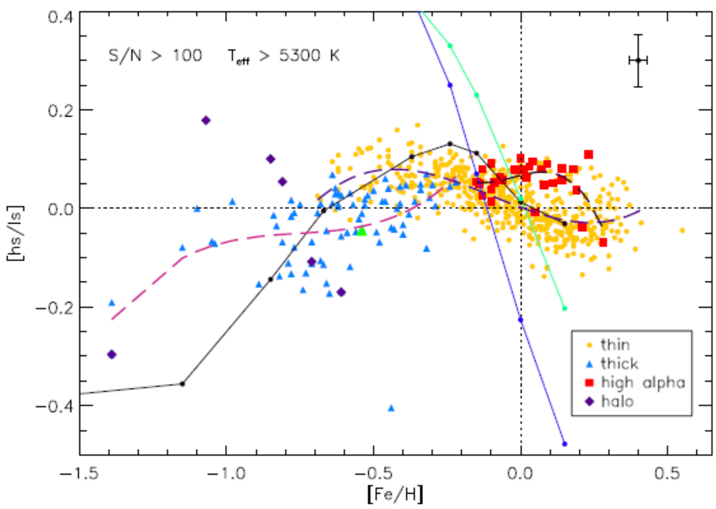

Figure 3.30: *Ratios of heavy-s to light-s as a function of [Fe/H] for stars with T_{eff} > 5300K and S/N > 100. The blue, green, and black lines are AGB models of 2 $M_\odot$, 3 $M_\odot$, and 6 $M_\odot$, respectively, from Cristallo et al. (2015a). The long-dashed lines are polynomial fits to the different populations. From Delgado Mena et al. (2017).*

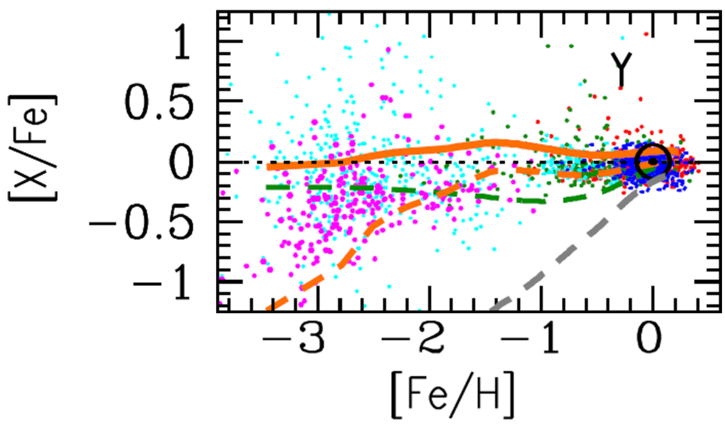

Figure 3.31: *Evolution of abundance ratio [Y/Fe] as a function of [Fe/H] and comparison to observational data. Prantzos et al. (2018) model including AGB/LIMS, rotating massive and r-process stellar yields is in solid orange curve; the same model but with non-rotating massive star yields is in dashed green curve; model including AGB/LIMS, rotating massive but without r-process stellar yields in orange dashed curve and finally model including AGB/LIMS but without rotating massive nor r-process yields in gray dashed curve. Observational data from Bensby et al. (2014), Roederer et al. (2014a) and Mishenina et al. (2013) based on LTE assumptions. From Prantzos et al. (2018).*

3.6.2 [Y/Mg] ratio as a proxy for stellar age

Finally, there is linear relation between the [Y/Mg] ratio and stellar ages for solar-like

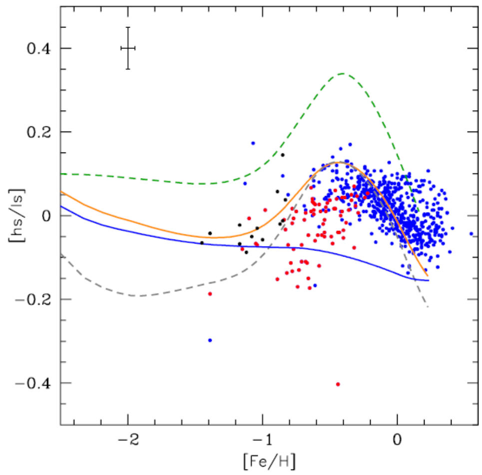

Figure 3.32: *Observed heavy-s (Ba, Ce, Nd) to light-s (Sr, Y, Zr) ratio [hs/ls] vs [Fe/H] compared with Prantzos et al. (2018) GCE model predictions. Observational data are from Delgado Mena et al. (2017) for thin (blue dots) and thick (red dots) disk stars. Black dots are the thick disk stars in Fishlock et al. (2017). Solid orange curve shows the prediction from Prantzos et al. (2018) baseline model, green dashed curve the one for the non-rotating massive stars, and gray dashed curve the non-rotating case where the r-component is not considered. The blue solid curve shows the prediction when the contribution from Low and Intermediate Mass Stars is omitted. From Prantzos et al. (2018).*

stars. The first evidence was obtained by da Silva et al. (2012), and later corroborated by Nissen (2015), Spina et al. (2016), Tucci Maia et al. (2016) and Feltzing et al. (2017).

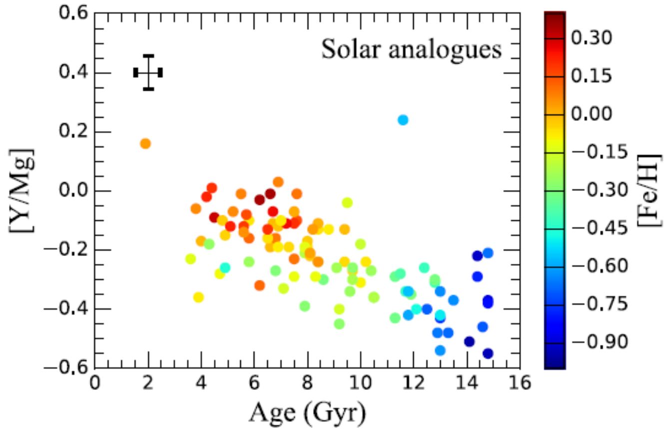

Figure 3.33: *[Y/Mg] as a function of age (in Gyr) for all stars with σ_Age < 1 Gyr from Bensby et al. (2014) that also have T_{eff} in the range of 5777 ± 100 K. From Feltzing et al. (2017).*

As above commented for the Sr (see latter section), lower mass AGB stars (1–4 $M_\odot$), in particular, produce large amounts of main s-process elements, meaning that the enrichment of the ISM (begun roughly 500 Myr after the formation of the first population of stars) with Y gradually increases with time (Travaglio et al. 2004) and therefore younger, metal richer stars will have larger Y abundances. In contrast, Mg, an α-element born in the final stages of massive stars becoming Supernovae SNeII (> 10 $M_{\odot}$), enriches the ISM much quicker after the first stars formation, being overabundant over the rest of elements.

The later evolution, with the contribution of additional sources as SNeIa, producing larger yields in Fe but not in α-elements, will reduce the Mg abundance ratio with respect to the Y. Leaving aside stars of different temperature and surface gravity, it is clear that the evolution of both Y and Mg with time is not independent of the evolution of Fe (see f.i. Sect. 1.3 in Chapt. 1 about the relation of Fe with the production of the first, second and third peaks of the main s-process). Hence, this relation might provide a very powerful tool for deriving ages of stars without the need to resort to determining their masses (evolutionary stage) very precisely (Feltzing et al. 2017).

3.7. Zirconium ($_{40}$Zr)

Zirconium is another light s-process element that belongs to the first peak of stability in the main s-process (see Sect. 1.3 in Chapt. 1). ^{90}Zr isotope shows increased stability due to its magic number of neutrons, 50 (see Fig. 1.16 in Chapt. 1) and accounts for 51% of Zr nuclei of the solar system (Travaglio et al. 2004, see Fig. 3.19). This stability makes these isotopes (^{88}Sr, ^{89}Y, ^{90}Zr) bottle necks in the main slow (s-process) neutron capture mechanism.

This process is developed in AGB/LIMS stars (Karakas & Lattanzio 2014) where the required free neutrons are supplied mainly by the reaction ^{13}C(α; n)^{16}O and to a lesser extent by the reaction ^{22}Ne(α; n)^{25}Mg (Delgado Mena et al. 2017, see Sect. 1.3). Once it is synthesized during thermal inter-pulse periods, it gets lifted and mixed up on the surface after the third dredge-up. The main s-process might account for ca 65% of the System Solar Zr abundance (see Fig. 1.24 in Chapt. 1) plus ca 2% from weak s-process contribution.

The discussion about chemical galaxy distribution, nucleosynthesis sites and time delay with respect other sources, show similar topics with respect to the main s-process first peak partners as Sr and Y. See Sect. 3.5, Sr element, for a general view equally applicable for Zr.

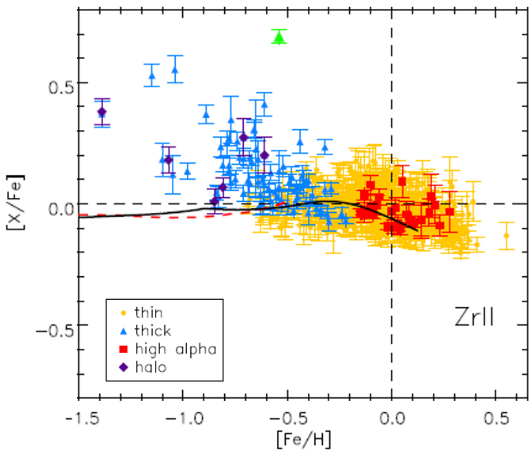

Figure 3.34: *[Zr/Fe] ratio as a function of metallicity for stars with T_{eff} > 5300 K (Zr II) and S/N > 100. The green bigger triangle is the s-enriched star HD 11397. GCE models are included from Bisterzo et al. (2017) for the thin disc (black lines) and the thick disc (red dashed lines). From Delgado Mena et al. (2017).*

3.7.1 Chemical galactic abundances

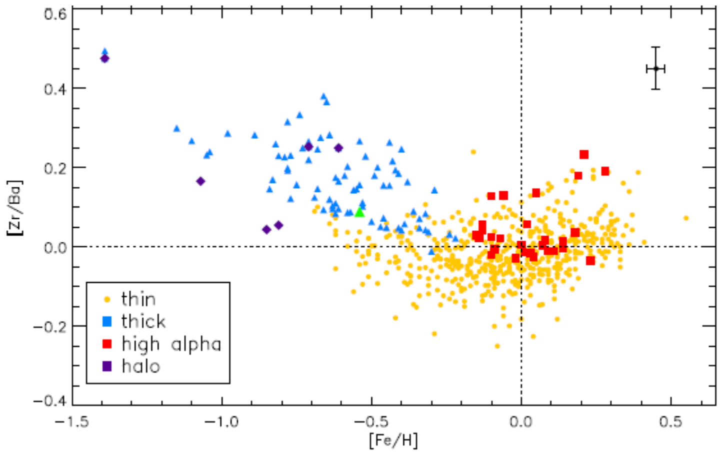

Figure 3.35: *Abundance ratios of a light-s element as Zr with respect to the heavy, main s-process second peak element Ba as a function of [Fe/H] for stars with T_{eff} > 5300 K and S/N > 100. From Delgado Mena et al. (2017).*

The Zr galaxy chemical abundance is shown in Fig. 3.34 by Delgado Mena et al. (2017) from the HARPS GTO survey. The included Bisterzo et al. (2017) GCE models fit the thin disk population abundances quite well, but does not reproduce the thick disk stars. These models are built considering the contributions of r-process (only significant in metal poorer stars), s-process, and the LEPP.

In the Fig. 3.35 the [Zr/Ba] ratio is observed. The same argument than in Subsect. 3.5 (Sr element) can be developed in relation with the increase of the ratio towards metal poor stars from [Fe/H] < -0.5 dex. This indicates an unexpected contribution of s-process light elements in this range. A full discussion about this subject and the relation of the first peak s-process elements with metallicity might be found in the commented subsection of Sr.

This gave origin to the LEPP hypothesis, a new and unknown source of light s-process elements proposed by Travaglio et al. (2004). However, this point is under discussion and some studies have been published arguing that known nucleosynthesis sources might explain this apparent anomaly.

Once more, see Subsect. 3.5 for a full development on this subject and abundance trend figures explanation. Or others as the increasing scatter of the stellar abundances towards metal poor stars (halo/EMP) and their proposed causes.

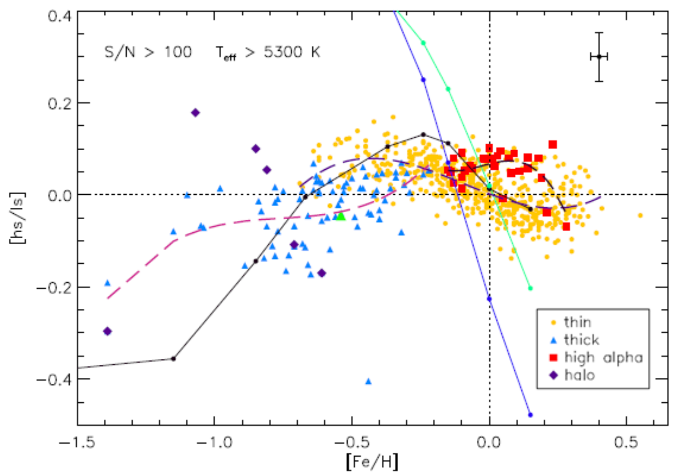

Figure 3.36: *Ratios of heavy-s to light-s as a function of [Fe/H] for stars with T_{eff} > 5300K and S/N > 100. The blue, green, and black lines are AGB models of 2 $M_\odot$, 3 $M_\odot$, and 6 $M_\odot$, respectively, from Cristallo et al. (2015a). The long-dashed lines are polynomial fits to the different populations. From Delgado Mena et al. (2017).*

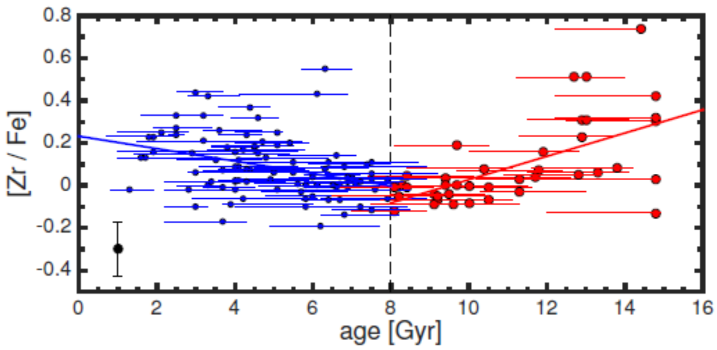

Figure 3.37: *[Zr/Fe] compared to age. Only stars with age uncertainties less than 3 Gyr are plotted. The vertical dotted line at 8 Gyr indicates an approximate age separation between thin and thick disk. Blue dots represent young thin disk stars, while red dots are for old thick disk stars. The blue and red lines indicate the best fit for thin and thick disk stars. The errors on the ages are from Bensby et al. (2014). The average error on the abundance ratio is indicated in black. From Battistini & Bensby (2016).*

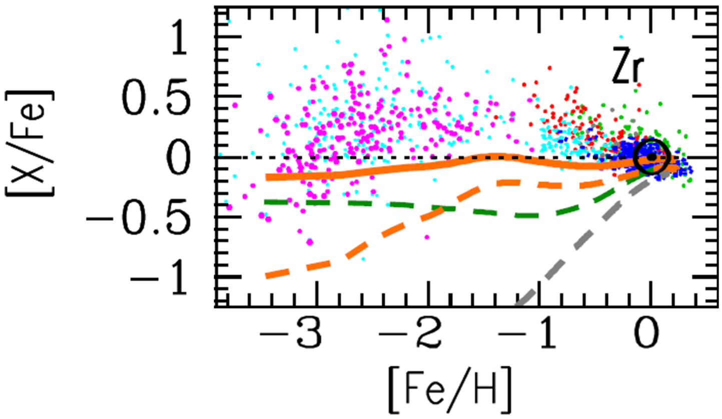

Figure 3.38: *Evolution of abundance ratio [Zr/Fe] as a function of [Fe/H] and comparison to observational data. Prantzos et al. (2018) model including AGB/LIMS, rotating massive and r-process stellar yields is in solid orange curve; the same model but with non-rotating massive star yields is in dashed green curve; model including AGB/LIMS, rotating massive but without r-process stellar yields in orange dashed curve and finally model including AGB/LIMS but without rotating massive nor r-process yields in gray dashed curve. Observational data from Roederer et al. (2014a), Battistini & Bensby (2016) and Mishenina et al. (2013) based on LTE assumptions. From Prantzos et al. (2018).*

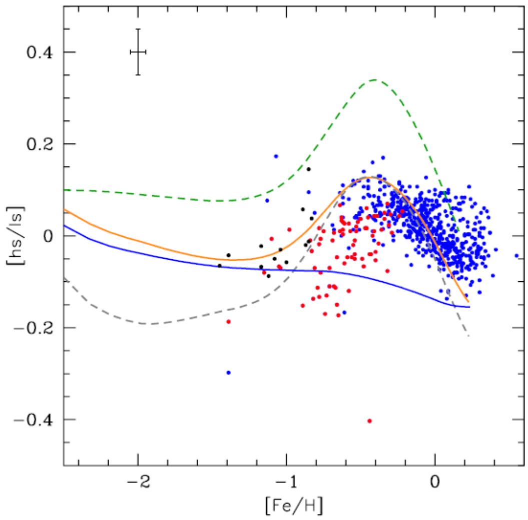

Figure 3.39: *Observed heavy-s (Ba, Ce, Nd) to light-s (Sr, Y, Zr) ratio [hs/ls] vs [Fe/H] compared with Prantzos et al. (2018) GCE model predictions. Observational data are from Delgado Mena et al. (2017) for thin (blue dots) and thick (red dots) disk stars. Black dots are the thick disk stars in Fishlock et al. (2017). Solid orange curve shows the prediction from Prantzos et al. (2018) baseline model, green dashed curve the one for the non-rotating massive stars, and gray dashed curve the non-rotating case where the r-component is not considered. The blue solid curve shows the prediction when the contribution from Low and Intermediate Mass Stars is omitted. From Prantzos et al. (2018).*

3.8. Barium ($_{56}$Ba)

Barium is an element that belongs to the second peak of stability in main s-process, the prototype of the heavy s-process element (see Sect. 1.3 in Chapt. 1).

^{138}Ba isotope shows increased stability due to its magic number of neutrons, 82 and accounts for the 71.7% of Ba nuclei of the solar system (Travaglio et al. 1999, see Fig. 3.40), of which ca 84-85% come from the s-process mechanism, see Fig. 3.1 by Simmerer et al. (2004) or 3.45 by Travaglio et al. (1999). Due to the increased stability makes some second peak isotopes as ^{138}Ba, ^{139}La or ^{140}Ce, become bottle necks in the main slow (s) neutron capture mechanism.

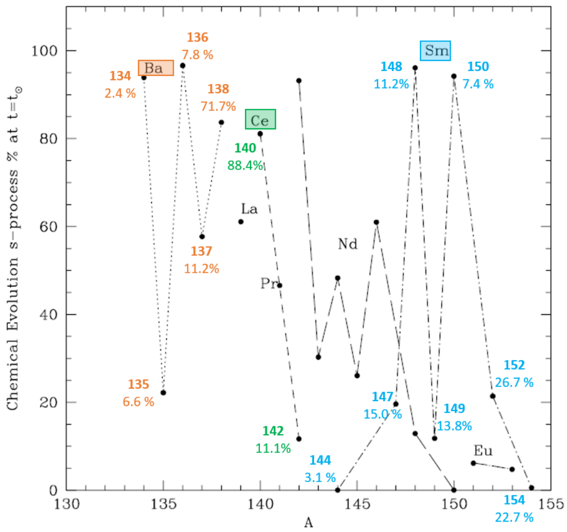

Figure 3.40: *Ba to Eu isotope s-fractions at t=t$_\odot$ according to Travaglio et al. (1999) standard model. For some isotopes are included the isotopic contribution to its element in the solar system. Adapted from Travaglio et al. (1999).*

This process is developed in AGB/LIMS stars (Karakas & Lattanzio 2014) where the required free neutrons are supplied mainly by the reaction $^{13}C(\alpha;\, n)^{16}O$ and to a lesser extent by the reaction $^{22}Ne(\alpha;\, n)^{25}Mg$ (Delgado Mena et al. 2017, see Sect. 1.3). Once it is synthesized during thermal inter-pulse periods, it gets lifted up and mixed on the surface after the third dredge-up.

As was explained for the first peak elements (Sr, Y and Zr), lower mass AGB stars (1–4 M$_\odot$), produce large amounts of main s-process elements (the lighter the star, the higher the fraction of heavy / light s-elements), meaning that the enrichment of the ISM (which begun roughly 500 Myr after the formation of the first population of stars) with s-process elements gradually increases with time (Travaglio et al. 2004) and therefore younger stars will have higher abundances.

This is additionally linked with the metallicity. An excess of Fe over the neutron flux limits the final point of the main s-process production to the lighter elements, the first peak of stability (see Fig. 1.15 and 1.18 in Chapt. 1). The linear reaction is unable to push beyond, to the second or third peaks, due to the scarceness of neutrons. They are eagerly captured by the excess of Fe to form heavier isotopes of Fe or light Fe-peak elements (e.g. see Fig. 1.17 in Sect. 1.3).

As shown in the Fig. 1.18 in Sect. 1.3 by Travaglio et al. (2004) a maximum of second peak production (Ba) is expected for a 1.5 $M_{\odot}$ star at metallicity [Fe/H] $\simeq$ -0.5 dex. This is an intermediate metallicity between the maximum production of first peak elements or the third, as Pb. The latter needs a metal poor environment (higher/excess of neutron flux ratio per Fe nuclei) for overcoming the stability of the first and second peaks, pushing ahead the neutron capture reaction to the termination point (strong s-process), the third peak.

In addition, primitive massive stars provide a promising site for the early production of the neutron-capture elements by the r-process throughout classical neutrino-driven winds of core-collapse SNeII. Or by the weak s-process. This is because the short evolution time needed in contrast with the longer time necessary to develop the main s-process in AGB/LIMS. Although it is short with respect to other sources, the enrichment of the interstellar medium (ISM) with main s-process material only begins roughly 500 Myr after the formation of the first population of stars (Sneden et al. 2008).

Nevertheless the origin remains uncertain but at least three sources have been proposed Mishenina et al. (2013). They are listed below. The first two were already mentioned in the Subsect. 3.5 of the Sr element and related to its scatter of abundances in the halo/EMP stars (equally applicable for Y and Zr):

r-process Sources Early Universe

- The neutrino-driven winds from the core-collapse supernovae, SNeII (Woosley et al. 1994).
- Polar jets from rotating Magnetohydrodynamics (MHD) core-collapse supernovae (Nishimura et al. 2006; Winteler et al. 2012).
- The enriched neutron-rich matter from merging neutron stars (Freiburghaus et al. 1999) and/or neutron-star/black hole mergers (Surman et al. 2008). They are called Compact Binary Merger events, CBM (see Sect. 1.5).

More complete details about these sources are found in Sect. 3.9 about an r-element, europium (Eu). They will have their impact in the abundance trend and GCE models, which will be discussed below.

3.8.1 Chemical galactic abundances

Barium is one of the most abundant and best observable chemical elements produced in neutron capture reactions. Ba II is the dominant ionization stage in the F-G stars atmospheres and lines at 4554, 4934, 5853, 6141 and 6496 Å, can be easily detected, even in extremely metal-poor stars for some of them (e.g. 4554 or 6141 Å ones) (Mashonkina et al. 1999).

As numerous are the Ba chemical abundance studies in dwarf stars. The Fig. 3.41 shows some of them in relation to the thin and thick disk populations, included within the Trevisan & Barbuy (2014) study.

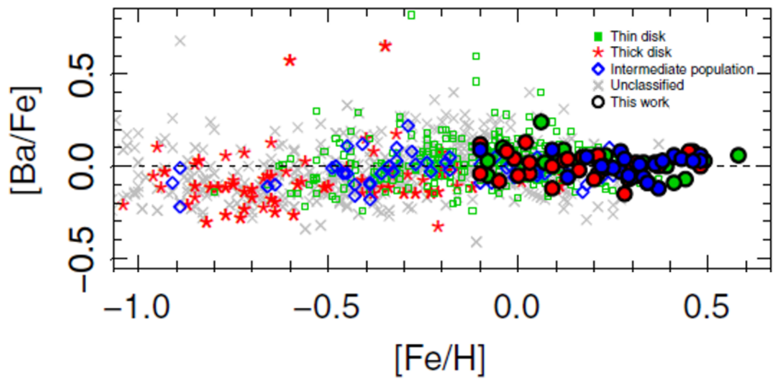

Figure 3.41: *Abundance of Ba vs. metallicity. The abundances derived in this work (circles) are compared with the thin- (green squares) and thick-disk (red stars) stars and the intermediate population (blue diamonds) from Edvardsson et al. (1993), Reddy et al. (2003, 2006), Bensby et al. (2005), Nissen & Schuster (2011), Mishenina et al. (2013) and Ishigaki et al. (2013). Grey crosses represent stars with no available U, V, and W velocities, therefore no membership assignment was possible. The symbols representing the Trevisan & Barbuy (2014) sample stars are filled according to their membership classification: thin disk (green), thick disk (red) and intermediate population (blue). From Trevisan & Barbuy (2014).*

In the Fig. 3.42, the sample of 1111 FGK dwarf stars from the HARPS GTO survey by Delgado Mena et al. (2017). The included Bisterzo et al. (2017) GCE models fit quite well to the thin disk population abundances. However, the same delay in the maximum abundances as in Sr, Y and Zr is observed. The maximum abundance is reached at solar metallicity, but in the models at [Fe/H] ≃ -0.35 dex, closer to the theoretical maximum of the dominant main s-process second peak production in AGB/LIMS (see repeatedly referred Fig. 1.18). As happens for light-s elements in the Delgado Mena et al. (2017) survey, all of the thick disk models fail to reproduce the observational data.

These models are built considering the contributions of r-process (only significant in

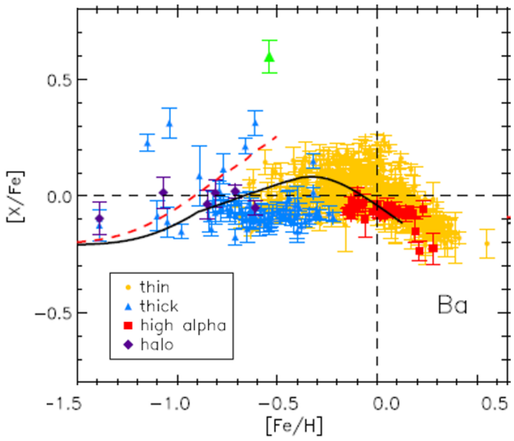

Figure 3.42: *[Ba/Fe] ratio as a function of metallicity for stars with T_{eff} > 5300 K and S/N > 100. The green bigger triangle is the s-enriched star HD 11397. GCE models are included from Bisterzo et al. (2017) for the thin disc (black lines) and the thick disc (red dashed lines). From Delgado Mena et al. (2017).*

metal poorer stars), s-process, and LEPP. For further details about LEPP, see light-s elements as Sr, Y, Zr but summarising, this nucleosynthesis site is not fully accepted or needed in some other GCE models for explaining chemical trends as it would be comment later (e.g. in reference to Prantzos et al. 2018 GCE models).

There is to notice a discrepancy about the thin disk trends observed at solar and supersolar metallicities depending on the studies. E.g. the Delgado Mena et al. (2017) data from the HARPS GTO sample (1111 FGK dwarfs) shows a clear fall of Ba abundances for thin disc stars from a maximum [Ba/Fe] ≃ 0.25 dex at solar metallicity to [Ba/Fe] < –0.2 dex at super-solar metallicities, similar to the values reported by Israelian et al. (2014) and Bensby et al. (2014). However this trend is not so clear, almost flat, in previous studies (e.g. Trevisan & Barbuy (2014)).

Like in the case of light s elements, the Ba scatter greatly increases towards halo extremely metal poor stars. It is observed in the Fig. 3.43 by Trevisan & Barbuy (2014) and 3.44 by Prantzos et al. (2018). As above commented, GCE models as for example from Bisterzo et al. (2017) used in the Delgado Mena et al. (2017) study, include the LEPP contribution, whose nature is not well understood. Likewise it was pointed that this nucleosynthesis site providing extra light-s elements is not fully accepted and trends can be addressed by known nucleosynthesis sites as it is the case of the GCE models used by Prantzos et al. (2018) in Fig. 3.44.

Indeed, the Prantzos et al. (2018) models account for different prescriptions relative to yield sources as LIMS/AGB (main s process), massive stars (early r process) and enhancement of yields in massive fast rotators (spin-stars), these last two yield sources making stronger incidence at the metal poor range. It is observed how the inclusion of r-process contribution at early stages of the universe due to their short time evolution with respect to the AGB production, and the Ba yield enhancement in fast rotators, greatly improve the fit of the abundance data at metal poor metallicity. And additionally fits reasonable well solar and supersolar thin disk population, reproducing the falling trend found by Delgado Mena et al. (2017) and other authors (Bensby et al. 2014 and Battistini & Bensby 2016), without the need of the LEPP contribution (and reproducing similar GCE Bisterzo et al. 2017 model prediction that includes it).

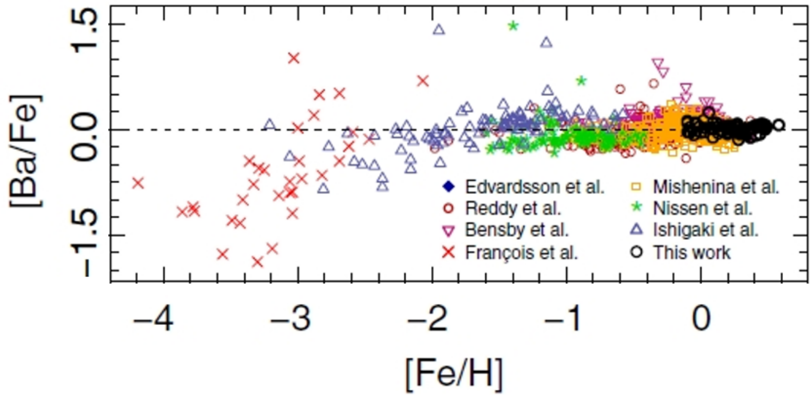

Figure 3.43: *Abundance Ba vs. metallicity. The sample obtained by Trevisan & Barbuy (2014) are indicated by black open circles. Halo stars studied by François et al. (2007) and Ishigaki et al. (2013) are represented by red crosses and blue triangles, respectively. The disk stars are shown as blue diamonds (Edvardsson et al. 1993), red open circles (Reddy et al. 2003), magenta triangles (Bensby et al. 2005), green stars (Nissen & Schuster 2011) and yellow squares (Mishenina et al. 2013). From Trevisan & Barbuy (2014).*

In this direction, the role of the spinstars/fast rotators were studied by Cescutti et al. (2013) and Cescutti & Chiappini (2014), constraining in addition the early s- and r-process contribution. The observed scatter in the halo metal-poor stars is explained by Cescutti & Chiappini (2014) (as a general reference to s-process elements though not including Zr in their study) assuming different scenarios, developing an inhomogeneous GCE model for the galactic halo as a result of combining contributions from weak s-process production in fast rotators (spinstars) and both r-process elements coming from massive stars by electron-capture Supernovae and by Magnetorotationally (MHD) driven Supernovae (Nishimura et al. 2006; Winteler et al. 2012), a rare progenitor configuration characterized by a high rotation rate and a strong magnetic field necessary for the formation of bipolar jets (see Fig. 1.34), already proposed by Mishenina et al. (2013) (see the beginning of the Ba section) as an additional nucleosynthesis site with an important contribution at early stages of the universe.

However, both r-process contributions are not clearly distinguishable in observational data. Both are able to reproduce the fraction of r-process-rich stars fairly well in the early galaxy abundance. Independently of the r-process scenarios adopted, the weak s-process

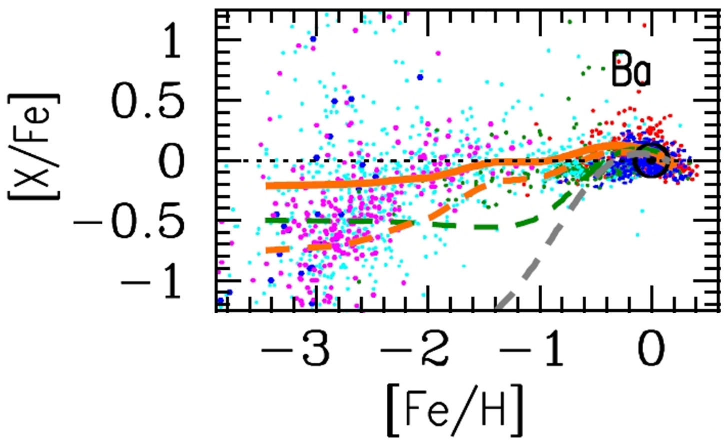

Figure 3.44: *Evolution of abundance ratio [Ba/Fe] as a function of [Fe/H] and comparison to observational data. Prantzos et al. (2018) model including AGB/LIMS, rotating massive and r-process stellar yields is in solid orange curve; the same model but with non-rotating massive star yields is in dashed green curve; model including AGB/LIMS, rotating massive but without r-process stellar yields in orange dashed curve and finally model including AGB/LIMS but without rotating massive nor r-process yields in gray dashed curve. Observational data from Bensby et al. (2014), Roederer et al. (2014a) and Mishenina et al. (2013) based on LTE assumptions. From Prantzos et al. (2018).*

contribution from massive spin-stars is needed to reproduce the spread of s-process light elements (in the case of this article referring to Sr and Y) over the heavy neutron capture element, Ba (Cescutti & Chiappini 2014).

Nevertheless, Prantzos et al. (2018) argues that the inhomogeneous GCE model by Cescutti & Chiappini (2014) is not sufficient to fully explain the halo abundances scatter. They points to the need of an in-depth study taking into account additional factors as merging of sub-halos (each one with its own history and timescale for chemical enrichment) as a forming mechanism of the early Galaxy or the imperfect gas mixing.

The Prantzos et al. (2018) GCE model including rotating massive stars yields are found to have a dramatic impact in the predicted evolution of the Ba at low metallicity (see Fig. 3.44, solid orange model) but doesn't fully explain the abundance scatter in the halo, as commented by the same authors as above.

3.8.2 [Ba/Eu] ratio: s-process vs r-process nucleosynthesis evolution

Ba, as the second peak s-process prototype, has been extensively used by comparing it to an r-process prototype element as europium (Eu), for assessing the impact of s- and r-processes in the galaxy chemical evolution. As shown in Fig. 3.40 and 3.45, Eu isotopes *s*-PROCESS FRACTIONAL CONTRIBUTIONS FOR ISOTOPES FROM Ba TO Eu AT $t = t_\odot$ WITH RESPECT TO SOLAR SYSTEM ABUNDANCES

Element	Abundance (%)	Element	Abundance (%)	Element	Abundance (%)
^{134}Ba......	94	^{141}Pr	47	^{147}Sm......	20
^{135}Ba......	22	^{142}Nd......	93	^{148}Sm......	96
^{136}Ba......	97	^{143}Nd......	30	^{149}Sm......	12
^{137}Ba......	58	^{144}Nd......	48	^{150}Sm......	94
^{138}Ba......	84	^{145}Nd......	26	^{152}Sm......	21
^{139}La......	61	^{146}Nd......	61	^{154}Sm......	0.5
^{140}Ce......	81	^{148}Nd......	13	^{151}Eu	6
^{142}Ce......	12	^{150}Nd......	0.02	^{153}Eu	5

Figure 3.45: *Ba to Eu isotope s-fractions at t=$t_\odot$ according to Travaglio et al. (1999) standard model. From Travaglio et al. (1999).*

are a net r-process element and only a minor fraction is contributed by the s-process.

The Fig. 3.46, though metallicity range is centered to to the thin disk stars (even at solar and supersolar values) and the metal poor thick disk stars sample is limited, is already hinting a trend that would be confirmed by extended surveys to metal poor stars: At very low metallicities the r-process is expected to dominate the production of heavy elements since massive stars were the first to explode as core-collapse SNeII and enrich the ISM with their material before the AGB stars (s-process, as already above commented needed at least roughly 500 Myr) contributed to the main s-process (Delgado Mena et al. 2017). Already, early studies on very metal-poor stars reported the enrichment of Eu when compared to other n-capture elements (Spite & Spite 1978).

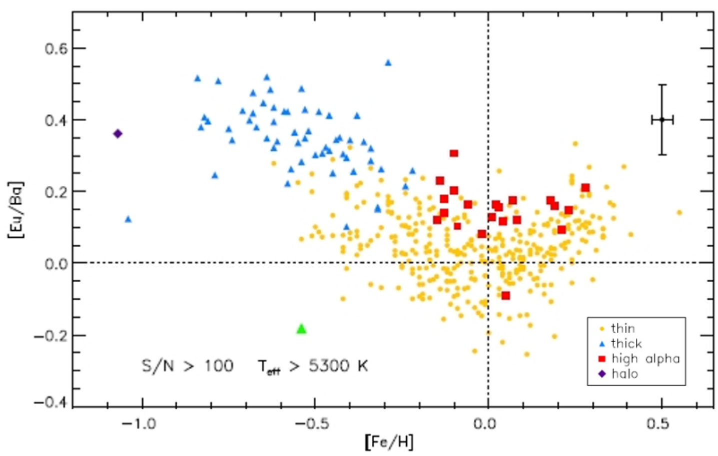

Figure 3.46: *Abundance ratios between the r-process element Eu and the heavy-s element Ba, as a function of [Fe/H] for stars with T_{eff} > 5300K and S/N > 100. From Delgado Mena et al. (2017).*

From this point of view, another interesting ratio provided by Delgado Mena et al. (2017) is the [Ba/O] (see Fig. 3.47). Travaglio et al. (1999) showed that the best progenitors for reproducing the r-process contribution to the enrichment of the Galaxy are SNe II from stars with masses 8–10 $M_{\odot}$. The more massive SNeII progenitors > 15 $M_{\odot}$, enriched the ISM with oxygen at earlier times since those massive stars evolve faster. As a consequence the ratio [Eu/O] in metal poor stars is negative with a moderate slope (see Fig. 3.48, indicating certain coupling (SNeII source although with different yields). However, the slope of the [Ba/O] ratio is striking (see Fig. 3.47), pointing once more to the domination of massive stars core-collapse supernovae over AGB production at early stages of the universe as the main source of enrichment to the ISM, because of the longer time delay.

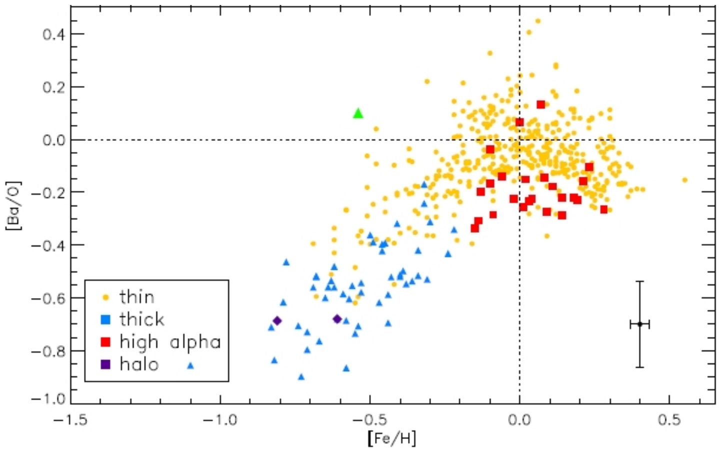

Figure 3.47: *Abundance ratios between the α element O and the n-capture element Ba, as a function of [Fe/H] for stars with T_{eff} > 5300K and S/N > 100. From Delgado Mena et al. (2017).*

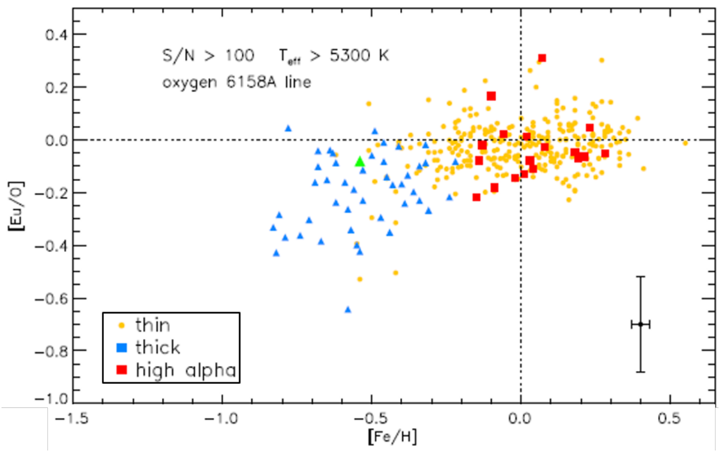

Figure 3.48: *Abundance ratios between the α element O and the rapid n-capture element Eu, as a function of [Fe/H] for stars with T_{eff} > 5300K and S/N > 100. From Delgado Mena et al. (2017).*

Another interesting observation in the Fig. 3.46 is the raise in the ratio from solar to supersolar metallicity. This change of trend matches with the observed decrease of Ba abundance in this range (see Fig. 3.42) as consequence of the continuous decrease of these heavy-s elements when metallicity increases. The sweet spot of the second peak s-process elements production as Ba (see repeatedly referred Fig. 1.18 by Travaglio et al. 2004) is already overcome (though delayed in observational data, as above commented, with respect to the GCE models) favouring the production of light (first peak) s-process elements. The reason as also above commented is the lower ratio of neutrons per Fe at higher metallicities which monopolize the neutron capture, preventing the necessary excess of neutron flux for overcoming the first peak of increased stability and avoiding to push ahead the neutron capture reactions to the second peak elements as Ba.

The Fig. 3.49 provides a larger sample of metal poor stars but is not so complete at supersolar metallicity. Nevertheless, it supports the same trends above highlighted in the Delgado Mena et al. (2017) survey: the r-process dominant role at early stages of the universe, to metal poor stars and the uptick, though only hinted due to the smaller sample in this range, of the ratio at supersolar metallicity by the decreasing of the second peak s-process yields (Ba). Likewise, there is to count with the decrease of second peak s-process yields when the metallicity gets poorer. The main s-process is favouring the production of heavier elements than the Ba, the ones from the third peak of stability as Pb. This is due to the increasing neutron per Fe nuclei ratio. This excess of neutrons is available for overcoming the first and second high stability peaks pushing ahead the neutron capture reaction to the terminal point (Pb) towards metal poorer metallicities (see once more Fig. 1.18 by Travaglio et al. (2004)).

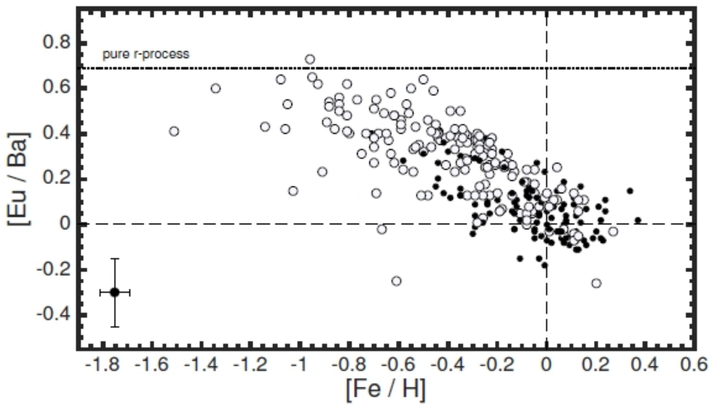

Figure 3.49: *[Eu/Ba] as a function of [Fe/H]. The full sample is divided into thin and thick disks according to the Battistini & Bensby (2016) age-selection criterion. The dotted line represents a pure r-process ratio derived from Bisterzo et al. (2014). From Battistini & Bensby (2016).*

3.9. Europium ($_{63}$Eu)

Europium is an r-process element prototype. Both stable nuclei ^{151}Eu and ^{153}Eu, are almost entirely produced by the r-process in the solar system. The rapid neutron capture points to the needed intense flux of neutrons that overwhelms the β-decay time allowing the creation of elements outside the valley of β stability (see Fig. 1.32 in Chapt. 1) where the slow s-process ocurr with a much lower neutron flux. And in which the β-disintegration is needed to create new higher atomic number elements (see Fig. 1.17).

Nevertheless, the origin of heavy r-process elements remains uncertain (Mishenina et al. 2013) and the dominant production site of the r-process elements has not yet been unambiguously identified (Matteucci et al. 2014; Thielemann et al. 2010).

But at least three sources have been proposed as was previously mentioned about the impact of early r-process production in first (Sr, Y, Zr) and second peak (Ba) s-process elements. They are going to be once more introduced but in a more extended way, namely:

r-process Early Universe: Neutrino-Driven Winds

The classic scenario for r-process production, the neutrino-driven winds from the core-collapse supernovae, SNeII (>10 M$_{\odot}$) (Woosley et al. 1994).
Extremely energetic neutrinos are produced during the collapse of the SNII, and they are potentially able to interact with the dense material that is falling onto the core of the star (see Fig. 1.31 in Chapt. 1). This interaction can heat the material, giving to it the additional energy needed to recreate the energy output observed of $\simeq 10^{51}$ erg (Battistini & Bensby 2016).
Neutrino-driven winds from proto-NS (neutron stars) following the delayed explosions of very massive stars (> 20 M$_{\odot}$, Hypernovae) have been suggested as a promising site to form the solar r-process abundances (Matteucci et al. 2014).
However, recent hydrodynamical simulations have shown that the neutrino winds are proton rich (Arcones et al. 2007; Fischer et al. 2010; Hüdepohl et al. 2010) but never very neutron rich, only slightly enriched as best (Martínez Pinedo et al. 2012; Roberts et al. 2012), unlike the pioneer simulations by Woosley et al. (1994) and Takahashi et al. (1994).
These studies cast serious doubts on the validity of the neutrino wind scenario and it seems now established that neutrino-driven winds from proto-NS cannot be the main origin of the r-process elements beyond $A \simeq 110$. Prompt explosions of massive stars in the 8–10 M$_{\odot}$ range may lead to an ejected amount of r-process matter consistent with the observed Galactic abundances but it is not clear whether these prompt explosions do occur and the right yields (Matteucci et al. 2014).

r-process Early Universe: MHD SNeII

Polar jets from rotating Magnetohydrodynamics (MHD) core-collapse supernovae (Nishimura et al. 2006; Winteler et al. 2012). This is a recently proposed strong r-process site that would greatly impact the metal poor abundance trends and nucleosynthesis at early stages of the galaxy as commented in the first and second s-process peak elements sections.
An important step in the study of neutron-capture elements was the discovery that metal-poor stars show high relative abundances of certain neutron-capture elements compared to Fe, meaning that the r- and s-processes were already active at early times. But in special the significant number of stars with high levels of r-process elements as Eu, at very low metallicities (galactic halo stars) show up the early impact of r-process. As repeatedly commented, s-process (AGB/LIMS) need at least roughly a 500 Myr time delay, after the formation of the first population of stars (Sneden et al. 2008). However r-process linked with core-collapse of massive stars might develop very soon after the appearance of the first stars.
MHD SNeII, characterized by high rotation rates and large magnetic fields, are observed as an interesting and promising site for the strong r-process observed in the early Galaxy that deserve further investigation. The rarity of the MHD-SNeII progenitors, might provide a natural explanation for the observed scatter in the abundances of r-process elements (and indirectly for the s-process ones) in extremely metal poor stars at a very early stage of the universe.

r-process Early Universe: CBM Mergers

The enriched neutron-rich matter from merging neutron stars (Freiburghaus et al. 1999) and/or neutron-star/black hole mergers (Surman et al. 2008).
The resulting abundance patterns from a double NS and a NS black hole merger are practically indistinguishable and are uniquely referred to as compact binary mergers (CBM). More than 10^{-2} $M_{\odot}$ of r-process matter may be ejected in a single coalescence event, orders of magnitude higher than the average r-process ejecta required from SNeII, though the rate of CBM events should be significantly lower (though still unknown, gravitational waves interferometry technique will help to) than the core-collapse ones in the galaxy, so it remains unclear which site is dominant in the r-process production. CBM might be another natural explanation for the scatter of r-process element abundances at low metallicity, given their rarity and high r-process element production (Matteucci et al. 2014).

The abundance studies of Eu, as a r-process prototype, therefore are key for constraining r-processes and understand the galaxy chemical evolution. And they are abundant.

3.9.1 Chemical galactic abundances

The Fig. 3.50 by Delgado Mena et al. (2017), a recent sample of FGK dwarf stars from the HARPS GTO program, shows and α-like behaviour at poor-moderate metallicities ([Fe/H] > -1.0 dex). In some way, it is understandable due to one common nucleosynthesis site, as SNeII though their nucleosynthesis occur at different stages of the core-collapse massive star.

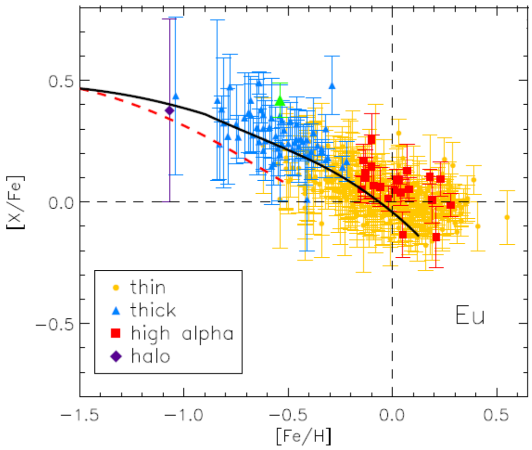

Figure 3.50: *[Eu/Fe] ratio as a function of metallitiçy for stars with T_{eff} > 5300 K and S/N > 100. The green bigger triangle is the s-enriched star HD 11397. GCE models are included from Bisterzo et al. (2017) for the thin disc (black lines) and the thick disc (red dashed lines). From Delgado Mena et al. (2017).*

The abundance data from this study is coincident with historical surveys that show similar trends as observed in Fig. 3.51 used by the Trevisan & Barbuy (2014) paper.

The Bisterzo et al. (2017) GCE model used in the Fig. 3.50 and based on a synthetic primary process in massive stars exploding as SNe II, strikingly matches the thin disk abundance, however underestimates the abundances of the thick disc population. This is the reason for the inclusion of an additional nucleosynthesis source by Prantzos et al. (2018) in their GCE models, especially relevant for the metal poor stars: spin-stars/ fast rotators yields.

When the range is extended to metal poor stars, as in Fig. 3.52 and 3.53, similar scatter can be observed as for s-process elements like Sr, Y, Zr or Ba.

As above commented, rare MHD-SNeII or compact binary mergers (CBM), exceptional events that provide high production yields, might be natural explanations for the scatter of r-process element abundances at low metallicity.

Some used inhomogeneous GCE models, as the Cescutti & Chiappini (2014) model, that try to explain scatter (see Fig. 3.54), are not sufficient. As suggested by Prantzos et al.

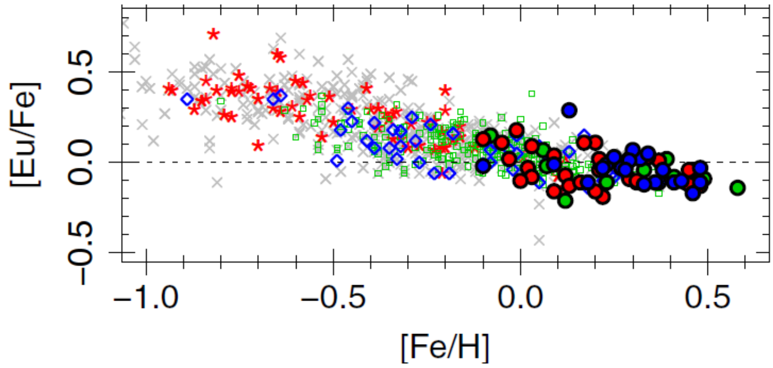

Figure 3.51: *Abundance of Eu vs. metallicity. The abundances derived in this work (circles) are compared with the thin- (green squares) and thick-disk (red stars) stars and the intermediate population (blue diamonds) from Edvardsson et al. (1993), Reddy et al. (2003, 2006), Bensby et al. (2005), Nissen & Schuster (2011), Mishenina et al. (2013) and Ishigaki et al. (2013). Grey crosses represent stars with no available U, V, and W velocities, therefore no membership assignment was possible. The symbols representing the Trevisan & Barbuy (2014) sample stars are filled according to their membership classification: thin disk (green), thick disk (red) and intermediate population (blue). From Trevisan & Barbuy (2014).*

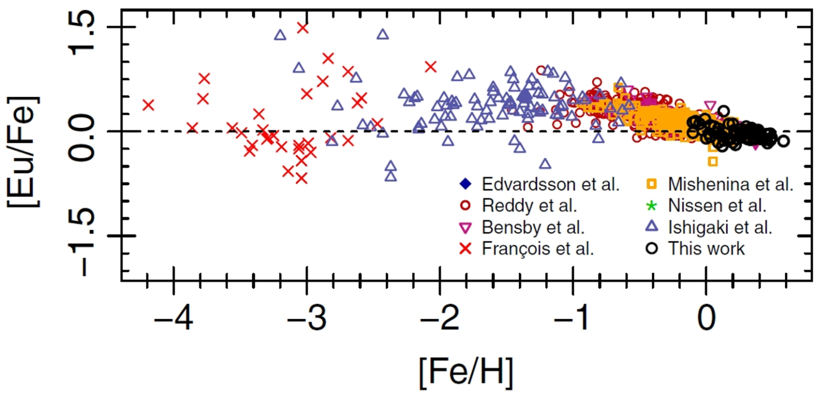

Figure 3.52: *Abundance Eu vs. metallicity. The sample obtained by Trevisan & Barbuy (2014) are indicated by black open circles. Halo stars studied by François et al. (2007) and Ishigaki et al. (2013) are represented by red crosses and blue triangles, respectively. The disk stars are shown as blue diamonds (Edvardsson et al. 1993), red open circles (Reddy et al. 2003), magenta triangles (Bensby et al. 2005), green stars (Nissen & Schuster 2011) and yellow squares (Mishenina et al. 2013). From Trevisan & Barbuy (2014).*

(2018), it is needed in-depth study taking into account additional factors. As merging of sub-halos (each one with its own history and timescale for chemical enrichment) as a forming mechanism of the early Galaxy or the imperfect gas mixing.

The Prantzos et al. (2018) GCE model, as above commented, offers an additional nucleosynthesis factor, the impact of massive spin-stars/fast rotators more frequent at early

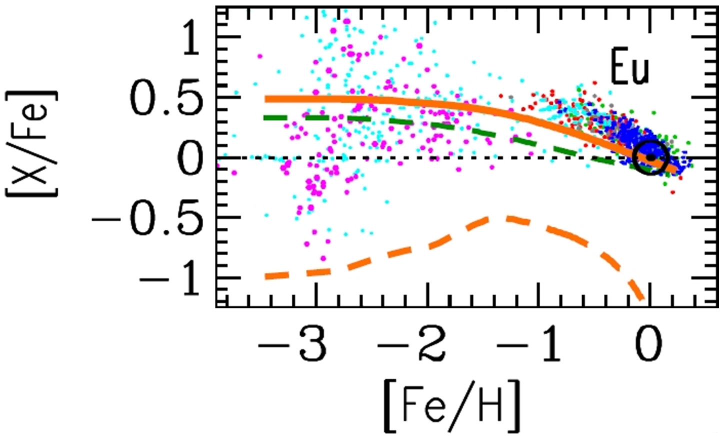

Figure 3.53: *Evolution of abundance ratio [Eu/Fe] as a function of [Fe/H] and comparison to observational data. Prantzos et al. (2018) model including AGB/LIMS, rotating massive and r-process stellar yields is in solid orange curve; the same model but with non-rotating massive star yields is in dashed green curve; model including AGB/LIMS, rotating massive but without r-process stellar yields in orange dashed curve and finally model including AGB/LIMS but without rotating massive nor r-process yields in gray dashed curve. Observational data from Roederer et al. (2014a), Battistini & Bensby (2016) and Mishenina et al. (2013) based on LTE assumptions. From Prantzos et al. (2018).*

stages of the universe. As it was noted in the Bisterzo et al. (2017) GCE model used by Delgado Mena et al. (2017, see Fig. 3.50) and mainly based on SNeII yields, the fit was acceptable for thin disk stars. However, at moderate metal poor range (thick disk stars) the model looks like underestimating the real abundances. This underestimation is also present in the Prantzos et al. (2018) GCE models as observed in Fig. 3.53. This model takes into account LIMS/AGB and r-process yields (as the green dashed prediction) but without the enhancement in yields provided by rotating massive stars (orange fit). Although there is striking improvement in the fit to the observational data at extremely metal poor ranges, it does not explain the great scatter.

Chemical evolution studies should offer a way to discriminate among different sites for the r-process element production, through the comparison of model predictions with the observations. Unfortunately, the different studies have reached different conclusions (Matteucci et al. 2014).

The complexity of likely introduced nucleosynthesis sources (SNeII, MHD-SNeII, CBM, spin-rotators enhancements) and galaxy particular evolutionary factors, as sub-halos merger episodes or imperfect gas mixing, altogether might be behind the observed scatter.

And as an additional factor that might contribute to the scatter in the metal poor range, the weakness of the Eu lines, Eu II 4205, 6437, 6645 and the typical 4129 Å used in the different studies.

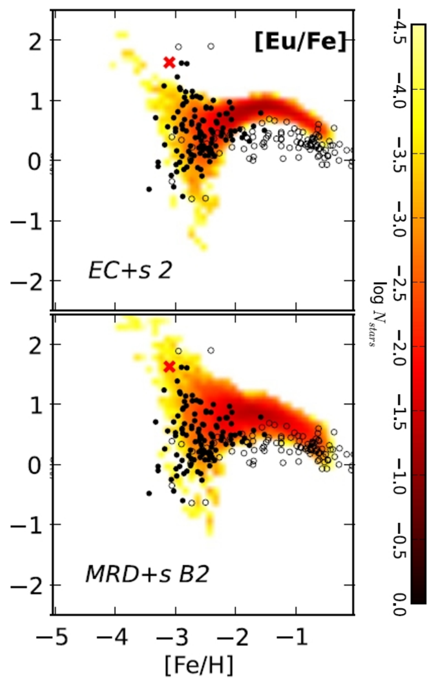

Figure 3.54: *Stellar distribution [Eu/Fe] vs. [Fe/H] in the halo; the density plot is the distribution of simulated long-living stars for two different nucleosynthesis prescriptions included in the Cescutti & Chiappini (2014) models, see side bar for the color scale; superimposed, they are shown the abundances for halo stars (data from Frebel (2010); Aoki et al. (2013)). The symbols for the Frebel (2010) data are black dots for normal stars, a red x marker for a carbon enhanced metal poor CEM-r star, and black open circle for stars without carbon measurement; for the Aoki et al. (2013) data are adopted the same symbols, but instead of dots are used squares. Adapted from Cescutti & Chiappini (2014).*

3.9.2 [Ba/Eu] ratio: s-process vs r-process nucleosynthesis evolution

As was shown in Sect. 3.8.2 (Ba element section), Eu as an r-process element prototype is extensively used jointly with Ba as the second peak s-process prototype, for assessing the impact of s-processes and r-processes in the galaxy chemical evolution.

The discussion about this ratio can be entirely followed in that section. Also with respect to other interesting and related ratios as [Eu/O] and [Ba/O].

3.9.3 [Eu/Mg] ratio: α vs r-process nucleosynthesis evolution

Another interesting ratio is the [Eu/Mg] in Fig. 3.55. The r-process component of the heavy elements and the α-elements, in particular magnesium, are thought to be mainly produced in SNeII, though at different stages and sites. The tight flat correlation between Mg and Eu indicates that they are mainly produced in constant proportions in 8-10 $M_\odot$ SNe type II, less massive than the oxygen SNeII progenitors, throughout all ages. Nevertheless there is the incipient scatter observed in the metal poor range linked with the observed scatter in Eu and the in-homogeneous factors that might be impacting the r-process at early stages of the galaxy/universe (SNeII, MHD-SNeII, CBM, spin-rotators enhancements, weakness of lines...).

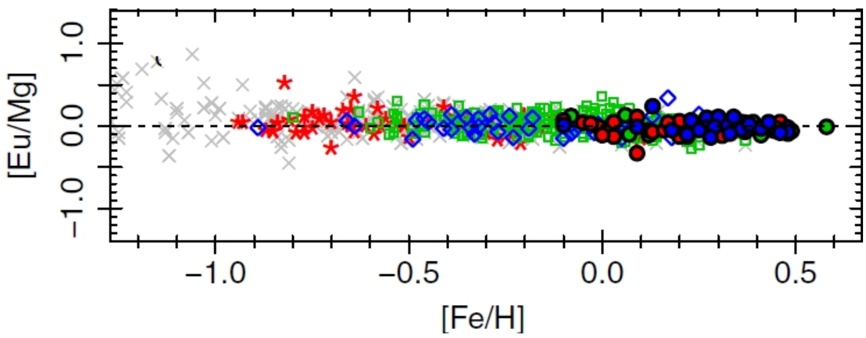

Figure 3.55: *Abundance ratio between neutron-capture (r-process) element as Eu and magnesium (α-element) as a function of metallicity.The sample obtained by Trevisan & Barbuy (2014) are indicated by black open circles. Halo stars studied by François et al. (2007) and Ishigaki et al. (2013) are represented by red crosses and blue triangles, respectively. The disk stars are shown as blue diamonds (Edvardsson et al. 1993), red open circles (Reddy et al. 2003), magenta triangles (Bensby et al. 2005), green stars (Nissen & Schuster 2011) and yellow squares (Mishenina et al. 2013). From Trevisan & Barbuy (2014).*

3.10. Lead ($_{82}$Pb)

Lead is produced by two neutron capture processes that have different timescales, i.e., in the slow s-process occurring during the thermally pulsing asymptotic giant branch (AGB) phase of intermediate-mass (2-8 $M_{\odot}$) stars and the rapid r-process (Mashonkina et al. 2012). Simmerer et al. (2004) account 79% of Solar System Pb abundance from s-process in LIMS/AGB stars and 21% from r-process (see Fig.3.1).

There are four stable isotopes: ^{204}Pb (1.4% in SS), ^{206}Pb (24.1%), ^{207}Pb (22.1%), ^{208}Pb (52.4%). The last three are radiogenic as products of decay chains from ^{238}U, ^{235}U and ^{232}Th (see Fig. 3.56) and as consequence of the r-process.

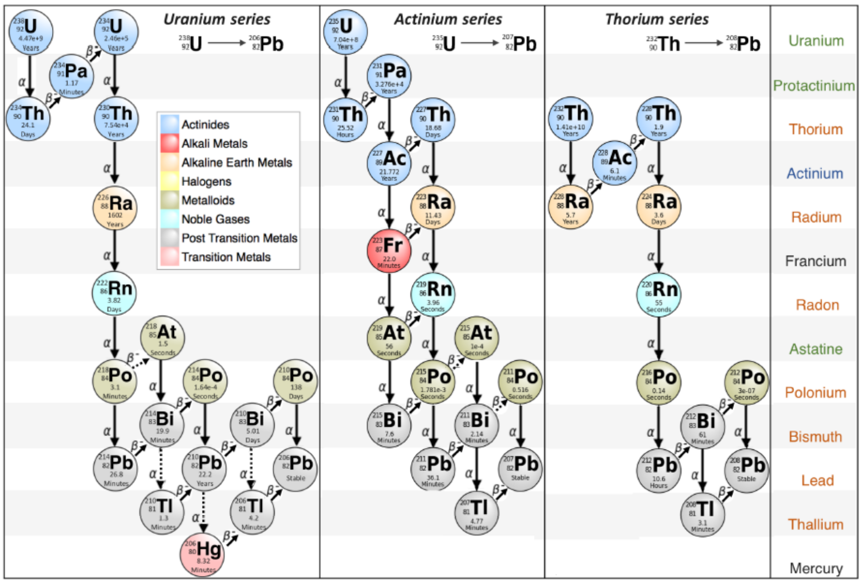

Figure 3.56: *Decay series of uranium-238, uranium-235, and thorium-232. Full names of elements shared by all three decay series are in coral, by the two uranium series in green, by 235U and 232Th in blue, and unique to 238U or 235U in black. From Tan (2016) as a modified image from wikipedia.*

As in the Sect. 1.3 commented, the Pb is the termination point of the main s-process neutron capture reaction (see Fig. 3.57).

Likewise commented, theoretical studies of the s-process have shown that in low-metallicity environment, heavy s-nuclei similar to those of Pb are more efficiently produced than lighter nuclei owing to both the larger ratio of free neutrons to Fe-peak seeds and an extended period of s-process nucleosynthesis (Gallino et al. 1998; Travaglio et al. 2001a).

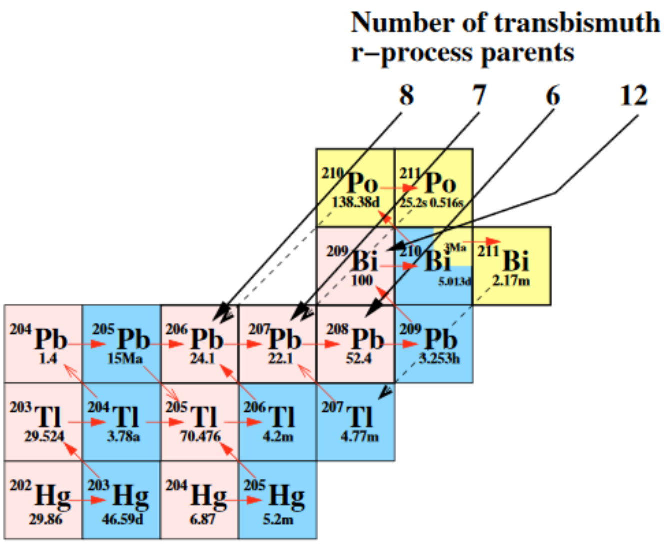

Figure 3.57: *Nucleosynthesis path of the s-process in the Pb-Bi region. The number of short lived transbismuth isotopes contributing to the r-process nucleosynthesis of these elements (see the latter Fig.3.56) is shown with solid black arrows. When stable (pink), is indicated the % of the isotope with respect the total element abundance in Solar System, when do not, the half-life time of decay. Red arrows are indicating the typical neutron capture and β^- decay of the main s-process. From Domingo-Pardo et al. (2008).*

At higher metallicity, the excess of Fe monopolizes the neutron capture leading to the formation of light elements only. The reaction is not able to overcome the increased stability of the first or second peak elements (see e.g. Fig.1.16) as efficiently, due to the lack of neutrons needed to push the reaction ahead.

Theoretical productions of some prototypical main s-process peaks elements in function of metallicity, are observed in a figure that is once more showed in this section (Fig. 3.58).

Due to the time delay of the AGB production, the contribution of heavy elements as Pb (most in < 4 $M_{\odot}$ mass star) appears at [Fe/H] $\sim$ -1.5 dex. However, one has to take into account that a contribution of light first peak elements as Sr, Y and Zr might be present sooner, at -2.0 dex (Kobayashi et al. 2020a), due to a smaller contribution of the weak s-process in intermediate mass AGB stars (4-8 $M_{\odot}$). Although it is at solar metallicity when the first peak elements total abundance is higher and predominant due to the enhanced main s-process production from low mass AGBs (< 4 $M_{\odot}$), as shown by Fig. 3.58.

However, as later will be introduced, at the extremely metal poor range, the studies found that the Pb origin is likely due to a pure r-process. In fact, MHD-SNeII are very good candidates for the rapid enrichment of the universe, as they are massive core-collapse supernovae with a very short time-delay (10 Myr), meanwhile other likely sources as CBM mergers do not produce Pb, but Th and U (Kobayashi et al. 2020a).

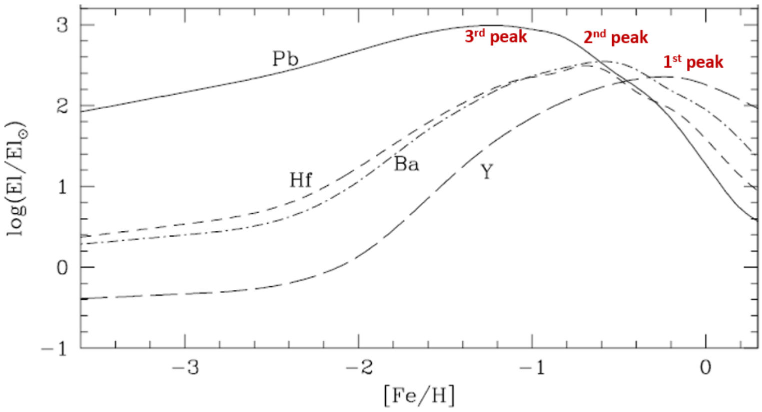

Figure 3.58: *Production of s-process elements in function of metallicity for a 1.5 $M_\odot$ AGB (Travaglio et al. 2004). To lower metallicity, the neutron capture is seeded of an excess of neutrons per Fe for displacing the production to the termination point, Pb.*

Nevertheless, there are reported some Carbon-enhanced objects in the metal poor range, which are believed to be affected by mass transfer across binary systems from asymptotic giant branch (AGB) stars, and have been providing a useful constraint on the s-process in low-metallicity AGB stars (Aoki & Honda 2008).

3.10.1 Chemical galactic abundances

The used Pb I 4057 Å line is weak and embedded in the near-UV range and might suffer strong NLTE effect corrections due to ultraviolet photo-ionization that strongly depletes abundances under LTE assumptions, especially in the metal poor range (Mashonkina et al. 2012).

The Fig. 3.59 and 3.60 belong to the freshly delivered paper by Kobayashi et al. (2020a). Their models include the smaller contribution of r-process at a very early stage of the universe due to MHD-SNeII that very soon (10 Myr after first star appearance) enriches the ISM as observed in Fig. 3.60 as the likely r-production source at the early universe.

Unfortunately, there are very few Pb abundance determinations to constraint the contribution of the other stellar sources (aside LIMS/AGB) in the production of this element at sub-solar metallicities (Prantzos et al. 2018), due to the weakness of the available line.

Roederer et al. (2010a) found that the stellar Pb/Eu abundance ratios form a plateau in the metallicity range 2.3 < [Fe/H] < 1.4, and that Pb/Eu increases towards higher metallicity (Mashonkina et al. 2012). The increase in Pb/Eu at [Fe/H] > 1.4 suggests a growing contribution to the stellar lead abundance from the s-process opening in AGB stars (see Fig. 3.61).

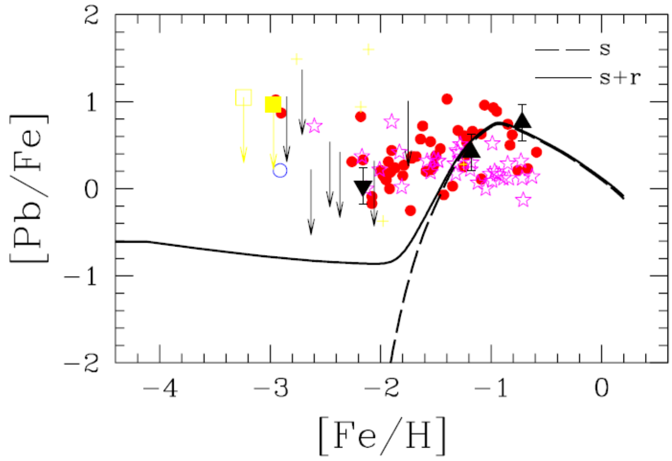

Figure 3.59: *[Pb/Fe]–[Fe/H] relation. Observational data sources are: red circles, Mashonkina et al. (2012) (NLTE); blue open circle, Barbuy et al. (2011); magenta stars, Hansen et al. (2012); yellow plus, Roederer et al. (2014a) for C-normal stars; black filled triangles, Roederer et al. (2012); black filled upside-down triangle, Ivans et al. (2006); and upper limits, Roederer et al. (2010b, 2012, 2014b); Mashonkina et al. (2014); The large yellow filled and open squares indicate the Sneden, Sneden et al. (2003a) and Honda stars, Roederer et al. (2014a), respectively. From Kobayashi et al. (2020a).*

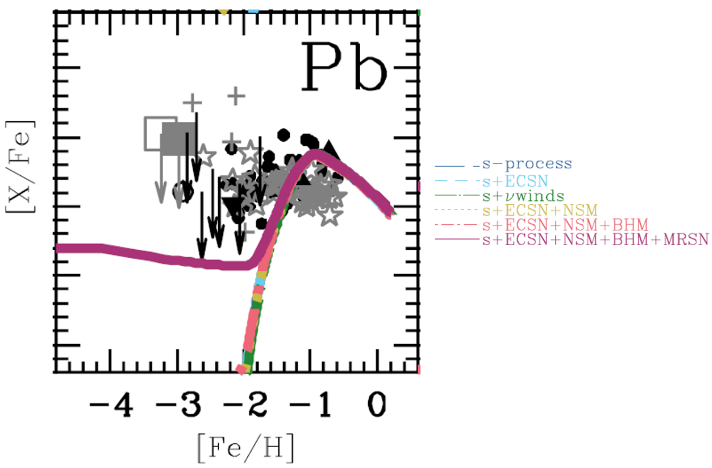

Figure 3.60: *[Pb/Fe]–[Fe/H] relation. Similar to previous figure but including the evolution for the models with s-process from AGB stars only (blue long-dashed lines); with s-process and ECSNe (Electron Capture Supernovae) (light-blue short-dashed lines); with s-process, ECSNe, and ν-driven winds (green dot-long-dashed lines); with s-process, ECSNe , and NS-NS (neutron star-neutron star) mergers (olive dotted lines); with s-process, ECSNe, and NS-NS/NS-BH (black hole) mergers (orange dot-short-dashed lines); with s-process, ECSNe, NS-NS/NS-BH mergers, and MRSNe (or named MHD-SNeII) (red solid lines). From Kobayashi et al. (2020a).*

This plateau indicates that Pb in stars of lower metallicity should be of pure r-process origin as Eu is, from fast sources which quickly enriches the early universe as is argued by Kobayashi et al. (2020a) GCE model (MHD-SNeII).

Nevertheless it is observed in the same figure a sub-sample of enhanced Pb abundances that correspond to s-process coupled to C-enhanced stars/objects.

The overwhelming majority of the 28 stars in the Roederer et al. (2010a) s- and r+s-subset have strong C-enhancements ([C/Fe]> +1.5), presumably produced together with the s-process. Many of the stars that they claim to lack s-process material ("no-s", standard stars) have sub-solar, standard [C/Fe] ratios.

The carbon enhanced and rich s-process metal-poor stars (CEMP-s) issue is developed in the C element Sect. 2.2. They are related with binary systems with mass-transfer from evolved AGB in binary systems at the early universe, enhancing the companion's C and coupled s-process element abundances.

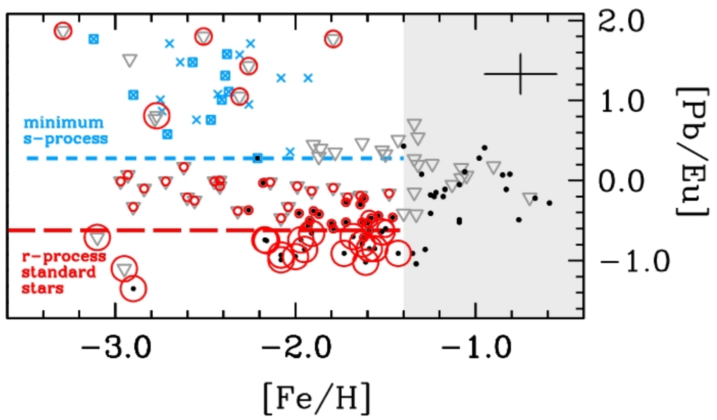

Figure 3.61: *Abundance ratio of [Pb/Eu] as a function of [Fe/H]. All measurements are indicated by small black circles, and all upper limits are indicated by downward-facing triangles. All red circles represent stars lacking any detectable trace of s-process material. The long-dashed line indicates [Pb/Eu] ≤ -0.6 (the upper extent of the range for the r-process standard stars), and the short-dashed lines indicate [Pb/Eu] ≤ +0.3, the approximate minimum ratios expected from AGB pollution. For comparison, small blue "×"s denote stars enriched ins-process material, and small open squares around these "×"s indicate that the star shows RV variations. The shaded regions indicate metallicities where the s-process predictions may not be appropriate. A representative uncertainty is shown in the top right corner of each panel. From Roederer et al. (2010a).*

Chapter 4

Summary: Deconstructing Periodic Table

Chapt. 2 and 3 have visited the elements with relevant lines in optical and near-IR spectral range (basically from 4000 to 9000 Å) from which their abundances can be derived. This is the approximate range usually covered by high resolution spectrographs coupled in optical telescopes. In a basic way, the atomic elements nucleosynthesis have been described from their contribution sources and underlying mechanisms, warning about the remaining uncertainties in origins and yields.

Nevertheless, when one observes the periodic table (Fig. 4.2) and compares with the present elements selection, it is noticed that the number of elements not included in the present selection, is high. Abundances from those elements can not be obtained from optical spectra of dwarf stars. Different observational instruments and additional spectral ranges, whose descriptions are out from the scope of this document, are employed.

However, atomic nucleosynthesis shows some common features in groups of elements. As example, it is possible to track the main keys of the α-elements nucleosynthesis knowing only one of them, to say, silicon (Si). Although every α-element shows its own peculiarities, the main features of the Si abundance profile are common with the other α-elements. All will show a characteristic chemical abundance gap between the thin and the thick disks. And a negative slope from the abundance plateau at [Fe/H]= -1.0 dex to solar values as a result of stellar and galactic evolutionary reasons as explained in Sect. 1.4. The same can be said about their main nucleosynthesis site and mechanism involved, the α-capture reaction in burning stages previous to SNeII core-collapse explosion in massive stars. F.i. as Ne or Ar, not included in this manuscript. Other elements groups in the periodic table share similar nucleosynthesis features among their components.

Especially in the case of the heavier elements of the periodic table. They are thought

Figure 4.1: *Horsehead nebula (Barnard 33), NGC2023, NGC2024 and IC434 nebulae. Takahashi TSA120 amateur telescope.*

to be mainly produced by r-process in extremely energetic and cataclysmic events as NS or NS+BH pair mergers. The gravitational wave signal GW170817 as a product of a NS pair merger, detected by LIGO/Virgo in 2017, allowed to study its electromagnetic counterpart and find evidences of r-process elements nucleosynthesis. However, there is not yet consensus on the role of this CBM in the production and evolution of r-elements. There are other nucleosythesis sources that need further studies as f.i., MHD-SNeII. Regarding the heavier elements topic, all of them share this uncertainty about their origins.

Here we will briefly summarize the most significant neucleosynthesis features of these elements...

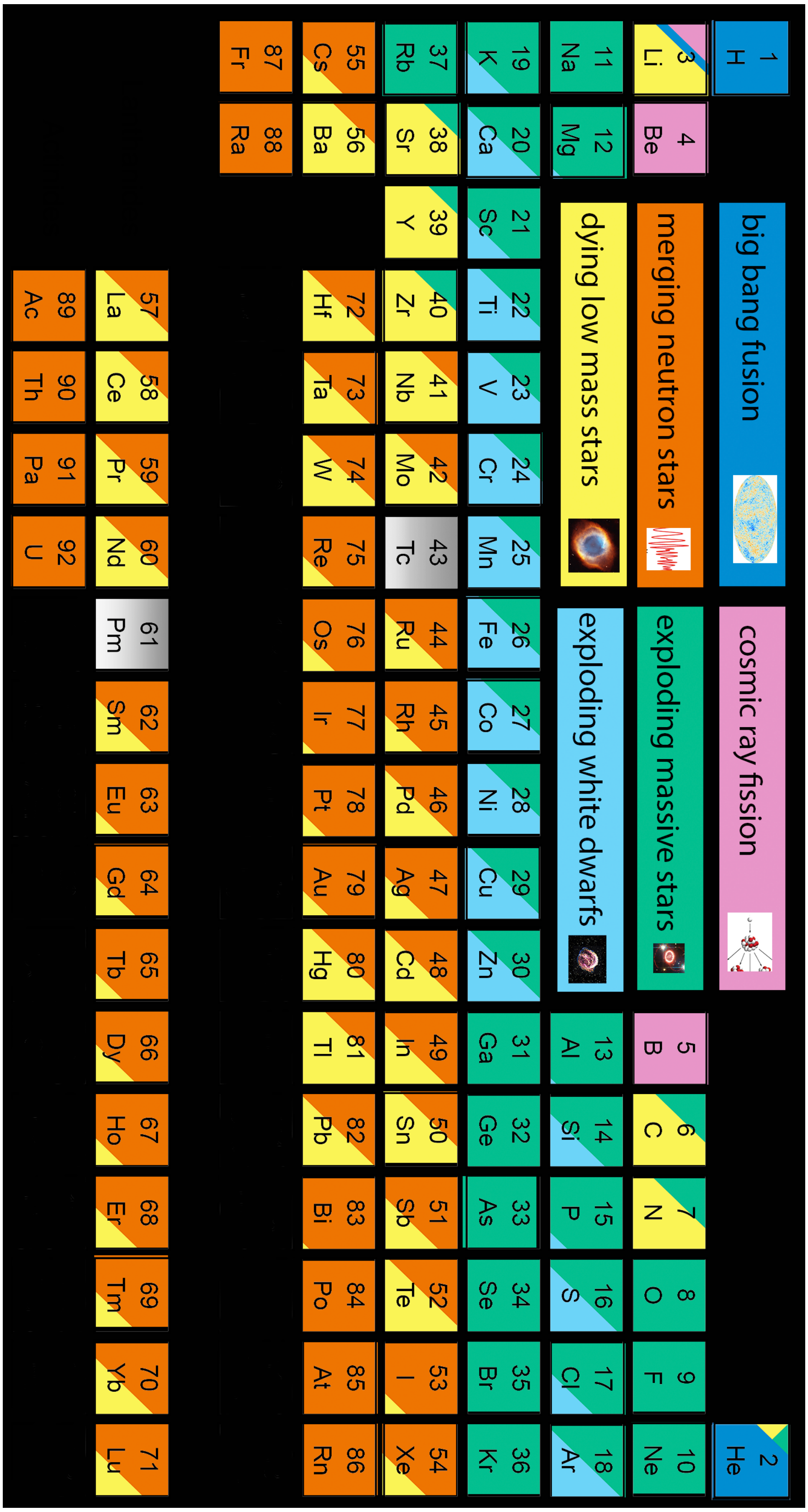

Figure 4.2: *Periodic table. Graphic created by Jennifer Johnson. Astronomical Image Credits: ESA/NASA/AASNOVA*

Hydrogen was utterly obtained from the Big Bang and the recombination, 300000-400000 years later, when the physical conditions of the antique hot universe, due to its expansion, permitted the dense plasma of particles to cool enough for the binding of electrons and protons.

As was Helium, in a ca 24:76 He:H proportion. However He, has increased its abundance in universe (to ca. 26%) at expense of the H. This is because the stellar nucleosynthesis of He in MS stars by the PP chains mechanism (predominantly in LIMS) or the CNO cycle (predominantly in massive stars, with metallic CNO seeds acting as catalysts), see Sect. 1.1. This He production is later injected into the ISM in the Post-AGB (LIMS) stages or the SNeII core-collapsed explosions (massive stars).

Likewise, trace amounts of Lithium were produced in the Big Bang nucleosynthesis (SBBN). Together with some unstable Beryllium that however was easily destroyed. Although important uncertainties remain about the different contributions, some models estimate that around a 30% of the Li is due to the SBBN and spallation of the GCR interacting on the ISM medium (CNO nuclei and particles). A 20% due to core-collapsed SNeII explosion of massive stars and a 50% from AGB production (LIMS, especially in intermediate mass stars throughout HBB) and SNeIa. But as above mentioned, the yields and some depletion mechanisms are poorly constrained and understood. As example, the recently obtained observational data from a SNIa by the Miller (2015) study suggested a production of Li from 3 to 10 times the theoretical expected in thermonuclear supernovae. Li nucleosynthesis remains as the most challenging element from the periodic table.

Apart from some traces production in the SBBN, almost all the Beryllium and Boron are produced by the spallation of the GCR interacting on the ISM medium (CNO nuclei and particles).

Carbon and Nitrogen, as in their respective sections mentioned, are still challenging elements whose nucleosynthesis are not completely understood. E.g. the C was traditionally considered an element predominantly produced in LIMS/AGB by triple-α reaction plus an important but minority contribution from massive stars, via SNeII. However, taking into account of nucleosynthesis sources as rotating massive stars, especially during the early stages of the universe, is changing the balance between LIMS/AGB or massive stars contributions. For instance, in the recently published GCE study by Kobayashi et al. (2020a), at t= 9.2 Gyr their contributions are almost balanced. In the case of the N, their production is especially activated, via the CN cycle, in intermediate mass stars in which the HBB mechanism has been triggered by their higher temperatures. Although the GCE studies are indicating a predominant production from AGB, it remains similar uncertainties about the role of fast rotating massive stars in its production and yields.

Oxygen, an α-element, however, although also produced in LIMS/AGB, is predominantly synthesized in hydrostatic He burning stages preceding the core-collapsed supernovae of massive stars (SNeII). The enrichment of the ISM in O is assumed to be produced very fast after the appearance of the first stars with respect to the r-process neutron capture elements as Eu. This is indicated by their abundance trends and ratio in the metallicity poor range at the very early universe. They indicate higher oxygen yields from more massive (> 15 $M_{\odot}$) short-live stars than the production from r-process in less massive ones (~ 8-10 $M_{\odot}$) and their time delayed core-collapsed SNeII explosions. As another striking feature, this element shows strong NLTE effects that impact its strongest available lines (O I triplet at 7770 Å). This introduces important uncertainties on their derived abundances under LTE assumptions. In-depth 3D NLTE effect studies, already available, will help future abundance and GCE studies.

In spite of the nucleosynthesis color indication in the Fig. 4.2, the Fluorine nucleosynthesis sites are diverse and the yields uncertain and not well constrained by GCE models: AGB (TP-AGB) via neutron or proton captures, neutrino spallation ν-process in core collapse SNeII, core He-burning in Wolf-Rayet stars, fast rotating massive stars at the early universe and dwarf mergers. In the recently published GCE study by Kobayashi et al. (2020a), the balance at t= 9.2 Gyr is only slightly favourable to the AGB over SNeII production, with a ratio 51:49. Although one has to take into account the likely extra production from Wolf-Rayet stars, a source not included in their study.

Neon, an α-element, therefore predominantly produced by a net reaction of α-particle capture in burning stages preceding SNeII in massive stars. In its case, during the hydrostatic C burning stage. Ne contribution from AGBs, is very small and mostly comes from mass loss. This statement could be similarly used for heavier elements than Ne, up to and including Ge (Kobayashi et al. 2020a).

An Odd-Z element, Sodium, is produced in hydrostatic C burning stages preceding core-collapse SNeII in massive stars. But it is also minority contributed from LIMS/AGB in high temperature H-burning regions via the NeNa cycle. Thermonuclear SNeIa or Classical Novae, are other nucleosynthesis suspected sources.

Magnesium, another α-element, therefore mainly produced by a net reaction of α-particle capture in burning stages preceding SNeII in massive stars. In its case, during hydrostatic C- and ensuing Ne-burning stages.

Aluminum, an Odd-Z element linked to Na, produced in C and Ne burning stages preceding core-collapse SNeII in massive stars and the NeNaMgAl cycle in LIMS/AGB, especially in intermediate mass stars in which the HBB mechanism has been triggered by their higher temperatures. But unlike Na, it shows an α-like (Mg-like) behaviour in terms of galactic chemical abundance. This fact might indicate an incomplete understanding of the nucleosynthesis sources and mechanisms related with both elements.

Silicon, an α-element, thus predominantly produced in Ne and O burning stages preceding SNeII in massive stars, but with an appreciable contribution from thermonuclear SNeIa, 22% according to the last GCE study by Kobayashi et al. (2020a).

An Odd-Z element, the only stable isotope of Phosphorous ^{31}P, is thought to be formed by neutron capture on ^{29}Si and ^{30}Si in massive stars (in the O- and Ne-burning shells) by core-collapse SNeII supernovae. A small or negligible contribution is expected from SNeIa (Cescutti et al. 2012).

As an α-element, Sulphur, is predominantly produced in O and Si burning stages preceding SNeII in massive stars. Also with an appreciable production from SNeIa, 29% according to the last GCE study by Kobayashi et al. (2020a).

The two stable isotopes ^{35}Cl and ^{37}Cl of Chlorine, an Odd-Z element, are thought to be formed during hydrostatic and explosive O burning stages in core-collapse SNeII supernovae of massive stars. ^{35}Cl is primarily produced when ^{34}S captures a proton. The isotope ^{37}Cl from radioactive β^{+} decay of ^{37}Ar (Maas et al. 2016).

As an α-element, Argon, is predominantly produced in burning stages preceding SNeII in massive stars. And similar to its close neighbours in the periodic table, Si, S and Ca α-elements partners, with an appreciable contribution from SNeIa, 34% according to the last GCE study by Kobayashi et al. (2020a).

Potassium, an Odd-Z element, almost completely synthesized in hydrostatic and explosive O burning preceding SNeII. Like O, it is an element affected by strong NLTE effects on their available lines as K I 7664 and 7699 Å . The GCE models don't fit at all the observational data but taking into account of the contribution from rotating massive stars at early stages of the universe, greatly improves them. It is expected a minority or negligible contribution from SNeIa, depending on the GCE study selected.

Calcium, another α-element, produced in Si and O burning stages preceding SNeII in massive stars. With an important production from SNeIa, 39% according to the last GCE study by Kobayashi et al. (2020a).

From this point, the elements are entering in the Fe-peak group territory. The contribution of thermonuclear supernovae SNeIa increases in this group, being the main nucleosynthesis site for elements as Cr, Mn, Fe and Ni.

Scandium, an Odd-Z Fe-peak element, however showing an α-like behaviour due to being produced in common sites to α-elements. In this case, Ne burning or explosive O and Si burning stages preceding SNeII in massive stars. Nevertheless, its nucleosynthesis looks more complex with additional contributions from neutrino spallation ν-process or jet-like SNeII explosions. Depending on the GCE study, there might also be a negligible to small contribution from SNeIa sources.

Titanium, as an α-element is predominantly produced in hydrostatic Si and explosive O burnings in SNeII of massive stars. It is an element used as a proxy for stellar ages. Other possible nucleosynthesis sources might be neutrino spallation ν-process or jet-like HNe explosions. It is expected an important contribution from SNeIa supernovae, although yields depend on the used models.

Vanadium, and Odd-Z Fe-peak element, produced in explosive Si burning in SNeII and SNeIa, but contributed by other nucleosynthesis sources in poorly constrained amounts, similar to the case of Sc: Dependent yields on the initial chemical and physical parameters of the SNeII progenitors, fast rotating massive stars and HNe jet-like explosion especially at early stages of the universe.

Chromium, an Even-Z Fe-peak element, thought to be produced in explosive Si burning of thermonuclear SNeIa by factor of ~ 2/3 with the remaining ~ 1/3 originating from SNeII.

Manganese, an Odd-Z Fe-peak element, similarly to Cr, produced in explosive incomplete Si burning outer layers of SNeII and with majority production in SNeIa. Although their NLTE effects are moderate, they are increasingly stronger at low metallicity range, greatly impacting the interpretation of the nucleosynthesis sites from the GCE model fit to the observational data, whose slope is changed by the corrections.

Iron, classically was thought to be almost solely produced by SNeIa thermonuclear supernovae, but although it remains the majority source, some GCE studies have decreased its contribution. As example, in the freshly published GCE study by Kobayashi et al. (2020a), it represents the 60% contribution of the total Fe in the universe. ^{56}Fe is the more common endpoint of fusion chains inside extremely massive stars. Also as product of radioactive β^{+} decay of ^{56}Ni to ^{56}Co, and the later decay to ^{56}Fe in SNeIa (Kuchner et al. 1994).

Beyond the Iron, nuclear fusion reactions are not energetically favoured, although still explosive burning processes are able to produce dominant abundances of elements as Co, Ni, Cu or Zn. The contribution from neutron capture processes, s-process by LIMS/AGB or r-process in SNeII/HNe massive stars or cataclysmic events as NS or NS+BH pair merger, has an increasingly dominant role from this point.

Cobalt, a Fe-peak element, is produced in both, explosive Si burning in SNeII (central complete-Si-burning regions of the supernova ejecta) and SNIa. The proportion between them vary depending on the used study. Energetic HNe might have made important contributions, especially at the early universe. As an element beyond Fe, the s-process is already modestly contributing to the general abundance, either main-s (LIMS/AGB stars) or weak-s (massive stars) but hardly attaining 9% of its prevalence in the solar system.

A similar statement can be made for Nickel, another Fe-peak element, contributed by both SNeII and SNeIa in Si explosive burning layers, with a negligible contribution of s-process (f.i. hardly 1% in the Ni of the solar system). In the Ni case the SNeIa is the majority contributor, being an element strongly coupled to the Fe abundance along all the universe evolution.

In the case of Copper, another Fe-peak element, however the contribution from s-process, especially weak-s in massive stars (25% in solar system) plus a modest main-s one in LIMS/AGB (5%), is becoming more significant. Its nucleosynthesis is complex but the remainder comes from explosive burning in SNeII/HNe and SNeIa supernovae. However SNeIa yield and its contribution to the galactic Cu abundances is not clear. Depending on the GCE study, can range from significant to negligible. The latter is the obtained conclusion in the freshly published GCE study by Kobayashi et al. (2020a). As in Co, the HNe seem greatly to contribute to the Cu abundance, especially during the early stages of the universe. Taking into account of the extra contribution from fast rotating massive stars at early stages of the universe, enhances the fit of GCE models with the observational data, especially in the metal poor range. As additional difficulty, important NLTE effects look to be impacting the abundances at the metal poor range and that is indicating the need of 3D-NLTE correction studies, which are currently not available.

Zinc, as the last Fe-peak element seems to share nucleosynthesis sites with copper but in different yields or additional sources. It shows the same difficult interpretation on the SNeIa yields. The enhancement of Zn visible in the [Zn/Fe] ratio is striking at the metal poor range (early universe), pointing to the dramatic improvement in efficiency of one synthetic channel or the impact of additional sources as the proposed contribution from Pop II core-collapse very massive stars (500-1000 $M_{\odot}$). GCE models look unable to obtain a reasonable fit to observational data except when a large fraction of energetic Hypernovae is included as was the case of the Cu element. The s-process contribution is modest (11% in solar system).

At Gallium, the kingdom of the fusion contributions, in hydrostatic or explosive burnings in SNeII is over. Neutron capture processes, either s- (LIMS/AGB) or r-process (SNeII/HNe massive stars, MHD-SNeII, neutron stars or neutron+black hole merger), dominate the periodic table from here on. And the uncertainties are high in relation to the r-process yields in those extremely energetic events.

The higher contributions of s-process with respect to r-process (in solar system) are obtained in the three s-process peaks of special stability (see Fig. 1.15 and 3.1). The first light s-elements as Strontium, Yttrium, Zirconium, Niobium, Molybdenum. The second heavy s-elements as Barium, Lanthanum, Cerium, Praseodymium, and Neodymium. And the third peak, s-process termination point, Lead (Thallium and Bismuth).

Europium is the only net r-process element included in this document. Neutrino-driven winds from SNeII is the classic r-process nucleosynthesis channel. But a promising r-process source studied the last years is a rare kind of SNeII, Magnetohydrodynamics core-collapse supernovae (MHD-SNeII), characterized by high rotation rates and large magnetic fields that might naturally explain the Eu and other r-process elements scatter at metal poor metallicity range.

NS or NS+BH pair mergers (CBM) in spite of their low rate of frequency might show high r-process yields due to their large ejecta, similarly explaining the great scatter of abundances in extremely metal poor stars at the early universe. NS pair mergers may be the dominant contributors to r-process production in the Galaxy, and could account for all the Gold, Platinum and many other heavy elements. However as mentioned in the chapter introduction, there is not consensus yet on the role of these events in the production and evolution of r-elements.

Many uncertainties remain on the nucleosynthesis sites of some elements. Many factors that might impact the interpretation of their galactic chemical evolution from their abundance trends. The most of them have been reviewed and basically described along this document:

Uncertainties about oscillator strengths of lines from which abundances are derived, about the impact of NLTE effects on those lines, uncertainties about the mechanisms of the galaxy formation and chemical nature or origin of their components (halo, disk), how the initial physical parameters of the stars are related with the yields for each source, incomplete understanding of infrequent nucleosynthesis events as CBM that however are expected to produce large yields in the heavier elements or about yields of rare SNeII configurations as MHS-SNeII that greatly could impact the production of r-process elements at the early universe, uncertainties about the fraction and yields of Hypernovae or fast rotating massive stars that especially enhanced some elements at the early universe and in short, all the possible unknown or poorly constrained mechanisms that might change the understanding of the formation and galactic evolution of some elements.

Nevertheless, the advancement of the technology and the increasing available observational data might face and finally overcome these difficulties. Although on the other side, they raise new challenges as the mining of the relevant information from the huge flow of data in surveys as e.g. GAIA. Or the improvement in the instrumental sensitivity of observational techniques as the next generations of spectrographs. Or in the brand new ones, as the gravitational-wave interferometry.

Gravitational-wave interferometry is a perfect example about how advancement of technology might push ahead the research about nucleosynthesis, opening new lines of study. The detection by LIGO/Virgo observatories in 2017 of the gravitational waves from the GW170817 event, a neutron stars merger, triggered an unprecedented multidisciplinary study of the emissions in the full extent of the electromagnetic range, providing for the first time, an integral experimental information of such event, in "real time".

Finally, the Fig. 4.3 has been used by some authors, to illustrate how local conditions might be impacting the understanding of the nucleosynthesis sites. In the Fig. 3.55 of Sect. 3.9 about the r-process element, Eu, we can observe the tight correlation between Europium and the α-element, Mg. That might be quite understandable, both although throughout different processes have a common nucleosynthesis site, in core-collapsed SNeII at the low end of massive stars.

Hence, if both, r-process and α-elements, were created throughout the same mecha-

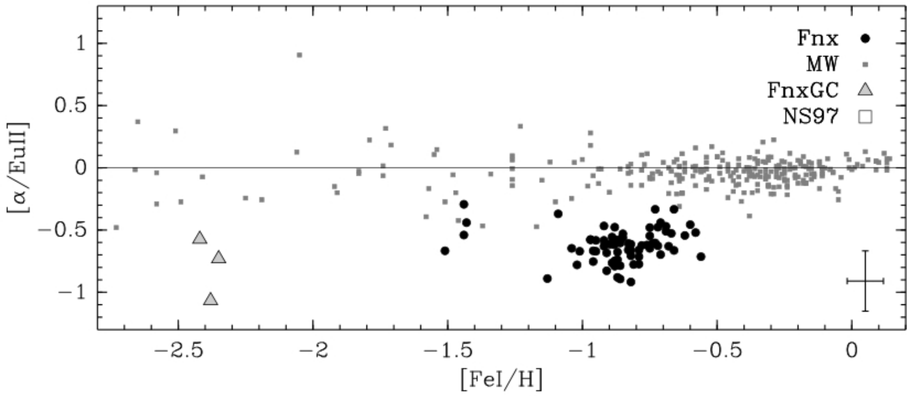

Figure 4.3: *[α/Eu] as a function of [Fe/H]. The Fornax field stars are plotted as solid black circles, the Milky Way stars of Venn et al. (2004) as small grey squares and some Fornax globular clusters as triangles. From doctoral thesis* `https://www.rug.nl/research/portal/files/2809676/12_thesis.pdf` *by Bruno Letarte.*

nisms in every galaxy, the ratio of [Eu/α] should be the same in every system and show the likewise flat and coupled trend. However, when the Fig. 4.3 is observed, the abundance of the dwarf galaxy Fornax's stars show an striking low [α/Eu] ratio, suggesting a decoupled nucleosynthesis of Eu and α-elements. That might be a recall of the great impact of local environments in the chemical evolution and the uncertainties in relation with the nucleosynthesis sites and mechanisms only based on the observational data from our galaxy.

Figure 4.4: *Whirlpool galaxy (M51a) interacting with companion (M51b). Takahashi TSA120 amateur telescope.*

Calar Alto Observatory, Almeria, Spain

Compiled using LaTeX

Chapter 5

Main Lines and their Features

tablefootnote

In the previous chapters, there have tried to provide an overview of the nucleosynthesis topic of certain atomic elements present in the stellar atmospheres of main sequence dwarf stars. There has been circumscribed to those elements with relevant lines in spectra obtained with telescopes and spectrographs that work in the visible and very near infrared range (approximately 4000-10000 Å). Which lines are they? How are originated, and which their main features? But before getting into it, some basic spectroscopic notions.

5.1. Spectral information

From the study of spectra, there has been possible to recompose the chemical (and structural) evolution of our galaxy. But the spectroscopic information is not limited to providing abundances of certain chemical elements. The kind of electronic transitions involved can tell us not only the element to whom it belongs, but its ionization state as well. This is intimately connected with the physical conditions in which the transition is produced and especially with one parameter, the temperature. What it is the same, the dwarf star mass (see Fig. 5.1).

Dwarf (FGK spectral class) main sequence stars show photosphere temperatures from 3700 to 7500 K approximately:

- K spectral class: 3700-5200 K approx.
- G spectral class: 5200-6000 K approx.
- F spectral class: 6000-7500 K approx.

The temperature rules the dominant oxidation states of the atomic elements as neutral,

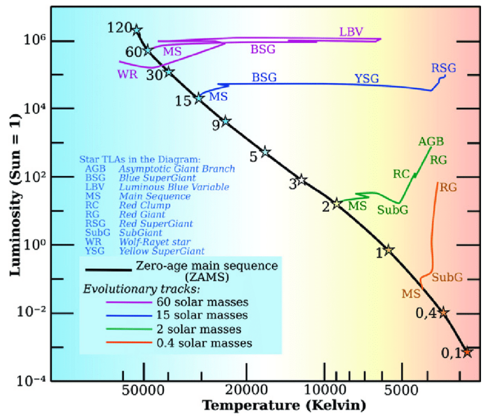

Figure 5.1: *Relationship between luminosity, mass and effective temperature of stars. From Mattsson (2009). Including some evolutionary tracks.*

firstly or secondly ionized species whose fractions vary in function of the specific chemical element and the photospheric temperature, as observed for the iron in Fig. 5.2.

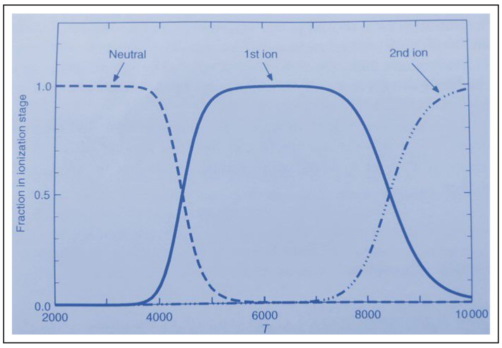

Figure 5.2: *For iron, fractions of ionization species in function of temperature by computing simulation. 1 dyne/cm^2 of electron pressure is used in calculations. From Gray (2008).*

The temperature, jointly with additional physical conditions, impacts on the lines profile as well. Thus, the study of the latter provides information about the temperature but the surrounding environment pressure under which they are produced. This is an important factor to be taken into account, as it is suggesting the caption of the Fig. 5.2. Higher density of chemical species (including subatomic particles as electrons), means more frequent collisions between them. As a consequence, the local velocity of one specific atomic element changes the rest position wavelength of the emitted or absorbed line given by the Doppler equation as shown below. The full dynamical motion/thermal range for all the particles of a specific element, leads to the final line broadening showed in the spectrum.

$\frac{v}{c} = \frac{\Delta\lambda}{\lambda}$ ...

...where v is the source velocity (local or from the star) of the emitting or absorbing

element, λ the rest position wavelength of the line corresponding with its electronic transition and c the light velocity. $\Delta\lambda$ is the wavelength displacement produced by the velocity source and the Doppler effect.

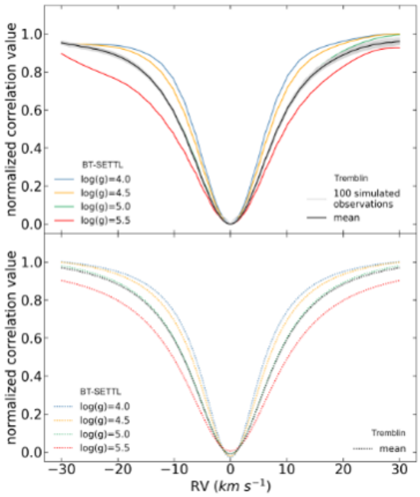

Figure 5.3: *Higher gravity means higher frequency of collisions and dynamical motion range, leading to a broadening of line by Doppler effect. Here, simulations of the impact of surface gravity (logg) on the lines profiles of substellar objects (planets and brown dwarfs) by Speedie, J. and Lafrenière, D. (2019), The iScientist, Vol. IV, 4(1), 3-14. This trend can be extended to stellar ones.*

But what it is right for the local environment, it is also true for the motion of the star itself. The latter leads not to a broadening of the lines, but to a general and close to uniform drift of the lines' wavelength with respect to their rest positions, whatever the chemical element or the lines studied.

The Doppler effect, gives the star velocity with respect to our sight direction according to the equation as shown above, and this is key information in astronomy. From this, f.i. one can deduce the orbital periods in binary systems. Or the presence of exoplanets orbiting one star as one of the more successful methods for discovering exoplanets. The periodic wobble effect on the motion of the star exerted by the gravitational effect of the planet is recorded in the displacement of the lines on a high resolution spectrum.

And it has also been responsible for the understanding of the evolution of the universe and our position on it. The study of the Doppler effect of lines in spectra led Hubble to state the uniform expansion of the universe and, as a consequence, settle the base for the Big Bang Theory.

Finally, the presence of magnetic fields and their intensity can also be deduced from spectra. They lead to the split of lines coming from electronic transitions between level of states with angular momentum (Zeeman effect). Energy degeneration of these states

Figure 5.4: *High resolution spectrograph CARMENES, built for the 3.5m telescope at the Calar Alto Observatory (Almería, Spain). Looking for exoplanets surrounding M stars.*

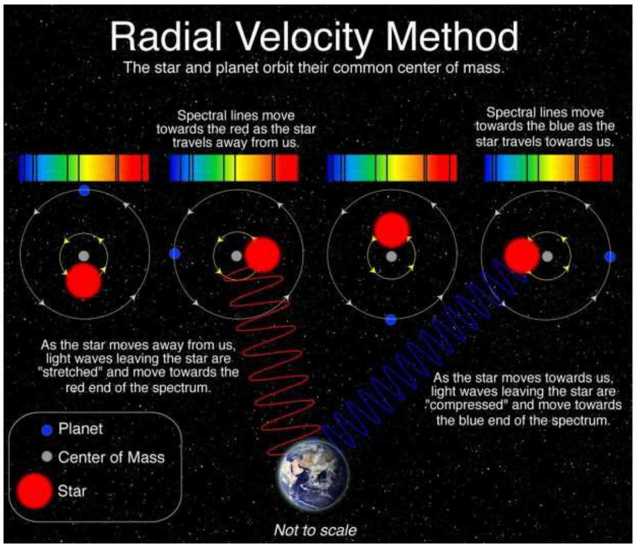

Figure 5.5: *Radial velocity method diagram for the searching of exoplanets. Credit: Las Cumbres Observatory.*

are slightly broken in the presence of magnetic fields (see Fig. 5.8), leading to two o more distinct transitions (so, different close related lines) whose separation is a function of the magnetic field's strength.

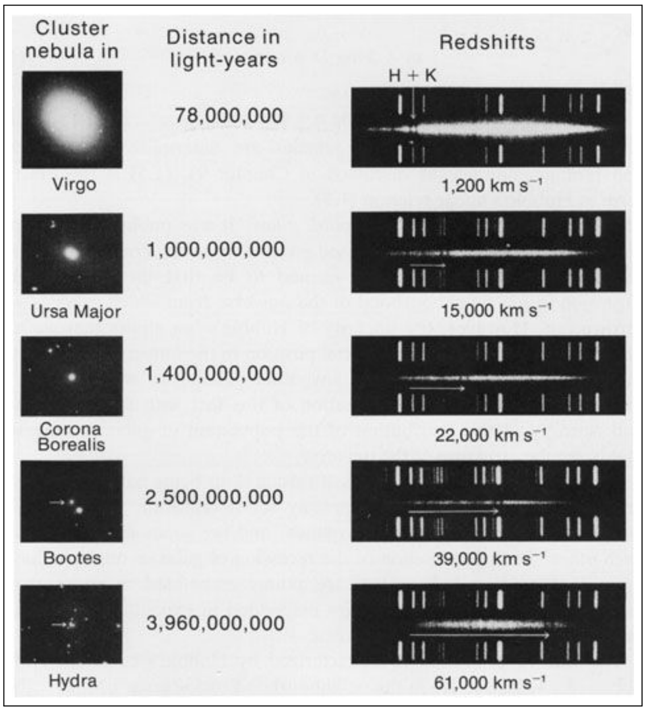

Figure 5.6: *Observations by V.M. Slipher showed the drift of lines (here Ca lines H+K) to redwards in "nebulae", what is the same, higher velocities of scape from us for "nebulae" that looked like to be further. Hubble realized this relation, using the Cepheids method by Henrietta Swan Leavitt, for calculating the distance of those nebulae.*

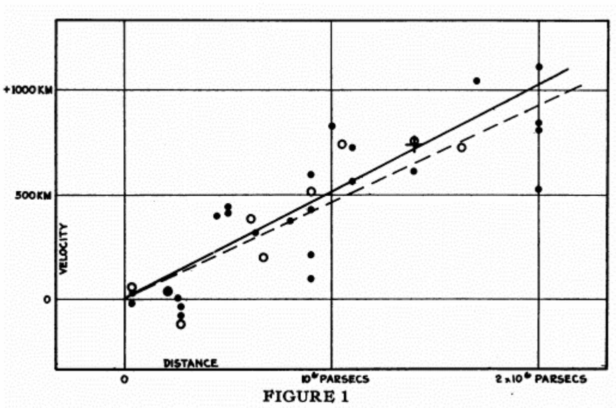

Figure 5.7: *Hubble's diagram as appeared in the historical article by Hubble (1929). He realized the relation between distance with respect to us and the increasing scape velocity of the galaxies. This demonstrated a general expansion of the universe.*

5.2. Absorption Lines: Energy, intensity and probability

The core of the star provides a continuum light source approximating to a black

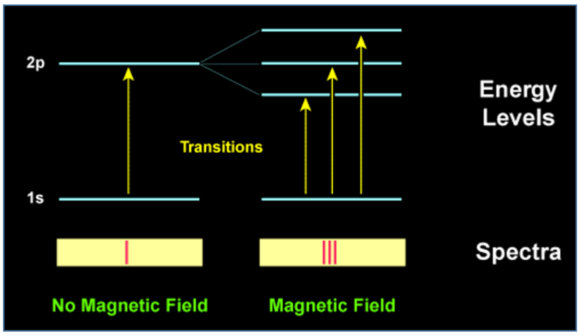

Figure 5.8: *Zeeman effect illustration. P orbitals have an angular momentum quantum number L=1, leading to three (2*L+1) orbitals p with degenerated energies. This degeneration is broken on the presence of a magnetic field.*

body curve with the temperature of the star. Absorption spectral lines appear against this continuous as electronic jumps between two quantized energy levels of the atomic (neutral or ionized) chemical elements present in the photosphere, following the Plank law:

$E = h \cdot \nu = \frac{hc}{\lambda}$ ...

...where ν is the frequency of the absorption line, c the speed of light and h the Plank's constant. λ, the corresponding wavelength of the absorption line.

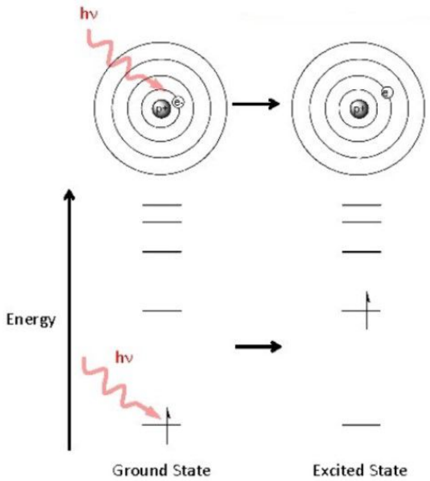

Figure 5.9: *Illustration of an absorption electronic transition between the ground and first excited energy levels.*

The intensity with which an atom in level i absorbs light to jump to level j is given by

$N_i h\nu_{ji} B_{ji} \rho_\nu$ ...

...where N_i is the number of atoms in state i, ρ_ν is the density of radiation with frequency ν. B_{ji} is the Einstein B coefficient, the transition probability for absorption as transitions

per second of an atom from the low i to the excited level j.

Other way to quantify the absorption transition probability is using the oscillator strength (f). This is an unambiguous and dimensionless parameter, in which is usually presented laboratory data for atomic systems (Tennyson 2005).

$f_{ij} = \frac{4\pi\epsilon_0 m_e}{e^2\pi} h\nu_{ji} B_{ij}$ ...

...where ϵ_0 is the permittivity of a vacuum, m_e the electron mass and e the charge on an electron.

Nevertheless, oscillator strength is usually tabulated as $\log(gf)$, where g is the statistical weight, intended as the number of degenerate quantum states in an energy level (in this case, the arrival j level).

5.3. The medium: Optical depth and critical density

Optical depth quantifies the transparency/opacity of the medium. If a chemical specie is very concentrated along the line of sight, not all the atoms may be absorbing the light frequency of a certain electronic transition. It is defined:

$\tau = \int_0^z \alpha \, dz$ ...

...where α is the extinction coefficient, and represents the product of the number of atoms and their opacity at the wavelength in question.

When $\tau >> 1$, the transition is optically thick (saturated) and the total absorption is not directly related to the number of absorbers. Thus, under this circumstance, the density column can not be measured from the spectrum. On the contrary, if $\tau << 1$, transition optically thin, the intensity is directly proportional to the number of absorbers and the spectrum can be used to measure the column density directly (Tennyson 2005).

Other parameter related with the surrounding medium is the critical density as the density of collision partners (usually electrons) above which the collisional de-excitation from the upper level occurs quickly than the radiative de-excitation. Above this limit, it is intended that the emitting species is in thermodynamic equilibrium with its local environment (LTE), and the emission is thermal, directly related with the temperature. On the contrary, under this limit, the emitting species is not in thermodynamic equilibrium with its local environment (NLTE), and the emission is not completely related with the temperature of the medium (free electrons). However, as each collisional excitation leads to an emission, this can provide information on the density of the collision partners (Tennyson 2005).

Although LTE and NLTE conditions, are directly related with the emission mechanism, and like it was noted in the precedent chapters, they also have their impact on the intensity of the absorption lines. Studies of chemical abundance in the past often used LTE models for main sequence dwarfs. However, increasingly chemical abundance studies are taken into account NLTE effects on the results, even changing dramatically the understanding of the galactic chemical evolution in certain elements.

5.4. H atom description: An overview

This document is intended as a basic one, therefore is not getting into a thorough and profound description of the H atom developed by quantum mechanics, using the Schrödinger equation. Nevertheless, it is needed an understanding about some notions behind this description for a basic background.

5.4.1 Energy and quantum numbers

The hydrogen atom (one proton and one electron, H) is the simplest case for a successful solution of the Schrödinger wave equation. Heavier atoms, given their structural complexity, require furthers approximations for its resolution.

For H, the Energy of bound states is given by:

$E = -R\frac{Z^2}{n^2}$ ...

...where R is the constant of Rydberg (though depending on the reduced mass of the system, and taking slightly different values for different hydrogen species. This makes possible to distinguish between the hydrogen or deuterium in moderate resolution spectra), Z is the atomic number, here 1 for hydrogen, and finally n is the principal number quantum.

According to this equation, energy is only dependent on the principal quantum number, n, related with the levels of the electronic shells in atoms. Nevertheless, additional quantum numbers are needed for an electronic description of the hydrogen atom. These states are energetically degenerated (whatever n is the same), although this is not completely true under certain circumstances, as will be later explained. Here, a brief enumeration of them (Tennyson 2005):

- **n** Principal quantum number, taking values n= 1, 2, 3..., ∞ when ionized.
- **l** Electron orbital angular momentum quantum number, taking l= 0 (or s), 1 (or p), 2 (or d), 3 (or f), ..., n-1. See Fig. 5.10.
- $\mathbf{m}_l$ Magnetic quantum number, related with the projection (m$\hbar$, where $\hbar$ is the reduced Plank's constant) of **l** along the z-axis of the system. It can take (2l+1) values= -l, -l+1, ..., 0, ..., l-1, l. See Fig. 5.10.

- **s** Electron spin quantum number. The electron spin angular momentum is given by $\hbar[\mathrm{s(s+1)}]^{\frac{1}{2}}$. In the case of H, one electron always has s=1/2, so its unique angular momentum is equal to $\frac{\sqrt{3}}{2}\hbar$.
- $\mathbf{m}_s$ Quantum number related with the projection ($m_s\hbar$) of **s** along the z-axis of the system. It can take (2s+1) values= -s, -s+1, ..., 0, ..., s-1, s. In the case of H atom, as s=1/2 for one electron, s_z can only take 1/2 or -1/2.

As above commented, **n** determines the energy of the different levels, degenerated when **n** is hold. The electronic jumps between the different n levels arise the known series of hydrogen, as observed in Fig. 5.11.

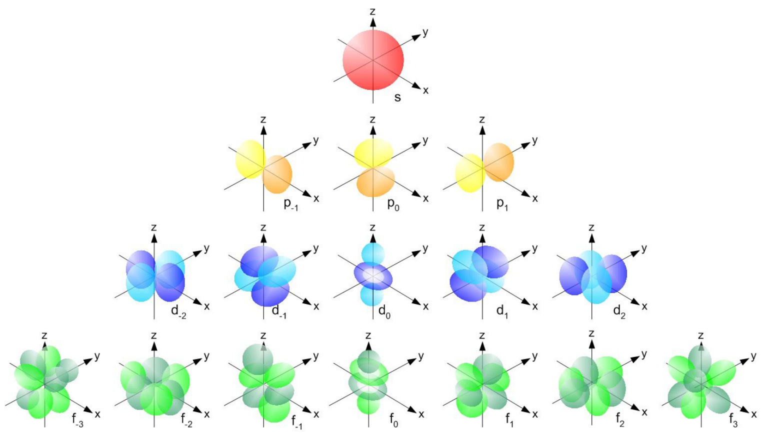

Figure 5.10: *Orbitals l: s (0), p (1), d (2) and f (3) and their magnetic number in subindex. Their forms and orientations correspond to the probability density to find the electron. Electronic occupation of the orbitals in the upper (and open)* **n** *shell of the atom (valence shell), determines its chemical properties and ability to stablish bonds (and orientation) with other atomic elements. Credit* `http://chemgroups.ucdavis.edu/~larsen/ChemWiki.htm`.

However, this is not completely true, under certain conditions, as the presence of magnetic fields (see Fig. 5.8 in section 5, Zeeman effect) and including relativistic effects.

The coupling among the different angular momentum contributions (orbital, electronic spin and nuclear), rules the slight differences of energies given rise to the fine and hyperfine structure of the hydrogen atom. This is of limited use in astronomical applications because to be very small. However, its importance grows greatly in heavy elements in especial beyond the iron. And additionally, a little surprise is hidden in the hyperfine structure of the H that gives place to one of the most powerful tools in Astronomy. An overview into this topic is provided next.

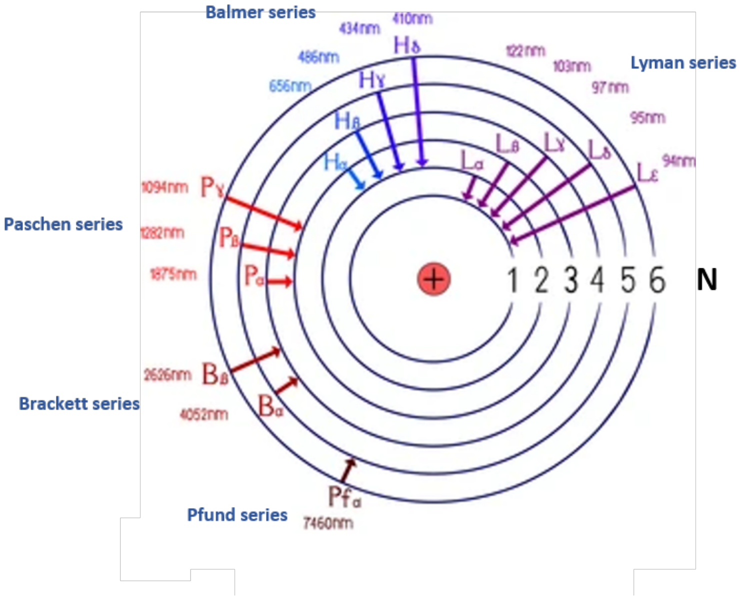

Figure 5.11: *Hydrogen series, depending on the lower energy state (what is to say, its* **n** *quantum number). Here, as emissions from higher to lower levels. Adapted figure.*

5.4.2 Fine and hyperfine structure in the H atom. Notation

Fine and hyperfine structures arisen from the combination of different contributions of angular momentum of the electrons and nuclei:

- Electron orbital angular momentum **l**.
- Electron spin angular momentum **s**.
- Nuclear spin angular momentum **i**.

For taking into account and its comprehension, regarding the incoming info, the vectorial sum is quantized in quantum mechanics as next described:

$$\bar{a} + \bar{b} = \bar{c} = |a - b|, |a - b|{+}1, ..., a + b - 1, a + b$$

Fine structure

The fine structure of the hydrogen is given by the coupling of the angular momentum of the electron: **l** and **s**

$$\bar{\mathbf{l}} + \bar{\mathbf{s}} = \bar{\mathbf{j}}$$

j determines the energetic split of levels. Each level is noted in a term as next:

$^{2S+1}L^{o}_{J}$ ...

Table 5.1: *For different electronic configuration, angular momentum coupling between l and s for obtaining j levels after vectorial sum. Including their spectroscopic notation.*

Config	l	s	j	Term	Levels
ns	0	1/2	1/2	$n\,^2S$	$n\,^2S_{1/2}$
np	1	1/2	1/2 , 3/2	$n\,^2P^o$	$n\,^2P^o_{1/2}$, $n\,^2P^o_{3/2}$
nd	2	1/2	3/2 , 5/2	$n\,^2D$	$n\,^2D_{3/2}$, $n\,^2D_{5/2}$
nf	3	1/2	5/2 , 7/2	$n\,^2F^o$	$n\,^2F^o_{5/2}$, $n\,^2F^o_{7/2}$

...where S is the electronic spin, always 1/2 for an electron, L the corresponding orbital quantum number and J the corresponding coupling state. Superscript **o***, has to do with a concept, parity of the wavefunction. Practically, for one electron in the case of hydrogen, it is marked when* **l** *is odd and not included when is even. For heavier atoms, it is extended to the total sum of* **l** *from each electron of the configuration.*

Now, using the sum of vectors, it is easy obtaining the fine structure terms for the configurations of one electron in the hydrogen atom, whatever the **n** shell (the principal number quantum) in which is located, as next (Tennyson 2005):

Thus, at the ground level (n=1 l=0, 1s), do not suffer splitting by magnetic fields presence. Unlike any other orbitals when **l** is different from 0 (orbitals p, d or f).

f.i. An electronic transition from 1s to an orbital 2p under a magnetic field presence, will show a doublet with very slight difference of frequency because of the coupling of **l** and **s** angular momentum in 2p orbital ($2\,^2P^o_{1/2}, 2\,^2P^o_{3/2}$).

Hyperfine structure and the 1.42 GHz line

However, once again, this is not completely true. The coupling of an additional source of angular momentum, the nuclear spin **i** to the total electron angular momentum **j**, arisen the hyperfine structure of the hydrogen and the final angular momentum, **f**:

$$f = j \pm \frac{1}{2}$$

Coming back to the ground state, 1s or its term $1\,^2S_{1/2}$, is no longer true to be an unique energetic level with j = 1/2. The coupling of nuclear spin with the total electron angular momentum under the presence of magnetic fields, provokes its splitting into two levels, **s**=0 and **s**=1. A transition between the two levels (see Fig. 5.12) corresponds to an energy of $6 \cdot 10^{-5} eV$, what is the same, 1420.406 MHz or a wavelength of 21 cm (Tennyson 2005).

Nevertheless, the more stable configuration in this case it is the parallel coupling of both, electron and nuclear spins. The relaxation is a forbidden transition but can occur as a magnetic dipole transition with an Einstein A coefficient extremely low, $2.9 \cdot 10^{-15} s^{-1}$, one time every approx. 10 million of years. However, the large amount of neutral hydrogen

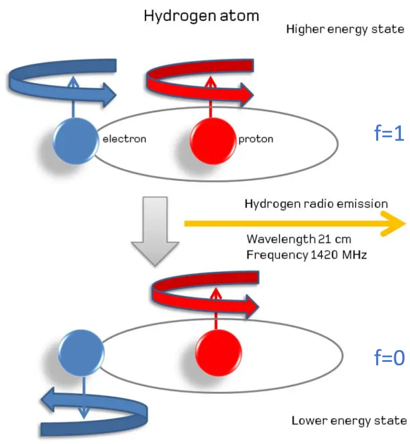

Figure 5.12: *Hyperfine transition in the level* $1\,^2S_{1/2}$ *by the nuclear spin coupling to the total electron angular momentum. Credit* https://www.skao.int/.

in the universe and their collisions favouring the transition, make the use of this frequency possible in radio astronomy for mapping the universe, given its ubiquity. Not only for describing structures and location but their velocities (f.i, rotational curves in galaxies).

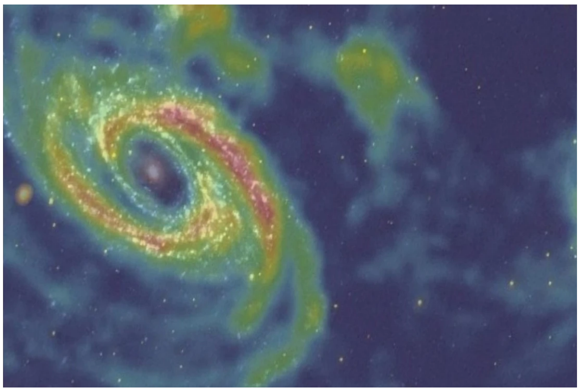

Figure 5.13: *Galaxy Messier 81, constructed from data taken with the Very Large Array, maps out this spiral-armed, star-forming galaxy in 21 centimetre emissions. Credit NRAO/AUI/NSF.*

Allowed transitions

Deriving from the quantum mechanism, the selection rules that determines if a transition is allowed or not are next:

- Δ**n** any.
- Δ**l** = ±1.

- $\Delta \mathbf{s} = 0$ (always satisfied, because s=1/2).
- $\Delta \mathbf{j} = 0, \pm 1$.
- $\Delta \mathbf{m}_j = 0, \pm 1$ (only important when magnetic field present).

These transitions are driven by electric dipoles. Weaker ones, driven by both, electric quadrupoles and magnetic dipoles, are observed but are not important for hydrogen (but the very remarkable exception, 21 cm line).

5.5. Complex atoms

Here, it is not intended to develop the formal description by the quantum mechanics of complex atoms. Suffice it to say, that the electronic core of the atom it is approximated to a central field of potential (depending on the distance to the nucleus) over each electron. This approach, and additional, lead to a solution for a simplified Schrödinger equation. Now, there is no degeneration of energy in orbitals with different angular momentum **l**. Each n**l**, have 2l+1 orbitals with magnetic quantum different numbers (see Fig. 5.10). For instance, angular momentum quantum number l=1 (orbitals p), provides 3 possible orbitals depending on their magnetic quantum number $\mathbf{m}_l$ (p_{-1}, p_0, p_1).

n is not longer the unique quantum number what rules the energy of the electronic configurations in the atom. Even orbitals with higher **n** could have less relative energy than other with lower **n**, if the form and orientation of the orbitals (**l**) penetrates better into the core of the atom. This makes, following the central field approach, the electron possible to be stabilized more efficiently, via coulomb attraction, by the nucleus. And give arise to the filling order of shells/orbitals observed in Fig. 5.14. As above commented, the outer electronically open configuration shell (valence shell) gives the chemical features of the elements and their position in the Periodic Table. Those elements, with similar electronic configuration valence shell (vertical row in Periodic Table) will share main chemical properties.

Pauli's exclusion principle and the electron degeneracy pressure

This principle arises naturally from the formal equations and proposes that no two electrons can occupy the same spin-orbital. This means that for each orbital with a specific magnetic quantum number, the electron has two possibilities of spin $\mathbf{m}_s$= 1/2 or -1/2, and two electrons could occupy it always that their spin (m_s) is different (+1/2,-1/2) but never (+1/2,+1/2) or (-1/2,-1/2), see Fig. 5.15.

Thus, each quantum number **l**, could be occupied by $2 \cdot (2l + 1)$ possible electrons. This principle is key in astronomy because it provides the electronic degeneracy pressure (see Fig. 5.16 which holds up the gravitational collapse of white dwarfs (Tennyson 2005). This

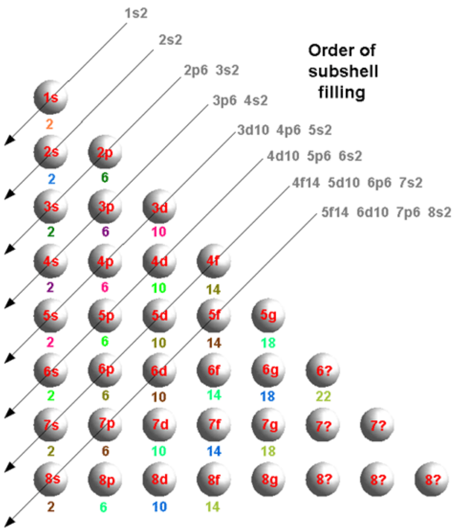

Figure 5.14: *Filling order of orbitals depending on their* **n** *and* **l** *quantum numbers. Under spheres, the maxima of electrons filling for each* **nl** *orbitals.*

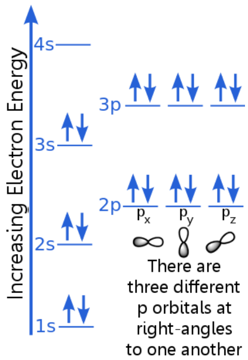

Figure 5.15: *Electronic filling in pairs, of orbitals* **ls** *following the Pauli's exclusion principle.*

principle is also applied to the neutron particles in nuclei and will provide a similar but higher counter-pressure to the collapse of neutron stars in black holes.

5.5.1 Angular momenta

For the calculation of the total electronic angular momentum, two schemes can be applied. Both yield the same $\bar{\mathbf{J}}$ but they are used under different circumstances.

Considering a non-relativistic point of view in which states with the same **L** and **S** have

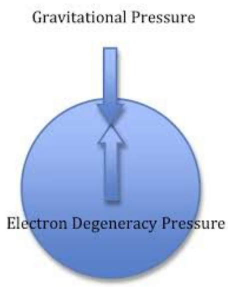

Figure 5.16: *Forces interacting in white dwarf.*

the same energy, the Russell-Saunders (L-S) scheme would fit well. Although this is not exactly true, even in light elements. In practice, relativistic effects split this degeneracy, but the effect is so weak that the approximation to a degenerated state is very close for lighter elements than iron.

For heavy elements in which the relativistic effects are much stronger, however, the j-j coupling method is more appropriate. Nevertheless, light elements are more prevalent in astronomical spectra and the L-S method is largely used (Tennyson 2005).

Method L-S or Russell-Saunders coupling

The orbital and spin angular momenta for one electron give pass to their total angular momenta as next:

$$\bar{\mathbf{L}}_\mathbf{i} = \sum_i^n \bar{\mathbf{l}}_\mathbf{i}$$

$$\bar{\mathbf{S}}_\mathbf{i} = \sum_i^n \bar{\mathbf{s}}_\mathbf{i}$$

Remember how the vectorial sum is developed in quantum mechanics. Now, for obtaining the total electron angular momentum:

$$\bar{\mathbf{J}} = \bar{\mathbf{L}} + \bar{\mathbf{S}}$$

As a result of the Pauli's Principle, electronically closed/completed shells have always the angular momenta **L**=0 and **S**=0. Therefore, it is only needed to consider the electronic configuration of the open or partially-filled orbitals/shells.

Method j-j coupling

Here, the approach is considering the direct vectorial sum of $\bar{l}_i$ and $\bar{s}_i$:

$$\bar{\mathbf{j}}_\mathbf{i} = \bar{\mathbf{l}}_\mathbf{i} + \bar{\mathbf{s}}_\mathbf{i}$$

Then, for the total electron angular momentum: $\bar{\mathbf{J}}_\mathbf{i} = \sum_i^n \bar{\mathbf{j}}_\mathbf{i}$

Here, the total angular momentum J is the one conserved, so J=0 for closed shells and sub-shells. Only needed to considered electronic configuration in the electronically open outer shells.

5.5.2 Notation. Laporte and Hund's rules

Notation was described in section 5:

$^{2S+1}L_J^o$

But now, these terms are referring to the total angular momenta L, S and J. Now S is not longer always 1/2, because more than one single electron, as was in the hydrogen, is considered in the electronic configuration. This arises additional levels.

For superscript **o**, the wave function parity term, from a practical point of view, will be included when:

$(-1)^{l_1+l_1...+l_n}$ is negative (odd parity)...

...and not, when positive (even parity). There is only to consider electrons in open shells/orbitals.

The strong transitions driven by electric dipoles connect opposite parity states levels (even-odd or odd-even). This is known as the ***Laporte's Rule***.

In complex atom, simple n-l configurations can lead to a bunch of terms with slight differences of energy. Let's consider now some basic rules by Hund that help to order lower and higher energy levels, following some examples for a better comprehension (Tennyson 2005):

- ***1st Hunds's Rule***: for a given configuration, the term with the maximum spin multiplicity (2S+1) lies lowest in energy.

  Example: Considering the Helium excited configuration with one electron in 1s and one electron in 2s orbitals (1s2s), see next table:

Table 5.2: *Electronic excited configuration of He, 1s2s. Arisen terms. Always remember how the vectorial sum is developed in quantum mechanics and the terms' notation.*

Conf.	$\bar{l}_i$	$\bar{L}$	$\bar{s}_i$	$\bar{S}$	(L,S)	$\bar{J}$	Levels-Terms
1s	0	0	1/2	0,1	(0,0)	0	$^1S_0$ or also ^1S
2s	0		1/2		(0,1)	1	$^3S_1$

Thus, two terms arise from this electronic configuration and the lowest energy corresponds to the term with maximum spin multiplicity, $^3S_1$. The real splitting between them is 0.80 eV.

This rule determines the filling order of electrons in incomplete subshells with the

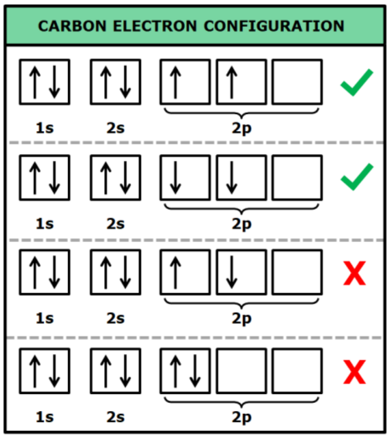

Figure 5.17: *The 1st Multiplicity Hund's rule determining the spin orientation (and so the filling order), for minimizing energy, of* **p** *orbitals in the neutral carbon (C I). Credit* https://study.com/academy/lesson/atomic-structures-pauli-exclusion-principle-aufbau-principle-hunds-rule.html.

same n and l quantum numbers, privileging those in which spin is the same (whenever **m** is different) as shown in Fig. 5.17.

- ***2nd Hunds's Rule***: for a given configuration, and spin multiplicity, the term with the largest value of L lies lowest in energy.

  Example: Firstly, we will consider an apparent paradox regarding the Carbon excited and ground configurations $1s^2 2s^2 2p3p$ and $1s^2 2s^2 2p^2$. Let us start first with the excited electronic configuration, $1s^2 2s^2 2p3p$. As above commented, orbitals/shells electronically completed ($1s^2 2s^2$) do not contribute to a net angular momentum ($\bar{\mathbf{L}}$ = 0 and $\bar{\mathbf{S}}$=0). We can ignore them. See next table with the arisen terms:

Table 5.3: *Electronic excited configuration of C, $1s^2 2s^2 2p3p$. Arisen terms.*

Conf.	$\bar{l}_i$	$\bar{L}$	$\bar{s}_i$	$\bar{S}$	(L,S)	$\bar{J}$	Levels-Terms
2**p**	1	0, 1, 2	1/2	0,1	(0,0)	0	${}^1S_0$
					(0,1)	1	${}^3S_1$
					(1,0)	1	${}^1P_1$
3**p**	1		1/2		(1,1)	0,1,2	${}^3P_0, {}^3P_1, {}^3P_2$
					(2,0)	2	${}^1D_2$
					(2,1)	1,2,3	${}^3D_1, {}^3D_2, {}^3D_3$

All even parity terms (see above how to determinate the parity of wavefunction).

Here, it comes the apparent paradox. When we consider the ground electronic configuration of the C ground state, $1s^2 2s^2 2p^2$. If the same development is followed for the two electrons located in the open subshell $2p^2$ ($l_1 = l_2 = 1$ and $s_1 = s_2 = 1/2$), the same terms are attained!.

However, the Pauli exclusion principle has to be taken into account here, given that both electrons have the same **n** and f.i. there are certain states (f.i.^3D) in which is possible $m_1 = m_2$ and $m_{1s} = m_{2s} = +1/2$ or $m_{1s} = m_{2s} = -1/2$, what it is the same, all the quantum numbers (n-l-m_l-m_s) would be identical, and two electrons would occupy the same orbital **p** with the same m_s spin. This is allowed when **n** is different (as in the former C excited example) and they occupy **p** orbitals of different shells, but not when they do in the same orbital itself (unless other quantum number as $\mathbf{m}_l$ is different). These are the cases shown by the Fig. 5.18.

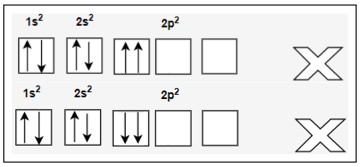

Figure 5.18: *Wrong electronic filling order of* **p** *orbitals against the Pauli's exclusion principle.*

As a direct method to know which terms are allowed when electrons are equivalent (same **n,l**), **L+S** for these electrons must be even for accomplishing the Pauli's exclusion principle. Following this rough, but efficient method, we can exclude from the Table 5.4 some terms not valid in the ground electronic state.

Table 5.4: *Electronic ground configuration of C, $1s^2 2s^2 2p^2$. Arisen terms and not valid by Pauli's exclusion.*

Conf.	$\bar{l}_i$	$\bar{L}$	$\bar{s}_i$	$\bar{S}$	(L,S)	$\bar{J}$	Levels-Terms
					(0,0)	0	$^1S_0$
2**p**	1		1/2		$\cancel{(0,1)}$	$\cancel{1}$	$\cancel{^3S_1}$
		0, 1, 2		0,1	$\cancel{(1,0)}$	$\cancel{1}$	$\cancel{^1P_1}$
					(1,1)	0,1,2	$^3P_0, ^3P_1, ^3P_2$
2**p**	1		1/2		(2,0)	2	$^1D_2$
					$\cancel{(2,1)}$	$\cancel{1,2,3}$	$\cancel{^3D_1, ^3D_2, ^3D_3}$

Applying the 1st Hund's principle, we find that the term with the lowest energy is ^3P. But which one is the next ^1D or ^1S?

Here, 2nd Hund's principle comes in our help: the term with the highest total angular orbital momentum is the one with the lowest energy. So, the right order: $^3P < {}^1D < {}^1S$.

But, what about the fine structure: $^3P_0,^3P_1,^3P_2$? See next principle.

- ***3rd Hunds's Rule***: for a given configuration, and same spin multiplicity (2S+1), the term with the lowest energy is obtained for the lowest J in the "normal" case and for the highest one in the "inverted" case.

  Firstly, we need to know what is this statement referring to, with normal or inverted cases. Normal is when the orbitals (same orbital quantum number **l**) from one shell are partially occupied, less than the half of their capacity. Following the case of the neutral carbon (C I), one can observe (see Fig, 5.17) how the valence orbital 2p^2, is only partially occupied in 2 from the total possible 6 electrons of capacity, what it is the same, less than half of their capacity. This is the "normal" case.

  Like so, in the case of the neutral carbon, now we can order the ^3P fine structure in the next energy order: $^3P_0 <^3 P_1 <^3 P_2$.

  However, let us consider the fine structure of the oxygen (O I), with its electronic configuration in the valence orbitals 2p^4 (see Fig. 5.19). The p orbitals are filled with 4 electrons from the 6 of capacity, more than the half one. This is the "inverted" case.

  Like so, in the case of the neutral oxygen, now we can order the ^3P fine structure in the next energy order:$^3P_2 <^3 P_1 <^3 P_0$.

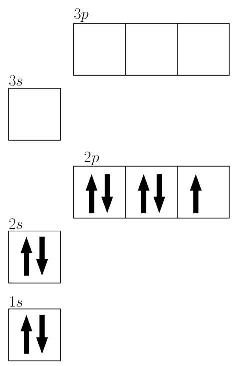

Figure 5.19: *Neutral oxygen (O I) electronic configuration.*

5.5.3 Allowed or forbidden transitions

Strong allowed transitions are driven by electric dipoles. They must always obey some rules (rigorous). Others (propensity rules) can be violated, leading to weaker transitions (forbidden transitions). Typically, they have Einstein coefficients bigger than 10^6 per second (Tennyson 2005). Transitions driven by electric quadrupole or magnetic dipole are also considered forbidden. In the Table Fig. 5.5 are summarized the selection rules in the different transitions driven types.

Table 5.5: *Selection rules for atomic spectra. Rules 1, 2 and 3 must always be obeyed. For electric dipole transitions, intercombination lines violate the rule 4 and forbidden lines violate rule 5 and / or 6. Electric quadrupole and magnetic dipole transitions are also considered as forbidden (Tennyson 2005).*

Rule	Electric dipole	Electric quadrupole	Magnetic dipole
1.	$\Delta J = 0, \pm1$ Not J = 0-0	$\Delta J = 0, \pm1, \pm2$ Not J = 0-0, 1/2-1/2, 0-1	$\Delta J = 0, \pm1$ Not J = 0-0
2.	$\Delta M_J = 0, \pm1$	$\Delta M_J = 0, \pm1, \pm2$	$\Delta M_J = 0, \pm1$
3.	Parity changes	Parity unchanged	Parity unchanged
4.	$\Delta S = 0$	$\Delta S = 0$	$\Delta S = 0$
5.	One electron jumps Δn any $\Delta l = 0, \pm1$	One or no electron jumps Δn any $\Delta l = 0, \pm2$	No electron jumps $\Delta n = 0$ $\Delta l = 0$
6.	$\Delta L = 0, \pm1$ Not L = 0-0	$\Delta L = 0, \pm1, \pm2$ Not L = 0-0, 0-1	$\Delta L = 0$

In heavy atoms or ions, relativistic effects can lead to a change of S and therefore $\Delta S \neq 0$. This violation arises **intercombination lines**. They are noted using one square bracket f.i. C III]. Dielectric dipole transitions violating the propensity rules 5 and/or 6, arise the **forbidden transitions**, labelled by square brackets, f.i. [C III].

Forbidden transitions are generally weaker than intercombination lines and much more than allowed ones. Transitions driven by higher electric multipoles (quadrupoles) or magnetic moments (magnetic dipoles), even satisfying rules of the Table 5.5, are either much weaker than the allowed electric dipole transitions. Thus, they are also referred to as forbidden transitions (Tennyson 2005).

Typical lifetimes (inverse of Einstein coefficients) for allowed decays via each mechanism are:

$$\tau_{dipole} \sim 10^{-8} s,\ \tau_{magnetic} \sim 10^{-3} s,\ \tau_{quadrupole} \sim 1 s$$

Clearly, when available, decay routes via allowed transitions will be the only mechanism used. Only metastables, excited states with a long life in a close to a free-collisions environment (low density) can decay via forbidden transitions. Hence, they could be important in hot, low density such as H II regions, planetary nebulae or stars corona.

Forbidden lines are normally only important for low-lying states, because higher states nearly always have possible radiative decay routes via allowed transitions. This leads to the lines, for neutral or low ionized atoms, to be observed in infrared. A common source of forbidden lines arises from the relaxation of excited terms within the ground state configuration and levels within the ground state term, completely forbidden by the Laporte's rule and via magnetic transitions (Tennyson 2005).

Finally, like in the case of the hydrogen, we could consider the contribution of angular momentum and the coupling of the nuclear spin. This adds new rules for electric dipoles transition based in the final angular momentum:

$\Delta F = 0, \pm 1$ and Not F = 0-0 transition

5.6. Relevant lines

Features of the main lines for each atomic element, with relevant ones in the visible and the very near infrared range for dwarf main sequence stars, will be deployed in the next sections. They will be selected regarding the importance for the abundant calculations of the atomic element. Therefore, the first two primordials elements, major constituents in stars as hydrogen and helium are treated for informational purposes, from a general point of view, only remarking some interesting aspects of their presence in visible spectra. Somehow, iron, given the abundance of their lines across the whole visible spectra, will be approached from this general point of view as well, not giving details about particular lines.

General plots at the beginning of each element section will be included. They have been obtained from the NIST database [1], using the Saha-LTE Spectrum generator, under "ad hoc" premises of electron temperature 0.5 eV and electron density of 2.7x10^{12} cm^{-3}.

Next, there will be supplied information regarding the most relevant spectral lines based on bibliographic sources and experience. Nevertheless, attention has to be paid to the circumstances in which the spectra are taken. For example, if one is studying MS in a binary system as the wide period hot subdwarf one, some lines can be overlapped and interfered by the hot subdwarf lines, especially in the blue part of the spectra. On the other hand, some spectral ranges could not be available by the spectrograph configuration.

The spectral information of lines are obtained from NIST database. There are included the next fields:

- Atomic ionization of the line and line character.
  Intercombination lines are indicated as element], forbidden ones as [element].
- Ritz wavelength in air of the line, calculated from the energy levels.
- log(gf) oscillator strength
  They can be obtained departing from the probability/Einstein emission coefficients A_{ki} (s^{-1}):
  - Absorption oscillator strength (f-value) for all the multipole types:
    $f_{ik} = A_{ki} \cdot 1.49919 \cdot 10^{-16} g_k / g_i \lambda^2$
    ...where A_{ki} is expressed here in units of $10^8 s^{-1}$, g_k and g_i are the statistical weight of the upper and lower level respectively, and λ wavelength in Å

[1] https://www.nist.gov/pml/atomic-spectra-database

Like this, $\log_{10}(g_i f_{ik})$ is finally dependent on the g_k, the arrival level statistical weight:

$g_i f_{ik} = A_{ki} \cdot 1.49919 \cdot 10^{-16} \cancel{g_i} \cdot g_k / \cancel{g_i} \lambda^2$ *...where* $g_k = 2J_k+1$

For obtaining line strengths (S), multiply Einstein coefficients by the next list (NIST info):

- Electric dipole (E1) $4.935525 \cdot 10^{-19} \cdot g_k \lambda^3$
- Magnetic dipole (M1) $3.707342 \cdot 10^{-14} \cdot g_k \lambda^3$
- Electric quadrupole (E2) $8.928970 \cdot 10^{-19} \cdot g_k \lambda^5$
- Magnetic quadrupole (M2) $6.707037 \cdot 10^{-14} \cdot g_k \lambda^5$

...where g_k is the statistical weight of the upper level and λ wavelength in Å.

- Accuracy, indicated by a code letter corresponding to their strength uncertainties as listed below. In general, they reflect estimates of predominantly systematic effects:
  - AAA $\leq$ 0.3%
  - AA $\leq$ 1%
  - A+ $\leq$ 2%
  - A $\leq$ 3%
  - B+ $\leq$ 7%
  - B $\leq$ 10%
  - C+ $\leq$ 18%
  - C $\leq$ 25%
  - D+ $\leq$ 40%
  - D $\leq$ 50%
  - E > 50%
- Electronic configuration of the lower and upper levels and fine structure terms involved in the transition

About the accuracy field, just one remark: this is not intended as a classification about fineness regarding the abundance study. For example, the line Na I 5889 Å is an intense and fine absorption line, classified as bf AA (strength uncertainty < 1%). However, it could be not a good line for studying the Na abundance by the reasons developed in section 5.6. Other reasons, as commented above regarding binary or multiple systems, could advise or force the use of lines of lower reliability if they are unblended.

5.6.1 Hydrogen ($_1$H)

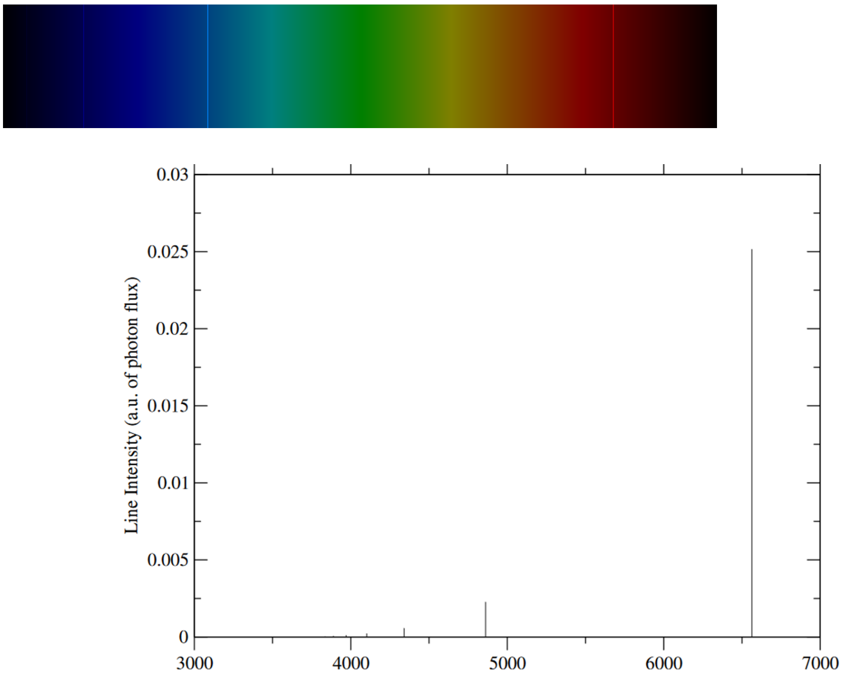

Figure 5.20: *Hydrogen lines intensity (Balmer series). Saha-LTE Spectrum (NIST) from ad hoc conditions: electron temperature 0.5 eV and electron density of 2.7x10^{12} cm^{-3}.*

The hydrogen spectra, in main sequence dwarfs, show the typical broad bands of the Balmer series due to the electronic transitions from n=2 to successive higher levels (see Fig. 5.11 in section 5). Hydrogen is the main component, by very far, of main sequence stars. Their high density, some orders larger than electron number density in sun-alike stars, determines a broad dynamical range of collisions and different velocity with respect to the rest position. Additional transitions involving the fine structure levels of the hydrogen contribute to the broadening of the main lines of the serie. Altogether, it is the explanation of the great intensity and broadening of these lines (see Fig. 5.21)

Hydrogen and keplerian disks

Modifications of the hydrogen lines core might offer information about additional topics as the presence of circumstellar keplerian disks. This can provoke f.i. the H_α core to appear as depleted or in emission. At the same time, this could be valuable information about the angle of the disk with respect to our sight line as depending on this, the H_α could be observed like a typical hydrogen absorption line or on the contrary, as a net emission (see Fig. 5.22 and 5.23). Although the latter example comes from a massive star (B-type spectral class), it could be applied approximately to less massive stars or special cases involving MS

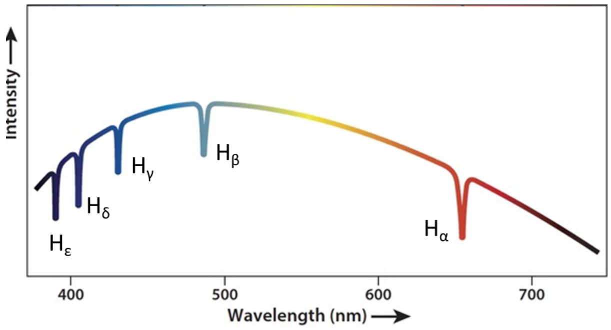

Figure 5.21: *Typical rough profile of spectra of main sequences dominated by intense hydrogen lines from Balmer series.*

stars (f.i. binary systems including circumbinary disks).

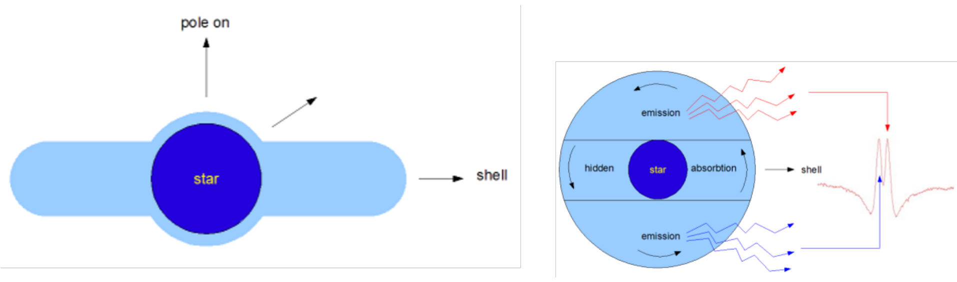

Figure 5.22: *Structure of a massive Be star and its keplerian disk, from equatorial or axial point of view. Relation with the absorption/emitting components of the H_α line (Kogure & Hirata 1982).*

Next, the main lines of the Balmer serie, are enumerated (constrained to the 3900 Å lower limit and Ritz wavelength air values). Not included, the transitions arisen from the hydrogen fine structure.

Line	Wave.Ritz Air (Å)	Prob. A_{ki} (s^{-1})	Energy (cm^{-1})	Levels (n)
H_α	6562.819	4.4101e+07	82259.158 → 97492.304	2 → 3
H_β	4861.333	8.4193e+06	82259.158 → 102823.904	2 → 4
H_γ	4340.471	2.5304e+06	82259.158 → 105291.657	2 → 5
H_δ	4101.7415	9.7320e+05	82259.158 → 106632.1681	2 → 6
H_ϵ	3970.0788	4.3889e+05	82259.158 → 107440.4508	2 → 7

Lyman-alpha forest

As shown in Fig. 5.11 in section 5, Lyman series (low level n=1) get into the UV range. For example, α line wavelength is 1215.7 Å . Although not concerning the studied range here, visible and near infrared spectra, indirectly they can have their impact there. The cause, the

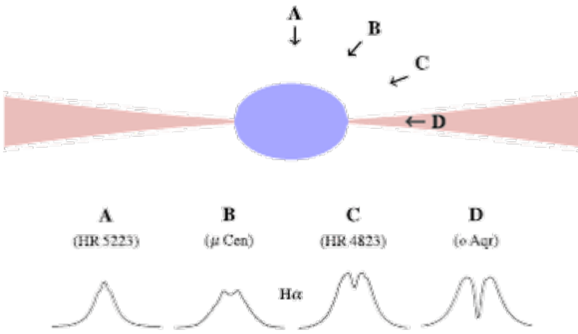

Figure 5.23: *Schematic view of a massive Be star. The lower part shows example spectral Be stars profiles arisen from the different points of sight with respect to their respective disks (Rivinius et al. 2013).*

redshift due to the universe expansion in α-Lyman emitted light coming from quasars or distant galaxies.

This redshifted light, and its absorption by H I clouds at different distances of the interstellar medium, produce a typical profile in spectra known as Lyman-α forest (see Fig.5.24).

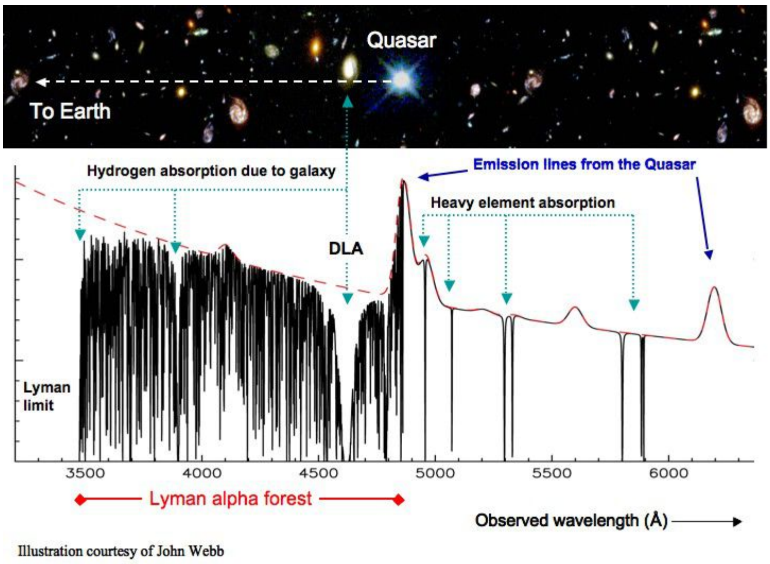

Figure 5.24: *Lyman-α forest of emitted light from a quasar, getting into the visible range. Credit* `https://people.lam.fr/pieri.matthew/lymana.html`.

This is a valuable tool in astronomy. Firstly, it gives information about the interstellar medium, making possible to determine the frequency and density of clouds containing neutral hydrogen and their temperature. Besides for redshift z~6, it is showing the end of the reionization epoch of the universe.

Before the reionization and after the recombination epoch, the neutral hydrogen was so abundant and dense that the absorption of the emitted light is utterly absorbed given arise to a different profile, the Gunn–Peterson trough (see Fig. 5.25).

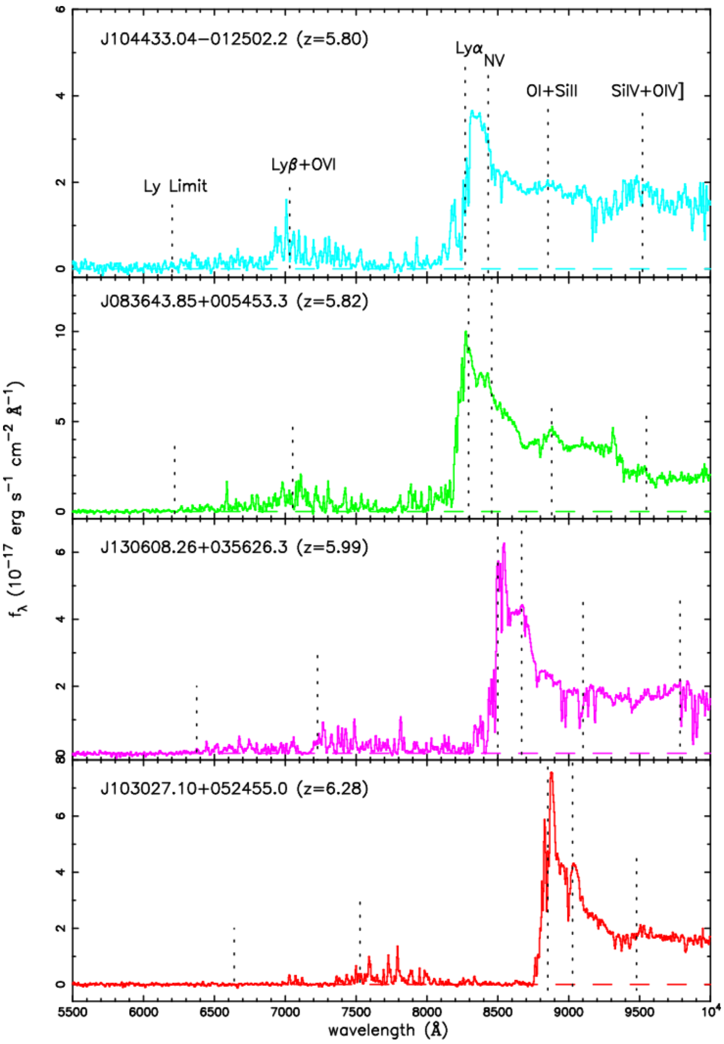

Figure 5.25: *Gunn–Peterson trough, at around z~6. Before completing reionization epoch of the universe, the neutral hydrogen was so abundant and the medium optically depth, that absorption was total for the alpha-Lyman light emitted by the quasar or distant galaxy. Several quasar examples close to z=6 in which it is possible to observe how wavelengths below the α-Lyman emission has been nearly absorbed (Fan 2003).*

5.6.2 Helium ($_2$He)

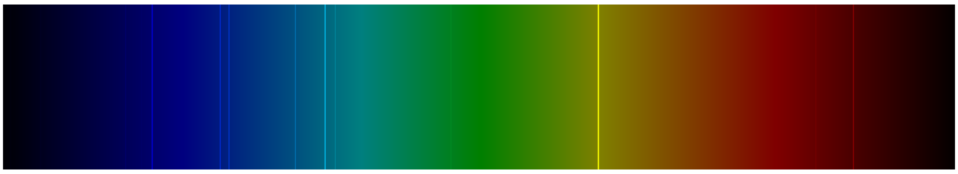

The unique Helium specie observed in main dwarf sequence stars is neutral, given the surface temperature of these stars.

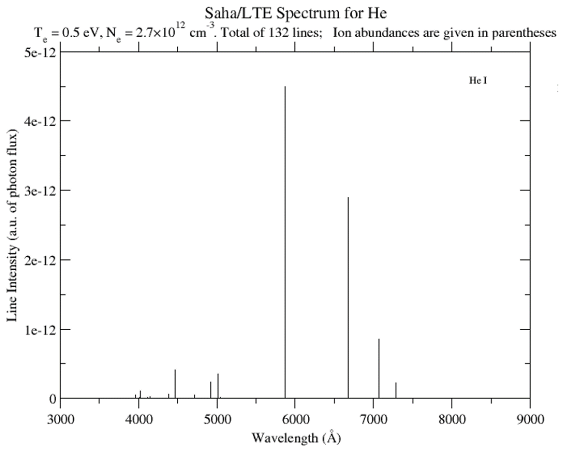

Figure 5.26: *Helium lines intensity. Saha-LTE Spectrum (NIST) from ad hoc conditions: electron temperature 0.5 eV and electron density of 2.7x10^{12} cm^{-3}.*

As commented at the beginning of this section, this element is only approached from a general point of view and no spectral details about each line will be offered. However, a general scheme of the transitions involved, and the main lines observed, can be found in the Fig. 5.27.

The helium transitions are producing from two He kind of states, showing singlet or triplet multiplicity. Which is the same, states showing the two electrons with antiparallel (+1/2 and -1/2, para-helium) or parallel (ortho-helium) spins m$_s$. The term ^{3}S corresponding to the 1s2s electronic configuration is the ground state (2^{3}S) of the orthohelium (transition from/to 1s^2 is forbidden). This is a metastable state with 7800 s of lifetime, as shown in Fig. 5.28.

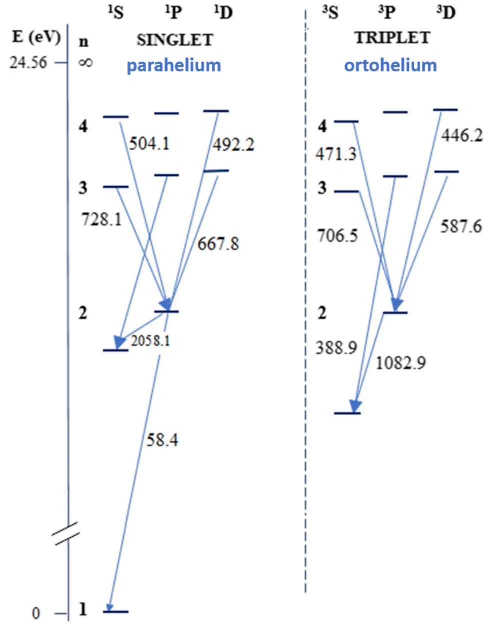

Figure 5.27: *Main transitions regarding the fine structure terms of the helium. Wavelengths are included in nm. Transitions can be split into two categories, involving singlet (parahelium, when m_s of the two electrons are antiparallel +1/2 and -1/2) or triplet (orthohelium, when both are showing the same orientation) terms. Here, diagram from the emission point of view. From* Şahin & Tanışlı *(*2020*).*

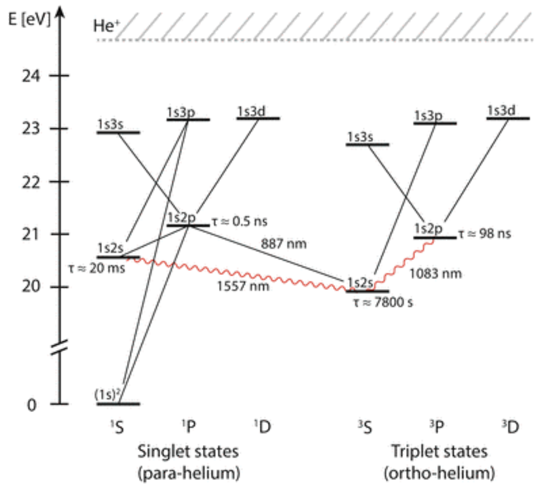

Figure 5.28: *Level scheme and transition wavelengths for low-lying states of helium ($n < 4$). Included lifetimes of n=2 terms. From* Vassen et al. *(*2016*).*

5.6.3 Lithium ($_3$Li)

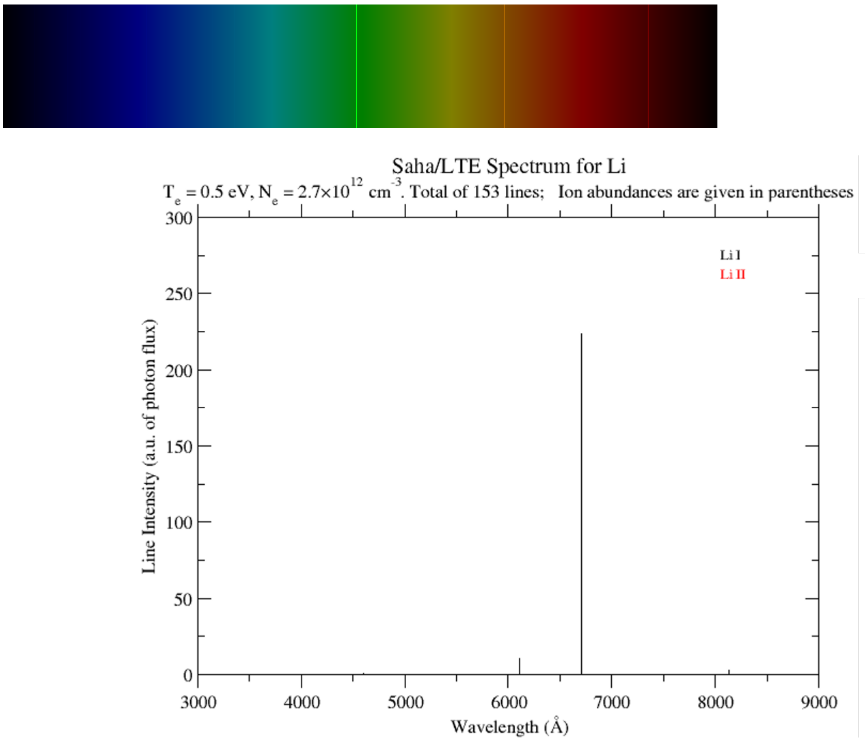

Figure 5.29: *Lithium lines intensity. Saha-LTE Spectrum (NIST) from ad hoc conditions: electron temperature 0.5 eV and electron density of 2.7x10^{12} cm^{-3}.*

Its detection is very difficult in regular main sequence stars (see Section 2.1). The only chance for studying abundance of lithium in main sequence stars is constrained to the doublet Li I 6708 Å line. It is also offered the information of the alternative extremely faint Li I 6104 Å line, but useless here.

Line	Ritz Air (Å)	log($g_i f_{ik}$)	Accuracy	Config. **Level**
Li I	6103.53	0.106	AAA	$1s^2 2p\ ^2\mathbf{P}^o_{1/2} \rightarrow 1s^2 3d\ ^2\mathbf{D}_{3/2}$
Li I	6103.66	-0.593	AAA	$1s^2 2p\ ^2\mathbf{P}^o_{3/2} \rightarrow 1s^2 3d\ ^2\mathbf{D}_{3/2}$
Li I	6707.76	-0.002	AAA	$1s^2 2s\ ^2\mathbf{S}_{1/2} \rightarrow 1s^2 2p\ ^2\mathbf{P}^o_{3/2}$
Li I	6707.91	-0.303	AAA	$1s^2 2s\ ^2\mathbf{S}_{1/2} \rightarrow 1s^2 2p\ ^2\mathbf{P}^o_{1/2}$

Clearly, the absorption from the ground level, being more populated, yields a more intense line Li I 6708 Å. Nevertheless, this intrinsically asymmetric line because of the blended doublet components, can often be too weak to be reliably measured, and is more or less blended with the neighbouring lines of other species, especially with Fe I 6707.4 Å (Takeda & Kawanomoto 2005).

5.6.4 Carbon ($_6$C)

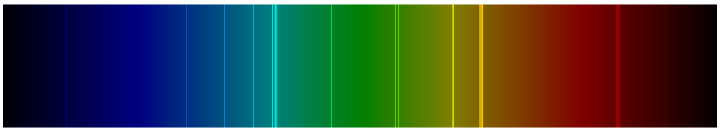

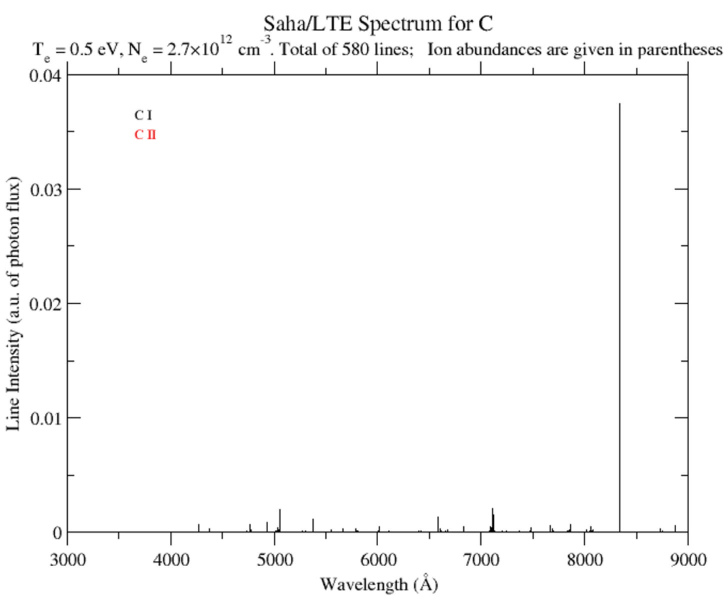

Figure 5.30: *Carbon lines intensity. Saha-LTE Spectrum (NIST) from ad hoc conditions: electron temperature 0.5 eV and electron density of 2.7x10^{12} cm^{-3}.*

No doubt, the line C I 8335 Å it is the strongest line by far. However, it has to be paid some attention, because it could be partially overlapped by telluric lines, depending on either, the radial velocity of the star or its line broadening. In spite of this, it is the most useful line for C abundance determination.

Nevertheless, additional lines in the range of 7100-7120, although much less intense, are useful and a nice check of the obtained abundance. However, their use is limited when studying metal poor stars.

5.6.5 Nitrogen ($_7$N)

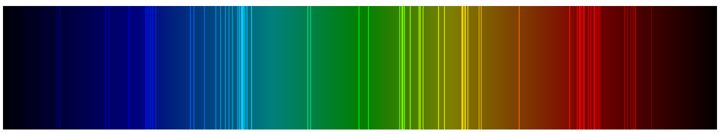

Line	Ritz Air (Å)	log($g_i f_{ik}$)	Accuracy	Config. **Level**
C I	7111.4579	-1.08	B	$2s^2 2p3p\ ^3\mathbf{D_1} \rightarrow 2s^2 2p4d\ ^3\mathbf{F^o_2}$
C I	7113.1656	-0.77	B	$2s^2 2p3p\ ^3\mathbf{D_3} \rightarrow 2s^2 2p4d\ ^3\mathbf{F^o_4}$
C I	7115.1710	-1.47	B	$2s^2 2p3p\ ^3\mathbf{D_1} \rightarrow 2s^2 2p5s\ ^3\mathbf{P^o_0}$
C I	7115.1789	-0.93	B	$2s^2 2p3p\ ^3\mathbf{D_2} \rightarrow 2s^2 2p4d\ ^3\mathbf{F^o_3}$
C I	7116.9776	-0.91	B	$2s^2 2p3p\ ^3\mathbf{D_3} \rightarrow 2s^2 2p5s\ ^3\mathbf{P^o_2}$
C I	7119.6559	-1.15	B	$2s^2 2p3p\ ^3\mathbf{D_2} \rightarrow 2s^2 2p5s\ ^3\mathbf{P^o_1}$
C I	8335.1447	-0.44	B+	$2s^2 2p3s\ ^1\mathbf{P^o_1} \rightarrow 2s^2 2p3p\ ^1\mathbf{S_0}$

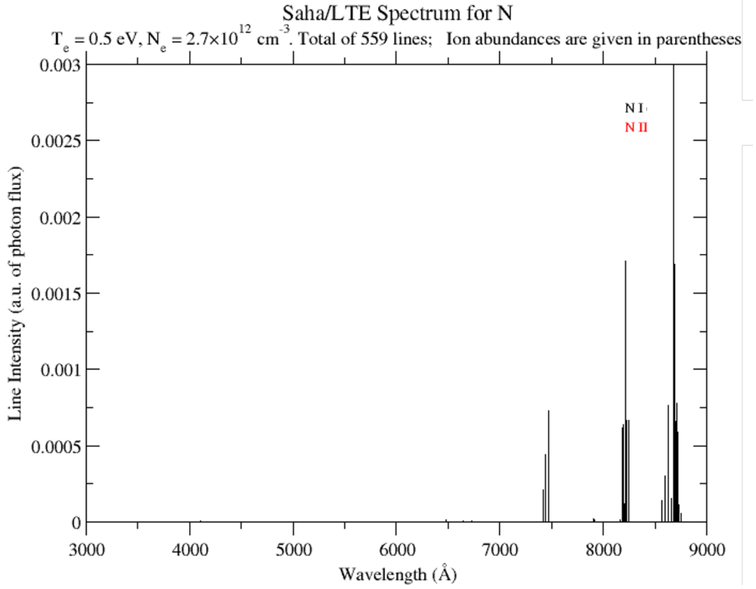

Figure 5.31: *Nitrogen lines intensity. Saha-LTE Spectrum (NIST) from ad hoc conditions: electron temperature 0.5 eV and electron density of 2.7x10^{12} cm^{-3}.*

Nitrogen it is a tricky element to study, especially in metal poor stars. As commented in Section 2.3, nitrogen does not present readily available lines in visible or near IR range (4000-9000 Å), but some extremely weak and blended lines in the near IR.

The N I 8683 Å line was used in the study of Takeda & Honda (2005), as others like 8680, 8703 or 8719 are suspected to be appreciably blended with lines of other species. Nevertheless, its use is constrained to metallicity higher than -0.4 dex, due to its extreme weakness. And even so, there are high uncertainties on the derived abundances and the results might not be very reliable. Anyway, these lines are included in the next table, given the few available options.

Line	Ritz Air (Å)	log($g_i f_{ik}$)	Accuracy	Config. **Level**
N I	8680.282	0.359	B+	$2s^2 2p^2 (^3\mathbf{P}) 3s\ ^4\mathbf{P}_{5/2} \rightarrow 2s^2 2p^2 (^3\mathbf{P}) 3p\ ^4\mathbf{D}^o_{7/2}$
N I	8683.403	0.105	B+	$2s^2 2p^2 (^3\mathbf{P}) 3s\ ^4\mathbf{P}_{3/2} \rightarrow 2s^2 2p^2 (^3\mathbf{P}) 3p\ ^4\mathbf{D}^o_{5/2}$
N I	8686.149	-0.284	B+	$2s^2 2p^2 (^3\mathbf{P}) 3s\ ^4\mathbf{P}_{1/2} \rightarrow 2s^2 2p^2 (^3\mathbf{P}) 3p\ ^4\mathbf{D}^o_{3/2}$
N I	8703.247	-0.310	B+	$2s^2 2p^2 (^3\mathbf{P}) 3s\ ^4\mathbf{P}_{1/2} \rightarrow 2s^2 2p^2 (^3\mathbf{P}) 3p\ ^4\mathbf{D}^o_{1/2}$
N I	8711.703	-0.233	B+	$2s^2 2p^2 (^3\mathbf{P}) 3s\ ^4\mathbf{P}_{3/2} \rightarrow 2s^2 2p^2 (^3\mathbf{P}) 3p\ ^4\mathbf{D}^o_{3/2}$
N I	8718.837	-0.349	B+	$2s^2 2p^2 (^3\mathbf{P}) 3s\ ^4\mathbf{P}_{5/2} \rightarrow 2s^2 2p^2 (^3\mathbf{P}) 3p\ ^4\mathbf{D}^o_{5/2}$

5.6.6 Oxygen ($_8$O)

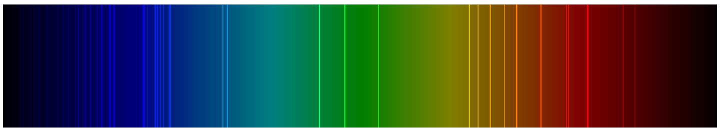

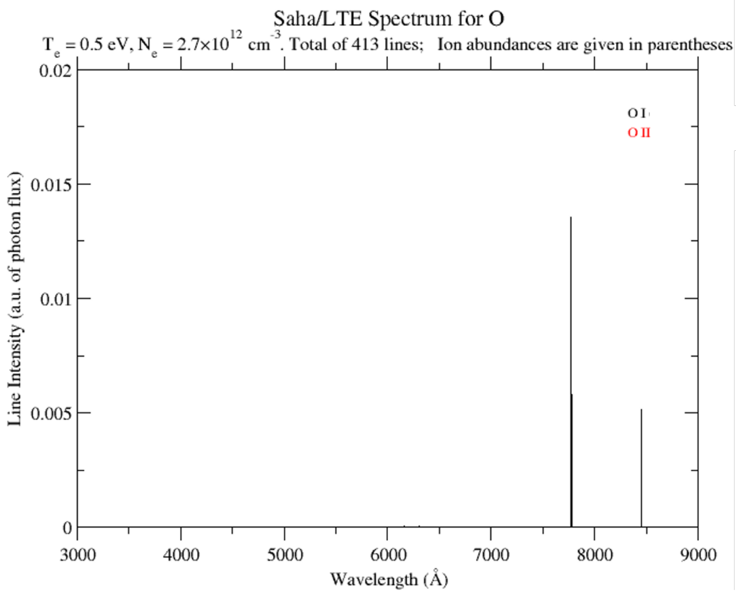

Figure 5.32: *Oxygen lines intensity. Saha-LTE Spectrum (NIST) from ad hoc conditions: electron temperature 0.5 eV and electron density of 2.7x10^{12} cm^{-3}.*

The oxygen abundance studies use the intense triplet at 777 nm. However, as reminded in Section 2.4, they are severely impacted by NLTE effects. Different authors have studied these effects, reaching corrections not always in agreement (Takeda & Honda 2005; Bensby et al. 2004; Amarsi et al. 2015, 2019b). This uncertainty is why the oxygen has been not included in the α-element index in studies like the ones by Duong et al. (2018) or Adibekyan et al. (2013).

Other lines, in visible range, have been used as the forbidden [O I] 6300 and 6363

Å lines, but they are very gravity-dependent and very weak or not present in dwarfs and sub-giants (Fulbright & Johnson 2003). Besides, the [O I] 6300 Å line is severely blended by Ni I line at high metallicities (Allende Prieto et al. 2001) and the surrounding interval, is impacted by telluric bands.

Line	Ritz Air (Å)	$\log(g_i f_{ik})$	Accuracy	Config. **Level**
	7771.944	0.369	A	$2s^2 2p^3(^4\mathbf{S}^o)3s\ ^5\mathbf{S}^o_2 \rightarrow 2s^2 2p^3(^4\mathbf{S}^o)3p\ ^5\mathbf{P}_3$
O I	7774.166	0.223	A	$2s^2 2p^3(^4\mathbf{S}^o)3s\ ^5\mathbf{S}^o_2 \rightarrow 2s^2 2p^3(^4\mathbf{S}^o)3p\ ^5\mathbf{P}_2$
	7775.388	0.002	A	$2s^2 2p^3(^4\mathbf{S}^o)3s\ ^5\mathbf{S}^o_2 \rightarrow 2s^2 2p^3(^4\mathbf{S}^o)3p\ ^5\mathbf{P}_1$
	8446.247	-0.463	B	$2s^2 2p^3(^4\mathbf{S}^o)3s\ ^3\mathbf{S}^o_1 \rightarrow 2s^2 2p^3(^4\mathbf{S}^o)3p\ ^3\mathbf{P}_0$
O I	8446.359	0.236	B	$2s^2 2p^3(^4\mathbf{S}^o)3s\ ^3\mathbf{S}^o_1 \rightarrow 2s^2 2p^3(^4\mathbf{S}^o)3p\ ^3\mathbf{P}_2$
	8446.758	0.014	B	$2s^2 2p^3(^4\mathbf{S}^o)3s\ ^3\mathbf{S}^o_1 \rightarrow 2s^2 2p^3(^4\mathbf{S}^o)3p\ ^3\mathbf{P}_1$

5.6.7 Sodium ($_{11}$Na)

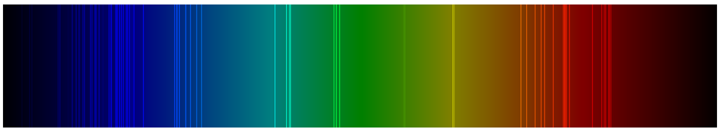

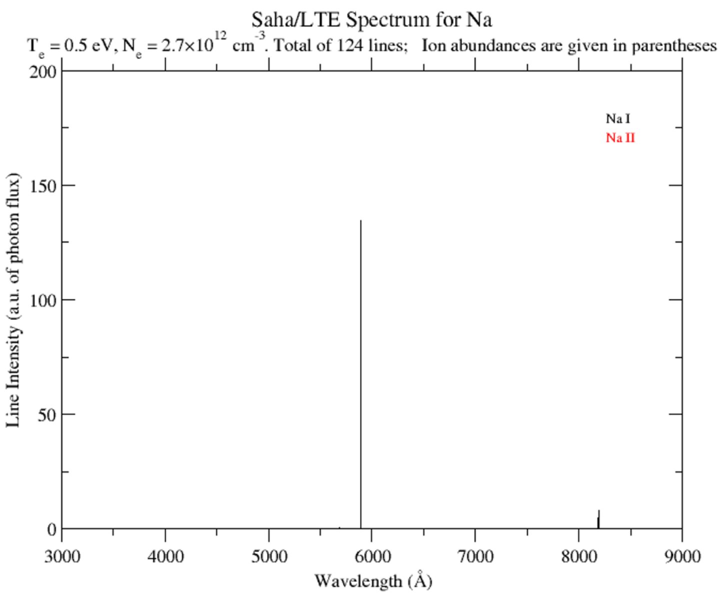

Figure 5.33: *Sodium lines intensity. Saha-LTE Spectrum (NIST) from ad hoc conditions: electron temperature 0.5 eV and electron density of 2.7x10^{12} cm^{-3}.*

The sodium is a tricky element for the abundance study. In one hand, it has a wonderful, intense doublet lines of Na I at 5890 and 5896 Å (Na-D lines). However, these lines are usually contaminated by both, artificial pollution and especially by the interstellar ISM contribution. In the Fig. 5.34 it is observed this latter contribution at a different radial velocity than the MS lines. This is not always the usual, and the lines of the ISM contribution is too often overlapping the MS ones. This contribution could be not detected, although usually it produces asymmetric or not Gaussian/Lorentzian profiles, on the contrary as expected for the unblended MS lines.

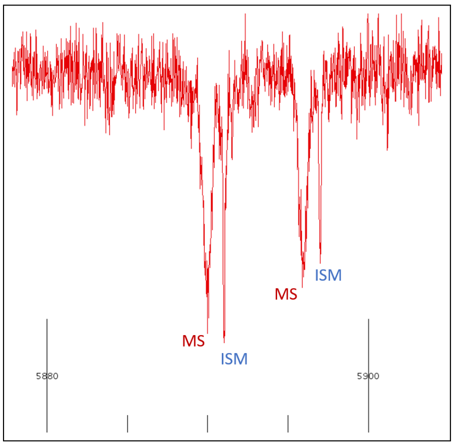

Figure 5.34: *Sodium D-lines in an MS spectrum. It is observed a redshifted duplication because the ISM contribution at different radial velocity than the MS.*

As a result, if this contribution is not disentangled, the Na abundance obtained from these lines could be strongly biased. Additionally, this resonance doublet is impacted by strong NLTE effects.

Other Na lines along the spectral range can be used, as the ones offered in the next table. Unfortunately, they are much less intense than the Na-D lines.

Line	Ritz Air (Å)	$\log(g_i f_{ik})$	Accuracy	Config. **Level**
Na I	5688.1933	-1.406	A	$2p^6 3p\ ^2\mathbf{P}^o_{3/2} \rightarrow 2p^6 4d\ ^2\mathbf{D}_{3/2}$
	5688.2047	-0.452	A	$2p^6 3p\ ^2\mathbf{P}^o_{3/2} \rightarrow 2p^6 4d\ ^2\mathbf{D}_{5/2}$
Na I	5889.9509	0.108	AA	$2p^6 3s\ ^2\mathbf{S}_{1/2} \rightarrow 2p^6 3p\ ^2\mathbf{P}^o_{3/2}$
	5895.9242	-0.194	AA	$2p^6 3s\ ^2\mathbf{S}_{1/2} \rightarrow 2p^6 3p\ ^2\mathbf{P}^o_{1/2}$
Na I	6154.2253	-1.547	A	$2p^6 3p\ ^2\mathbf{P}^o_{1/2} \rightarrow 2p^6 5s\ ^2\mathbf{S}_{1/2}$
Na I	6160.7471	-1.246	A	$2p^6 3p\ ^2\mathbf{P}^o_{3/2} \rightarrow 2p^6 5s\ ^2\mathbf{S}_{1/2}$

5.6.8 Magnesium ($_{12}$Mg)

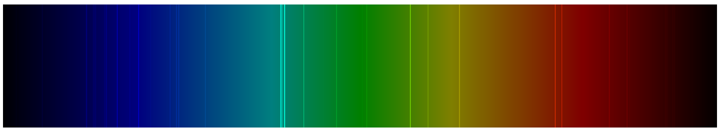

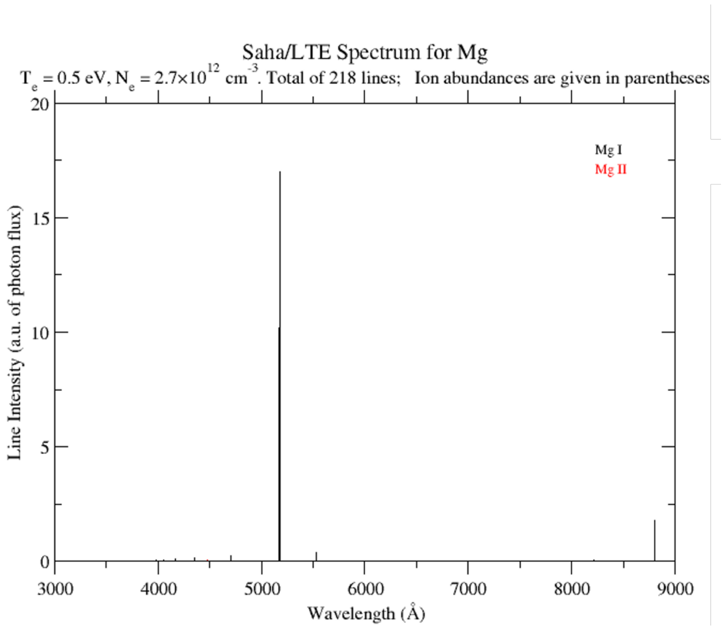

Figure 5.35: *Magnesium lines intensity. Saha-LTE Spectrum (NIST) from ad hoc conditions: electron temperature 0.5 eV and electron density of 2.7x10^{12} cm^{-3}.*

The triplet Mg I at 516-8 nm interval are the strongest available lines. As commented in Section 2.7, could be impacted by NLTE effects, though moderately (-0.2 dex at most, Romano et al. (2010)), at metal poor range. Besides, they are saturated lines and less sensitive to the abundances.

Nevertheless, other less intense but non-saturated lines are available. Main are included in the next table. However, some of them, are showing high uncertainties in their strength determinations.

5.6.9 Aluminium ($_{13}$Al)

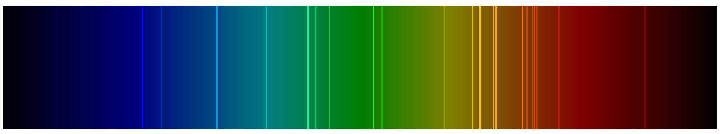

Line	Ritz Air (Å)	$\log(g_i f_{ik})$	Accuracy	Config. **Level**
Mg I]	4571.0956	-5.623	D	$2p^6 3s^2\ ^1\mathbf{S}_0 \rightarrow 3s3p\ ^3\mathbf{P}^o_0$
Mg I	4702.9908	-0.440	B+	$3s3p\ ^1\mathbf{P}^o_1 \rightarrow 3s5d\ ^1\mathbf{D}_2$
Mg I	4730.0286	-2.347	C+	$3s3p\ ^1\mathbf{P}^o_1 \rightarrow 3s6s\ ^1\mathbf{S}_0$
Mg I	5167.3213	-0.870	B+	$3s3p\ ^3\mathbf{P}^o_0 \rightarrow 3s4s\ ^3\mathbf{S}_1$
Mg I	5172.6844	-0.393	B+	$3s3p\ ^3\mathbf{P}^o_1 \rightarrow 3s4s\ ^3\mathbf{S}_1$
Mg I	5183.6043	-0.167	A	$3s3p\ ^3\mathbf{P}^o_2 \rightarrow 3s4s\ ^3\mathbf{S}_1$
Mg I	5711.0880	-1.724	B	$3s3p\ ^1\mathbf{P}^o_1 \rightarrow 3s5s\ ^1\mathbf{S}_0$
Mg I	8717.825	-0.941	D+	$3s4p\ ^3\mathbf{P}^o_2 \rightarrow 3s7d\ ^3\mathbf{D}_3$
Mg I	8736.006	-0.886	D+	$3s3d\ ^3\mathbf{D}_2 \rightarrow 3s7f\ ^3\mathbf{F}^o_3$
	8736.020	-0.725	C	$3s3d\ ^3\mathbf{D}_3 \rightarrow 3s7f\ ^3\mathbf{F}^o_4$
	8736.029	-1.056	D+	$3s3d\ ^3\mathbf{D}_1 \rightarrow 3s7f\ ^3\mathbf{F}^o_2$

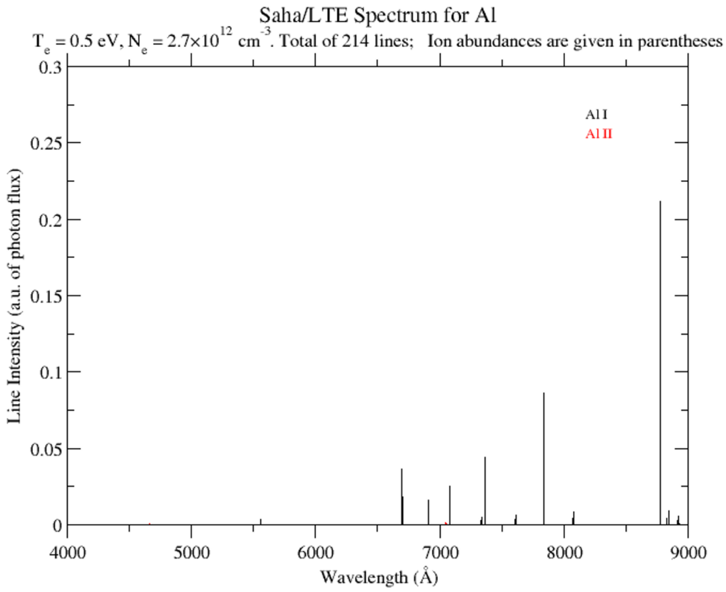

Figure 5.36: *Aluminium lines intensity. Saha-LTE Spectrum (NIST) from ad hoc conditions: electron temperature 0.5 eV and electron density of 2.7x10^{12} cm^{-3}. For avoiding excessive scaling (resonance lines) and improving detail of minority lines, range < 4000 Å has been cut.*

Resonance lines, at 3944 and 3961 Å, have been historically used. However, they suffer from large uncertainties, and are located in the vicinity of the H and K Ca lines. Besides, the line 3944 Å is often severely blended by CH lines. This is why other less strong doublets as the included in the following table are used for the aluminium abundance studies.

Line	Ritz Air (Å)	$\log(g_i f_{ik})$	Accuracy	Config. **Level**
Al I	3944.0060	-0.635	B+	$3s^2 3p\ ^2\mathbf{P}^o_{1/2} \rightarrow 3s^2 4s\ ^2\mathbf{S}_{1/2}$
Al I	3961.5201	-0.333	B+	$3s^2 3p\ ^2\mathbf{P}^o_{3/2} \rightarrow 3s^2 4s\ ^2\mathbf{S}_{1/2}$
Al I	6696.018	-1.569	C+	$3s^2 4s\ ^2\mathbf{S}_{1/2} \rightarrow 3s^2 5p\ ^2\mathbf{P}^o_{3/2}$
	6698.667	-1.870	C+	$3s^2 4s\ ^2\mathbf{S}_{1/2} \rightarrow 3s^2 5p\ ^2\mathbf{P}^o_{1/2}$
Al I	7835.309	-1.834	B	$3s^2 3d\ ^2\mathbf{D}_{3/2} \rightarrow 3s^2 6f\ ^3\mathbf{F}^o_{5/2}$
	7836.134	-1.834	C+	$3s^2 3d\ ^2\mathbf{D}_{5/2} \rightarrow 3s^2 6f\ ^3\mathbf{F}^o_{5/2}$
	7836.134	-0.534	B+	$3s^2 3d\ ^2\mathbf{D}_{5/2} \rightarrow 3s^2 6f\ ^3\mathbf{F}^o_{7/2}$
Al I	8772.871	-0.349	B+	$3s^2 3d\ ^2\mathbf{D}_{3/2} \rightarrow 3s^2 5f\ ^2\mathbf{F}^o_{5/2}$
	8773.902	-0.192	B+	$3s^2 3d\ ^2\mathbf{D}_{5/2} \rightarrow 3s^2 5f\ ^2\mathbf{F}^o_{7/2}$
	8773.905	-1.495	C+	$3s^2 3d\ ^2\mathbf{D}_{5/2} \rightarrow 3s^2 5f\ ^2\mathbf{F}^o_{5/2}$

5.6.10 Silicon ($_{14}$Si)

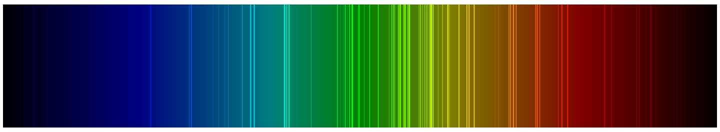

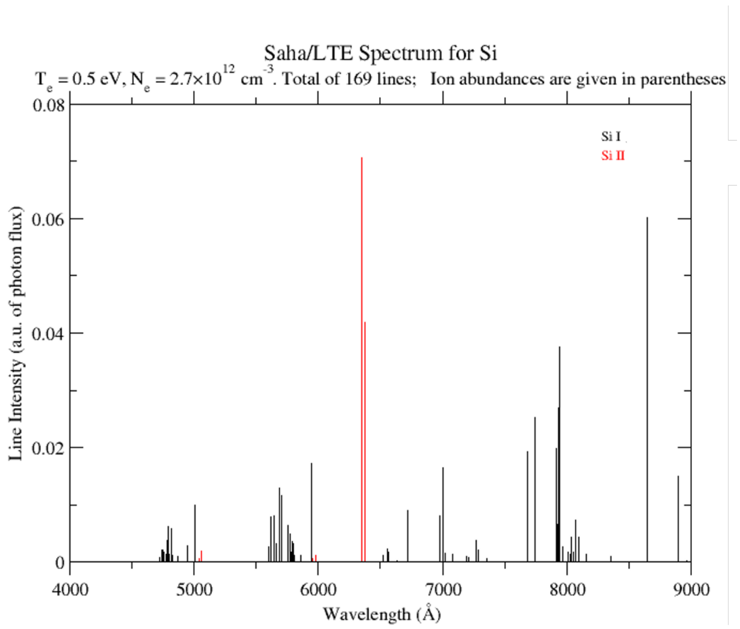

Figure 5.37: *Silicon lines intensity. Saha-LTE Spectrum (NIST) from ad hoc conditions: electron temperature 0.5 eV and electron density of 2.7x10^{12} cm^{-3}. For avoiding excessive scaling (lines 3905 and 4102) and improving detail of minority lines, range < 4200 Å has been cut.*

Regarding the Si lines, see discussion in section 2.9. Summarizing, strong lines Si I, at

3905 and 4102 Å are affected by different considerations that advice against their use in abundance studies.

Si I or Si II lines are impacted by significant NLTE effects. Positive in the case of Si I lines and negative when involving Si II lines as 6347 and 6371 Å ones (Shi et al. 2009). Nevertheless, weaker lines than 3905 and 4102 Å, are less impacted, and used for deriving abundances.

The number of available lines is large, and some of the main bibliographic lines used in abundance studies are included in the next table.

Line	Ritz Air (Å)	$\log(g_i f_{ik})$	Accuracy	Config. **Level**
Si I	5701.104	-2.050	D	$3s^2 3p4s\ ^3\mathbf{P}^o_1 \rightarrow 3s^2 3p5p\ ^3\mathbf{P}_0$
Si I	5772.146	-1.750	D+	$3s^2 3p4s\ ^1\mathbf{P}^o_1 \rightarrow 3s^2 3p5p\ ^1\mathbf{P}_0$
Si I	6142.487[a]	–1.48	*	$3s3p^3\ ^3\mathbf{D}^o_3 \rightarrow 5f\ ^3\mathbf{D}_3$
Si I	6145.015[a]	–1.39	*	$3s3p^3\ ^3\mathbf{D}^o_2 \rightarrow 5f\ ^3\mathbf{G}_3$
Si I	6155.134[a]	-0.78	*	$3s3p^3\ ^3\mathbf{D}^o_3 \rightarrow 5f\ ^3\mathbf{G}_4$
Si I	6237.320[a]	-1.08	*	$3s3p^3\ ^3\mathbf{D}^o_1 \rightarrow 5f\ ^3\mathbf{F}_2$
Si I	6243.813[a]	-1.29	*	$3s3p^3\ ^3\mathbf{D}^o_2 \rightarrow 5f\ ^3\mathbf{F}_3$
Si I	6244.468[a]	-1.29	*	$3s3p^3\ ^3\mathbf{D}^o_2 \rightarrow 5f\ ^1\mathbf{D}_2$
Si II	6347.11	0.149	B+	$3s^2 4s\ ^2\mathbf{S}_{1/2} \rightarrow 3s^2 4p\ ^2\mathbf{P}^o_{3/2}$
Si II	6371.37	-0.082	C+	$3s^2 4s\ ^2\mathbf{S}_{1/2} \rightarrow 3s^2 4p\ ^2\mathbf{P}^o_{1/2}$
Si I	6721.848	-0.94	D	$3s^2 3p4p\ ^1\mathbf{P}_1 \rightarrow 3s^2 3p6d\ ^1\mathbf{D}^o_2$
Si I	6741.64[a]	–1.57	*	$3s^2 3p4p\ ^3\mathbf{D}^o_3 \rightarrow 8s\ ^3\mathbf{P}_2$
Si I	8728.011[a]	-0.38	*	$3s^2 3p3d\ ^3\mathbf{F}^o_2 \rightarrow 5f\ ^3\mathbf{F}_3$
Si I	8742.451[a]	-0.36	*	$3s^2 3p3d\ ^1\mathbf{D}^o_2 \rightarrow 5f\ ^3\mathbf{F}_3$
Si I	8752.009[a]	-0.19	*	$3s^2 3p3d\ ^1\mathbf{D}^o_2 \rightarrow 4f\ ^1\mathbf{F}_3$

a: Ritz, not available in NIST. Instead, observed wave. log(gf) and electronic transitions from Shi et al. (2011).

5.6.11 Sulphur ($_{16}$S)

Sulphur lines and their correspondent abundance studies are controversial. For the lines discussion and, especially, their implications in the abundance studies, please see section 2.10. Summarizing, historical abundance studies have based in high excitation lines in the near-IR as 8693.2 & 8694.0 & 8694.6 or 9212.9 & 9228.1 & 9237.5 Å. However, the galactic evolution abundance profiles arisen has not been always coincident.

The 8693/8694 lines, after applying NLTE corrections, seem systematically yielding higher abundances over the 9212 and 9237 lines studies. Other historically used line, at

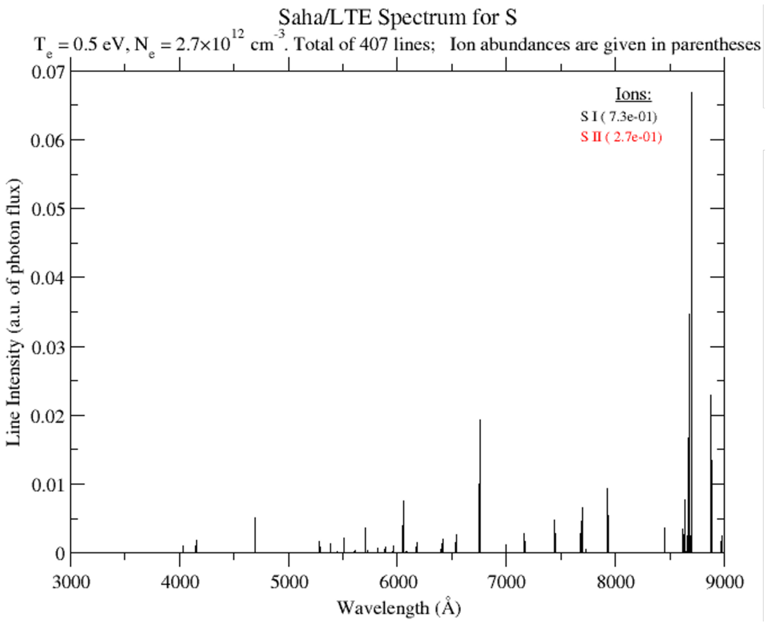

Figure 5.38: *Sulphur lines intensity. Saha-LTE Spectrum (NIST) from ad hoc conditions: electron temperature 0.5 eV and electron density of 2.7x10*^{12} *cm*$^{-3}$*. The range is limited up to 9000 Å, and therefore, the strong S* I *lines at 9213 and 9237 are not included in this plot.*

8680 Å, is blended with a Si I line. On the other hand, the 9212 and 9237 lines, suffer from strong NLTE effects. In addition, they can be impacted by the wings of the Paschen-ζ hydrogen line at 9229, or telluric lines as well. Eventually, they are lines that can out range the limits of the available spectrum.

Additional lines at 6743 and 6757 Å have been lately used. However, they could be too faint for developing studies in extremely metal poor stars. This has led to the exploring of an IR line at 1045 nm in some studies.

Line	Ritz Air (Å)	log($g_i f_{ik}$)	Accuracy	Config. **Level**
S I	6743.54	-1.065	D+	$3s^23p^3(^4\mathbf{S}^o)4p\ ^5\mathbf{P}_1 \rightarrow 3s^23p^3(^4\mathbf{S}^o)5d\ ^5\mathbf{D}^o_2$
S I	6748.79	-0.638	D+	$3s^23p^3(^4\mathbf{S}^o)4p\ ^5\mathbf{P}_2 \rightarrow 3s^23p^3(^4\mathbf{S}^o)5d\ ^5\mathbf{D}^o_3$
S I	6757.15	-0.351	D+	$3s^23p^3(^4\mathbf{S}^o)4p\ ^5\mathbf{P}_3 \rightarrow 3s^23p^3(^4\mathbf{S}^o)5d\ ^5\mathbf{D}^o_4$
S I	8680.46	-0.237	C	$3s^23p^3(^4\mathbf{S}^o)4p\ ^5\mathbf{P}_2 \rightarrow 3s^23p^3(^4\mathbf{S}^o)4d\ ^5\mathbf{D}^o_3$
S I	8693.16	-1.380	D+	$3s^23p^3(^4\mathbf{S}^o)4p\ ^5\mathbf{P}_3 \rightarrow 3s^23p^3(^4\mathbf{S}^o)5d\ ^5\mathbf{D}^o_2$
S I	8693.98	-0.535	D+	$3s^23p^3(^4\mathbf{S}^o)4p\ ^5\mathbf{P}_3 \rightarrow 3s^23p^3(^4\mathbf{S}^o)5d\ ^5\mathbf{D}^o_3$
S I	8694.71	0.052	C	$3s^23p^3(^4\mathbf{S}^o)4p\ ^5\mathbf{P}_3 \rightarrow 3s^23p^3(^4\mathbf{S}^o)5d\ ^5\mathbf{D}^o_4$
S I	9212.863	0.395	C	$3s^23p^3(^4\mathbf{S}^o)4s\ ^5\mathbf{S}^o_2 \rightarrow 3s^23p^3(^4\mathbf{S}^o)4p\ ^5\mathbf{P}_3$
S I	9237.538	0.025	C	$3s^23p^3(^4\mathbf{S}^o)4s\ ^5\mathbf{S}^o_2 \rightarrow 3s^23p^3(^4\mathbf{S}^o)4p\ ^5\mathbf{P}_1$

5.6.12 Potassium ($_{19}$K)

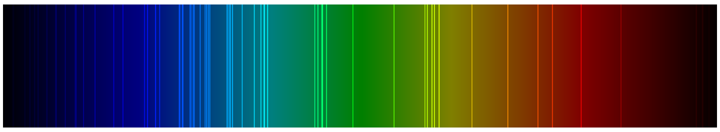

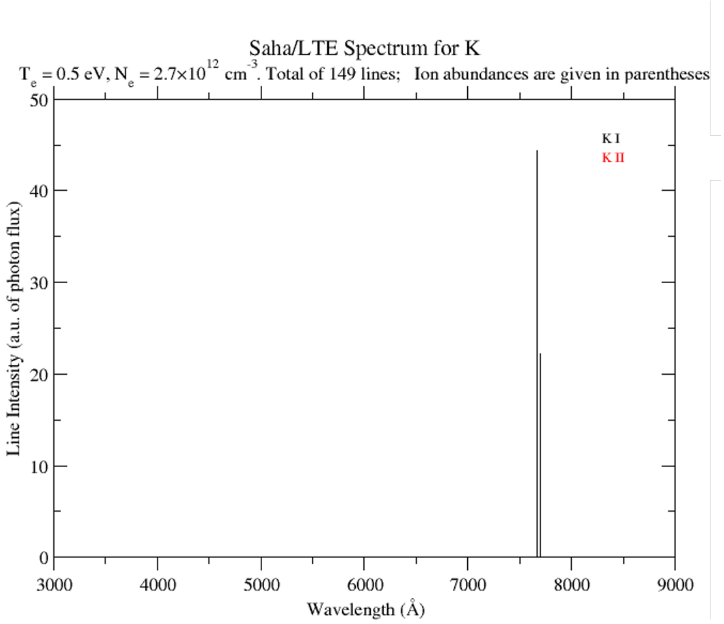

Figure 5.39: *Potassium lines intensity. Saha-LTE Spectrum (NIST) from ad hoc conditions: electron temperature 0.5 eV and electron density of 2.7x10^{12} cm^{-3}.*

Two are the only available lines, the resonance K I 7664 and 7698 Å, for using in potassium abundance studies. Both strong and reliably determined oscillator strengths. However, they suffer from important NLTE effects (see Fig. 2.74 in section 2.11).

Especially, the K I 7664 line is embedded into a telluric interval, and there is to apply a disentangling method for its use. On the other hand, although not often, they could be blended with ISM's neutral atomic potassium contribution.

Line	Ritz Air (Å)	log($g_i f_{ik}$)	Accuracy	Config. **Level**
K I	7664.899	0.125	AAA	$3p^6 4s\ ^2\mathbf{S}_{1/2} \rightarrow 3p^6 4p\ ^2\mathbf{P}^o_{3/2}$
K I	7698.965	-0.178	AAA	$3p^6 4s\ ^2\mathbf{S}_{1/2} \rightarrow 3p^6 4p\ ^2\mathbf{P}^o_{1/2}$

5.6.13 Calcium ($_{20}$Ca)

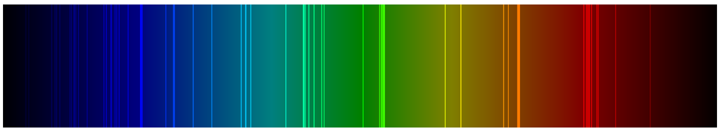

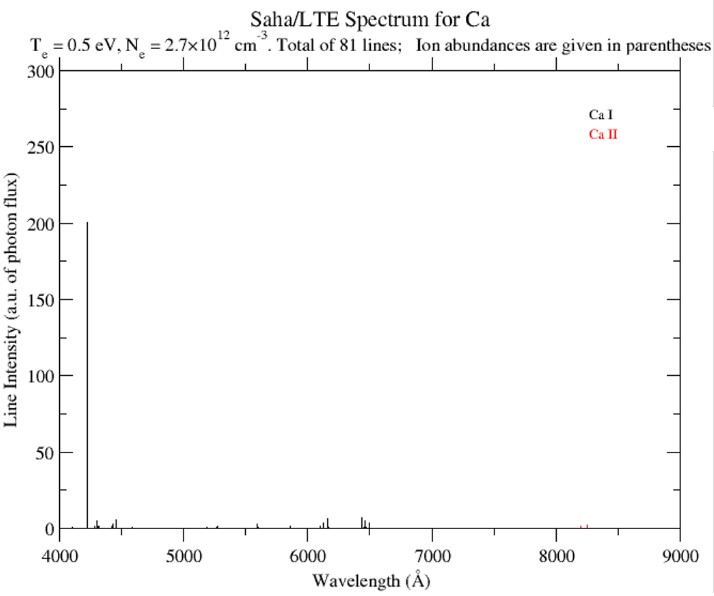

Figure 5.40: *Calcium lines intensity. Saha-LTE Spectrum (NIST) from ad hoc conditions: electron temperature 0.5 eV and electron density of 2.7x10^{12} cm^{-3}. The range is limited up to 8400 Å, and a minimum limit of 4000 Å and therefore, strong although problematic Ca II resonance lines at 3933 and 3968, and the IR triplet at 8498, 8542 and 8662, greatly exceeding the intensity scale of this plot, are not included.*

As commented in the caption of the saha spectrum figure, strong resonance Ca H+K lines at 3933 and 3968 are avoided. In one hand, they are formed in at slightly different heights in the chromosphere, therefore they are not photospheric and thus dependent on the chromospheric activities. And on the other, they are usually contaminated by a strong ISM contributions.

Regarding the strong triplet lines at IR, they suffer significant departures from LTE conditions (Osorio et al. 2022), and on the other hand, they could saturate in metal rich stars. In addition, great care has to be paid in their spectra reduction, as the triplet interval could overlap with a multitude of strong sky emission lines if they are not properly subtracted (Usher et al. 2019). Thus, their use is often limited to the study of extremely metal poor stars, in which they are among the few features available for inferring the star metallicity.

In the abundance studies of mildly metal poor stars, other non-saturated, weaker Ca I lines along the spectrum are used as the sample of lines from the next table.

Line	Ritz Air (Å)	$\log(g_i f_{ik})$	Accuracy	Config. **Level**
Ca I	4512.27	-2.02[a]	*	*
Ca I	4526.928	-0.42	D	$3p^63d4s\ ^1\mathbf{D}_2 \rightarrow 3p^64snp\ \mathbf{w}^1\mathbf{P}^o_1$
Ca I	4578.551	-0.558	C	$3p^63d4s\ ^3\mathbf{D}_1 \rightarrow 3p^64s4f\ ^3\mathbf{F}^o_2$
Ca I	4581.395	-0.337	C	$3p^63d4s\ ^3\mathbf{D}_2 \rightarrow 3p^64s4f\ ^3\mathbf{F}^o_3$
Ca I	4581.467	-1.26	D	$3p^63d4s\ ^3\mathbf{D}_2 \rightarrow 3p^64s4f\ ^3\mathbf{F}^o_2$
Ca I	4585.865	-0.187	C	$3p^63d4s\ ^3\mathbf{D}_3 \rightarrow 3p^64s4f\ ^3\mathbf{F}^o_4$
Ca I	4585.964	-1.26	D	$3p^63d4s\ ^3\mathbf{D}_3 \rightarrow 3p^64s4f\ ^3\mathbf{F}^o_3$
Ca I	5261.704	-0.73	D	$3p^63d4s\ ^3\mathbf{D}_1 \rightarrow 3p^63d4p\ ^3\mathbf{P}^o_1$
Ca I	5349.47	-0.581[b]	*	$3p^63d4s\ ^1\mathbf{D}_2 \rightarrow 3p^63d4p\ ^1\mathbf{F}^o_3$
Ca I	5867.56	–1.592[b]	*	*
Ca I	6122.217	-0.315	C	$3p^64s4p\ ^3\mathbf{P}^o_1 \rightarrow 3p^64s5s\ ^3\mathbf{S}_1$
Ca I	6156.023	-2.18	E	$3p^63d4s\ ^3\mathbf{D}_1 \rightarrow 3p^64s5p\ ^3\mathbf{P}^o_2$
Ca I	6161.297	-1.03	D	$3p^63d4s\ ^3\mathbf{D}_2 \rightarrow 3p^64s5p\ ^3\mathbf{P}^o_2$
Ca I	6166.439	-0.90	D	$3p^63d4s\ ^3\mathbf{D}_1 \rightarrow 3p^64s5p\ ^3\mathbf{P}^o_0$
Ca I	6169.042	-0.54	D	$3p^63d4s\ ^3\mathbf{D}_2 \rightarrow 3p^64s5p\ ^3\mathbf{P}^o_1$
Ca I	6169.563	-0.27	D	$3p^63d4s\ ^3\mathbf{D}_3 \rightarrow 3p^64s5p\ ^3\mathbf{P}^o_2$
Ca I	6439.075	0.47	D	$3p^63d4s\ ^3\mathbf{D}_3 \rightarrow 3p^63d4p\ ^3\mathbf{F}^o_4$
Ca I	6449.808	-0.55	D	$3p^63d4s\ ^3\mathbf{D}_1 \rightarrow 3p^63d4p\ ^1\mathbf{D}^o_2$
Ca I	6455.598	-1.36	E	$3p^63d4s\ ^3\mathbf{D}_2 \rightarrow 3p^63d4p\ ^1\mathbf{D}^o_2$
Ca I	6471.662	-0.59	D	$3p^63d4s\ ^3\mathbf{D}_3 \rightarrow 3p^63d4p\ ^3\mathbf{F}^o_3$
Ca I	6717.681	-0.61	E	$3p^63d4s\ ^1\mathbf{D}_2 \rightarrow 3p^64s5p\ ^1\mathbf{P}^o_1$

a: Not available in NIST. Wave and log(gf) from Bensby et al. (2014).
b: Not available in NIST. Wave and log(gf) from Neves et al. (2009).

5.6.14 Scandium ($_{21}$Sc)

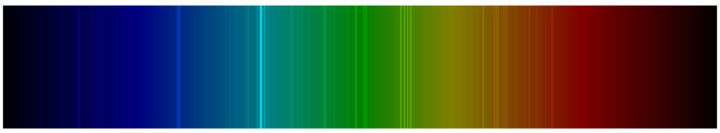

Lines from ionized scandium are generally used. However, their strongest lines are located in the UV-A range. Other weaker Sc II lines spread along the visible range are instead available. Most relevant are shown in the next table.

There is no in-depth study on NLTE effects, although it is expected to be negligible from the only study by Zhang et al. (2008) applied to Sun Sc II lines.

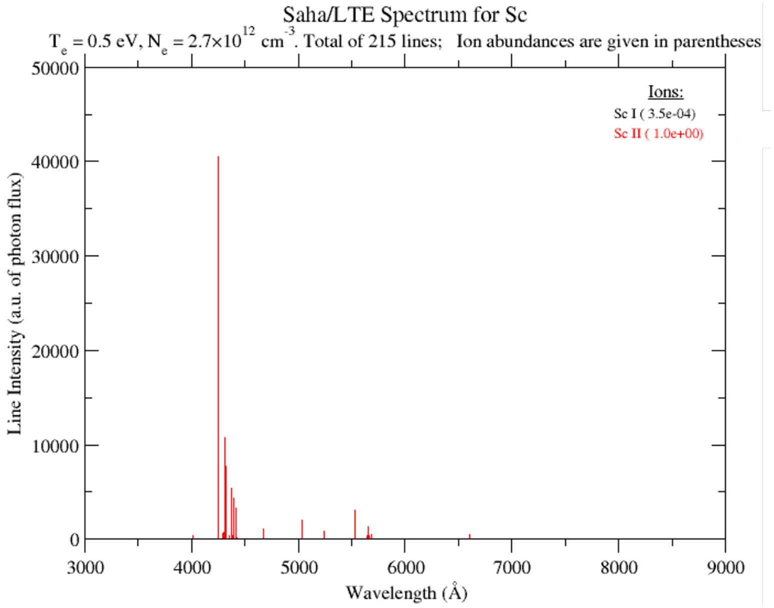

Figure 5.41: *Scandium lines intensity. Saha-LTE Spectrum (NIST) from ad hoc conditions: electron temperature 0.5 eV and electron density of 2.7x10^{12} cm^{-3}.*

Line	Ritz Air (Å)	log($g_i f_{ik}$)	Accuracy	Config. **Level**
Sc II	4246.822	0.242	A’	$3p^6 3d4s\ ^1\mathbf{D_2} \rightarrow 3p^6 3d4p\ ^1\mathbf{D}^o_2$
Sc II	4400.389	-0.54	B’	$3p^6 3d^2\ ^3\mathbf{F_3} \rightarrow 3p^6 3d4p\ ^3\mathbf{F}^o_3$
Sc II	4670.407	-0.58	B’	$3p^6 3d^2\ ^1\mathbf{D_2} \rightarrow 3p^6 3d4p\ ^1\mathbf{F}^o_3$
Sc II	5031.021	-0.40	B’	$3p^6 3d^2\ ^1\mathbf{D_2} \rightarrow 3p^6 3d4p\ ^1\mathbf{P}^o_1$
Sc II	5239.813	-0.77	B’	$3p^6 4s^2\ ^1\mathbf{S_0} \rightarrow 3p^6 3d4p\ ^1\mathbf{P}^o_1$
Sc II	5526.790	0.02	C+	$3p^6 3d^2\ ^1\mathbf{G_4} \rightarrow 3p^6 3d4p\ ^1\mathbf{F}^o_3$
Sc II	5641.001	-1.13	C+	$3p^6 3d^2\ ^3\mathbf{P_1} \rightarrow 3p^6 3d4p\ ^3\mathbf{P}^o_2$
Sc II	5657.896	-0.60	B’	$3p^6 3d^2\ ^3\mathbf{P_2} \rightarrow 3p^6 3d4p\ ^3\mathbf{P}^o_2$
Sc II	6245.637	–1.022[a]	*	$3p^6 3d^2\ ^3\mathbf{P_2} \rightarrow 3p^6 3d4p\ ^3\mathbf{D}^o_3$
Sc II	6604.601	-1.31	D+	$3p^6 3d^2\ ^1\mathbf{D_2} \rightarrow 3p^6 3d4p\ ^1\mathbf{D}^o_2$

a: Not available in NIST. Log(gf) from Neves et al. (2009).

5.6.15 Titanium ($_{22}$Ti)

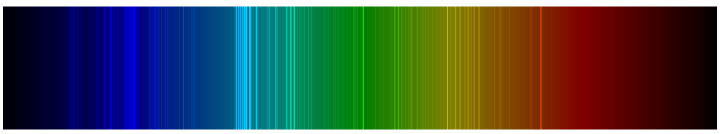

The available Ti I and Ti II lines are wide in the bluer interval of the visible spectra. Next, only a sample of the numerous lines used in bibliography.

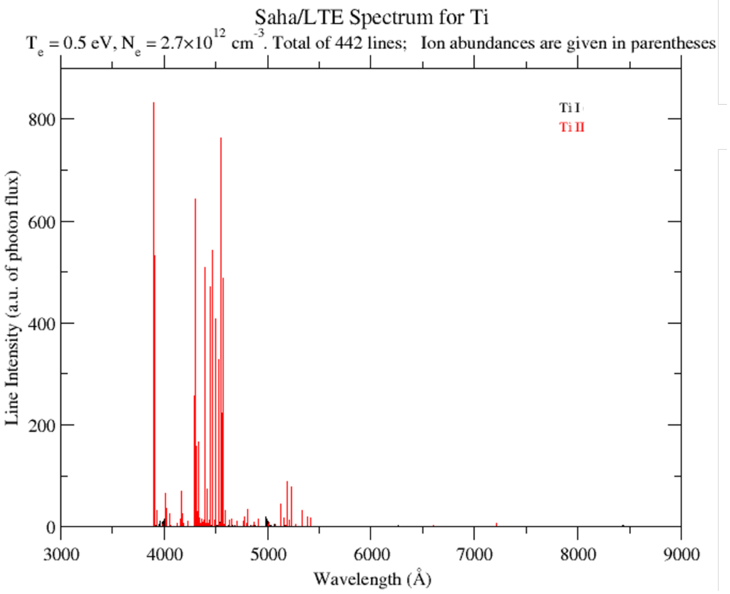

Figure 5.42: *Titanium lines intensity. Saha-LTE Spectrum (NIST) from ad hoc conditions: electron temperature 0.5 eV and electron density of 2.7x10^{12} cm^{-3}.*

Line	Ritz Air (Å)	$\log(g_i f_{ik})$	Accuracy	Config. **Level**
Ti I	4512.7339	-0.480	C+	$3d^3(^4\mathbf{F})4s\ \mathbf{a^5F_4} \rightarrow 3d^3(^4\mathbf{F})4f\ \mathbf{y^5F^o_5}$
Ti I	4518.0220	-0.324	C+	$3d^3(^4\mathbf{F})4s\ \mathbf{a^5F_3} \rightarrow 3d^3(^4\mathbf{F})4f\ \mathbf{y^5F^o_4}$
Ti I	4555.4829	-0.488	C+	$3d^3(^4\mathbf{F})4s\ \mathbf{a^5F_5} \rightarrow 3d^3(^4\mathbf{F})4f\ \mathbf{y^5F^o_4}$
Ti I	4562.6271	-2.594	A	$3d^24s^2\ \mathbf{a^3F_3} \rightarrow 3d^2(^3\mathbf{F})4s4p(^3\mathbf{P}^o)\ \mathbf{z^1D^o_2}$
Ti I	4617.2689	0.389	C+	$3d^3(^4\mathbf{P})4s\ \mathbf{a^5P_3} \rightarrow 3d^3(^4\mathbf{P})4p\ \mathbf{w^5D^o_4}$
Ti I	4623.0972	0.110	C+	$3d^3(^4\mathbf{P})4s\ \mathbf{a^5P_2} \rightarrow 3d^3(^4\mathbf{P})4p\ \mathbf{w^5D^o_3}$
Ti I	4656.4693	-1.283	A	$3d^24s^2\ \mathbf{a^3F_2} \rightarrow 3d^2(^3\mathbf{F})4s4p(^3\mathbf{P}^o)\ \mathbf{z^3G^o_3}$
Ti I	4758.1178	0.425	C+	$3d^3(^2\mathbf{H})4s\ \mathbf{a^3H_5} \rightarrow 3d^3(^2\mathbf{H})4p\ \mathbf{x^3H^o_5}$
Ti I	4820.4094	-0.439	C+	$3d^24s^2\ \mathbf{a^1G_4} \rightarrow 3d^2(^1\mathbf{D})4s4p(^1\mathbf{P}^o)\ \mathbf{y^1F^o_3}$
Ti I	4840.8737	-0.510	C+	$3d^24s^2\ \mathbf{a^1D_2} \rightarrow 3d^2(^1\mathbf{D})4s4p(^1\mathbf{P}^o)\ \mathbf{y^1D^o_2}$
Ti I	4913.6134	0.161	C+	$3d^3(^2\mathbf{G})4s\ \mathbf{a^3G_3} \rightarrow 3d^3(^2\mathbf{G})4p\ \mathbf{y^3H^o_4}$
Ti I	4981.7305	0.504	C+	$3d^3(^4\mathbf{F})4s\ \mathbf{a^5F_5} \rightarrow 3d^3(^4\mathbf{F})4p\ \mathbf{y^5G^o_6}$
Ti I	5016.1609	-0.574	C+	$3d^3(^4\mathbf{F})4s\ \mathbf{a^5F_5} \rightarrow 3d^3(^4\mathbf{F})4p\ \mathbf{y^5G^o_5}$
Ti I	5022.8679	-0.434	C+	$3d^3(^4\mathbf{F})4s\ \mathbf{a^5F_3} \rightarrow 3d^3(^4\mathbf{F})4p\ \mathbf{y^5G^o_3}$
Ti I	5024.8444	-0.602	C+	$3d^3(^4\mathbf{F})4s\ \mathbf{a^5F_2} \rightarrow 3d^3(^4\mathbf{F})4p\ \mathbf{y^5G^o_2}$
Ti I	5039.9574	-1.068	A	$3d^24s^2\ \mathbf{a^3F_3} \rightarrow 3d^2(^3\mathbf{F})4s4p(^3\mathbf{P}^o)\ \mathbf{z^3D^o_2}$
Ti I	5064.6526	-0.929	A	$3d^24s^2\ \mathbf{a^3F_4} \rightarrow 3d^2(^3\mathbf{F})4s4p(^3\mathbf{P}^o)\ \mathbf{z^3D^o_3}$
Ti I	5113.4401	-0.783	C+	$3d^3(^4\mathbf{F})4s\ \mathbf{b^3F_3} \rightarrow 3d^2(^3\mathbf{P})4s4p(^3\mathbf{P}^o)\ \mathbf{v^3D^o_2}$
Ti I	5145.4602	-0.574	C+	$3d^3(^4\mathbf{F})4s\ \mathbf{b^3F_4} \rightarrow 3d^2(^3\mathbf{P})4s4p(^3\mathbf{P}^o)\ \mathbf{v^3D^o_3}$
Ti I	5219.7015	-2.26	C+	$3d^24s^2\ \mathbf{a^3F_3} \rightarrow 3d^2(^3\mathbf{F})4s4p(^3\mathbf{P}^o)\ \mathbf{z^3F^o_2}$
Ti I	5426.2494	-2.944	A	$3d^24s^2\ \mathbf{a^3F_3} \rightarrow 3d^2(^3\mathbf{F})4s4p(^3\mathbf{P}^o)\ \mathbf{z^5S^o_3}$
Ti I	5490.1477	-0.933	C+	$3d^3(^4\mathbf{F})4s\ \mathbf{b^3F_4} \rightarrow 3d^3(^4\mathbf{F})4p\ \mathbf{x^5D^o_3}$
Ti I	5662.1516	0.01	B+	$3d^2(^3\mathbf{F})4s4p(^3\mathbf{P}^o)\ \mathbf{z^5D^o_4} \rightarrow 3d^24s(^4\mathbf{F})5s\ \mathbf{e^5F_5}$
Ti I	5866.4513	-0.840	C+	$3d^24s^2\ \mathbf{a^3P_2} \rightarrow 3d^3(^4\mathbf{F})4p\ \mathbf{y^3D^o_3}$
Ti I	6064.6260	-1.944	C+	$3d^24s^2\ \mathbf{a^3P_0} \rightarrow 3d^2(^3\mathbf{P})4s4p(^3\mathbf{P}^o)\ \mathbf{z^3S^o_1}$
Ti I	6091.1710	-0.423	C+	$3d^3(^2\mathbf{G})4s\ \mathbf{b^1G_4} \rightarrow 3d^3(^2\mathbf{G})4p\ \mathbf{z^1H^o_5}$
Ti I	6126.2161	-1.424	C+	$3d^24s^2\ \mathbf{a^3P_2} \rightarrow 3d^2(^3\mathbf{P})4s4p(^3\mathbf{P}^o)\ \mathbf{z^3S^o_1}$
Ti I	6258.1016	-0.355	C+	$3d^3(^4\mathbf{F})4s\ \mathbf{b^3F_3} \rightarrow 3d^2(^3\mathbf{F})4s4p(^1\mathbf{P}^o)\ \mathbf{y^3G^o_4}$
Ti I	6258.7069	-0.24	C	$3d^3(^4\mathbf{F})4s\ \mathbf{b^3F_4} \rightarrow 3d^2(^3\mathbf{F})4s4p(^1\mathbf{P}^o)\ \mathbf{y^3G^o_5}$
Ti I	6261.0988	-0.479	C+	$3d^3(^4\mathbf{F})4s\ \mathbf{b^3F_2} \rightarrow 3d^2(^3\mathbf{F})4s4p(^1\mathbf{P}^o)\ \mathbf{y^3G^o_3}$
Ti I	6599.1058	-2.085	C+	$3d^24s^2\ \mathbf{a^1D_2} \rightarrow 3d^2(^3\mathbf{F})4s4p(^3\mathbf{P}^o)\ \mathbf{z^1F^o_3}$
Ti I	8377.861	-1.59	B	$3d^3(^4\mathbf{F})4s\ \mathbf{a^3F_3} \rightarrow 3d^2(^3\mathbf{F})4s4p(^3\mathbf{P}^o)\ \mathbf{z^5D^o_3}$
Ti I	8412.357	-1.39	B	$3d^3(^4\mathbf{F})4s\ \mathbf{a^5F_2} \rightarrow 3d^2(^3\mathbf{F})4s4p(^3\mathbf{P}^o)\ \mathbf{z^5D^o_1}$
Ti I	8426.507	-1.20	B	$3d^3(^4\mathbf{F})4s\ \mathbf{a^5F_3} \rightarrow 3d^2(^3\mathbf{F})4s4p(^3\mathbf{P}^o)\ \mathbf{z^5D^o_2}$
Ti I	8434.954	-0.83	B	$3d^3(^4\mathbf{F})4s\ \mathbf{a^5F_5} \rightarrow 3d^2(^3\mathbf{F})4s4p(^3\mathbf{P}^o)\ \mathbf{z^5D^o_4}$
Ti I	8435.653	-1.02	B	$3d^3(^4\mathbf{F})4s\ \mathbf{a^5F_4} \rightarrow 3d^2(^3\mathbf{F})4s4p(^3\mathbf{P}^o)\ \mathbf{z^5D^o_3}$
Ti II	4583.4091	-2.72	D	$3d^3\ \mathbf{a^4P_{3/2}} \rightarrow 3d^2(^3\mathbf{F})4p\ \mathbf{z^2F^o_{5/2}}$
Ti II	4657.2006	-2.15	D	$3d^2(^3\mathbf{P})4s\ \mathbf{b^4P_{5/2}} \rightarrow 3d^2(^3\mathbf{F})4p\ \mathbf{z^2F^o_{7/2}}$
Ti II	4708.6627	-2.336	B'	$3d^3\ \mathbf{a^2P_{3/2}} \rightarrow 3d^2(^3\mathbf{F})4p\ \mathbf{z^2F^o_{5/2}}$
Ti II	4911.1944	-0.609	B+	$3d4s^2\ \mathbf{c^2D_{5/2}} \rightarrow 3d^2(^3\mathbf{P})4p\ \mathbf{y^2P^o_{3/2}}$
Ti II	5211.5303	-1.165	B'	$3d^3\ \mathbf{b^2F_{7/2}} \rightarrow 3d^2(^1\mathbf{D})4p\ \mathbf{y^2F^o_{7/2}}$
Ti II	5381.0216	-1.921	C+	$3d^3\ \mathbf{b^2D2_{3/2}} \rightarrow 3d^2(^3\mathbf{F})4p\ \mathbf{z^2F^o_{5/2}}$
Ti II	5418.7678	-2.002	C+	$3d^3\ \mathbf{b^2D2_{5/2}} \rightarrow 3d^2(^3\mathbf{F})4p\ \mathbf{z^2F^o_{5/2}}$

5.6.16 Vanadium ($_{23}$V)

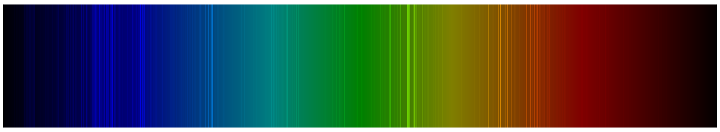

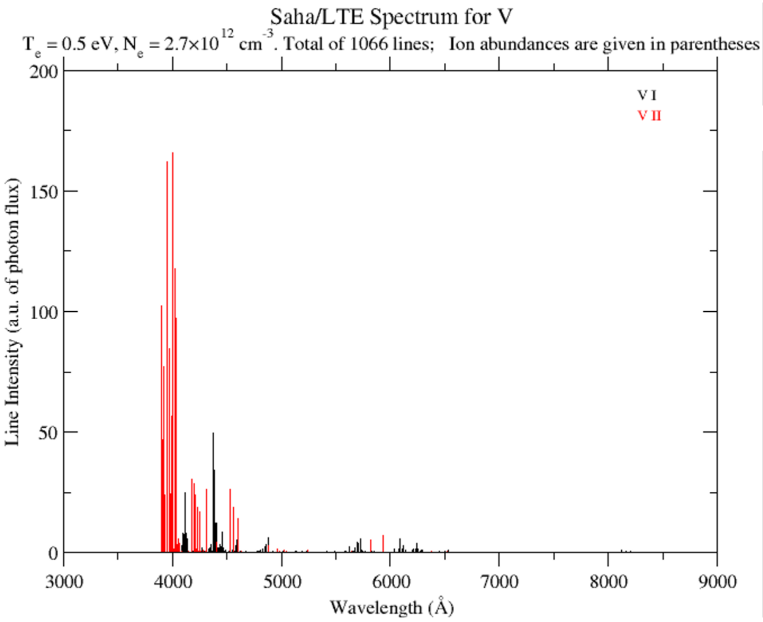

Figure 5.43: *Vanadium lines intensity. Saha-LTE Spectrum (NIST) from ad hoc conditions: electron temperature 0.5 eV and electron density of 2.7x10^{12} cm^{-3}.*

Most intense lines of vanadium are located close to the UVA interval, so in an overcrowded range of spectra. Other lines in the blue or red visible range are shown in the next table.

Line	Ritz Air (Å)	log($g_i f_{ik}$)	Accuracy	Config. **Level**
V I	5670.8480	-0.43	B	$3d^4(^5\mathbf{D})4s\ \mathbf{a^4D_{7/2}} \rightarrow 3d^3(^4\mathbf{F})4s4p(^3\mathbf{P}^o)\ \mathbf{z^2G^o_{9/2}}$
V I	5737.0616	-0.74	C+	$3d^4(^5\mathbf{D})4s\ \mathbf{a^4D_{5/2}} \rightarrow 3d^4(^5\mathbf{D})4p\ \mathbf{y^4F^o_{5/2}}$
V I	6081.4422	-0.61	B	$3d^4(^5\mathbf{D})4s\ \mathbf{a^4D_{3/2}} \rightarrow 3d^4(^5\mathbf{D})4p\ \mathbf{z^4P^o_{3/2}}$
V I	6251.8231	-1.373	B+	$3d^4(^5\mathbf{D})4s\ \mathbf{a^6D_{7/2}} \rightarrow 3d^3(^4\mathbf{F})4s4p(^3\mathbf{P}^o)\ \mathbf{z^6D^o_{7/2}}$
V I	6274.6524	-1.694	B+	$3d^4(^5\mathbf{D})4s\ \mathbf{a^6D_{3/2}} \rightarrow 3d^3(^4\mathbf{F})4s4p(^3\mathbf{P}^o)\ \mathbf{z^6D^o_{1/2}}$

5.6.17 Chromium ($_{24}$Cr)

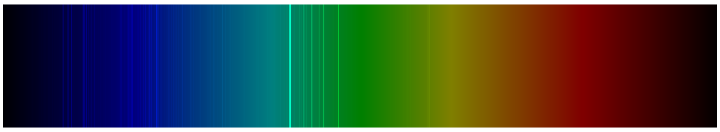

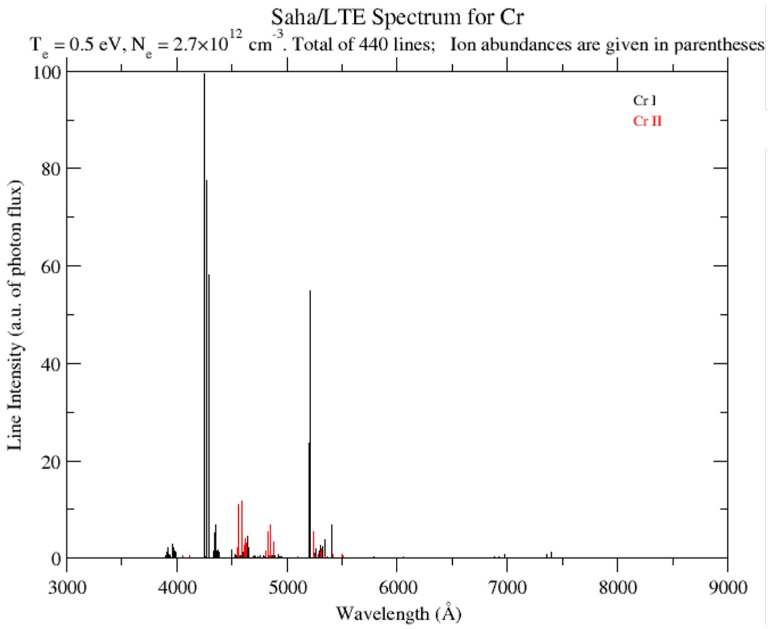

Figure 5.44: *Chromium lines intensity. Saha-LTE Spectrum (NIST) from ad hoc conditions: electron temperature 0.5 eV and electron density of 2.7x10^{12} cm^{-3}.*

As commented in section 2.16, chromium abundance is coupled with the iron one in the galactic chemical evolution. This is pointing to common nucleosynthesis sites.

Cr I are mostly used for obtaining abundances. However, there has been suggested that they could be underestimating the overall chromium abundance (see that section for a further explanation).

On the other hand, there is not a clear consensus about intensity of the NLTE effects, although metallicity seems to be the controlling parameter over temperature or surface gravity. Some of the main lines Cr I are shown in the next table.

Line	Ritz Air (Å)	$\log(g_i f_{ik})$	Accuracy	Config. **Level**
Cr I	4511.8905	-0.343	B	$3d^5(^4\mathbf{G})4s\ \mathbf{a^3G_4} \rightarrow 3d^5(^4\mathbf{G})4p\ \mathbf{y^3G^o_4}$
Cr I	4545.9530	-1.38	B	$3d^5(^6\mathbf{S})4s\ \mathbf{a^5S_2} \rightarrow 3d^4(^5\mathbf{D})4s4p(^3\mathbf{P}^o\ \mathbf{y^5P^o_2}$
Cr I	4600.7483	-1.26	B	$3d^44s^2\ \mathbf{a^5D_3} \rightarrow 3d^4(^5\mathbf{D})4s4p(^3\mathbf{P}^o\ \mathbf{y^5P^o_3}$
Cr I	4626.1734	-1.32	B	$3d^44s^2\ \mathbf{a^5D_1} \rightarrow 3d^4(^5\mathbf{D})4s4p(^3\mathbf{P}^o\ \mathbf{y^5P^o_1}$
Cr I	4708.0126	0.110	B	$3d^4(^5\mathbf{D})4s4p(^3\mathbf{P}^o\ \mathbf{z^7F^o_5} \rightarrow 3d^44s5s\ \mathbf{f^7D_4}$
Cr I	4730.7101	-0.192	B	$3d^5(^4\mathbf{G})4s\ \mathbf{a^3G_3} \rightarrow 3d^5(^4\mathbf{G})4p\ \mathbf{y^3F^o_2}$
Cr I	5247.5651	-1.63	B	$3d^44s^2\ \mathbf{a^5D_0} \rightarrow 3d^5(^6\mathbf{S})4p\ \mathbf{z^5P^o_1}$
Cr I	5296.6911	-1.41	B	$3d^44s^2\ \mathbf{a^5D_2} \rightarrow 3d^5(^6\mathbf{S})4p\ \mathbf{z^5P^o_1}$
Cr I	5300.7456	-2.13	B	$3d^44s^2\ \mathbf{a^5D_2} \rightarrow 3d^5(^6\mathbf{S})4p\ \mathbf{z^5P^o_3}$
Cr I	5783.0643	-0.50	D	$3d^5(^6\mathbf{S})4p\ \mathbf{z^5P^o_1} \rightarrow 3d^5(^6\mathbf{S})4d\ \mathbf{e^5D_1}$
Cr I	5783.8501	-0.295	B	$3d^5(^6\mathbf{S})4p\ \mathbf{z^5P^o_2} \rightarrow 3d^5(^6\mathbf{S})4d\ \mathbf{e^5D_2}$
Cr I	5787.9188	-0.083	B	$3d^5(^6\mathbf{S})4p\ \mathbf{z^5P^o_2} \rightarrow 3d^5(^6\mathbf{S})4d\ \mathbf{e^5D_3}$
Cr I	6330.0913	-2.91	D	$3d^5(^6\mathbf{S})4p\ \mathbf{a^5S_2} \rightarrow 3d^5(^6\mathbf{S})4p\ \mathbf{z^7D^o_3}$

5.6.18 Manganese ($_{25}$Mn)

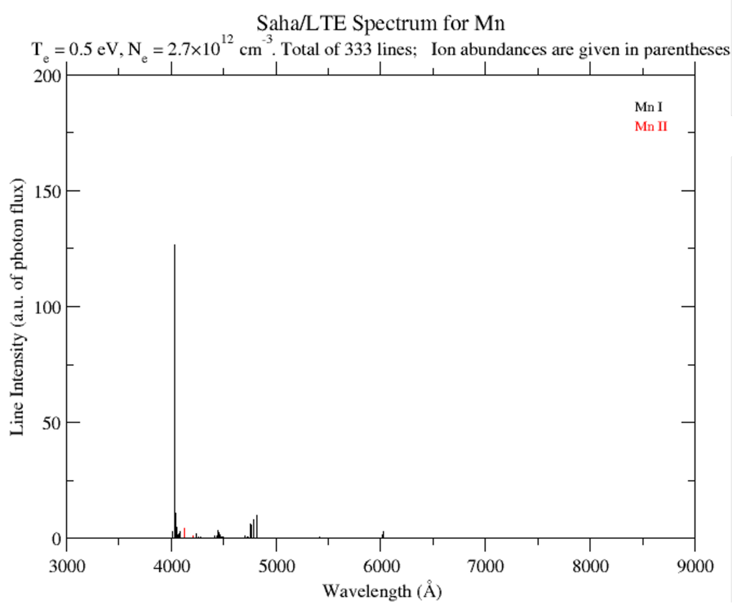

Figure 5.45: *Manganese lines intensity. Saha-LTE Spectrum (NIST) from ad hoc conditions: electron temperature 0.5 eV and electron density of 2.7x10^{12} cm^{-3}.*

Some studies are pointing to severe NLTE effects at lower metallicities due to a photoionization process (see section 2.115 for a further explanation). This could dramatically change the assessment of the galactic chemical evolution, depending on the study base, LTE or NLTE assumptions (see Fig. 2.117 and 2.118 in above commented section).

The main Mn lines are observed at bluer intervals. Some of them are listed next.

Line	Ritz Air (Å)	log($g_i f_{ik}$)	Accuracy	Config. **Level**
Mn I	4502.213	-0.344	B	$3d^6(^5\mathbf{D})4s\ \mathbf{a^4D_{5/2}} \rightarrow 3d^6(^5\mathbf{D})4p\ \mathbf{z^4D^o_{7/2}}$
Mn I	4739.087	-0.490	B	$3d^6(^5\mathbf{D})4s\ \mathbf{a^4D_{3/2}} \rightarrow 3d^6(^5\mathbf{D})4p\ \mathbf{z^4F^o_{3/2}}$
Mn I	4754.042	-0.085	B	$3d^5(^6\mathbf{S})4s4p(^3\mathbf{P^0})\ \mathbf{z^8P^o_{5/2}} \rightarrow 3d^5 4s(^7\mathbf{S})5s\ \mathbf{e^8S_{7/2}}$
Mn I	4762.367	0.426	B	$3d^6(^5\mathbf{D})4s\ \mathbf{a^4D_{7/2}} \rightarrow 3d^6(^5\mathbf{D})4p\ \mathbf{z^4F_{9/2}}$
Mn I	4783.427	0.042	B	$3d^5(^6\mathbf{S})4s4p(^3\mathbf{P^0})\ \mathbf{z^8P^o_{7/2}} \rightarrow 3d^5 4s(^7\mathbf{S})5s\ \mathbf{e^8S_{7/2}}$
Mn I	4823.524	0.144	B	$3d^5(^6\mathbf{S})4s4p(^3\mathbf{P^0})\ \mathbf{z^8P^o_{9/2}} \rightarrow 3d^5 4s(^7\mathbf{S})5s\ \mathbf{e^8S_{7/2}}$
Mn I	4823.524	0.144	B	$3d^5(^6\mathbf{S})4s4p(^3\mathbf{P^0})\ \mathbf{z^8P^o_{9/2}} \rightarrow 3d^5 4s(^7\mathbf{S})5s\ \mathbf{e^8S_{7/2}}$
Mn I	6013.51	-0.252	C+	$3d^5(^6\mathbf{S})4s4p(^3\mathbf{P^0})\ \mathbf{z^6P^o_{3/2}} \rightarrow 3d^5 4s(^7\mathbf{S})5s\ \mathbf{e^6S_{5/2}}$
Mn I	6021.82	0.035	C+	$3d^5(^6\mathbf{S})4s4p(^3\mathbf{P^0})\ \mathbf{z^6P^o_{7/2}} \rightarrow 3d^5 4s(^7\mathbf{S})5s\ \mathbf{e^6S_{5/2}}$

5.6.19 Iron ($_{26}$Fe)

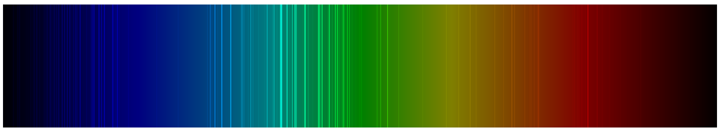

No point in highlighting any special iron lines due to the countless available Fe I and Fe II ones along the whole spectrum, most, strong enough for their study. Nevertheless, it is worth taking a look into the extra info possible to obtain from them.

A wide range of methods are available for the gravity determination, most reliable based on asteroseismology or from dynamic mass and radius measurements in eclipsing binary systems. Nevertheless, GAIA mission and their extremely precise astrometric data provide a simpler method, the trigonometric gravity determination via spectroscopic data. This is derived following the next expression (Tsantaki et al. 2019):

$$log(g/g_{\odot}) = \log(\mathrm{M}/\mathrm{M}_{\odot}) + 4 \cdot log(T_{eff}/T_{eff\odot}) + 0.4 \cdot (V + BC) + 2 \cdot log\pi + 0.104$$

...being M, stellar mass; T, surface temperature; V, visual magnitude; BC, the bolometric correction; π, the parallax in mas.

Other methods make use of light-curves, comparison with theoretical isochrones, spectroscopic parameters as the equivalent widths of certain lines, the study of the wings of strong lines given their dependence on the collision broadening (hence the gas pressure) or the study of molecular species whose molecular equilibria are pressure sensitive.

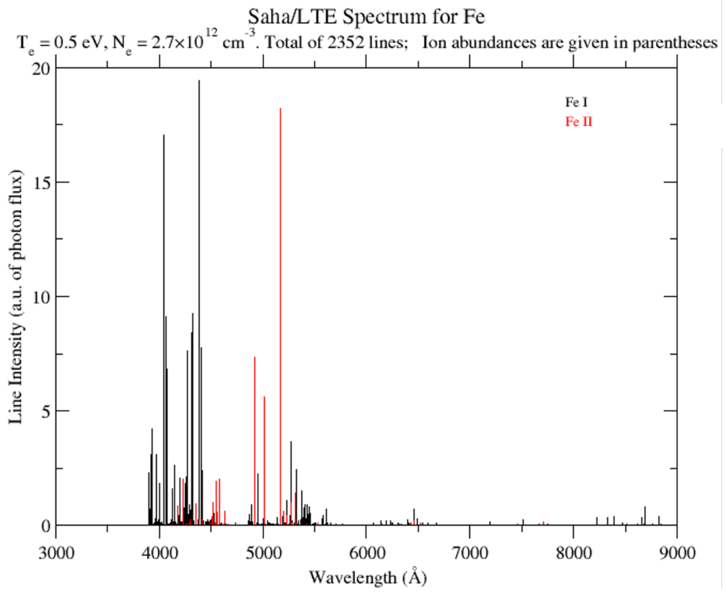

Figure 5.46: *Iron lines intensity. Saha-LTE Spectrum (NIST) from ad hoc conditions: electron temperature 0.5 eV and electron density of 2.7x10^{12} cm^{-3}.*

However, in spectroscopy, the gravity determination is usually achieved assessing the ionization equilibrium between known species as Fe I and Fe II (or others as Ti I/Ti II). The ionization is determined by the change of electron pressure. Therefore, surface gravity can be obtained, demanding that abundances from ionized lines equal those from neutral ones (Bell et al. 1985), and otherwise, no correlation between iron abundance and equivalent widths and excitation potential is attained.

In fact, this Fe I and Fe II excitation equilibrium can be used, besides of log$g$, for obtaining stellar parameters as effective temperature (T_{eff}), metallicity ([Fe/H]), and micro-turbulent velocity (ξ), computing and interpolating in a grid of theoretical stellar atmosphere models such as f.i. the ones of Kurucz (1993). In binary systems, an additional parameter can be obtained by the latter method, the spectral dilution.

5.6.20 Cobalt ($_{27}$Co)

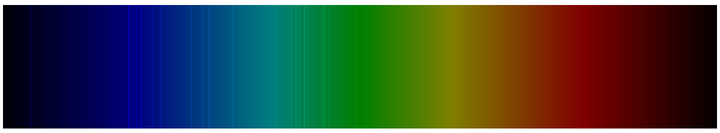

Stronger lines are concentrated on the bluer interval of the spectra. NLTE effect on the

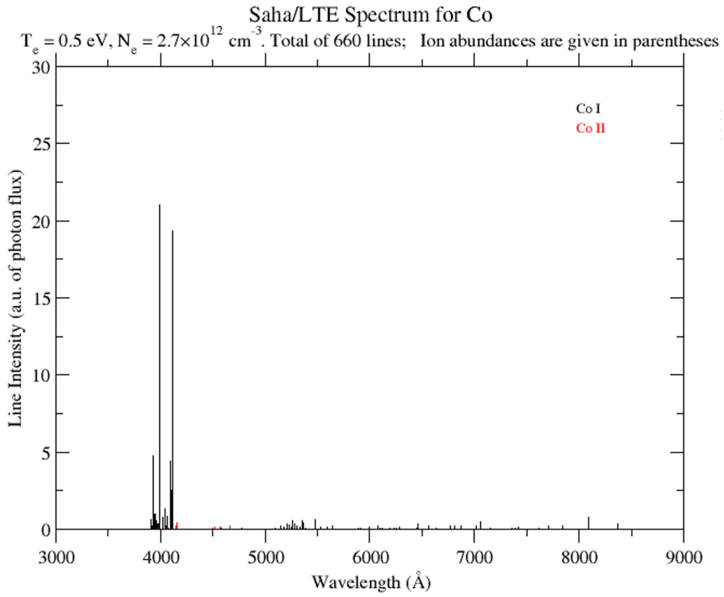

Figure 5.47: *Cobalt lines intensity. Saha-LTE Spectrum (NIST) from ad hoc conditions: electron temperature 0.5 eV and electron density of 2.7x10^{12} cm^{-3}.*

Co I lines could be severe, depending on the metallicity, gravity or temperature (see section 3.1). Next some interesting lines from bibliography, some weaker in redder intervals of the spectrum.

Line	Ritz Air (Å)	log($g_i f_{ik}$)	Accuracy	Config. **Level**
Co I	3995.302	-0.22	C+	$3p^63d^8(^3\mathbf{F})4s\ \mathbf{a^2F_{7/2}} \rightarrow 3p^63d^8(^3\mathbf{F})4p\ \mathbf{y^4G^o_{9/2}}$
Co I	4110.530	-1.08	D	$3p^63d^8(^3\mathbf{F})4s\ \mathbf{a^2F_{5/2}} \rightarrow 3p^63d^7(^4\mathbf{F})4s4p(^3\mathbf{P^0})\ \mathbf{z^2F^o_{5/2}}$
Co I	4118.767	-0.49	C	$3p^63d^8(^3\mathbf{F})4s\ \mathbf{a^2F_{5/2}} \rightarrow 3p^63d^7(^4\mathbf{F})4s4p(^3\mathbf{P^0})\ \mathbf{z^2G^o_{7/2}}$
Co I	4121.311	-0.32	C	$3p^63d^8(^3\mathbf{F})4s\ \mathbf{a^2F_{7/2}} \rightarrow 3p^63d^7(^4\mathbf{F})4s4p(^3\mathbf{P^0})\ \mathbf{z^2G^o_{9/2}}$
Co I	5212.691	-0.11	B	$3p^63d^7(^4\mathbf{F})4s4p(^3\mathbf{P^0})\ \mathbf{z^4F^o_{9/2}} \rightarrow 3p^63d^74s(^5\mathbf{F})5s\ \mathbf{f^4F_{9/2}}$
Co I	5280.629	-0.03	D	$3p^63d^7(^4\mathbf{F})4s4p(^3\mathbf{P^0})\ \mathbf{z^4G^o_{9/2}} \rightarrow 3p^63d^74s(^5\mathbf{F})5s\ \mathbf{f^4F_{7/2}}$
Co I	5301.039	-1.99	C	$3p^63d^74s^2\ \mathbf{a^4P_{5/2}} \rightarrow 3p^63d^8(^3\mathbf{F})4p\ \mathbf{y^4D^o_{5/2}}$
Co I	5352.045	0.06	B	$3p^63d^7(^4\mathbf{F})4s4p(^3\mathbf{P^0})\ \mathbf{z^4G^o_{11/2}} \rightarrow 3p^63d^74s(^5\mathbf{F})5s\ \mathbf{f^4F_{9/2}}$
Co I	5647.23	-1.56	C	$3p^63d^8(^3\mathbf{P})4s\ \mathbf{a^2P_{3/2}} \rightarrow 3p^63d^8(^3\mathbf{F})4p\ \mathbf{y^2D^o_{5/2}}$
Co I	5647.23	-1.56	C	$3p^63d^8(^3\mathbf{P})4s\ \mathbf{a^2P_{3/2}} \rightarrow 3p^63d^8(^3\mathbf{F})4p\ \mathbf{y^2D^o_{5/2}}$

5.6.21 Nickel ($_{28}$Ni)

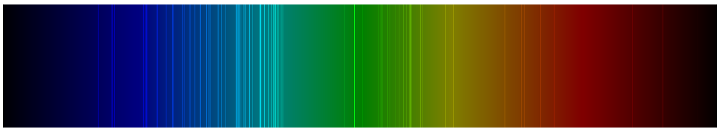

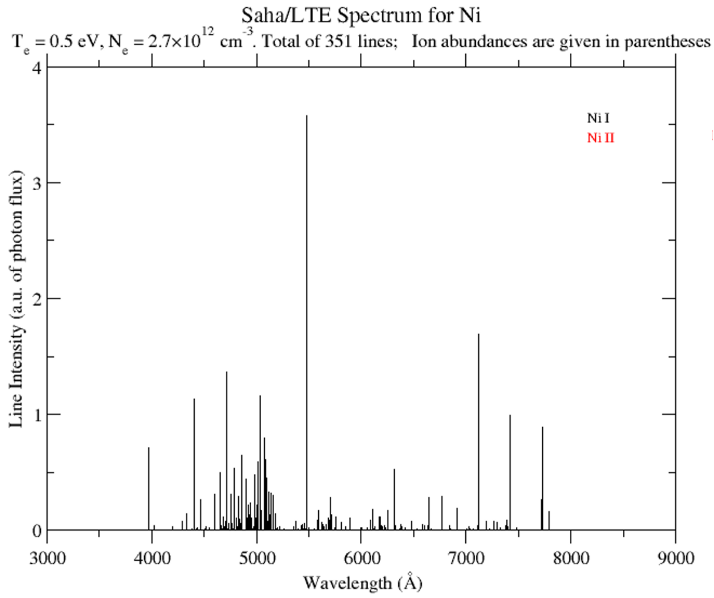

Figure 5.48: *Nickel lines intensity. Saha-LTE Spectrum (NIST) from ad hoc conditions: electron temperature 0.5 eV and electron density of 2.7x10^{12} cm^{-3}.*

The available and bibliographic Nickel lines from abundance studios are abundant along the visible interval spectra. Like this, the selection possibility is wide and only a few of them are shown as a particular sample along the spectrum in the next table. Up to now, no in-depth NLTE effects studio has been developed for this element.

Line	Ritz Air (Å)	$\log(g_i f_{ik})$	Accuracy	Config. **Level**
Ni I	4686.213	-0.64	D	$3d^8(^3\mathbf{F})4s4p(^3\mathbf{P^0})\ ^5\mathbf{G}^o_2 \rightarrow 3d^84s(^4\mathbf{F})5s\ ^5\mathbf{F_2}$
Ni I	4831.176	-0.41	D	$3d^8(^3\mathbf{F})4s4p(^3\mathbf{P^0})\ ^5\mathbf{F}^o_4 \rightarrow 3d^84s(^4\mathbf{F})5s\ ^5\mathbf{F_3}$
Ni I	4855.411	0.00	D	$3d^9(^2\mathbf{D})4p\ ^3\mathbf{P}^o_2 \rightarrow 3d^9(^2\mathbf{D_{5/2}})4d\ ^2\mathbf{[3/2]_2}$
Ni I	4904.412	-0.17	D	$3d^9(^2\mathbf{D})4p\ ^3\mathbf{P}^o_2 \rightarrow 3d^9(^2\mathbf{D_{5/2}})4d\ ^2\mathbf{[1/2]_2}$
Ni I	5081.110	0.30	D	$3d^9(^2\mathbf{D})4p\ ^1\mathbf{F}^o_3 \rightarrow 3d^9(^2\mathbf{D_{3/2}})4d\ ^2\mathbf{[7/2]_4}$
Ni I	5094.411	-1.08	D	$3d^9(^2\mathbf{D})4p\ ^3\mathbf{D}^o_1 \rightarrow 3d^9(^2\mathbf{D_{3/2}})4d\ ^2\mathbf{[1/2]_1}$
Ni I	5115.392	-0.11	D	$3d^8(^3\mathbf{F})4s4p(^3\mathbf{P^0})\ ^3\mathbf{G}^o_5 \rightarrow 3d^84s(^4\mathbf{F})5s\ ^3\mathbf{F_4}$
Ni I	5392.331	-1.32	D	$3d^8(^3\mathbf{F})4s4p(^3\mathbf{P^0})\ ^3\mathbf{D}^o_3 \rightarrow 3d^84s(^4\mathbf{F})5s\ ^3\mathbf{F_2}$
Ni I	5435.858	-2.60	D+	$3d^8(^3\mathbf{P})4s^2\ ^3\mathbf{P_0} \rightarrow 3d^8(^3\mathbf{F})4s4p(^3\mathbf{P^0})\ ^3\mathbf{D}^o_1$
Ni I	5587.858	-2.14	C+	$3d^8(^3\mathbf{P})4s^2\ ^3\mathbf{P_2} \rightarrow 3d^8(^3\mathbf{F})4s4p(^3\mathbf{P^0})\ ^3\mathbf{D}^o_3$
Ni I	5754.656	-2.34	C+	$3d^8(^3\mathbf{P})4s^2\ ^3\mathbf{P_2} \rightarrow 3d^9(^2\mathbf{D})4p\ ^1\mathbf{P}^o_1$
Ni I	5805.217	-0.64	D	$3d^8(^3\mathbf{F})4s4p(^3\mathbf{P^0})\ ^3\mathbf{D}^o_2 \rightarrow 3d^9(^2\mathbf{D\_3/2})4d\ ^2\mathbf{[5/2]_3}$
Ni I	5996.730	-1.06	D	$3d^8(^3\mathbf{F})4s4p(^3\mathbf{P^0})\ ^3\mathbf{F}^o_2 \rightarrow 3d^9(^2\mathbf{D\_3/2})4d\ ^2\mathbf{[5/2]_2}$
Ni I	6086.282	-0.51	D	$3d^8(^3\mathbf{F})4s4p(^3\mathbf{P^0})\ ^3\mathbf{D}^o_1 \rightarrow 3d^9(^2\mathbf{D\_3/2})4d\ ^2\mathbf{[5/2]_2}$
Ni I	6108.116	-2.44	D+	$3d^8(^1\mathbf{D})4s^2\ ^1\mathbf{D_2} \rightarrow 3d^9(^2\mathbf{D})4p\ ^3\mathbf{D}^o_2$
Ni I	6111.070	-0.87	D	$3d^8(^3\mathbf{F})4s4p(^3\mathbf{P^0})\ ^3\mathbf{F}^o_4 \rightarrow 3d^9(^2\mathbf{D_{5/2}})4d\ ^3\mathbf{[7/2]_4}$
Ni I	6130.135	-0.96	D	$3d^8(^3\mathbf{F})4s4p(^3\mathbf{P^0})\ ^3\mathbf{D}^o_1 \rightarrow 3d^9(^2\mathbf{D_{3/2}})4d\ ^2\mathbf{[3/2]_1}$
Ni I	6176.811	-0.53	D	$3d^8(^3\mathbf{F})4s4p(^3\mathbf{P^0})\ ^3\mathbf{F}^o_4 \rightarrow 3d^9(^2\mathbf{D_{5/2}})4d\ ^2\mathbf{[9/2]_5}$
Ni I	6204.604	-1.14	D	$3d^8(^3\mathbf{F})4s4p(^3\mathbf{P^0})\ ^3\mathbf{F}^o_4 \rightarrow 3d^84s(^4\mathbf{F})5s\ ^5\mathbf{F_4}$
Ni I	6204.604	-1.14	D	$3d^8(^3\mathbf{F})4s4p(^3\mathbf{P^0})\ ^3\mathbf{F}^o_4 \rightarrow 3d^84s(^4\mathbf{F})5s\ ^5\mathbf{F_4}$
Ni I	6230.089	-1.26	E	$3d^8(^3\mathbf{F})4s4p(^3\mathbf{P^0})\ ^3\mathbf{F}^o_3 \rightarrow 3d^9(^2\mathbf{D_{5/2}})4d\ ^2\mathbf{[3/2]_2}$
Ni I	6378.250	-0.90	D	$3d^8(^3\mathbf{F})4s4p(^3\mathbf{P^0})\ ^3\mathbf{D}^o_3 \rightarrow 3d^9(^2\mathbf{D_{5/2}})4d\ ^2\mathbf{[9/2]_4}$
Ni I	6598.598	-0.98	D	$3d^8(^3\mathbf{F})4s4p(^3\mathbf{P^0})\ ^3\mathbf{F}^o_2 \rightarrow 3d^9(^2\mathbf{D_{5/2}})4d\ ^2\mathbf{[7/2]_3}$
Ni I	6635.122	-0.83	D	$3d^8(^3\mathbf{F})4s4p(^3\mathbf{P^0})\ ^1\mathbf{F}^o_3 \rightarrow 3d^9(^2\mathbf{D_{3/2}})4d\ ^2\mathbf{[7/2]_4}$
Ni I	6643.630	-2.30	D	$3d^8(^1\mathbf{D})4s^2\ ^1\mathbf{D_2} \rightarrow 3d^9(^2\mathbf{D})4p\ ^3\mathbf{P}^o_2$
Ni I	6767.772	-2.17	D	$3d^10\ ^1\mathbf{S_0} \rightarrow 3d^9(^2\mathbf{D})4p\ ^3\mathbf{P}^o_1$
Ni I	6772.315	-0.99	D	$3d^9(^2\mathbf{D})4p\ ^1\mathbf{P}^o_1 \rightarrow 3d^9(^2\mathbf{D_{3/2}})5s\ ^2\mathbf{[3/2]_2}$

5.6.22 Copper ($_{29}$Cu)

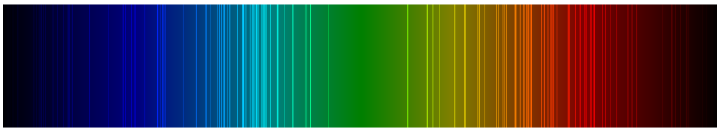

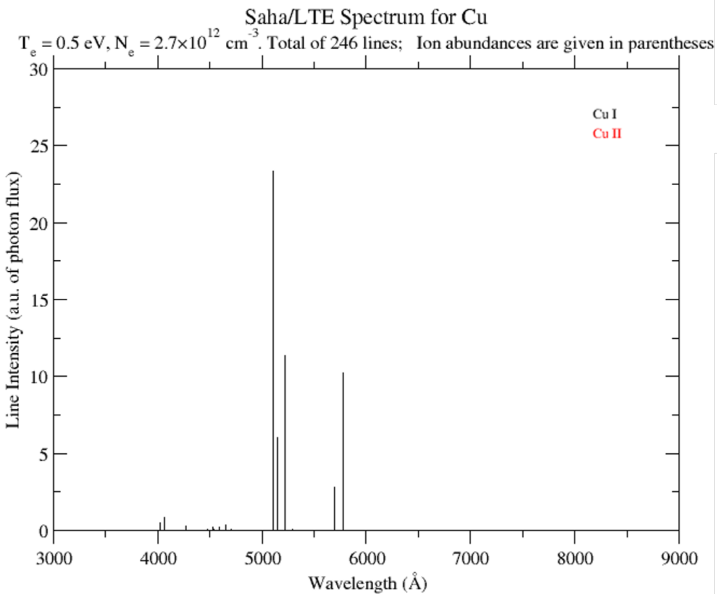

Figure 5.49: *Copper lines intensity. Saha-LTE Spectrum (NIST) from ad hoc conditions: electron temperature 0.5 eV and electron density of 2.7x10^{12} cm^{-3}.*

Copper lines are problematic. Few are the available lines and in addition they are affected by some problems, one of them, the severe impact of NLTE effects at lower metallicities. The next table summarizes the available options.

Line	Ritz Air (Å)	log($g_i f_{ik}$)	Accuracy	Config. **Level**
Cu I	5105.548	-1.50	C+	$3d^9 4s^2\ {}^2\mathbf{D}_{5/2} \rightarrow 3d^{10} 4p\ {}^2\mathbf{P}^o_{3/2}$
Cu I	5153.238	-0.02	C+	$3d^{10} 4p\ {}^2\mathbf{P}^o_{1/2} \rightarrow 3d^{10} 4d\ {}^2\mathbf{D}_{3/2}$
Cu I	5218.202	0.26	C+	$3d^{10} 4p\ {}^2\mathbf{P}^o_{3/2} \rightarrow 3d^{10} 4d\ {}^2\mathbf{D}_{5/2}$
Cu I	5220.070	-0.610	C+	$3d^{10} 4p\ {}^2\mathbf{P}^o_{3/2} \rightarrow 3d^{10} 4d\ {}^2\mathbf{D}_{3/2}$
Cu I	5700.240	-2.33	C+	$3d^9 4s^2\ {}^2\mathbf{D}_{3/2} \rightarrow 3d^{10} 4p\ {}^2\mathbf{P}^o_{3/2}$
Cu I	5782.126	-1.781	C+	$3d^9 4s^2\ {}^2\mathbf{D}_{3/2} \rightarrow 3d^{10} 4p\ {}^2\mathbf{P}^o_{1/2}$

5.6.23 Zinc ($_{30}$Zn)

Saha plot has been avoided for this element, as there is only a unique transition probability in the NIST database for the entire visible range involving Zn I lines. Hence, the next table includes lines with oscillator strengths obtained from a different source. As observed, only a few lines strong enough are available in the visible range for the determination of Zn abundance.

Line	Ritz Air (Å)	log($g_i f_{ik}$)	Accuracy	Config. **Level**
Zn I	4722.1569	-0.338^a	*	$3d^{10}4s4p\ \mathbf{^3P^o_1} \rightarrow 3d^{10}4s5s\ \mathbf{^3S_1}$
Zn I	4810.5321	-0.137^a	*	$3d^{10}4s4p\ \mathbf{^3P^o_2} \rightarrow 3d^{10}4s5s\ \mathbf{^3S_1}$
Zn I	6362.3458	0.16	C	$3d^{10}4s4p\ \mathbf{^1P^o_1} \rightarrow 3d^{10}4s4d\ \mathbf{^1D_2}$

a: Not available in NIST. log(gf) from Delgado Mena et al. (2017).

5.6.24 Strontium ($_{38}$Sr)

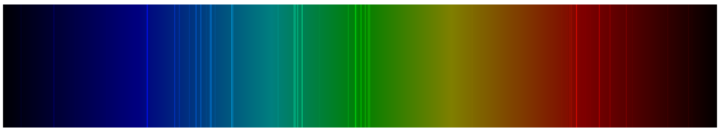

The two resonance Sr II lines at 4077 and 4215 Å are the only shots available for abundance determination, especially when metal poor stars are involved. They overwhelm the intensities of the Sr I lines, and both have been avoided in the Fig. 5.50 for a better detail of the distribution of the latter. Only the Sr I line at 4607 Å provides intensity enough for its use in abundance determinations. Hence, the scope of the available options is limited.

Line	Ritz Air (Å)	log($g_i f_{ik}$)	Accuracy	Config. **Level**
Sr II	4077.7094	0.148	AA	$4p^6 5d\ \mathbf{^2S_{1/2}} \rightarrow 4p^6 5p\ \mathbf{^2P^o_{3/2}}$
Sr II	4215.5193	-0.166	AA	$4p^6 5d\ \mathbf{^2S_{1/2}} \rightarrow 4p^6 5p\ \mathbf{^2P^o_{1/2}}$
Sr I	4607.3330	0.283	AA	$5s^2\ \mathbf{^1S_0} \rightarrow 5s5p\ \mathbf{^1P^o_1}$

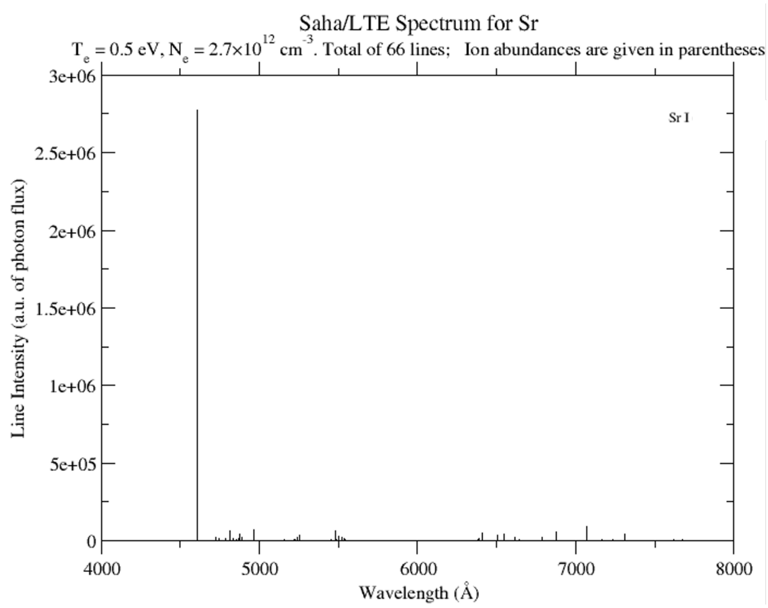

Figure 5.50: *Strontium lines intensity. Saha-LTE Spectrum (NIST) from ad hoc conditions: electron temperature 0.5 eV and electron density of 2.7x10^{12} cm^{-3}. Resonance Sr* II *lines at 4077 and 4215 Å have been avoided for a better detail in the Sr* I *lines' distribution.*

5.6.25 Yttrium ($_{39}$Y)

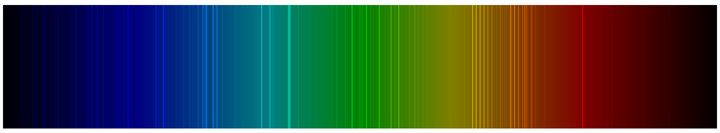

Unlike its first peak s-element companion, Sr, the available options of lines are a bit wider. Nevertheless, they are weak and could be partially blended (f.i. Y II line at 4900 Å).

Line	Ritz Air (Å)	log($g_i f_{ik}$)	Accuracy	Config. **Level**
Y II	4374.933	0.155	A	4d5s $\mathbf{a^1D_2} \rightarrow$ 4d5p $\mathbf{z^1D^o_2}$
Y II	4398.010	-0.999	A+	4d5s $\mathbf{a^3D_2} \rightarrow$ 5s5p $\mathbf{z^3P^o_1}$
Y II	4854.861	-0.38	B	4d^2 $\mathbf{a^3F_2} \rightarrow$ 4d5p $\mathbf{z^3D^o_1}$
Y II	4883.682	0.07	B	4d^2 $\mathbf{a^3F_4} \rightarrow$ 4d5p $\mathbf{z^3D^o_3}$
Y II	4900.119	-0.09	B	4d^2 $\mathbf{a^3F_3} \rightarrow$ 4d5p $\mathbf{z^3D^o_2}$
Y II	5087.419	-0.17	B	4d^2 $\mathbf{a^3F_3} \rightarrow$ 4d5p $\mathbf{z^3F^o_4}$
Y II	5200.410	-0.573	B+	4d^2 $\mathbf{a^3F_2} \rightarrow$ 4d5p $\mathbf{z^3F^o_2}$
Y II	5205.723	-0.35	B+	4d^2 $\mathbf{a^3F_3} \rightarrow$ 4d5p $\mathbf{z^3F^o_3}$
Y II	5402.774	-0.630[a]	*	4d^2 $\mathbf{b^1B_2} \rightarrow$ 4d5p $\mathbf{z^1F^o_3}$

a: Not available in NIST. log(gf) from Delgado Mena et al. (2017).

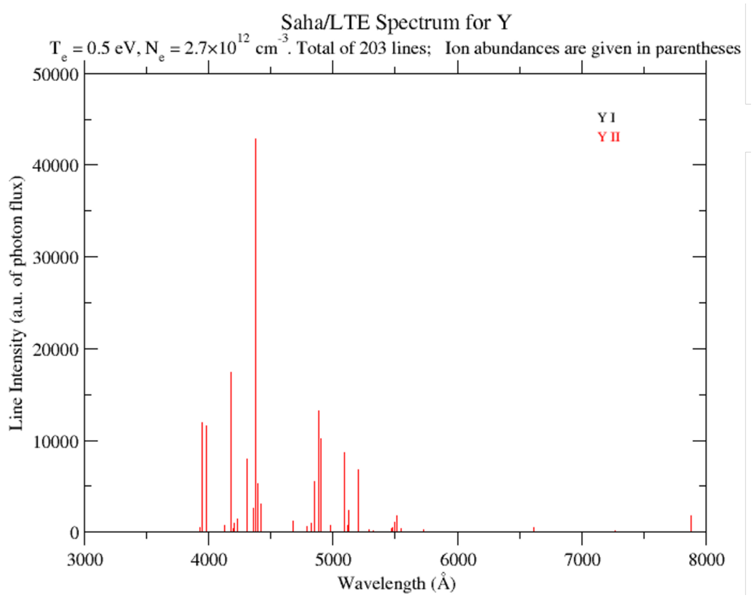

Figure 5.51: *Yttrium lines intensity. Saha-LTE Spectrum (NIST) from ad hoc conditions: electron temperature 0.5 eV and electron density of 2.7x10^{12} cm^{-3}.*

5.6.26 Zirconium ($_{40}$Zr)

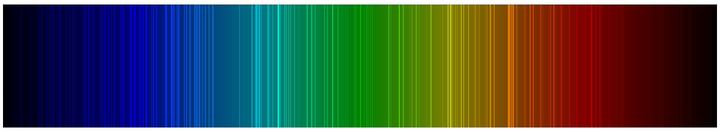

Weak lines are the only options for abundance determination of this element. No transition probability is obtained from the NIST database for Zr I or Zr ɪɪ species. Best shots deal with Zr ɪɪ lines, blended in some cases (f.i. Zr ɪɪ 4048 or 4149).

Line	Wave Air (Å)[a]	log($g_i f_{ik}$)	Accuracy	Config. **Level**[a]
Zr ɪɪ	4048.67	-0.53[b]	5%[b]	$4d^2(^3F)5s\ \mathbf{a^2F_{7/2}} \rightarrow 4d^2(^3F)5p\ \mathbf{z^2D^o_{5/2}}$
Zr ɪɪ	4050.33	-1.06[b]	6%[b]	$4d^2(^3F)5s\ \mathbf{a^2F_{5/2}} \rightarrow 4d^2(^3F)5p\ \mathbf{z^2D^o_{3/2}}$
Zr ɪɪ	4061.53	-0.72[c]	*	$4d^2(^3F)5s\ \mathbf{a^2F_{5/2}} \rightarrow 4d^2(^3F)5p\ \mathbf{z^4F^o_{3/2}}$
Zr ɪɪ	4149.20	-0.04[b]	5%[b]	$4d^2(^3F)5s\ \mathbf{a^2F_{7/2}} \rightarrow 4d^2(^3F)5p\ \mathbf{z^2F^o_{7/2}}$
Zr ɪɪ	4208.98	-0.51[b]	4%[b]	$4d^2(^3F)5s\ \mathbf{a^2F_{5/2}} \rightarrow 4d^2(^3F)5p\ \mathbf{z^2F^o_{5/2}}$
Zr ɪɪ	4317.31	-1.45[b]	8%[b]	$4d^2(^3F)5s\ \mathbf{a^2F_{5/2}} \rightarrow 4d^2(^3F)5p\ \mathbf{z^4G^o_{7/2}}$
Zr ɪɪ	4379.78	-0.356[d]	*	$4d^3\ \mathbf{a^2H_{11/2}} \rightarrow 4d^2(^3F)5p\ \mathbf{z^2G^o_{9/2}}$
Zr ɪɪ	5112.27	-0.85[b]	5%[b]	$4d^3\ \mathbf{b^2D_{3/2}} \rightarrow 4d^2(^3P)5p\ \mathbf{y^2D^o_{3/2}}$

a: Observed air wave and electronic configuration from Grotrian project database (http://grotrian.nsu.ru/).
b: Not available in NIST. log(gf) and f uncertainties (in % against f) from Ljung et al. (2006).
c: Not available in NIST. log(gf) from Siqueira Mello et al. (2014).
d: Not available in NIST. log(gf) from Delgado Mena et al. (2017).

5.6.27 Barium ($_{56}$Ba)

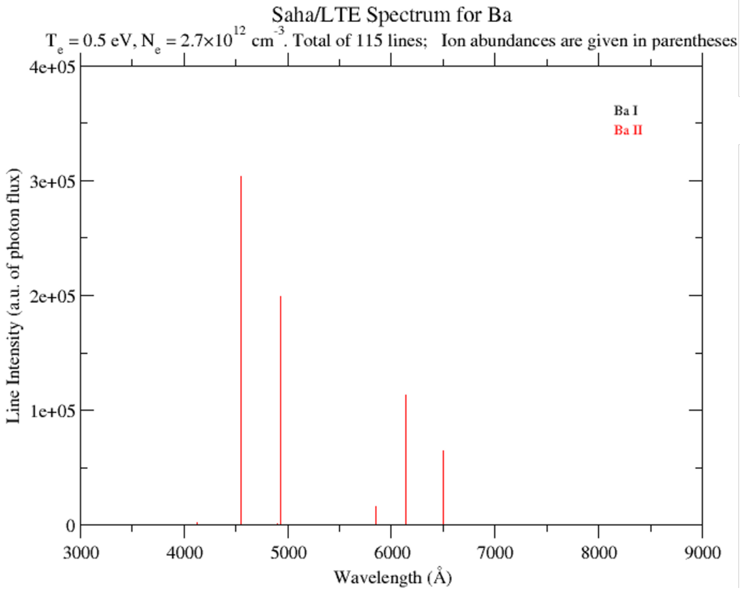

Figure 5.52: *Barium lines intensity. Saha-LTE Spectrum (NIST) from ad hoc conditions: electron temperature 0.5 eV and electron density of 2.7x10^{12} cm^{-3}.*

Five Ba II lines are available for abundance studies, intense and sharp (except 5853 line), though partially blended in different grades (severe in the case of the 6496 Å line with Fe I). The two resonance lines at 4554 and 4934 Å are sensitive to hyperfine structure effects and therefore strongly dependent on the Ba isotope ratio. This is why they can be used to infer the role of s- and r-processes (regarding this subject, see Fig. 3.40 in section 3.8). Unlike the lines at 5853 and 6141 Å, which are almost independent of the isotopic ratios (Cescutti et al. 2021).

The bibliography makes use, especially, of lines at 4554 and 6141 Å. Like it does of the 5853 one, although weaker.

Line	Ritz Air (Å)	log($g_i f_{ik}$)	Accuracy	Config. **Level**
Ba II	4554.033	0.140	B	6s $^2\mathbf{S}_{1/2} \rightarrow$ 6p $^2\mathbf{P}^o_{3/2}$
Ba II	4934.077	-0.16	B	6s $^2\mathbf{S}_{1/2} \rightarrow$ 6p $^2\mathbf{P}^o_{1/2}$
Ba II	5853.675	-0.908	B	5d $^2\mathbf{D}_{3/2} \rightarrow$ 6p $^2\mathbf{P}^o_{3/2}$
Ba II	6141.713	-0.032	B	5d $^2\mathbf{D}_{5/2} \rightarrow$ 6p $^2\mathbf{P}^o_{3/2}$
Ba II	6496.898	-0.407	B	5d $^2\mathbf{D}_{3/2} \rightarrow$ 6p $^2\mathbf{P}^o_{1/2}$

5.6.28 Lanthanum ($_{57}$La)

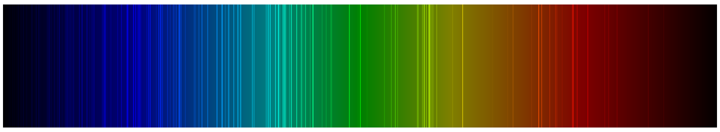

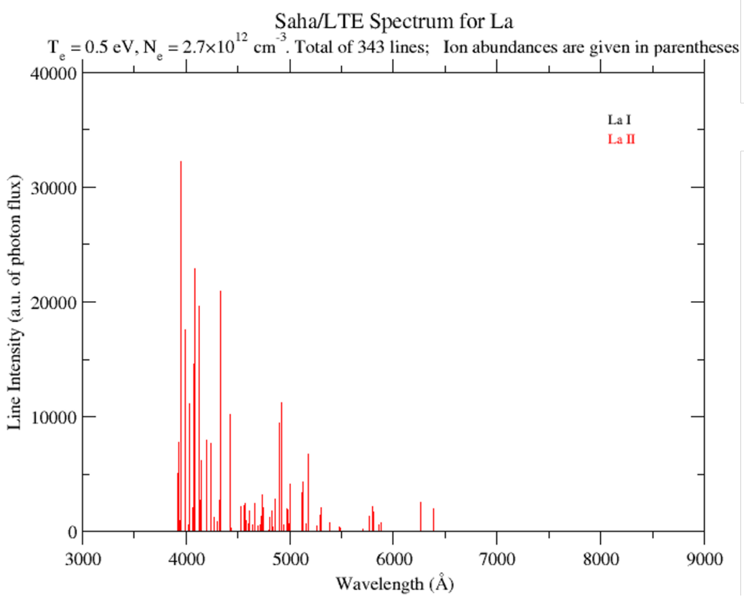

Figure 5.53: *Lanthanum lines intensity. Saha-LTE Spectrum (NIST) from ad hoc conditions: electron temperature 0.5 eV and electron density of 2.7x10^{12} cm^{-3}.*

Weak and blended La II lines, most towards the bluer intervals, are the only shots for abundance study of this tricky element. These are general features of the second peak s-process element partners (cerium, neodymium or samarium) but barium, given their low abundances.

Line	Ritz Air (Å)	$\log(g_i f_{ik})$	Accuracy	Config. **Level**
La II	3949.102	0.491	B+	5d6s $\mathbf{a^3D_3} \rightarrow$ 5d6p $\mathbf{x^3F^o_4}$
La II	3988.515	0.21	B	5d6s $\mathbf{a^3D_3} \rightarrow$ 5d6p $\mathbf{x^3D^o_3}$
La II	3995.745	-0.064	B+	5d^2 **2** $\rightarrow$ 5d6p $\mathbf{x^3F^o_2}$
La II	4031.686	-0.08	B	5d6s $\mathbf{a^3D_2} \rightarrow$ 5d6p $\mathbf{y^3D^o_2}$
La II	4042.901	0.33[a]	B	5d^2 $\mathbf{a^1G_4} \rightarrow$ 5d6p $\mathbf{x^1F^o_3}$
La II	4077.342	-0.059	B+	5d6s $\mathbf{a^3D_1} \rightarrow$ 5d6p $\mathbf{x^3F^o_2}$
La II	4086.709	-0.07	B+	5d^2 $\mathbf{a^3F_2} \rightarrow$ 5d6p $\mathbf{y^1D^o_2}$
La II	4123.218	0.127	B+	5d6s $\mathbf{a^3D_2} \rightarrow$ 5d6p $\mathbf{x^3F^o_3}$
La II	4196.546	-0.30	B+	5d6s $\mathbf{a^3D_2} \rightarrow$ 5d6p $\mathbf{x^3F^o_2}$
La II	4238.37	-0.26	B+	5d6s $\mathbf{a^3D_3} \rightarrow$ 5d6p $\mathbf{x^3F^o_3}$
La II	4333.75	-0.059	B+	5d^2 **2** $\rightarrow$ 5d6p $\mathbf{y^1D^o_2}$
La II	4429.91	-0.351	B+	5d6s $\mathbf{a^3D_1} \rightarrow$ 5d6p $\mathbf{y^1D^o_2}$

a: Not available in NIST. log(gf) from Zhiguo et al. (1999).

5.6.29 Cerium ($_{58}$Ce)

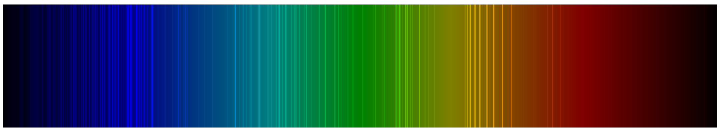

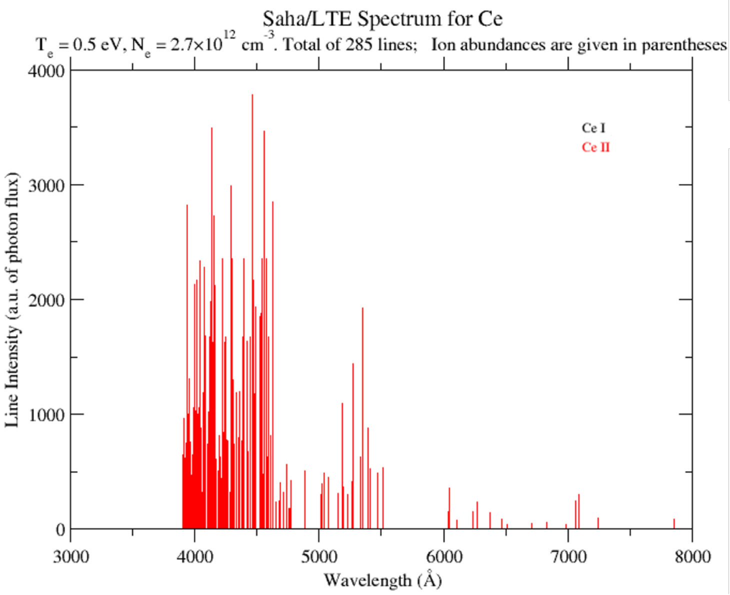

Figure 5.54: *Cerium lines intensity. Saha-LTE Spectrum (NIST) from ad hoc conditions: electron temperature 0.5 eV and electron density of 2.7x10^{12} cm^{-3}.*

As commented for lanthanum, given the low abundances of the second peak s-process elements, their lines are generally weak but the barium ones. Next, a list of some bibliographic Ce II lines.

Line	Ritz Air (Å)	log($g_i f_{ik}$)	Accuracy	Config. **Level**
Ce II	3999.2368	0.06	B+	$4f5d(^1\mathbf{G}^o)6s\ \mathbf{o_{9/2}} \rightarrow 4f5d(^1\mathbf{G}^o)6p\ \mathbf{_{11/2}}$
Ce II	4053.5031	-0.61	B+	$4f(^2\mathbf{F}^o)5d^2(^3\mathbf{F})\ ^4\mathbf{H}^o_{7/2} \rightarrow 4f5d(^1\mathbf{G}^o)6p\ \mathbf{_{9/2}}$
Ce II	4073.4744	0.21	B+	$4f^2(^3\mathbf{H})6s\ ^4\mathbf{H_{7/2}} \rightarrow 4f^2(^3\mathbf{H_4})6p_{3/2}\ \mathbf{(4,3/2)^o_{5/2}}$
Ce II	4083.2218	0.27	B+	$4f5d(^3\mathbf{H}^o)6s\ ^4\mathbf{H}^o_{11/2} \rightarrow 4f5d(^3\mathbf{H}^o)6p\ ^4\mathbf{H_{11/2}}$
Ce II	4137.6453	0.40	B+	$4f^2(^3\mathbf{H})6s\ ^4\mathbf{H_{9/2}} \rightarrow 4f^2(^3\mathbf{H_4})6p_{3/2}\ \mathbf{(4,3/2)^o_{11/2}}$
Ce II	4186.5941	0.813[a]	*	$4f^2(^3\mathbf{H})6s\ ^4\mathbf{H_{13/2}} \rightarrow 4f^2(^3\mathbf{H_6})6p_{3/2}\ \mathbf{(6,3/2)^o_{15/2}}$
Ce II	4222.597	-0.15	B+	$4f(^2\mathbf{F}^o)5d^2(^3\mathbf{F})\ \mathbf{o_{9/2}} \rightarrow 4f5d(^1\mathbf{G}^o)6p\ \mathbf{_{9/2}}$
Ce II	4382.165	0.13	B+	$4f^2(^3\mathbf{H})6s\ ^4\mathbf{H_{11/2}} \rightarrow 4f^2(^3\mathbf{H_4})6p_{3/2}\ \mathbf{(4,3/2)^o_{11/2}}$
Ce II	4418.780	0.27	B+	$4f^2(^3\mathbf{H})6s\ ^4\mathbf{H_{13/2}} \rightarrow 4f^2(^3\mathbf{H_5})6p_{3/2}\ \mathbf{(5,3/2)^o_{13/2}}$
Ce II	4460.207	0.28	B+	$4f^2(^3\mathbf{H})6s\ ^4\mathbf{H_{7/2}} \rightarrow 4f^2(^3\mathbf{H_4})6p_{1/2}\ \mathbf{(4,1/2)^o_{7/2}}$
Ce II	4523.075	-0.08	B+	$4f^2(^3\mathbf{H})6s\ ^4\mathbf{H_{9/2}} \rightarrow 4f^2(^3\mathbf{H_4})6p_{1/2}\ \mathbf{(4,1/2)^o_{7/2}}$
Ce II	4562.359	0.21	B+	$4f^2(^3\mathbf{H})6s\ ^4\mathbf{H_{7/2}} \rightarrow 4f^2(^3\mathbf{H_4})6p_{1/2}\ \mathbf{(4,1/2)^o_{9/2}}$
Ce II	4628.161	0.14	B+	$4f^2(^3\mathbf{H})6s\ ^4\mathbf{H_{9/2}} \rightarrow 4f^2(^3\mathbf{H_4})6p_{1/2}\ \mathbf{(4,1/2)^o_{9/2}}$

a: Not available in NIST. log(gf) from http://kurucz.harvard.edu/ linelists/gfnew/gfall08oct17.dat

5.6.30 Neodymium ($_{60}$Nd)

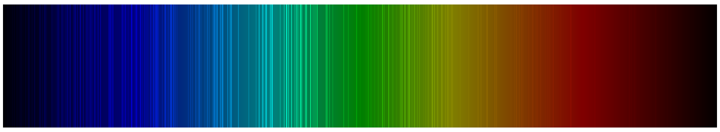

Given its low abundance, very weak and blended Nd II lines are the only options for this second peak s-process element.

Line	Ritz Air (Å)	log($g_i f_{ik}$)	Accuracy	Config. **Level**
Nd II	4040.7918	0.117	B+	$4f^4(^5\mathbf{I})6s\ ^6\mathbf{I_{11/2}} \rightarrow \mathbf{o_{13/2}}$
Nd II	4061.0799	0.550	B+	$4f^4(^5\mathbf{I})6s\ ^6\mathbf{I_{15/2}} \rightarrow 4f^4(^5\mathbf{I})6p\ ^6\mathbf{K}^o_{17/2}$
Nd II	4109.0711	-0.163	B+	$4f^4(^5\mathbf{I})6s\ ^6\mathbf{I_{9/2}} \rightarrow \mathbf{o_{11/2}}$
Nd II	4109.4478	0.350	B+	$4f^4(^5\mathbf{I})6s\ ^6\mathbf{I_{13/2}} \rightarrow 4f^4(^5\mathbf{I})6p\ ^6\mathbf{K}^o_{15/2}$
Nd II	4156.0778	0.164	B+	$4f^4(^5\mathbf{I})6s\ ^6\mathbf{I_{11/2}} \rightarrow 4f^4(^5\mathbf{I})6p\ ^6\mathbf{K}^o_{13/2}$
Nd II	4177.3196	-0.101	B+	$4f^4(^5\mathbf{I})6s\ ^6\mathbf{I_{9/2}} \rightarrow 4f^4(^5\mathbf{I})6p\ ^6\mathbf{K}^o_{11/2}$
Nd II	4247.365	-0.212	B+	$4f^4(^5\mathbf{I})6s\ ^6\mathbf{I_{7/2}} \rightarrow \mathbf{o_{9/2}}$
Nd II	4303.571	0.084	B+	$4f^4(^5\mathbf{I})6s\ ^6\mathbf{I_{7/2}} \rightarrow 4f^4(^5\mathbf{I})6p\ ^6\mathbf{K}^o_{9/2}$
Nd II	4451.563	0.07	B+	$4f^4(^5\mathbf{I})6s\ ^4\mathbf{I_{11/2}} \rightarrow 4f^4(^5\mathbf{I})6p\ ^6\mathbf{K}^o_{13/2}$

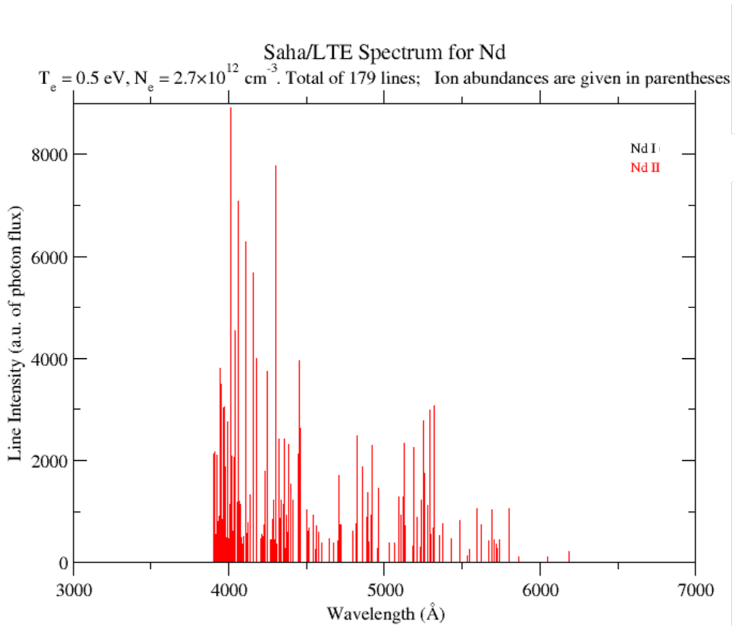

Figure 5.55: *Neodymium lines intensity. Saha-LTE Spectrum (NIST) from ad hoc conditions: electron temperature 0.5 eV and electron density of 2.7x10^{12} cm^{-3}.*

5.6.31 Europium ($_{63}$Eu)

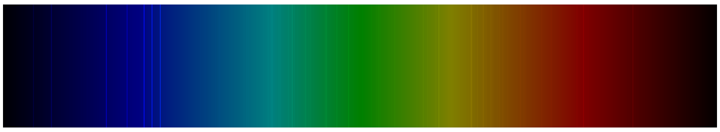

Europium is an r-process element, often used to assess evolutionary questions, contrasting with respect to the s-process elements like barium. Eu II 4129 Å line, although partially blended, is the most used line for abundance studies. In the bluest extreme of the spectra is possible to find others useful, as the ones included in the next table.

Line	Ritz Air (Å)	log($g_i f_{ik}$)	Accuracy	Config. **Level**
Eu II	3930.499	0.24	*	$4f^7(^8S^o)6s\ \mathbf{a^7S^o_3} \rightarrow 4f^7(^8S^o_{7/2})6p_{3/2}\ \mathbf{(7/2,3/2)_3}$
Eu II	3971.972	0.28	*	$4f^7(^8S^o)6s\ \mathbf{a^7S^o_3} \rightarrow 4f^7(^8S^o_{7/2})6p_{3/2}\ \mathbf{(7/2,3/2)_4}$
Eu II	4129.725	0.19	*	$4f^7(^8S^o)6s\ \mathbf{a^9S^o_4} \rightarrow 4f^7(^8S^o_{7/2})6p_{1/2}\ \mathbf{(7/2,1/2)_4}$
Eu II	4205.04	0.12	*	$4f^7(^8S^o)6s\ \mathbf{a^9S^o_4} \rightarrow 4f^7(^8S^o_{7/2})6p_{1/2}\ \mathbf{(7/2,1/2)_3}$

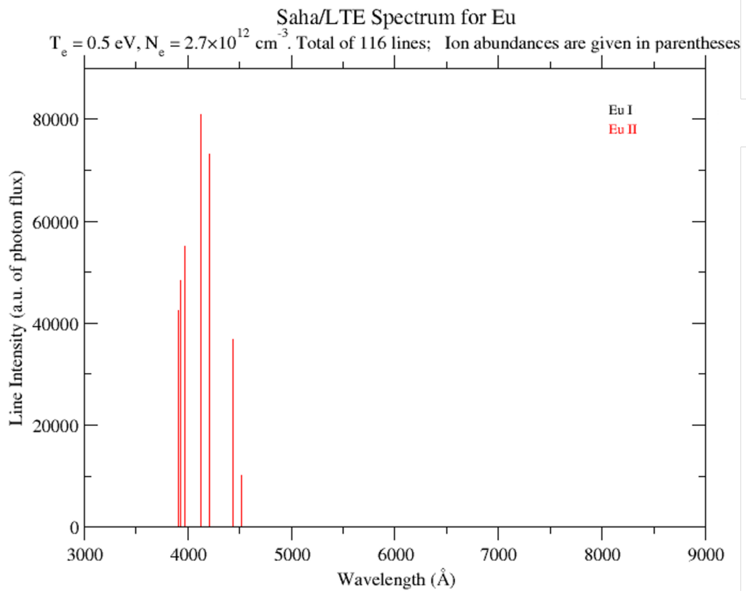

Figure 5.56: *Europium lines intensity. Saha-LTE Spectrum (NIST) from ad hoc conditions: electron temperature 0.5 eV and electron density of 2.7x10^{12} cm^{-3}.*

Calar Alto Observatory, Almeria, Spain

Compiled using LaTeX

Epilogue

Even for a neophyte, when faces the factors that determine the abundance trends of each atomic element in the galaxy, is easy to understand and get overwhelmed by the Homeric task which astronomers and astrophysicists have to confront on the nucleosynthesis understanding matter.

Indeed, they must offer a consistent narration about how stellar inner layers physical and chemical conditions change in relation with mass, metallicity and stellar age and the stages the stars are getting through with the help of stellar models.

With the somehow limited experimental data from the photospheres of the stars, a thinner and much colder layer than the rest of the star's inner, abundances for some elements are derived. And based on this and helped by other astrophysics fields information, they must trace a complete relate of the galaxy evolution: How the galaxy was formed, how it is structured, which events conformed their parts, how old are they, from which kind of stars are made up of, how have they evolved...and once more, helped by theoretical models, what nucleosynthesis sites are contributing to each element abundance in each evolutionary stage of the universe and why the trends look like as they are.

And everything, in spite of a path plenty of difficulties, uncertainties, possibilities and unknowns channels or mechanisms still to be researched or constrained. But knowledge emerges from such tremendous, and in some way touching, human effort of understanding.

The entire history of the universe, the Milky Way evolution, the stellar evolution, chemical and physical knowledge, spectroscopic knowledge, decades of technical advancing and above all, collective and individual human effort, are condensed and delivered in the form of an apparently simple figure as the shown periodic table, that however, is telling a plain story to the rest of us about where we come from and what we are made up of, those 2% of atomic elements heavier than the primordial hydrogen and helium, one way or another, forged within the stars for 13.000 million years of evolution.

Appendix A

Galactic Chemical Evolution (GCE) Models

Galactic chemical evolution models are an useful tool for the analysis of observational data and the chemical abundances trends of elements. They show how well the nucleosynthesis sites, yields and galactic evolution is understood for each element. Indeed, for some elements the theoretical predictions of the models and observational data fit quite well. Unfortunately, it is not the case for an appreciable bunch of elements revealing the need of new observations and the constraining of new or poorly known mechanisms or sites of nucleosynthesis. The most important factor of uncertainty is the set of nucleosynthesis yields.

The subject, obviously, is extraordinary complex and far away from the scope of a beginner on the matter but it is worth, in an extreme lightly way, to provide a shallow glimpse into the basic features of some widely used GCE models (see chapters 2 and 3), without any deepening at all in formalism or specific parameters.

A.1. Only a glimpse into three GCE studies

As mentioned, this subject is extraordinary complex and far away from the knowledge and understanding of this beginner. In spite of this handicap, it will be tried in the next pages the description of the models from three GCE studies, used in this manuscript. There will be merely extracted the direct information found in their articles of some general assumptions for their building. Even with a partial understanding, it might illustrate the mentioned complexity of the matter. And on the other side, although they are literal information pieces that can be consulted in their articles, the gathered info might be useful in some aspect or at least as a first glimpse on the corresponding model.

A.1.1 Prantzos et al. (2018) model

The Prantzos et al. (2018) model is based on one-zone model (Goswami & Prantzos 2000), updated in Kubryk et al. (2015), and in which local disk is built by infall of gas at an exponentially decreasing rate and a characteristic time-scale of 10 Gyr. The star formation rate is given by a Schmidt-Kennicutt law in both sub-systems (disk and halo):

$$\Psi(t) = \alpha \cdot \Sigma_G(t)^{1.5}$$

Where Σ_G is the local gas surface density and the coefficient α is chosen as to obtain a gas fraction of ~20% at the end of the simulation.

Therefore this simple approach of both disks and the halo, does not aspire to develop a close to realistic description of them. And this aspect is aware by authors that claim the model is poorly reflecting the physical processes in both the halo and the disk.

For instance, part of the scatter of the chemical abundances in stars at very low metallicities ([Fe/H]< -2.0 dex) probably reflects chemical inhomogeneities in the interstellar medium at very early epochs in the evolution of the Galaxy. For heavy elements though, dispersion may result both from inhomogeneities in the ISM (e.g. Cescutti et al. 2013) and from production in sub-haloes evolving at different rates. It is well established that the Galactic halo did not evolve in a "monolithic collapse" but rather by hierarchical merging of smaller sub-haloes. In that case, there is no unique relation between metallicity and time, since the different sub-haloes evolved at a different pace (Prantzos 2006).

And on the other hand the Milky Way disk is more complex than described by 1-zone model as seen, along this manuscript, from the distinct chemical abundances in the thin or the thick disks. This is suggesting the requirement of some mixing of stellar populations with different histories.

However, this kind of 1-models are still playing their role in studies of galactic chemical evolution since they allow one to probe some key features, like e.g. the dependence of yields on metallicity, the relative importance of various metal sources evolving on different timescales (e.g. massive stars vs. SNIa or LIM stars), the local star formation history (through the G-dwarf distribution), etc. And in the present study to test the implications and impact of their new grid of stellar yields from rotating massive stars.

Additional assumptions. Adopted initial mass function (IMF) of Kroupa (2002) in the mass range 0.1-120 $M_\odot$. Regarding stellar life-times depending on metallicity and mass, $\tau(M, Z)$, of Cristallo et al. (2015b) for stars in the mass range 1-7 $M_\odot$. Those from Limongi & Chieffi (2018) for > 7 $M_\odot$. The latter includes mass loss, rotation and yields of the stellar explosion. The yields of massive stars used are based on a grid of models in the mass range 13-20 $M_\odot$ and initial metallicities corresponding to [Fe/H] = 0; -1; -2; -3. For each metallicity they computed models for three initial rotational velocities, namely v_{rot} = 0; 150; 300 $\mathrm{km \cdot s^{-1}}$ (see Fig. A.1).

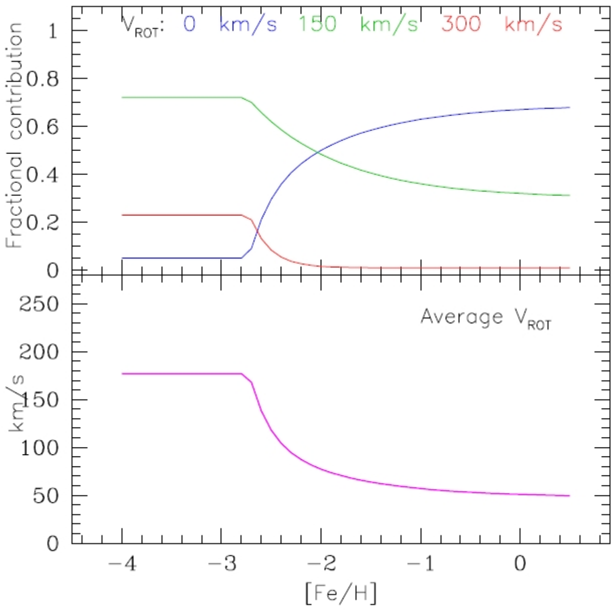

Figure A.1: ***Top***: *Adopted fractional contribution with metallicity of the yields of rotating massive stars.* ***Bottom***: *Resulting average initial rotational velocity of massive stars as a function of metallicity. From Prantzos et al. (2018).*

The model adopts fiduciary yields for the r-isotopes since most heavy elements have a mixed origin. Core collapse supernovae (CCSN/SNeII) have long been considered as the main site of the r-process but detailed nucleosynthesis studies in those objects have failed up to now to account satisfactorily for the production of the full range of r-process elements. As shown in the Eu section (see Sect. 3.9) other sources are suspected importantly to contribute as neutron stars or neutron and black hole pair mergers (CBM mergers). Or MHD-SNeII a rare kind of supernovae of very massive stars characterized by high rotation rates and large magnetic fields. Both additional sources are though to have enriched the medium in very early stages of the universe in r-process elements.

The detection of the gravitational waves of a pair of NS stars merger by LIGO/Virgo, GW170817, allow to find evidences of r-process elements nucleosynthesis (see Sect. 1.5). However, there is still no consensus on the role of that class of objects in the production and evolution of r-elements. This model assumes that they are produced in CCSN/SNeII and their yields for a star of mass M and metallicity Z are scaled to the yield of oxygen $Y_{^{16}O}$(M,Z). The choice of ^{16}O, produced exclusively by massive stars, as reference isotope ensures that if its solar abundance is well reproduced in the simulation, so will be the r-fractions of heavy elements. This allow them to study the behavior of the other isotopes (of mixed origin), as well as the behavior of the elements and to constrain the adopted s-element yields.

The model includes 285 stable isotopes from H to U. Radioactive decay within long lived stars and in the ISM are taken into account for those isotopes whose lifetime shorter than the Universe age.

Yields in GCE calculations requires interpolation in the mass range of the super-AGB stars and low mass CCSN/SNeII, ~ 7 to 12 $M_\odot$, where no complete grids of yields were available at the study date.

For the rate of thermonuclear supernovae (SNIa) the model adopts a semi-empirical approach: the observational data of surveys concerning the Delayed Time Distribution (DTD) are described well by a power-law in time, of the form $\propto t^{-1}$. This approach, leads to 1.3 SNIa per 1000 $M_\odot$ of stars formed. SNIa yields are adopted from Iwamoto et al. (1999) for Z=0 and $Z=Z_\odot$, interpolating logarithmically in metallicity between those values.

We do not extent into other specific details taken into account, but this info directly taken from the Prantzos et al. (2018) article is enough for describing the main characteristics. Although they might be not fully understand by a neophyte on the matter, one can be aware of the complexity of factors involved in the task of building a GCE model and developing such study.

Maybe from the Prantzos et al. (2018) there is to highlight the use of one-zone formalism for describing the formation of galactic disk and halo. Although it is poorly reflecting the physical processes in both the halo and the disk, as the same authors claim, its use is helpful for the purpose of the article: The impact of their new grid of stellar yields from rotating massive stars and the comparison with results when are not included in the model. Surely, although unknown for this beginner, part of the reason for this choice has to do with a simplification of the computational calculations and the decreasing of computational time cost.

A.1.2 Romano et al. (2010) models

Romano et al. (2010) used in their article a large grid of models that combined different prescriptions of single star yields from several authors (see Fig. A.2).

Models are not going to be fully described but some swallow features. In spite of the different combinations of stellar yields for single stars, the galaxy chemical evolution model chosen is the two-infall model (their case B) developed by Chiappini et al. (1997, 2001), adopting their formalism and basic equations.

The overlaying concept of this description of the galaxy formation has been already described in some sections of this manuscripts. However, it is once more explained in a schematic way:

The inner halo and thick disc of the Milky Way are assumed to form on a relatively short time-scale (about 1 Gyr) out of a first infall episode, whereas the thin disc forms inside-

Model	Adopted stellar yields LIMSs	Massive stars	Comments
1	vdHG97, η_{AGB} var	WW95, case B	Reference model
2	vdHG97, η_{AGB} var	WW95, case A	Mass cut changed
3	vdHG97, η_{AGB} var	WW95, case B + M92 pre-SN yields	Winds from $Z = Z_\odot$ massive stars included
4	vdHG97, η_{AGB} var	K06, $\varepsilon_{HN} = 0$	SNII yields changed
5	vdHG97, η_{AGB} var	K06, $\varepsilon_{HN} = 1$	HN nucleosynthesis included
6	vdHG97, η_{AGB} var	K06, $\varepsilon_{HN} = 1$ + Geneva pre-SN yields, $\upsilon_{ini} \neq 0$	Stellar rotation included
7	vdHG97, η_{AGB} var	K06, $\varepsilon_{HN} = 1$ + Geneva pre-SN yields, $\upsilon_{ini} = 0$	
8	vdHG97, η_{AGB} const	K06, $\varepsilon_{HN} = 1$ + Geneva pre-SN yields, $\upsilon_{ini} \neq 0$	Mass loss along the AGB changed
9	vdHG97, minimum HBB	K06, $\varepsilon_{HN} = 1$ + Geneva pre-SN yields, $\upsilon_{ini} \neq 0$	HBB extent reduced
10	M01, $\alpha = 1.68$	K06, $\varepsilon_{HN} = 1$ + Geneva pre-SN yields, $\upsilon_{ini} \neq 0$	LIMS yields changed
11	M01, $\alpha = 2.50$	K06, $\varepsilon_{HN} = 1$ + Geneva pre-SN yields, $\upsilon_{ini} \neq 0$	HBB strength increased
12	M01, $\alpha = 1.68$	K06, $\varepsilon_{HN} = 1$ + [Geneva, $\upsilon_{ini} \neq 0$ + M92] pre-SN yields	
13	KL07, with extra pulses	K06, $\varepsilon_{HN} = 1$ + Geneva pre-SN yields, $\upsilon_{ini} \neq 0$	AGB yields from detailed stellar models
14	KL07, with extra pulses	K06, $\varepsilon_{HN} = 1$ + [Geneva, $\upsilon_{ini} \neq 0$ + M92] pre-SN yields	
15	K10, without extra pulses	K06, $\varepsilon_{HN} = 1$ + Geneva pre-SN yields, $\upsilon_{ini} \neq 0$	Up-to-date nuclear reaction rates for LIMSs

Notes. vdHG97: van den Hoek & Groenewegen (1997); WW95: Woosley & Weaver (1995); M92: Maeder (1992); K06: Kobayashi et al. (2006); M01: Marigo (2001); KL07: Karakas & Lattanzio (2007); K10: Karakas (2010). The models adopting the yields by Marigo (2001) for LIMSs use self-consistent nucleosynthesis prescriptions from Portinari et al. (1998) for stars of initial mass m = 6 $M_\odot$ and m = 7 $M_\odot$.

Figure A.2: *Some nucleosynthesis prescriptions of the models used in the theoretical GCE study by Romano et al. (2010).*

out on longer time-scales (7 Gyr in the solar vicinity and more than a Hubble time at the outermost radii) during a second independent episode of extragalactic gas infall.The Galactic disc is approximated by several independent rings, 2 kpc wide. The stellar formation rate adopted is proportional to both the total mass and the gas surface densities. The efficiency of conversion of gas into stars is higher during the halo/thick-disc phase than during the thin-disc phase. Furthermore, it drops to zero every time the gas density drops below a critical density threshold.

Basic formalism as the accretion rate equation in each independent 2 kpc shell that is approximating the Galactic disk is taken from Matteucci & Francois (1989). No exchange of matter between them is assumed:

$$\frac{\Sigma_I(R,t)}{dt} = A(R)e^{-\frac{t}{\tau_H}} + B(R)e^{-\frac{(t-t_{max})}{\tau_D}}$$

Where $\Sigma_I(R,t)$ is the surface mass density of the infalling material, which is assumed to have primordial chemical composition; t_{max} is the time of maximum gas accretion onto the disk, coincident with the end of the halo/thick-disk phase and set as previously commented in 1 Gyr ; τ_H and τ_D are respectively the timescales for mass accretion onto the halo/thick-disk and thin disk components. In particular, $\tau_H = 0.8\,Gyr$ and, according to the inside-out scenario, $\tau_D = 1.03 \cdot R\,(kpc^{-1}) - 1.27\,Gyr$. A linear approximation for the variation of τ_D is adopted. The quantities A(R) and B(R) are derived from the condition of reproducing the current total mass surface density distribution in the halo and along the disk, at the present Rana (1991).

The stellar lifetimes are taken into account in details. As for the stellar IMF, the Kroupa et al. (1993) IMF is assumed in the 0.1–100 $M_\odot$ mass range. The rate of SNIa explosions is calculated as in the Matteucci & Greggio (1986) study. The yields of SNIa are taken from Iwamoto et al. (1999), model W7.

For single stars, different sets of stellar yields are adopted as shown in Table A.2. This factor is the only difference among the 15 models tested. For LIMS, the authors consider the yields by:

LIMS yields

- van den Hoek & Groenewegen (1997) for two choices of the mass-loss rate and minimum core mass for hot bottom burning
- Marigo (2001) for two choices of the mixing-length parameter
- Karakas & Lattanzio (2007) standard set, taking the contribution from "extra pulses" into account
- Karakas (2010) who recomputed Karakas & Lattanzio (2007) with updated nuclear reaction rates and enlarged the grid of masses and metallicities.

For massive stars, the authors consider the yields by:

Massive star yields

- Woosley & Weaver (1995), computed without mass loss and without rotation
- Kobayashi et al. (2006), including metallicity-dependent mass loss
- The Geneva group Meynet & Maeder (2002b); Hirschi et al. (2005); Hirschi (2007); Ekström et al. (2008) limited to the presupernova stage, but computed with both mass loss and rotation
- Older yields by Maeder (1992) for solar-metallicity stars (with higher mass-loss rates but without rotation) are considered as well

All of the adopted yield sets are metallicity dependent and are provided for various metallicity values. For instance, the Geneva group yields which include rotation, show different rotation velocity dependent on metallicity (see Fig. A.3), impacting the final yields and their references chosen.

Similar dependency on metallicity might be found in the ejected mass as shown for some elements in Fig. A.4.

Further and thorough details of every set of yields are developed in the article. They are beyond from the scope and purpose of this schematic review.

Z_{ini}	$m_{ini}(v_{ini})$	Ref.
0	9(500), 15(800), 25(800), 40(800), 60(800), 85(800)	1
10^{-8}	9(500), 20(600), 40(700), 60(800), 85(800)	2
10^{-5}	9(300), 15(300), 20(300), 40(300), 60(300)	3
0.004	9(300), 12(300), 15(300), 20(300), 25(300), 40(300), 60(0)	3
0.02	12(300), 15(300), 20(300), 25(300), 40(300), 60(300)	4

Figure A.3: *Yields for massive stars from pre-supernova Geneva models including mass loss and rotation. Listed are: the initial metallicity of the stars, Z_{ini}, the initial stellar masses (in $M_\odot$) and rotational velocities (in km·s^{-1}), $m_{ini}(v_{ini})$, and the reference papers from which the yields have been picked up: (1) Ekström et al. (2008); (2) Hirschi (2007); (3) Meynet & Maeder (2002b); (4) Hirschi et al. (2005).*

A.1.3 Kobayashi, Karakas and Lugaro (2020) model

Kobayashi et al. (2020a) construct their Galactic chemical evolution (GCE) models for all stable elements from C to U using theoretical nucleosynthesis yields and event rates of all chemical enrichment sources. From their article, we want to highlight the concise and, for a beginner, extraordinary useful summary of the chemical nucleosynthesis sources. Meanwhile they describe the complex setup of factors and yields taken into account, additionally they develop a remarkable piece of information, accessible for a beginner, about the state-of-the-art in the nucleosynthesis sources subject.

The basic equations, star formation rates and galactic formation description of this GCE, are not included in this Anexo. We consider that the main didactic purpose has been accomplished in the preceding models information.

Here, we focus on the information regarding the decisions taken about nucleosynthesis sources and yields. The authors take into account the next list of galactic chemical enrichment sources:

Stellar winds in AGBs and core-collapse supernovae

All dying stars return a fraction or all of their envelope mass to the interstellar medium (ISM) by stellar winds. These winds (for massive stars occurring before the final supernova explosions) carry newly processed metals and the unprocessed metals that were trapped inside the star at its formation and is returned to the ISM. The wind mass is given by:
$M_{wind} = M_{init} - M_{remnant} - \Sigma_i p_{z_i m}$
M_{init} is the initial mass and $M_{remnant}$ the remnant mass (BH, NS or WD). $p_{z_i m}$ is the nucleosynthesis yield of each element/isotope. In function of the initial masses, remnant masses and nucleosynthesis yields are set up as in Kobayashi et al. (2006, 2011b).

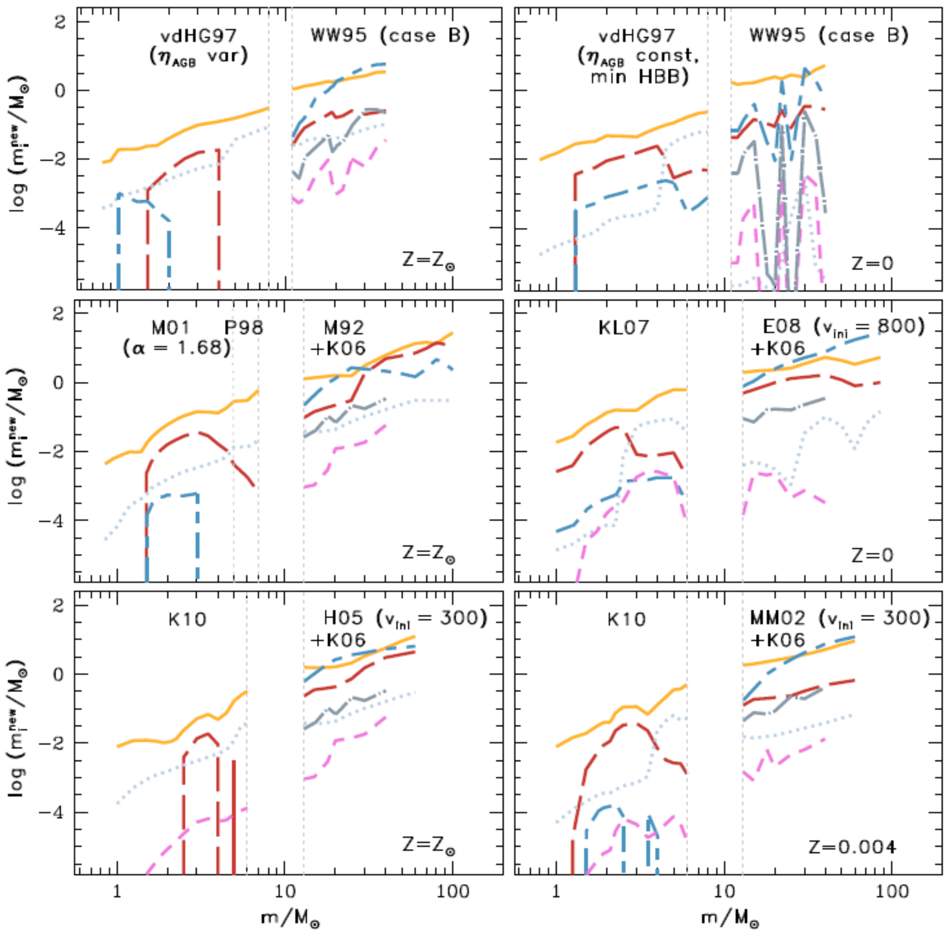

Figure A.4: *Ejected masses of newly produced elements as a function of the stellar initial mass, from different authors...*
vdHG97:van den Hoek & Groenewegen (1997); WW95:Woosley & Weaver (1995); M01:Marigo (2001); P98:Portinari et al. (1998); M92:Maeder (1992); K06:Kobayashi et al. (2006); KL07:Karakas & Lattanzio (2007); E08:Ekström et al. (2008); K10:Karakas (2010); H05:Hirschi et al. (2005); MM02:Meynet & Maeder (2002b)
...and for different initial metallicities.
Solid (orange) lines: He; long-dashed (red) lines: C; dotted (light blue) lines: N; short-dashed-long-dashed (blue) lines: O; short-dashed (magenta) lines: Na; dot-dashed (gray) lines: Mg.

Asymptotic Giant Branch (AGB) stars

Stars with initial masses between roughly 0.9 - 8 $M_\odot$ (depending on metallicity) pass through the thermally-pulsing AGB phase. The He-burning shell is thermally unstable and can drive mixing of material from the core into the envelope, which has been processed by nuclear reactions. This mixing is known as third dredge-up

(TDU), and is responsible for enriching the surface in ^{12}C and other products of He-burning, as well as s-process elements.

In AGB stars with initial masses $\geq$ 4 $M_{\odot}$, the base of the convective envelope becomes hot enough to sustain proton-capture nucleosynthesis (hot bottom burning). HBB can change the surface composition because the entire envelope is exposed to the hot burning region a few thousand times per interpulse period. The CNO cycles operate to convert the freshly synthesized ^{12}C into primary ^{14}N, and the NeNa and MgAl chains may also operate to produce ^{23}Na and Al.

At the deepest extent of each TDU, it is assumed that the bottom of the H-rich convective envelope penetrates into the ^{12}C-rich intershell layer resulting into a partial mixing zone (PMZ) leading to the formation of a ^{13}C pocket via the ^{12}C(p,γ)^{13}N(β^{+})^{13}C reaction chain. While many physical processes have been proposed, there is still not full agreement on which process(es) drives the mixing. The inclusion of ^{13}C pockets in theoretical calculations of AGB stars is still one of the most significant uncertainties affecting predictions of the s-process and in particular the absolute values of the yields (Karakas & Lugaro 2016; Buntain et al. 2017). Other major uncertainties come from the rates of the neutron source reactions ^{13}C(α,n)^{16}O and ^{22}Ne(α,n)^{25}Mg (Bisterzo et al. 2015) and the neutron-capture cross sections of some key isotopes (Cescutti et al. 2018).

The authors of this model take the nucleosynthesis yields including s-process and WD masses primarily from Lugaro et al. (2012) for Z = 0.0001, Fishlock et al. (2014) for Z = 0.001, Karakas et al. (2018) for Z = 0.0028, and Karakas & Lugaro (2016) for Z = 0.007, 0.014 and 0.03. In these post-processing nucleosynthesis, protons are added to the top layers of the He-intershell at the deepest extent of each TDU episode by means of an artificial PMZ. The mass of the PMZ, i.e., how deep it reaches below the base of the convective envelope, is given by a free parameter M_{mix} as a function of mass and metallicity, as discussed in detail by Karakas & Lugaro (2016). In addition, for this paper the authors calculated some selected low-mass star models with Z = 0.014, 0.007 and 0.0028 using a smaller PMZ mass; namely these models set the PMZ mass to be 0.001 $M_{\odot}$ compared to the standard size, 0.002 $M_{\odot}$ used in Karakas & Lugaro (2016). The adopted PMZ mass of their fiducial model is summarized in Table A.5.

Non time-dependent convective overshooting, which essentially only affects the depth of the TDU and not the formation of the PMZ, is also included in some models (in function of stellar mass and metallicity).

The newly produced metal yields, $p_{z_i m}$, are calculated as the difference between the amount of the species in the winds and the initial amount in the envelope of the progenitor star. The initial abundances are set as the scaled proto-solar abundances, which are calculated from Asplund et al. (2009).

Z	0.0001	0.001	0.0028	0.007	0.014	0.03
$M_{\rm mix} = 0$	-		$1M_\odot$	$1 - 1.25M_\odot$	$1 - 1.25M_\odot$	$1 - 2.25M_\odot$
$M_{\rm mix} = 2 \times 10^{-3}$	$0.9 - 2.25M_\odot$	$1 - 2.5M_\odot$	-	-	-	-
$M_{\rm mix} = 1 \times 10^{-3}$	$2.5 - 3M_\odot$	$2.75M_\odot$	$1.15 - 2.75M_\odot$	$1.5 - 3.75M_\odot$	$1.5 - 4M_\odot$	$2.5 - 4M_\odot$
$M_{\rm mix} = 5 \times 10^{-4}$	-	$3M_\odot$	$3 - 3.5M_\odot$	-	-	-
$M_{\rm mix} = 1 \times 10^{-4}$	-	-	$3.75 - 4M_\odot$	$4 - 4.25M_\odot$	$4.25 - 5M_\odot$	$4.25 - 5M_\odot$
$M_{\rm mix} = 0$	$3.5 - 6M_\odot$	$3.25 - 7M_\odot$	$4.5 - 7M_\odot$	$4.5 - 7.5M_\odot$	$5.5 - 8M_\odot$	$5.5 - 8M_\odot$
Z	0.0001	0.001	0.004	0.008	0.02	-
$M_{\rm mix} = 0$	$6.5 - 7.5M_\odot$	$7.5M_\odot$	$7.5 - 8M_\odot$	$8 - 8.5M_\odot$	$8.5 - 9M_\odot$	

Figure A.5: *The mass of partial mixing zones, $M_{\rm mix}$, adopted for the AGB and super-AGB models as a function of initial mass and metallicity.*

Super AGB stars

The fate of stars with initial masses between about 8-10 $M_\odot$ (at Z = 0.02) is uncertain (Doherty et al. 2017, for a review). The upper limit of AGB stars, $M_{up,C}$, is defined as the minimum mass for carbon ignition, and is estimated to be larger at high metallicity and also for metallicities lower than Z ~ 10^{-4} (Gil-Pons et al. 2007; Siess 2007).

Just above $M_{up,C}$, neutrino cooling and contraction leads to the off-centre ignition of a C flame, which moves inward but does not propagate to the centre. This may form a hybrid C+O+Ne WD (see Kobayashi et al. 2015, for more details). These hybrid WDs can be progenitors of a sub-class of SNeIa, called SNeIax (Foley et al. 2013), which are expected preferably in dwarf galaxies (Kobayashi et al. 2015; Cescutti & Kobayashi 2017). The authors take the nucleosynthesis yields of an SNIax from Fink et al. (2014).

Above this mass range, the off-centre C ignition moves inward all the way to the centre (≤ 9 $M_\odot$), or stars undergo central carbon ignition (≥ 9 $M_\odot$). For both cases, a strongly degenerate O+Ne+Mg core is formed (O+Ne dominant, but Mg is essential for electron capture). If the stellar envelope is lost by winds or binary interaction, an O+Ne+Mg WD may be formed. This upper mass limit is defined as the minimum mass for the Ne ignition, $M_{up,Ne}$ ~ 9 ± 1 $M_\odot$ and is smaller for lower metallicities (Siess 2007; Doherty et al. 2015).

Stars with $M_{up,Ne}$ < M < 10 $M_\odot$ may have cores as massive as ≥ 1.35 $M_\odot$ and ignite Ne off-centre. If Ne burning is not ignited at the centre (for a core mass < 1.37 $M_\odot$, Nomoto 1984), or if off-centre Ne burning does not propagate to the centre (M = 8.8 $M_\odot$, Jones et al. 2014), it has been believed that such a core eventually undergoes an electron-capture induced collapse. Electron-Capture Supernovae (ECSN, see Nomoto et al. 2013, for more details) are one of the candidate r-process sites. Recent 3D simulations showed that the fate of the O+Ne+Mg core may depend on the density, and the explosion may result in thermonuclear disruption leaving behind an

O+Ne+Fe WD instead (Jones et al. 2016).
The mass ranges of the C+O+Ne WDs, O+Ne+Mg WDs, and ECSNe are taken from Doherty et al. (2015). Ne burning is not followed in Doherty et al. (2015); the lower-limit of ECSNe is defined with the temperature ~ $1.2 \cdot 10^9$ K, and the upper limit is defined with the core mass = 1.375 $M_\odot$ at the end of C burning. These may underestimate the ECSN rate. These mass ranges are highly affected by convective overshooting and mass-loss. There is no region where the core mass is larger than the Chandrasekhar mass limit in the models considered by (Doherty et al. 2015); if there were, the stars could explode as so-called Type 1.5 SNe, although no signature of such supernovae has yet been observed. The nucleosynthesis yields (up to and including Ni) of super AGB stars are taken from Doherty et al. (2014a,b). The initial abundances are the scaled solar abundances from Grevesse et al. (1996).

Core-collapse supernovae

Although a few groups have presented multi-dimensional simulations of exploding 10 - 25 $M_\odot$ stars (Marek & Janka 2009; Kotake et al. 2012; Bruenn et al. 2013; Burrows 2013), the explosion mechanism of core-collapse (Type II, Ib, and Ic) supernovae is still uncertain; the ejected iron mass in explosion simulations is not as large as observed (Bruenn et al. 2016) and the formation of black holes is also not followed in most cases, except for (Kuroda et al. 2018). The authors use the nucleosynthesis yields from one-dimensional (1D) calculations of Kobayashi et al. (2006, 2011b).
The uncertainties include the reaction rates (namely, of $^{12}C(\alpha,\gamma)^{16}O$), mixing in stellar interiors, rotationally induced mixing processes, and mass loss via stellar winds, which affect the yields of elements/isotopes formed during hydrostatic burning. Furthermore, the most important uncertainty in the yields is associated with the formation of remnants (i.e., neutron stars or blackholes) in massive stars, and different methods have been used to address this problem.
As in Kobayashi et al. (2006), the ejected explosion energy and ^{56}Ni mass (which decays to ^{56}Fe) are determined to meet an independent observational constraint: the light curves and spectral fitting of individual supernova (Nomoto et al. 2013). As a result it is found that many core-collapse supernovae ($M \geq 20\ M_\odot$) have an explosion energy that is more than 10 times that of a regular supernova ($E_{51} \equiv E/10^{51}$ erg ≥ 10), as well as production of more iron and α elements. These are called Hypernovae (HNe), while all other supernovae with E51 = 1 are refereed to as SNeII. The nucleosynthesis yields are provided separately for SNeII and HNe as a function of the progenitor mass and metallicity. As mentioned above, the yield tables provide the amount of processed metals ($p_{z_i m}$) in the ejecta (in $M_\odot$), and the unprocessed metals are added in the GCE. The fraction of HNe at any given time is uncertain and

is set $\epsilon_{HN} = 0.5$ for masses M $\geq$ 20 $M_\odot$ following previous works (Kobayashi et al. 2006, 2011b), while a metal-dependent fraction ϵ_{HN} = 0.5, 0.5, 0.4, 0.01, and 0.01 for Z = 0, 0.001, 0.004, 0.02, and 0.05 was introduced in Kobayashi & Nakasato (2011) in order to match the observed rate of broad-line SNe Ibc at the present day (e.g., Podsiadlowski et al. 2004).

It is known that multi-dimensional effects are particularly important for some elements, e.g., Sc, V, Ti, and Co (Maeda & Nomoto 2003; Tominaga 2009). The authors calculated the K15 GCE model, which is plotted in Sneden et al. (2016) and Zhao et al. (2016), applying constant factors, +1.0, 0.45, 0.3, 0.2, and 0.2 dex for [(Sc, Ti, V, Co, and ^{64}Zn)/Fe] yields, respectively, which takes the 2D jet effects of HNe into account. The authors also show this K15 model for some elements in the paper.

Stellar rotation induce mixing of C into the H-burning shell, producing a large amount of primary nitrogen, which is mixed back into the He burning shell (Meynet & Maeder 2002a; Hirschi 2007). For high initial rotational velocities at low metallicity ("spin-stars"), this process results in the production of s-process elements, even at low metallicities (Frischknecht et al. 2016; Limongi & Chieffi 2018; Choplin et al. 2018).

Chiappini et al. (2006) showed that rotation is necessary to explain the observed N/O–O/H relations with a GCE model and the same result was shown in Kobayashi et al. (2011b). However, using more self-consistent cosmological simulations, Vincenzo & Kobayashi (2018) reproduced the observed relation not with rotation but with inhomogeneous enrichment from AGB stars. Therefore, the authors do not include yields from rotating massive stars in this paper. Prantzos et al. (2018) showed a GCE model assuming a metallicity-dependent function of the rotational velocities, and concluded that because of the contribution from rotating massive stars a further light element primary process (LEPP) is not necessary to explain the elemental abundances with A < 100. The authors show that they do not need to include fast rotating stars for these elements neither since other sources are present in their models.

Failed supernovae

The upper limit of SNeII supernovae, $M_{u,2}$, is not well known owing to uncertainties in the physics of blackhole formation, and was set as $M_{u,2}$ = 50 $M_\odot$ in Kobayashi et al. (2006, 2011b), which is the same for HNe. However, recently it has been questioned if massive SNe II can explode or not, both observationally and theoretically. In searching for the progenitor stars at the locations of nearby SNe IIP, no progenitor stars have been found with initial masses M > 30 $M_\odot$ (Smartt 2009). In multidimensional simulations of supernova explosions, it seems very difficult to explode stars $\geq$ 25 $M_\odot$ with the neutrino mechanism (e.g., Janka 2012), and similar results are obtained with parametrized 1D models (Ugliano et al. 2013; Müller et al. 2016). At lower metallicities, since the stellar cores become more compact, it might even be harder to explode. However, the metallicity dependence is probably not very straight forward and may be non-monotonic (Pejcha & Thompson 2015). Therefore, in this paper the authors include new nucleosynthesis yields of 'failed' supernovae (Kobayashi Tominaga 2020, in prep.) at the massive end of SNe II, while keeping the contributions from HNe. It is assumed that all CO cores fall onto black holes and is not ejected to the ISM, since the timescales of the multi-dimensional simulations are not long enough to follow this process. The upper mass limit of SNeII, $M_{u,2}$, is treated as a free parameter, while the upper mass limit of HNe is the same as the upper limit of initial mass function, M_u. In their fiducial model $M_{u,2} = 30\ M_\odot$ and $M_u = 50\ M_\odot$ are adopted (at > 30 $M_\odot$, the yields are interpolated between the values at 30 $M_\odot$ and 0 at 40 $M_\odot$). If it is assumed all ejecta collapses onto black holes, the evolution of C and N is slightly different, but there is no significant difference in the evolution of heavier elements.

Confusingly, failed supernovae are not related to faint supernovae (Nomoto et al. 2013; Ishigaki et al. 2014, 2018), which are suggested by completely different observational results. At [Fe/H] ≤ 2.5, a large fraction of stars are carbon enhanced relative to iron (CEMP stars, [C/Fe] > 0.7 in Aoki et al. 2007, but see Beers & Christlieb 2005 for a different definition), with increasing the fraction toward lower metallicities (e.g., Placco et al. 2014). CEMP stars with an s-process enrichment (CEMP-s, [Ba/Fe] > 1) are well explained by the binary mass transfer from AGB stars, while CEMP with no s-process enhancement (CEMP-no stars, [Ba/Fe] < 0) are observed to be both single and binaries (Hansen et al. 2016b) and several scenarios suggested (see Nomoto et al. 2013 and the references therein). Faint supernovae are core-collapse supernovae from massive (≥ 13 $M_\odot$) stars possibly only at Z = 0, with normal or large explosion energy (i.e., faint SNe or faint HNe) that leave relatively large black holes and eject C-rich envelope. Because of the small ejecta mass, the contribution to GCE is negligible and thus the authors do not include the yields of faint supernovae and exclude CEMP stars from most of figures in this paper.

Pair-instability supernovae

Stars with 100 $M_\odot \leq M \leq 300\ M_\odot$ encounter the electron-positron pair instability and do not reach the temperature of iron photodisintegration. Pair-instability supernovae (PISNe) are predicted to produce a large amount of metals such as S and Fe (Barkat et al. 1967; Heger & Woosley 2002; Umeda & Nomoto 2002). Despite searching for many years, no conclusive signature of PISNe has been detected in metal poor stars in the solar neighborhood (Umeda & Nomoto 2002; Cayrel et al. 2004; Keller et al. 2014), the bulge (Howes et al. 2015), or in metal-poor damped Lyman α

system (Kobayashi et al. 2011c). Therefore, the authors do not include PISNe in this paper. Table A.6 summarizes the possible necessary conditions for the different types of core-collapse supernovae. Note that these are very uncertain, and should be investigated with 3D/GR/MHD simulations of supernova explosions.

	stellar mass [$M_\odot$]	rotation	magnetic field
ECSN	$\sim 8.8 - 9$	no	no
SNII/Ibc	$10 - 30$	no	no
failed SN	$30 - 50$	no	no
HN	$20 - 50$	yes	weak?
MRSN	$25 - 50$	yes	strong

Figure A.6: *The mass ranges of core-collapse supernovae used in our fiducial GCE model, and necessary conditions for the explosions.*

Electron-capture supernovae (ECSNe)

After the super-AGB phase, because of electron captures ^{24}Mg(e$^-$, ν)^{24}Na(e$^-$, ν)^{24}Ne and ^{20}Ne(e$^-$, ν)^{20}F(e$^-$, ν)^{20}O, the electron fraction Y_e decreases, which can trigger collapse (Miyaji et al. 1980; Nomoto 1987). The collapsing O+Ne+Mg cores have a steep surface density gradient and loosely bound H/He envelope, which can cause prompt explosions. Indeed, Kitaura et al. (2006) obtained self consistent explosions with a 1D hydrodynamical code with neutrino transport. This is the case for SN1054 that formed the Crab Nebula (Nomoto et al. 1982). Although 1D nucleosynthesis calculations did not have low enough Y_e (Hoffman et al. 2008; Wanajo et al. 2009) for heavy r-process elements, 2D calculations showed Y_e down to 0.40 (Wanajo et al. 2011), which leads to a weak r-process up to A ~ 110. The authors apply the nucleosynthesis yields from the 2D calculation of an ECSN from an 8.8 $M_\odot$ star (Wanajo et al. 2013) for all ECSNe. Note that neutrino oscillations may affect the nucleosynthesis yields of ECSNe (Wu et al. 2014; Pllumbi et al. 2015).

Neutrino-driven winds (ν-winds)

Neutron stars (NSs) are born as hot and dense environments from which neutrinos diffuse out leading to a process of mass loss known as ν-driven winds. 1D hydrodynamical codes with neutrino transport showed that the conditions of these winds are not suitable for the occurrence of the r-process (Arcones et al. 2007; Fischer et al. 2010). Wanajo et al. (2013) confirmed this with semi-analytic nucleosynthesis calculations, and showed the dependence of proto-NS mass. Although proto-NSs with masses > 2.0 $M_\odot$ can eject heavy r-process elements, the others eject light trans-iron elements made by quasi nuclear statistical equilibrium (Sr, Y, and Zr) and by a weak r-process up to A ~ 110. Based on the initial mass to NS mass relation from 1D hydrodynamical simulations by Arcones et al. (2007), the authors add the nucleosynthesis yields of ν-driven winds from the proto-NS masses 1.4, 1.6, 1.8, and 2.0 $M_\odot$ (Wanajo et al. 2013) to their SNeII yields of 13, 15, 20, and 40 $M_\odot$ stars, respectively. Similar results as Arcones et al. (2007) are obtained with 2D simulations (Arcones & Janka 2011), although the impact of multi-dimensional modelling on nucleosynthesis yields needs to be studied further.

Neutron-star mergers (NSMs)

Compact binary mergers, i.e., NS-NS and NS-BH mergers, have been considered as a possible site of the r-process (e.g., Lattimer & Schramm 1974). Recently, the existence of such an event was confirmed by the gravitational wave source GW170817 (Abbott et al. 2017b), associated with an astronomical transient AT2017gfo (Smartt et al. 2017; Valenti et al. 2017) and a short γ-ray burst GRB170817A (Abbott et al. 2017a). The spectra of AT2017gfo can be well explained with the emissions peaking in near-infrared from the dynamical ejecta with heavy r-process elements including lanthanides, and the emissions peaking at optical wavelengths from the outflow from BH discs (Metzger & Fernández 2014; Tanaka et al. 2017).

Newtonian (Ruffert et al. 1997; Rosswog et al. 1999) and approximate general-relativity (GR) (Bauswein et al. 2013) 3D simulations showed unbound matter of ~ 10^{-2} $M_\odot$ after NSMs. The ejecta had extremely low $Y_e < 0.1$ (Freiburghaus et al. 1999; Bauswein et al. 2013), which can explain the "universal" r-process pattern (Sneden et al. 2008) at $A \geq 130$ but not at $A \leq 130$. However, in a full-GR 3D simulation with approximate neutrino transport, the dynamical ejecta exhibit a wide range of $Y_e \sim 0.09$-0.45, which gives good agreement with the "universal" r-process pattern for A ~ 90-240. The authors use the nucleosynthesis yields from the 3D-GR calculation of a NS-NS merger (1.3 $M_\odot$ +1.3 $M_\odot$, Wanajo et al. 2013) both for NS-NS and NS-BH mergers. Note that, however, double NS systems with a mass ratio < 1 (Ferdman & PALFA Collaboration 2018) might lead tidal disruption and larger r-process production. Also, a recent full-GR simulation of a NS-BH merger (1.35 $M_\odot$ + 5.4 $M_\odot$) shows a smaller outflow but the ejecta is very neutron rich (Kyutoku et al. 2018), so that the nucleosynthesis yields may be significantly different. Furthermore, the overall outflow may be dominated by winds from the accretion disks formed after merger (Radice et al. 2018). The rate of NS-NS mergers is estimated as 10^{-5} per year per galaxy from the Galactic pulsar population (e.g., van den Heuvel & Lorimer 1996). The delay-time distributions of NSMs are predicted from binary population synthesis codes (e.g., Tutukov & Yungelson 1993; Mennekens & Vanbeveren 2014; Belczynski et al. 2018; Kruckow et al. 2018; Vigna-Gómez et al. 2018), but the results depend on many parameters that describe uncertain physics such as Roche lobe overflow and common envelope evolution, as well as on the distribution of initial binary parameters. The authors adopt the delay-time distributions of the standard model from Mennekens & Vanbeveren (2014) for Z = 0.002 and Z = 0.02, which are shown in Fig. 3 of Mennekens & Vanbeveren (2016), assuming a binary fraction of 100%; the authors use the rates at Z = 0.002 and Z = 0.02 for Z ≤ 0.002 and Z ≥ 0.02, respectively. Supernova kick is also one of the most important assumptions for NSMs rates, and the average velocity 450 $\mathrm{km \cdot s^{-1}}$ is adopted in these rates. With 265 $\mathrm{km \cdot s^{-1}}$ (Hobbs et al. 2005), the NS-NS and NS-BH merger rates are increased by a factor of 1.6 and 1.2, respectively, and with other parameters, these rates can be increased by a factor of ~ 20 and ~ 30, respectively (Mennekens & Vanbeveren 2014).

Magneto-rotational supernovae (MRSNe or MHDSNe)

While the explosions of normal core-collapse supernovae (SNeII) are likely to be triggered by a standing accretion shock instability (e.g., Janka 2012), strong magnetic fields and/or fast rotation could also induce core-collapse supernovae. Such magneto-rotational supernovae are also considered as an r-process site (Symbalisty 1984; Cameron 2003). Followed by a few axisymmetric magneto-hydrodynamic (MHD) simulations (e.g. Takiwaki et al. 2009), a full 3D MHD simulation is performed for 15 $M_\odot$ star with $5{\cdot}10^{12}$G, which shows a clear jet-like explosion (Winteler et al. 2012). Mösta et al. (2014) showed in a 3D MHD GR simulation for 25 $M_\odot$ star with 10^{12}G that the jet is disturbed and no runaway explosion is obtained during the simulation time. It is not sure whether they can explode and produce enough r-process elements or not. Nishimura et al. (2015) calculated nucleosynthesis yields as a post-process based on 2D special relativistic MHD simulations for a 25 $M_\odot$ star (Takiwaki et al. 2009) depending on the strength of magnetic fields and the rotational energy. Actually, Takiwaki et al. (2009) calculated 1.69 $M_\odot$ iron core from a star with initial mass 25 $M_\odot$, solar metallicity, and equatorial rotational velocity of ~ 200 $\mathrm{km \cdot s^{-1}}$ (Heger & Langer 2000). The late phase evolution of jet propagation and shock-breakout is not followed. Therefore, it is unknown whether the envelope of the iron core is also ejected or falls back onto the remnant. The proto-NSs have 10^{15}G and could be the origin of the magnetars, but probably do not become long gamma-ray burst or HNe since the jet is only mildly relativistic. Because of the necessary conditions of rotation and some magnetic fields, MRSNe and HNe may be related but not the same. In this paper, the authors replace 3% of 25-50 $M_\odot$ HNe with MRSNe. In the model with the metal-dependent HN fraction, the MRSN rate also depends on the metallicity: ϵ_{MRSN}(Z) = 0.03 ϵ_{HN}(Z). This fraction of MRSNe relative to HNe is chosen from the observed [Eu/Fe]-[Fe/H] relation in the solar neighborhood, but may differ in the Galactic bulge. If the authors also allow 20 $M_\odot$ or 15 $M_\odot$ stars for MRSNe, the rate can be larger by a factor of ~2 or ~4, respectively, but the chemical enrichment timescale is not so different.

Type Ia Supernovae (SNeIa)

The progenitor systems of SNeIa are still a matter of extensive debate; plausible scenarios are (1) deflagrations or delayed detonations of Chandrasekhar (Ch) mass WDs from single degenerate systems, (2) sub-Ch-mass explosions from double degenerate systems, or (3) double detonation of sub-Ch-mass WDs in single or double degenerate systems (e.g., Hillebrandt & Niemeyer 2000, for a review). Observationally, the progenitors of the majority of 'normal' SNeIa are most likely to be Ch-mass WDs (Scalzo et al. 2014). From the nucleosynthetic point of view, Kobayashi et al. (2020b) showed that more than 75% of SNeIa should be Ch-mass explosions (see also Seitenzahl et al. 2013a), using the nucleosynthesis yields calculated with their 2D hydrodynamical code both for Ch and sub-Ch mass explosions. Therefore, in the paper the authors adopt the same yield set but only for delayed detonations in Ch-mass C+O WDs, as a function of metallicity (Z = 0, 0.002, 0.01, 0.02, 0.04, 0.06, and 0.10). This new yield set solved the Ni overproduction problem in the yields of Nomoto et al. (1997) and Iwamoto et al. (1999). The adopted progenitor systems are the binaries of C+O WDs with main-sequence (MS) or red-giants (RG) secondary stars (see Kobayashi & Nomoto 2009), for more details, hereafter KN09), and the mass ranges of the secondary stars depend on the metallicity because the optically thick winds from WDs are essential for the evolution of these progenitor systems (Kobayashi et al. 1998, hereafter K98). In GCE, the lifetime distribution function of SNeIa is calculated with Eq.[2] in KN09, with the metallicity dependence of the WD winds (K98) and the mass-stripping effect on the binary companion stars (KN09). MS+WD systems have timescales of ~ 0.1-1 Gyr, which are dominant in star-forming galaxies (the so-called prompt population), while RG+WD systems have lifetimes of ~ 1 20 Gyr, which are dominant in early-type galaxies. The binary parameters of MS+WD and RG+WD systems, b_{MS} and b_{RG}, are mainly determined from the observed [O/Fe]–[Fe/H] relation at [Fe/H] > 1. The total number of SNeIa ($\sim b_{MS}$, b_{RG}) is determined from the [O/Fe] slope, and b_{RG} is determined from the metal-rich tail of the metallicity distribution function. (b_{RG}, b_{MS}) are set to be (0.02, 0.04) for the new models in this paper, while (0.023, 0.023) were used for the Kobayashi et al. (2011b) and Kobayashi et al. (2015) models. Both sets give very similar [O/Fe]–[Fe/H] relations. Note that these parameters do not only account for the binary fractions, but include a suitable range of binary separations and any other conditions that are necessary for the systems to explode as SNeIa (see Kobayashi & Nomoto 2009, for more details). The resultant delay-time/lifetime distribution is very similar to that observed at Z ~ 0.02 (see Fig. 12 of Kobayashi et al. 2020b).

Type Iax Supernovae (SNeIax)

There is also a significant number of faint or super-luminous SNe Ia (e.g., Gal-Yam 2017) that are likely to be from sub-Ch or super-Ch WDs (Scalzo et al. 2019). The rate of super-luminous SNe Ia is so small that we do not include them in this paper. Possibly the subset of faint SNe Ia are included as SNe Iax in the following sections. Since the secondary star of an SN Iax is observed (McCully et al. 2014), we adopt the single degenerate model from Kobayashi et al. (2015). It is assumed that the progenitors are hybrid C+O+Ne WDs, and we take the mass ranges from the results of super AGB calculations (Doherty et al. 2015) depending on the metallicity.

A.2. Conclusion

As mentioned the latter descriptions of these couple of GCE models are a short and extraordinary shallow glimpse into the complexity of the factors to be taken into account in their building. The info has been literally taken from the corresponding studies and only concern to some particular and partial aspects of the GCE models. But it is enough for the schematic purpose of this Anexo.

Models are fed and dependent on the observational data which might help to constraint nucleosynthesis sources yields and the understanding of astrophysical events, today already are not still fully understood. Observational data help for their improvement, increasing accuracy and completeness. On the other hand, the fit or not of the GCE models to the observational data warn about the incomplete understanding of nucleosynthesis mechanisms regarding some elements or the role and contributions of the different nuclosynthesis sites involved in the production of one element and its galactic evolution.

Better and more complete observational data produce better GCE models. Better GCE models produce better understanding of the galactic chemical evolution and the observational data.

Figure A.7: *Trifid Nebula, M20. Takahashi TSA120 amateur telescope*

Appendix B

Abundance Scales

Mass fractions

$X = H$
$Y = He$
$Z =$ metals (non H or He)
$X + Y + Z = 1$

[ ] scale

$[X/H] = log(n_X/n_H)^* - log(n_X/n_H)_\odot$

$[X/Fe] = [X/Fe]^* - [X/Fe]_\odot =$
$= log(n_X/n_{Fe})^* - log(n_X/n_{Fe})_\odot =$
$= log[(n_X/n_H)/(n_{Fe}/n_H)]^* - log[(n_X/n_H)/(n_{Fe}/n_H)]_\odot =$
$= log(n_X/n_H)^* - log(n_X/n_H)_\odot - log(n_{Fe}/n_H)^* + log(n_{Fe}/n_H)_\odot =$
$= [X/H] - [Fe/H]$

$[X/Y] =$ same development than above or $= [X/Fe] - [Y/Fe]$

12 scale

$log\, \epsilon(X) = log(n_X/n_H) + 12$

Equivalency

$$[X/Fe] = [log\,\epsilon(X)^{*} - log\,\epsilon(X)_{\odot}] - [log\,\epsilon(Fe)^{*} - log\,\epsilon(Fe)_{\odot}]$$

$$[X/Y] = [log\,\epsilon(X)^{*} - log\,\epsilon(X)_{\odot}] - [log\,\epsilon(Y)^{*} - log\,\epsilon(Y)_{\odot}]$$

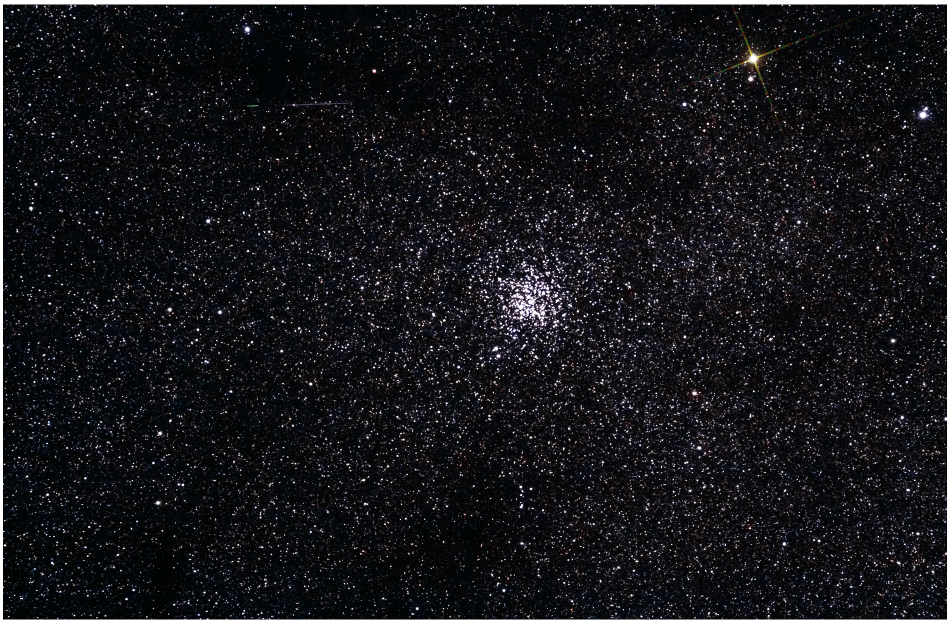

Figure B.1: *Globular Cluster, M11. Takahashi TSA120 amateur telescope*

Appendix C

Glossary & Acronyms

This glossary has been elaborated with basic definitions and info. Therefore, the use of references has been avoided. The sources are diverse, in some cases as simple as valid definitions from Wikipedia. Others, from articles or books.

Click over wished term or acronym: **GLOSSARY INDEX**

AGB

Asymptotic Giant Branch. This is a late period of the stellar evolution of low- to intermediate-mass stars. It is characterized by a central inert core of carbon and oxygen surrounded by hellium and hydrogen burning shells. Glossary Index

α-elements

O, Ne, Mg, Si, S, Ar, Ca and Ti elements. C shows particular features but it is also considered as an α-element. They are obtained by a net α particle capture reaction.

Their nucleosynthesis mainly occur in burning stages prior SNII. Glossary Index

α-Freeze-outs

Nucleosynthesis mechanism triggered during the core-collapse supernova (SNII). In the initial heating of the inner most regions of the ejecta, when the supernova shock wave passes through the Si-rich shell of the star, post-shock temperatures are sufficiently high that nuclei are broken down into nucleons and α-particles. As the material subsequently expands and cools, the nucleons and α-particles reassemble to form heavy nuclei. However, not all α-particles reassemble, and, as a result, the final abundances freeze out with a significant number α-particles remaining. Glossary Index

α-particle

${}^{4}_{2}He^{+2}$. Glossary Index

APOGEE

The Apache Point Observatory Galactic Evolution Experiment. This is one of the programs in the Sloan Digital Sky Survey III (SDSS-III). It uses the Sloan 2.5 m telescope, collecting a half million high-resolution (R ~ 22500), high signal-to-noise ratio (>100), near-infrared (1.51–1.70 m) spectra for 146000 stars. Glossary Index

β-disintegration

Radioactive decay in which a beta particle, fast energetic positron or electron, is emitted from an atomic nucleus.

β^- disintegration

$n \rightarrow p^+ + e^- + antineutrino$

${}^{A}_{Z}X \rightarrow {}^{A}_{Z+1}\ Y + e^-$

β^+ disintegration

$p^+ \rightarrow n + e^+ + \nu_e$

${}^{A}_{Z}X \rightarrow {}^{A}_{Z-1}\ Y + e^+$

Glossary Index

BH

Black Hole. Glossary Index

Blueshift

Decrease in wavelength and increase in frequency (increase in energy), of an electromagnetic wave due to the movement of the source (moving close, Doppler effect). Glossary Index

BUMP

RGB bump is an increase of the differential luminosity function noticed in studying globular clusters. It has been related in the stellar evolution with the RGB evolution point later than the convective cell, due to the FDU, reaches the maximum depth (as termination point of the FDU). Due to some instability after this point, the star briefly descend the RGB for stabilizing and recovering later the RGB ascend. As a consequence, the star gets through the same luminosity point several times in the RGB ascend, provoking the excess of the luminosity function.
The RGB bump as a separation point between the low-RGB and up-RGB, and related with some chemical changes produced on the stellar atmosphere. Glossary Index

CBM

Compact Binary Merger: NS+NS, NS+BH or BH+BH. Glossary Index

CE

Common envelope. A common envelope is formed in a binary star system when the orbital separation decreases rapidly or one of the stars expands rapidly. The donor star will start mass transfer and the receiving star is unable to accept all material, which leads to the formation of a common envelope engulfing the companion star. Glossary Index

CEMP

Carbon enhanced metal poor star. Stars enhanced in carbon abundance, exceeding [C/Fe] > +0.5 to +1.0 depending on the criteria at metal poor range [Fe/H] < -1 dex. It includes different formation origin (single or binary systems) and chemical features (s-process elements enhancement or not). Glossary Index

Chandrasekhar limit

Maximum mass of a stable white dwarf star, 1.4 $M_{\odot}$. The Chandrasekhar limit is the mass above which electron degeneracy pressure in the star's core is insufficient to balance the star's own gravitational self-attraction. This happens in massive stars (exceeding 8 $M_\odot$ of total mass) leading to the collapse of the core and the explosion of the star as a supernova. The core remnant forms a neutron star or black hole. Glossary Index

Classical Nova

A close binary system formed by a WD and a MS, sub-giant or red giant star with orbital period lower than 12 hours. The WD accretes matter from the companion producing thermonuclear runaway. It occurs only on the surface of the star, allowing the white dwarf and the binary system to remain intact. Glossary Index

CNO cycle

Nucleosynthesis mechanism in the main sequence stage for producing helium from hydrogen. It is triggered in stars with mass > 1.3 $M_\odot$ and temperature in the core exceeding $17{\cdot}10^6$ K. It involves the previous enrichment of the star in C, N and O acting as catalyst of the reaction. Glossary Index

Damped Lyman-alpha (Ly-α) systems

Concentrations of neutral hydrogen gas that are detected in the spectra of quasars (kind of Active Galactic Nuclei, AGN). Their impact in spectra consist of neutral hydrogen Lyman alpha absorption lines which are broadened by radiation damping, a synchrotron radiation mechanism. They can be observed at relatively high redshifts of 2-4 offering the opportunity to study the dynamics of the gas at early stages of a galaxy formation. Glossary Index

Dwarf

Different meaning depending on the context. In this manuscript, it refers to a star of relatively small size and low luminosity in the main sequence stage. Mainly F, G or K spectral class stars. Glossary Index

Dredge-up: FDU/SDU/TDU

First, Second and Third Dredge-Up. During these periods the surface convection zone extends down into the inner layers undergoing nuclear fusion. The fusion products are lifted-up and mixed onto the stellar atmosphere and outer layers. The mixing of shells produces additional nucleosynthesis of some elements.
The first dredge-up occurs when a main-sequence star enters the red-giant branch (RGB). $^{12}C/^{13}C$ and C/N ratios are lowered.

The second dredge-up occurs in stars with 4–8 $M_\odot$ when helium fusion comes to an end at the core, convection mixes the products of the CNO cycle. This increases the abundance of ^{4}He and ^{14}N in the stellar atmosphere, whereas the amount of ^{12}C and ^{16}O decreases.
The third dredge-up occurs in the asymptotic giant branch (AGB). TDU causes helium, carbon and the s-process products to be mixed into the surface. The C abundance relative to oxygen increases with each new thermal pulse, and can create a carbon star. Glossary Index

EMP

Extremely metal poor star. Metal poor stars with metallicity [Fe/H] < 3 dex, including Group II and III population stars, formed at early stages of the galaxy and universe. Glossary Index

Explosive Burning

In opposition to hydrostatic burning. It refers to the fusion reactions and nucleosynthesis when the star has lost its equilibrium and the gravitational core collapse produces a dramatic increase of temperature due to the radially moving shock wave. The nucleosynthesis is richer in non-alpha-nucleus isotopes than during the hydrostatic burnings. Glossary Index

Fast rotators/rotating stars/spinstars

Theoretical models of the formation of the first stars indicates that stars of very metallicity should have very high rotational velocities. The prototype model of a spinstar is a massive star with low metallicity, fast rotation, strong mixing processes and a high mass loss rate. Mixing of shells produces additional nucleosynthesis and an extra contribution of elements at early stages of the universe. Rotational velocity average of the stars decreased with the universe evolution. Glossary Index

FEROS

The FEROS instrument is a high-resolution Échelle spectrograph (R=48000). It is operated at the European Southern Observatory (ESO) in La Silla, Chile. Glossary Index

GAIA

Gaia is a mission to chart a three-dimensional map of the Milky Way. It will provide accurate positional and radial velocity measurements of about one billion stars. It refers to the name of the satellite probe launched in 2013 by ESA for accomplishing this mission. Glossary Index

Gaia-Enceladus

Name of a hypothetical dwarf galaxy that theoretical models show it collides with the Milky Way approximately 11.5 Gyr ago. Glossary Index

GCE

It refers to Galactic Chemical Evolution Models. Glossary Index

GCR

Galactic cosmic rays. High-energy protons and atomic nuclei which move through space at nearly the speed of light. In the galaxy context, particles usually formed and accelerated in Supernovae events. In this environment they might contribute as an additional nucleosynthesis site for some light elements as Lithium. This is as a result of the spallation they produce on interstellar matter nuclei. Glossary Index

HARPS

High Accuracy Radial velocity Planet Searcher. It is a high-precision echelle planet-finding spectrograph installed on the ESO's 3.6 m telescope at La Silla Observatory in Chile. Glossary Index

HB

Horizontal Branch stage. A stellar evolution stage that immediately follows the red giant branch (RGB) in stars whose masses are similar to the Sun's. It is characterized by helium fusion in the core for producing carbon and oxygen as a byproduct (triple-alpha reaction) and by hydrogen fusion (CNO cycle) in the shell surrounding the core. Glossary Index

HBB

Hot Bottom Burning. This is an alternative nucleosynthesis site and mechanism in AGBs with masses higher than 4 $M_\odot$. it is produced in the hot bottom of the hydrogen burning shell (> $100{\cdot}10^6$ K) in which new reactions take place when the convective envelope reaches it after a thermal pulse. Then, the new elements synthesized are lifted and mixed up on the stellar atmosphere by TDU. Glossary Index

Heavy s-elements

It refers to second and third peak main s-process elements as Ba, La, Ce, Pr, Nd, Pb and Bi in opposition to light-s elements of the first peak as Sr, Y and Zr. Their ratio (heavy- against light-s) is an useful information of stellar or galactic evolution. Glossary Index

HNe

Hypernovae. It is a very energetic kind of core collapse supernovae (10^{52} erg, one order of magnitude over standard supernovae). Typically it occurs in massive stars exceeding 20 $M_\odot$. Glossary Index

Hydrostatic Burning

The fusion reactions are produce meanwhile the star maintain an equilibrium, and the particles follow a thermal distribution. In massive stars it refers to helium burning, carbon burning, oxygen burning, and silicon burning stages before core collapse supernova. They synthesize especially the α-elements (A = 2Z). Glossary Index

Intermediate mass stars

Definition might vary regarding different criteria. As general criteria it is said of the star with a mass exceeding 2.25 $M_\odot$ and a maximum limit of 8 $M_\odot$. A star exceeding 2.25 $M_\odot$ will produce a non-degenerate core helium ignition. Meanwhile, the 8 $M_\odot$ limit is the border for avoiding the carbon burning. Like the low mass, the intermediate mass stars enter the AGB with an electron-degenerate carbon oxygen (C-O) core and are unable to reach the $800{\cdot}10^6$ K for producing carbon burning. This criterion depends on the chemical composition and metallicity of the stars and it is only valid for sun-like composition stars. Glossary Index

ISM

Interstellar medium. Electromagnetic radiation and matter (including ionic, atomic and molecular gas, dust and cosmic rays) between stars. Glossary Index

Jet-like core collapse explosions

Or bipolar supernova explosion. It is a proposed mechanism of core collapse especially in very massive stars as hypernovae. This is expected to be a more frequent mechanism at early stages of the universe, involvong metal poor stars from the III and II populations.
During the core collapse, if the very massive stars are rotating, they will not become a black hole at once, but they form an equatorial accretion disk around the central remnant, typically smaller than 2-3 $M_\odot$. After forming the accretion disk, two opposed jet-like explosions toward the polar direction may occur by extracting energy from the accretion disk and/or the black hole itself.
This mechanism provides a new nucleosynthesis site as the polar jets shock-wave and additional enrichment of the medium with some elements. Glossary Index

LEPP

Lighter Element Primary Process. This is an unknown s-process proposed by Travaglio et al. (2004) as a contribution to explain an extra overabundance observed and not expected of light-s elements with respect to heavy ones at lower metallicities regarding thick disk stars ([Fe/H] ~ -0.5 to -1.0). However at present, this extra s-elements contribution has been argued to be provided by existent nucleosynthesis sites, within the uncertainties of the models or extra weak-s contributions from rotating stars at early stages of the galaxy. Glossary Index

Light-s elements

It refers to the first peak of main s-process elements as Sr, Y and Zr in opposition to heavy-s elements of second and third peaks as Ba, La, Ce, Pr, Nd, Pb and Bi. Their ratio (heavy- against light-s) is an useful information of stellar or galactic evolution. Glossary Index

LIGO

Laser Interferometer Gravitational-wave Observatory. Gravitational wave observatory comprising two enormous laser interferometers located 3000 kilometers apart, Hanford Site (Washington) and Livingston (Louisiana), LIGO exploits the physical properties of light and of space itself to detect and understand the origins of gravitational waves (GW). It detected GW150914, the first direct observation of a GW in 2015. Glossary Index

LIMS

Low and intermediate mass stars. With masses between about 0.8 to 8 $M_\odot$. They evolve through central hydrogen and helium burning and enter the AGB stage with an electron-degenerate carbon oxygen (C-O) core. The core does not reach the required temperature for carbon burning ($800{\cdot}10^6$ K) and it is surrounded by helium and hydrogen burning shells at this stage. They will end their life as dying white dwarfs without nuclear activity and only emitting thermal radiation once they lose their outer layers. Glossary Index

Low mass stars

Definition might vary regarding different criteria. As general criteria it is said of the star with a mass under 2.25 $M_\odot$ and a minimum limit of 0.8 $M_\odot$. A star under 2.25 $M_\odot$ will produce a degenerate core helium ignition. 0.8 $M_\odot$ is the minimum mass required to ignite helium and evolve through central helium burning. They enter the AGB stage with an electron-degenerate carbon oxygen (C-O) core.
This criterion depends on the chemical composition and metallicity of the stars and it is only valid for sun-like composition stars. Glossary Index

LTE/NLTE

Local Thermodynamic Equilibrium or Non-Local Thermodynamic Equilibrium. When it is assumed LTE environment, electromagnetic emission behaves as if the emitting species is in thermodynamic equilibrium with its local environment, following a thermal distribution of electronic levels populations. This stage is obtained above a critical density that is the density of collision partners, often electrons or protons, above which the collisional de-excitation from the upper level occurs more quickly than the radiative de-excitation. In this case the emissions behave as if they are thermal and can be used as a measure of stellar atmosphere temperature.
Below the critical density, each collisional excitation leads to an emission and, given knowledge of both the line strength and the collision cross section, the emissions can provide information on the density of the collision partners but they are not thermal and no info of temperature of the surrounded medium can be obtained.
NLTE environment can be provided by different factors as a powerful UV source that rules the distribution of the electronic level populations of the emitting species, even producing photoionization and preventing a thermal distribution. Radiative factors dominate over collisional/thermal one. Glossary Index

Macroturbulence

Non thermal velocity associated to granulation, super-granulation, oscillations, and other large-scale motions. They are, jointly with rotational velocity, the primary cause of line profile broadening in the spectra of F, G and K main sequence stars. Glossary Index

Massive stars

Stars with mass exceeding 8 $M_{\odot}$. They mostly evolve through the central carbon, neon, oxygen and silicon burning stages and end their lives as core collapse supernovae. Glossary Index

Metallicity

The abundance of elements heavier than hydrogen or helium. Depending on the used scale, called Z or [M/H]. It is often defined using the total iron content of the star, as iron is among the easiest to measure with spectral observations and it is coupled to the total metallicity evolution in the galaxy. Glossary Index

MgAl cycle

Nucleosynthesis chain of reactions produced in AGB stage of LIMS. It is linked to the NeNa cycle (forming the NeNaMgAl) and it is responsible for a contribution to the abundances of some Mg and Al isotopes. This cycle is triggered above $50{\cdot}10^6$ K but it would be at temperatures exceeding $70{\cdot}10^6$ K, in AGBs of intermediate mass stars experiencing HBB, when the cycle pushes forward the production for ^{27}Al accumulation, the main stable isotope produced by this cycle. Glossary Index

MHD-SNeII

MHD-SNeII, is a rare kind of supernovae of very massive stars at early stages of the universe characterized by high rotation rates and large magnetic fields. It is observed as an interesting and promising site for the fast r-process elements enrichment observed in the early Galaxy, due to their powerful theoretical ejecta and enhanced nucleosynthesis in their bipolar jets explosion (see jet-like core collapse explosions). Glossary Index

Microturbulence

The microturbulent velocity is defined as the micro-scale non-thermal component of the gas velocity in the region of spectral line formation. It is the distribution of these velocities along the line of sight that produces the microturbulence broadening of the absorption lines in low mass stars that have convective envelopes. Stellar micro-turbulence varies with the effective temperature and the surface gravity. Glossary Index

MS

Main Sequence stars. Main and longer stage of the stars in which they fusion hydrogen atoms to form helium in their cores. Glossary Index

NeNa cycle

Nucleosynthesis chain of reactions produced in LIMS, being responsible of the enhancement in photospheric Na. It is linked to the MgAl cycle (forming the NeNaMgAl).
The Na production by the NeNa cycle might be lifted and mixed to the stellar photosphere during First Dredge-Up (FDU) though it is not clear to what extent. Theoretical models predict that mixing is deep enough to change Na abundance only in giants (RGB) above 1.5-2 $M_{\odot}$but particularly in intermediate-mass above 4 V. Observationally, it is well known that evolved intermediate-mass stars show some Na enhancement after the FDU. Glossary Index

NS

Neutron star. Glossary Index

Nu process (ν-process) SNII

Nucleosynthesis process produced as the core of a massive star collapses to form a neutron star. The flux of neutrinos in the overlying shells of heavy elements becomes so great that, despite the small cross section, substantial nuclear transmutation is induced. Neutrinos excite heavy elements and even helium to particle unbound levels. The evaporation of a single neutron or proton, and the back reaction of these nucleons on other species present, significantly alters the outcome of traditional nucleosynthesis calculations. Glossary Index

PNS

Proto-neutron star. It is the first phase of life of a neutron star originated from a core-collapse supernova. Glossary Index

Population III of stars

So far, not observed stars population, hypothetically composed entirely of primordial gas (hydrogen, helium and very small amounts of lithium and beryllium), the pristine material left over from the Big Bang. These stars would have a Z close to 0 ([M/H] ~ -10 dex) and would constitute the very first generation of stars. Glossary Index

Post-AGB

Rapid transition stage from the Asymptotic Giant Branch (AGB) towards the Planetary Nebula Phase (PN), before the stellar remnant cools down as a White Dwarf (WD). The stars in Post-AGB evolve in a fast track to hotter effective temperature but are not hot enough yet to photoionize the circumstellar envelope. The strong mass loss during AGB will eject the stellar atmosphere in time scales of 10^4 - 10^5 yr forming an expanding, spherical envelope around the star. At some time at the very end of AGB or during the post-AGB stage, the geometry of mass ejection should drastically change: the typical spherical geometry of the AGB envelopes is lost and most PNe present axis-symmetric (bipolar and elliptical) morphologies. The duration of the post-AGB phase strongly depends on the initial mass. Although for the less massive objects the transition time may be as large as 30.000-40.000 yr, more massive objects may last in the post-AGB phase only a few decades/centuries. Glossary Index

pp chain

Nuclear fusion reactions by which stars convert hydrogen to helium. It is the dominant mechanism of helium production during main sequence in low mass stars. Glossary Index

Primary/Secondary nucleosynthesis

In the case of a primary nucleosynthesis, the element is expected to originate from H-burning on fresh heavier elements than hydrogen and helium generated by the parent star. Unlike the secondary nucleosynthesis of one element, in which one or several involved elements in its production is already present in the formation of the parent star and not freshly produced. Glossary Index

Radiogenic nuclide/isotope

It is produced by a process of radioactive decay. Glossary Index

Redshift

Increase in wavelength and decrease in frequency (decrease in energy), of an electromagnetic wave due to the movement of the source (moving away, Doppler effect). Other motifs for redshifting are due to the universe expansion known as cosmological redshift or to relativistic effects by strong gravitational fields known as gravitational redshift. Glossary Index

RG

Red Giant star.Glossary Index

RGB

Red Giant Branch. It is a stage that follows the main sequence for low- to intermediate-mass stars before helium ignition. Red-giant-branch stars have an inert helium core surrounded by a shell of hydrogen burning. Glossary Index

RLOF

Roche Lobe Overflow. In binary systems when a star's surface, usually due to evolution reasons, extends out beyond its Roche lobe and the material which lies outside the Roche lobe can fall off into the companion's Roche lobe via the first Lagrangian point producing a mass transfer and accretion by the companion. Glossary Index

Roche Lobe

The Roche lobe is the region around a star in a binary system within which orbiting material is gravitationally bound to that star. Glossary Index

SBBN

Standard Big Bang nucleosynthesis (SBBN) describes the formation of the lightest elements by a sequence of reactions and predicts their abundances as a function of baryon density. The expansion and cooling of the Universe limited this epoch to the first few minutes after big bang.
Standard BBN predicts that only the lightest elements H, He, and Li can be synthesized as the primordial nucleosynthesis. Glossary Index

SMBH

Supermassive black hole, with mass on the order of millions to billions of $M_{\odot}$. Accretion of interstellar gas onto supermassive black holes is the process responsible for powering active galactic nuclei (AGN) and quasars. Glossary Index

SNeIa

Thermonuclear Supernovae. They are formed by binary interactions between a white dwarf (WD) and an evolved companion (Red Giant) or another white dwarf. The matter accretion by the white dwarf that finally surpasses a critical mass point, the Chandrasekhar limit (ca 1.4 $M_{\odot}$), produces the collapse of the core by an uncontrolled fusion reaction, leading to the explosion that might eject the companion, leaving behind a neutron star or black hole. Glossary Index

SNeII

Core collapse Supernovae. In massive stars, once the burning fuels are exhausted, gravity provokes that the successive layers fall violently at a fraction of the speed of light (around 23%) against the core, that reaches 10^{11} K and contracts to the limit of the electronic degeneracy.
When the compacted core mass exceeds the Chandrasekhar limit (1.4 $M_{\odot}$), even this matter resistance is overwhelmed and the core implosions, collapsing, only stopped by the neutron degeneracy, the last resistance of the star's core to becoming a black hole. Outer layers rebound over this collapsed core, provoking an expanding shock-wave, completely disrupting the rest of the star and the ejection of the outer layers as a supernova explosion.
Behind, the collapsed core has become a neutron star or black hole depending on the initial mass of the star and experienced gravity pressure. Glossary Index

Thermal pulses

They characterized great part of the AGB stage in LIMS. It happens by the thermal runaway caused by helium burning confined in a relatively thin shell surrounding an inactive carbon/oxygen core. The provoked instability triggers some physical changes on the stellar structure, mixing shells and producing nucleosynthesis of some isotopes and elements, lifted and mixed up on the stellar atmosphere by TDU during the interpulse periods. The surface of the AGB is usually, depending on the stellar mass, enhanced in carbon (becoming a carbon star) and s-process elements. Glossary Index

TP-AGB

This period in the AGB stage of LIMS starts after the helium shell runs out of fuel. The star derives its energy from fusion of hydrogen in a thin shell, which restricts the inner helium shell to a very thin layer and prevents it fusing stably that provocke thermal pulses as a consequence of thermal runaways. This instability triggers some physical and chemical changes in the AGB and their mass loss in the form of stellar winds. Glossary Index

Triple α-reaction

Nuclear fusion reactions by which helium (α particles) are transformed into carbon (and oxygen as a by-product). Glossary Index

UV

Ultraviolet wavelength range. In this manuscript, wavelengths under 400 nm but as well for indicating intervals close to that limit in the blue part of the spectrum. Glossary Index

UVES

Ultraviolet and Visual Echelle Spectrograph attached to the Very Large Telescope (VLT, ESO), with a R ~ 40000 (1 arcsec slit). Glossary Index

Virgo

It is a large interferometer designed to detect gravitational waves, located in Santo Stefano a Macerata, near the city of Pisa, Italy. It is part of a scientific collaboration of laboratories from six countries: Italy, France, the Netherlands, Poland, Hungary and Spain. Sensitivity was enhanced by a factor of 10 in 2016. On 14 August 2017, LIGO and Virgo jointly detected a signal, GW170814. It was the first binary black hole merger detected by both observatories. Glossary Index

WD

White dwarf. A stellar core remnant (mostly carbon and oxygen) composed of electron-degenerate matter, formed from AGB in LIMS by the loss of outer layers. White dwarfs are thought to be the final evolutionary state of stars whose mass is not high enough to become a neutron star. The nuclear reactions have ceased and the remnant core only emits thermal energy. Glossary Index

WAMP

Wilkinson Microwave Anisotropy Probe. This is NASA spacecraft operating from 2001 to 2010 which measured temperature differences across the sky in the cosmic microwave background (CMB), the radiant heat remaining from the Big Bang. The CBM was produced by photons freed by the recombination of electrons and protons forming neutral hydrogen atoms, 300000-400000 yr after Big Bang, and the decoupling of radiation and matter. This happens when the universe cooled under ca 3000 K. Glossary Index

ZAMS

Zero age main sequence. It is the time when the proto-star first joins the main sequence on the Hertzsprung-Russell diagram by burning hydrogen in its core through fusion reactions. After this time the star enters a phase of stellar evolution that is quite stable, in which they spend most of their life, steadily processing hydrogen into helium by PP or CNO nucleosynthesis mechanisms. Glossary Index

Figure C.1: *Leo Triplet, M66 Group. Takahashi TSA120 amateur telescope*

Bibliography

Abadi, M. G., Navarro, J. F., Steinmetz, M., & Eke, V. R. 2003, Astrophysical Journal, 591, 499

Abate, C., Pols, O. R., Karakas, A. I., & Izzard, R. G. 2015, Astronomy & Astrophysics, 576, A118

Abbott, B. P., Abbott, R., Abbott, T. D., et al. 2017a, Astrophysical Journal Letters, 848, L13

Abbott, B. P., Abbott, R., Abbott, T. D., et al. 2017b, Physical Review Letters, 119, 161101

Abia, C., Cristallo, S., Cunha, K., de Laverny, P., & Smith, V. V. 2019, Astronomy & Astrophysics, 625, A40

Abia, C., Cunha, K., Cristallo, S., & de Laverny, P. 2015, Astronomy & Astrophysics, 581, A88

Abia, C., Cunha, K., Cristallo, S., et al. 2010, Astrophysical Journal Letters, 715, L94

Abia, C., Domínguez, I., Gallino, R., et al. 2002, Astrophysical Journal, 579, 817

Abia, C., Hedrosa, R. P., Domínguez, I., & Straniero, O. 2017, Astronomy & Astrophysics, 599, A39

Adibekyan, V. Z., Figueira, P., Santos, N. C., et al. 2013, Astronomy & Astrophysics, 554, A44

Adibekyan, V. Z., Sousa, S. G., Santos, N. C., et al. 2012, Astronomy & Astrophysics, 545, A32

Afflerbach, A., Churchwell, E., & Werner, M. W. 1997, Astrophysical Journal, 478, 190

Agostini, M., Altenmüller, K., Appel, S., et al. 2020, arXiv e-prints, arXiv:2006.15115

Aguilera-Gómez, C., Chanamé, J., Pinsonneault, M. H., & Carlberg, J. K. 2016, Astrophysical Journal, 829, 127

Akerman, C. J., Carigi, L., Nissen, P. E., Pettini, M., & Asplund, M. 2004, Astronomy & Astrophysics, 414, 931

Akeson, R. L., Chen, X., Ciardi, D., et al. 2013, Publications of the Astronomical Society of the Pacific, 125, 989

Allende Prieto, C., Barklem, P. S., Lambert, D. L., & Cunha, K. 2004, Astronomy & Astrophysics, 420, 183

Allende Prieto, C., Lambert, D. L., & Asplund, M. 2001, Astrophysical Journal Letters, 556, L63

Amarsi, A. M., Asplund, M., Collet, R., & Leenaarts, J. 2015, Monthly Notices of the Royal Astronomical Society, 454, L11

Amarsi, A. M., Nissen, P. E., Asplund, M., Lind, K., & Barklem, P. S. 2019a, Astronomy & Astrophysics, 622, L4

Amarsi, A. M., Nissen, P. E., & Skúladóttir, Á. 2019b, Astronomy & Astrophysics, 630, A104

Andrievsky, S., Bonifacio, P., Caffau, E., et al. 2018, Monthly Notices of the Royal Astronomical Society, 473, 3377

Andrievsky, S. M., Spite, F., Korotin, S. A., et al. 2011, Astronomy & Astrophysics, 530, A105

Andrievsky, S. M., Spite, M., Korotin, S. A., et al. 2010, Astronomy & Astrophysics, 509, A88

Andrievsky, S. M., Spite, M., Korotin, S. A., et al. 2007, Astronomy & Astrophysics, 464, 1081

Aoki, W. 2010, in Chemical Abundances in the Universe: Connecting First Stars to Planets, ed. K. Cunha, M. Spite, & B. Barbuy, Vol. 265, 111–116

Aoki, W., Beers, T. C., Christlieb, N., et al. 2007, Astrophysical Journal, 655, 492

Aoki, W., Beers, T. C., Lee, Y. S., et al. 2013, Astronomical Journal, 145, 13

Aoki, W. & Honda, S. 2008, Publications of the Astronomical Society of Japan, 60, L7

Aoki, W., Honda, S., Beers, T. C., et al. 2005, Astrophysical Journal, 632, 611

Aoki, W., Norris, J. E., Ryan, S. G., Beers, T. C., & Ando, H. 2002, Astrophysical Journal, 567, 1166

Arcones, A. & Janka, H. T. 2011, Astronomy & Astrophysics, 526, A160

Arcones, A., Janka, H. T., & Scheck, L. 2007, Astronomy & Astrophysics, 467, 1227

Arentsen, A., Starkenburg, E., Shetrone, M. D., et al. 2019, Astronomy & Astrophysics, 621, A108

Argast, D., Samland, M., Gerhard, O. E., & Thielemann, F. K. 2000, Astronomy & Astrophysics, 356, 873

Argast, D., Samland, M., Thielemann, F. K., & Gerhard, O. E. 2002, Astronomy & Astrophysics, 388, 842

Arnett, W. D. 1982, Astrophysical Journal, 253, 785

Arnett, W. D. & Thielemann, F. K. 1985, Astrophysical Journal, 295, 589

Arnould, M., Goriely, S., & Jorissen, A. 1999, Astronomy & Astrophysics, 347, 572

Asplund, M., Grevesse, N., Sauval, A. J., & Scott, P. 2009, Annual Review of Astronomy & Astrophysics, 47, 481

Asplund, M., Lambert, D. L., Nissen, P. E., Primas, F., & Smith, V. V. 2006, Astrophysical Journal, 644, 229

Aver, E., Olive, K. A., & Skillman, E. D. 2015, Journal of Cosmology and Astroparticle Physics, 2015, 011

Barbuy, B., Cayrel, R., Spite, M., et al. 1997, Astronomy & Astrophysics, 317, L63

Barbuy, B., Spite, M., Hill, V., et al. 2011, Astronomy & Astrophysics, 534, A60

Barbuy, B., Spite, M., Spite, F., et al. 2005, Astronomy & Astrophysics, 429, 1031

Barkat, Z., Rakavy, G., & Sack, N. 1967, Physical Review Letters, 18, 379

Barklem, P. S., Christlieb, N., Beers, T. C., et al. 2005, Astronomy & Astrophysics, 439, 129

Battistini, C. & Bensby, T. 2015, Astronomy & Astrophysics, 577, A9

Battistini, C. & Bensby, T. 2016, Astronomy & Astrophysics, 586, A49

Bauswein, A., Goriely, S., & Janka, H. T. 2013, Astrophysical Journal, 773, 78

Bear, E. & Soker, N. 2018, Monthly Notices of the Royal Astronomical Society, 480, 3702

Beers, T. C. & Christlieb, N. 2005, Annual Review of Astronomy & Astrophysics, 43, 531

Beers, T. C., Preston, G. W., & Shectman, S. A. 1992, Astronomical Journal, 103, 1987

Belczynski, K., Askar, A., Arca-Sedda, M., et al. 2018, Astronomy & Astrophysics, 615, A91

Bell, R. A., Edvardsson, B., & Gustafsson, B. 1985, Monthly Notices of the Royal Astronomical Society, 212, 497

Bensby, T. & Feltzing, S. 2006, Monthly Notices of the Royal Astronomical Society, 367, 1181

Bensby, T., Feltzing, S., & Lundström, I. 2004, Astronomy & Astrophysics, 415, 155

Bensby, T., Feltzing, S., Lundström, I., & Ilyin, I. 2005, Astronomy & Astrophysics, 433, 185

Bensby, T., Feltzing, S., & Oey, M. S. 2014, Astronomy & Astrophysics, 562, A71

Bergemann, M. 2011, Monthly Notices of the Royal Astronomical Society, 413, 2184

Bergemann, M. & Cescutti, G. 2010, Astronomy & Astrophysics, 522, A9

Bergemann, M. & Gehren, T. 2008, Astronomy & Astrophysics, 492, 823

Bergemann, M., Pickering, J. C., & Gehren, T. 2010, Monthly Notices of the Royal Astronomical Society, 401, 1334

Bihain, G., Israelian, G., Rebolo, R., Bonifacio, P., & Molaro, P. 2004, Astronomy & Astrophysics, 423, 777

Bisterzo, S., Gallino, R., Käppeler, F., et al. 2015, Monthly Notices of the Royal Astronomical Society, 449, 506

Bisterzo, S., Gallino, R., Pignatari, M., et al. 2004, Memorie della Società Astronomica Italiana, 75, 741

Bisterzo, S., Gallino, R., Straniero, O., Cristallo, S., & Käppeler, F. 2011, Monthly Notices of the Royal Astronomical Society, 418, 284

Bisterzo, S., Travaglio, C., Gallino, R., Wiescher, M., & Käppeler, F. 2014, Astrophysical Journal, 787, 10

Bisterzo, S., Travaglio, C., Wiescher, M., Käppeler, F., & Gallino, R. 2017, Astrophysical Journal, 835, 97

Boeltzig, A., Bruno, C. G., Cavanna, F., et al. 2016, European Physical Journal A, 52, 75

Bonifacio, P., Molaro, P., Sivarani, T., et al. 2007, Astronomy & Astrophysics, 462, 851

Bonifacio, P., Spite, M., Cayrel, R., et al. 2009, Astronomy & Astrophysics, 501, 519

Bortolas, E., Mapelli, M., & Spera, M. 2017, Monthly Notices of the Royal Astronomical Society, 469, 1510

Bravo, E. & Martínez-Pinedo, G. 2012, Physical Review C, 85, 055805

Brewer, M.-M. & Carney, B. W. 2006, Astronomical Journal, 131, 431

Brook, C. B., Gibson, B. K., Martel, H., & Kawata, D. 2005, Astrophysical Journal, 630, 298

Brook, C. B., Kawata, D., Gibson, B. K., & Freeman, K. C. 2004, Astrophysical Journal, 612, 894

Brown, J. A., Sneden, C., Lambert, D. L., & Dutchover, Edward, J. 1989, Astrophysical Journal Supplement Series, 71, 293

Bruenn, S. W., Lentz, E. J., Hix, W. R., et al. 2016, Astrophysical Journal, 818, 123

Bruenn, S. W., Mezzacappa, A., Hix, W. R., et al. 2013, Astrophysical Journal Letters, 767, L6

Buntain, J. F., Doherty, C. L., Lugaro, M., et al. 2017, Monthly Notices of the Royal Astronomical Society, 471, 824

Burrows, A. 2013, Reviews of Modern Physics, 85, 245

Caffau, E., Bonifacio, P., Faraggiana, R., et al. 2005, Astronomy & Astrophysics, 441, 533

Caffau, E., Bonifacio, P., Faraggiana, R., & Steffen, M. 2011, Astronomy & Astrophysics, 532, A98

Caffau, E., Bonifacio, P., Oliva, E., et al. 2019, Astronomy & Astrophysics, 622, A68

Caffau, E., Sbordone, L., Ludwig, H. G., Bonifacio, P., & Spite, M. 2010, Astronomische Nachrichten, 331, 725

Cameron, A. G. W. 2003, Astrophysical Journal, 587, 327

Cameron, A. G. W. & Fowler, W. A. 1971, Astrophysical Journal, 164, 111

Campbell, S. W. & Lattanzio, J. C. 2008, Astronomy & Astrophysics, 490, 769

Carigi, L. & Peimbert, M. 2011, Revista Mexicana de Astronomía y Astrofísica, 47, 139

Carigi, L., Peimbert, M., Esteban, C., & García-Rojas, J. 2005, Astrophysical Journal, 623, 213

Carney, B. W., Latham, D. W., Stefanik, R. P., Laird, J. B., & Morse, J. A. 2003, Astronomical Journal, 125, 293

Casagrande, L., Schönrich, R., Asplund, M., et al. 2011, Astronomy & Astrophysics, 530, A138

Casey, A. R., Ruchti, G., Masseron, T., et al. 2016, Monthly Notices of the Royal Astronomical Society, 461, 3336

Cayrel, R., Depagne, E., Spite, M., et al. 2004, Astronomy & Astrophysics, 416, 1117

Cescutti, G. & Chiappini, C. 2014, Astronomy & Astrophysics, 565, A51

Cescutti, G., Chiappini, C., Hirschi, R., Meynet, G., & Frischknecht, U. 2013, Astronomy & Astrophysics, 553, A51

Cescutti, G., Hirschi, R., Nishimura, N., et al. 2018, Monthly Notices of the Royal Astronomical Society, 478, 4101

Cescutti, G. & Kobayashi, C. 2017, Astronomy & Astrophysics, 607, A23

Cescutti, G., Matteucci, F., Caffau, E., & François, P. 2012, Astronomy & Astrophysics, 540, A33

Cescutti, G., Matteucci, F., McWilliam, A., & Chiappini, C. 2009, Astronomy & Astrophysics, 505, 605

Cescutti, G., Morossi, C., Franchini, M., et al. 2021, Astronomy & Astrophysics, 654, A164

Charbonnel, C. & Balachandran, S. C. 2000, Astronomy & Astrophysics, 359, 563

Charbonnel, C. & Primas, F. 2005, Astronomy & Astrophysics, 442, 961

Chen, Y. Q., Nissen, P. E., Zhao, G., & Asplund, M. 2002, Astronomy & Astrophysics, 390, 225

Chen, Y. Q., Nissen, P. E., Zhao, G., Zhang, H. W., & Benoni, T. 2000, Astronomy & Astrophysics Supplement Series, 141, 491

Chiaki, G., Susa, H., & Hirano, S. 2018, Monthly Notices of the Royal Astronomical Society, 475, 4378

Chiappini, C., Ekström, S., Meynet, G., et al. 2008, Astronomy & Astrophysics, 479, L9

Chiappini, C., Hirschi, R., Meynet, G., et al. 2006, Astronomy & Astrophysics, 449, L27

Chiappini, C., Matteucci, F., & Gratton, R. 1997, Astrophysical Journal, 477, 765

Chiappini, C., Matteucci, F., & Meynet, G. 2003, Astronomy & Astrophysics, 410, 257

Chiappini, C., Matteucci, F., & Romano, D. 2001, Astrophysical Journal, 554, 1044

Chiba, M. & Yoshii, Y. 1998, Astronomical Journal, 115, 168

Choplin, A., Hirschi, R., Meynet, G., et al. 2018, Astronomy & Astrophysics, 618, A133

Cohen, J. G., Christlieb, N., McWilliam, A., et al. 2004, Astrophysical Journal, 612, 1107

Cohen, J. G., Christlieb, N., Thompson, I., et al. 2013, Astrophysical Journal, 778, 56

Cohen, J. G., McWilliam, A., Shectman, S., et al. 2006, Astronomical Journal, 132, 137

Cooke, R. J., Pettini, M., & Steidel, C. C. 2017, Monthly Notices of the Royal Astronomical Society, 467, 802

Costa Silva, A. R., Delgado Mena, E., & Tsantaki, M. 2020, Astronomy & Astrophysics, 634, A136

Côté, B., Jones, S., Herwig, F., & Pignatari, M. 2020, Astrophysical Journal, 892, 57

Cristallo, S., Abia, C., Straniero, O., & Piersanti, L. 2015a, Astrophysical Journal, 801, 53

Cristallo, S., Di Leva, A., Imbriani, G., et al. 2014, Astronomy & Astrophysics, 570, A46

Cristallo, S., Piersanti, L., Straniero, O., et al. 2011, Astrophysical Journal Supplement Series, 197, 17

Cristallo, S., Straniero, O., Piersanti, L., & Gobrecht, D. 2015b, Astrophysical Journal Supplement Series, 219, 40

Şahin, N. & Tanışlı, M. 2020, European Physical Journal Plus, 135, 653

Cunha, K., Smith, V. V., & Gibson, B. K. 2008, Astrophysical Journal Letters, 679, L17

da Silva, R., Porto de Mello, G. F., Milone, A. C., et al. 2012, Astronomy & Astrophysics, 542, A84

de Bennassuti, M., Salvadori, S., Schneider, R., Valiante, R., & Omukai, K. 2017, Monthly Notices of the Royal Astronomical Society, 465, 926

de la Reza, R., Drake, N. A., Oliveira, I., & Rengaswamy, S. 2015, Astrophysical Journal, 806, 86

Decressin, T., Meynet, G., Charbonnel, C., Prantzos, N., & Ekström, S. 2007, Astronomy & Astrophysics, 464, 1029

Delgado Mena, E., Tsantaki, M., Adibekyan, V. Z., et al. 2017, Astronomy & Astrophysics, 606, A94

Delgado Mena, E., Tsantaki, M., Sousa, S. G., et al. 2016, Astronomy & Astrophysics, 587, A66

Denissenkov, P. A. 2012, Astrophysical Journal Letters, 753, L3

Dierickx, M., Klement, R., Rix, H.-W., & Liu, C. 2010, Astrophysical Journal Letters, 725, L186

Doherty, C. L., Gil-Pons, P., Lau, H. H. B., Lattanzio, J. C., & Siess, L. 2014a, Monthly Notices of the Royal Astronomical Society, 437, 195

Doherty, C. L., Gil-Pons, P., Lau, H. H. B., et al. 2014b, Monthly Notices of the Royal Astronomical Society, 441, 582

Doherty, C. L., Gil-Pons, P., Siess, L., & Lattanzio, J. C. 2017, Publications of the Astronomical Society of Australia, 34, e056

Doherty, C. L., Gil-Pons, P., Siess, L., Lattanzio, J. C., & Lau, H. H. B. 2015, Monthly Notices of the Royal Astronomical Society, 446, 2599

Domingo-Pardo, C., Abbondanno, U., Aerts, G., et al. 2008

Duong, L., Freeman, K. C., Asplund, M., et al. 2018, Monthly Notices of the Royal Astronomical Society, 476, 5216

Ecuvillon, A., Israelian, G., Santos, N. C., et al. 2004, Astronomy & Astrophysics, 418, 703

Edvardsson, B., Andersen, J., Gustafsson, B., et al. 1993, Astronomy & Astrophysics, 500, 391

Ekström, S., Meynet, G., Chiappini, C., Hirschi, R., & Maeder, A. 2008, Astronomy & Astrophysics, 489, 685

El Eid, M. F. 2015, in American Institute of Physics Conference Series, Vol. 1645, American Institute of Physics Conference Series, 132–138

Esteban, C., Peimbert, M., Torres-Peimbert, S., & Escalante, V. 1998, Monthly Notices of the Royal Astronomical Society, 295, 401

Fabbian, D., Nissen, P. E., Asplund, M., Pettini, M., & Akerman, C. 2009, Astronomy & Astrophysics, 500, 1143

Fan, X. 2003, in American Astronomical Society Meeting Abstracts, Vol. 203, American Astronomical Society Meeting Abstracts, 129.01

Feltzing, S., Fohlman, M., & Bensby, T. 2007, Astronomy & Astrophysics, 467, 665

Feltzing, S., Howes, L. M., McMillan, P. J., & Stonkutė, E. 2017, Monthly Notices of the Royal Astronomical Society, 465, L109

Ferdman, R. D. & PALFA Collaboration. 2018, in Pulsar Astrophysics the Next Fifty Years, ed. P. Weltevrede, B. B. P. Perera, L. L. Preston, & S. Sanidas, Vol. 337, 146–149

Fich, M. & Silkey, M. 1991, Astrophysical Journal, 366, 107

Fink, M., Kromer, M., Seitenzahl, I. R., et al. 2014, Monthly Notices of the Royal Astronomical Society, 438, 1762

Fischer, T., Whitehouse, S. C., Mezzacappa, A., Thielemann, F. K., & Liebendörfer, M. 2010, Astronomy & Astrophysics, 517, A80

Fishlock, C. K., Karakas, A. I., Lugaro, M., & Yong, D. 2014, Astrophysical Journal, 797, 44

Fishlock, C. K., Yong, D., Karakas, A. I., et al. 2017, Monthly Notices of the Royal Astronomical Society, 466, 4672

Flörs, A., Spyromilio, J., Maguire, K., et al. 2018, Astronomy & Astrophysics, 620, A200

Foley, R. J., Challis, P. J., Chornock, R., et al. 2013, Astrophysical Journal, 767, 57

Forestini, M., Goriely, S., Jorissen, A., & Arnould, M. 1992, Astronomy & Astrophysics, 261, 157

François, P., Depagne, E., Hill, V., et al. 2007, Astronomy & Astrophysics, 476, 935

François, P., Matteucci, F., Cayrel, R., et al. 2004, Astronomy & Astrophysics, 421, 613

Franchini, M., Morossi, C., Di Marcantonio, P., et al. 2020, Astrophysical Journal, 888, 55

Francois, P. 1987, Astronomy & Astrophysics, 176, 294

Francois, P. 1988, Astronomy & Astrophysics, 195, 226

Frebel, A. 2010, Astronomische Nachrichten, 331, 474

Frebel, A., Christlieb, N., Norris, J. E., et al. 2006, Astrophysical Journal, 652, 1585

Freiburghaus, C., Rosswog, S., & Thielemann, F. K. 1999, Astrophysical Journal Letters, 525, L121

Frischknecht, U., Hirschi, R., Pignatari, M., et al. 2016, Monthly Notices of the Royal Astronomical Society, 456, 1803

Fröhlich, C., Hauser, P., Liebendörfer, M., et al. 2006, Astrophysical Journal, 637, 415

Fryer, C. L., Woosley, S. E., & Heger, A. 2001, Astrophysical Journal, 550, 372

Fuhrmann, K. 1998, Astronomy & Astrophysics, 338, 161

Fulbright, J. P. 2000, Astronomical Journal, 120, 1841

Fulbright, J. P. & Johnson, J. A. 2003, Astrophysical Journal, 595, 1154

Gaia Collaboration, Brown, A. G. A., & et al. 2018, Astronomy & Astrophysics, 616, A1

Gal-Yam, A. 2017, Observational and Physical Classification of Supernovae, ed. A. W. Alsabti & P. Murdin, 195

Gallino, R., Arlandini, C., Busso, M., et al. 1998, Astrophysical Journal, 497, 388

Gallino, R., Bisterzo, S., Straniero, O., Ivans, I. I., & Käppeler, F. 2006, Memorie della Società Astronomica Italiana, 77, 786

García Pérez, A. E., Aoki, W., Inoue, S., et al. 2009, Astronomy & Astrophysics, 504, 213

Gehren, T., Liang, Y. C., Shi, J. R., Zhang, H. W., & Zhao, G. 2004, Astronomy & Astrophysics, 413, 1045

Gehren, T., Shi, J. R., Zhang, H. W., Zhao, G., & Korn, A. J. 2006, Astronomy & Astrophysics, 451, 1065

Gil-Pons, P., Gutiérrez, J., & García-Berro, E. 2007, Astronomy & Astrophysics, 464, 667

Gilmore, G. & Reid, N. 1983, Monthly Notices of the Royal Astronomical Society, 202, 1025

Gilmore, G., Wyse, R. F. G., & Jones, J. B. 1995, Astronomical Journal, 109, 1095

Goswami, A. & Prantzos, N. 2000, Astronomy & Astrophysics, 359, 191

Gratton, R. G. 1989, Astronomy & Astrophysics, 208, 171

Gratton, R. G., Carretta, E., Claudi, R., Lucatello, S., & Barbieri, M. 2003, Astronomy & Astrophysics, 404, 187

Gratton, R. G. & Sneden, C. 1987a, Astronomy & Astrophysics Supplement Series, 68, 193

Gratton, R. G. & Sneden, C. 1987b, Astronomy & Astrophysics, 178, 179

Gratton, R. G. & Sneden, C. 1991, Astronomy & Astrophysics, 241, 501

Gratton, R. G., Sneden, C., Carretta, E., & Bragaglia, A. 2000, Astronomy & Astrophysics, 354, 169

Gray, D. F. 2008, The Observation and Analysis of Stellar Photospheres

Grevesse, N., Noels, A., & Sauval, A. J. 1996, in Astronomical Society of the Pacific Conference Series, Vol. 99, Cosmic Abundances, ed. S. S. Holt & G. Sonneborn, 117

Griffith, E., Johnson, J. A., & Weinberg, D. H. 2019, Astrophysical Journal, 886, 84

Guerço, R., Cunha, K., Smith, V. V., et al. 2019, Astrophysical Journal, 885, 139

Gummersbach, C. A., Kaufer, A., Schaefer, D. R., Szeifert, T., & Wolf, B. 1998, Astronomy & Astrophysics, 338, 881

Hansen, C. J., Hansen, T. T., Koch, A., et al. 2019, Astronomy & Astrophysics, 623, A128

Hansen, C. J., Nordström, B., Hansen, T. T., et al. 2016a, Astronomy & Astrophysics, 588, A37

Hansen, C. J., Primas, F., Hartman, H., et al. 2012, Astronomy & Astrophysics, 545, A31

Hansen, T., Hansen, C. J., Christlieb, N., et al. 2014, Astrophysical Journal, 787, 162

Hansen, T. T., Andersen, J., Nordström, B., et al. 2016b, Astronomy & Astrophysics, 586, A160

Hartwig, T. & Yoshida, N. 2019, Astrophysical Journal Letters, 870, L3

Hartwig, T., Yoshida, N., Magg, M., et al. 2018, Monthly Notices of the Royal Astronomical Society, 478, 1795

Haywood, M., Di Matteo, P., Lehnert, M. D., Katz, D., & Gómez, A. 2013, Astronomy & Astrophysics, 560, A109

Haywood, M., Lehnert, M. D., Di Matteo, P., et al. 2016, Astronomy & Astrophysics, 589, A66

Hedrosa, R. P., Abia, C., Busso, M., et al. 2013, Astrophysical Journal Letters, 768, L11

Heger, A., Fryer, C. L., Woosley, S. E., Langer, N., & Hartmann, D. H. 2003, Astrophysical Journal, 591, 288

Heger, A. & Langer, N. 2000, Astrophysical Journal, 544, 1016

Heger, A. & Woosley, S. E. 2002, Astrophysical Journal, 567, 532

Helmi, A., Babusiaux, C., Koppelman, H. H., et al. 2018, Nature, 563, 85

Henry, R. B. C., Edmunds, M. G., & Köppen, J. 2000, Astrophysical Journal, 541, 660

Hernanz, M., Jose, J., Coc, A., & Isern, J. 1996, Astrophysical Journal, 465, L27

Hilditch, R. W. 2001, An Introduction to Close Binary Stars

Hill, V., Barbuy, B., Spite, M., et al. 2000, Astronomy & Astrophysics, 353, 557

Hillebrandt, W. & Niemeyer, J. C. 2000, Annual Review of Astronomy & Astrophysics, 38, 191

Hillen, M. 2013, Interferometric studies of AGB and post-AGB stars. Phd thesis

Hinkel, N. R., Timmes, F. X., Young, P. A., Pagano, M. D., & Turnbull, M. C. 2014, Astronomical Journal, 148, 54

Hirschi, R. 2007, Astronomy & Astrophysics, 461, 571

Hirschi, R., Meynet, G., & Maeder, A. 2005, Astronomy & Astrophysics, 433, 1013

Hix, W. R. & Thielemann, F.-K. 1999, Astrophysical Journal, 511, 862

Hoang, B.-M., Naoz, S., Kocsis, B., Rasio, F. A., & Dosopoulou, F. 2018, Astrophysical Journal, 856, 140

Hobbs, G., Lorimer, D. R., Lyne, A. G., & Kramer, M. 2005, Monthly Notices of the Royal Astronomical Society, 360, 974

Hoffman, R. D., Müller, B., & Janka, H. T. 2008, Astrophysical Journal Letters, 676, L127

Höfner, S. & Olofsson, H. 2018, , 26, 1

Honda, S., Aoki, W., Kajino, T., et al. 2004, Astrophysical Journal, 607, 474

Howes, L. M., Casey, A. R., Asplund, M., et al. 2015, Nature, 527, 484

Hoyle, F. & Fowler, W. A. 1960, Astrophysical Journal, 132, 565

Hubble, E. 1929, Proceedings of the National Academy of Science, 15, 168

Hüdepohl, L., Müller, B., Janka, H. T., Marek, A., & Raffelt, G. G. 2010, Physical Review Letters, 104, 251101

Hurley, J. R., Tout, C. A., & Pols, O. R. 2002, Monthly Notices of the Royal Astronomical Society, 329, 897

Iocco, F., Mangano, G., Miele, G., Pisanti, O., & Serpico, P. D. 2009, Physics Reports, 472, 1

Ishigaki, M. N., Aoki, W., & Chiba, M. 2013, Astrophysical Journal, 771, 67

Ishigaki, M. N., Tominaga, N., Kobayashi, C., & Nomoto, K. 2014, Astrophysical Journal Letters, 792, L32

Ishigaki, M. N., Tominaga, N., Kobayashi, C., & Nomoto, K. 2018, Astrophysical Journal, 857, 46

Israelian, G., Bertran de Lis, S., Delgado Mena, E., & Adibekyan, V. Z. 2014, Memorie della Società Astronomica Italiana, 85, 265

Israelian, G., Ecuvillon, A., Rebolo, R., et al. 2004, Astronomy & Astrophysics, 421, 649

Israelian, G. & Rebolo, R. 2001, Astrophysical Journal Letters, 557, L43

Ivanova, D. V. & Shimanskiĭ, V. V. 2000, Astronomy Reports, 44, 376

Ivans, I. I., Simmerer, J., Sneden, C., et al. 2006, Astrophysical Journal, 645, 613

Iwamoto, K., Brachwitz, F., Nomoto, K., et al. 1999, Astrophysical Journal Supplement Series, 125, 439

Izotov, Y. I., Schaerer, D., & Charbonnel, C. 2001, Astrophysical Journal, 549, 878

Izotov, Y. I. & Thuan, T. X. 1999, Astrophysical Journal, 511, 639

Izotov, Y. I., Thuan, T. X., & Guseva, N. G. 2014, Monthly Notices of the Royal Astronomical Society, 445, 778

Janka, H.-T. 2012, Annual Review of Nuclear and Particle Science, 62, 407

Janka, H. T., Langanke, K., Marek, A., Martínez-Pinedo, G., & Müller, B. 2007, Physics Reports, 442, 38

Ji, A. P., Frebel, A., & Bromm, V. 2015, Monthly Notices of the Royal Astronomical Society, 454, 659

Jones, S., Hirschi, R., & Nomoto, K. 2014, Astrophysical Journal, 797, 83

Jones, S., Röpke, F. K., Pakmor, R., et al. 2016, Astronomy & Astrophysics, 593, A72

Jönsson, H., Ryde, N., Harper, G. M., et al. 2014a, Astronomy & Astrophysics, 564, A122

Jönsson, H., Ryde, N., Harper, G. M., Richter, M. J., & Hinkle, K. H. 2014b, Astrophysical Journal Letters, 789, L41

Jönsson, H., Ryde, N., Nissen, P. E., et al. 2011, Astronomy & Astrophysics, 530, A144

Jönsson, H., Ryde, N., Spitoni, E., et al. 2017, Astrophysical Journal, 835, 50

Jordan, G. C., Gupta, S. S., & Meyer, B. S. 2003, Physical Review C, 68, 065801

Jorissen, A., Smith, V. V., & Lambert, D. L. 1992, Astronomy & Astrophysics, 261, 164

Jorissen, A., Van Eck, S., Van Winckel, H., et al. 2016, Astronomy & Astrophysics, 586, A158

Karakas, A. & Lattanzio, J. C. 2007, Publications of the Astronomical Society of Australia, 24, 103

Karakas, A. I. 2010, Monthly Notices of the Royal Astronomical Society, 403, 1413

Karakas, A. I. & Lattanzio, J. C. 2014, Publications of the Astronomical Society of Australia, 31, e030

Karakas, A. I., Lattanzio, J. C., & Pols, O. R. 2002, Publications of the Astronomical Society of Australia, 19, 515

Karakas, A. I. & Lugaro, M. 2016, Astrophysical Journal, 825, 26

Karakas, A. I., Lugaro, M., Carlos, M., et al. 2018, Monthly Notices of the Royal Astronomical Society, 477, 421

Karlsson, T., Bromm, V., & Bland-Hawthorn, J. 2013, Reviews of Modern Physics, 85, 809

Kasen, D., Metzger, B., Barnes, J., Quataert, E., & Ramirez-Ruiz, E. 2017, Nature, 551, 80

Keenan, P. C. 1942, Astrophysical Journal, 96, 101

Keller, S. C., Bessell, M. S., Frebel, A., et al. 2014, Nature, 506, 463

Kirby, E. N., Guhathakurta, P., Zhang, A. J., et al. 2016, Astrophysical Journal, 819, 135

Kitaura, F. S., Janka, H. T., & Hillebrandt, W. 2006, Astronomy & Astrophysics, 450, 345

Kobayashi, C., Izutani, N., Karakas, A. I., et al. 2011a, Astrophysical Journal Letters, 739, L57

Kobayashi, C., Karakas, A. I., & Lugaro, M. 2020a, Astrophysical Journal, 900, 179

Kobayashi, C., Karakas, A. I., & Umeda, H. 2011b, Monthly Notices of the Royal Astronomical Society, 414, 3231

Kobayashi, C., Leung, S.-C., & Nomoto, K. 2020b, Astrophysical Journal, 895, 138

Kobayashi, C. & Nakasato, N. 2011, Astrophysical Journal, 729, 16

Kobayashi, C. & Nomoto, K. 2009, Astrophysical Journal, 707, 1466

Kobayashi, C., Nomoto, K., & Hachisu, I. 2015, Astrophysical Journal Letters, 804, L24

Kobayashi, C., Tominaga, N., & Nomoto, K. 2011c, Astrophysical Journal Letters, 730, L14

Kobayashi, C., Tsujimoto, T., Nomoto, K., Hachisu, I., & Kato, M. 1998, Astrophysical Journal Letters, 503, L155

Kobayashi, C., Umeda, H., Nomoto, K., Tominaga, N., & Ohkubo, T. 2006, Astrophysical Journal, 653, 1145

Kobulnicky, H. A. & Skillman, E. D. 1996, Astrophysical Journal, 471, 211

Kogure, T. & Hirata, R. 1982, Bulletin of the Astronomical Society of India, 10, 281

Korn, A. J. & Ryde, N. 2005, Astronomy & Astrophysics, 443, 1029

Korotin, S. A., Andrievsky, S. M., & Zhukova, A. V. 2018, Monthly Notices of the Royal Astronomical Society, 480, 965

Kotake, K., Sumiyoshi, K., Yamada, S., et al. 2012, Progress of Theoretical and Experimental Physics, 2012, 01A301

Krauss, L. M. 2012, A Universe from Nothing: Why There is Something Rather than Nothing, ed. Atria Books

Kroupa, P. 2002, in Astronomical Society of the Pacific Conference Series, Vol. 285, Modes of Star Formation and the Origin of Field Populations, ed. E. K. Grebel & W. Brandner, 86

Kroupa, P., Tout, C. A., & Gilmore, G. 1993, Monthly Notices of the Royal Astronomical Society, 262, 545

Kruckow, M. U., Tauris, T. M., Langer, N., Kramer, M., & Izzard, R. G. 2018, Monthly Notices of the Royal Astronomical Society, 481, 1908

Kubryk, M., Prantzos, N., & Athanassoula, E. 2015, Astronomy & Astrophysics, 580, A126

Kuchner, M. J., Kirshner, R. P., Pinto, P. A., & Leibundgut, B. 1994, Astrophysical Journal Letters, 426, L89

Kumar, Y. B., Reddy, B. E., & Lambert, D. L. 2011, Astrophysical Journal Letters, 730, L12

Kuroda, T., Kotake, K., Takiwaki, T., & Thielemann, F.-K. 2018, Monthly Notices of the Royal Astronomical Society, 477, L80

Kurucz, R. 1993, ATLAS9 Stellar Atmosphere Programs and 2 km/s grid. Kurucz CD-ROM No. 13. Cambridge, 13

Kyutoku, K., Kiuchi, K., Sekiguchi, Y., Shibata, M., & Taniguchi, K. 2018, , 97, 023009

Lagarde, N., Decressin, T., Charbonnel, C., et al. 2012, Astronomy & Astrophysics, 543, A108

Lai, D. K., Bolte, M., Johnson, J. A., et al. 2008, Astrophysical Journal, 681, 1524

Lai, D. K., Johnson, J. A., Bolte, M., & Lucatello, S. 2007, Astrophysical Journal, 667, 1185

Lambert, D. L. & Reddy, B. E. 2004, Monthly Notices of the Royal Astronomical Society, 349, 757

Lattimer, J. M. & Schramm, D. N. 1974, Astrophysical Journal Letters, 192, L145

Lazarus, P., Tauris, T. M., Knispel, B., et al. 2014, Monthly Notices of the Royal Astronomical Society, 437, 1485

Lederer, C. M., Hollander, J. M., & Perlman, I. 1967, Table of isotopes

Li, H. N., Ludwig, H. G., Caffau, E., Christlieb, N., & Zhao, G. 2013, Astrophysical Journal, 765, 51

Li, Z., Li, E., Su, J., et al. 2011, Science China Physics, Mechanics, and Astronomy, 54, 67

Liang, Y. C., Zhao, G., & Shi, J. R. 2001, Astronomy & Astrophysics, 374, 936

Limongi, M. & Chieffi, A. 2003, Astrophysical Journal, 592, 404

Limongi, M. & Chieffi, A. 2018, Astrophysical Journal Supplement Series, 237, 13

Liu, C. & van de Ven, G. 2012, Monthly Notices of the Royal Astronomical Society, 425, 2144

Ljung, G., Nilsson, H., Asplund, M., & Johansson, S. 2006, Astronomy & Astrophysics, 456, 1181

Lodders, K. & Fegley, B., J. 1995, Meteoritics, 30, 661

Lodders, K. & Palme, H. 2009, Meteoritics and Planetary Science Supplement, 72, 5154

Longland, R., Lorén-Aguilar, P., José, J., et al. 2011, Astrophysical Journal Letters, 737, L34

Lu, L., Sargent, W. L. W., Barlow, T. A., Churchill, C. W., & Vogt, S. S. 1996, Astrophysical Journal Supplement Series, 107, 475

Lucatello, S., Beers, T. C., Christlieb, N., et al. 2006, Astrophysical Journal Letters, 652, L37

Lucatello, S., Gratton, R., Cohen, J. G., et al. 2003, Astronomical Journal, 125, 875

Lucatello, S., Masseron, T., Johnson, J. A., Pignatari, M., & Herwig, F. 2011, Astrophysical Journal, 729, 40

Lucatello, S., Tsangarides, S., Beers, T. C., et al. 2005, Astrophysical Journal, 625, 825

Lugaro, M., Davis, A. M., Gallino, R., et al. 2003, Astrophysical Journal, 593, 486

Lugaro, M., Karakas, A. I., Stancliffe, R. J., & Rijs, C. 2012, Astrophysical Journal, 747, 2

Lyman, J. D., Lamb, G. P., Levan, A. J., et al. 2018, Nature Astronomy, 2, 751

Maas, T., Van Winckel, H., & Lloyd Evans, T. 2005, Astronomy & Astrophysics, 429, 297

Maas, Z. G., Pilachowski, C. A., & Cescutti, G. 2017, Astrophysical Journal, 841, 108

Maas, Z. G., Pilachowski, C. A., & Hinkle, K. 2016, Astronomical Journal, 152, 196

Maeda, K. & Nomoto, K. 2003, Astrophysical Journal, 598, 1163

Maeder, A. 1992, Astronomy & Astrophysics, 264, 105

Maeder, A., Grebel, E. K., & Mermilliod, J.-C. 1999, Astronomy & Astrophysics, 346, 459

Maeder, A. & Meynet, G. 2012, Reviews of Modern Physics, 84, 25

Maeder, A., Meynet, G., & Chiappini, C. 2015, Astronomy & Astrophysics, 576, A56

Magic, Z., Collet, R., Asplund, M., et al. 2013, Astronomy & Astrophysics, 557, A26

Magkotsios, G., Timmes, F. X., & Wiescher, M. 2011, Astrophysical Journal, 741, 78

Maiorca, E., Uitenbroek, H., Uttenthaler, S., et al. 2014, Astrophysical Journal, 788, 149

Maoz, D. & Graur, O. 2017, Astrophysical Journal, 848, 25

Marek, A. & Janka, H. T. 2009, Astrophysical Journal, 694, 664

Marigo, P. 2001, Astronomy & Astrophysics, 370, 194

Martayan, C., Frémat, Y., Hubert, A. M., et al. 2007, Astronomy & Astrophysics, 462, 683

Martínez Pinedo, G., Fischer, T., Lohs, A., & Huther, L. 2012, in Journal of Physics Conference Series, Vol. 403, Journal of Physics Conference Series, 012037

Mashonkina, L., Christlieb, N., & Eriksson, K. 2014, Astronomy & Astrophysics, 569, A43

Mashonkina, L., Gehren, T., & Bikmaev, I. 1999, Astronomy & Astrophysics, 343, 519

Mashonkina, L., Gehren, T., Shi, J. R., Korn, A. J., & Grupp, F. 2011, Astronomy & Astrophysics, 528, A87

Mashonkina, L., Gehren, T., Travaglio, C., & Borkova, T. 2003, Astronomy & Astrophysics, 397, 275

Mashonkina, L., Korn, A. J., & Przybilla, N. 2007, Astronomy & Astrophysics, 461, 261

Mashonkina, L., Ryabtsev, A., & Frebel, A. 2012, Astronomy & Astrophysics, 540, A98

Mashonkina, L. I., Shimanskiĭ, V. V., & Sakhibullin, N. A. 2000, Astronomy Reports, 44, 790

Masseron, T., Johnson, J. A., Lucatello, S., et al. 2012, Astrophysical Journal, 751, 14

Masseron, T., Johnson, J. A., Plez, B., et al. 2010, Astronomy & Astrophysics, 509, A93

Matrozis, E., Ryde, N., & Dupree, A. K. 2013, Astronomy & Astrophysics, 559, A115

Matteucci, F. & Francois, P. 1989, Monthly Notices of the Royal Astronomical Society, 239, 885

Matteucci, F. & Greggio, L. 1986, Astronomy & Astrophysics, 154, 279

Matteucci, F., Romano, D., Arcones, A., Korobkin, O., & Rosswog, S. 2014, Monthly Notices of the Royal Astronomical Society, 438, 2177

Mattsson, L. 2009, On the winds of carbon stars and the origin of carbon: A theoretical study, PhD thesis, Uppsala University, Sweden

Mattsson, L. 2010, Astronomy & Astrophysics, 515, A68

Mayer, M. G. 1948, Physical Review, 74, 235

Mayer, M. G. 1949, Physical Review, 75, 1969

McClure, R. D. 1984, Astrophysical Journal Letters, 280, L31

McClure, R. D. & Woodsworth, A. W. 1990, Astrophysical Journal, 352, 709

McCully, C., Jha, S. W., Foley, R. J., et al. 2014, Nature, 512, 54

McWilliam, A., Preston, G. W., Sneden, C., & Shectman, S. 1995, Astronomical Journal, 109, 2736

Mennekens, N. & Vanbeveren, D. 2014, Astronomy & Astrophysics, 564, A134

Mennekens, N. & Vanbeveren, D. 2016, Astronomy & Astrophysics, 589, A64

Metzger, B. D. & Berger, E. 2012, Astrophysical Journal, 746, 48

Metzger, B. D. & Fernández, R. 2014, Monthly Notices of the Royal Astronomical Society, 441, 3444

Meyer, B. S. 2005, in Workshop on Oxygen in the Earliest Solar System, Vol. 1278, 32

Meynet, G. & Arnould, M. 2000, Astronomy & Astrophysics, 355, 176

Meynet, G., Hirschi, R., Ekstrom, S., et al. 2010, Astronomy & Astrophysics, 521, A30

Meynet, G. & Maeder, A. 2000, Astronomy & Astrophysics, 361, 101

Meynet, G. & Maeder, A. 2002a, Astronomy & Astrophysics, 390, 561

Meynet, G. & Maeder, A. 2002b, Astronomy & Astrophysics, 381, L25

Mikolaitis, Š., de Laverny, P., Recio-Blanco, A., et al. 2017, Astronomy & Astrophysics, 600, A22

Miller, J. L. 2015, Physics Today, 68, 16

Mishenina, T. V., Kovtyukh, V. V., Soubiran, C., Travaglio, C., & Busso, M. 2002, Astronomy & Astrophysics, 396, 189

Mishenina, T. V., Pignatari, M., Korotin, S. A., et al. 2013, Astronomy & Astrophysics, 552, A128

Miyaji, S., Nomoto, K., Yokoi, K., & Sugimoto, D. 1980, Publications of the Astronomical Society of Japan, 32, 303

Mocák, M., Campbell, S. W., Müller, E., & Kifonidis, K. 2010, Astronomy & Astrophysics, 520, A114

Monaco, L., Boffin, H. M. J., Bonifacio, P., et al. 2014, Astronomy & Astrophysics, 564, L6

Mooley, K. P., Nakar, E., Hotokezaka, K., et al. 2018, Nature, 554, 207

Mösta, P., Richers, S., Ott, C. D., et al. 2014, Astrophysical Journal Letters, 785, L29

Müller, B., Heger, A., Liptai, D., & Cameron, J. B. 2016, Monthly Notices of the Royal Astronomical Society, 460, 742

Nakamura, T., Umeda, H., Iwamoto, K., et al. 2001, Astrophysical Journal, 555, 880

Nault, K. A. & Pilachowski, C. A. 2013, Astronomical Journal, 146, 153

Navarro, J. F., Abadi, M. G., Venn, K. A., Freeman, K. C., & Anguiano, B. 2011, Monthly Notices of the Royal Astronomical Society, 412, 1203

Neves, V., Santos, N. C., Sousa, S. G., Correia, A. C. M., & Israelian, G. 2009, Astronomy & Astrophysics, 497, 563

Nishimura, N., Takiwaki, T., & Thielemann, F.-K. 2015, Astrophysical Journal, 810, 109

Nishimura, S., Kotake, K., Hashimoto, M.-a., et al. 2006, Astrophysical Journal, 642, 410

Nissen, P. E. 2015, Astronomy & Astrophysics, 579, A52

Nissen, P. E., Akerman, C., Asplund, M., et al. 2007, Astronomy & Astrophysics, 469, 319

Nissen, P. E., Chen, Y. Q., Asplund, M., & Pettini, M. 2004, Astronomy & Astrophysics, 415, 993

Nissen, P. E., Chen, Y. Q., Carigi, L., Schuster, W. J., & Zhao, G. 2014, Astronomy & Astrophysics, 568, A25

Nissen, P. E., Chen, Y. Q., Schuster, W. J., & Zhao, G. 2000, Astronomy & Astrophysics, 353, 722

Nissen, P. E. & Schuster, W. J. 2010, Astronomy & Astrophysics, 511, L10

Nissen, P. E. & Schuster, W. J. 2011, Astronomy & Astrophysics, 530, A15

Nomoto, K. 1984, Astrophysical Journal, 277, 791

Nomoto, K. 1987, Astrophysical Journal, 322, 206

Nomoto, K., Iwamoto, K., Nakasato, N., et al. 1997, Nuclear Physics A, 621, 467

Nomoto, K., Kobayashi, C., & Tominaga, N. 2013, Annual Review of Astronomy & Astrophysics, 51, 457

Nomoto, K., Sparks, W. M., Fesen, R. A., et al. 1982, Nature, 299, 803

Nomoto, K., Tominaga, N., Umeda, H., Kobayashi, C., & Maeda, K. 2006, Nuclear Physics A, 777, 424

Norris, J. E., Ryan, S. G., & Beers, T. C. 1997, Astrophysical Journal, 488, 350

Norris, J. E., Yong, D., Bessell, M. S., et al. 2013, Astrophysical Journal, 762, 28

Ohkubo, T., Umeda, H., Maeda, K., et al. 2006, Astrophysical Journal, 645, 1352

Osorio, Y., Aguado, D. S., Allende Prieto, C., Hubeny, I., & González Hernández, J. I. 2022, Astrophysical Journal, 928, 173

Otsuka, M., Izumiura, H., Tajitsu, A., & Hyung, S. 2008, The Astrophysical Journal, 682, 682

Palacios, A., Charbonnel, C., Talon, S., & Siess, L. 2006, Astronomy & Astrophysics, 453, 261

Peimbert, A., Peimbert, M., & Luridiana, V. 2016, Revista Mexicana de Astronomía y Astrofísica, 52, 419

Pejcha, O. & Thompson, T. A. 2015, Astrophysical Journal, 801, 90

Pettini, M., Zych, B. J., Steidel, C. C., & Chaffee, F. H. 2008, Monthly Notices of the Royal Astronomical Society, 385, 2011

Pignatari, M., Gallino, R., Heil, M., et al. 2010, Astrophysical Journal, 710, 1557

Pignatari, M., Herwig, F., Hirschi, R., et al. 2016, Astrophysical Journal Supplement Series, 225, 24

Pilachowski, C. A. & Pace, C. 2015, Astronomical Journal, 150, 66

Placco, V. M., Frebel, A., Beers, T. C., & Stancliffe, R. J. 2014, Astrophysical Journal, 797, 21

Pllumbi, E., Tamborra, I., Wanajo, S., Janka, H.-T., & Hüdepohl, L. 2015, Astrophysical Journal, 808, 188

Podsiadlowski, P., Mazzali, P. A., Nomoto, K., Lazzati, D., & Cappellaro, E. 2004, Astrophysical Journal Letters, 607, L17

Portinari, L., Chiosi, C., & Bressan, A. 1998, Astronomy & Astrophysics, 334, 505

Prantzos, N. 2006, arXiv e-prints, astro

Prantzos, N. 2012a, Astronomy & Astrophysics, 538, A80

Prantzos, N. 2012b, Astronomy & Astrophysics, 542, A67

Prantzos, N., Abia, C., Limongi, M., Chieffi, A., & Cristallo, S. 2018, Monthly Notices of the Royal Astronomical Society, 476, 3432

Prantzos, N., Aubert, O., & Audouze, J. 1996, Astronomy & Astrophysics, 309, 760

Pratten, G., Schmidt, P., & Hinderer, T. 2020, Nature Communications, 11, 2553

Preston, G. W. & Sneden, C. 2001, Astronomical Journal, 122, 1545

Prochaska, J. X., Naumov, S. O., Carney, B. W., McWilliam, A., & Wolfe, A. M. 2000, Astronomical Journal, 120, 2513

Quinn, P. J., Hernquist, L., & Fullagar, D. P. 1993, Astrophysical Journal, 403, 74

Radice, D., Perego, A., Hotokezaka, K., et al. 2018, Astrophysical Journal, 869, 130

Raghavan, D., McAlister, H. A., Henry, T. J., et al. 2010, Astrophysical Journal Supplement Series, 190, 1

Rana, N. C. 1991, Annual Review of Astronomy & Astrophysics, 29, 129

Recio-Blanco, A., de Laverny, P., Worley, C., et al. 2012, Astronomy & Astrophysics, 538, A117

Reddy, A. B. S. & Lambert, D. L. 2016, Astronomy & Astrophysics, 589, A57

Reddy, B. E., Lambert, D. L., & Allende Prieto, C. 2006, Monthly Notices of the Royal Astronomical Society, 367, 1329

Reddy, B. E., Tomkin, J., Lambert, D. L., & Allende Prieto, C. 2003, Monthly Notices of the Royal Astronomical Society, 340, 304

Reggiani, H., Amarsi, A. M., Lind, K., et al. 2019, Astronomy & Astrophysics, 627, A177

Reifarth, R., Altstadt, S., Göbel, K., et al. 2016, in Journal of Physics Conference Series, Vol. 665, Journal of Physics Conference Series, 012044

Renda, A., Fenner, Y., Gibson, B. K., et al. 2004, Monthly Notices of the Royal Astronomical Society, 354, 575

Rivinius, T., Carciofi, A. C., & Martayan, C. 2013, , 21, 69

Roberts, L. F., Reddy, S., & Shen, G. 2012, Physical Review C, 86, 065803

Roederer, I. U., Cowan, J. J., Karakas, A. I., et al. 2010a, Astrophysical Journal, 724, 975

Roederer, I. U., Lawler, J. E., Cowan, J. J., et al. 2012, Astrophysical Journal Letters, 747, L8

Roederer, I. U., Preston, G. W., Thompson, I. B., et al. 2014a, Astronomical Journal, 147, 136

Roederer, I. U., Schatz, H., Lawler, J. E., et al. 2014b, Astrophysical Journal, 791, 32

Roederer, I. U., Sneden, C., Lawler, J. E., & Cowan, J. J. 2010b, Astrophysical Journal Letters, 714, L123

Romano, D., Franchini, M., Grisoni, V., et al. 2020, Astronomy & Astrophysics, 639, A37

Romano, D., Karakas, A. I., Tosi, M., & Matteucci, F. 2010, Astronomy & Astrophysics, 522, A32

Romano, D. & Matteucci, F. 2007, Monthly Notices of the Royal Astronomical Society, 378, L59

Romano, D., Matteucci, F., Zhang, Z.-Y., Ivison, R. J., & Ventura, P. 2019, Monthly Notices of the Royal Astronomical Society, 490, 2838

Rosswog, S., Liebendörfer, M., Thielemann, F. K., et al. 1999, Astronomy & Astrophysics, 341, 499

Roškar, R., Debattista, V. P., Quinn, T. R., & Wadsley, J. 2012, Monthly Notices of the Royal Astronomical Society, 426, 2089

Rudolph, A. L., Simpson, J. P., Haas, M. R., Erickson, E. F., & Fich, M. 1997, Astrophysical Journal, 489, 94

Ruffert, M., Janka, H. T., Takahashi, K., & Schaefer, G. 1997, Astronomy & Astrophysics, 319, 122

Ryan, S. G., Norris, J. E., & Beers, T. C. 1996, Astrophysical Journal, 471, 254

Ryde, N. & Lambert, D. L. 2004, Astronomy & Astrophysics, 415, 559

Sackmann, I. J. & Boothroyd, A. I. 1999, Astrophysical Journal, 510, 217

Salaris, M., Cassisi, S., & Weiss, A. 2002, Publications of the Astronomical Society of the Pacific, 114, 375

Sales, L. V., Helmi, A., Abadi, M. G., et al. 2009, Monthly Notices of the Royal Astronomical Society, 400, L61

Salpeter, E. E. 1952, Astrophysical Journal, 115, 326

Samland, M. 1998, Astrophysical Journal, 496, 155

Savage, B. D. & Sembach, K. R. 1996, Annual Review of Astronomy & Astrophysics, 34, 279

Sbordone, L., Bonifacio, P., Caffau, E., et al. 2010, Astronomy & Astrophysics, 522, A26

Scalzo, R. A., Parent, E., Burns, C., et al. 2019, Monthly Notices of the Royal Astronomical Society, 483, 628

Scalzo, R. A., Ruiter, A. J., & Sim, S. A. 2014, Monthly Notices of the Royal Astronomical Society, 445, 2535

Schaye, J., Crain, R. A., Bower, R. G., et al. 2015, Monthly Notices of the Royal Astronomical Society, 446, 521

Schönrich, R. & Binney, J. 2009, Monthly Notices of the Royal Astronomical Society, 399, 1145

Schönrich, R. & McMillan, P. J. 2017, Monthly Notices of the Royal Astronomical Society, 467, 1154

Seitenzahl, I. R., Cescutti, G., Röpke, F. K., Ruiter, A. J., & Pakmor, R. 2013a, Astronomy & Astrophysics, 559, L5

Seitenzahl, I. R., Ciaraldi-Schoolmann, F., Röpke, F. K., et al. 2013b, Monthly Notices of the Royal Astronomical Society, 429, 1156

Seitenzahl, I. R. & Townsley, D. M. 2017, Nucleosynthesis in Thermonuclear Supernovae, ed. A. W. Alsabti & P. Murdin, 1955

Sellwood, J. A. & Binney, J. J. 2002, Monthly Notices of the Royal Astronomical Society, 336, 785

Sharma, M., Theuns, T., Frenk, C. S., & Cooke, R. J. 2018, Monthly Notices of the Royal Astronomical Society, 473, 984

Shaver, P. A., McGee, R. X., Newton, L. M., Danks, A. C., & Pottasch, S. R. 1983, Monthly Notices of the Royal Astronomical Society, 204, 53

Shi, J. R., Gehren, T., Mashonkina, L., & Zhao, G. 2009, Astronomy & Astrophysics, 503, 533

Shi, J. R., Gehren, T., & Zhao, G. 2011, Astronomy & Astrophysics, 534, A103

Shi, J. R., Takada-Hidai, M., Takeda, Y., et al. 2012, Astrophysical Journal, 755, 36

Shimansky, V. V., Bikmaev, I. F., Galeev, A. I., et al. 2003, Astronomy Reports, 47, 750

Siess, L. 2007, Astronomy & Astrophysics, 476, 893

Silva Aguirre, V., Ruchti, G. R., Hekker, S., et al. 2014, Astrophysical Journal Letters, 784, L16

Simmerer, J., Sneden, C., Cowan, J. J., et al. 2004, Astrophysical Journal, 617, 1091

Siqueira Mello, C., Hill, V., Barbuy, B., et al. 2014, Astronomy & Astrophysics, 565, A93

Sitnova, T. M., Mashonkina, L. I., Ezzeddine, R., & Frebel, A. 2019, Monthly Notices of the Royal Astronomical Society, 485, 3527

Sitnova, T. M., Mashonkina, L. I., & Ryabchikova, T. A. 2016, Monthly Notices of the Royal Astronomical Society, 461, 1000

Sivarani, T., Bonifacio, P., Molaro, P., et al. 2004, Astronomy & Astrophysics, 413, 1073

Smartt, S. J. 2009, Annual Review of Astronomy & Astrophysics, 47, 63

Smartt, S. J., Chen, T. W., Jerkstrand, A., et al. 2017, Nature, 551, 75

Smiljanic, R., Franciosini, E., Bragaglia, A., et al. 2018, Astronomy & Astrophysics, 617, A4

Smiljanic, R., Romano, D., Bragaglia, A., et al. 2016, Astronomy & Astrophysics, 589, A115

Sneden, C. & Cowan, J. J. 2003, Science, 299, 70

Sneden, C., Cowan, J. J., & Gallino, R. 2008, Annual Review of Astronomy & Astrophysics, 46, 241

Sneden, C., Cowan, J. J., Kobayashi, C., et al. 2016, Astrophysical Journal, 817, 53

Sneden, C., Cowan, J. J., Lawler, J. E., et al. 2003a, Astrophysical Journal, 591, 936

Sneden, C., Preston, G. W., & Cowan, J. J. 2003b, Astrophysical Journal, 592, 504

Soares-Santos, M., Holz, D. E., Annis, J., et al. 2017, Astrophysical Journal Letters, 848, L16

Spina, L., Meléndez, J., Karakas, A. I., et al. 2016, Astronomy & Astrophysics, 593, A125

Spite, F. & Spite, M. 1982, Astronomy & Astrophysics, 115, 357

Spite, M., Andrievsky, S. M., Spite, F., et al. 2012, Astronomy & Astrophysics, 541, A143

Spite, M., Caffau, E., Andrievsky, S. M., et al. 2011, Astronomy & Astrophysics, 528, A9

Spite, M., Caffau, E., Bonifacio, P., et al. 2013, Astronomy & Astrophysics, 552, A107

Spite, M., Cayrel, R., Hill, V., et al. 2006, Astronomy & Astrophysics, 455, 291

Spite, M., Cayrel, R., Plez, B., et al. 2005, Astronomy & Astrophysics, 430, 655

Spite, M. & Spite, F. 1978, Astronomy & Astrophysics, 67, 23

Spitoni, E., Matteucci, F., Jönsson, H., Ryde, N., & Romano, D. 2018, Astronomy & Astrophysics, 612, A16

Spitoni, E., Silva Aguirre, V., Matteucci, F., Calura, F., & Grisoni, V. 2019, Astronomy & Astrophysics, 623, A60

Stacy, A., Bromm, V., & Loeb, A. 2011, Monthly Notices of the Royal Astronomical Society, 413, 543

Starkenburg, E., Shetrone, M. D., McConnachie, A. W., & Venn, K. A. 2014, Monthly Notices of the Royal Astronomical Society, 441, 1217

Steigman, G. 2010, in Light Elements in the Universe, ed. C. Charbonnel, M. Tosi, F. Primas, & C. Chiappini, Vol. 268, 19–26

Stephan, A. P., Naoz, S., Ghez, A. M., et al. 2019, Astrophysical Journal, 878, 58

Stephan, A. P., Naoz, S., Ghez, A. M., et al. 2016, Monthly Notices of the Royal Astronomical Society, 460, 3494

Surman, R., McLaughlin, G. C., Ruffert, M., Janka, H. T., & Hix, W. R. 2008, Astrophysical Journal Letters, 679, L117

Symbalisty, E. M. D. 1984, Astrophysical Journal, 285, 729

Takada-Hidai, M., Takeda, Y., Sato, S., et al. 2002, Astrophysical Journal, 573, 614

Takahashi, K., Witti, J., & Janka, H. T. 1994, Astronomy & Astrophysics, 286, 857

Takeda, Y. 2020, arXiv e-prints, arXiv:2001.04588

Takeda, Y., Hashimoto, O., Taguchi, H., et al. 2005, Publications of the Astronomical Society of Japan, 57, 751

Takeda, Y. & Honda, S. 2005, Publications of the Astronomical Society of Japan, 57, 65

Takeda, Y., Honda, S., Ohnishi, T., et al. 2013, Publications of the Astronomical Society of Japan, 65, 53

Takeda, Y., Kato, K.-I., Watanabe, Y., & Sadakane, K. 1996, Publications of the Astronomical Society of Japan, 48, 511

Takeda, Y. & Kawanomoto, S. 2005, Publications of the Astronomical Society of Japan, 57, 45

Takeda, Y., Zhao, G., Takada-Hidai, M., et al. 2003, Chinese Journal of Astronomy Astrophysics, 3, 316

Takiwaki, T., Kotake, K., & Sato, K. 2009, Astrophysical Journal, 691, 1360

Tan, C. 2016, Answers Research Journal, 9, 9

Tan, K., Shi, J., Takada-Hidai, M., Takeda, Y., & Zhao, G. 2016, Astrophysical Journal, 823, 36

Tanaka, M., Utsumi, Y., Mazzali, P. A., et al. 2017, Publications of the Astronomical Society of Japan, 69, 102

Tautvaišienė, G., Drazdauskas, A., Bragaglia, A., Randich, S., & Ženovienė, R. 2016, Astronomy & Astrophysics, 595, A16

Tennyson, J. 2005, Astronomical spectroscopy : an introduction to the atomic and molecular physics of astronomical spectra, Vol. 2

The, L.-S., El Eid, M. F., & Meyer, B. S. 2007, Astrophysical Journal, 655, 1058

Thielemann, F. K. & Arnett, W. D. 1985, Astrophysical Journal, 295, 604

Thielemann, F. K., Dillmann, I., Farouqi, K., et al. 2010, in Journal of Physics Conference Series, Vol. 202, Journal of Physics Conference Series, 012006

Thielemann, F. K., Fröhlich, C., Hirschi, R., et al. 2007, Progress in Particle and Nuclear Physics, 59, 74

Thuan, T. X., Izotov, Y. I., & Lipovetsky, V. A. 1995, Astrophysical Journal, 445, 108

Thurston, T. R., Edmunds, M. G., & Henry, R. B. C. 1996, Monthly Notices of the Royal Astronomical Society, 283, 990

Timmes, F. X., Woosley, S. E., & Weaver, T. A. 1995, Astrophysical Journal Supplement Series, 98, 617

Toloza, O., Breedt, E., De Martino, D., et al. 2019, Bulletin of the American Astronomical Society, 51, 168

Tominaga, N. 2009, Astrophysical Journal, 690, 526

Travaglio, C., Galli, D., Gallino, R., et al. 1999, Astrophysical Journal, 521, 691

Travaglio, C., Gallino, R., Arnone, E., et al. 2004, Astrophysical Journal, 601, 864

Travaglio, C., Gallino, R., Busso, M., & Gratton, R. 2001a, Astrophysical Journal, 549, 346

Travaglio, C., Randich, S., Galli, D., et al. 2001b, Astrophysical Journal, 559, 909

Trevisan, M. & Barbuy, B. 2014, Astronomy & Astrophysics, 570, A22

Trippella, O., Busso, M., Palmerini, S., Maiorca, E., & Nucci, M. C. 2016, Astrophysical Journal, 818, 125

Troja, E., Piro, L., van Eerten, H., et al. 2017, Nature, 551, 71

Truran, J. W. & Arnett, W. D. 1971, Astrophysics and Space Science, 11, 430

Tsantaki, M., Santos, N. C., Sousa, S. G., et al. 2019, Monthly Notices of the Royal Astronomical Society, 485, 2772

Tsebrenko, D. & Soker, N. 2015, Monthly Notices of the Royal Astronomical Society, 453, 166

Tsujimoto, T., Nomoto, K., Yoshii, Y., et al. 1995, Monthly Notices of the Royal Astronomical Society, 277, 945

Tsujimoto, T. & Shigeyama, T. 1998, Astrophysical Journal Letters, 508, L151

Tucci Maia, M., Ramírez, I., Meléndez, J., et al. 2016, Astronomy & Astrophysics, 590, A32

Tutukov, A. V. & Yungelson, L. R. 1993, Monthly Notices of the Royal Astronomical Society, 260, 675

Ugliano, M., Janka, H. T., Arcones, A., & Marek, A. 2013, in GRBs and their Hosts as Tracers of the High Redshift Universe, 18

Umeda, H. & Nomoto, K. 2002, Astrophysical Journal, 565, 385

Umeda, H. & Nomoto, K. 2005, Astrophysical Journal, 619, 427

Usher, C., Beckwith, T., Bellstedt, S., et al. 2019, Monthly Notices of the Royal Astronomical Society, 482, 1275

Uttenthaler, S., Aringer, B., Lebzelter, T., et al. 2008, Astrophysical Journal, 682, 509

Valenti, S., Sand, D. J., Yang, S., et al. 2017, Astrophysical Journal Letters, 848, L24

van den Heuvel, E. P. J. & Lorimer, D. R. 1996, Monthly Notices of the Royal Astronomical Society, 283, L37

van den Hoek, L. B. & Groenewegen, M. A. T. 1997, Astronomy & Astrophysics Supplement Series, 123, 305

van Zee, L., Salzer, J. J., Haynes, M. P., O'Donoghue, A. A., & Balonek, T. J. 1998, Astronomical Journal, 116, 2805

Vangioni-Flam, E. & Cassé, M. 1999, Astrophysics and Space Science, 265, 77

Vangioni-Flam, E., Cassé, M., & Audouze, J. 2000, Physics Reports, 333, 365

Vassen, W., Notermans, R. P. M. J. W., Rengelink, R. J., & van der Beek, R. F. H. J. 2016, Applied Physics B: Lasers and Optics, 122, 289

Venn, K. A., Irwin, M., Shetrone, M. D., et al. 2004, Astronomical Journal, 128, 1177

Ventura, P. & D'Antona, F. 2010, Monthly Notices of the Royal Astronomical Society, 402, L72

Ventura, P., Dell'Agli, F., Schneider, R., et al. 2014a, Monthly Notices of the Royal Astronomical Society, 439, 977

Ventura, P., Di Criscienzo, M., Carini, R., & D'Antona, F. 2013, Monthly Notices of the Royal Astronomical Society, 431, 3642

Ventura, P., di Criscienzo, M., D'Antona, F., et al. 2014b, Monthly Notices of the Royal Astronomical Society, 437, 3274

Vigna-Gómez, A., Neijssel, C. J., Stevenson, S., et al. 2018, Monthly Notices of the Royal Astronomical Society, 481, 4009

Vilchez, J. M. & Esteban, C. 1996, Monthly Notices of the Royal Astronomical Society, 280, 720

Villalobos, Á. & Helmi, A. 2008, Monthly Notices of the Royal Astronomical Society, 391, 1806

Vincenzo, F. & Kobayashi, C. 2018, Monthly Notices of the Royal Astronomical Society, 478, 155

Wanajo, S., Janka, H.-T., & Müller, B. 2011, Astrophysical Journal Letters, 726, L15

Wanajo, S., Janka, H.-T., & Müller, B. 2013, Astrophysical Journal Letters, 767, L26

Wanajo, S., Nomoto, K., Janka, H. T., Kitaura, F. S., & Müller, B. 2009, Astrophysical Journal, 695, 208

Wang, B., Zhou, W. H., Zuo, Z. Y., et al. 2017, Monthly Notices of the Royal Astronomical Society, 464, 3965

Werner, K., Rauch, T., & Kruk, J. W. 2005, Astronomy & Astrophysics, 433, 641

Wheeler, J. C., Sneden, C., & Truran, James W., J. 1989, Annual Review of Astronomy & Astrophysics, 27, 279

Winteler, C., Käppeli, R., Perego, A., et al. 2012, Astrophysical Journal Letters, 750, L22

Witzel, G., Ghez, A. M., Morris, M. R., et al. 2014, Astrophysical Journal Letters, 796, L8

Witzel, G., Sitarski, B. N., Ghez, A. M., et al. 2017, Astrophysical Journal, 847, 80

Woosley, S. E., Arnett, W. D., & Clayton, D. D. 1973, Astrophysical Journal Supplement Series, 26, 231

Woosley, S. E., Hartmann, D. H., Hoffman, R. D., & Haxton, W. C. 1990, Astrophysical Journal, 356, 272

Woosley, S. E. & Haxton, W. C. 1988, Nature, 334, 45

Woosley, S. E. & Hoffman, R. D. 1992, Astrophysical Journal, 395, 202

Woosley, S. E. & Weaver, T. A. 1995, Astrophysical Journal Supplement Series, 101, 181

Woosley, S. E., Wilson, J. R., Mathews, G. J., Hoffman, R. D., & Meyer, B. S. 1994, Astrophysical Journal, 433, 229

Wu, M.-R., Fischer, T., Huther, L., Martínez-Pinedo, G., & Qian, Y.-Z. 2014, , 89, 061303

Wyse, R. F. G. & Gilmore, G. 1995, Astronomical Journal, 110, 2771

Yan, H. L., Shi, J. R., & Zhao, G. 2015, Astrophysical Journal, 802, 36

Yong, D., Norris, J. E., Bessell, M. S., et al. 2013, Astrophysical Journal, 762, 26

Yoon, J., Beers, T. C., Placco, V. M., et al. 2016, Astrophysical Journal, 833, 20

Yoshida, T., Umeda, H., & Nomoto, K. 2008, Astrophysical Journal, 672, 1043

Zhang, H. W., Gehren, T., Butler, K., Shi, J. R., & Zhao, G. 2006, Astronomy & Astrophysics, 457, 645

Zhang, H. W., Gehren, T., & Zhao, G. 2008, arXiv e-prints, arXiv:0802.2609

Zhang, H. W., Gehren, T., & Zhao, G. 2014, in IAU Symposium, Vol. 298, Setting the scene for Gaia and LAMOST, ed. S. Feltzing, G. Zhao, N. A. Walton, & P. Whitelock, 453–453

Zhao, G., Mashonkina, L., Yan, H. L., et al. 2016, Astrophysical Journal, 833, 225

Zhiguo, Z., Zhongshan, L., & Zhankui, J. 1999, European Physical Journal D, 7, 499

Zoccali, M., Hill, V., Lecureur, A., et al. 2008, Astronomy & Astrophysics, 486, 177

Institut für Physik und Astronomie, Universität Potsdam
Astronomical Institute of the Czech Academy of Sciences
Dpto. de Química "Prof. José Carlos Vílchez Martín", Univ. de H

NUCLEOSYNTHESIS AND ABUNDANCES OF ELEMENTS WITH RELEVANT OPTICAL LINES IN DWARFS

Author:
Francisco Molina

Supervisor:
Dr Joris Vos

Cover: Sunset from the Calar Alto Observatory (Almería, Spain). August, 2020

Back cover: Starry Night in Partaloa (Almería, Spain). August, 2020